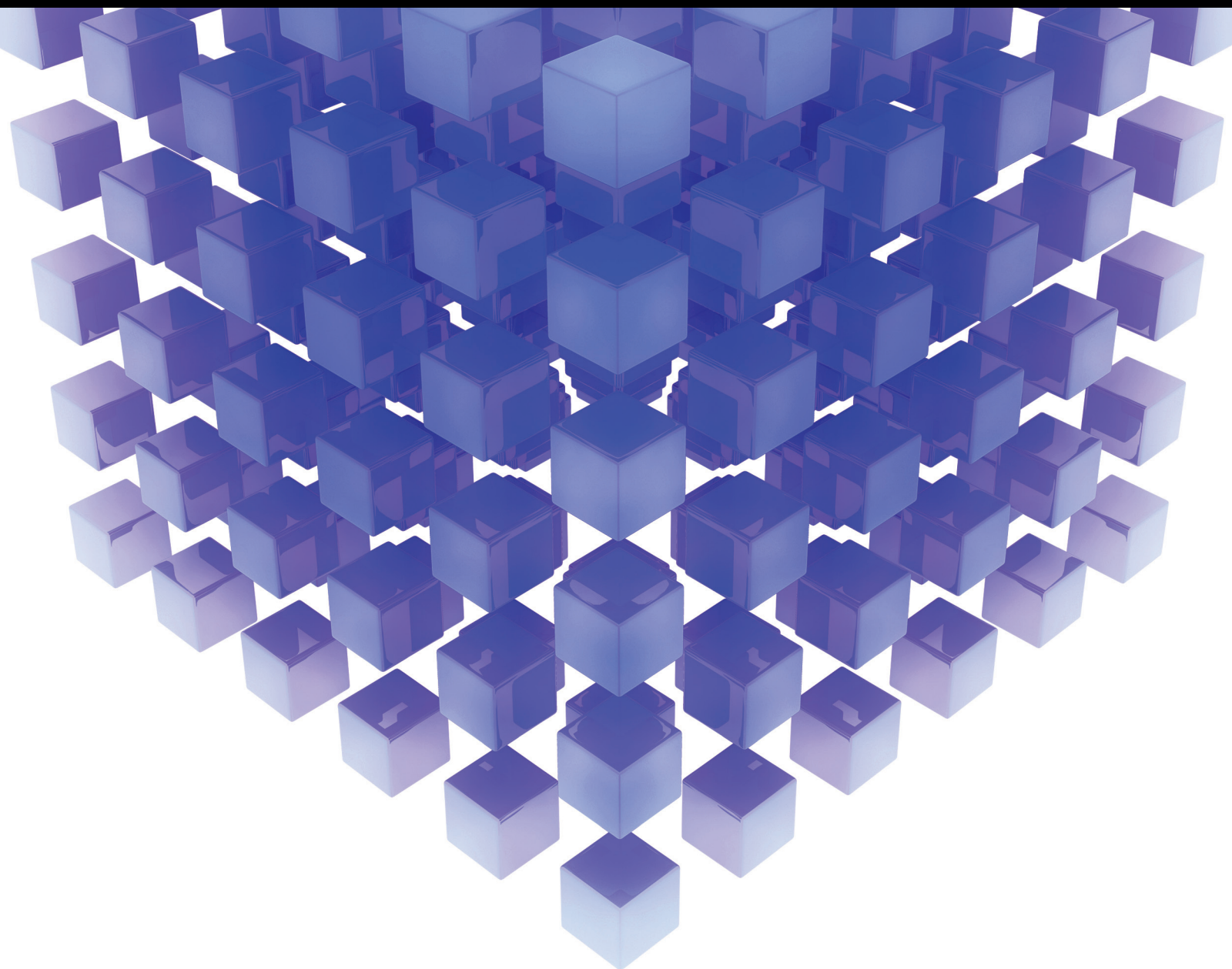


Mathematical Problems in Engineering

# Applied Mathematics for Engineering Problems in Biomechanics and Robotics

Lead Guest Editor: Carlos Llopis-Albert

Guest Editors: Francisco Rubio, Shouzhen Zeng, and Huchang Liao





---

# **Applied Mathematics for Engineering Problems in Biomechanics and Robotics**

Mathematical Problems in Engineering

---

**Applied Mathematics for Engineering Problems  
in Biomechanics and Robotics**

Lead Guest Editor: Carlos Llopis-Albert

Guest Editors: Francisco Rubio, Shouzhen Zeng,  
and Huchang Liao



---

Copyright © 2019 Hindawi. All rights reserved.

This is a special issue published in “Mathematical Problems in Engineering.” All articles are open access articles distributed under the Creative Commons Attribution License, which permits unrestricted use, distribution, and reproduction in any medium, provided the original work is properly cited.

## Editorial Board

- Mohamed Abd El Aziz, Egypt  
AITOUCHE Abdelouhab, France  
Leonardo Acho, Spain  
José A. Acosta, Spain  
Daniela Addressi, Italy  
Paolo Adesso, Italy  
Claudia Adduce, Italy  
Ramesh Agarwal, USA  
Francesco Aggogeri, Italy  
Juan C. Agüero, Australia  
Ricardo Aguilar-Lopez, Mexico  
Tarek Ahmed-Ali, France  
Elias Aifantis, USA  
Muhammad N. Akram, Norway  
Guido Ala, Italy  
Andrea Alaimo, Italy  
Reza Alam, USA  
Nicholas Alexander, UK  
Salvatore Alfonzetti, Italy  
Mohammad D. Aliyu, Canada  
Juan A. Almendral, Spain  
José Domingo Álvarez, Spain  
Cláudio Alves, Portugal  
J. P. Amezcuita-Sanchez, Mexico  
Lionel Amodeo, France  
Sebastian Anita, Romania  
Renata Archetti, Italy  
Felice Arena, Italy  
Sabri Arik, Turkey  
Francesco Aristodemo, Italy  
Fausto Arpino, Italy  
Alessandro Arsie, USA  
Edoardo Artioli, Italy  
Fumihito Ashida, Japan  
Farhad Aslani, Australia  
Mohsen Asle Zaem, USA  
Romain Aubry, USA  
Matteo Aureli, USA  
Richard I. Avery, USA  
Viktor Avrutin, Germany  
Francesco Aymerich, Italy  
Sajad Azizi, Belgium  
Michele Baccocchi, Italy  
Seungik Baek, USA  
Adil Bagirov, Australia  
Khaled Bahlali, France  
Laurent Bako, France  
Pedro Balaguer, Spain  
Stefan Balint, Romania  
Ines Tejado Balsera, Spain  
Alfonso Banos, Spain  
Jerzy Baranowski, Poland  
Roberto Baratti, Italy  
Andrzej Bartoszewicz, Poland  
David Bassir, France  
Chiara Bedon, Italy  
Azeddine Beghdadi, France  
Denis Benasciutti, Italy  
Ivano Benedetti, Italy  
Rosa M. Benito, Spain  
Elena Benvenuti, Italy  
Giovanni Berselli, Italy  
Giorgio Besagni, Italy  
Michele Betti, Italy  
Jean-Charles Beugnot, France  
Pietro Bia, Italy  
Carlo Bianca, France  
Simone Bianco, Italy  
Vincenzo Bianco, Italy  
Vittorio Bianco, Italy  
Gennaro N. Bifulco, Italy  
David Bigaud, France  
Antonio Bilotta, Italy  
Paul Bogdan, USA  
Guido Bolognesi, UK  
Rodolfo Bontempo, Italy  
Alberto Borboni, Italy  
Paolo Boscaroli, Italy  
Daniela Boso, Italy  
Guillermo Botella-Juan, Spain  
Boulaïd Boulkroune, Belgium  
Fabio Bovenga, Italy  
Francesco Braghin, Italy  
Ricardo Branco, Portugal  
Maurizio Brocchini, Italy  
Julien Bruchon, France  
Matteo Bruggi, Italy  
Michele Brun, Italy  
Vasilis Burganos, Greece  
Tito Busani, USA  
Raquel Caballero-Águila, Spain  
Filippo Cacace, Italy  
Pierfrancesco Cacciola, UK  
Salvatore Caddemi, Italy  
Roberto Caldelli, Italy  
Alberto Campagnolo, Italy  
Eric Campos-Canton, Mexico  
Marko Canadija, Croatia  
Salvatore Cannella, Italy  
Francesco Cannizzaro, Italy  
Javier Cara, Spain  
Ana Carpio, Spain  
Caterina Casavola, Italy  
Sara Casciati, Italy  
Federica Caselli, Italy  
Carmen Castillo, Spain  
Inmaculada T. Castro, Spain  
Miguel Castro, Portugal  
Giuseppe Catalanotti, UK  
Nicola Caterino, Italy  
Alberto Cavallo, Italy  
Gabriele Cazzulani, Italy  
Luis Cea, Spain  
Song Cen, China  
Miguel Cerrolaza, Venezuela  
M. Chadli, France  
Gregory Chagnon, France  
Ludovic Chamoin, France  
Ching-Ter Chang, Taiwan  
Qing Chang, USA  
Michael J. Chappell, UK  
Kacem Chehdi, France  
Peter N. Cheimets, USA  
Xinkai Chen, Japan  
Luca Chiapponi, Italy  
Francisco Chicano, Spain  
Nicholas Chileshe, Australia  
Adrian Chmielewski, Poland  
Ioannis T. Christou, Greece  
Hung-Yuan Chung, Taiwan  
Simone Cinquemani, Italy  
Roberto G. Citarella, Italy  
Joaquim Ciurana, Spain  
John D. Clayton, USA  
Francesco Clementi, Italy

Piero Colajanni, Italy  
Giuseppina Colicchio, Italy  
Vassilios Constantoudis, Greece  
Enrico Conte, Italy  
Francesco Conte, Italy  
Alessandro Contento, USA  
Mario Cools, Belgium  
Jean-Pierre Corriou, France  
J.-C. Cortés, Spain  
Carlo Cosentino, Italy  
Paolo Crippa, Italy  
Andrea Crivellini, Italy  
Erik Cuevas, Mexico  
Maria C. Cunha, Portugal  
Peter Dabnichki, Australia  
Luca D'Acerno, Italy  
Weizhong Dai, USA  
Andrea Dall'Asta, Italy  
Purushothaman Damodaran, USA  
Bhabani S. Dandapat, India  
Farhang Daneshmand, Canada  
Giuseppe D'Aniello, Italy  
Sergey Dashkovskiy, Germany  
Fabio De Angelis, Italy  
Samuele De Bartolo, Italy  
Abílio De Jesus, Portugal  
Pietro De Lellis, Italy  
Alessandro De Luca, Italy  
Stefano de Miranda, Italy  
Filippo de Monte, Italy  
M. do Rosário de Pinho, Portugal  
Michael Defoort, France  
Alessandro Della Corte, Italy  
Xavier Delorme, France  
Laurent Dewasme, Belgium  
Angelo Di Egidio, Italy  
Roberta Di Pace, Italy  
Ramón I. Diego, Spain  
Yannis Dimakopoulos, Greece  
Zhengtao Ding, UK  
M. Djemai, France  
Alexandre B. Dolgui, France  
Georgios Dounias, Greece  
Florent Duchaine, France  
George S. Dulikravich, USA  
Bogdan Dumitrescu, Romania  
Horst Ecker, Austria  
Saeed Eftekhari Azam, USA  
Ahmed El Hajjaji, France  
Antonio Elipe, Spain  
Fouad Erchiqui, Canada  
Anders Eriksson, Sweden  
R. Emre Erkmen, Canada  
G. Espinosa-Paredes, Mexico  
Leandro F. F. Miguel, Brazil  
Andrea L. Facci, Italy  
Giacomo Falcucci, Italy  
Giovanni Falsone, Italy  
Hua Fan, China  
Nicholas Fantuzzi, Italy  
Yann Favennec, France  
Fiorenzo A. Fazzolari, UK  
Giuseppe Fedele, Italy  
Roberto Fedele, Italy  
Arturo J. Fernández, Spain  
Jesus M. Fernandez Oro, Spain  
Massimiliano Ferraioli, Italy  
Massimiliano Ferrara, Italy  
Francesco Ferrise, Italy  
Eric Feulvarch, France  
Barak Fishbain, Israel  
S. Douwe Flapper, Netherlands  
Thierry Floquet, France  
Eric Florentin, France  
Alessandro Formisano, Italy  
Francesco Franco, Italy  
Elisa Francomano, Italy  
Tomonari Furukawa, USA  
Juan C. G. Prada, Spain  
Mohamed Gadala, Canada  
Matteo Gaeta, Italy  
Mauro Gaggero, Italy  
Zoran Gajic, USA  
Erez Gal, Israel  
Jaime Gallardo-Alvarado, Mexico  
Ugo Galvanetto, Italy  
Akemi Gálvez, Spain  
Rita Gamberini, Italy  
Maria L. Gandarias, Spain  
Arman Ganji, Canada  
Zhiwei Gao, UK  
Zhong-Ke Gao, China  
Giovanni Garcea, Italy  
Luis Rodolfo Garcia Carrillo, USA  
Jose M. Garcia-Aznar, Spain  
Akhil Garg, China  
Alessandro Gasparetto, Italy  
Gianluca Gatti, Italy  
Oleg V. Gendelman, Israel  
Stylios Georgantzinos, Greece  
Fotios Georgiades, UK  
Parviz Ghadimi, Iran  
Mergen H. Ghayesh, Australia  
Georgios I. Giannopoulos, Greece  
Agathoklis Giaralis, UK  
Pablo Gil, Spain  
Anna M. Gil-Lafuente, Spain  
Ivan Giorgio, Italy  
Gaetano Giunta, Luxembourg  
Alessio Gizzi, Italy  
Jefferson L.M.A. Gomes, UK  
Emilio Gómez-Déniz, Spain  
Antonio M. Gonçalves de Lima, Brazil  
David González, Spain  
Chris Goodrich, USA  
Rama S. R. Gorla, USA  
Kannan Govindan, Denmark  
Antoine Grall, France  
George A. Gravvanis, Greece  
Fabrizio Greco, Italy  
David Greiner, Spain  
Simonetta Grilli, Italy  
Jason Gu, Canada  
Federico Guarracino, Italy  
Michele Guida, Italy  
Zhaoxia Guo, China  
José L. Guzmán, Spain  
Quang Phuc Ha, Australia  
Petr Hájek, Czech Republic  
Weimin Han, USA  
Zhen-Lai Han, China  
Thomas Hanne, Switzerland  
Mohammad A. Hariri-Ardebili, USA  
Xiao-Qiao He, China  
Luca Heltai, Italy  
Nicolae Herisanu, Romania  
Alfredo G. Hernández-Díaz, Spain  
M.I. Herreros, Spain  
Eckhard Hitzer, Japan  
Paul Honeine, France  
Jaromir Horacek, Czech Republic

Muneo Hori, Japan  
András Horváth, Italy  
S. H. Hosseinnia, Netherlands  
Gordon Huang, Canada  
Sajid Hussain, Canada  
Asier Ibeas, Spain  
Orest V. Iftime, Netherlands  
Przemyslaw Ignaciuk, Poland  
Giacomo Innocenti, Italy  
Emilio Insfran Pelozo, Spain  
Alessio Ishizaka, UK  
Nazrul Islam, USA  
Benoit Jung, France  
Benjamin Ivorra, Spain  
Payman Jalali, Finland  
Mahdi Jalili, Australia  
Łukasz Jankowski, Poland  
Samuel N. Jator, USA  
Juan C. Jauregui-Correa, Mexico  
Reza Jazar, Australia  
Khalide Jbilou, France  
Piotr Jędrzejowicz, Poland  
Isabel S. Jesus, Portugal  
Linni Jian, China  
Bin Jiang, China  
Zhongping Jiang, USA  
Emilio Jiménez Macías, Spain  
Ningde Jin, China  
Xiaoliang Jin, USA  
Liang Jing, Canada  
Dylan F. Jones, UK  
Palle E. Jorgensen, USA  
Vyacheslav Kalashnikov, Mexico  
Tamas Kalmar-Nagy, Hungary  
Tomasz Kapitaniak, Poland  
Julius Kaplunov, UK  
Haranath Kar, India  
K. Karamanos, Belgium  
Krzysztof Kecik, Poland  
Jean-Pierre Kenne, Canada  
Ch. M. Khaliq, South Africa  
Do Wan Kim, Republic of Korea  
Nam-Il Kim, Republic of Korea  
Jan Koci, Czech Republic  
Ioannis Kostavelis, Greece  
Sotiris B. Kotsiantis, Greece  
Manfred Krafczyk, Germany

Frederic Kratz, France  
Petr Krysl, USA  
Krzysztof S. Kulpa, Poland  
Shailesh I. Kundalwal, India  
Jurgen Kurths, Germany  
Cedrick A. K. Kwuimy, USA  
Kyandoghere Kyamakya, Austria  
Davide La Torre, Italy  
Risto Lahdelma, Finland  
Hak-Keung Lam, UK  
Giovanni Lancioni, Italy  
Jimmy Lauber, France  
Antonino Laudani, Italy  
Hervé Laurent, France  
Aimé Lay-Ekuakille, Italy  
Nicolas J. Leconte, France  
Dimitri Lefebvre, France  
Eric Lefevre, France  
Marek Lefik, Poland  
Yaguo Lei, China  
Kauko Leiviskä, Finland  
Thibault Lemaire, France  
Roman Lewandowski, Poland  
Chen-Feng Li, China  
Jian Li, USA  
Yang Li, China  
Huchang Liao, China  
En-Qiang Lin, USA  
Zhiyun Lin, China  
Peide Liu, China  
Peter Liu, Taiwan  
Wanquan Liu, Australia  
Bonifacio Llamazares, Spain  
Alessandro Lo Schiavo, Italy  
Jean Jacques Loiseau, France  
Francesco Lolli, Italy  
Paolo Lonetti, Italy  
Sandro Longo, Italy  
António M. Lopes, Portugal  
Sebastian López, Spain  
Pablo Lopez-Crespo, Spain  
Luis M. López-Ochoa, Spain  
Ezequiel López-Rubio, Spain  
Vassilios C. Loukopoulos, Greece  
Jose A. Lozano-Galant, Spain  
haiyan Lu, Australia  
Gabriel Luque, Spain

Valentin Lychagin, Norway  
Antonio Madeo, Italy  
José María Maestre, Spain  
Alessandro Magnani, Italy  
Fazal M. Mahomed, South Africa  
Noureddine Manamanni, France  
Paolo Manfredi, Italy  
Didier Maquin, France  
Giuseppe Carlo Marano, Italy  
Damijan Markovic, France  
Francesco Marotti de Sciarra, Italy  
Rui Cunha Marques, Portugal  
Rodrigo Martinez-Bejar, Spain  
Guiomar Martín-Herrán, Spain  
Denizar Cruz Martins, Brazil  
Benoit Marx, France  
Elio Masciari, Italy  
Franck Massa, France  
Paolo Massioni, France  
Alessandro Mauro, Italy  
Fabio Mazza, Italy  
Laura Mazzola, Italy  
Driss Mehdi, France  
Roderick Melnik, Canada  
Pasquale Memmolo, Italy  
Xiangyu Meng, USA  
Jose Merodio, Spain  
Alessio Merola, Italy  
Mahmoud Mesbah, Iran  
Luciano Mescia, Italy  
Laurent Mevel, France  
Mariusz Michta, Poland  
Aki Mikkola, Finland  
Giovanni Minafò, Italy  
Hiroyuki Mino, Japan  
Pablo Mira, Spain  
Dimitrios Mitsotakis, New Zealand  
Vito Mocella, Italy  
Sara Montagna, Italy  
Roberto Montanini, Italy  
Francisco J. Montáns, Spain  
Gisele Mophou, France  
Rafael Morales, Spain  
Marco Morandini, Italy  
Javier Moreno-Valenzuela, Mexico  
Simone Morganti, Italy  
Caroline Mota, Brazil

Aziz Moukrim, France  
Dimitris Mourtzis, Greece  
Emiliano Mucchi, Italy  
Josefa Mula, Spain  
Jose J. Muñoz, Spain  
Giuseppe Muscolino, Italy  
Marco Mussetta, Italy  
Hakim Naceur, France  
Alessandro Naddeo, Italy  
Hassane Naji, France  
Mariko Nakano-Miyatake, Mexico  
Keivan Navaie, UK  
AMA Neves, Portugal  
Luís C. Neves, UK  
Dong Ngoduy, New Zealand  
Nhon Nguyen-Thanh, Singapore  
Tatsushi Nishi, Japan  
Xesús Nogueira, Spain  
Ben T. Nohara, Japan  
Mohammed Nouari, France  
Mustapha Nourelfath, Canada  
Włodzimierz Ogryczak, Poland  
Roger Ohayon, France  
Krzysztof Okarma, Poland  
Mitsuhiro Okayasu, Japan  
Alberto Olivares, Spain  
Enrique Onieva, Spain  
Calogero Orlando, Italy  
Alejandro Ortega-Moñux, Spain  
Sergio Ortobelli, Italy  
Naohisa Otsuka, Japan  
Erika Ottaviano, Italy  
Pawel Packo, Poland  
Arturo Pagano, Italy  
Alkis S. Paipetis, Greece  
Roberto Palma, Spain  
Alessandro Palmeri, UK  
Pasquale Palumbo, Italy  
Weifeng Pan, China  
Jürgen Pannek, Germany  
Elena Panteley, France  
Achille Paolone, Italy  
George A. Papakostas, Greece  
Xosé M. Pardo, Spain  
Vicente Parra-Vega, Mexico  
Manuel Pastor, Spain  
Petr Páta, Czech Republic  
Pubudu N. Pathirana, Australia  
Surajit Kumar Paul, India  
Sitek Paweł, Poland  
Luis Payá, Spain  
Alexander Paz, Australia  
Igor Pažanin, Croatia  
Libor Pekař, Czech Republic  
Francesco Pellicano, Italy  
Marcello Pellicciari, Italy  
Haipeng Peng, China  
Mingshu Peng, China  
Zhengbiao Peng, Australia  
Zhi-ke Peng, China  
Marzio Pennisi, Italy  
Maria Patrizia Pera, Italy  
Matjaz Perc, Slovenia  
A. M. Bastos Pereira, Portugal  
Ricardo Perera, Spain  
Francesco Pesavento, Italy  
Ivo Petras, Slovakia  
Francesco Petrini, Italy  
Lukasz Pieczonka, Poland  
Dario Piga, Switzerland  
Paulo M. Pimenta, Brazil  
Antonina Pirrotta, Italy  
Marco Pizzarelli, Italy  
Vicent Pla, Spain  
Javier Plaza, Spain  
Kemal Polat, Turkey  
Dragan Poljak, Croatia  
Jorge Pomares, Spain  
Sébastien Poncet, Canada  
Volodymyr Ponomaryov, Mexico  
Jean-Christophe Ponsart, France  
Mauro Pontani, Italy  
Cornelio Posadas-Castillo, Mexico  
Francesc Pozo, Spain  
Christopher Pretty, New Zealand  
Luca Pugi, Italy  
Krzysztof Puszynski, Poland  
Giuseppe Quaranta, Italy  
Vitomir Racic, Italy  
Jose Ragot, France  
Carlo Rainieri, Italy  
K. Ramamani Rajagopal, USA  
Ali Ramazani, USA  
Higinio Ramos, Spain  
Alain Rassinoux, France  
S.S. Ravindran, USA  
Alessandro Reali, Italy  
Jose A. Reinoso, Spain  
Oscar Reinoso, Spain  
Carlo Renno, Italy  
Fabrizio Renno, Italy  
Nidhal Rezg, France  
Ricardo Riaza, Spain  
Francesco Riganti-Fulginei, Italy  
Gerasimos Rigatos, Greece  
Francesco Ripamonti, Italy  
Jorge Rivera, Mexico  
Eugenio Roanes-Lozano, Spain  
Bruno G. M. Robert, France  
Ana Maria A. C. Rocha, Portugal  
José Rodellar, Spain  
Luigi Rodino, Italy  
Rosana Rodríguez López, Spain  
Ignacio Rojas, Spain  
Alessandra Romolo, Italy  
Debasish Roy, India  
Gianluigi Rozza, Italy  
Jose de Jesus Rubio, Mexico  
Rubén Ruiz, Spain  
Antonio Ruiz-Cortes, Spain  
Ivan D. Rukhlenko, Australia  
Mazen Saad, France  
Kishin Sadarangani, Spain  
Andrés Sáez, Spain  
Mehrddad Saif, Canada  
John S. Sakellariou, Greece  
Salvatore Salamone, USA  
Vicente Salas, Spain  
Jose Vicente Salcedo, Spain  
Nunzio Salerno, Italy  
Miguel A. Salido, Spain  
Roque J. Saltarén, Spain  
Alessandro Salvini, Italy  
Sylwester Samborski, Poland  
Ramon Sancibrian, Spain  
Giuseppe Sanfilippo, Italy  
Vittorio Sansalone, France  
José A. Sanz-Herrera, Spain  
Nickolas S. Sapidis, Greece  
Evangelos J. Sapountzakis, Greece  
Luis Saucedo-Mora, Spain

Marcelo A. Savi, Brazil  
Andrey V. Savkin, Australia  
Roberta Sburlati, Italy  
Gustavo Scaglia, Argentina  
Thomas Schuster, Germany  
Oliver Schütze, Mexico  
Lotfi Senhadji, France  
Junwon Seo, USA  
Joan Serra-Sagrista, Spain  
Gerardo Severino, Italy  
Ruben Sevilla, UK  
Stefano Sfarra, Italy  
Mohamed Shaat, Egypt  
Mostafa S. Shadloo, France  
Leonid Shaikhet, Israel  
Hassan M. Shanechi, USA  
Bo Shen, Germany  
Suzanne M. Shontz, USA  
Babak Shotorban, USA  
Zhan Shu, UK  
Nuno Simões, Portugal  
Christos H. Skiadas, Greece  
Konstantina Skouri, Greece  
Neale R. Smith, Mexico  
Bogdan Smolka, Poland  
Delfim Soares Jr., Brazil  
Alba Sofi, Italy  
Francesco Soldovieri, Italy  
Raffaele Solimene, Italy  
Jussi Sopenan, Finland  
Marco Spadini, Italy  
Bernardo Spagnolo, Italy  
Paolo Spagnolo, Italy  
Ruben Specogna, Italy  
Vasilios Spitas, Greece  
Sri Sridharan, USA  
Ivanka Stamova, USA  
Rafał Stanisławski, Poland  
Florin Stoican, Romania  
Salvatore Strano, Italy  
Yakov Strelniker, Israel  
Ning Sun, China  
Sergey A. Suslov, Australia  
Thomas Svensson, Sweden  
Andrzej Swierniak, Poland  
Andras Szekrenyes, Hungary  
Kumar K. Tamma, USA

Yang Tang, Germany  
Hafez Tari, USA  
Alessandro Tasora, Italy  
Sergio Teggi, Italy  
Ana C. Teodoro, Portugal  
Alexander Timokha, Norway  
Gisella Tomasini, Italy  
Francesco Tornabene, Italy  
Antonio Tornambe, Italy  
Javier Martinez Torres, Spain  
Mariano Torrisi, Italy  
George Tsiatas, Greece  
Antonios Tsourdos, UK  
Federica Tubino, Italy  
Nerio Tullini, Italy  
Andrea Tundis, Italy  
Emilio Turco, Italy  
Ilhan Tuzcu, USA  
Efstratios Tzirtzilakis, Greece  
Filippo Ubertini, Italy  
Francesco Ubertini, Italy  
Mohammad Uddin, Australia  
Hassan Ugail, UK  
Giuseppe Vairo, Italy  
Eusebio Valero, Spain  
Pandian Vasant, Malaysia  
Marcello Vasta, Italy  
Carlos-Renato Vázquez, Mexico  
Miguel E. Vázquez-Méndez, Spain  
Josep Vehi, Spain  
Martin Velasco Villa, Mexico  
K. C. Veluvolu, Republic of Korea  
Fons J. Verbeek, Netherlands  
Franck J. Vernerey, USA  
Georgios Veronis, USA  
Vincenzo Vespri, Italy  
Renato Vidoni, Italy  
V. Vijayaraghavan, Australia  
Anna Vila, Spain  
Rafael J. Villanueva, Spain  
Francisco R. Villatoro, Spain  
Uchechukwu E. Vincent, UK  
Gareth A. Vio, Australia  
Francesca Vipiana, Italy  
Stanislav Vítek, Czech Republic  
Thuc P. Vo, UK  
Jan Vorel, Czech Republic

Michael Vynnycky, Sweden  
Hao Wang, USA  
Liliang Wang, UK  
Shuming Wang, China  
Yongqi Wang, Germany  
Roman Wan-Wendner, Austria  
Jarosław Wąs, Poland  
P.H. Wen, UK  
Waldemar T. Wójcik, Poland  
Changzhi Wu, China  
Desheng D. Wu, Sweden  
Yuqiang Wu, China  
Michalis Xenos, Greece  
Guangming Xie, China  
Xue-Jun Xie, China  
Gen Q. Xu, China  
Hang Xu, China  
Joseph J. Yame, France  
Xinggang Yan, UK  
Jixiang Yang, China  
Mijia Yang, USA  
Yongheng Yang, Denmark  
Luis J. Yebra, Spain  
Peng-Yeng Yin, Taiwan  
Yuan Yuan, UK  
Qin Yuming, China  
Elena Zaitseva, Slovakia  
Arkadiusz Zak, Poland  
Daniel Zaldivar, Mexico  
Francesco Zammori, Italy  
Vittorio Zampoli, Italy  
Rafal Zdunek, Poland  
Ibrahim Zeid, USA  
Haopeng Zhang, USA  
Huaguang Zhang, China  
Kai Zhang, China  
Qingling Zhang, China  
Xianming Zhang, Australia  
Xuping Zhang, Denmark  
Zhao Zhang, China  
Yifan Zhao, UK  
Jian G. Zhou, UK  
Quanxin Zhu, China  
Mustapha Zidi, France  
Gaetano Zizzo, Italy  
Zhixiang Zou, Germany  
J. A. Fonseca de Oliveira Correia, Portugal

# Contents

## **Applied Mathematics for Engineering Problems in Biomechanics and Robotics**

Carlos Llopis-Albert , Francisco Rubio , Shouzhen Zeng , and Huchang Liao   
Editorial (3 pages), Article ID 2578916, Volume 2019 (2019)

## **Modal Decoupled Dynamics Feed-Forward Active Force Control of Spatial Multi-DOF Parallel Robotic Manipulator**

Xinjian Niu, Chifu Yang , Bowen Tian, Xiang Li , and Junwei Han  
Research Article (13 pages), Article ID 1835308, Volume 2019 (2019)

## **Extended Version of Linguistic Picture Fuzzy TOPSIS Method and Its Applications in Enterprise Resource Planning Systems**

Shouzhen Zeng , Muhammad Qiyas, Muhammad Arif , and Tariq Mahmood  
Research Article (8 pages), Article ID 8594938, Volume 2019 (2019)

## **EO Sensor Planning for UAV Engineering Reconnaissance Based on NIIRS and GIQE**

Jingbo Bai , Yangyang Sun , Liang Chen , Yufang Feng, and Jianyong Liu   
Research Article (9 pages), Article ID 6837014, Volume 2018 (2019)

## **Existence and Stability of Periodic Solution Related to Valveless Pumping**

B. Dorociaková , M. Michalková , R. Olach , and M. Sága  
Research Article (8 pages), Article ID 3982432, Volume 2018 (2019)

## **Evaluation of the Use of the Yeoh and Mooney-Rivlin Functions as Strain Energy Density Functions for the Ground Substance Material of the Annulus Fibrosus**

Héctor E. Jaramillo S.   
Research Article (10 pages), Article ID 1570142, Volume 2018 (2019)

## **A Reliability-Based Consensus Model for Multiattribute Group Decision-Making with Analytically Evidential Reasoning Approach**

Yuan-Wei Du , Ning Yang, Wen Zhou , and Chang-Xing Li  
Research Article (14 pages), Article ID 1651857, Volume 2018 (2019)

## **An Evacuation Route Model of Crowd Based on Emotion and Geodesic**

Bangquan Liu , Zhen Liu , Dechao Sun , and Chunyue Bi   
Research Article (10 pages), Article ID 5397071, Volume 2018 (2019)

## **Position Tracking Control of PMSM Based on Fuzzy PID-Variable Structure Adaptive Control**

Pei Pei , Zhongcai Pei, Zhiyong Tang , and Han Gu   
Research Article (15 pages), Article ID 5794067, Volume 2018 (2019)

## **Human-Robot Interaction and Demonstration Learning Mode Based on Electromyogram Signal and Variable Impedance Control**

Rui Wu , He Zhang , Tao Peng, Le Fu, and Jie Zhao   
Research Article (11 pages), Article ID 8658791, Volume 2018 (2019)

**Mass Collaboration-Driven Method for Recommending Product Ideas Based on Dempster-Shafer Theory of Evidence**

Yuan-Wei Du , Yu-Kun Shan, Chang-Xing Li, and Rui Wang   
Research Article (10 pages), Article ID 1980152, Volume 2018 (2019)

**Decision-Maker's Risk Preference Based Intuitionistic Fuzzy Multiattribute Decision-Making and Its Application in Robot Enterprises Investment**

Liangdong Zhou  and Qifeng Wang   
Research Article (6 pages), Article ID 1720189, Volume 2018 (2019)

**Extension Dependent Degree Method with Mapping Transformation for Three-Parameter Interval Number Decision Making**

Li-Bo Xu , Xing-Sen Li, Jun-kai Shao, and Kai-jie Wang  
Research Article (12 pages), Article ID 1831086, Volume 2018 (2019)

**Bifurcation Analysis of Stick-Slip Motion of the Vibration-Driven System with Dry Friction**

Peng Li  and Ziwang Jiang  
Research Article (10 pages), Article ID 2305187, Volume 2018 (2019)

**Nonlinear Vibration of an Elastic Soft String: Large Amplitude and Large Curvature**

De-Min Zhao, Shan-Peng Li, Yun Zhang, and Jian-Lin Liu   
Research Article (11 pages), Article ID 7909876, Volume 2018 (2019)

**A Study on the Application of Coordinated TOPSIS in Evaluation of Robotics Academic Journals**

Liping Yu, Wenhua Yang, Yunlong Duan , and Xinwen Long  
Research Article (7 pages), Article ID 5456064, Volume 2018 (2019)

**Workspace Analysis of a Hybrid Kinematic Machine Tool with High Rotational Applications**

Haiqiang Zhang, Hairong Fang , Yuefa Fang, and Bingshan Jiang  
Research Article (12 pages), Article ID 2607497, Volume 2018 (2019)

## Editorial

# Applied Mathematics for Engineering Problems in Biomechanics and Robotics

**Carlos Llopis-Albert** <sup>1</sup>, **Francisco Rubio** <sup>1</sup>, **Shouzhen Zeng** <sup>2</sup>, and **Huchang Liao** <sup>3</sup>

<sup>1</sup>*Centro de Investigación en Ingeniería Mecánica (CIIM), Universitat Politècnica de València, Camino de Vera s/n, 46022 Valencia, Spain*

<sup>2</sup>*Ningbo University, Ningbo 315211, China*

<sup>3</sup>*Sichuan University, Chengdu, Sichuan 610065, China*

Correspondence should be addressed to Huchang Liao; [liaohuchang@163.com](mailto:liaohuchang@163.com)

Received 5 February 2019; Accepted 6 February 2019; Published 21 April 2019

Copyright © 2019 Carlos Llopis-Albert et al. This is an open access article distributed under the Creative Commons Attribution License, which permits unrestricted use, distribution, and reproduction in any medium, provided the original work is properly cited.

This special issue brings together a collection of mathematical work relating to the disciplines of biomechanics and robotics, which are increasingly closely linked. On the one hand, biomechanics is the application of the principles and techniques of mechanics to the structure and functions of living organisms. On the other hand, robotics is the branch of science and technology that deals with the design, construction, operation, and application of robots and automated mechanical systems. They promise to be two of the most influential lines of research in the twenty-first century, since they generate innovation in a wide range of research fields. They encompass areas such as medicine, healthcare, sports, logistics and distribution, manufacturing industries, and business technology. Both disciplines are inherently multidisciplinary by nature, involving mathematics, physics, biology, and computing. The intention of this special issue is therefore to deal with mathematical work related to medical imaging and visualization, bioinformatics, exoskeletons, microelectromechanical systems and nanotechnology, new biomaterials and sensors, medical robotics, healthcare robots, injury prevention and rehabilitation, enhancement of patient and worker safety and quality, ergonomics, production, logistics and distribution applications, socioeconomic and management issues, and decision-making processes related to these disciplines.

This special issue is devoted to applied mathematics in both biomechanics and robotics and to their integration. Consequently, the objective is to disseminate advanced

mathematical research on biomechanics and robotics and their applications while promoting integration between these disciplines. The published articles address significant issues and contribute to the development of new concepts, methodologies, applications, trends, and knowledge in science. In this regard, the topics covered by this special issue include the following: biomechanics and robotics: use of techniques from computational mechanics, such as Finite Element Analysis (FEA) and Multibody Dynamics Analysis (MDA); new mathematical approaches, innovations, and challenges in biomechanics and robotics; biomechanics and robotics: new trends in modeling and simulation; kinematics, dynamics, and optimization procedures in biomechanics and robotics; computer-based methods in biomechanics, biomedical engineering, and robotics; applied mathematics to deal with manufacturing, production, logistics and distribution, product design, ergonomics, management and socioeconomic aspects, and (fuzzy) decision-making processes related to biomechanics and robotics; topics related to mathematical approaches to human motion analysis, virtual prototypes, diagnosis, injury prevention, treatment, and rehabilitation; sports performance, training techniques, and development of materials and equipment by means of biomechanics and robotics; biomechanics and robotics applications in medicine, work efficiency, and risk factors among assembly line workers.

For this special issue, we requested high-quality original research articles in the above-mentioned topics. The number

of accepted submissions in the special issue is 16, which have been published after a fair and rigorous review process organized by the guest editorial team. The accepted papers cover a wide range of topics and a concise description of them follows.

In the paper entitled “Existence and Stability of Periodic Solution Related to Valveless Pumping” by B. Dorociaková et al., an application in nanotechnology is presented using a valveless pumping approach, also known as the Liebau effect. It was described as the unidirectional flow of liquid in a system without valves that is caused by the asymmetrical placement of the periodically working pump.

H. E. Jaramillo set out and discussed the importance of the intervertebral disc in the mechanical behavior of the human spine using a finite element model of the human spine in the paper “Evaluation of the Use of the Yeoh and Mooney-Rivlin Functions as Strain Energy Density Functions for the Ground Substance Material of the Annulus Fibrosus”.

The paper entitled “A Reliability-Based Consensus Model for Multiattribute Group Decision-Making with Analytically Evidential Reasoning Approach” by Y.-W. Du et al. presents a study that provides a reliability-based consensus model for multiattribute group decision making with an analytically evidential reasoning approach.

B. Liu et al. developed a real-time evacuation route approach based on emotion and geodesics under the influence of individual emotion and multihazard circumstances in the paper entitled “An Evacuation Route Model of Crowd Based on Emotion and Geodesic”.

Dealing with position tracking control in the paper “Position Tracking Control of PMSM Based on Fuzzy PID-Variable Structure Adaptive Control”, P. Pei et al. propose a novel fuzzy PID-variable structure adaptive control for position tracking of a permanent magnet synchronous motor, which is used in an electric extremity exoskeleton robot.

In the paper entitled “Human-Robot Interaction and Demonstration Learning Mode Based on Electromyogram Signal and Variable Impedance Control”, R. Wu et al. simulate the properties of a variable admittance controller and a variable impedance controller, showing the good performance of these two controllers under trajectory tracking and physical interaction. In addition, a new mode of learning from demonstration that conforms to human intuition was developed by combining the electromyogram (EMG) signals and variable impedance (admittance) controller in a dragging demonstration.

Y.-W. Du et al. introduce a “Mass Collaboration-Driven Method for Recommending Product Ideas Based on Dempster-Shafer Theory of Evidence”.

In the paper entitled “Decision-Maker’s Risk Preference Based Intuitionistic Fuzzy Multiattribute Decision-Making and Its Application in Robot Enterprises Investment”, L. Zhou and Q. Wang developed an intuitionistic fuzzy dependent hybrid weighted operator and proposed an intuitionistic fuzzy multiattribute decision-making method, which was verified in a robot manufacturing investment case study.

In the paper entitled “Extension Dependent Degree Method with Mapping Transformation for Three-Parameter Interval Number Decision Making”, L.-B. Xu et al. put

forward a new decision-making approach and framework based on extension simple dependent degree. It makes it possible not only to perform uncertain analysis of decision results by different settings of attitude coefficients, but also to take dynamic analysis and rule finding by some extension of the interval mapping transformation method.

In the paper entitled “Bifurcation Analysis of Stick-Slip Motion of the Vibration-Driven System with Dry Friction” regarding the problem of vibration-driven systems, which can move due to the periodic motion of the internal mass and the dry friction, P. Li and Z. Jiang proposed to model their system as a Filippov system with the property of stick-slip motion.

In the paper entitled “Nonlinear Vibration of an Elastic Soft String: Large Amplitude and Large Curvature”, D.-M. Zhao et al. addressed the nonlinear vibration of an elastic string with a large amplitude and large curvature, which was systematically investigated using the Hamilton principle, the modified complex normal form method, and the finite difference scheme.

L. Yu et al. dealt with multicriteria decision analysis methods by presenting a new assessment approach based on the analysis of Technique for Order of Preference by Similarity to Ideal Solution (TOPSIS) evaluation methods in the paper entitled “A Study on the Application of Coordinated TOPSIS in Evaluation of Robotics Academic Journals”.

In the paper entitled “Workspace Analysis of a Hybrid Kinematic Machine Tool with High Rotational Applications”, H. Zhang et al. proposed a novel parallel manipulator with one translational and two rotational degrees of freedom that can be used to form a five-degree-of-freedom hybrid kinematic machine tool for large heterogeneous complex structural component machining in aerospace field.

The paper entitled “Extended Version of Linguistic Picture Fuzzy TOPSIS Method and Its Applications in Enterprise Resource Planning Systems” by S. Zeng et al. uses uncertain information in terms of linguistic picture fuzzy numbers. The decision-maker provides membership, neutral, and non-membership fuzzy linguistic terms to represent uncertain assessments information of alternatives in linguistic multicriteria decision making, in which a new hamming distance measure between two linguistic picture fuzzy numbers is defined in order to introduce the extended version of TOPSIS method.

J. Bai et al. in the paper entitled “EO Sensor Planning for UAV Engineering Reconnaissance Based on NIIRS and GIQE” developed a method to solve the problem of poor image quality caused by the flight altitude not meeting the mission requirements based on National Imagery Interpretability Rating Scale (NIIRS), the general image quality equation (GIQE), and the geometrical property of the ground sampled distance (GSD).

In the paper entitled “Modal Decoupled Dynamics Feed-Forward Active Force Control of Spatial Multi-DOF Parallel Robotic Manipulator”, X. Niu et al. proposed an intelligent robotic spine brace for the treatment of scoliosis. In order to solve the disadvantages of the parallel mechanism, they present a novel active force control structure, modal space dynamic feed-forward (MSDF) force control strategy.

### **Conflicts of Interest**

The guest editors declare that there are no conflicts of interest regarding the publication of this special issue.

### **Acknowledgments**

We would like to thank all the authors for their excellent contributions and the reviewers for their valuable help; their feedback was very useful in improving the quality of the papers submitted.

*Carlos Llopis-Albert  
Francisco Rubio  
Shouzhen Zeng  
Huchang Liao*

## Research Article

# Modal Decoupled Dynamics Feed-Forward Active Force Control of Spatial Multi-DOF Parallel Robotic Manipulator

Xinjian Niu,<sup>1</sup> Chifu Yang ,<sup>1</sup> Bowen Tian,<sup>2</sup> Xiang Li ,<sup>3</sup> and Junwei Han<sup>1</sup>

<sup>1</sup>State Key Laboratory of Robotics and System, Harbin Institute of Technology, Harbin 150001, China

<sup>2</sup>Department of Economic and Trade, School of Business Administration, Zhongnan University of Economics and Law, Wuhan 430000, China

<sup>3</sup>Department of Mechatronics Engineering, Harbin Institute of Technology, Harbin 150001, China

Correspondence should be addressed to Xiang Li; [lxiang0818@163.com](mailto:lxiang0818@163.com)

Received 10 June 2018; Revised 16 August 2018; Accepted 19 September 2018; Published 16 April 2019

Guest Editor: Carlos Llopis-Albert

Copyright © 2019 Xinjian Niu et al. This is an open access article distributed under the Creative Commons Attribution License, which permits unrestricted use, distribution, and reproduction in any medium, provided the original work is properly cited.

According to the parallel mechanism theory, this paper proposes a novel intelligent robotic spine brace for the treatment of scoliosis. Nevertheless, this type of parallel mechanism has the following disadvantages: strong dynamic coupling in task space or joint space, adverse effect of system's gravity, and lower response frequency in roll and pitch orientations, which seriously affect the performance of the system. In order to solve those boring problems, this paper presents a novel active force control structure, modal space dynamic feed-forward (MSDF) force control strategy. Besides, this paper expresses the intelligent robotic brace system model including the dynamic and kinematic models and the electric actuator model with Kane strategy. The stability of the intelligent system with the novel control strategy is proved. In order to evaluate the performance of the presented MSDF force control method, this paper builds the parallel mechanism experimental platform. It can be seen from experimental results that the proposed motion control method solves these boring problems well.

## 1. Instruction

Scoliosis is a three-dimensional (3D) abnormal curvature of the spine [1]. However, current braces are mainly used to treat the lateral curvature of the spine, which are little effective for the anterior and posterior curvature of the spine [2–5]. Besides, since corrective forces are applied on human spine passively using current braces, it is difficult to control the forces accurately, which brings difficulties in the treatment of the scoliosis. A new intelligent parallel manipulator system is designed in this paper for exerting 3D active corrective forces on the spine of patients [6]. A spatial multi-degree of freedom (multi-DOF) parallel robotic manipulator actuated by electrical actuators is used as the robotic brace in this paper, since this parallel structure has high precision, high reliability, and high power weight ratio and offers 3D active corrective forces [7–9]. However, this type of parallel mechanism has the following disadvantages, strong dynamic coupling in task space or joint space, adverse effect of system's gravity and lower response frequency in roll and pitch orientations,

which seriously affect the performance of the system. Because of the above boring problems of the parallel mechanism, it is difficult to improve the performance of the system just with the typical proportion-integral-derivative (PID) control method in traditional physical space [10–12]. Fortunately, the dynamic feed-forward control strategy in modal space can solve these problems excellently.

A lot of studies have reported this parallel mechanism widely [13–16], and this structure was used in many areas practically [17, 18]. For solving those inherent properties, a lot of control methods have been presented for parallel structure [19–21]. Those control strategies were all presented in traditional physical space, joint space, or task space [22–25]. Without taking into account the system dynamics and system kinematics, a series control strategy with the disturbance observer for parallel mechanism was designed in joint space [26]. This study increases the anti-interference characteristics of the system, which improves the performance of the system. However, they ignored the influence of the gravity term, which is important for the system. Yang et al. developed

a proportion-derivative (PD) control strategy with gravity compensation for the hydraulic 6-DOF parallel manipulator to solve the problem of the device's gravity, which improve the track tracking performance well [27]. However, they did not consider coupling problem of the parallel mechanism in all six directions, which infected tracking precision serious. Based on the observer, a backstepping control algorithm for forward kinematics solver is studied taking into account the actuator's friction [28]. In order to improve the performance of the system, the friction of the actuator is considered in this literature. Nevertheless, the gravity of the system was also ignored in this study, which had bad effects on the parallel system. In previous literatures only the problem of tracking motion trajectories using a variety of basic and advanced control methods is considered. However, it is critical for most parallel robotic applications to detect contact force between robot and environment, for example, assembly robots, grinding robots, surgery robots, and rehabilitation robots which involve extensive contact with environment. The development of force control strategy for parallel robotic manipulators is later than that of motion control. Noshadi et al. presented an active force control strategy combined with the classical PID controller for a 3-RRR (revolute-revolute-revolute) 3-DOF planar parallel robotic manipulator [29]. Bera et al. proposed a virtual foundations force control in parallel robotic manipulator using bond graph modeling [30]. Lopes et al. reported a method to obtain high performance of active force control by combing a robotic controlled impedance device (RCID) with a commercial industrial robot [31]. Goertzen et al. proposed a new application of a velocity-based force control method used for robotic biomechanical testing [32]. Wen et al. presented a fuzzy identification strategy for achieving the system model of the multi-DOF spatial redundantly actuated parallel robot [33]. Since those inherent shortcomings of the parallel mechanism, the performance of parallel robotic manipulator cannot be achieved satisfactorily using the above-mentioned force control strategies in joint space and work space. For solving those inherent properties, a decoupling motion control method is studied in modal space [34, 35]. Nevertheless, this control structure is designed just for motion control of parallel robotic manipulator. Yang et al. proposed a novel modal space decouple control method for force trajectory tracking, which solved the dynamic coupling in force field [36]. However, this novel control structure is developed based on the classical PID control strategy, which decoupled the dynamic coupling, but neglected gravity term of the robot system. Thus, the current force control strategies for the parallel mechanism are all controlled in joint space or workspace which could not solve the dynamic coupling problem of the parallel manipulator. Besides, most current control methods ignored the gravity term of the device which is critical for achieving high-precision corrective forces. This paper develops a novel force control strategy, which solves those boring inherent properties of the parallel system.

The main contribution of this article is to design a new control structure, modal space dynamic feed-forward (MSDF) active force control for parallel robotic manipulators which can eliminate the bad effects of those inherit properties such as dynamic coupling, low response frequency, and

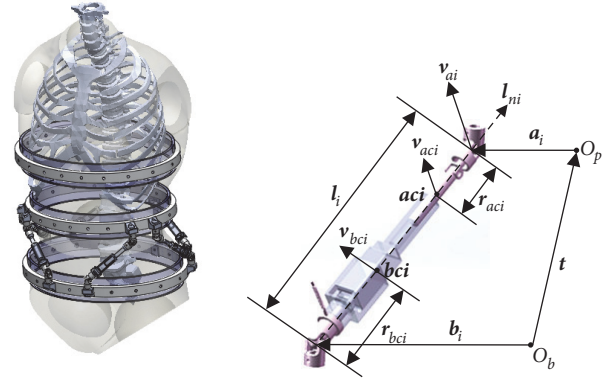


FIGURE 1: Structure of the novel brace.

gravity term in six directions. In comparison to those control structures in traditional physical space, the proposed control strategy improves performances of parallel mechanism effectively.

## 2. System Model

The intelligent robotic system consists of two Stewart platforms in series. As can be seen in Figure 1, this intelligent system is driven with twelve actuators and there is a kinematic chain of universal prismatic spherical (UPS) in each leg. Since the upper platform has the same structure with the lower platform, this paper just describes the system model of the lower platform.

*2.1. Dynamics Model.* When using the rigid body modeling theory and establishing the dynamic model of the parallel robotic manipulator system, there are the following assumptions: (1) the moving platform and fixed platform are both rigid bodies. (2) The piston rod and cylinder are both rigid bodies. (3) Hinges and other connectors are all rigid connectors with negligible masses. According to above assumptions, the system consists of 13 rigid bodies including 6 piston rods, 6 cylinders, and one moving platform, respectively. Based on the Newton's second law and angular momentum theory, inertia force and inertia moment of the system are expressed as

$$\mathbf{F}_p = m_p \ddot{\mathbf{t}} \quad (1)$$

$$\mathbf{M}_p = \mathbf{I}_p \dot{\boldsymbol{\omega}}^L + \boldsymbol{\omega}^L \times \mathbf{I}_p \boldsymbol{\omega}^L \quad (2)$$

in which  $\mathbf{F}_p$  is the inertia force.  $\mathbf{M}_p$  is the inertia moment and  $m_p$  means the mass of the motion upper platform.  $\mathbf{t}$  is the linear vector of the body framework relative to the fixed framework.  $\boldsymbol{\omega}^L$  is the upper platform's angular velocity vector in fixed framework.  $\mathbf{I}_p$  means the inertia tensor in inertial framework and can be expressed as

$$\mathbf{I}_p = \mathbf{R} \mathbf{I}_p^p \mathbf{R}^T \quad (3)$$

in which  $I_p^P$  means inertia tensor in body framework.  $R$  denotes the transformation matrix from the body framework to the inertia framework and  $R^T$  is the transpose of  $R$ .

Based on (1) and (2), the generalized inertia force of motion platform is expressed as

$$\begin{aligned} F_p^* &= -M_p \ddot{\bar{q}} - C_p \dot{\bar{q}} \\ &= \begin{pmatrix} m_p I & 0 \\ 0 & I_p \end{pmatrix} \begin{bmatrix} \dot{\bar{t}} \\ \dot{\omega}^L \end{bmatrix} - \begin{pmatrix} 0_{3 \times 3} & 0 \\ 0_{3 \times 3} & \tilde{\omega}^L I_p \end{pmatrix} \begin{bmatrix} \dot{\bar{t}} \\ \omega^L \end{bmatrix} \end{aligned} \quad (4)$$

in which  $\tilde{\omega}^L$  means the angular velocity's skew symmetric matrix in inertia framework.  $\dot{\bar{q}}$  and  $\ddot{\bar{q}}$  are the generalized velocity and acceleration in the inertia framework.  $C_p$  is the damping coefficient of the system.

In the same way, according to the angular momentum theorem and Newton's second law, inertia moment force and moment of piston rod is described as

$$F_{rvi} = m_a \dot{v}_{aci} \quad (5)$$

$$M_{rwi} = I_{ai} \dot{\omega}_{li} + \omega_{li} \times I_{ai} \omega_{li} \quad (6)$$

where  $F_{rvi}$ ,  $M_{rwi}$  are inertia force and inertia moment of piston rod.  $m_a$  means the mass of piston rod.  $v_{aci}$  denotes piston rod's centroid velocity.  $\omega_{li}$  means the leg's angular velocity.  $I_{ai}$  denotes the piston rod's inertia tensor.

The leg's angular velocity and the piston rod's centroid velocity are expressed with the motion platform's generalized velocity.

$$v_{aci} = J_{aci,ai} J_{ai,\bar{q}} \dot{\bar{q}} \quad (7)$$

$$\omega_{li} = J_{wi,ai} J_{ai,\bar{q}} \dot{\bar{q}} \quad (8)$$

where  $J_{aci,ai}$  means the Jacobi matrix from the velocity of upper hinge point to the piston rod's centroid velocity.  $J_{ai,\bar{q}}$  denotes the Jacobi matrix from the motion platform's generalized velocity to the velocity of upper hinge point.  $J_{wi,ai}$  is the Jacobi matrix from the velocity of upper hinge point to the leg's angular velocity.

Based on (5), (6), (7), and (8), the piston rod's generalized inertia force in fixed framework is gotten

$$\begin{aligned} F_{ri}^* &= J_{ai,\bar{q}}^T J_{aci,ai}^T F_{rvi} + J_{ai,\bar{q}}^T J_{wi,ai}^T M_{rwi} \\ &= J_{ai,\bar{q}}^T \left( J_{aci,ai}^T m_a J_{aci,ai} + J_{wi,ai}^T I_{ai} J_{wi,ai} \right) J_{ai,\bar{q}} \ddot{\bar{q}} \\ &+ \left\{ J_{ai,\bar{q}}^T \left[ \frac{J_{aci,ai}^T m_a d(J_{aci,ai} J_{ai,\bar{q}})}{dt} \right] \right. \\ &+ J_{ai,\bar{q}}^T J_{wi,ai}^T \left[ \frac{I_{ai} d(J_{wi,ai} J_{ai,\bar{q}})}{dt} + J_{wi,ai} J_{ai,\bar{q}} \dot{\bar{q}} \right. \\ &\left. \left. \times I_{ai} J_{wi,ai} J_{ai,\bar{q}} \right] \right\} \dot{\bar{q}} \end{aligned} \quad (9)$$

where  $F_{ri}^*$  is the generalized inertia force of piston rod in the inertial coordinate framework.  $J_{aci,ai}^T$ ,  $J_{wi,ai}^T$ ,  $J_{ai,\bar{q}}^T$  are the transpose of matrix  $J_{aci,ai}$ ,  $J_{wi,ai}$ ,  $J_{ai,\bar{q}}$ .

In the same way, the cylinder's generalized force in fixed framework is expressed as

$$\begin{aligned} F_{ci}^* &= J_{ai,\bar{q}}^T J_{bci,ai}^T F_{cvi} + J_{ai,\bar{q}}^T J_{wi,ai}^T M_{cwi} \\ &= J_{ai,\bar{q}}^T \left( J_{bci,ai}^T m_b J_{bci,ai} + J_{wi,ai}^T I_{bi} J_{wi,ai} \right) J_{ai,\bar{q}} \ddot{\bar{q}} \\ &+ \left\{ J_{ai,\bar{q}}^T \left[ \frac{J_{bci,ai}^T m_b d(J_{bci,ai} J_{ai,\bar{q}})}{dt} \right] \right. \\ &+ J_{ai,\bar{q}}^T J_{wi,ai}^T \left[ \frac{I_{bi} d(J_{wi,ai} J_{ai,\bar{q}})}{dt} + J_{wi,ai} J_{ai,\bar{q}} \dot{\bar{q}} \right. \\ &\left. \left. \times I_{bi} J_{wi,ai} J_{ai,\bar{q}} \right] \right\} \dot{\bar{q}} \end{aligned} \quad (10)$$

where  $F_{ci}^*$  is the generalized inertia force of the cylinder.  $m_b$  is the cylinder's mass.  $I_{bi}$  is the cylinder's inertia tensor.  $J_{bci,ai}$  means the Jacobi matrix from the velocity of upper hinge point to the cylinder's centroid velocity.  $J_{bci,ai}^T$  is the transpose of matrix.  $F_{cvi}$ ,  $M_{cwi}$  are inertia force and inertia moment of the cylinder.

According to Kane approach and based on (4), (9), and (10), the dynamic model of the intelligent robotic system is described as

$$\tau - F_c + F_p^* + \sum_{i=1}^6 F_{ri}^* + \sum_{i=1}^6 F_{ci}^* + G^* = 0 \quad (11)$$

in which  $F_c$  means the contact force.  $G^*$  is the device's gravity.  $\tau$  denotes the generalized force and is expressed as

$$\tau = J_{l\bar{q}}^T F_a \quad (12)$$

in which  $J_{l\bar{q}}^T$  denotes the Jacobi matrix from the generalized velocity to the leg's velocity.  $F_a$  means the net output force of the actuator.

Base on (11), the standard formula of the system model in task space is written as

$$M(\bar{q}) \ddot{\bar{q}} + N(\bar{q}, \dot{\bar{q}}) \dot{\bar{q}} + G(\bar{q}) + F_c = \tau \quad (13)$$

in which  $M$  is the system's mass matrix.  $N$  means the centrifugal term.  $G$  denotes the device's gravity term.  $\bar{q}$  means the motion platform's generalized pose.

In addition (13) is rewritten in joint space

$$M_l(l) \ddot{l} + C_l(l, \dot{l}) \dot{l} + G_l(l) + F_{cl} = F_a \quad (14)$$

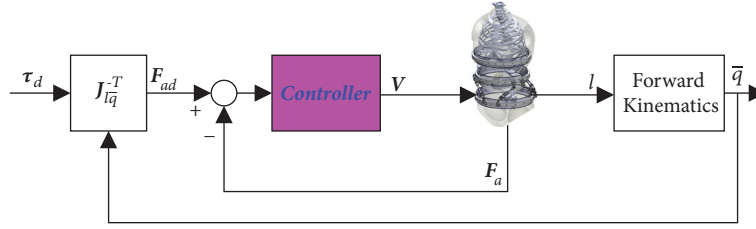


FIGURE 2: Active force control strategy in traditional physical space.

in which  $M_l$  means mass matrix.  $C_l$  denotes centrifugal force.  $G_l$  shows the gravity term. With the Jacobi matrix  $J_{l\bar{q}}$ , the work space and the joint space are connected as follows:

$$\begin{aligned} \dot{l} &= J_{l\bar{q}} \dot{\bar{q}} \\ M_l &= J_{l\bar{q}}^{-T} M J_{l\bar{q}}^{-1} \\ C_l &= J_{l\bar{q}}^{-T} (M \dot{J}_{l\bar{q}}^{-1} + N J_{l\bar{q}}^{-1}) \\ F_{cl} &= J_{l\bar{q}}^{-T} F_c \\ G_l &= J_{l\bar{q}}^{-T} G \end{aligned} \quad (15)$$

In joint space, the system's mass matrix is a real symmetric and positive definite matrix [37].

**2.2. Kinematics Model.** Current studies have developed the kinematics of parallel mechanism widely [38, 39]. Hence, this paper just describes the kinematics briefly. According to Figure 1, the inverse kinematics is described with the geometric approach

$$l_i = \sqrt{\mathbf{l}_i^T \mathbf{l}_i} = \sqrt{(\mathbf{t} + \mathbf{R}\mathbf{a}_i^p - \mathbf{b}_i)^T (\mathbf{t} + \mathbf{R}\mathbf{a}_i^p - \mathbf{b}_i)} \quad (16)$$

in which  $l_i$  means the actuator's length.  $\mathbf{a}_i^p$  is the upper joint point's radius vector in body framework.  $\mathbf{b}_i$  is the lower joint point's radius vector in inertia framework.

The upper platform's position can be achieved from the analysis of the forward kinematic using the given leg's length. In this section, the upper platform's position is obtained with the Newton-Raphson iterative algorithm. This algorithm's iterative sequence is described as

$$\bar{q}_{j+1} = \bar{q}_j + J_{l\bar{q}}^{-1} (l_m - l_j) \quad (17)$$

where  $l_m$  means the measured limb position.

**2.3. Actuator Dynamics.** The parallel robotic manipulator is driven by 12 miniature electrical actuators. In this paper, the friction of the actuator is ignored. Thus, the force equilibrium equation can be described as

$$\mathbf{F}_p = \mathbf{F}_a \quad (18)$$

In which  $\mathbf{F}_p$  means the actuator's output force.  $\mathbf{F}_a$  is measured by the force sensor.

Based on the motor output force principle and parameters of the motor, the actuator's output force  $\mathbf{F}_p$  is expressed as

$$\mathbf{F}_p = k_t \mathbf{I}_t \quad (19)$$

in which  $k_t$  means the motor's force coefficient.  $\mathbf{I}_t$  denotes the equivalent current resulted from the current loop and this equivalent current can be expressed as

$$\mathbf{I}_t = \frac{1}{\tau_0 s + 1} \mathbf{U} \quad (20)$$

in which  $\tau_0$  means the time constant of the current loop and  $\mathbf{U}$  denotes the input of the current loop that is described as

$$U_i = U_{ri} - k_e \dot{l}_i \quad (21)$$

in which  $k_e$  shows the equivalent electromotive force (EMF) coefficient.  $U_{ri}$  means the  $i$ th motor's control voltage.

### 3. Control Design

**3.1. Active Force Control Strategy in Traditional Physical Space.** The traditional physical control space consists of workspace and joint space. Since it is difficult to measure poses of end-effector, joint space control strategy (JSCS) is widely used in engineering. Therefore, this paper just presents the JSCS control method in traditional physical space in Figure 2.

In Figure 2,  $\tau_d$  is the desired force of the system in task space and  $\mathbf{V}$  is the control law in traditional joint space.

Because the typical PID control approach is applied extensively in engineering, a classical P control strategy is used as the force controller.

$$\mathbf{V} = k_p \mathbf{e} = k_p (\mathbf{F}_{ad} - \mathbf{F}_a) \quad (22)$$

in which  $k_p$  means the P control gain and is tuned in experimental process.  $\mathbf{F}_{ad}$  is the desired force of the actuator.

**3.2. Active Force Control Strategy in Modal Space.** Because of the strong dynamic coupling of parallel robotic manipulator in joint space and task space, it is impossible to control multiple input and multiple output (MIMO) dynamic system independently. In order to decouple the dynamic coupling system and improve the system performance, modal space decoupling technique is used in this paper. Each channel control parameters are tuned in experimental process independently in modal space [36]. As shown in Figure 3, the

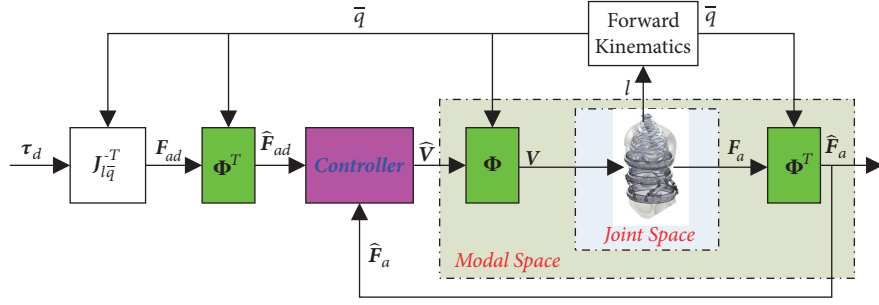


FIGURE 3: Active force control strategy in modal space.

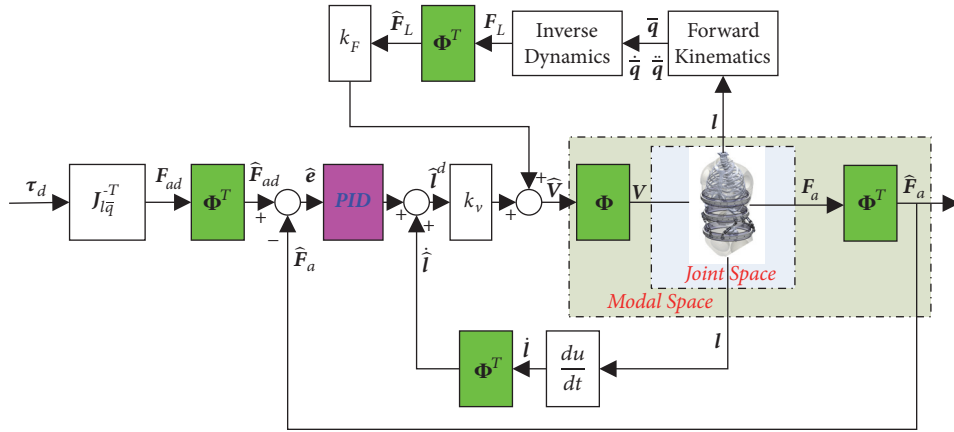


FIGURE 4: Modal space dynamic feed-forward (MSDF) force control strategy.

MIMO system is controlled in modal space where each channel is controlled independently.

In Figure 3,  $\Phi$  means the modal translation matrix.  $\Phi^T$  is the transpose of matrix  $\Phi$ .  $\hat{F}_{ad}$  denotes the reference modal driven force.  $\hat{F}_a$  means the measured feedback force from the load cell.  $\hat{V}$  denotes the modal input voltage.  $V$  is the parallel mechanism's control input and  $F_a$  is the feedback force of the intelligent manipulator. The output of the modal controller is  $\hat{V}$  and  $\hat{F}_a$  is the modal feedback force.

Each force channel is controlled in modal space independently [36]. For revealing the property, the modal control law adopts the typical P control method

$$\hat{V} = \hat{K}_p \hat{e} = \begin{bmatrix} \hat{k}_1 & & & & & \\ & \hat{k}_2 & & & & \\ & & \ddots & & & \\ & & & \hat{k}_6 & & \end{bmatrix} \begin{bmatrix} \hat{F}_{ad1} - \hat{F}_{a1} \\ \hat{F}_{ad2} - \hat{F}_{a2} \\ \vdots \\ \hat{F}_{ad6} - \hat{F}_{a6} \end{bmatrix} \quad (23)$$

in which  $\hat{k}_i$  denotes the  $i$ th P control gain.  $\hat{e}$  means the modal control error,  $\hat{e} = \hat{F}_{ad} - \hat{F}_a$

**3.3. Dynamics Feed-Forward Active Force Control Strategy in Modal Space.** For improving performances of the parallel mechanism, the MSDF active force control strategy is presented in this paper. MSDF control strategy is constructed

by adding a dynamic feed-forward to the modal space PID (MSPID) control method. MSDF control strategy can greatly improve the dynamic trajectory tracking performance of the parallel robotic manipulator without affecting the robust stability of MSPID control. The principle of MSDF is shown in Figure 4.

In Figure 4,  $k_v$  means the feed-forward gain of velocity.  $k_F$  denotes the dynamic feed-forward gain.  $F_L$  is the compensation force of the system.  $\hat{F}_L$  is the modal compensation force.  $\hat{l}^d$  is the velocity error of actuator in modal space.  $\hat{l}$  is the modal velocity of actuator.

According to the feed-forward strategy, this paper proposed the modal control law without destroying MSPID system stability.

$$\hat{V} = k_v \hat{l}^d + k_F \hat{F}_L \quad (24)$$

$$\hat{l}^d = \hat{l} + \hat{K}_p \hat{e} = \hat{l} + \hat{K}_p (\hat{F}_{ad} - \hat{F}_a) \quad (25)$$

$$\hat{F}_L = \Phi^T (\hat{G}_l + \hat{M}_l \hat{l}) \quad (26)$$

Equation (26) is expressed as

$$\hat{F}_L = \hat{G}_l + \hat{M}_l \hat{l} \quad (27)$$

in which  $\hat{M}_l$  is the mass matrix modal space,  $\hat{M}_l = \text{diag}\{\hat{M}_{l1} \cdots \hat{M}_{l6}\}$ .  $\hat{G}_l$  means the gravity term in modal space,  $\hat{G}_l = [\hat{G}_{l1} \cdots \hat{G}_{l6}]$ .

According to the Laplace transformation, (24), (25), and (27) are described as

$$\widehat{\mathbf{V}} = k_v \widehat{\mathbf{I}}^d(s) + k_F \widehat{\mathbf{F}}_L(s) \quad (28)$$

$$\widehat{\mathbf{I}}^d = s \widehat{\mathbf{I}} + \widehat{\mathbf{K}}_p (\widehat{\mathbf{F}}_{ad} - \widehat{\mathbf{F}}_a) \quad (29)$$

$$\widehat{\mathbf{F}}_L = \widehat{\mathbf{G}}_l + s^2 \widehat{\mathbf{M}}_l \widehat{\mathbf{I}} \quad (30)$$

Combing (29) and (30) with (28), the modal force control law is achieved

$$\widehat{\mathbf{V}}(s) = k_v \widehat{\mathbf{K}}_p \left[ \left( k_F \widehat{\mathbf{K}}_p^{-1} \widehat{\mathbf{M}}_l s^2 + \widehat{\mathbf{K}}_p^{-1} s \right) \widehat{\mathbf{I}} + (\widehat{\mathbf{F}}_{ad} - \widehat{\mathbf{F}}_a) \right] + k_F \widehat{\mathbf{G}}_l \quad (31)$$

Equation (31) is expressed as

$$\widehat{\mathbf{V}}_i(s) = k_v k_{pi} \left[ \left( \frac{k_F \widehat{M}_{li}}{k_{pi}} s + \frac{1}{k_{pi}} \right) \dot{\widehat{I}}_i + (\widehat{F}_{adi} - \widehat{F}_{ai}) \right] + k_F \widehat{G}_{li} \quad (32)$$

As shown in (32), according to the MSPID control method, the MSDF control law of each channel consists of a gravity compensation term and a velocity feedback differentiation loop independently. The controller design and parameters adjustment of MSDF are carried out in each channel independently. According to the performance of each modal channel, the designed controller makes the performance of each channel optimal in modal space, thus achieving the best overall control performance of the parallel robotic manipulator system.

#### 4. Stability Analysis

Stability shows the critical property of the parallel mechanism. Since the dynamic feed-forward control strategy does not destroy the whole system stability, this paper just derives the MSPID system stability.

According to (19), (20), and (21), it can be obtained

$$k_t' (\mathbf{U}_r - k_e \dot{\mathbf{l}}) = \mathbf{F}_p \quad (33)$$

where  $k_t' = k_t(1/(\tau_0 s + 1))$

Based on Laplace transformation, (34) is described as

$$sl = \frac{1}{k_e} \left( \mathbf{U}_r - \frac{1}{k_t'} \mathbf{F}_p \right) \quad (34)$$

Based on (14) and (18), EQ (35) is obtained

$$\mathbf{M}_l(l) \ddot{\mathbf{l}} + \mathbf{C}_l(l, \dot{\mathbf{l}}) \dot{\mathbf{l}} + \mathbf{G}_l(l) + \mathbf{F}_{cl} = \mathbf{F}_p \quad (35)$$

Since the parallel robotic spine brace works in low speed area, the centrifugal term  $\mathbf{C}_l$  is so small that can be ignored [36]. Thus, (35) is expressed as

$$\mathbf{M}_l(l) \ddot{\mathbf{l}} + \mathbf{G}_l(l) + \mathbf{F}_{cl} = \mathbf{F}_p \quad (36)$$

Based on Laplace transformation, (37) is obtained

$$s^2 \mathbf{M}_l(l) \mathbf{l} = \mathbf{F}_p - (\mathbf{G}_l(l) + \mathbf{F}_{cl}) \quad (37)$$

Combine (34) with (37)

$$s \mathbf{M}_l(l) \mathbf{U}_r = \left( k_e \mathbf{I} + \frac{1}{k_t'} s \mathbf{M}_l(l) \right) \mathbf{F}_p - k_e (\mathbf{G}_l(l) + \mathbf{F}_{cl}) \quad (38)$$

Based on the transformational relation from the joint space to the modal space, it can be obtained

$$\mathbf{M}_l = \Phi \widehat{\mathbf{M}}_l \Phi^T \quad (39)$$

Combine (39) with (38)

$$\Phi (s \widehat{\mathbf{M}}_l) \Phi^T \mathbf{U}_r = \Phi \left( k_e \mathbf{I} + \frac{1}{k_t'} s \widehat{\mathbf{M}}_l \right) \Phi^T \mathbf{F}_p - k_e (\mathbf{G}_l(l) + \mathbf{F}_{cl}) \quad (40)$$

where

$$\begin{aligned} \widehat{\mathbf{U}}_r &= \Phi^T \mathbf{U}_r, \\ \widehat{\mathbf{F}}_p &= \Phi^T \mathbf{F}_p \end{aligned} \quad (41)$$

in which  $\widehat{\mathbf{U}}_r$  is the modal motor voltage.  $\widehat{\mathbf{F}}_p$  is the output force of actuator in modal space.

Based on (40) and (41), (42) is described as

$$(s \widehat{\mathbf{M}}_l) \widehat{\mathbf{U}}_r = \left( k_e \mathbf{I} + \frac{1}{k_t'} s \widehat{\mathbf{M}}_l \right) \widehat{\mathbf{F}}_p - k_e \Phi^T (\mathbf{G}_l(l) + \mathbf{F}_{cl}) \quad (42)$$

According to (18) and (42), the transfer function from  $\widehat{\mathbf{U}}_r$  to  $\widehat{\mathbf{F}}_a$  can be obtained

$$\frac{k_t \widehat{M}_{li} s}{\tau_0 \widehat{M}_{li} s^2 + \widehat{M}_{li} s + k_t k_e} \widehat{U}_{ri} = \widehat{F}_{ai} \quad (43)$$

Because of  $\widehat{U}_{ri} = \widehat{V}_i$  (43) is expressed as

$$\frac{k_t \widehat{M}_{li} s}{\tau_0 \widehat{M}_{li} s^2 + \widehat{M}_{li} s + k_t k_e} \widehat{V}_i = \widehat{F}_{ai} \quad (44)$$

Based on (23) and (44), the open-loop transfer function of the MSPID system can be obtained

$$\begin{aligned} \widehat{G}_i(s) &= \frac{\widehat{F}_{ai}}{\widehat{F}_{adi}} \\ &= \frac{(k_{pi} \widehat{M}_{li} / k_e) s}{s^2 / (k_t k_e / \tau_0 \widehat{M}_{li}) + 2 \xi_i s / \sqrt{k_t k_e / \tau_0 \widehat{M}_{li}} + 1} \end{aligned} \quad (45)$$

in which  $\xi_i$  means the damping coefficient,  $\xi_i = 1/2 \sqrt{k_t k_e \tau_0 / \widehat{M}_{li}}$ . Equation (45) is described as

$$\widehat{G}_i(s) = \frac{(k_{pi} \widehat{M}_{li} / k_e) s}{s^2 / \widehat{\omega}_{ni}^2 + 2 \xi_i s / \widehat{\omega}_{ni} + 1} \quad (46)$$

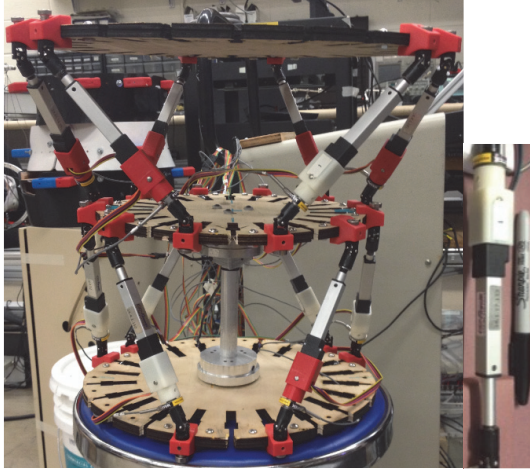


FIGURE 5: Experimental parallel spine brace.

in which  $\widehat{\omega}_{ni}$  denotes the system's natural frequency,  $\widehat{\omega}_{ni} = \sqrt{k_t k_e / \tau_0 \widehat{M}_{li}}$ .

Based on the Bode stability criterion, for guaranteeing the MSPID system stability, the system control parameters should satisfy (47).

$$\frac{k_{pi} \widehat{M}_{li}}{k_e} < 2 \widehat{\xi}_i \widehat{\omega}_{ni} \quad (47)$$

As shown in (47), in order to guarantee the MSPID system stability, the modal gain matrix  $\widehat{K}_p$  should be chosen appropriately. Thus, the MSDF system is robustly stable.

## 5. Experiment

Using the proposed MSDF force control method, some experiments are carried out for evaluating performances of the intelligent robotic system. Compared with the MSPID force control algorithm, the MSDF control strategy can achieve better performances.

**5.1. Experiment Setup.** For implementing and evaluating performances of the presented MSDF force control method, this section builds the parallel intelligent mechanism in Figure 5. This parallel system has several features: (1) 12 linear electric cylinders, (2) a real-time controller, and (3) a monitor computer. The force given signals are provided by the monitor computer. Besides, the force controller is running in a real-time controller. Geometric parameters of the brace system are shown in Table 1 and the sampling time for the experimental system is set to 20ms.

**5.2. Experiment Results.** Scoliosis is a 3D deformity. In order to achieve better orthopedic effect, this paper proposed an MSDF control structure for the robotic manipulator. For verifying the performance of the system with this presented

TABLE 1: Parameters of the experimental parallel intelligent manipulator.

Parameters	Values
Ellipse's long distance of upper joint (mm)	150
Ellipse's short distance of upper joint (mm)	142
Ellipse's long distance of lower joint (mm)	170
Ellipse's long distance of lower joint (mm)	149
Maximal stroke of linear electric cylinder (mm)	50
Initial length of linear electric cylinder (mm)	160
Masses of moving platform and joints (Kg)	0.33

control method, several force signals are given to the robotic system. The modal space P controllers are tuned to be

$$\widehat{K}_p = \text{diag} [16 \ 16 \ 16 \ 16 \ 16 \ 16] \quad (48)$$

The dynamic feed-forward control parameters  $k_v$  and  $k_F$  are tuned to be

$$k_v = \text{diag} [5.5 \ 5.5 \ 5.5 \ 5.5 \ 5.5 \ 5.5] \quad (49)$$

$$k_F = \text{diag} [1.6 \ 1.6 \ 1.6 \ 1.6 \ 1.6 \ 1.6]$$

As shown in Figure 6, step signals (surge: 8 N, sway: 8 N, heave: 10 N, roll: 1.5 Nm, pitch: 1.5 Nm, yaw: 1.5 Nm) are given to the robotic system in all six directions to detect the performance of the system. It can be seen from Figure 6 that the celerity of MSDF controller is superior to MSPID controller. In addition, the steady-state error of MSDF controller is smaller than that of MSPID controller. The maximal steady-state error is 0.1 N in linear directions and 0.05 Nm in angular directions with the proposed MSDF control strategy, 0.5 N in linear directions and 0.1 Nm in angular directions under the traditional MSPID control method. Furthermore, the dynamic system with the MSDF controller responds to desired force signals more quickly than that of the MSPID controller in all six directions.

As shown in (50a), (50b), (50c), (50d), (50e), and (50f) the reference special force signals are exerted on the robotic spine brace system respectively. Responses to the desired special force signals are shown in Figures 7 and 8 depicting the dynamic errors of the robotic system.

$$F_x = 3 \sin(0.377t) + 4 \sin(0.314t) + 5 \sin(0.253t) \quad (50a)$$

$$F_y = 4 \sin(0.314t) + 3 \sin(0.188t) + 5 \sin(0.253t) \quad (50b)$$

$$F_z = 2 \sin(0.314t) + 3 \sin(0.188t) + 5 \sin(0.253t) \quad (50c)$$

$$M_x = 0.8 \sin(0.440t) + 1.0 \sin(0.377t) + 1.2 \sin(0.314t) \quad (50d)$$

$$M_y = 0.8 \sin(0.377t) + 1.0 \sin(0.314t) + 1.2 \sin(0.440t) \quad (50e)$$

$$M_z = 0.8 \sin(0.377t) + 1.0 \sin(0.314t) + 1.2 \sin(0.440t) \quad (50f)$$

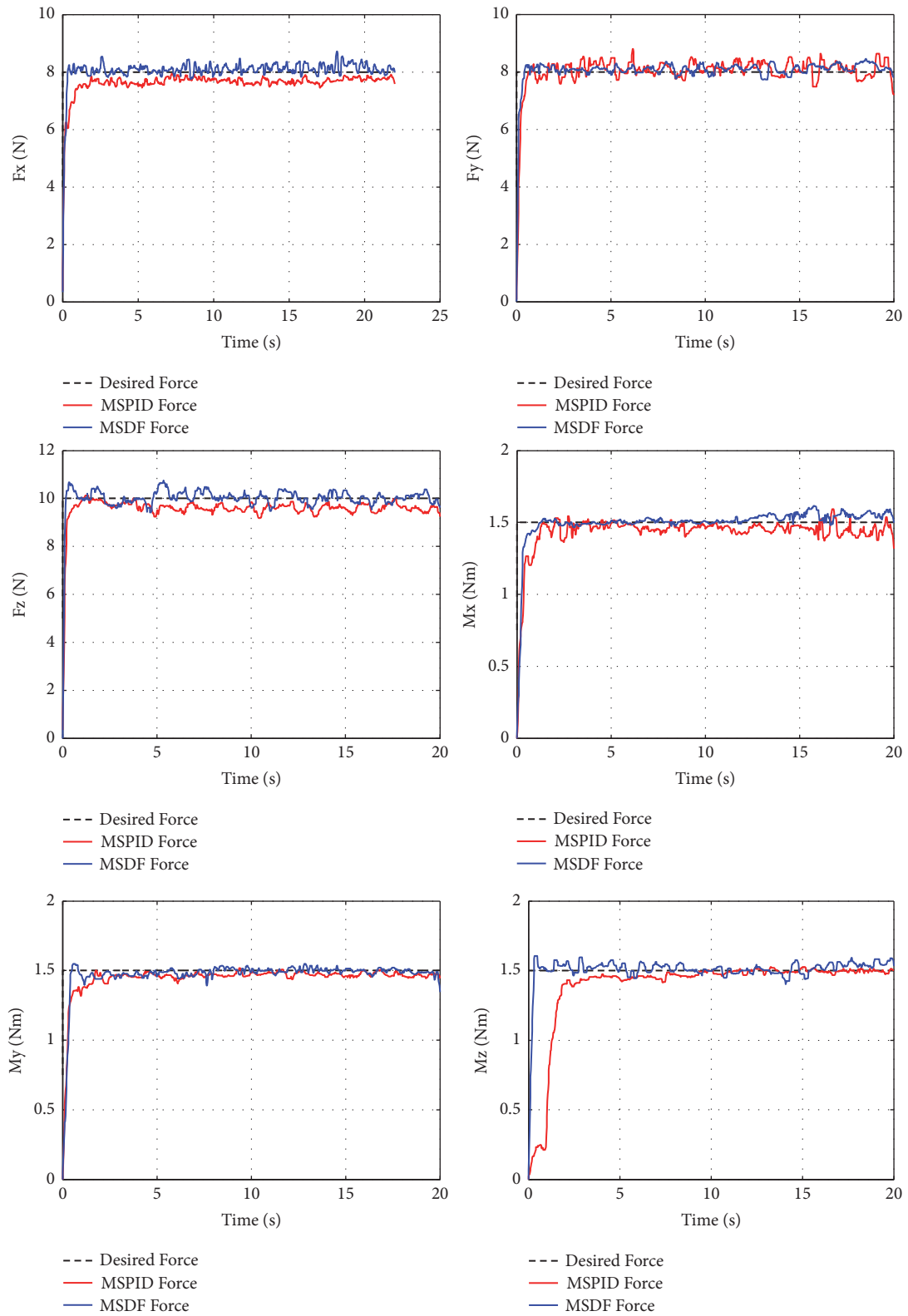


FIGURE 6: Responses to the desired step force signals with MSPID and MSDF controllers.

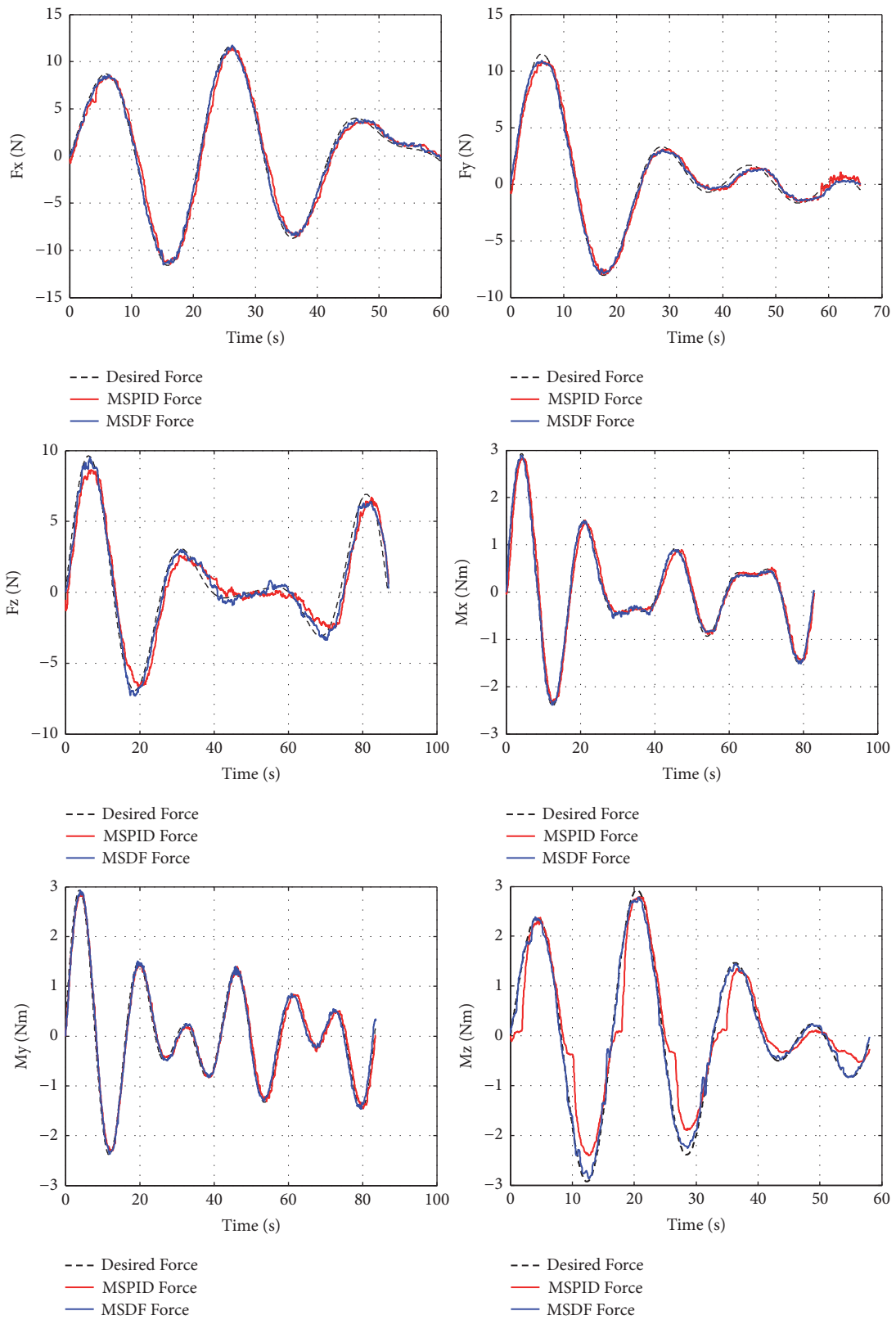


FIGURE 7: Responses to the desired special force signals with MSPID and MSDF controllers.

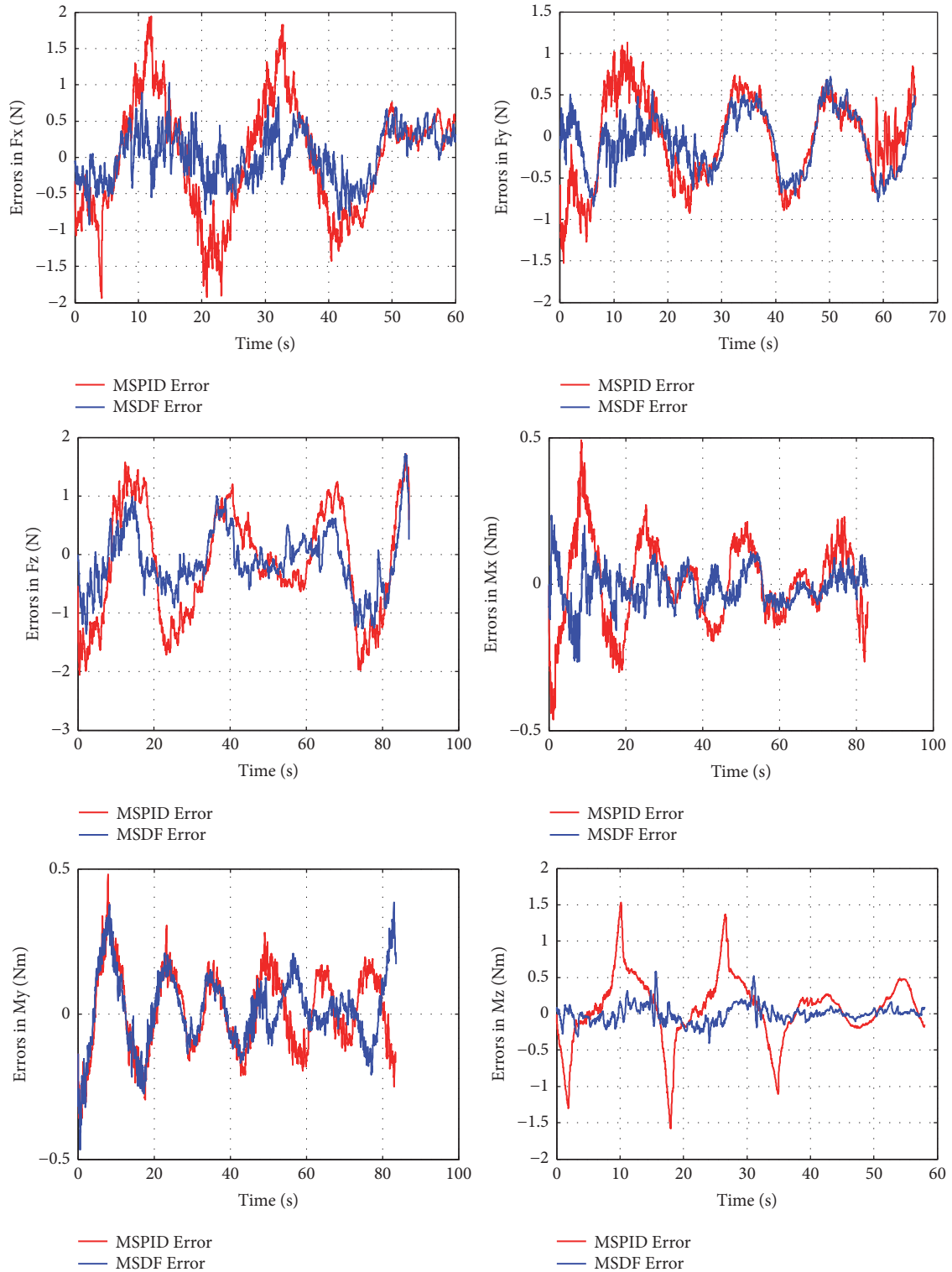


FIGURE 8: Dynamic tracking errors of parallel robotic manipulator with MSPID and MSDF controllers.

As shown in Figures 7 and 8, the dynamic response performance of the proposed MSDF controller in time domain is much better than that of MSPID controller in all directions. In comparison to the typical MSPID control method, the attenuation amplitude reduces 21% at least and

the lag phase is 47% at least with the presented MSDF force control strategy. Thus, the designed MSDF force control strategy can improve the control performance and dynamic tracking accuracy of the parallel robotic manipulator.

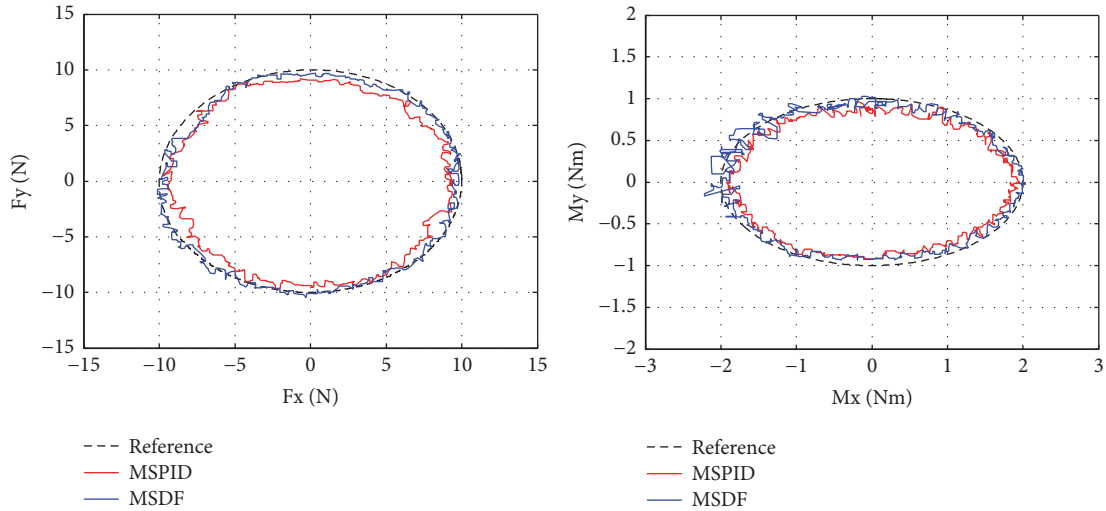


FIGURE 9: Responses to the combined force commands with MSPID and MSDF controllers.

However, the above experiments are all single-DOF. Thus, the combine force signals are desired for evaluating the performance of the robotic brace system. The desired force signals are applied on the parallel manipulator in EQ (51a), (51b), (51d), and (51e) and the responses are shown in Figure 9.

$$F_x = 10 \cos(0.377t) \quad (51a)$$

$$F_y = 10 \sin(0.377t) \quad (51b)$$

$$M_x = 2.0 \sin(0.314t) \quad (51d)$$

$$M_y = 1.0 \cos(0.314t) \quad (51e)$$

As can be seen from Figure 9, the robotic brace responds to the desired combined force signals much better under the MSDF control strategy than that of MSPID control strategy. MSDF controller has smaller track errors than the MSPID controller.

As can be deduced from Figures 6–9, the single freedom dynamic tracking performance of the robotic brace system with the presented MSDF controller is superior to that with the MSPID controller and the composite dynamic trajectory tracking performance is also better than the MSPID control strategy. MSDF controller not only solves the dynamic coupling in traditional physical space but compensates the gravity of the system. Besides, the steady-state error of the system with MSDF control method is also smaller than that of the MSPID control strategy. Thus, MSDF control can track the desired dynamic trajectory more quickly and accurately and applying high-precision 3D corrective forces on human spine.

## 6. Conclusion

This paper investigates modal space dynamic feed-forward control structure for parallel robotic manipulator, to overcome those boring problems. The system models are developed, including the dynamic model of the robotic spine brace, the actuator's dynamic model, and the forward kinematics

and inverse kinematics models of the system. Besides, the stability of the MSDF control strategy is analyzed and the novel controller reveals excellent robustness. Based on the typical PID force control method, those boring problems of parallel robotic manipulator greatly affect performances of the intelligent system in traditional physical space. For those boring problems, the MSDF active force control strategy is designed based on the dynamic feed-forward control algorithm and the modal decoupling approach. In order to verify performances of the parallel mechanism, experimental given signals are applied on the intelligent system with the proposed MSDF force control method. According to those experimental results, the MSDF force control algorithm can track the desired force dynamic trajectory more quickly and accurately, and apply high-precision 3D corrective forces on human spine. Compared with MSPID control method, the proposed MSDF control strategy presents excellent performance for the robotic spine brace. The system is stable and the state-errors of the system because of the boring problems tend to zero asymptotically.

Although performance of the system is excellent using the novel MSDF control strategy, there are some improvements needed to be done for this robotic spine brace in the future. Currently, this control strategy ignores disturbers from system nonlinearity, modeling errors, and other external interferences. In the future, an antidisturbance observer strategy should be developed to improve the performance and robustness of this robotic brace system. Furthermore, the current control method does not consider the model of human spine which is important for the control system. Thus, one of the next steps is building the three-dimensional model of human spine.

## Data Availability

The Matlab Source Code data used to support the findings of this study are available from the corresponding author upon request.

## Conflicts of Interest

The authors declare that there are no conflicts of interest regarding the publication of this paper.

## Authors' Contributions

Mr. Niu provided the ideas for this article and wrote this paper. Prof. Yang helped build the test platform and provided financial support for this paper. Dr. Tian made contributions to data collection and English check of the paper. Dr. Li made contributions to formula deduction of the paper and the revision of the review comments. Prof. Han made contributions to English check and collection of references and typesetting of this paper.

## Acknowledgments

The authors would also like to thank Dr. Sunil K Agrawal for the help of putting forward the concept of this robotic structure. The work was supported by the National Natural Science Foundation of China (grant number 51305095) and the Natural Science Foundation of Heilongjiang Province (grant number QC2013C045).

## References

- [1] S. L. Weinstein, L. A. Dolan, J. C. Cheng, A. Danielsson, and J. A. Morcuende, "Adolescent idiopathic scoliosis," *The Lancet*, vol. 371, no. 9623, pp. 1527–1537, 2008.
- [2] R. S. Fayssoux, R. H. Cho, and M. J. Herman, "A history of bracing for idiopathic scoliosis in north America," *Clinical Orthopaedics and Related Research*, vol. 468, no. 3, pp. 654–664, 2010.
- [3] M. A. Asher and D. C. Burton, "Adolescent idiopathic scoliosis: natural history and long term treatment effects," *Scoliosis*, vol. 1, pp. 2-2, 2006.
- [4] S. Negrini, S. Minozzi, J. Bettany-Saltikov, F. Zaina, N. Chockalingam, and T. B. Grivas, *Braces for Idiopathic Scoliosis in Adolescents*, John Wiley and Sons Ltd, 2007.
- [5] H.-R. Weiss and M. Werkmann, "Retraction: Soft braces in the treatment of Adolescent Idiopathic Scoliosis (AIS) - Review of the literature and description of a new approach," *Scoliosis*, vol. 8, no. 1, p. 7, 2013.
- [6] J.-H. Park, P. Stegall, and S. K. Agrawal, "Dynamic brace for correction of abnormal postures of the human spine," in *Proceedings of the 2015 IEEE International Conference on Robotics and Automation, ICRA 2015*, pp. 5922–5927, USA, May 2015.
- [7] J. P. Merlet, "Parallel robots," *Solid Mechanics and Its Applications*, vol. 128, pp. 2091–2127, 2010.
- [8] J. Wang and C. M. Gosselin, "Kinematic analysis and design of kinematically redundant parallel mechanisms," *Journal of Mechanical Design*, vol. 126, no. 1, pp. 109–118, 2004.
- [9] Y. Lou, Y. Zhang, R. Huang, X. Chen, and Z. Li, "Optimization algorithms for kinematically optimal design of parallel manipulators," *IEEE Transactions on Automation Science and Engineering*, vol. 11, no. 2, pp. 574–584, 2014.
- [10] T. Nozaki, T. Mizoguchi, and K. Ohnishi, "Decoupling strategy for position and force control based on modal space disturbance observer," *IEEE Transactions on Industrial Electronics*, vol. 61, no. 2, pp. 1022–1032, 2014.
- [11] A. A. Allais, J. E. McInroy, and J. F. O'Brien, "Locally decoupled micromanipulation using an even number of parallel force actuators," *IEEE Transactions on Robotics*, vol. 28, no. 6, pp. 1323–1334, 2012.
- [12] J. E. McInroy, J. F. O'Brien, and A. A. Allais, "Designing micromanipulation systems for decoupled dynamics and control," *IEEE/ASME Transactions on Mechatronics*, vol. 20, no. 2, pp. 553–563, 2015.
- [13] C. Gosselin and S. Foucault, "Dynamic point-to-point trajectory planning of a two-DOF cable-suspended parallel robot," *IEEE Transactions on Robotics*, vol. 30, no. 3, pp. 728–736, 2014.
- [14] M. Carricato and J. Merlet, "Stability analysis of underconstrained cable-driven parallel robots," *IEEE Transactions on Robotics*, vol. 29, no. 1, pp. 288–296, 2013.
- [15] J. Borras, F. Thomas, and C. Torras, "New geometric approaches to the analysis and design of stewart-gough platforms," *IEEE/ASME Transactions on Mechatronics*, vol. 19, no. 2, pp. 445–455, 2014.
- [16] K. A. Arrouk, B. C. Bouzgarrou, and G. Gogu, "CAD-based unified graphical methodology for solving the main problems related to geometric and kinematic analysis of planar parallel robotic manipulators," *Robotics and Computer-Integrated Manufacturing*, vol. 37, pp. 302–321, 2016.
- [17] J. Pile and N. Simaan, "Modeling, design, and evaluation of a parallel robot for cochlear implant surgery," *IEEE/ASME Transactions on Mechatronics*, vol. 19, no. 6, pp. 1746–1755, 2014.
- [18] P. K. Jamwal, S. Q. Xie, S. Hussain, and J. G. Parsons, "An adaptive wearable parallel robot for the treatment of ankle injuries," *IEEE/ASME Transactions on Mechatronics*, vol. 19, no. 1, pp. 64–75, 2014.
- [19] Y. Li and Q. Xu, "Dynamic modeling and robust control of a 3-PRC translational parallel kinematic machine," *Robotics and Computer-Integrated Manufacturing*, vol. 25, no. 3, pp. 630–640, 2009.
- [20] A. M. Mohammed and S. Li, "Dynamic neural networks for kinematic redundancy resolution of parallel stewart platforms," *IEEE Transactions on Cybernetics*, vol. 46, no. 7, pp. 1538–1550, 2016.
- [21] A. Dumlu and K. Erenturk, "Trajectory tracking control for a 3-DOF parallel manipulator using fractional-order PIAD $\mu$  control," *IEEE Transactions on Industrial Electronics*, vol. 61, pp. 3417–3426, 2014.
- [22] S.-H. Chen and L.-C. Fu, "Output feedback sliding mode control for a stewart platform with a nonlinear observer-based forward kinematics solution," *IEEE Transactions on Control Systems Technology*, vol. 21, no. 1, pp. 176–185, 2013.
- [23] S. Mishra, P. S. Londhe, S. Mohan, S. K. Vishvakarma, and B. M. Patre, "Robust task-space motion control of a mobile manipulator using a nonlinear control with an uncertainty estimator," *Computers and Electrical Engineering*, vol. 67, pp. 729–740, 2018.
- [24] S. A. Moosavian and E. Papadopoulos, "Modified transpose Jacobian control of robotic systems," *Automatica*, vol. 43, no. 7, pp. 1226–1233, 2007.
- [25] S. Kim, Y. J. Shin, K. Kim, and S. Kim, "Design and control of robot manipulator with a distributed actuation mechanism," *Mechatronics*, vol. 24, no. 8, pp. 1223–1230, 2014.
- [26] Y. Pi and X. Wang, "Observer-based cascade control of a 6-DOF parallel hydraulic manipulator in joint space coordinate," *Mechatronics*, vol. 20, no. 6, pp. 648–655, 2010.

- [27] C. Yang, Q. Huang, H. Jiang, O. Ogbobe Peter, and J. Han, "PD control with gravity compensation for hydraulic 6-DOF parallel manipulator," *Mechanism and Machine Theory*, vol. 45, no. 4, pp. 666–677, 2010.
- [28] S. Chen and L. Fu, "Observer-based backstepping control of a 6-dof parallel hydraulic manipulator," *Control Engineering Practice*, vol. 36, pp. 100–112, 2015.
- [29] A. Noshadi, M. Mailah, and A. Zolfagharian, "Active force control of 3-RRR planar parallel manipulator," *International Conference on Mechanical and Electrical Technology*, pp. 77–81, 2010.
- [30] T. K. Bera, R. Merzouki, B. Ould Bouamama, and A. K. Samantaray, "Force control in a parallel manipulator through virtual foundations," *Proceedings of the Institution of Mechanical Engineers, Part I: Journal of Systems and Control Engineering*, vol. 226, no. 8, pp. 1088–1106, 2012.
- [31] A. Lopes and F. Almeida, "A force-impedance controlled industrial robot using an active robotic auxiliary device," *Robotics and Computer Integrated Manufacturing*, vol. 24, pp. 299–309, 2008.
- [32] D. J. Goertzen and G. N. Kawchuk, "A novel application of velocity-based force control for use in robotic biomechanical testing," *Journal of Biomechanics*, vol. 42, no. 3, pp. 366–369, 2009.
- [33] S. Wen, H. Yu, B. Zhang et al., "Fuzzy identification and delay compensation based on the force/position control scheme of the 5-DOF redundantly actuated parallel robot," *International Journal of Fuzzy Systems*, vol. 19, no. 1, pp. 124–140, 2017.
- [34] C. Yang, Z. Qu, and J. Han, "Decoupled-space control and experimental evaluation of spatial electrohydraulic robotic manipulators using singular value decomposition algorithms," *IEEE Transactions on Industrial Electronics*, vol. 61, no. 7, pp. 3427–3438, 2014.
- [35] C. Yang and J. Han, "Dynamic coupling analysis of a spatial 6-DOF electro-hydraulic parallel manipulator using a modal decoupling method," *International Journal of Advanced Robotic Systems*, vol. 10, p. 1, 2013.
- [36] C. Yang, J. Zhao, L. Li, and S. K. Agrawal, "Design and implementation of a novel modal space active force control concept for spatial multi-DOF parallel robotic manipulators actuated by electrical actuators," *ISA Transactions*, vol. 72, pp. 273–286, 2018.
- [37] M. W. Spong, *Robot Dynamics and Control*, John Wiley and Sons, 1989.
- [38] L. Baron and J. Angeles, "The on-line direct kinematics of parallel manipulators under joint-sensor redundancy," *IEEE Transactions on Robotics & Automation*, vol. 16, no. 1, pp. 12–19, 2000.
- [39] S. Staicu, "Dynamics of the 6-6 Stewart parallel manipulator," *Robotics and Computer-Integrated Manufacturing*, vol. 27, no. 1, pp. 212–220, 2011.

## Research Article

# Extended Version of Linguistic Picture Fuzzy TOPSIS Method and Its Applications in Enterprise Resource Planning Systems

Shouzhen Zeng <sup>1,2</sup>, Muhammad Qiyas,<sup>3</sup> Muhammad Arif <sup>3</sup> and Tariq Mahmood<sup>4</sup>

<sup>1</sup>School of Management, Fudan University, Shanghai 200433, China

<sup>2</sup>School of Business, Ningbo University, Ningbo 315211, China

<sup>3</sup>Department of Mathematics, Abdul Wali Khan University Mardan, Pakistan

<sup>4</sup>Department of Electronics, University of Engineering and Technology, Taxila Sub-Campus Chakwal, Pakistan

Correspondence should be addressed to Muhammad Arif; marifmaths@awkum.edu.pk

Received 19 July 2018; Accepted 2 January 2019; Published 27 January 2019

Academic Editor: Mariusz Michta

Copyright © 2019 Shouzhen Zeng et al. This is an open access article distributed under the Creative Commons Attribution License, which permits unrestricted use, distribution, and reproduction in any medium, provided the original work is properly cited.

The main objective of the proposed research in this paper is introducing an extended version of the linguistic picture fuzzy TOPSIS technique and then solving the problems in enterprise resource planning systems. In this article, we use the uncertain information in terms of linguistic picture fuzzy numbers; the decision maker provides membership, neutral, and nonmembership fuzzy linguistic terms to represent uncertain assessments information of alternatives in linguistic multicriteria decision making (LMCDMs). In order to introduce the extended version of TOPSIS method, we defined a new hamming distance measure between two linguistic picture fuzzy numbers. Further, we apply the proposed method to problem of enterprise resource planning systems and discuss numerical implementation of the proposed method of LMCDM.

## 1. Introduction

In our daily life, we face some tasks and activities to handle with the help of decision making. Basically, decision making is an intellectual process which depends on different spiritual and reasoning processes; in the decision making process we choose a good alternative from the set of all available alternatives. For a single decision maker, it is mostly difficult to examine all related conditions of a problem due to the increasing complication of the socioeconomic environment. In everyday life, many decision making measures take place in group information. However, under more conditions, for the real multiple attribute decision making problems, the decision information about alternatives is usually uncertain or fuzzy due to the increasing complication of the socioeconomic situation and the ambiguity of inherent subjective attribute of human thinking; thus, numerical values are incomplete or partial for exemplary real-life decision problems. However, in practice, the attribute values of decision problems are not ever disposed by crisp information because of the fuzziness, and many of them are more considerable

to be stated by fuzzy information; see [1–5], such as fuzzy numbers, intuitionistic fuzzy numbers [6], and linguistic variable [7, 8].

Fuzzy set theory was firstly defined by Zadeh's in 1965 [9], which is a framework to encounter confusion, ambiguity, and exaggeration and perform a degree of membership for each member of the nature of discussion to a subset of it. Therefore, we have a forum of true values. The degree of nonmembership was added by Atanassov in 1983 to FS; Atanassov defined the notion of intuitionistic fuzzy set (IFS) [10], which is mostly permissible to handle the ambiguity quantification and give the occasion to correctly model the problem based on existing judgment and experience [11]. The two of these structures are assumed to be a soft approach which, in turn, start soft computing and approximate analysis [12].

Later on in 2014, Cuong proposed the concept of picture fuzzy set (PFS) and studied its basic operations and properties. The picture fuzzy set is designated by the membership, neutral, and nonmembership degree. The only restraint is that the sum of the membership, neutral, and nonmembership degrees must not exceed 1. PFS are basically used for those

models, which cannot be expressed in the traditional PS and IFS, like the opinions of the people which have answers of the following types: yes, abstain, no, and refusal. Already some promotion has happened in the research of the PFS theory. In (2014) P. H. Phong discussed the composition of picture fuzzy relation [13], and Singh studied the correlation coefficients for picture fuzzy set and tested the correlation coefficient for clustering analysis with picture fuzzy information. Son et al. developed many novel fuzzy clustering algorithms based on picture fuzzy sets and applications to time series forecasting and weather forecasting (Thong and Son, 2015). Wei [14] proposed picture fuzzy cross-entropy model for multiple attribute decision making problems. S. jun et al. (2017) defined picture uncertain linguistic aggregation operators [15]. In 2017 Phong and Cuong introduced the notion of picture linguistic set and handled MCGDM problem under PLNs environment [16].

In 1981 Hwang and Yoon introduced the idea of TOPSIS method; the idea that the selected alternative must be the closest from the positive ideal solution and the farthest from negative ideal solution is an outstanding multicriteria decision making method [17]. In (1996) Triantaphyllou et al. continued the TOPSIS strategy for decision making problem with fuzzy data [18]. Many authors extended TOPSIS methods and applied these on multiple attribute decision making [19, 20]. Chen (2000) stretches out TOPSIS to fuzzy group decision making problems [21]. Ashtiani et al. [22] used the TOPSIS method to solve decision making problem with the interval valued fuzzy sets. To deal with multiple attribute decision making problem with intuitionistic fuzzy sets, He and Gong [23] developed a natural generalization of the TOPSIS method. Liu et al. [24] proposed a new TOPSIS method for decision making problems with interval-valued intuitionistic fuzzy data.

The remainder of the article is structured as follows. In Section 2, we briefly discussed basic definitions and linguistic picture fuzzy numbers. In Section 3, we defined the Hamming distance between the two linguistic picture fuzzy sets and found the distance between the two PFSs. In Section 4, we discussed the framework of the linguistic picture fuzzy set TOPSIS method and explained an algorithm to solve the LMCDM problem with linguistic picture fuzzy environment. In Section 5, we solved an LMCDM problem to expose the achievement and practicality of the linguistic picture fuzzy set TOPSIS method, and we wrote the conclusion in the last section.

## 2. Preliminaries

*Definition 1* (see [12]). Let  $Y \neq \emptyset$  be a universal set. Then we defined the picture fuzzy set as

$$H = \{ \langle y, a_H(y), b_H(y), c_H(y) \rangle \mid y \in Y \} \quad (1)$$

Where  $a_H(y), b_H(y), c_H(y) : Y \rightarrow [0, 1]$ . For each  $y \in Y$ .  $a_H(y), b_H(y)$ , and  $c_H(y)$  are respectively, known as positive degree, neutral degree, and negative degree of  $Y$  in  $R$ , which satisfy the condition

$$a_H(y) + b_H(y) + c_H(y) \leq 1, \quad \forall y \in Y. \quad (2)$$

The refusal degree of  $Y$  in  $H$  is defined as  $\sigma_H(y) = 1 - a_H(y) - b_H(y) - c_H(y)$ , and if  $\sigma_H(y) = 0, \forall y \in Y$ , then  $H$  is reduced to an IFS [10], and if  $\sigma_H(y) = b_H(y) = 0$  for all  $y \in Y$ ,  $H$  is degenerated to an FS.

*Definition 2* (see [25, 26]). Let  $\check{L} = (\xi_0, \xi_1, \dots, \xi_{g-1})$  be the absolute order distinct term finite set. Then  $\check{L}$  is called a linguistic term set, where  $g$  is the odd cardinality with  $g > 0$ . Generally  $g$  is considered as 3, 5, 7, etc. For example, when  $g = 7$  the linguistic term set is as follows:

$$\check{L} = \langle \xi_0, \xi_1, \xi_2, \xi_3, \xi_4, \xi_5, \xi_6 \rangle \quad (3)$$

= (v. poor, poor, slightly poor, fair, slightly good, good, v. good)

If  $\xi_f, \xi_g \in \check{L}$ , then the following characteristics are satisfied:

- (1) The order of set as:  $\xi_f < \xi_g, \iff f < g$ ;
- (2) The operator of negation as:  $\text{neg}(\xi_f) = \xi_{g-1-f}$ ;
- (3) Maximum  $(\xi_f, \xi_g) = \xi_f$ , if  $f \geq g$ ;
- (4) Minimum  $(\xi_f, \xi_g) = \xi_g$ , if  $f \leq g$ .

*Definition 3* (see [16]). Let  $Y$  be a nonempty set; then we defined the picture linguistic number set  $R$  in  $Y$  as

$$H = \{ \langle y, \langle \xi_{\theta(y)}, a_H(y), b_H(y), c_H(y) \rangle \rangle \mid y \in Y \} \quad (4)$$

Which is designated by a linguistic term  $\xi_{\theta(x)} \in \check{L}$ , a positive degree, a neutral degree, and a negative degree  $a_H(y), b_H(y), c_H(y) \in [0, 1]$ , respectively, the element  $y$  to  $\xi_{\theta(y)}$  with the following condition:

$$a_H(y) + b_H(y) + c_H(y) \leq 1, \quad \forall y \in Y. \quad (5)$$

and  $\sigma_R(y) = 1 - a_H(y) - b_H(y) - c_H(y)$  is said to be the refusal degree of  $y$  to  $\xi_{\theta(y)}$  for all  $y \in Y$ .

If  $\sigma_H(Y) = 0, \forall y \in Y$ , in this case the picture linguistic set is reduced to the intuitionistic linguistic set.

*Definition 4*. Let  $\xi_a, \xi_b, \xi_c \in \check{L}_{[0,g]}$  and  $\alpha = \langle \xi_a, \xi_b, \xi_c \rangle$ , if  $a + b + c \leq g$ . Then,  $\alpha$  is called the linguistic picture fuzzy numbers on  $\check{L}_{[0,g]}$ . If  $\xi_a, \xi_b, \xi_c \in \check{L}$ , then we consider  $\alpha$  the original linguistic picture fuzzy numbers, and virtual linguistic picture fuzzy numbers, otherwise.

$\Gamma_{[0,g]} = \langle \langle \xi_a, \xi_b, \xi_c \rangle \mid \xi_a, \xi_b, \xi_c \in \check{L}_{[0,g]} \rangle$  represent all linguistic picture fuzzy numbers defined on  $\check{L}_{[0,g]}$ .

**Definition 5.** Let  $\langle \xi_a, \xi_b, \xi_c \rangle, \langle \xi_{a_1}, \xi_{b_1}, \xi_{c_1} \rangle, \langle \xi_{a_2}, \xi_{b_2}, \xi_{c_2} \rangle \in \Gamma_{[0,g]}$ . Then, the following operators hold by operations of picture fuzzy sets:

$$\begin{aligned}
 & \cdot \langle \xi_{a_1}, \xi_{b_1}, \xi_{c_1} \rangle \cup \langle \xi_{a_2}, \xi_{b_2}, \xi_{c_2} \rangle \\
 &= \langle \max(\xi_{a_1}, \xi_{a_2}), \min(\xi_{b_1}, \xi_{b_2}), \min(\xi_{c_1}, \xi_{c_2}) \rangle; \\
 & \cdot \langle \xi_{a_1}, \xi_{b_1}, \xi_{c_1} \rangle \cap \langle \xi_{a_2}, \xi_{b_2}, \xi_{c_2} \rangle \\
 &= \langle \min(\xi_{a_1}, \xi_{a_2}), \min(\xi_{b_1}, \xi_{b_2}), \max(\xi_{c_1}, \xi_{c_2}) \rangle; \\
 & \cdot \langle \xi_a, \xi_b, \xi_c \rangle^c = \langle \xi_c, \xi_b, \xi_a \rangle; \\
 & \cdot \langle \xi_{a_1}, \xi_{b_1}, \xi_{c_1} \rangle \subseteq \langle \xi_{a_2}, \xi_{b_2}, \xi_{c_2} \rangle \text{ iff } \xi_{a_1} \leq \xi_{a_2}, \xi_{b_1} \\
 & \geq \xi_{b_2} \text{ and } \xi_{c_1} \geq \xi_{c_2}; \\
 & \cdot \langle \xi_{a_1}, \xi_{b_1}, \xi_{c_1} \rangle = \langle \xi_{a_2}, \xi_{b_2}, \xi_{c_2} \rangle \text{ iff } \xi_{a_1} = \xi_{a_2}, \xi_{b_1} \\
 & = \xi_{b_2} \text{ and } \xi_{c_1} = \xi_{c_2}.
 \end{aligned} \tag{6}$$

**Definition 6.** Let  $\langle \xi_a, \xi_b, \xi_c \rangle, \langle \xi_{a_1}, \xi_{b_1}, \xi_{c_1} \rangle, \langle \xi_{a_2}, \xi_{b_2}, \xi_{c_2} \rangle \in \Gamma_{[0,g]}, \lambda > 0$ . Then we defined the following operations of linguistic picture fuzzy numbers:

$$\begin{aligned}
 & \cdot \langle \xi_{a_1}, \xi_{b_1}, \xi_{c_1} \rangle \oplus \langle \xi_{a_2}, \xi_{b_2}, \xi_{c_2} \rangle \\
 &= \langle \xi_{a_1+a_2-a_1a_2/g}, \xi_{b_1+b_2-b_1b_2/g}, \xi_{c_1+c_2-c_1c_2/g} \rangle; \\
 & \cdot \lambda \langle \xi_a, \xi_b, \xi_c \rangle = \langle \xi_{g-g(1-a/g)^\lambda}, \xi_{g(b/g)^\lambda}, \xi_{g(c/g)^\lambda} \rangle;
 \end{aligned} \tag{7}$$

**Definition 7.** Let  $\alpha_i = \langle \xi_{a_i}, \xi_{b_i}, \xi_{c_i} \rangle \in \Gamma_{[0,g]} (i = 1, 2, \dots, m)$  and  $\omega_i$  be the weighting vector of  $\alpha_i$ , satisfying  $0 \leq \omega_i \leq 1 (i = 1, 2, \dots, m)$  and  $\sum_{i=1}^m \omega_i = 1$ . Then, we defined the linguistic picture fuzzy weighted averaging operator as

$$\begin{aligned}
 & LPFWA(\alpha_1, \alpha_2, \dots, \alpha_m) \\
 &= \langle \xi_{g-g \prod_{i=1}^m (1-a_i/g)^{\omega_i}}, \xi_{g \prod_{i=1}^m (b_i/g)^{\omega_i}}, \xi_{g \prod_{i=1}^m (c_i/g)^{\omega_i}} \rangle
 \end{aligned} \tag{8}$$

As a special case, if  $\omega = (1/n, 1/n, \dots, 1/n)$ , then equation (8) is reduced to the following form:

$$\begin{aligned}
 & LPFWA(\alpha_1, \alpha_2, \dots, \alpha_m) \\
 &= \langle \xi_{g-g \prod_{i=1}^m (1-a_i/g)^{1/n}}, \xi_{g \prod_{i=1}^m (b_i/g)^{1/n}}, \xi_{g \prod_{i=1}^m (c_i/g)^{1/n}} \rangle
 \end{aligned} \tag{9}$$

**Example 8.** Let  $X = \langle x_1, x_2, x_3 \rangle, C = \langle c_1, c_2, c_3 \rangle$  be the sets of alternatives and criteria, respectively. The linguistic set  $\check{L} = \xi_0$  (nothing),  $\xi_1$  (very very low),  $\xi_2$  (very low),  $\xi_3$  (low),  $\xi_4$  (medium),  $\xi_5$  (high),  $\xi_6$  (very high),  $\xi_7$  (very very high),  $\xi_8$  (perfect). The decision makers provide the linguistic picture fuzzy assessments as shown in Table 1.

### 3. The Distance between Two Linguistic Picture Fuzzy Numbers

In TOPSIS method the distance measure is an important concept. We can define the following Hamming distance between two linguistic picture fuzzy sets.

**Definition 9.** Let  $A = \langle \xi_{a_1}, \xi_{b_1}, \xi_{c_1} \rangle$  and  $B = \langle \xi_{a_2}, \xi_{b_2}, \xi_{c_2} \rangle$  be the two linguistic picture fuzzy numbers. Then we defined the Hamming distance between  $A$  and  $B$  as

$$d(A, B) = \frac{|a_1 - a_2| + |b_1 - b_2| + |c_1 - c_2| + |\tau_1 - \tau_2|}{2g} \tag{10}$$

**Example 10.** In Example 8, for  $A_1 = \langle \xi_2, \xi_3, \xi_3 \rangle$  of  $x_1, A_2 = \langle \xi_1, \xi_5, \xi_2 \rangle$  of  $x_2$  and  $A_3 = \langle \xi_4, \xi_1, \xi_4 \rangle$  of  $x_3$ , in addition,  $\tau_1 = 9 - 2 - 3 - 3 = 1, \tau_2 = 9 - 1 - 5 - 2 = 1$ , and  $\tau_3 = 9 - 4 - 1 - 4 = 0$ ,

$$\begin{aligned}
 d(A_1, A_2) &= \frac{|2 - 1| + |3 - 5| + |3 - 2| + |1 - 1|}{2(9)} = \frac{4}{18} \\
 &= 0.22, \\
 d(A_1, A_3) &= \frac{|2 - 4| + |3 - 1| + |3 - 4| + |1 - 0|}{2(9)} = \frac{6}{18} \\
 &= 0.33, \\
 d(A_2, A_3) &= \frac{|1 - 4| + |5 - 1| + |2 - 4| + |1 - 0|}{2(9)} = \frac{10}{18} \\
 &= 0.56,
 \end{aligned} \tag{11}$$

## 4. The Linguistic Picture Fuzzy Set TOPSIS Method

To solve the LMCDMs problem, we present the linguistic picture fuzzy set TOPSIS method, which consists of the following steps.

**Step 1.** Construct the linguistic picture fuzzy decision matrix,

**Step 2.** With the help of averaging operator, find the positive and negative ideal solutions of alternatives.

**Step 3.** For every alternative, find the relative closeness degree.

**Step 4.** Give rank to the alternatives, based on relative closeness degree.

**4.1. The Linguistic Picture Fuzzy Decision Matrix.** Let  $A_{ji} = \langle \xi_{a_{ji}}, \xi_{b_{ji}}, \xi_{c_{ji}} \rangle$  be the linguistic picture fuzzy assessment of the alternatives  $x_i$  provided by the decision makers  $d_j$  with respect to the criteria  $C = \langle c_1, c_2, \dots, c_m \rangle$  and let  $\omega = \langle \omega_1, \omega_2, \dots, \omega_m \rangle$  be the weight of criteria. Then the linguistic picture fuzzy decision matrix of a LMCDM is written as

$$\begin{aligned}
 D &= \langle A_{ji} \rangle_{n \times m} \\
 &= \begin{pmatrix} & C(\omega_1) & \dots & C(\omega_m) \\ x_1 & \langle \xi_{a_{11}}, \xi_{b_{11}}, \xi_{c_{11}} \rangle & \dots & \langle \xi_{a_{1m}}, \xi_{b_{1m}}, \xi_{c_{1m}} \rangle \\ x_2 & \langle \xi_{a_{21}}, \xi_{b_{21}}, \xi_{c_{21}} \rangle & \dots & \langle \xi_{a_{2m}}, \xi_{b_{2m}}, \xi_{c_{2m}} \rangle \\ \vdots & \vdots & \ddots & \vdots \\ \vdots & \vdots & \ddots & \vdots \\ \vdots & \vdots & \ddots & \vdots \\ x_n & \langle \xi_{a_{n1}}, \xi_{b_{n1}}, \xi_{c_{n1}} \rangle & \dots & \langle \xi_{a_{nm}}, \xi_{b_{nm}}, \xi_{c_{nm}} \rangle \end{pmatrix} \tag{12}
 \end{aligned}$$

TABLE 1: Linguistic picture assessments of alternatives.

		$c_1$	$c_2$	$c_3$
$d$	$x_1$	$\langle \mathfrak{E}_2, \mathfrak{E}_3, \mathfrak{E}_3 \rangle$	$\langle \mathfrak{E}_4, \mathfrak{E}_2, \mathfrak{E}_1 \rangle$	$\langle \mathfrak{E}_1, \mathfrak{E}_3, \mathfrak{E}_5 \rangle$
	$x_2$	$\langle \mathfrak{E}_1, \mathfrak{E}_5, \mathfrak{E}_2 \rangle$	$\langle \mathfrak{E}_3, \mathfrak{E}_4, \mathfrak{E}_1 \rangle$	$\langle \mathfrak{E}_2, \mathfrak{E}_3, \mathfrak{E}_4 \rangle$
	$x_3$	$\langle \mathfrak{E}_4, \mathfrak{E}_1, \mathfrak{E}_4 \rangle$	$\langle \mathfrak{E}_4, \mathfrak{E}_1, \mathfrak{E}_3 \rangle$	$\langle \mathfrak{E}_3, \mathfrak{E}_2, \mathfrak{E}_3 \rangle$

*Example 11.* In Example 8, suppose that  $\omega = \langle 0.3, 0.4, 0.3 \rangle$  are the weight of criteria  $C = \langle c_1, c_2, c_3 \rangle$ ; then the linguistic picture fuzzy decision matrix of the LMCDM is

$$D = \langle A_{ji} \rangle_{3 \times 3} = \begin{pmatrix} c_1 \langle 0.3 \rangle & c_2 \langle 0.4 \rangle & c_3 \langle 0.3 \rangle \\ x_1 \langle \mathfrak{E}_2, \mathfrak{E}_3, \mathfrak{E}_3 \rangle & \langle \mathfrak{E}_4, \mathfrak{E}_2, \mathfrak{E}_1 \rangle & \langle \mathfrak{E}_1, \mathfrak{E}_3, \mathfrak{E}_5 \rangle \\ x_2 \langle \mathfrak{E}_1, \mathfrak{E}_5, \mathfrak{E}_2 \rangle & \langle \mathfrak{E}_3, \mathfrak{E}_4, \mathfrak{E}_1 \rangle & \langle \mathfrak{E}_2, \mathfrak{E}_3, \mathfrak{E}_4 \rangle \\ x_3 \langle \mathfrak{E}_4, \mathfrak{E}_1, \mathfrak{E}_4 \rangle & \langle \mathfrak{E}_4, \mathfrak{E}_1, \mathfrak{E}_3 \rangle & \langle \mathfrak{E}_3, \mathfrak{E}_2, \mathfrak{E}_3 \rangle \end{pmatrix} \quad (13)$$

*4.2. The Positive and Negative Ideal Solutions of Alternatives.* To determine the positive ideal solution and negative ideal solution of the alternatives, we apply the  $\cup$  and  $\cap$  operation of the linguistic picture fuzzy numbers and the linguistic picture fuzzy weighted averaging operator on the linguistic picture fuzzy matrix.

Operation  $\cup$  and  $\cap$  of linguistic picture fuzzy sets for each column is defined as

$$\begin{aligned} \vee c_j &= \langle \mathfrak{E}_{\vee a_j}, \mathfrak{E}_{\vee b_j}, \mathfrak{E}_{\vee c_j} \rangle = \bigcup_{j=1}^n A_{ji} = \bigcup_{j=1}^n \langle \mathfrak{E}_{a_{ji}}, \mathfrak{E}_{b_{ji}}, \mathfrak{E}_{c_{ji}} \rangle \\ &= \langle \max(\mathfrak{E}_{a_{1i}}, \mathfrak{E}_{a_{2i}}, \dots, \mathfrak{E}_{a_{ni}}), \min(\mathfrak{E}_{b_{1i}}, \mathfrak{E}_{b_{2i}}, \dots, \mathfrak{E}_{b_{ni}}), \\ &\quad \min(\mathfrak{E}_{c_{1i}}, \mathfrak{E}_{c_{2i}}, \dots, \mathfrak{E}_{c_{ni}}) \rangle \\ \wedge c_j &= \langle \mathfrak{E}_{\wedge a_j}, \mathfrak{E}_{\wedge b_j}, \mathfrak{E}_{\wedge c_j} \rangle = \bigcap_{j=1}^n A_{ji} = \bigcap_{j=1}^n \langle \mathfrak{E}_{a_{ji}}, \mathfrak{E}_{b_{ji}}, \\ &\quad \mathfrak{E}_{c_{ji}} \rangle = \langle \min(\mathfrak{E}_{a_{1i}}, \mathfrak{E}_{a_{2i}}, \dots, \mathfrak{E}_{a_{ni}}), \\ &\quad \min(\mathfrak{E}_{b_{1i}}, \mathfrak{E}_{b_{2i}}, \dots, \mathfrak{E}_{b_{ni}}), \max(\mathfrak{E}_{c_{1i}}, \mathfrak{E}_{c_{2i}}, \dots, \mathfrak{E}_{c_{ni}}) \rangle \end{aligned} \quad (14)$$

On the basis of  $\vee c_j, \wedge c_j$  and weight  $\omega = \langle \omega_1, \omega_2, \dots, \omega_m \rangle$  of criteria  $C = \langle c_1, c_2, \dots, c_m \rangle$ , to find the positive and negative ideal solutions of alternatives, using the linguistic picture fuzzy weighted averaging operator,

$$PIS = \langle \mathfrak{E}_{a_p}, \mathfrak{E}_{b_p}, \mathfrak{E}_{c_p} \rangle = LPFWA \langle \vee c_1, \vee c_2, \dots, \vee c_m \rangle \quad (15)$$

$$\begin{aligned} &= \langle \mathfrak{E}_{g-g \prod_{i=1}^m (1-\vee a_i/g)^{\omega_i}}, \mathfrak{E}_{g \prod_{i=1}^m (\vee b_i/g)^{\omega_i}}, \mathfrak{E}_{g \prod_{i=1}^m (\vee c_i/g)^{\omega_i}} \rangle \\ NIS &= \langle \mathfrak{E}_{a_n}, \mathfrak{E}_{b_n}, \mathfrak{E}_{c_n} \rangle = LPFWA \langle \wedge c_1, \wedge c_2, \dots, \wedge c_m \rangle \quad (16) \\ &= \langle \mathfrak{E}_{g-g \prod_{i=1}^m (1-\wedge a_i/g)^{\omega_i}}, \mathfrak{E}_{g \prod_{i=1}^m (\wedge b_i/g)^{\omega_i}}, \mathfrak{E}_{g \prod_{i=1}^m (\wedge c_i/g)^{\omega_i}} \rangle \end{aligned}$$

*Example 12.* According to  $D$  in Example 8, we have

$$\begin{aligned} \vee c_1 &= \bigcup_{j=1}^3 A_{j1} = \langle \max(\mathfrak{E}_2, \mathfrak{E}_3, \mathfrak{E}_3), \min(\mathfrak{E}_1, \mathfrak{E}_5, \mathfrak{E}_2), \\ &\quad \min(\mathfrak{E}_4, \mathfrak{E}_1, \mathfrak{E}_4) \rangle = \langle \mathfrak{E}_3, \mathfrak{E}_1, \mathfrak{E}_1 \rangle, \\ \wedge c_1 &= \bigcap_{j=1}^3 A_{j1} = \langle \min(\mathfrak{E}_2, \mathfrak{E}_3, \mathfrak{E}_3), \min(\mathfrak{E}_1, \mathfrak{E}_5, \mathfrak{E}_2), \\ &\quad \max(\mathfrak{E}_4, \mathfrak{E}_1, \mathfrak{E}_4) \rangle = \langle \mathfrak{E}_2, \mathfrak{E}_1, \mathfrak{E}_4 \rangle, \\ \vee c_2 &= \bigcup_{j=1}^3 A_{j2} = \langle \max(\mathfrak{E}_4, \mathfrak{E}_2, \mathfrak{E}_1), \min(\mathfrak{E}_3, \mathfrak{E}_4, \mathfrak{E}_1), \\ &\quad \min(\mathfrak{E}_4, \mathfrak{E}_1, \mathfrak{E}_3) \rangle = \langle \mathfrak{E}_4, \mathfrak{E}_1, \mathfrak{E}_1 \rangle, \\ \wedge c_2 &= \bigcap_{j=1}^3 A_{j2} = \langle \min(\mathfrak{E}_4, \mathfrak{E}_2, \mathfrak{E}_1), \min(\mathfrak{E}_3, \mathfrak{E}_4, \mathfrak{E}_1), \\ &\quad \max(\mathfrak{E}_4, \mathfrak{E}_1, \mathfrak{E}_3) \rangle = \langle \mathfrak{E}_1, \mathfrak{E}_1, \mathfrak{E}_4 \rangle, \\ \vee c_3 &= \bigcup_{j=1}^3 A_{j3} = \langle \max(\mathfrak{E}_1, \mathfrak{E}_3, \mathfrak{E}_5), \min(\mathfrak{E}_2, \mathfrak{E}_3, \mathfrak{E}_4), \\ &\quad \min(\mathfrak{E}_3, \mathfrak{E}_2, \mathfrak{E}_3) \rangle = \langle \mathfrak{E}_5, \mathfrak{E}_2, \mathfrak{E}_2 \rangle, \\ \wedge c_3 &= \bigcap_{j=1}^3 A_{j3} = \langle \min(\mathfrak{E}_1, \mathfrak{E}_3, \mathfrak{E}_5), \min(\mathfrak{E}_2, \mathfrak{E}_3, \mathfrak{E}_4), \\ &\quad \max(\mathfrak{E}_3, \mathfrak{E}_2, \mathfrak{E}_3) \rangle = \langle \mathfrak{E}_1, \mathfrak{E}_2, \mathfrak{E}_3 \rangle \end{aligned} \quad (17)$$

Based on equations (15) and (16), we calculate PIS and NIS of  $D$ ,

$$\begin{aligned} PIS &= \langle \mathfrak{E}_{a_p}, \mathfrak{E}_{b_p}, \mathfrak{E}_{c_p} \rangle = LPFWA \langle \vee c_1, \vee c_2, \dots, \vee c_m \rangle \\ &= \langle \mathfrak{E}_{9-9 \prod_{i=1}^3 (1-\vee a_i/9)^{\omega_i}}, \mathfrak{E}_{9 \prod_{i=1}^3 (\vee b_i/9)^{\omega_i}}, \mathfrak{E}_{9 \prod_{i=1}^3 (\vee c_i/9)^{\omega_i}} \rangle \\ &= \mathfrak{E}_{9-9[(1-3/9)^{0.3} \times (1-4/9)^{0.4} \times (1-5/9)^{0.3}]} \mathfrak{E}_{9[(1/9)^{0.7} \times (2/9)^{0.3}]} \\ &\quad \mathfrak{E}_{9[(1/9)^{0.7} \times (2/9)^{0.3}] = \langle \mathfrak{E}_{4.10}, \mathfrak{E}_{1.26}, \mathfrak{E}_{1.22} \rangle \quad (18) \\ NIS &= \langle \mathfrak{E}_{a_n}, \mathfrak{E}_{b_n}, \mathfrak{E}_{c_n} \rangle = LPFWA \langle \wedge c_1, \wedge c_2, \dots, \wedge c_m \rangle \\ &= \langle \mathfrak{E}_{g-g \prod_{i=1}^m (1-\wedge a_i/g)^{\omega_i}}, \mathfrak{E}_{g \prod_{i=1}^m (\wedge b_i/g)^{\omega_i}}, \mathfrak{E}_{g \prod_{i=1}^m (\wedge c_i/g)^{\omega_i}} \rangle \\ &= \mathfrak{E}_{9-9[(1-2/9)^{0.3} \times (1-1/9)^{0.7}]} \mathfrak{E}_{9[(1/9)^{0.7} \times (2/9)^{0.3}]} \\ &\quad \mathfrak{E}_{9[(4/9)^{0.7} \times (3/9)^{0.3}] = \langle \mathfrak{E}_{1.29}, \mathfrak{E}_{1.22}, \mathfrak{E}_{3.68} \rangle \end{aligned}$$

4.3. *The Relative Closeness and the Ranking of Alternatives.* For the alternatives ranking, we find for every alternative the relative close degree, where the relative close degree is determined by distance between the linguistic picture fuzzy assessment of each alternative and the positive and negative ideal solutions. Based on the decision matrix, we obtain the linguistic picture fuzzy set  $A_j$  of  $x_j$ , using the linguistic picture fuzzy weighted averaging operator:

$$A_j = LPFWA \langle A_{j1}, A_{j2}, \dots, A_{jm} \rangle \tag{19}$$

$$= \langle \xi_{g-g\prod_{i=1}^m (1-a_{ji}/g)^{\omega_i}}, \xi_{g\prod_{i=1}^m (b_{ji}/g)^{\omega_i}}, \xi_{g\prod_{i=1}^m (c_{ji}/g)^{\omega_i}} \rangle$$

Based on  $A_j$  of  $x_j$ , the Hamming distance between the linguistic picture fuzzy set of individual alternative and the positive and negative ideal solutions is obtained utilizing PIS (equation (15)) and NIS (equation (16)) and equation (10):

$$d \langle A_j, PIS \rangle = \frac{|a_j - a_p| + |b_j - b_p| + |c_j - c_p| + |\tau_j - \tau_p|}{2g} \tag{20}$$

$$d \langle A_j, NIS \rangle = \frac{|a_j - a_n| + |b_j - b_n| + |c_j - c_n| + |\tau_j - \tau_n|}{2g} \tag{21}$$

Where  $\tau_j = g - a_j - b_j - c_j$ ,  $\tau_p = g - a_p - b_p - c_p$ ,  $\tau_n = g - a_n - b_n - c_n$

Originating from the TOPSIS method, the ranking of alternatives is the following bases “select the shortest distance and the farthest distance from the positive and negative ideal solutions, respectively”; formally, it is fulfilled by the relative close degree of each alternative in existing TOPSIS methods. Based on Hamming distance between the linguistic picture fuzzy set of each alternative and the positive and negative ideal solutions (Eqs. (20) and (21)), we supply for each alternative  $x_i$  the following relative closeness degree  $C(x_j)$ :

$$d_{\max}^- = \max \langle d(A_1, NIS), d(A_2, NIS), \dots, d(A_n, NIS) \rangle \tag{22}$$

$$d_{\min}^+ = \min \langle d(A_1, PIS), d(A_2, PIS), \dots, d(A_n, PIS) \rangle \tag{23}$$

$$C(x_i) = \frac{1}{2} \left\langle \frac{d(A_j, NIS)}{d_{\max}^-} + \frac{d_{\min}^+}{d(A_j, PIS)} \right\rangle \tag{24}$$

Basically,  $C(x_i) \in [0, 1]$  for any alternative  $x_i$ ; that is,  $C(x_i)$  is increasing for  $d(A_j, NIS)$ , and decreasing for  $d(A_j, PIS)$ . The alternative rankings are obtained based on the relative closeness degree of alternatives as follows:  $\forall x_j, x_j^* \in X$ ,

$$x_j < x_j^* \iff C(x_j) \leq C(x_j^*) \tag{25}$$

*Example 13.* According to  $D$  in Example 8, and equation (19), we collect the linguistic picture fuzzy assessment of each alternative as follows:

$$A_1 = LPFWA \{ \langle \xi_2, \xi_3, \xi_3 \rangle, \langle \xi_4, \xi_2, \xi_1 \rangle, \langle \xi_1, \xi_3, \xi_5 \rangle \}$$

$$= \langle \xi_{9-9[(1-2/9)^{0.3} \times (1-4/9)^{0.4} \times (1-1/9)^{0.3}]}, \xi_{9[(3/9)^{0.7} \times (2/9)^{0.3}]}, \xi_{9[(3/9)^{0.3} \times (1/9)^{0.4} \times (5/9)^{0.3}]} \rangle = \langle \xi_{2.65}, \xi_{2.53}, \xi_{2.17} \rangle$$

$$A_2 = LPFWA \{ \langle \xi_1, \xi_5, \xi_2 \rangle, \langle \xi_3, \xi_4, \xi_1 \rangle, \langle \xi_2, \xi_3, \xi_4 \rangle \}$$

$$= \langle \xi_{9-9[(1-1/9)^{0.3} \times (1-3/9)^{0.4} \times (1-2/9)^{0.3}]}, \xi_{9[(5/9)^{0.3} \times (4/9)^{0.4} \times (3/9)^{0.3}]}, \xi_{9[(2/9)^{0.3} \times (1/9)^{0.4} \times (4/9)^{0.3}]} \rangle$$

$$= \langle \xi_{2.19}, \xi_{3.87}, \xi_{1.71} \rangle$$

$$A_3 = LPFWA \{ \langle \xi_4, \xi_1, \xi_4 \rangle, \langle \xi_4, \xi_1, \xi_3 \rangle, \langle \xi_3, \xi_2, \xi_3 \rangle \}$$

$$= \langle \xi_{9-9[(1-4/9)^{0.7} \times (1-3/9)^{0.3}]}, \xi_{9[(1/9)^{0.7} \times (2/9)^{0.3}]}, \xi_{9[(4/9)^{0.3} \times (3/9)^{0.7}]} \rangle = \langle \xi_{3.66}, \xi_{1.23}, \xi_{3.25} \rangle$$

Based on PIS and NIS in Example 12 and Equations (20) and (21), we obtain

$$d(A_1, PIS) = \frac{|2.65 - 4.10| + |2.53 - 1.26| + |2.17 - 1.22| + |1.65 - 2.42|}{2(9)} \tag{27}$$

$$= 0.25$$

and

$$d(A_1, NIS) = \frac{|2.65 - 1.29| + |2.53 - 1.22| + |2.17 - 3.36| + |1.65 - 3.13|}{2(9)} \tag{28}$$

$$= 0.28$$

Similarly,  $d(A_2, PIS) = 0.34$  and  $d(A_2, NIS) = 0.39$ ,  $d(A_3, PIS) = 0.21$  and  $d(A_3, NIS) = 0.25$ .

Now we get the following results, applying equations (22), (23), and (24):

$$d_{\max}^- = \langle 0.28, 0.39, 0.25 \rangle = 0.39$$

$$d_{\min}^+ = \langle 0.25, 0.34, 0.21 \rangle = 0.21$$

$$C(x_1) = \frac{1}{2} \left\langle \frac{0.28}{0.39} + \frac{0.21}{0.25} \right\rangle = 0.78 \tag{29}$$

$$C(x_2) = \frac{1}{2} \left\langle \frac{0.39}{0.39} + \frac{0.21}{0.34} \right\rangle = 0.79$$

$$C(x_3) = \frac{1}{2} \left\langle \frac{0.25}{0.39} + \frac{0.21}{0.21} \right\rangle = 0.81$$

According to equation (25), the ranking is as follows:

$$x_3 > x_2 > x_1 \tag{30}$$

Hence,  $x_3$  is the best alternative.

*Algorithm 14.*

*Step 1.* According to the membership, neutral, and nonmembership fuzzy linguistic assessments, the decision matrix  $D$  of the LMCDM problem is constructed.

*Step 2.* Calculate  $\forall c_i$  and  $\wedge c_i$ , for each column, using the linguistic picture fuzzy weighted averaging operator to determine the PIS and NIS.

*Step 3.* To find the linguistic picture fuzzy assessment  $A_j$  of each  $x_j$ , use the linguistic picture fuzzy weighted averaging operator.

*Step 4.* Find the Hamming distance  $d(A_j, PIS)$  and  $d(A_j, NIS)$  between each  $A_j$  and PIS (NIS) are calculated; the maximum Hamming distance  $d_{\max}^-$  of all  $d(A_j, NIS)$  and minimum Hamming distance  $d_{\min}^+$  of all  $d(A_j, PIS)$  are obtained; then calculate the relative close degree  $C(x_j)$  of every alternative  $x_j$ .

*Step 5.* Rank the alternatives using equation (25).

**5. Example**

A multinational company chooses an enterprise resource planning system to apply from three candidates  $A = (a_1, a_2, a_3)$ . To develop other considerable decisions, the Chief Information Officer (CIO) of the company evaluates the applicant enterprise resource planning systems in terms of three criteria, that is,  $c_1$  (energy cost),  $c_2$  (business), and  $c_3$  (procedure complication), where (0.3, 0.5, 0.2) are the weight of the criteria. Since the given criteria are qualitative, the estimated values are in the form of linguistic term, which are shown in Table 2.

*Step 2.* For each column of  $D$ , we have

$$\begin{aligned}
 \forall c_1 &= \langle \max(\mathfrak{L}_4, \mathfrak{L}_3, \mathfrak{L}_2), \min(\mathfrak{L}_2, \mathfrak{L}_3, \mathfrak{L}_2), \\
 &\quad \min(\mathfrak{L}_2, \mathfrak{L}_3, \mathfrak{L}_2) \rangle = \langle \mathfrak{L}_4, \mathfrak{L}_2, \mathfrak{L}_2 \rangle, \\
 \forall c_2 &= \langle \max(\mathfrak{L}_4, \mathfrak{L}_2, \mathfrak{L}_3), \min(\mathfrak{L}_3, \mathfrak{L}_5, \mathfrak{L}_4), \\
 &\quad \min(\mathfrak{L}_1, \mathfrak{L}_1, \mathfrak{L}_2) \rangle = \langle \mathfrak{L}_4, \mathfrak{L}_3, \mathfrak{L}_1 \rangle, \\
 \forall c_3 &= \langle \max(\mathfrak{L}_6, \mathfrak{L}_3, \mathfrak{L}_7), \min(\mathfrak{L}_1, \mathfrak{L}_2, \mathfrak{L}_1), \\
 &\quad \min(\mathfrak{L}_2, \mathfrak{L}_4, \mathfrak{L}_1) \rangle = \langle \mathfrak{L}_7, \mathfrak{L}_1, \mathfrak{L}_1 \rangle, \\
 \wedge c_1 &= \langle \min(\mathfrak{L}_4, \mathfrak{L}_3, \mathfrak{L}_2), \min(\mathfrak{L}_2, \mathfrak{L}_3, \mathfrak{L}_2), \\
 &\quad \max(\mathfrak{L}_2, \mathfrak{L}_3, \mathfrak{L}_2) \rangle = \langle \mathfrak{L}_2, \mathfrak{L}_2, \mathfrak{L}_3 \rangle, \\
 \wedge c_2 &= \langle \min(\mathfrak{L}_4, \mathfrak{L}_2, \mathfrak{L}_3), \min(\mathfrak{L}_3, \mathfrak{L}_5, \mathfrak{L}_4), \\
 &\quad \max(\mathfrak{L}_1, \mathfrak{L}_1, \mathfrak{L}_2) \rangle = \langle \mathfrak{L}_2, \mathfrak{L}_3, \mathfrak{L}_2 \rangle, \\
 \wedge c_3 &= \langle \min(\mathfrak{L}_4, \mathfrak{L}_3, \mathfrak{L}_2), \min(\mathfrak{L}_2, \mathfrak{L}_3, \mathfrak{L}_2), \\
 &\quad \max(\mathfrak{L}_2, \mathfrak{L}_3, \mathfrak{L}_2) \rangle = \langle \mathfrak{L}_2, \mathfrak{L}_2, \mathfrak{L}_3 \rangle.
 \end{aligned} \tag{31}$$

Using equations (15) and (16), we find that the positive and negative ideal solutions are

$$\begin{aligned}
 PIS &= LPFWA \langle \forall c_1, \forall c_2, \dots, \forall c_m \rangle \\
 &= \mathfrak{L}_{9^{-9[(1-4/9)^{0.3} \times (1-4/9)^{0.5} \times (1-7/9)^{0.2}]}} \\
 &\quad \mathfrak{L}_{9^{[(2/9)^{0.3} \times (3/9)^{0.5} \times (1/9)^{0.2}]}} \mathfrak{L}_{9^{[(2/9)^{0.3} \times (1/9)^{0.5} \times (1/9)^{0.2}]} \\
 &= \langle \mathfrak{L}_{4.80}, \mathfrak{L}_{2.15}, \mathfrak{L}_{1.26} \rangle \\
 NIS &= \langle \mathfrak{L}_{a_n}, \mathfrak{L}_{b_n}, \mathfrak{L}_{c_n} \rangle = LPFWA \langle \wedge c_1, \wedge c_2, \dots, \wedge c_m \rangle \\
 &= \mathfrak{L}_{9^{-9[(1-2/9)^{0.3} \times (1-2/9)^{0.5} \times (1-2/9)^{0.2}]}} \\
 &\quad \mathfrak{L}_{9^{[(2/9)^{0.3} \times (3/9)^{0.5} \times (2/9)^{0.2}]}} \mathfrak{L}_{9^{[(3/9)^{0.3} \times (2/9)^{0.5} \times (3/9)^{0.2}]} \\
 &= \langle \mathfrak{L}_{1.99}, \mathfrak{L}_{2.47}, \mathfrak{L}_{2.41} \rangle
 \end{aligned} \tag{32}$$

*Step 3.* Using (19), for each row of  $D$ , then

$$\begin{aligned}
 A_1 &= LPFWA \langle (\mathfrak{L}_4, \mathfrak{L}_2, \mathfrak{L}_2), (\mathfrak{L}_4, \mathfrak{L}_3, \mathfrak{L}_1), (\mathfrak{L}_6, \mathfrak{L}_1, \mathfrak{L}_2) \rangle \\
 &= \mathfrak{L}_{9^{-9[(1-4/9)^{0.3} \times (1-4/9)^{0.5} \times (1-6/9)^{0.2}]}} \\
 &\quad \mathfrak{L}_{9^{[(2/9)^{0.3} \times (3/9)^{0.5} \times (1/9)^{0.2}]}} \mathfrak{L}_{9^{[(2/9)^{0.3} \times (1/9)^{0.5} \times (2/9)^{0.2}]} \\
 &= \langle \mathfrak{L}_{4.50}, \mathfrak{L}_{2.15}, \mathfrak{L}_{1.45} \rangle \\
 A_2 &= LPFWA \langle (\mathfrak{L}_3, \mathfrak{L}_3, \mathfrak{L}_3), (\mathfrak{L}_2, \mathfrak{L}_5, \mathfrak{L}_1), (\mathfrak{L}_3, \mathfrak{L}_2, \mathfrak{L}_4) \rangle \\
 &= \langle \mathfrak{L}_{2.72}, \mathfrak{L}_{3.55}, \mathfrak{L}_{1.87} \rangle \\
 A_3 &= LPGWA \langle (\mathfrak{L}_2, \mathfrak{L}_2, \mathfrak{L}_2), (\mathfrak{L}_3, \mathfrak{L}_4, \mathfrak{L}_2), (\mathfrak{L}_7, \mathfrak{L}_1, \mathfrak{L}_1) \rangle \\
 &= \langle \mathfrak{L}_{3.92}, \mathfrak{L}_{2.48}, \mathfrak{L}_{1.74} \rangle
 \end{aligned} \tag{33}$$

*Step 4.* Using equations (20) and (21), to find the Hamming distance for each alternative

$$\begin{aligned}
 d(A_1, PIS) &= \frac{|4.50 - 4.80| + |2.15 - 2.15| + |1.45 - 1.26| + |0.9 - 0.7|}{2(9)} \\
 &= 0.038 \\
 d(A_1, NIS) &= \frac{|4.50 - 1.99| + |2.15 - 2.47| + |1.45 - 2.41| + |0.9 - 2.13|}{2(9)} \\
 &= 0.278. \\
 d(A_2, PIS) &= 0.236, \\
 d(A_2, NIS) &= 0.201, \\
 d(A_3, PIS) &= 0.102, \\
 d(A_3, NIS) &= 0.215.
 \end{aligned} \tag{34}$$

TABLE 2

		$c_1$	$c_2$	$c_3$
$D =$	$a_1$	$(\xi_4, \xi_2, \xi_2)$	$(\xi_4, \xi_3, \xi_1)$	$(\xi_6, \xi_1, \xi_2)$
	$a_2$	$(\xi_3, \xi_3, \xi_3)$	$(\xi_2, \xi_5, \xi_1)$	$(\xi_3, \xi_2, \xi_4)$
	$a_3$	$(\xi_2, \xi_2, \xi_2)$	$(\xi_3, \xi_4, \xi_2)$	$(\xi_7, \xi_1, \xi_1)$

The maximum and minimum Hamming distance and relative closeness degree of each alternative are obtained by using equations (22), (23), and (24), which are as follows:

$$\begin{aligned}
 d_{\max}^- &= \max(0.278, 0.201, 0.215) = 0.278, \\
 d_{\min}^+ &= \min(0.038, 0.236, 0.102) = 0.038, \\
 C(x_1) &= \frac{1}{2} \left( \frac{0.278}{0.278} + \frac{0.038}{0.038} \right) = 1, \\
 C(x_2) &= \frac{1}{2} \left( \frac{0.201}{0.278} + \frac{0.038}{0.236} \right) = 0.117 \\
 C(x_3) &= \frac{1}{2} \left( \frac{0.215}{0.278} + \frac{0.038}{0.102} \right) = 0.215
 \end{aligned}
 \tag{35}$$

According to equation (25), we rank the alternatives, as  $a_1 > a_3 > a_2$ , so the best alternative is  $A_1$ .

### 6. Conclusion

Inspired by linguistic picture fuzzy numbers, in this paper, uncertain estimate data in linguistic multicriteria decision making are expressed by linguistic picture fuzzy sets on linguistic terms set; then Hamming distance between two linguistic picture fuzzy sets and their properties are given and evaluated. Therefore, the linguistic picture fuzzy set TOPSIS method for LMCDM problems is proposed; different positive ideal solution, the negative ideal solution, and the relative closeness degrees of alternatives are provided; based on the designed algorithm, LMCDM problems with linguistic picture fuzzy sets can be automatically carried out. An example is also utilized to clarify the achievement, usefulness, and effectiveness of the linguistic picture fuzzy set TOPSIS method.

### Data Availability

No data were used to support this study.

### Conflicts of Interest

The authors declare that they have no conflicts of interest.

### Acknowledgments

This paper is supported by National Natural Science Foundation of China (no. 71671165), Statistical Scientific Key Research Project of Zhejiang (no. 18TJZZ24), Zhejiang Province Natural Science Foundation (no. LY18G010007),

Major Humanities and Social Sciences Research Projects in Zhejiang Universities (no. 2018QN058), and K. C. Wong Magna Fund in Ningbo University.

### References

- [1] T. Chen, C. Chang, and J. R. Lu, "The extended QUALIFLEX method for multiple criteria decision analysis based on interval type-2 fuzzy sets and applications to medical decision making," *European Journal of Operational Research*, vol. 226, no. 3, pp. 615–625, 2013.
- [2] S. J. Chuu, "Interactive group decision-making using a fuzzy linguistic approach for evaluating the flexibility in a supply chain," *European Journal of Operational Research*, vol. 213, no. 1, pp. 279–289, 2011.
- [3] F. Liu, W. G. Zhang, and Z. X. Wang, "A goal programming model for incomplete interval multiplicative preference relations and its application in group decision-making," *European Journal of Operational Research*, vol. 218, no. 3, pp. 747–754, 2012.
- [4] S. M. Mousavi and B. Vahdani, "Cross-docking Location Selection in Distribution Systems: A New Intuitionistic Fuzzy Hierarchical Decision Model," *International Journal of Computational Intelligence Systems*, vol. 9, no. 1, pp. 91–109, 2016.
- [5] J. Ye, "Fuzzy decision-making method based on the weighted correlation coefficient under intuitionistic fuzzy environment," *European Journal of Operational Research*, vol. 205, no. 1, pp. 202–204, 2010.
- [6] Z. Xu, "Intuitionistic fuzzy aggregation operators," *IEEE Transactions on Fuzzy Systems*, vol. 15, no. 6, pp. 1179–1187, 2007.
- [7] P. Liu and G. Tang, "Multi-criteria Group Decision-Making Based on Interval Neutrosophic Uncertain Linguistic Variables and Choquet Integral," *Cognitive Computation*, vol. 8, no. 6, pp. 1036–1056, 2016.
- [8] W. Yang, Y. Pang, and J. Shi, "Linguistic hesitant intuitionistic fuzzy cross-entropy measures," *International Journal of Computational Intelligence Systems*, vol. 10, no. 1, pp. 120–139, 2017.
- [9] L. A. Zadeh, "Fuzzy sets," *Information and Computation*, vol. 8, pp. 338–353, 1965.
- [10] K. T. Atanassov, "Intuitionistic fuzzy sets," *Fuzzy Sets and Systems*, vol. 20, no. 1, pp. 87–96, 1986.
- [11] I. K. Vlachos and G. D. Sergiadis, "Intuitionistic fuzzy information—applications to pattern recognition," *Pattern Recognition Letters*, vol. 28, no. 2, pp. 197–206, 2007.
- [12] L. A. Zadeh, "Fuzzy logic, Neural networks, and soft computing," *Communications of the ACM*, vol. 37, no. 3, pp. 77–84, 1994.
- [13] P. H. Phong and H. T. Dinh, "Some compositions of picture fuzzy relations," in *Fundamental and Applied IT Research*, 2014.
- [14] G. Wei, "Picture fuzzy cross-entropy for multiple attribute decision making problems," *Journal of Business Economics and Management*, vol. 17, no. 4, pp. 491–502, 2016.

- [15] S.-J. Wu and G.-W. Wei, "Picture uncertain linguistic aggregation operators and their application to multiple attribute decision making," *International Journal of Knowledge-Based and Intelligent Engineering Systems*, vol. 21, no. 4, pp. 243–256, 2017.
- [16] P. H. Phong and B. C. Cuong, "Multi-criteria Group Decision Making with Picture Linguistic Numbers," *VNU Journal of Science: Computer Science and Communication Engineering*, vol. 32, no. 3, pp. 39–53, 2017.
- [17] C. L. Hwang and K. Yoon, *Multiple Attribute Decision Making: Methods and Applications*, vol. 186, Springer-Verlag, Berlin, Germany, 1981.
- [18] E. Triantaphyllou and L. Chi-Tun, "Development and evaluation of five fuzzy multiattribute decision-making methods," *International Journal of Approximate Reasoning*, vol. 14, no. 4, pp. 281–310, 1996.
- [19] F. E. Boran, S. Genç, M. Kurt, and D. Akay, "A multi-criteria intuitionistic fuzzy group decision making for supplier selection with TOPSIS method," *Expert Systems with Applications*, vol. 36, no. 8, pp. 11363–11368, 2009.
- [20] Z. Yue, "An extended TOPSIS for determining weights of decision makers with interval numbers," *Knowledge-Based Systems*, vol. 24, no. 1, pp. 146–153, 2011.
- [21] C. Chen, "Extensions of the TOPSIS for group decision-making under fuzzy environment," *Fuzzy Sets and Systems*, vol. 114, no. 1, pp. 1–9, 2000.
- [22] B. Ashtiani, F. Haghhighirad, A. Makui, and G. A. Montazer, "Extension of fuzzy TOPSIS method based on interval-valued fuzzy sets," *Applied Soft Computing*, vol. 9, no. 2, pp. 457–461, 2009.
- [23] Y.-Y. He and Z.-W. Gong, "Extension of TOPSIS for intuitionistic fuzzy multiple attribute decision making and experimental analysis," *Advances in Information Sciences and Service Sciences*, vol. 4, no. 19, pp. 397–405, 2012.
- [24] S. Liu, F. Yu, W. Xu, and W. Zhang, "New approach to MCDM under interval-valued intuitionistic fuzzy environment," *International Journal of Machine Learning and Cybernetics*, vol. 4, no. 6, pp. 671–678, 2013.
- [25] B. C. Cuong and P. H. Phong, "Max-Min Composition of Linguistic Intuitionistic Fuzzy Relations and Application in Medical Diagnosis," *VNU Journal of Science: Computer Science and Communication Engineering*, vol. 30, no. 4, pp. 601–968, 2014.
- [26] F. Herrera and E. Herrera-Viedma, "Linguistic decision analysis: steps for solving decision problems under linguistic information," *Fuzzy Sets and Systems*, vol. 115, no. 1, pp. 67–82, 2000.

## Research Article

# EO Sensor Planning for UAV Engineering Reconnaissance Based on NIIRS and GIQE

Jingbo Bai , Yangyang Sun , Liang Chen , Yufang Feng, and Jianyong Liu 

Field Engineering College, Army Engineering University of PLA, Nanjing 210007, Jiangsu, China

Correspondence should be addressed to Jianyong Liu; [jianyong1212@126.com](mailto:jianyong1212@126.com)

Received 15 June 2018; Revised 5 October 2018; Accepted 11 October 2018; Published 31 December 2018

Guest Editor: Carlos Llopis-Albert

Copyright © 2018 Jingbo Bai et al. This is an open access article distributed under the Creative Commons Attribution License, which permits unrestricted use, distribution, and reproduction in any medium, provided the original work is properly cited.

When unmanned aerial vehicles (UAVs) support the Corps of Engineers in reconnaissance operations, in order to gather visible image information that should meet the mission's need, we grouped the engineering reconnaissance information interpretation tasks into 10 levels by using the National Imagery Interpretability Rating Scale (NIIRS). The quantitative relationship between the engineering targets, sensor performance, and flight altitude was established through the general image quality equation (GIQE) and the geometrical property of the ground sampled distance (GSD). Through some simulations, the influence of variable factors of the EO sensor imaging quality was analyzed, and the imaging height of the sensor for an engineering reconnaissance scenario was calculated. The results showed that this study could solve the problem of poor image quality caused by the flight altitude not meeting the mission requirements.

## 1. Introduction

The main task of engineering reconnaissance is to detect or identify the terrain, geology, hydrology, traffic conditions, the enemy's engineering facilities, the resources available locally on the battlefield, etc. When engineering corps reconnaissance operations are supported by unmanned aerial vehicles (UAVs), the mission planners of engineering corps may have limited knowledge about the use of UAV sensors, and because of the temporary assignment of engineering reconnaissance, the UAV operators of other units may not be familiar with the engineering targets. This brings uncertainty to the effectiveness of UAV engineering reconnaissance. In hostile and dangerous environments, UAV operators are generally willing to make the UAVs fly as high as possible; however, if the UAVs fly only at high altitude, some smaller targets will exceed the sensors' capabilities and might not be detected. In this case, the UAV operators will have to detect certain targets repeatedly, which is inefficient and will increase the risk of loss of the UAVs. If the UAV reconnaissance altitude corresponding to different types of engineering targets can be calculated in advance, the abovementioned problems could be avoided to some extent.

At present, there have been many research studies on the planning of the flight altitude of UAVs [1–4], but the main task of these studies was to avoid anti-aircraft fire or missiles, radar detection, obstacles, and other threats by adjusting flight altitude. This approach does not focus on the relationship between the sensor imaging height and quality. Most studies on imaging height and quality are about sensors of satellites [5, 6], and only small parts are about UAV sensors in order to provide theoretical methods for sensor design and performance evaluations [7, 8]. Qiao et al. [9] discussed a mission-oriented UAV path planning algorithm, and they pointed out that the quality of image information should be considered in mission planning. However, how to set the UAV to meet the image quality requirements was not discussed in their study.

This paper focuses solely on the imaging quality and height of EO sensors in UAVs supporting engineering reconnaissance. The problems of threat avoidance, flight paths, and resource consumption will not be discussed here. The main study is structured as follows. Section 2 is a general presentation of NIIRS and GIQE, and we group a series of engineering information interpretation tasks into 10 NIIRS levels according to military and civil visible NIIRS criteria.

Section 3 describes a method to build a quantitative relationship between the engineering targets, sensor performance, and flight altitude and to provide a solution for how high the UAV should fly in engineering reconnaissance operations. In Section 4, some simulations are carried out, and the results are discussed. Then, an engineering reconnaissance scenario is given to illustrate how to implement sensor planning. In Section 5, conclusions are given.

## 2. NIIRS and GIQE

**2.1. National Imagery Interpretability Rating Scale.** The NIIRS is a set of subjective image quality assessment criteria: a 10-level scale of 0 to 9 for image interpretability [10, 11]. NIIRS was developed under the auspices of the United States Government's Imagery Resolution Assessment and Reporting Standards (IRARS) committee. Each NIIRS level from 1 through 9 is defined by a series of interpretation tasks that range from very easy (requiring low image quality) to very difficult (requiring high levels of image quality). The tasks that define the NIIRS are related to an empirically derived perceptual image quality scale. Similar scales have been developed for use with radar, IR, and multispectral imagery. There are a large number of descriptive tasks in each scale that could not be listed here; refer to [12–14] if needed. NIIRS is probably the best measure of assessing the quality of images. It has been used extensively by the intelligence community. The performance of intelligence-surveillance-reconnaissance (ISR) sensors of UAVs was specified in NIIRS form, including "Global Hawk," "Dark Star," "Predator," and a large number of other platforms.

The NIIRS is predictable and is a subjective measure of information extraction. For nonprofessional users of remote sensing images, it is technically not dependent on a large number of data, and the subjective score of a target according to the NIIRS criteria guide is available [5, 15]. The NIIRS value and the spatial resolution (the ground sampled distance and relative edge response are measures of the system spatial resolution) have an ideal linear relationship [16], and the spatial resolution is defined as the minimum size that sensors can distinguish between targets whose length and width are at the same magnitude in the case of good contrast and similar background [17]. Therefore, for criteria not listed on the scale, NIIRS levels can be roughly estimated according to the shape, size, contrast, and other information of the targets.

**2.2. Visible NIIRS of Engineering Reconnaissance Operations.** For sensor planning of UAV, it is necessary to know the NIIRS levels of the engineering targets. Our solution is to extract the criteria that are relevant to the tasks of engineering reconnaissance from the current version of military and civil visible NIIRS and list a set of information interpretation tasks that are related to common engineering facilities, engineering equipment, personnel, the environment of the battlefield, and other targets according to the mission of UAV engineering reconnaissance. Next, we studied the background, state, shape, size, and other information of the engineering targets through a detailed comparison of the criteria of current

military and civil visible NIIRS. We grouped the engineering information interpretation tasks into corresponding levels according to the scales and merged them with the previous extracted criteria. Finally, we listed a rough estimated visible NIIRS of common engineering reconnaissance tasks in Table 1. As the focus of this study is sensor planning rather than image intelligence interpretation, some engineering targets were selected as similar features as the targets of the original criteria of visible NIIRS in order to avoid significant errors.

**2.3. General Image Quality Equation.** The NIIRS can express the requirements of reconnaissance mission well. It is meaningful to predict the NIIRS value when the sensor parameters of a UAV and information of reconnaissance targets are known. The general image quality equation (GIQE) is capable of completing this prediction. GIQE is an empirical model that is developed through a statistical analysis of the judgment of the image analyst. It originally predicted the interpretability of visible sampled imagery [18].

Although GIQE is subjective, it is impossible to predict the NIIRS by other methods. In the verification and comparison of image statistical models and estimation models, it is found that the two are correlated [13]. For example, an automobile salesman's ability is related to the number of automobiles that he sells. Without assessing his professional knowledge, we can verify the salesperson's ability through his sales performance. Image analysts are good predictors of image quality, and GIQE meets their needs well. Until a better method is developed, people will have to rely on this empirical model. The GIQE provides NIIRS predictions as a function of perceptual-quality attributes of scale, resolution, and sharpness, and of contrast and noise.

GIQE has undergone several revisions. The current version is 4.0:

$$NIIRS = 10.251 - a \lg GSD_{GM} + b \lg RER_{GM} - 0.656H_{GM} - 0.334 \left( \frac{G}{SNR} \right) \quad (1)$$

where  $GSD_{GM}$  is the geometric mean of the ground sampled distance in inches,  $RER_{GM}$  is the geometric mean of the normalized relative edge response,  $H_{GM}$  is the geometric mean height owing to edge overshoot resulting from modulation transfer function compensation (MTFC),  $G$  is the noise gain resulting from MTFC, and  $SNR$  is the signal-to-noise ratio.  $GSD_{GM}$  and  $RER_{GM}$  contribute as much as 92% of the NIIRS value. Other factors take up only 8% [19].

The definitions of parameters  $a$  and  $b$  are

$$a = \begin{cases} 3.32, & \text{if } RER_{GM} \geq 0.9 \\ 3.16, & \text{if } RER_{GM} < 0.9; \end{cases} \quad (2)$$

$$b = \begin{cases} 1.559, & \text{if } RER_{GM} \geq 0.9 \\ 2.817, & \text{if } RER_{GM} < 0.9 \end{cases}$$

TABLE 1: Estimated visible NIIRS of common engineering reconnaissance tasks.

---

**Rating Level 0**  
Interpretability of the imagery is precluded by obscuration, degradation, or very poor resolution.

**Rating Level 1**  
Distinguish between major land use classes (e.g., urban, agricultural, forest, water, barren).  
Detect a medium-sized port facility.  
Detect large highways or railway bridges on the water.  
Detect landing obstacle belts on a beachhead.

**Rating Level 2**  
Detect large buildings (e.g., hospitals, factories).  
Identify road patterns, like clover leaves, on major highway systems.  
Detect areas where the forest has been felled.  
Detect a multilane highway.

**Rating Level 3**  
Identify the shoreline of a major river.  
Detect a helipad by the configuration and markings.  
Detect individual houses in residential neighborhoods.  
Detect an engineering equipment in operation.  
Detect a floating bridge erected in the river.

**Rating Level 4**  
Identify tracked or wheeled engineering equipment, wheeled vehicles by general type when in groups.  
Identify the destruction of the riverbank after the haul road construction of the crossing site.  
Detect a bridge on small river or mechanized bridge equipment in engineering operation.  
Detect a hastily constructed military road when not camouflaged.  
Detect landslide or rockslide large enough to obstruct a single-lane road.  
Detect antitank ditch or trench in monotonous background.  
Detected pathways in obstacle field.  
Identify suitable area for constructing helipad.

**Rating Level 5**  
Identify the type of soil of riverbanks.  
Identify beach terrain suitable for amphibious landing operation.  
Identify whether there is a bypass route around the main road.  
Identify bridge structure and damages.  
Identify the type of trees.  
Identify tents (larger than two persons) at camping areas.  
Distinguish between pattern painting camouflages and cover camouflages of military facilities.

**Rating Level 6**  
Detect summer woodland camouflage netting large enough to cover a tank against a scattered tree background.  
Detect navigational channel markers and mooring buoys in water.

---

TABLE 1: Continued.

---

Detect recently installed minefields in ground forces deployment area based on a regular pattern of disturbed earth or vegetation.  
Identify obstacles in the road.  
Identify the type of large obstacles in obstacle belt (e.g., rail obstacle, antitank tetrahedron, etc.)  
Distinguish between wheeled bulldozers and loaders

**Rating Level 7**  
Distinguish between tanks, artillery, and their decoys.  
Identify the entrance of semiunderground works when not camouflaged.  
Detect underwater pier footings.  
Detect foxholes by ring of spoil outlining hole.

**Rating Level 8**  
Identify the number of personnel in engineering operations.  
Identify the shooting holes in the ground fortifications and detect scattered mines by minelaying vehicles.

**Rating Level 9**  
Identify individual barbs on a barbed wire fence.  
Identify equipment number painted on the engineering equipment.  
Identify braid of ropes 1 to 3 inches in diameter.

---

TABLE 2: Range of values in GIQE.

Parameters	Minimum	Maximum	Mean
GSD	3 in	80 in	20.6 in
RER	0.2	1.3	0.92
H	0.9	1.9	1.31
G	1	19	10.66
SNR	2	130	52.3

The revised GIQE is valid for the range of parameters listed in Table 2 [20]. The validity of the GIQE accuracy is uncertain if it is beyond this range.

The complete calculation of the parameters  $GSD_{GM}$ ,  $RER_{GM}$ ,  $H_{GM}$ ,  $G$ , and  $SNR$  in GIQE involves complex physical processes and is closely related to the specific physical parameters of the sensors. Therefore, we will not discuss the calculation here. The impact of the target (orientation, size, and contrast) is reflected in  $GSD_{GM}$  and implied in the  $SNR$ . The effects of the atmosphere are reflected in the  $SNR$ , and a standard target contrast is assumed for most applications. The impact of the sensor is included in  $GSD_{GM}$  and MTFC-related items (RER and lower-impact G and H). The effects of image processing include MTFC and grayscale transformations (dynamic range adjustment and gray-level transformation compensation), and the GIQE model assumes that the grayscale transformations are optimal [21].

### 3. Sensor Planning Method

According to the GIQE, factors that affect the value of NIIRS can be divided into two categories: one determined

by the intrinsic properties of sensors, the environment, or engineering targets, and the other is related to the specific use of the sensors. For sensor planning, the intrinsic properties part cannot be changed, so only using the sensor properly in engineering reconnaissance operations can meet the needs of NIIRS.

The parameters related to sensor planning are mainly reflected in  $GSD_{GM}$ .  $GSD_{GM}$  is determined by the sensor focal length, flight altitude of the UAV, imaging distance, and other factors. These are the operational parameters of the UAV in the course of an engineering reconnaissance mission, so they are very important to sensor planning. From the mathematical expression of GIQE, the influence of  $GSD_{GM}$  on NIIRS is significant. The influencing factors of  $GSD_{GM}$  are decomposed and discussed below.

$GSD_{GM}$  is the geometric mean of the horizontal and vertical ground sample distances based on a projection of the pixel pitch distance to the ground.  $GSD_{GM}$  is computed in inches in both the  $X$  and  $Y$  dimensions [18]:

$$GSD_{GM} = \sqrt{GSD_x \times GSD_y} \quad (3)$$

For systems in which the along-scan and cross-scan directions are not orthogonal,  $GSD_{GM}$  is modified by the angle  $\alpha$  between these directions:

$$GSD_{GM} = \sqrt{GSD_x \times GSD_y \times \sin \alpha} \quad (4)$$

For a CCD-array EO imaging sensor, the imaging scale depends on the focal length of the sensor and the flight altitude of the UAV. Assumption, Figure 1: a UAV flies from left to right, the EO sensor payload of the UAV has a focal length  $f$ , and the pixel pitches of the vertical and horizontal are  $DP$  and  $DP'$ , respectively. The pixel pitch is center-to-center distance of a pixel, relative to the pixel shape, usually the same as pixel edge length. The projection of the pixel is a trapezoidal area on the ground, the short edge of the trapezoid is  $x$ , the long edge is  $x'$ , and the hypotenuse is  $y'$ . The imaging height is  $h$ , the slant distance is  $r$ , and the look angle that is between the sensor to the target line and the ground horizontal line is  $\theta$ .

In Figure 1, the size of the pixel projection changes with the ground undulation, and for some military systems, it is not meaningful to compute the value on the ground. Thus, the usual practice is to compute the value on a plane perpendicular to the sensor sight, on which the sensor projection changes from a trapezoid on the ground to a rectangle or a square, and  $y'$  becomes  $y$ . In addition, the slant distance is kilometer-level, and GSD is centimeter-level, and the projection effect from ground to plane that vertical of sight on slant distance can be ignored. Thus, the distance from the sensor to the plane of the vertical sight can still be calculated by  $r$  here. If the pixel of an EO sensor is rectangular, this is known by the geometrical relation

$$\begin{aligned} x &= \frac{DP \cdot r}{f}, \\ y &= \frac{DP' \cdot r}{f} \end{aligned} \quad (5)$$

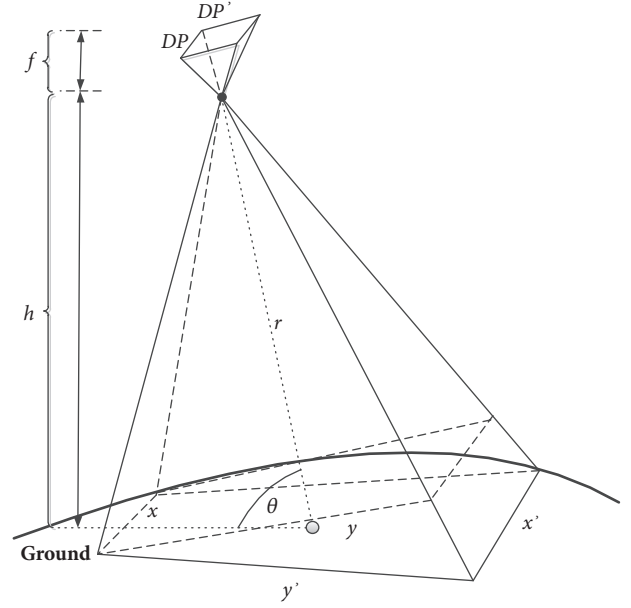


FIGURE 1: Projection of pixel to ground.

The rectangular area is

$$S = \frac{DP \cdot DP' \cdot r^2}{f^2} \quad (6)$$

According to (3), the value of  $GSD_{GM}$  is the square root of the rectangular area, and it is more direct and convenient to use the imaging height in calculations. Here, we use  $h/\sin \theta$  to replace  $r$ , and because the unit of  $GSD_{GM}$  is the inch, it needs to be converted to meters for calculation:

$$0.0254GSD_{GM} = \frac{\sqrt{DP \cdot DP'} \cdot h}{f \cdot \sin \theta} \quad (7)$$

Thus,

$$GSD_{GM} = \frac{39.37 \sqrt{DP \cdot DP'} \cdot h}{f \cdot \sin \theta} \quad (8)$$

Further,  $GSD_{GM}$  is brought into (1) to establish an association with the sensor:

$$\begin{aligned} NIIRS &= 10.251 NIIRS - a \lg \frac{39.37 \sqrt{DP \cdot DP'} \cdot h}{f \cdot \sin \theta} \\ &+ b \lg RER_{GM} - 0.656H_{GM} - 0.334 \left( \frac{G}{SNR} \right) \end{aligned} \quad (9)$$

Make  $10.751 + b \lg RER_{GM} - 0.656H_{GM} - 0.334(G/SNR) - NIIRS = K$ , and bring this into (9):

$$a \lg \frac{39.37 \sqrt{DP \cdot DP'} \cdot h}{f \cdot \sin \theta} = K \quad (10)$$

Then,

$$h = \frac{0.0254 f \sin \theta}{\sqrt{DP \cdot DP'}} \cdot 10^{K/a} \quad (11)$$

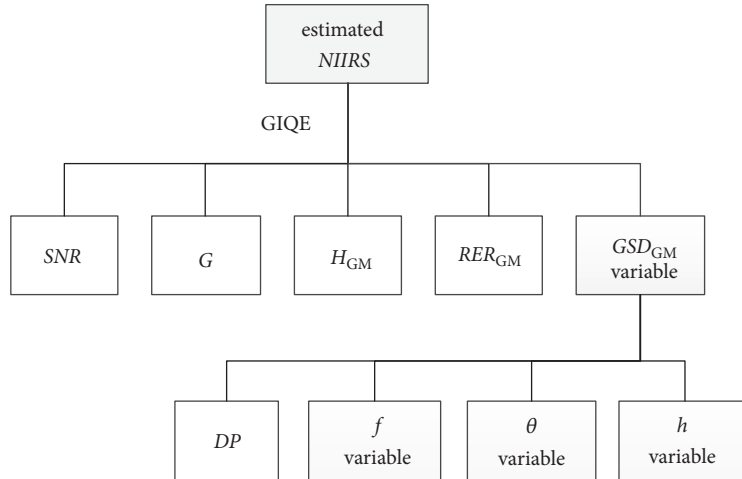


FIGURE 2: Model of sensor planning based on NIIRS and GIQE.

To sum up, when the NIIRS level is known before a reconnaissance operation, the model of sensor planning for UAVs based on NIIRS and GIQE is as shown in Figure 2.

#### 4. Simulation and Results Discussion

The EO equipment of “Global Hawk” and “Predator” was chosen as an example to carry out some simulations. A partial list of performance parameters [7, 13] for the EO camera of “Global Hawk” and “Predator” is shown in Table 3. When sensor planning for other types of UAVs, simply replace these with the parameters of the EO sensor payload of the other UAVs.

For the EO camera, the values of  $RER_{GM}$ ,  $H_{GM}$ , and  $G$  have the following typical data [8, 22]:  $RER_{GM} = 0.75$ ,  $H_{GM} = 1.4$ , and  $G = 10$ , making  $SNR = 66$ . Parameters such as  $RER_{GM}$ ,  $H_{GM}$ ,  $G$ , and  $SNR$  are generally fixed values, which are usually considered in the design of new EO equipment. Because  $RER_{GM} = 0.75$ , then  $a = 3.16$  and  $b = 2.817$  according to (1).

Assume that the along-scan and cross-scan directions are orthogonal. The pixel of the sensor array selected for the test is square, so that  $GSD_x = GSD_y = GSD$ . In the following, the relationship between the flight altitude, focal length of the sensor, angle of view, and the NIIRS will be analyzed, and an example of sensor planning of engineering reconnaissance supported by UAVs will be given to explain how to use NIIRS and GIQE for sensor planning.

**4.1. Relationship between Flight Altitude and NIIRS Level.** The EO sensor of “Global Hawk” is designed to provide a minimum NIIRS level of 6.5 [13] for visible light images (angle of view  $45^\circ$  and sensor-to-target distance of 28 km). The imaging height of 19,802 m can be calculated through a trigonometric relationship, that is, the maximum flight altitude of “Global Hawk,” rounded to 19,800 m for calculation. The EO sensor of “Predator” is designed to be at a  $45^\circ$  angle of view and at

TABLE 3: Partial parameters of EO camera of typical UAVs.

Parameters	“Global Hawk”	“Predator”
Focal length /mm	1000-1750	16-160
Pixel pitch/ $\mu\text{m}$	9*9	5*5
Maximum Flight altitude /m	19800	7620

a height of 15,000 ft (4570 m), providing a minimum NIIRS level of 6 for visible light images [23].

In order to study the relationship between the flight altitude and the NIIRS level of the EO sensor, to verify (9) by the NIIRS requirements for the sensor design, and to verify the reliability of  $GSD_{GM}$  calculated by  $DP$ ,  $f$ ,  $\theta$ , and  $h$ , a range of 11,000 m to 19,800 m of the flying altitude of “Global Hawk” was selected for the simulation. Because the sensor design requirement that stipulates the imaging quality should reach a certain level at a certain altitude, the focal length parameter value was set to the maximum focal length of 1.75 m. A range of cruising altitude of 4570 m to the maximum height of 7620 m for “Predator” was selected, and a focal length of 0.16 m was set. The relationship between the imaging height and the imaging quality was calculated by a simulation, as shown in Figure 3.

According to the results, the imaging height of “Global Hawk” increased from 11,000 m to 19,800 m, and the NIIRS level changed from 7.4 to 6.6. The imaging height of “Predator” increased from 4570 m to 7620 m, and the NIIRS level changed from 6.1 to 5.4. It can be seen directly from Figure 3 that the NIIRS value decreased as the imaging height increased, and the trend of value decreasing was slowing down.

When the imaging height of “Global Hawk” was 19,800 m, the NIIRS value was 6.6 (keeping two digits after the decimal point, the value was 6.55, and the result is marked with a red circle in Figure 3), and it met the design requirement of  $NIIRS > 6.5$ . When the imaging height of “Predator” was 4570 m, the NIIRS value was 6.1 (keeping two digits after the decimal

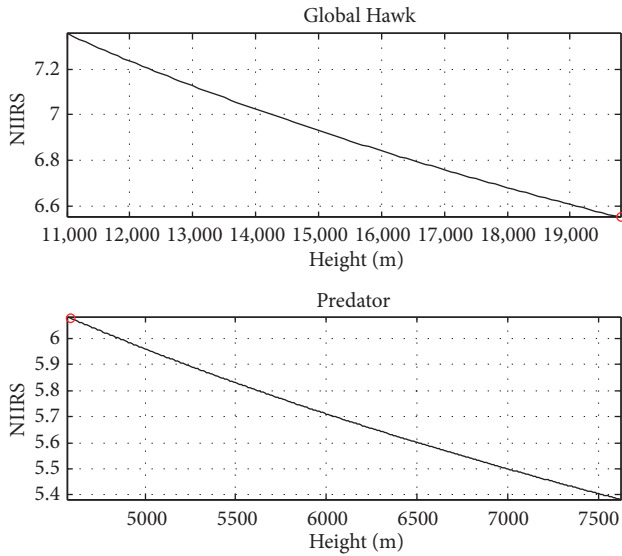


FIGURE 3: Relationship between flight altitude and NIIRS level.

point, the value was 6.08 and is also marked with a red circle in Figure 3). This also met the design requirement of  $NIIRS > 6$ . The calculation results can be further explained in that (9) was correct and reliable for calculating the NIIRS by using  $DP, f, \theta$ , and  $h$  to establish the relation with  $GSD_{GM}$ .

**4.2. Relationship between Focal Length of Sensor and NIIRS Level.** The instantaneous field of view (IFOV) can be adjusted by changing the focal length of an EO sensor. When the focal length is short, the IFOV is wide, and a large area can be detected, but the resolution is usually low. When the focal length is long, the IFOV is narrow, and the detector covers a small area, so the resolution is improved. However, this sacrifices the ground coverage, and very much like a "glimpse," the target detection is more difficult.

Therefore, it is necessary to set the focal length parameters reasonably in order to get the image to meet the task requirement and to improve the coverage of IFOV before engineering reconnaissance operations begin. For simulation parameters, the imaging height of the UAVs was set to their cruise altitude: "Global Hawk" was 18,000 m, "Predator" was 4570 m, and the angle of view was set to  $45^\circ$ . The results are shown in Figure 4.

The results showed that the focal length of "Global Hawk" was 1–1.75 m, the range of the NIIRS value was 5.9–6.7, and when the focal length of "Predator" was 0.016–0.16 m, the range of the NIIRS value increased from 2.9 to 6.1. The NIIRS value increased with the focal length of the sensor, and the trend of increasing speed of NIIRS slowed down with an increase in focal length. Because the EO sensor of "Global Hawk" has a zoom of only 1.75 $\times$ , the overall increase in the NIIRS value is small, but because of its long focal length, it can obtain high-quality images in case of a wide IFOV. The EO sensor of "Predator" has a zoom of 10 $\times$ ; therefore, the NIIRS value fluctuates greatly when the focal length changes. Because of the short focal length of

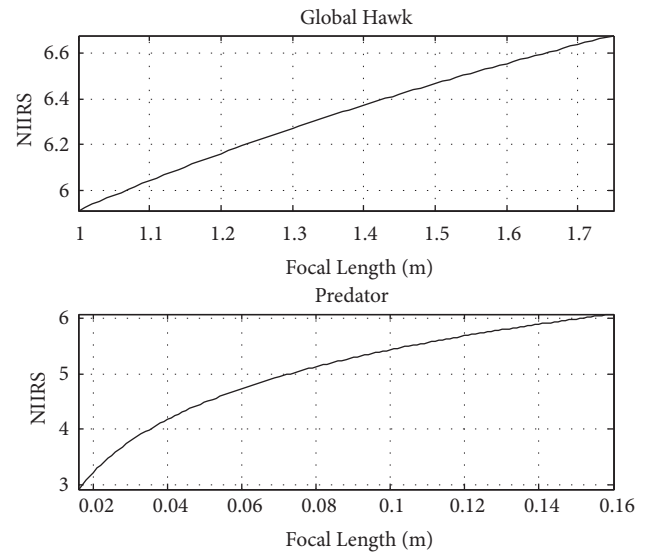


FIGURE 4: Relationship between focal length of sensor and NIIRS level.

the sensor, the image resolution of a wide IFOV can be lower.

**4.3. Relationship between Angle of View and NIIRS Level at Different IFOVs.** Here, the imaging height was the cruising altitude. According to the IFOV, the focal length was calculated by the minimum and maximum values, and the range of the angle of view was set to  $45^\circ$ – $90^\circ$ . The results are shown in Figure 5.

In case of a wide IFOV, when the angle of view increased from  $45^\circ$  to  $90^\circ$ , the range of the NIIRS value of "Global Hawk" was 5.9–6.4, and the range of the NIIRS value of "Predator" was 2.9–3.4. In case of a narrow IFOV, the range of the NIIRS value of "Global Hawk" was 6.7–7.2, and the range of the NIIRS value of "Predator" was 6.1–6.6. From the curve in Figure 5, we can see that the NIIRS value increased with an increase in the angle of view, the growth slowed down gradually, and it finally tended to be horizontal.

**4.4. Solution of Sensor Planning of a Scenario.** Taking engineering reconnaissance of landing attack supported by UAVs as an example, this paper shows how to plan the imaging height of the sensors in engineering reconnaissance operations. According to the operation methods of engineering reconnaissance supported by UAVs in landing attack and the estimated visible NIIRS of common engineering reconnaissance tasks (Table 1), the main reconnaissance tasks and the required NIIRS level are sorted as shown in Table 4. Among them, if multiple details need to be detected in a task, the image quality needs to be planned according to the highest NIIRS level.

For the parameter setting of the EO sensor of the UAV, the angle of view continues to be  $45^\circ$ , which was specified by the sensor design standards of NIIRS. Because the engineering reconnaissance task needs to detect more targets, a wide IFOV should be chosen as far as possible. The focal length of

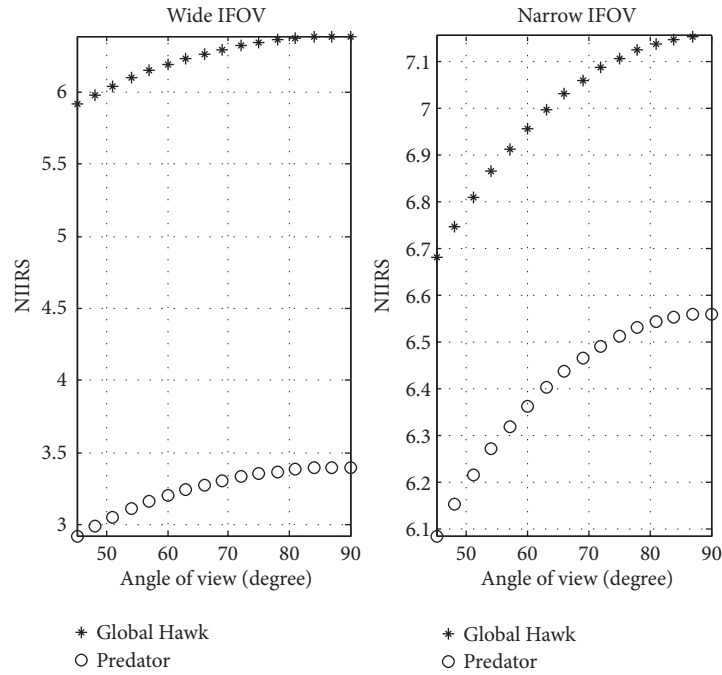


FIGURE 5: Relationship between angle of view and NIIRS level at different IFOVs.

TABLE 4: Tasks of engineering reconnaissance and NIIRS level requirement in landing combat.

Serial number	Missions	Main tasks that UAVs can support	NIIRS	NIIRS requirement
1	Reconnaissance of predetermined landing area.	Identify beach terrain suitable for amphibious landing operation.	5	5
2	Reconnaissance of antilanding obstacle field.	Identify the type of large obstacles in obstacle belt.	6	6
		Detected pathways in obstacle field.	4	
3	Reconnaissance of the road to depth.	Identify whether there is a bypass route around the main road.	5	6
		Identify obstacles in the road.	6	
4	Reconnaissance of river, ferry, and bridge area.	Identify the shoreline of a major river.	3	5
		Identify the type of soil of riverbanks.	5	
5	Reconnaissance of the original bridge.	Identify bridge structure and damages.	5	5
6	Reconnaissance of obstacles in depth.	Detect antitank ditch in monotonous background.	4	4
7	Reconnaissance of enemy's positions and fortifications.	Identify the entrance of semiunderground works when not camouflaged.	7	7
		Detect trench in monotonous background.	4	
8	Reconnaissance of enemy's camouflage.	Distinguish between pattern painting camouflages and cover camouflages of military facilities.	5	7
		Detect summer woodland camouflage netting large enough to cover a tank against a scattered tree.	6	
		Distinguish between tanks, artillery, and their decoys.	7	
9	Reconnaissance of enemy's engineering support capability.	Identify tracked or wheeled engineering equipment, wheeled vehicles by general type when in groups.	4	4
10	Reconnaissance of area for constructing helipad.	Identify suitable area for constructing helipad.	4	4

TABLE 5: Results of sensor planning.

Sensor platform	Focal length/m	Angle of view/degree	Imaging height/m									
			1	2	3	4	5	6	7	8	9	10
“Global Hawk”	1	45	18000	16877	16877	18000	18000	18000	8144	8144	18000	18000
“Predator”	0.08	45	5036	2430	2430	5036	5036	7620	1173	1173	7620	7620

the EO sensor of “Global Hawk” was set to 1 m. The range of the IFOV of “Predator” is  $2.3^\circ \times 1.7^\circ - 23^\circ \times 17^\circ$ . Because of its short focal length, the flight altitude of the UAV will descend to hundreds of meters if the IFOV is too wide, and this does not conform to practical use. Therefore, a  $5\times$  zoom was selected for which the IFOV was  $16.5^\circ \times 8.5^\circ$  and the focal length was 0.08 m. The values of  $RER_{GM}$ ,  $H_{GM}$ ,  $G$ ,  $DP$ ,  $a$ , and  $b$  were consistent with the previous text. The results of the EO sensor planning are shown in Table 5, and an imaging height requirement comparison of the two types of UAV is shown in Figure 6.

For tasks that demand a high NIIRS level, some other parameters of the sensor are fixed, so the flight altitude of the UAVs must be lowered to meet the imaging quality requirements. For a task with a lower demand of NIIRS level, the cruise altitude of “Global Hawk” is close to its ceiling, and the increasing part of the height has little effect on the image quality and detection range. Thus, the UAV should continue reconnaissance at the cruising altitude. By contrast, “Predator” has a different cruising altitude and maximum flight altitude, although it can easily obtain low-level NIIRS engineering target images without changing altitude. However, a large increase in the imaging height can increase the sensor’s detection range, and thus more targets will be detected and the efficiency of reconnaissance will be improved.

## 5. Conclusions

Aiming at the problem of how to obtain visible-light image intelligence in engineering reconnaissance operations supported by UAVs, the NIIRS and GIQE were studied in this paper. According to the NIIRS criteria and the properties of the engineering targets, the visible NIIRS level was specified for the engineering reconnaissance tasks, and the relationship between the NIIRS level of engineering reconnaissance tasks, the EO sensor performance, and the ground sampled distance was established through GIQE. Then, the ground sampled distance in the GIQE was further decomposed into sensor parameters such as pixel pitch, focal length, angle of view, and imaging height. A model for sensor planning was established by using a geometrical method. Finally, some simulations were carried out, and a scenario of an engineering reconnaissance operation was examined.

The results showed that the NIIRS level decreased with an increase in the imaging height and increased with an increase in the angle of view and the focal length. The value of the height in the results was the highest that a UAV could fly during an engineering reconnaissance task, and it was difficult to meet the imaging quality requirement if the flight

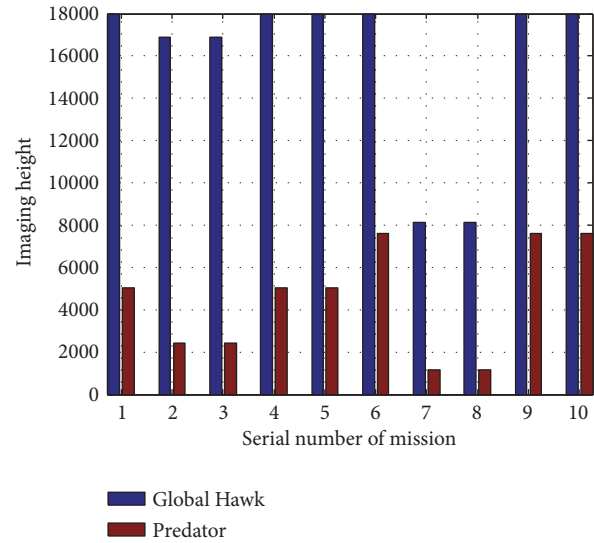


FIGURE 6: Imaging height requirement comparison of two types of UAV.

altitude was exceeded. Exceeding the flight altitude could lead to re-reconnaissance, increasing the time. In addition, in the model for sensor planning, several variables interacted with each other. The flight altitude is different when the angle of view and focal length are different for the same task. Thus, reasonable sensor planning should be combined with the requirements of specific engineering reconnaissance operations.

It is complicated to determine the flight altitude of UAVs in military operations. Threat avoidance, flight paths, and resource consumption should be considered in mission planning. The abovementioned problems will be studied in the future.

## Data Availability

These prior studies are cited at relevant places within the text as references [1–23].

## Conflicts of Interest

The authors declare that there are no conflicts of interest regarding the publication of this paper.

## Acknowledgments

This study was supported by the Military Science Project of the National Social Science Foundation of China (no.

15GJ003-141) and the Military Postgraduate Funding Project of the PLA (no. 2016JY370).

## References

- [1] Y. G. Fu, M. Y. Ding, and C. P. Zhou, "Phase angle-encoded and quantum-behaved particle swarm optimization applied to three-dimensional route planning for UAV," *IEEE Transactions on Systems, Man, and Cybernetics: Systems*, vol. 42, no. 2, pp. 511–526, 2012.
- [2] V. Roberge, M. Tarbouchi, and G. Labonte, "Comparison of parallel genetic algorithm and particle swarm optimization for real-time UAV path planning," *IEEE Transactions on Industrial Informatics*, vol. 9, no. 1, pp. 132–141, 2013.
- [3] A. Tsourdos, B. White, and M. Shanmugavel, *Cooperative Path Planning of Unmanned Aerial Vehicles*, John Wiley & Sons Ltd, 2010.
- [4] W. Naifeng, *Research on the small uav online path planning algorithms in complex and low-altitude environments*, Harbin Institute of Technology, Harbin, China, 2016, Research on the small uav online path planning algorithms in complex and low-altitude environments". *Harbin Institute of Technology*, 2016.
- [5] L. Li, H. Luo, M. She, and H. Zhu, "User-oriented image quality assessment of ZY-3 satellite imagery," *IEEE Journal of Selected Topics in Applied Earth Observations and Remote Sensing*, vol. 7, no. 11, pp. 4601–4609, 2014.
- [6] R. Ryan, B. Baldrige, R. A. Schowengerdt, T. Choi, D. L. Helder, and S. Blonski, "IKONOS spatial resolution and image interpretability characterization," *Remote Sensing of Environment*, vol. 88, no. 1-2, pp. 37–52, 2003.
- [7] B. Honggang, *A study on image quality evaluation of remote sensing systems based on NIIRS*, Xi'an Xidian University, Xi'an, China, 2010.
- [8] H. Xiao-juan, K. Sheng, and L. Kan, "Analysis of Image Quality Influencing Factors of Aero Visible Camera," *Optics & Optoelectronic Technology*, vol. 12, no. 4, pp. 65–68, 2014.
- [9] Q. Ming, Z. Xiao-lin, X. Wen-jun et al., "A Mission Oriented Path Planning Algorithm for Unmanned Reconnaissance Air Vehicles," *Journal of Air Force Engineering University: Natural Science Edition*, vol. 16, no. 2, pp. 38–42, 2015.
- [10] R. G. Driggers, M. Kelley, P. G. Cox, and G. C. Holst, "National imagery interpretation rating system (NIIRS) and the probabilities of detection, recognition, and identification," in *Proceedings of the Joint Precision Strike Demonstration Project Office SETA Member EOIR Measurements, Inc.*, pp. 349–360, Orlando, FL, 2007.
- [11] J. M. Irvine and J. C. Leachtenauer, "A Methodology for Developing Image Interpretability Scales," *ASPRS/ASCM Annual Convention Exhibition*, pp. 273–279, 1996.
- [12] R. G. Driggers, J. A. Ratches, J. C. Leachtenauer, and R. W. Kistner, "Synthetic aperture radar target acquisition model based on a national imagery interpretability rating scale to probability of discrimination conversion," *Optical Engineering*, vol. 42, no. 7, pp. 2104–2112, 2003.
- [13] J. C. Leachtenauer and R. G. Driggers, *Surveillance and Reconnaissance Imaging Systems-Modeling and Performance Prediction*, Artech House Publishers, 2000.
- [14] R. G. Driggers, M. Kruer, D. Scribner, P. Warren, and J. Leachtenauer, "Sensor performance conversions for infrared target acquisition and intelligence-surveillance-reconnaissance imaging sensors," *Applied Optics*, vol. 38, no. 28, pp. 5936–5943, 1999.
- [15] Imagery Resolution Assessments, and Reporting Standards (IRARS) Committee (1996), "Civil NIIRS Reference Guide", [http://www.fas.org/irp/imint/niirs\\_c/guide.htm](http://www.fas.org/irp/imint/niirs_c/guide.htm).
- [16] M. Abolghasemi and D. Abbasi-Moghadam, "Conceptual design of remote sensing satellites based on statistical analysis and NIIRS criterion," *Optical and Quantum Electronics*, vol. 47, no. 8, pp. 2899–2920, 2015.
- [17] Editorial Office of Equipment Reference, Ground resolution, *Equipment Reference*, no. 41, pp. 21-21, 2004.
- [18] J. C. Leachtenauer, W. Malila, J. Irvine, L. Colburn, and N. Salvaggio, "General image-quality equation: GIQE," *Applied Optics*, vol. 36, no. 32, pp. 8322–8328, 1997.
- [19] Q. Ye, X. Li, and Y. Chen, "Evaluating aerophoto image quality based on character statistics," *Remote Sensing*, vol. 5, pp. 20–23, 2006.
- [20] S. T. Thurman and J. R. Fienup, "Analysis of the general image quality equation," in *Proceedings of the SPIE Defense and Security Symposium*, pp. 69780F1–69780F13, Orlando, Fla, USA.
- [21] H. Mao, S. Tian, and A. Chao, *UAV Mission Planning*, National Defense Industry Press, 2015.
- [22] Y. Chang-feng, Y. Wen-Xian, and S. Yi, "The Situation Awareness Evaluation of S&R System," *Journal of National University of Defense Technology*, vol. 27, no. 3, pp. 49–53, 2005.
- [23] USAF, "Air combat command concept of operations for endurance unmanned aerial vehicles", [https://fas.org/irp/doddir/usaf/conops\\_uav/part02.htm](https://fas.org/irp/doddir/usaf/conops_uav/part02.htm).

## Research Article

# Existence and Stability of Periodic Solution Related to Valveless Pumping

B. Dorociaková <sup>1</sup>, M. Michalková <sup>1</sup>, R. Olach <sup>1</sup> and M. Sága<sup>2</sup>

<sup>1</sup>Department of Applied Mathematics, Faculty of Mechanical Engineering, University of Žilina, 010 26 Žilina, Slovakia

<sup>2</sup>Department of Applied Mechanics, Faculty of Mechanical Engineering, University of Žilina, 010 26 Žilina, Slovakia

Correspondence should be addressed to B. Dorociaková; bozena.dorociakova@fstroj.uniza.sk

Received 19 July 2018; Revised 28 September 2018; Accepted 29 October 2018; Published 28 November 2018

Guest Editor: Carlos Llopis-Albert

Copyright © 2018 B. Dorociaková et al. This is an open access article distributed under the Creative Commons Attribution License, which permits unrestricted use, distribution, and reproduction in any medium, provided the original work is properly cited.

Valveless pumping, also known as Liebau effect, can be described as the unidirectional flow of liquid in a system without valves that is caused by the asymmetry of placing of the periodically working pump. Recently, the research in this field has been reevoked, partially due to its possible application in nanotechnologies. In this paper, a configuration of one pipe and one tank is considered from the mathematical point of view. Qualitative properties of a class of nonlinear differential equations that model the assumed system configuration are investigated. New sufficient conditions for the existence of positive  $T$ -periodic solutions are given. Correspondingly, exponential stability of periodic solution is treated. Presented results are new. They extend and complement earlier ones in the literature.

## 1. Introduction

Valveless pumping represents a mechanism of fluid propagation in one direction in a system where valves are not presented. This type of mechanism was described by German cardiologist Gerhard Liebau for the first time in 1954. Working with patients suffering from severe aortic insufficiency led him to the idea that unidirectional blood propagation could be achieved without valves. To check his assumptions, he demonstrated a valveless pumping in a system consisting of two tanks connected by a rubber tube. Via periodic compression of the tube, located asymmetrically along the length of it, he pumped water from the lower tank to the upper one without the necessity of a valve to ensure a preferential direction of the flow [1]. As Liebau had assumed, the valveless circulation has been later observed in early stages of human embryonic life. In this stage, the heart is only tubular with complete absence of valves; however, the blood circulates in one direction through the cardiovascular system [2]. Many experimental and simulation works have been published on the subject of Liebau phenomenon in order to explain its physical nature, as well as the conditions of its occurrence (for example, [3–6]). Better understanding of the valveless pumping allowed transferring the knowledge to the

technical sphere where, for example, valveless micropumps have been designed [7].

In recent years efforts to investigate the analytical solution to the mathematical model of Liebau phenomenon have arisen. In [8], the existence of periodic solution for configurations of two tanks connected with rigid pipe and of three tanks connected with rigid pipes, respectively, is shown. On the one hand, the model with one tank and one rigid pipe is the simplest in configuration. On the other hand, it appeared to be the most difficult when the existence of solution is considered. The one pipe–one tank problem is more closely examined in [5, 6] where some significant results on the existence of positive periodic solutions are obtained. In [5], the mathematical model of this configuration is derived, resulting in the differential equation with singularities. Applying a suitable substitution, the aforementioned differential equation is transformed into regular one of the form

$$x''(t) + ax'(t) = \frac{e(t)}{\mu} x^{1-2\mu}(t) - \frac{c}{\mu} x^{1-\mu}(t), \quad (1)$$

$$t \in (0, T),$$

where  $a \geq 0, c > 0, 0 < \mu < 1/2$ , and  $e(t)$  is continuous and  $T$ -periodic on  $R$ . Likewise the authors in [6], we consider the generalization of this equation in the form

$$x''(t) + ax'(t) + q(t)x^\beta(t) - r(t)x^\alpha(t) = 0, \quad t \geq t_0, \quad (2)$$

where  $a \geq 0, q, r \in C([t_0, \infty), R)$ . Whereas the authors in [5, 6] consider only the case  $0 < \alpha < \beta < 1$ , we consider also more general case  $\alpha, \beta \in (0, \infty)$ .

Qualitative properties of solutions of differential equations are studied, for example, in [9–15]. In [13], the authors investigate Lasota and the Wazewska-Czyzewska model for the survival of red blood cells in an animal. Model is represented by the first order nonlinear delay differential equation. Another interesting model is treated in [9] where the authors study the periodicity of the Nicholson’s blowflies differential equations.

The purpose of this paper is primarily mathematical. We focus on the existence and exponential stability of a positive  $T$ -periodic solution of nonlinear differential equation (2) where  $a \geq 0, \alpha, \beta \in (0, \infty)$ , and  $q, r \in C([t_0, \infty), R)$ . In Section 2 there are given sufficient conditions for the existence of a positive  $T$ -periodic solution. Their application is illustrated on the example where the existence of  $2\pi$ -periodic solution of (2) is shown for given functions  $q(t)$  and  $r(t)$ . The exponential stability of a positive  $T$ -periodic solution is treated in Section 3. The obtained results are, consequently, applied on the problem of valveless pumping in one pipe–one tank configuration (Section 4). Sufficient conditions for the existence and exponential stability are reformulated for (1). Furthermore, the comparison of our main results and main results from [5, 6] for this equation is given in the Example 10. The results for the existence of positive  $T$ -periodic solution and its exponential stability, presented in this paper, are new, extending and complementing some earlier ones in the literature.

## 2. Existence of a Positive Periodic Solution

We study the existence of a positive  $T$ -periodic solution of (2) in this section. In the sequel, the following fixed point theorem will be used to prove some of the main results in the paper.

**Theorem 1** (Schauder’s fixed point theorem [14, 16]). *Let  $\Omega$  be a closed, convex, and nonempty subset of a Banach space  $X$ . Let  $S : \Omega \rightarrow \Omega$  be a continuous mapping such that  $S\Omega$  is a relatively compact subset of  $X$ . Then  $S$  has at least one fixed point in  $\Omega$ . That is, there exists an  $x \in \Omega$  such that  $Sx = x$ .*

Theorem 2 states sufficient conditions for the existence of the periodic solution of equation (2). Conditions (3)–(5) guarantee that the operator  $S : \Omega \rightarrow \Omega$ . In addition, conditions (4), (5) guarantee that  $(Sx)(t)$  is  $T$ -periodic function.

**Theorem 2.** *Suppose that there exist function  $k \in C([t_0, \infty), R)$  and constants  $m, M$  such that*

$$0 < m \leq \exp\left(\int_{t_0}^t [-a + k(s)] ds\right) \leq M, \quad t \geq t_0, \quad (3)$$

$$\int_t^{t+T} [-a + k(s)] ds = 0, \quad t \geq t_0, \quad (4)$$

$$\begin{aligned} &k(t) \exp\left(\int_{t_0}^t [-a + k(s)] ds\right) \\ &= \int_{t_0}^t \left[ r(s) \exp\left(\alpha \int_{t_0}^s [-a + k(v)] dv\right) \right. \\ &\quad \left. - q(s) \exp\left(\beta \int_{t_0}^s [-a + k(v)] dv\right) \right] ds, \end{aligned} \quad (5)$$

$t \geq t_0$ .

Then (2) has a positive  $T$ -periodic solution.

*Proof.* Let  $X = \{x \in C([t_0, \infty), R)\}$  be a Banach space with the norm  $\|x\| = \sup_{t \geq t_0} |x(t)|$ . We define a closed, bounded, and convex subset  $\Omega$  of  $X$  as

$$\begin{aligned} \Omega = \left\{ x \in X : x(t+T) = x(t), t \geq t_0, m \leq x(t) \right. \\ \left. \leq M, t \geq t_0, \frac{1}{x(t)} \int_{t_0}^t [r(s)x^\alpha(s) - q(s)x^\beta(s)] ds \right. \\ \left. = k(t), t \geq t_0 \right\}. \end{aligned} \quad (6)$$

and the operator  $S : \Omega \rightarrow X$  as

$$\begin{aligned} (Sx)(t) = \exp\left(\int_{t_0}^t (-a \right. \\ \left. + \frac{1}{x(s)} \int_{t_0}^s [r(v)x^\alpha(v) - q(v)x^\beta(v)] dv\right) ds, \end{aligned} \quad (7)$$

$t \geq t_0$ .

We need to show that for any  $x \in \Omega, Sx \in \Omega$ . According to (3), for every  $x \in \Omega$  and  $t \geq t_0$  we obtain

$$\begin{aligned} (Sx)(t) = \exp\left(\int_{t_0}^t (-a \right. \\ \left. + \frac{1}{x(s)} \int_{t_0}^s [r(v)x^\alpha(v) - q(v)x^\beta(v)] dv\right) ds \\ = \exp\left(\int_{t_0}^t [-a + k(s)] ds\right) \leq M \end{aligned} \quad (8)$$

as well as

$$\begin{aligned} (Sx)(t) &= \exp\left(\int_{t_0}^t (-a \right. \\ &+ \left. \frac{1}{x(s)} \int_{t_0}^s [r(v)x^\alpha(v) - q(v)x^\beta(v)] dv\right) ds \quad (9) \\ &= \exp\left(\int_{t_0}^t [-a + k(s)] ds\right) \geq m. \end{aligned}$$

With regard to (5), for every  $x \in \Omega$  and  $t \geq t_0$

$$\begin{aligned} k(t)(Sx)(t) &= k(t) \\ &\cdot \exp\left(\int_{t_0}^t \left(-a + \frac{1}{x(s)} \int_{t_0}^s [r(v)x^\alpha(v) - q(v)x^\beta(v)] dv\right) ds\right) \\ &= k(t) \exp\left(\int_{t_0}^t [-a + k(s)] ds\right) \\ &= \int_{t_0}^t \left[ r(s) \exp\left(\alpha \int_{t_0}^s [-a + k(v)] dv\right) \right. \\ &- \left. q(s) \exp\left(\beta \int_{t_0}^s [-a + k(v)] dv\right) \right] ds \\ &= \int_{t_0}^t [r(s)(Sx)^\alpha(s) - q(s)(Sx)^\beta(s)] ds. \end{aligned} \quad (10)$$

Finally, we show that for  $x \in \Omega$ ,  $t \geq t_0$ , the function  $(Sx)(t)$  is  $T$ -periodic. For  $x \in \Omega$ ,  $t \geq t_0$  and with regard to (4)

$$\begin{aligned} (Sx)(t+T) &= \exp\left(\int_{t_0}^{t+T} (-a \right. \\ &+ \left. \frac{1}{x(s)} \int_{t_0}^s [r(v)x^\alpha(v) - q(v)x^\beta(v)] dv\right) ds \\ &= \exp\left(\int_{t_0}^t (-a \right. \\ &+ \left. \frac{1}{x(s)} \int_{t_0}^s [r(v)x^\alpha(v) - q(v)x^\beta(v)] dv\right) ds \\ &\times \exp\left(\int_t^{t+T} (-a \right. \\ &+ \left. \frac{1}{x(s)} \int_{t_0}^s [r(v)x^\alpha(v) - q(v)x^\beta(v)] dv\right) ds \\ &= \exp\left(\int_{t_0}^t (-a \right. \\ &+ \left. \frac{1}{x(s)} \int_{t_0}^s [r(v)x^\alpha(v) - q(v)x^\beta(v)] dv\right) ds \\ &\times \exp\left(\int_t^{t+T} [-a + k(s)] ds\right) = (Sx)(t). \end{aligned} \quad (11)$$

This implies that  $(Sx)(t)$  is  $T$ -periodic on  $[t_0, \infty)$ . Thus, we have proved that  $Sx \in \Omega$  for any  $x \in \Omega$ .

Now we need to prove that  $S$  is completely continuous. First, we show that  $S$  is continuous. Let  $x_k = x_k(t) \in \Omega$  be such that  $x_k(t) \rightarrow x(t) \in \Omega$  as  $k \rightarrow \infty$ . For  $t \geq t_0$  we obtain

$$\begin{aligned} |(Sx_k)(t) - (Sx)(t)| &= \left| \exp\left(\int_{t_0}^t \left(-a + \frac{1}{x_k(s)} \int_{t_0}^s [r(v)x_k^\alpha(v) - q(v)x_k^\beta(v)] dv\right) ds\right) \right. \\ &- \left. \exp\left(\int_{t_0}^t \left(-a + \frac{1}{x(s)} \int_{t_0}^s [r(v)x^\alpha(v) - q(v)x^\beta(v)] dv\right) ds\right) \right|. \end{aligned} \quad (12)$$

With respect to the Lebesgue dominated convergence theorem

$$\lim_{k \rightarrow \infty} \|(Sx_k)(t) - (Sx)(t)\| = 0. \quad (13)$$

This means that  $S$  is continuous.

Further, we prove that  $S\Omega$  is relatively compact. It is sufficient to show by the Arzela-Ascoli theorem that the family of functions  $\{Sx : x \in \Omega\}$  is uniformly bounded and equicontinuous on every finite subinterval of  $[t_0, \infty)$ . The uniform boundedness follows from the definition of  $\Omega$ . For  $t \geq t_0, x \in \Omega$  we get

$$\left| \frac{d}{dt} (Sx)(t) \right| = \left| -a + \frac{1}{x(t)} \int_{t_0}^t [r(v)x^\alpha(v) - q(v) \right.$$

$$\begin{aligned} &\left. \cdot x^\beta(v)] dv \right| \times \exp\left(\int_{t_0}^t \left(-a + \frac{1}{x(s)} \right. \right. \\ &\left. \left. \cdot \int_{t_0}^s [r(v)x^\alpha(v) - q(v)x^\beta(v)] dv\right) ds\right) \\ &= |-a + k(t)| \exp\left(\int_{t_0}^t [-a + k(s)] ds\right) \leq M_1, \end{aligned} \quad (14)$$

$M_1 > 0.$

This shows the equicontinuity of the family  $S\Omega$ , (cf. [14], p. 265). Hence,  $S\Omega$  is relatively compact and therefore  $S$  is completely continuous. With respect to Theorem 1, there is an  $x_0 \in \Omega$  such that  $Sx_0 = x_0$ .

Consequently,  $x_0(t)$  is a positive  $T$ -periodic solution of (2). The proof is complete.  $\square$

*Example 3.* Consider the nonlinear differential equation (2) where  $a \geq 0$ ,  $\alpha, \beta \in (0, \infty)$ , and

$$\begin{aligned} q(t) &= -\frac{1}{\alpha^2} (\cos^2 t) \exp\left(\frac{1-\beta}{\alpha} (\sin t - \sin t_0)\right), \\ r(t) &= \frac{1}{\alpha} (a \cos t - \sin t) \exp\left(\frac{1-\alpha}{\alpha} (\sin t - \sin t_0)\right). \end{aligned} \quad (15)$$

Here  $t_0$  is such that  $\cos t_0 = -a\alpha$ ,  $0 \leq a\alpha \leq 1$ .

We set

$$k(t) = a + \frac{1}{\alpha} \cos t. \quad (16)$$

Condition (4) for  $T = 2\pi$  is

$$\int_t^{t+T} [-a + k(s)] ds = \frac{1}{\alpha} \int_t^{t+2\pi} \cos s ds = 0, \quad t \geq t_0. \quad (17)$$

For condition (5), we obtain

$$\begin{aligned} k(t) \exp\left(\int_{t_0}^t [-a + k(s)] ds\right) \\ = \left(a + \frac{1}{\alpha} \cos t\right) \exp\left(\frac{1}{\alpha} \int_{t_0}^t \cos s ds\right) \\ = \left(a + \frac{1}{\alpha} \cos t\right) \exp\left(\frac{1}{\alpha} (\sin t - \sin t_0)\right), \quad t \geq t_0. \end{aligned} \quad (18)$$

Also

$$\begin{aligned} \int_{t_0}^t \left[ r(s) \exp\left(\alpha \int_{t_0}^s [-a + k(v)] dv\right) - q(s) \right. \\ \left. \cdot \exp\left(\beta \int_{t_0}^s [-a + k(v)] dv\right) \right] ds \\ = \int_{t_0}^t \left[ \frac{1}{\alpha} (a \cos s - \sin s) \right. \\ \left. \cdot \exp\left(\frac{1-\alpha}{\alpha} (\sin s - \sin t_0)\right) \exp(\sin s - \sin t_0) \right. \\ \left. + \frac{1}{\alpha^2} (\cos^2 s) \exp\left(\frac{1-\beta}{\alpha} (\sin s - \sin t_0)\right) \right. \\ \left. \cdot \exp\left(\frac{\beta}{\alpha} (\sin s - \sin t_0)\right) \right] ds \\ = \int_{t_0}^t \left[ \frac{1}{\alpha} (a \cos s - \sin s) \exp\left(\frac{1}{\alpha} (\sin s - \sin t_0)\right) \right. \\ \left. + \frac{1}{\alpha^2} (\cos^2 s) \exp\left(\frac{1}{\alpha} (\sin s - \sin t_0)\right) \right] ds \\ = \int_{t_0}^t \frac{1}{\alpha} \left( a \cos s - \sin s + \frac{1}{\alpha} \cos^2 s \right) \\ \cdot \exp\left(\frac{1}{\alpha} (\sin s - \sin t_0)\right) ds \end{aligned}$$

$$\begin{aligned} &= \int_{t_0}^t \frac{d}{ds} \left[ \left( a + \frac{1}{\alpha} \cos s \right) \right. \\ &\cdot \exp\left(\frac{1}{\alpha} (\sin s - \sin t_0)\right) \Big] ds = \left( a + \frac{1}{\alpha} \cos t \right) \\ &\cdot \exp\left(\frac{1}{\alpha} (\sin t - \sin t_0)\right) - \left( a + \frac{1}{\alpha} \cos t_0 \right) = \left( a \right. \\ &\left. + \frac{1}{\alpha} \cos t \right) \exp\left(\frac{1}{\alpha} (\sin t - \sin t_0)\right), \quad t \geq t_0, \end{aligned} \quad (19)$$

since  $\cos t_0 = -a\alpha$ . It is easy to see that condition (3) also holds. Thus, the conditions of Theorem 2 are satisfied and (2) has a positive  $T = 2\pi$ -periodic solution.

### 3. Stability of a Positive Periodic Solution

Here we consider the exponential stability of a positive periodic solution of (2). Let  $x_1(t)$  denote the positive  $T$ -periodic solution of (2) with the initial condition  $x_1(t_0) = 1$ . Let  $x(t)$  denote another solution of (2) with initial condition  $x(t_0) = c_1 > 0$ ,  $c_1 \neq 1$ . Let  $y(t) = x(t) - x_1(t)$ ,  $t \in [t_0, \infty)$ , and  $x'(t_0) + ax(t_0) - x_1'(t_0) - ax_1(t_0) = 0$ .

After integration of (2), we get

$$\begin{aligned} \int_{t_0}^t x''(s) ds + a \int_{t_0}^t x'(s) ds \\ + \int_{t_0}^t [q(s) x^\beta(s) - r(s) x^\alpha(s)] ds = 0, \\ [x'(s)]_{t_0}^t \\ + a [x(s)]_{t_0}^t = \int_{t_0}^t [r(s) x^\alpha(s) - q(s) x^\beta(s)] ds \\ x'(t) - x'(t_0) + ax(t) \\ - ax(t_0) = \int_{t_0}^t [r(s) x^\alpha(s) - q(s) x^\beta(s)] ds. \end{aligned} \quad (20)$$

Similarly, integrating (2) for  $x_1(t)$  leads to

$$\begin{aligned} x_1'(t) - x_1'(t_0) + ax_1(t) - ax_1(t_0) \\ = \int_{t_0}^t [r(s) x_1^\alpha(s) - q(s) x_1^\beta(s)] ds. \end{aligned} \quad (21)$$

Consequently,

$$\begin{aligned} y'(t) = x'(t) - x_1'(t) = x'(t_0) + ax(t_0) - x_1'(t_0) \\ - ax_1(t_0) - a[x(t) - x_1(t)] \\ + \int_{t_0}^t [r(s) (x^\alpha(s) - x_1^\alpha(s)) \\ - q(s) (x^\beta(s) - x_1^\beta(s))] ds = -ay(t) \\ + \int_{t_0}^t [r(s) (x^\alpha(s) - x_1^\alpha(s)) \\ - q(s) (x^\beta(s) - x_1^\beta(s))] ds. \end{aligned} \quad (22)$$

By the mean value theorem, we obtain

$$\begin{aligned}
 y'(t) = & -ay(t) + \int_{t_0}^t [r(s)\alpha x_*^{\alpha-1}(s)(x(s) - x_1(s)) \\
 & - q(s)\beta x_0^{\beta-1}(s)(x(s) - x_1(s))] ds = -ay(t) \\
 & + \int_{t_0}^t [r(s)\alpha x_*^{\alpha-1}(s) - q(s)\beta x_0^{\beta-1}(s)] y(s) ds, \quad (23) \\
 & t \geq t_0.
 \end{aligned}$$

$x_*, x_0 \in [x, x_1]$  or  $x_*, x_0 \in [x_1, x]$ .

Let us assume that the function

$$\begin{aligned}
 f(t, x) = & -ax(t) + \int_{t_0}^t [r(s)x^\alpha(s) - q(s)x^\beta(s)] ds, \quad (24) \\
 & t \geq t_0
 \end{aligned}$$

satisfies Lipschitz-type condition with respect to  $m \leq x \leq M$ .

*Definition 4.* Let  $x_1(t)$  be a positive solution of (2). Let there exist constants  $K_{x_1}, \lambda > 0$  for every solution  $x(t)$  of (2) such that  $0 < m_* \leq x(t) \leq M_*, m_* \leq m, M_* \geq M, x'(t_0) + ax(t_0) - x'_1(t_0) - ax_1(t_0) = 0$  and  $|x(t) - x_1(t)| < K_{x_1} e^{-\lambda t}$  for all  $t > t_0$ .

Then  $x_1(t)$  is said to be exponentially stable.

In the next theorem, we establish sufficient conditions for the exponential stability of the positive solution  $x_1(t)$  of (2).

**Theorem 5.** Suppose that  $q, r \in C([t_0, \infty), (0, \infty))$  and there exist function  $k \in C([t_0, \infty), \mathbb{R})$  and constants  $m, M$  such that (3)–(5) hold. Let  $a > 0, 0 < \alpha < \beta < 1$  and there exist constants  $m_*, M_* \in (0, \infty)$  such that  $m_* \leq m, M_* \geq M$  and

$$\alpha m_*^{\alpha-1} r(t) - \beta M_*^{\beta-1} q(t) \leq 0 \quad \text{for } t \geq t_0. \quad (25)$$

Then (2) has a positive  $T$ -periodic solution which is exponentially stable.

*Proof.* Conditions (3)–(5) imply that (2) has a positive  $T$ -periodic solution  $x_1(t)$ . Let  $x(t)$  be a solution of (2) such that  $m_* \leq x(t) \leq M_*, x'(t_0) + ax(t_0) - x'_1(t_0) - ax_1(t_0) = 0$ . We show that there exists  $\lambda \in (0, \infty)$  such that

$$|x(t) - x_1(t)| < K_{x_1} e^{-\lambda t}, \quad t > t_0, \quad (26)$$

where  $K_{x_1} = e^{\lambda t_0} |y(t_0)| + 1$ .

We consider the Lyapunov function

$$L(t) = |y(t)| e^{\lambda t}, \quad t \geq t_0, \quad \lambda \in (0, a). \quad (27)$$

Let us claim that  $L(t) < K_{x_1}$  for  $t > t_0$ . Furthermore, let there exists  $t_* > t_0$  such that  $L(t_*) = K_{x_1}$  and  $L(t) < K_{x_1}$  for  $t \in [t_0, t_*)$ . Calculating the upper left derivative of  $L(t)$  along the solution of (23), we obtain

$$\begin{aligned}
 D^-(L(t)) \leq & -a|y(t)| e^{\lambda t} \\
 & + e^{\lambda t} \int_{t_0}^t [\alpha x_*^{\alpha-1}(s)r(s) - \beta x_0^{\beta-1}(s)q(s)] |y(s)| ds \quad (28) \\
 & + \lambda |y(t)| e^{\lambda t}, \quad t \geq t_0.
 \end{aligned}$$

For  $t = t_*$  we get

$$\begin{aligned}
 0 \leq D^-(L(t_*)) \leq & (\lambda - a) |y(t_*)| e^{\lambda t_*} \\
 & + e^{\lambda t_*} \int_{t_0}^{t_*} [\alpha x_*^{\alpha-1}(s)r(s) - \beta x_0^{\beta-1}(s)q(s)] \\
 & \cdot |y(s)| ds \leq (\lambda - a) |y(t_*)| e^{\lambda t_*} \quad (29) \\
 & + e^{\lambda t_*} \int_{t_0}^{t_*} [\alpha m_*^{\alpha-1} r(s) - \beta M_*^{\beta-1} q(s)] |y(s)| ds \\
 & \leq (\lambda - a) |y(t_*)| e^{\lambda t_*} = (\lambda - a) K_{x_1} < 0,
 \end{aligned}$$

which is a contradiction. Thus, we have

$$|y(t)| e^{\lambda t} < K_{x_1} \quad \text{for } t > t_0 \text{ and some } \lambda \in (0, a). \quad (30)$$

The proof is complete.  $\square$

#### 4. Application in a Pipe-Tank Configuration

In [5], authors J. Cid, G. Propst and M. Tvrdý established sufficient conditions for the existence and the asymptotic stability of a positive periodic solution for a pipe-tank flow configuration. Such flow configuration is a special case of valveless systems of moving fluid [5, 6].

According to authors Cid et al., the problem of fluid motion in the pipe in [5] can be reformulated as a periodic boundary value problem

$$\begin{aligned}
 u''(t) + au'(t) = & \frac{1}{u(t)} (e(t) - b(u'(t))^2) - c, \quad (31) \\
 & t \in [0, T],
 \end{aligned}$$

$$u(0) = u(T), \quad u'(0) = u'(T). \quad (32)$$

With regard to the physical meaning of the involved parameters, we may assume

$$a \geq 0, \quad b > 1, \quad c > 0 \quad (33)$$

and  $e(t)$  is continuous and  $T$ -periodic on  $\mathbb{R}$ .

The change of variables

$$u = x^\mu, \quad \text{where } \mu = \frac{1}{b+1} \quad (34)$$

transforms the singular problem (31) to the regular one

$$\begin{aligned}
 x''(t) + ax'(t) + q(t)x^\beta(t) - r(t)x^\alpha(t) = & 0, \\
 & t \in [0, T], \\
 x(0) = & x(T), \\
 x'(0) = & x'(T), \quad (35)
 \end{aligned}$$

where

$$\begin{aligned}
 r(t) = & \frac{e(t)}{\mu}, \\
 q(t) = & \frac{c}{\mu}, \quad (36) \\
 \alpha = & 1 - 2\mu, \\
 \beta = & 1 - \mu.
 \end{aligned}$$

From previous text, it follows that  $0 < \alpha < \beta < 1$ .

The main results of the paper [5] are summarized in Theorems 6 and 7.

**Theorem 6** (see [5]). Assume (33) and let  $a > 0$  and  $e_* > 0$ . Then problem (31) has a positive solution provided that the following inequality holds:

$$\frac{(b+1)c^2}{4e_*} < \left(\frac{\pi}{T}\right)^2 + \frac{a^2}{4}. \tag{37}$$

**Theorem 7** (see [5]). Assume (33) and let  $a > 0$  and  $e_* > 0$ . Then problem (31) has at least one asymptotically stable positive solution provided that the following inequalities hold:

$$\frac{c^2 [b(e^*)^2 - (b-1)(e_*)^2]}{e_*(e^*)^2} < \left(\frac{\pi}{T}\right)^2 + \frac{a^2}{4} \tag{38}$$

and

$$(b-1)e^* < be_*, \tag{39}$$

where  $e_* = \min\{e(t) : t \in [0, T]\}$ ,  $e^* = \max\{e(t) : t \in [0, T]\}$ .

The proofs of Theorems 6 and 7 rely on the method of lower and upper solution. For more details about the model and main results, we refer readers to [5, 6] and the references cited therein.

Our aim is to establish new sufficient conditions for the existence and the exponential stability of positive  $T$ -periodic solution of the equation

$$x''(t) + ax'(t) + \frac{1}{\mu} [cx^\beta(t) - e(t)x^\alpha(t)] = 0, \tag{40}$$

$t \geq t_0$ .

With respect to Theorems 2 and 5, we obtain the following result.

**Theorem 8.** Suppose that  $a \geq 0, 0 < \alpha < \beta < 1$  and there exist function  $k \in C([t_0, \infty), \mathbb{R})$  and constants  $m, M$  such that (3) and (4) hold and

$$\begin{aligned} &k(t) \exp\left(\int_{t_0}^t [-a + k(s)] ds\right) \\ &= \int_{t_0}^t \frac{1}{\mu} \left[ e(s) \exp\left(\alpha \int_{t_0}^s (-a + k(v)) dv\right) \right. \\ &\quad \left. - c \exp\left(\beta \int_{t_0}^s (-a + k(v)) dv\right) \right] ds, \quad t \geq t_0. \end{aligned} \tag{41}$$

Then (40) has a positive  $T$ -periodic solution.

**Theorem 9.** Suppose that  $e \in C([t_0, \infty), (0, \infty))$ ,  $a > 0, 0 < \alpha < \beta < 1$ , and  $c > 0$  and there exist function  $k \in C([t_0, \infty), \mathbb{R})$  and constants  $m, M$  such that (3), (4), and (41) hold. Let, in addition, there exist constants  $m_*, M_* \in (0, \infty)$  such that  $m_* \leq m, M_* \geq M$  and

$$\alpha m_*^{\alpha-1} e(t) - \beta M_*^{\beta-1} c \leq 0 \quad \text{for } t \geq t_0. \tag{42}$$

Then (40) has a positive  $T$ -periodic solution which is exponentially stable.

The results of Theorems 8 and 9 are illustrated by the example.

*Example 10.* Let us consider the nonlinear differential equation

$$x''(t) + ax'(t) + q(t)x^\beta(t) - r(t)x^\alpha(t) = 0, \tag{43}$$

$t \geq t_0$ ,

where  $a \in (0, \infty), 0 < \alpha < \beta < 1$  and

$$\begin{aligned} q(t) &= c(b+1) = \frac{c}{\mu}, \quad b > 1, c > 0, \\ r(t) &= \frac{a \cos t - \sin t}{d + \sin t_0} \left(\frac{d + \sin t_0}{d + \sin t}\right)^\alpha \\ &\quad + c(b+1) \left(\frac{d + \sin t}{d + \sin t_0}\right)^{\beta-\alpha} = \frac{e(t)}{\mu}, \quad d > 1, \end{aligned} \tag{44}$$

where  $t_0$  is such that  $a(d + \sin t_0) + \cos t_0 = 0$ .

We set

$$k(t) = a + \frac{\cos t}{d + \sin t}. \tag{45}$$

Then, for condition (4) and  $T = 2\pi$ , we get

$$\begin{aligned} \int_t^{t+T} [-a + k(s)] ds &= \int_t^{t+2\pi} \frac{\cos s}{d + \sin s} ds \\ &= \ln(d + \sin(t + 2\pi)) \\ &\quad - \ln(d + \sin t) = 0, \quad t \geq t_0. \end{aligned} \tag{46}$$

For condition (41), we obtain

$$\begin{aligned} &k(t) \exp\left(\int_{t_0}^t [-a + k(s)] ds\right) \\ &= \left(a + \frac{\cos t}{d + \sin t}\right) \exp\left(\int_{t_0}^t \frac{\cos s}{d + \sin s} ds\right) \\ &= \left(a + \frac{\cos t}{d + \sin t}\right) \exp\left(\ln \frac{d + \sin t}{d + \sin t_0}\right) \\ &= \left(a + \frac{\cos t}{d + \sin t}\right) \frac{d + \sin t}{d + \sin t_0} \\ &= \frac{a(d + \sin t) + \cos t}{d + \sin t_0}. \end{aligned} \tag{47}$$

We also get

$$\begin{aligned} &\int_{t_0}^t \left[ r(s) \exp\left(\alpha \int_{t_0}^s [-a + k(v)] dv\right) - q(s) \right. \\ &\quad \left. \cdot \exp\left(\beta \int_{t_0}^s [-a + k(v)] dv\right) \right] ds \\ &= \int_{t_0}^t \left[ \left(\frac{a \cos s - \sin s}{d + \sin t_0} \left(\frac{d + \sin t_0}{d + \sin s}\right)^\alpha \right. \right. \\ &\quad \left. \left. + c(b+1) \left(\frac{d + \sin s}{d + \sin t_0}\right)^{\beta-\alpha} \right) \right] \\ &\quad \times \exp\left(\alpha \int_{t_0}^s \frac{\cos v}{d + \sin v} dv\right) - c(b+1) \end{aligned}$$

$$\begin{aligned}
 & \cdot \exp\left(\beta \int_{t_0}^s \frac{\cos v}{d + \sin v} dv\right) ds \\
 &= \int_{t_0}^t \left( \left[ \frac{a \cos s - \sin s}{d + \sin t_0} \left( \frac{d + \sin t_0}{d + \sin s} \right)^\alpha \right. \right. \\
 &+ c(b+1) \left. \left. \left( \frac{d + \sin s}{d + \sin t_0} \right)^{\beta-\alpha} \right] \times \left( \frac{d + \sin s}{d + \sin t_0} \right)^\alpha \right. \\
 &- c(b+1) \left. \left( \frac{d + \sin s}{d + \sin t_0} \right)^\beta \right) ds \\
 &= \int_{t_0}^t \frac{a \cos s - \sin s}{d + \sin t_0} ds = \frac{1}{d + \sin t_0} (a \sin t + \cos t \\
 &- a \sin t_0 - \cos t_0) = \frac{a(d + \sin t) + \cos t}{d + \sin t_0},
 \end{aligned} \tag{48}$$

since  $a(d + \sin t_0) + \cos t_0 = 0$ . The condition (3) is also satisfied.

Thus, conditions (3), (4), and (41) of Theorem 8 are satisfied and (43) has a positive  $T = 2\pi$ -periodic solution

$$\begin{aligned}
 x(t) &= \exp\left(\int_{t_0}^t [-a + k(s)] ds\right) \\
 &= \exp\left(\int_{t_0}^t \frac{\cos s}{d + \sin s} ds\right) = \exp\left(\ln \frac{d + \sin t}{d + \sin t_0}\right) \tag{49} \\
 &= \frac{d + \sin t}{d + \sin t_0}, \quad t \geq t_0,
 \end{aligned}$$

$a(d + \sin t_0) + \cos t_0 = 0$ .  
For

$$\begin{aligned}
 t_0 &= \pi, \\
 a &= \frac{1}{4}, \\
 d &= 4, \\
 b &= 3, \\
 c &= 2,
 \end{aligned} \tag{50}$$

we get

$$\begin{aligned}
 \mu &= \frac{1}{b+1} = \frac{1}{4}, \\
 \alpha &= 1 - 2\mu = \frac{1}{2}, \\
 \beta &= 1 - \mu = \frac{3}{4},
 \end{aligned} \tag{51}$$

$$\begin{aligned}
 e(t) = \mu r(t) &= \frac{1}{4} \left[ \frac{1}{4} \left( \frac{1}{4} \cos t - \sin t \right) \left( \frac{4}{4 + \sin t} \right)^{0.5} \right. \\
 &\left. + 8 \left( \frac{4 + \sin t}{4} \right)^{0.25} \right]
 \end{aligned}$$

and  $e_* \approx 1.931$ ,  $e^* \approx 2.061$ . When we set constants  $m_* = 0.6 < m = 0.75$ ,  $M_* = 1.4 > M = 1.25$ , condition (42) has a form

$$\frac{1}{2} 0.6^{-0.5} e(t) - \frac{3}{2} 1.4^{-0.25} < 0, \quad t \geq \pi. \tag{52}$$

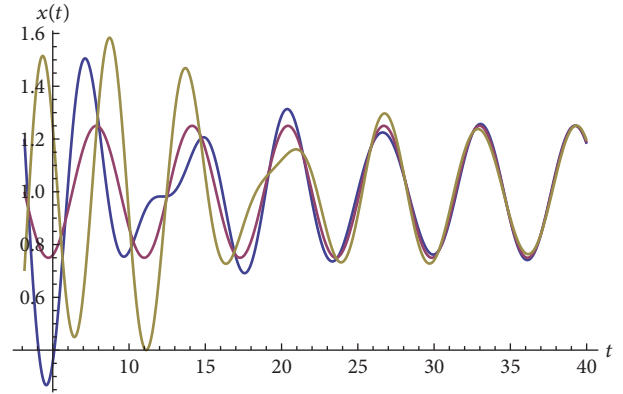


FIGURE 1: Numerical simulations of problem (43).

According to Theorem 9, solution  $x(t)$  is exponentially stable. The numerical simulation in Figure 1 supports the conclusion.

Let us check the existence and the asymptotic stability of the solution of (43) according to Theorems 6 and 7, respectively, with regard to considered values of parameters. We can see that conditions (37) and (38) are not satisfied. Also condition

$$q^* < \min \left\{ \left( \frac{\pi}{T} \right)^2 + \left( \frac{a}{2} \right)^2, r_* \right\}, \tag{53}$$

where  $q^* = \max\{q(t) : t \in [0, T]\}$ ,  $r_* = \min\{r(t) : t \in [0, T]\}$ , from Corollary 3.5 [6] is not satisfied.

As is illustrated on this example, our results provide extension to previously obtained results in [5, 6].

## Data Availability

No data were used to support this study.

## Conflicts of Interest

The authors declare that there are no conflicts of interest regarding the publication of this paper.

## Acknowledgments

This work was supported by the Grant 1/0812/17 of the Scientific Grant Agency of the Ministry of Education of the Slovak Republic and by the Grant No. 015ŽU-4/2017 of the Slovak Grant Agency KEGA.

## References

- [1] G. Liebau, "Über ein ventilloes Pumpprinzip," *Naturwissenschaften*, vol. 41, no. 14, p. 327, 1954.
- [2] J. Männer, A. Wessel, and T. M. Yelbuz, "How does the tubular embryonic heart work? Looking for the physical mechanism generating unidirectional blood flow in the valveless embryonic heart tube," *Developmental Dynamics*, vol. 239, no. 4, pp. 1035-1046, 2010.

- [3] A. Borzí and G. Propst, “Numerical investigation of the Liebau phenomenon,” *Z. Angew. Math. Phys.*, vol. 54, no. 6, pp. 1050–1072, 2003.
- [4] T. T. Bringley, S. Childress, N. Vandenberghe, and J. Zhang, “An experimental investigation and a simple model of a valveless pump,” *Physics of Fluids*, vol. 20, no. 3, p. 033602, 2008.
- [5] J. A. Cid, G. Propst, and M. Tvrdý, “On the pumping effect in a pipe/tank flow configuration with friction,” *Physica D: Nonlinear Phenomena*, vol. 273/274, pp. 28–33, 2014.
- [6] J. A. Cid, G. Infante, M. Tvrdý, and M. Zima, “A topological approach to periodic oscillations related to the Liebau phenomenon,” *Journal of Mathematical Analysis and Applications*, vol. 423, no. 2, pp. 1546–1556, 2015.
- [7] H. Andersson, W. van der Wijngaart, P. Nilsson, P. Enoksson, and G. Stemme, “A valve-less diffuser micropump for microfluidic analytical systems,” *Sensors and Actuators B: Chemical*, vol. 72, no. 3, pp. 259–265, 2001.
- [8] G. Propst, “Pumping effects in models of periodically forced flow configurations,” *Physica D: Nonlinear Phenomena*, vol. 217, no. 2, pp. 193–201, 2006.
- [9] L. Berezansky, E. Braverman, and L. Idels, “Nicholson’s blowflies differential equations revisited: main results and open problems,” *Applied Mathematical Modelling: Simulation and Computation for Engineering and Environmental Systems*, vol. 34, no. 6, pp. 1405–1417, 2010.
- [10] T. Candan, “Existence of positive periodic solutions of first-order neutral differential equations,” *Mathematical Methods in the Applied Sciences*, vol. 40, no. 1, pp. 205–209, 2017.
- [11] T. Candan, “Nonoscillatory solutions of higher order differential and delay differential equations with forcing term,” *Applied Mathematics Letters*, vol. 39, pp. 67–72, 2015.
- [12] J. Diblík and Z. Svoboda, “The solutions of second-order linear differential systems with constant delays,” in *Proceedings of the 14th International Conference of Numerical Analysis and Applied Mathematics (conference proceedings)*, vol. 1863, Rhodes, Greece, 2017.
- [13] B. Dorociaková and R. Olach, “Some notes to existence and stability of the positive periodic solutions for a delayed nonlinear differential equations,” *Open Mathematics*, vol. 14, pp. 361–369, 2016.
- [14] L. H. Erbe, Q. Kong, and B. G. Zhang, *Oscillation Theory for Functional-Differential Equations*, Marcel Dekker, New York, NY, USA, 1995.
- [15] X. Yang, “Existence of periodic solution for nonlinear differential equations,” *Applied Mathematics and Computation*, vol. 131, no. 2-3, pp. 433–438, 2002.
- [16] J. Schauder, “Der Fixpunktsatz in Funktionalräumen,” *Studia Mathematica*, vol. 2, no. 1, pp. 171–180, 1930.

## Research Article

# Evaluation of the Use of the Yeoh and Mooney-Rivlin Functions as Strain Energy Density Functions for the Ground Substance Material of the Annulus Fibrosus

Héctor E. Jaramillo S. 

*Departamento de Energética y Mecánica, Facultad de Ingeniería, Universidad Autónoma de Occidente, Cali 760031, Colombia*

Correspondence should be addressed to Héctor E. Jaramillo S.; [hjsuarez@uao.edu.co](mailto:hjsuarez@uao.edu.co)

Received 23 July 2018; Accepted 12 September 2018; Published 7 November 2018

Guest Editor: Carlos Llopis-Albert

Copyright © 2018 Héctor E. Jaramillo S. This is an open access article distributed under the Creative Commons Attribution License, which permits unrestricted use, distribution, and reproduction in any medium, provided the original work is properly cited.

Due to the importance of the intervertebral disc in the mechanical behavior of the human spine, special attention has been paid to it during the development of finite element models of the human spine. The mechanical behavior of the intervertebral disc is nonlinear, heterogeneous, and anisotropic and, due to the low permeability, is usually represented as a hyperelastic model. The intervertebral disc is composed of the nucleus pulposus, the endplates, and the annulus fibrosus. The annulus fibrosus is modeled as a hyperelastic matrix reinforced with several fiber families, and researchers have used different strain energy density functions to represent it. This paper presents a comparative study between the strain energy density functions most frequently used to represent the mechanical behavior of the annulus fibrosus: the Yeoh and Mooney-Rivlin functions. A finite element model of the annulus fibrosus of the L4-L5 segment under the action of three independent and orthogonal moments of 8 N-m was used, employing Abaqus software. A structured mesh with eight divisions along the height and the radial direction of annulus fibrosus and tetrahedron elements for the endplates were used, and an exponential energy function was employed to represent the mechanical behavior of the fibers. A total of 16 families were used; the fiber orientation varied with the radial coordinate from 25° on the outer boundary to 46° on the inner boundary, measuring it with respect to the transverse plane. The mechanical constants were taken from the reported literature. The range of motion was obtained by finite element analysis using different values of the mechanical constants and these results were compared with the reported experimental data. It was found that the Yeoh function showed a better fit to the experimental range of motion than the Mooney-Rivlin function, especially in the nonlinear region.

## 1. Introduction

Generally, biomechanics research uses the finite element (FE) method [1–6]. The first FE model of the spine was reported by Belytschko and Kulak [7] and included two vertebral bodies and the intervertebral disc (IVD). This model was axisymmetric and the tissues were represented as isotropic and linear elastic material. The nucleus pulposus (NP) was modeled as incompressible liquid and the annulus fibrosus (AF) as orthotropic linear material. However, the most important contributions to the modeling of the IVD were made by Shirazi-Adl et al. [8]. They reported a model of the L2-L3 segment that used geometry and nonlinear materials. The AF was represented as a matrix reinforced with collagen fibers, and this was possibly the first model of the AF in which it was modeled as a composite material. Also, the model

included the differences in the three kinds of bones of the vertebral bodies.

A few years later, Goel et al. [9] developed an FE model of the AF which takes into account the anisotropy of the fibers and their amount and orientation. However the fibers were considered as elastic material. More recently, Schmidt et al. [10] reported a new method of calibration of the properties of the AF (matrix and collagen fibers) using the experimental curves of the L4-L5 segment without NP. This method allows the individual contributions of the fibers and the matrix of the AF to be determined. On the other hand, a model developed by Ezquerro et al. [11] represented the NP as incompressible and hyperelastic using the Mooney-Rivlin energy function with two constants, and the AF was modeled as a fiber setup embedded into a matrix. They used a polynomial hyperelastic function for the matrix and

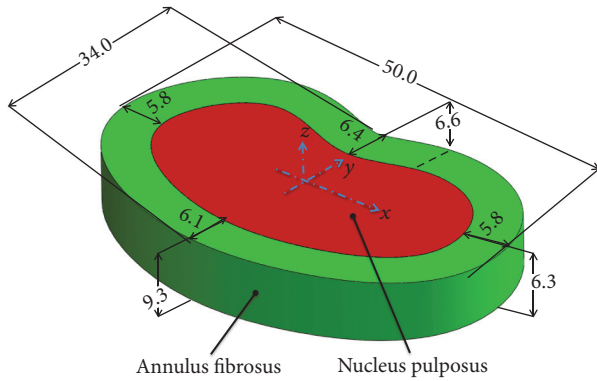


FIGURE 1: Shape and dimensions in mm for the annulus fibrosus of the L4-L5 segment.

stress-strain curves for the fibers. Guan et al. [12] reported an FE model in which the vertebrae were modeled as a rigid bodies, the NP as a hyperelastic Neo-Hookean material, the AF as a hyperelastic matrix fiber reinforced using a UMAT subroutine from Abaqus ([www.3ds.com](http://www.3ds.com), Dassault Systèmes, Francia), and the ligaments as Truss elements under tension, while Gap elements were used to simulate the contact between the joint facets.

In conclusion, many researchers have used different strain energy functions and techniques to model the mechanical behavior of the AF. Actually, the AF can be modeled as a reinforced matrix fiber. Particularly, the matrix or ground substance has been modeled using the energy functions of Mooney-Rivlin [13–18] and Yeoh [19–26]. However, we did not find any study that supported the use of these energy functions and how they affect the mechanical behavior of the AF. In this direction, this work compared the mechanical behavior of the AF determined using the two energy functions with the experimental data in order to find which strain energy function fit the experimental results better.

## 2. Methods and Materials

**2.1. Geometry.** The geometry of the AF of the L4-L5 segment (Figure 1) was taken from the FE model of the L4-L5-S1 segment reported by Jaramillo et al. [27]. The percentage of the transverse section of the AF with respect to the total area of the IVD was 50% according to reported works [28–30].

The AF model has a mesh with eight divisions along the height and eight in the radial direction (Figure 2). The AF was divided into five sections in order to take into account the regional variation of the material properties and to obtain a better fit to the experimental data [10]. Each radial division contains a total of 16 families of fibers [31–33], where the families were crisscrossed with one another. The orientation of the fibers varied radially from 25° on the outer boundary to 46° on the inner boundary using an increase of 3° [10, 23, 34, 35], and the angle was measured with respect to the horizontal axis.

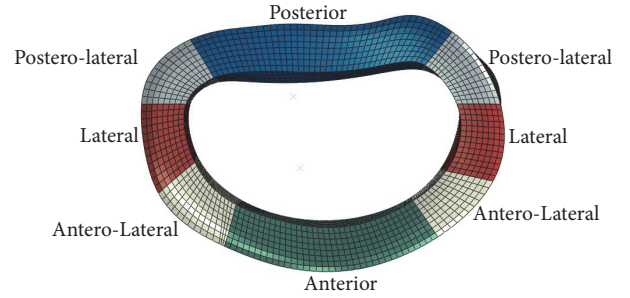


FIGURE 2: Final mesh and sections of the annulus fibrosus used to define their different properties.

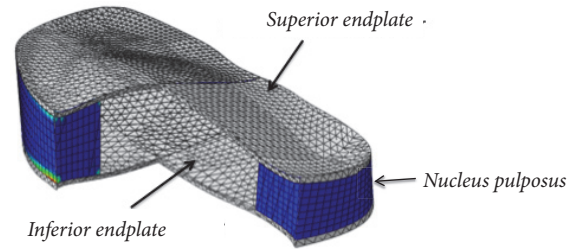


FIGURE 3: Section view of the finite element model.

TABLE 1: Type and number of elements used in the finite element model.

Part	Element type	Element number
Annulus fibrosus	Hexahedral, 8 nodes, C3D8H	7448
End plates	Tetrahedral, 10 nodes, C3D4	74134

The endplates were considered as a rigid body in order to apply the moments. A structured mesh of 7448 hexahedral elements with eight nodes was used for every model analyzed (Table 1). Due to the differences between the types of elements used to represent the AF and the endplates, the Tie option was used to join the two parts (Figure 3).

**2.2. Boundary Conditions and Loads.** The inferior endplate was fixed and three independent moments of 8 N-m were applied to the superior endplate. The moments were applied through the orthogonal axes in order to simulate the flexion, extension, lateral flexion, and axial rotation movements.

The range of motion (ROM) and the maximum stress in the families of fibers were selected as the output variables. The ROMs of the FE models were compared with the experimental data of the L4-L5 segment reported by Jaramillo et al. [36]. To compare the ROMs of the FE models with the experimental ROM, Equation (1) was employed, and the average ROM was calculated for 1, 2, 3, 4, 5, 6, 7, and 8 N-m in order to find how similar their behaviors were.

$$\% \text{ Aprox.} = \left( \frac{ROM_{Exp.} - ROM_{FEA}}{ROM_{Exp.}} \right) \times 100\% \quad (1)$$

Also, the influence of the mechanical constants on the maximum stress for the fiber families of the AF was obtained.

TABLE 2: Mechanical constants used to the fibers of the annulus fibrous.

Section	$a_1$ [MPa]	$a_2$ [Unit less]
Anterior	2.10	25.0
Antero-lateral	0.16	4.0
Lateral	0.16	4.0
Postero-lateral	0.16	4.0
Posterior	0.24	5.64

2.3. *Properties and Constitutive Equations.* A strain energy function was defined for the fibers (Equation (2)) and their mechanical constants (Table 2) were used for all the models.

$$W_f = \frac{a_1}{a_2} \left[ e^{a_2(I_4-1)^2} + e^{a_2(I_6-1)^2} - 2 \right], \quad (2)$$

where  $a_1$  and  $a_2$  are the material constants and  $I_4$  and  $I_6$  are the deviatoric invariants associated with the two families of fibers, which are defined as

$$I_4 = N^{(1)} \cdot C \cdot N^{(1)} \quad (3)$$

$$I_6 = N^{(2)} \cdot C \cdot N^{(2)} \quad (4)$$

where  $N^{(1)}$  and  $N^{(2)}$  are the unit vectors along the two fiber directions in the nondeformed configuration and  $C$  is the deviatoric right Green deformation tensor. The reinforcing fibers only work under a positive strain. This strain energy function was selected because it has been used by many researchers [22, 23, 37], and the experimental values for the mechanical constants have been reported [38–41].

Mooney-Rivlin and Yeoh strain energy functions were used to represent the ground substance. The Mooney-Rivlin function was defined as

$$W_m = c_{10} (I_1 - 3) + c_{01} (I_2 - 3) \quad (5)$$

where  $c_{10}$  and  $c_{01}$  are the material constants and  $I_1$  and  $I_2$  are the first and second deviatoric invariants of the deviatoric right Green deformation tensor. The mechanical constants (Table 3) were taken from values reported by Heuer et al. [42–44] and Rohlman et al. [45]. For the FE analysis, the constants were multiplied by 0, 25, 50, 75, 100, 200, 300, 400, and 500%. In the first step,  $c_{10}$  was varied and  $c_{01}$  was constant, and in the second step,  $c_{10}$  was constant and  $c_{01}$  was varied. For instance, for model 3 (M3),  $c_{10} = 0.56 \times 50\% = 0.28$  MPa and  $c_{01} = 0.14 \times 100\% = 0.14$  MPa. In this way, in models M1 to M9,  $c_{10}$  was varied and  $c_{01}$  was constant; in models M10 to M18,  $c_{10}$  was constant and  $c_{01}$  was varied.

The Yeoh function was defined as

$$W_m = c_1 (I_1 - 3) + c_2 (I_1 - 3)^2 + c_3 (I_1 - 3)^3 \quad (6)$$

where  $c_1$ ,  $c_2$ , and  $c_3$  are the mechanical constants of the material and  $I_1$  is the first deviatoric invariant of the deviatoric right Green deformation tensor. The experimental constants were taken from Ayturk et al. [23] (Table 4) and multiplied by 0, 25, 50, 75, 100, 200, 300, 400, and 500%. In the first step,  $c_1$  was varied and  $c_2$  and  $c_3$  were constant; in the second step,

TABLE 3: Mechanical constants for the strain energy function Mooney-Rivlin.

Section	$c_{10}$ [MPa]	$c_{01}$ [MPa]
Anterior	0.56	0.14
Antero-lateral	0.56	0.14
Lateral	0.56	0.14
Postero-lateral	0.56	0.14
Posterior	0.56	0.14

TABLE 4: Mechanical constants used for the Yeoh strain energy function.

Section	$c_1$ [MPa]	$c_2$ [MPa]	$c_3$ [MPa]
Anterior	0.0146	-0.0189	0.041
Antero-lateral	0.0146	-0.0189	0.041
Lateral	0.0146	-0.0189	0.041
Postero-lateral	0.0146	-0.0189	0.041
Posterior	0.0146	-0.0189	0.041

$c_2$  was varied and  $c_1$  and  $c_3$  were constant; finally, in the third step,  $c_3$  was varied and  $c_1$  and  $c_2$  were constant. For instance, in model 22 (M22),  $c_1 = 0.0146 \times 100\% = 0.0146$  MPa,  $c_2 = -0.0189 \times 100\% = -0.0189$  MPa, and  $c_3 = 0.041 \times 75\% = 0.03075$  MPa. In this way, in models M1 to M9,  $c_1$  was varied and  $c_2$  and  $c_3$  were constant; in models M10 to M18,  $c_2$  was varied and  $c_1$  and  $c_3$  were constant; and in models M19 to M27,  $c_3$  was varied and  $c_1$  and  $c_2$  were constant.

The Abaqus subroutine Uanisohyper was developed to implement the aforementioned energy functions. Also, due to the amount of data used, a subroutine in Python [46] was developed to execute every analysis automatically.

### 3. Results

3.1. *Range of Motion (ROM) Behavior.* Compared with the experimental ROM, the mechanical behavior of the Mooney-Rivlin function (Figures 4–7) fitted less well than the behavior obtained with the Yeoh function (Figures 8–11). In this direction, the Mooney-Rivlin approximations to the experimental data were 26.1% for the flexion movement, 35.7% for the extension movement, 19.2% for the lateral flexion movement, and 39.4% for the axial rotation movement, while the Yeoh function approximations were 87.0, 95.1, 78.6, and 91.1% for the flexion, extension, lateral flexion, and axial rotation, respectively.

3.1.1. *Using the Mooney-Rivlin Function as the Strain Energy Function for the Ground Substance.* The ROM behavior was similar for the four movements: as  $c_{10}$  and  $c_{01}$  increased, the ROM decreased, moving away from the experimental data. That is to say, when the mechanical constants increased, the ground substance contributed a greater part of the stiffness of the AF and as a consequence a lower ROM. Particularly, the set of mechanical constants with the better approximation to the experimental ROM was  $c_{10} = 0$  MPa and  $c_{01} = 0.14$  MPa, with experimental approximations of 74.2, 82.4, 59.0, and 77.9% for the flexion, extension, lateral flexion, and axial

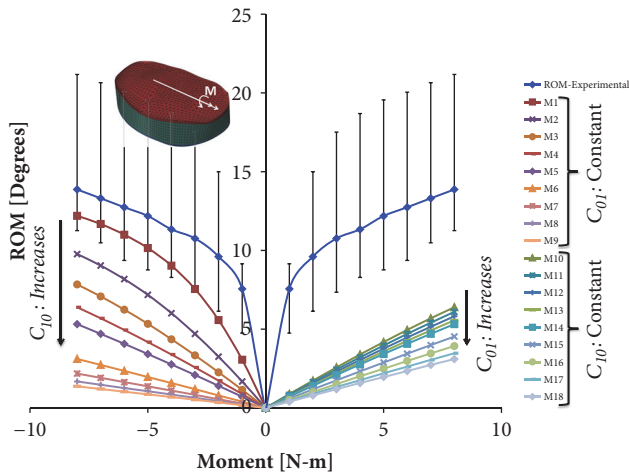


FIGURE 4: ROM versus Moment for the flexion movement using Mooney-Rivlin function for different values of  $c_{10}$  and  $c_{01}$ .

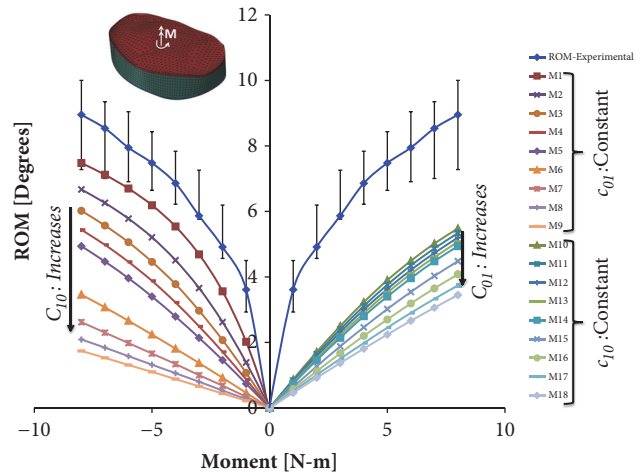


FIGURE 7: ROM versus Moment for the axial rotation movement using Mooney-Rivlin function for different values of  $c_{10}$  and  $c_{01}$ .

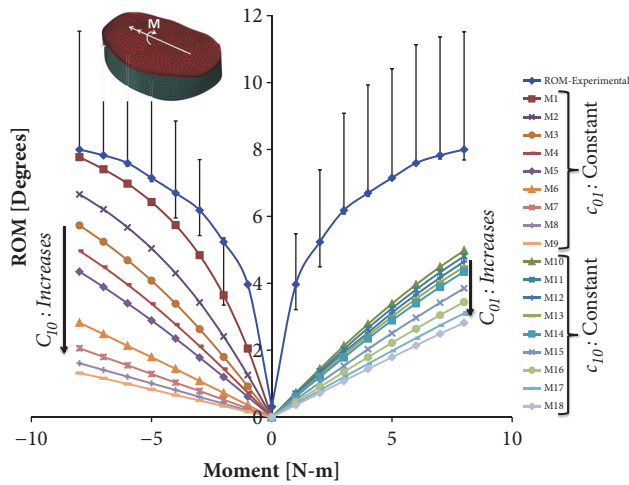


FIGURE 5: ROM versus Moment for the extension movement using Mooney-Rivlin function for different values of  $c_{10}$  and  $c_{01}$ .

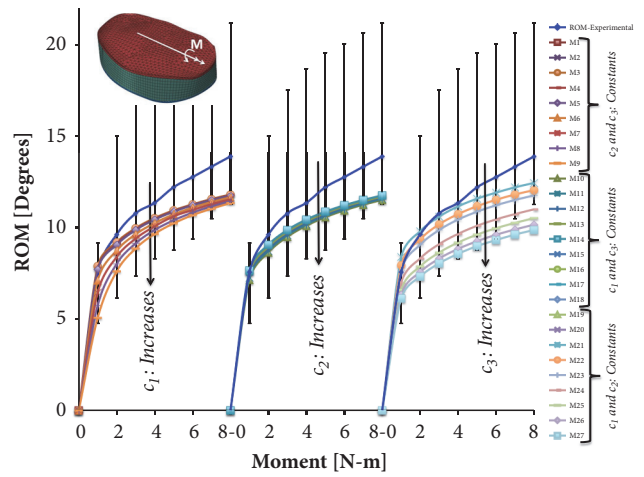


FIGURE 8: ROM versus Moment for the flexion movement using Yeoh function for different values of  $c_1$ ,  $c_2$ , and  $c_3$ .

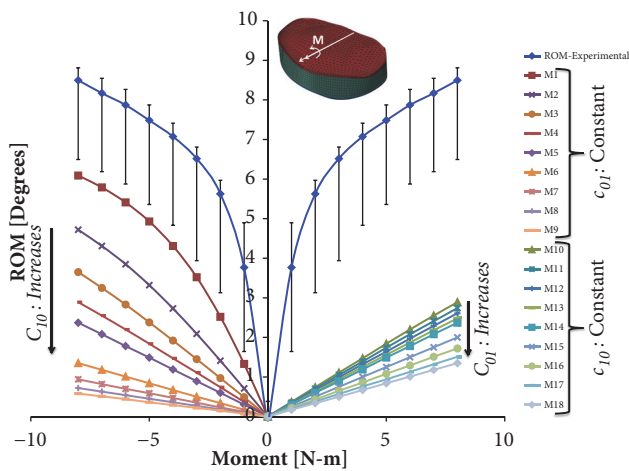


FIGURE 6: ROM versus Moment for the lateral flexion movement using Mooney-Rivlin function for different values of  $c_{10}$  and  $c_{01}$ .

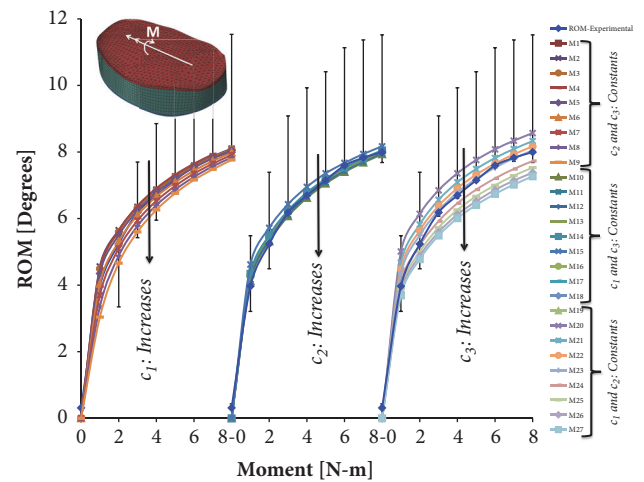


FIGURE 9: ROM versus Moment for the extension movement using Yeoh function for different values of  $c_1$ ,  $c_2$ , and  $c_3$ .

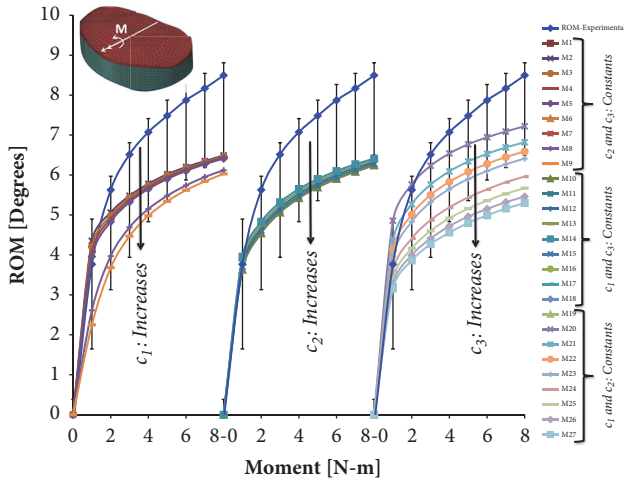


FIGURE 10: ROM versus Moment for the lateral flexion movement using Yeoh function for different values of  $c_1$ ,  $c_2$  and  $c_3$ .

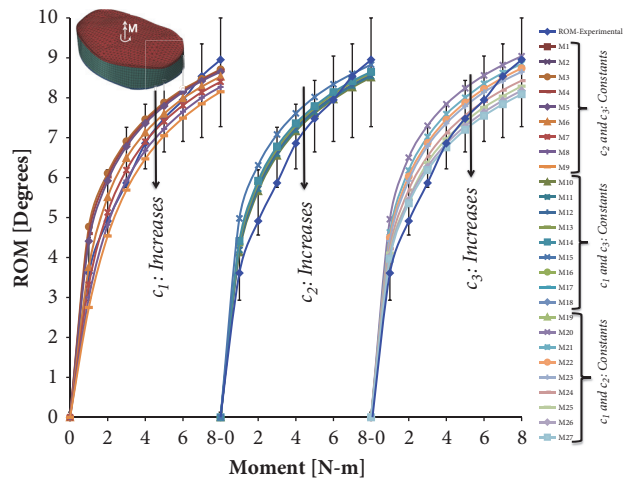


FIGURE 11: ROM versus Moment for the axial rotation movement using Yeoh function for different values of  $c_1$ ,  $c_2$  and  $c_3$ .

rotation, respectively (Figures 4–7). Then, the left sides of Figures 4–7 show the ROM behavior when  $c_{01}$  (0.14 MPa) is constant but  $c_{10}$  increases and the right sides show the ROM behavior when  $c_{10}$  (0.56 MPa) is constant but  $c_{01}$  increases, for all movements. In general, the  $c_{10}$  variation has a major impact than  $c_{01}$  over the ROM behavior.

**3.1.2. Using the Yeoh Function as the Strain Energy Function for the Ground Substance.** When the Yeoh function was used, the ROM showed a better fit to the experimental behavior. In this direction, the fits obtained were 94.1% for flexion movement using  $c_1 = 0.0146$  MPa,  $c_2 = -0.0189$  MPa, and  $c_3 = 0.0205$  MPa; 98.8% for extension movement using  $c_1 = 0.0292$  MPa,  $c_2 = -0.0189$  MPa, and  $c_3 = 0.041$  MPa; 88.4% for lateral flexion movement using  $c_1 = 0.0146$  MPa,  $c_2 = -0.0189$  MPa, and  $c_3 = 0.01025$  MPa; and 96.0% for axial rotation movement using  $c_1 = 0.0438$  MPa,  $c_2 = -0.0189$  MPa, and  $c_3 = 0.041$  MPa (Figures 8–11). Just four curves were outside the experimental range for flexion (Figure 8), extension (Figure 9), and lateral flexion

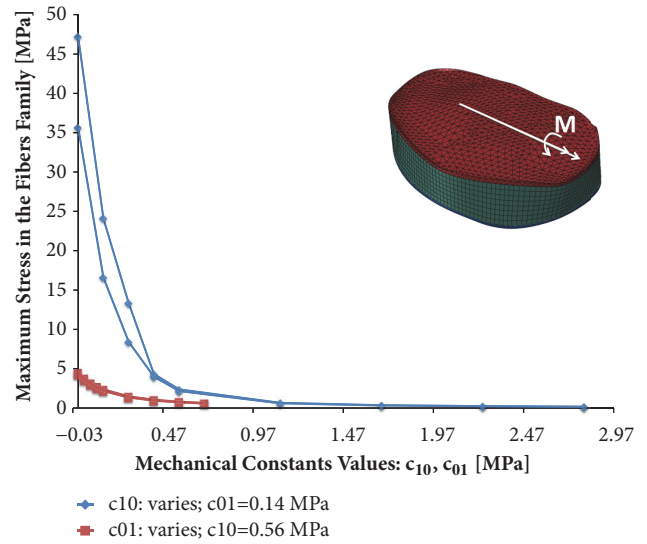


FIGURE 12: Maximum stress in the fibers family of AF versus mechanical constants values for the flexion movement, using Mooney-Rivlin function.

(Figure 10); these curves used the combination of  $c_1 = 0.0146$  MPa,  $c_2 = -0.0189$  MPa, and  $c_3 = 0.082, 0.123, 0.164,$  and  $0.205$  MPa. For the axial rotation movement, all curves were within the experimental range (Figure 11). Then, Figures 8–11 are composed by three groups of figures, the first group (left side) show the ROM behavior when  $c_2$  (-0.0189 MPa) and  $c_3$  (0.041) are constant but  $c_1$  increases, for the second group (middle)  $c_1$  (0.0146 MPa) and  $c_3$  (0.043) are constant but  $c_2$  increases, finally the third group (right side) show the ROM behavior when  $c_1$  (0.0146 MPa) and  $c_2$  (-0.0189 MPa) are constant but  $c_3$  increases, for all movements.

In general, the intervertebral disc stiffness increased due to the increase of the mechanical constants; however, a high impact of  $c_3$  on the ROM was found in all movements. This can be explained by the high dispersion area found in the ROM behavior when  $c_3$  varied (curves on the right side, Figures 8–11). In this case, the fits to the obtained experimental data were 84.6% for flexion, 93.4% for extension, 77.8% for lateral flexion, and 90.5% for axial rotation; these values of fit were under the average values obtained for all curves.

**3.2. Maximum Stress in the Families of Fibers.** In general, it was found that the ROM decreased due to increases of the mechanical constants of the ground substance ( $c_1$ ,  $c_2$ , and  $c_3$ ). This can be explained by the fact that when the moment is applied, part of it is taken by the fibers and another by the matrix or ground substance, so when the mechanical constants of the ground substance increase, the matrix takes a greater part of the moment.

**3.2.1. Using the Mooney-Rivlin Function as the Strain Energy Function for the Ground Substance.** Figures 12–15 show the stress behavior versus the mechanical constants variation for a moment maximum of 8 N-m applied. Then, for a maximum moment of 8 N-m, the stress in the fibers varied from 0.17 to 47.1 MPa in flexion (Figure 12), from 0.57 to 125.5 MPa in

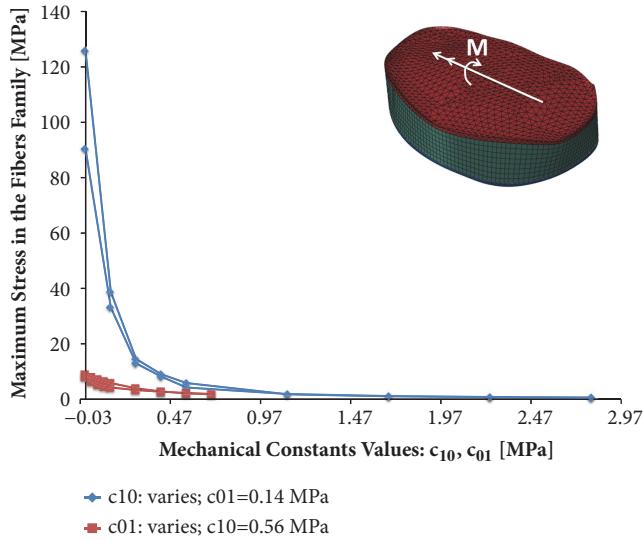


FIGURE 13: Maximum stress in the fibers family of AF versus mechanical constants values for the extension movement, using Mooney-Rivlin function.

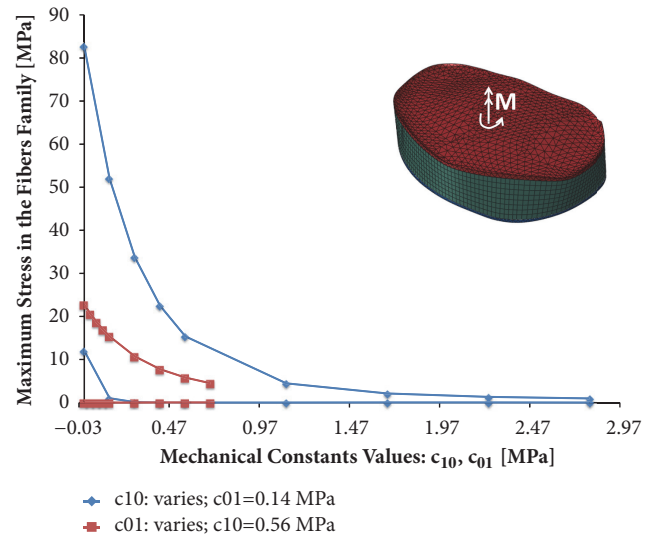


FIGURE 15: Maximum stress in the fibers family of AF versus mechanical constants values for the axial rotation movement, using Mooney-Rivlin function.

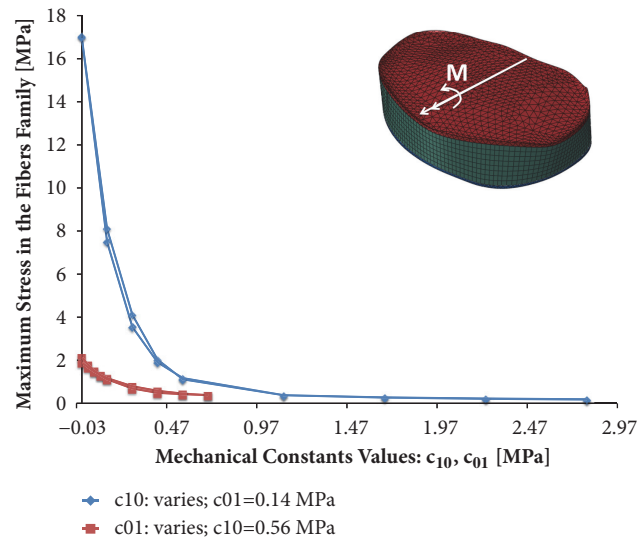


FIGURE 14: Maximum stress in the fibers family of AF versus mechanical constants values for the lateral flexion movement, using Mooney-Rivlin function.

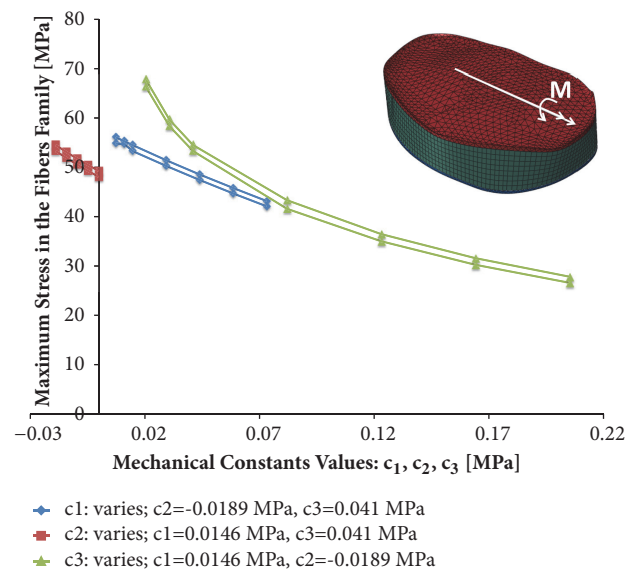


FIGURE 16: Maximum stress in the fibers family of AF versus mechanical constants values for the flexion movement, using Yeoh function.

extension (Figure 13), from 0.17 to 17.0 MPa in lateral flexion (Figure 14), and from 0.015 to 12.0 MPa in axial rotation (Figure 15). The percentage differences in the stresses between the fiber families were 16.5% for flexion, 12.8% for extension, 5.4% for lateral flexion, and 97.7% for axial rotation when  $c_{10}$  was varied and  $c_{01}$  was equal to 0.14 MPa. When  $c_{10}$  was constant (0.56 MPa) and  $c_{01}$  was varied, the differences between the stresses for the two families of fibers were 9.4% for flexion, 16.8% for extension, 7.8% for lateral flexion, and 99.8% for axial rotation. In general, for all values of  $c_{10}$  and  $c_{01}$ , the stress differences between the two families of fibers were 12.9% for flexion, 14.8% for extension, 6.6% for lateral flexion, and 98.7% for axial rotation.

3.2.2. *Using the Yeoh Function as the Strain Energy Function for the Ground Substance.* Figures 16–19 show the stress behavior versus the mechanical constants variation for a moment maximum of 8 N-m applied. Then, for a maximum moment of 8 N-m, the fiber stress varied from 26.6 to 67.7 MPa for flexion (Figure 16), from 48.7 MPa to 250.0 MPa for extension (Figure 17), from 14.6 to 33.9 MPa for lateral flexion (Figure 18), and from 10.3 to 158.9 MPa for axial rotation (Figure 19). In the case when  $c_1$  was varied and  $c_2$  (−0.0189 MPa) and  $c_3$  (0.041 MPa) were constant, the average differences in stresses between the two fiber families were 2.2% for flexion, 36.0% for extension, 14.1% for lateral flexion,

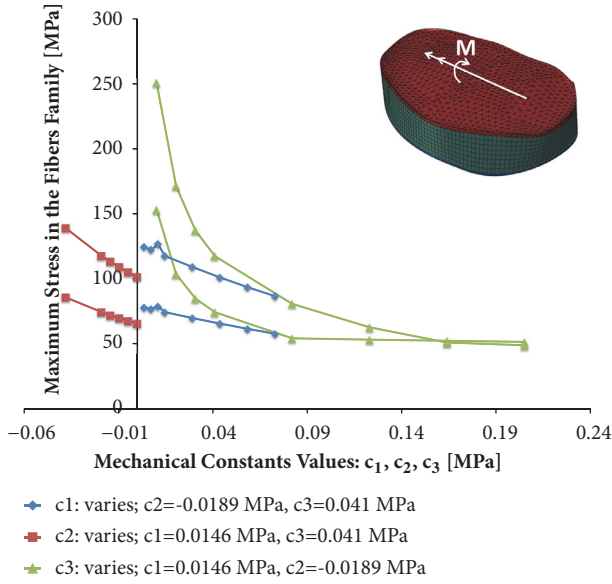


FIGURE 17: Maximum stress in the fibers family of AF versus mechanical constants values for the extension movement, using Yeoh function.

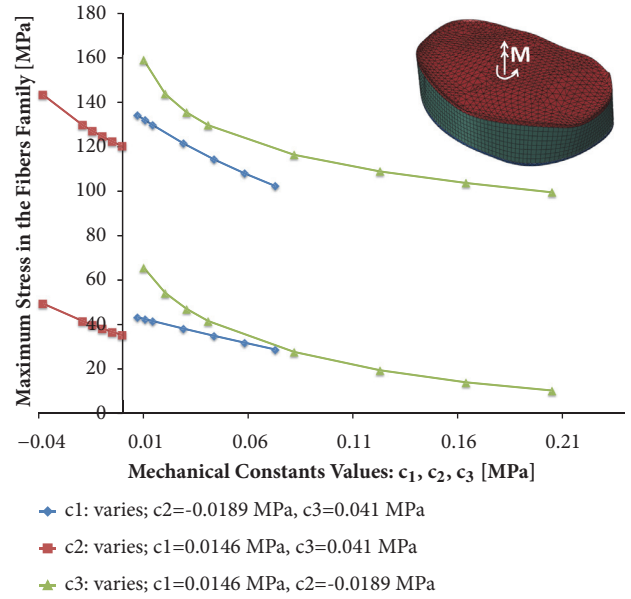


FIGURE 19: Maximum stress in the fibers family of AF versus mechanical constants values for the axial rotation movement, using Yeoh function.

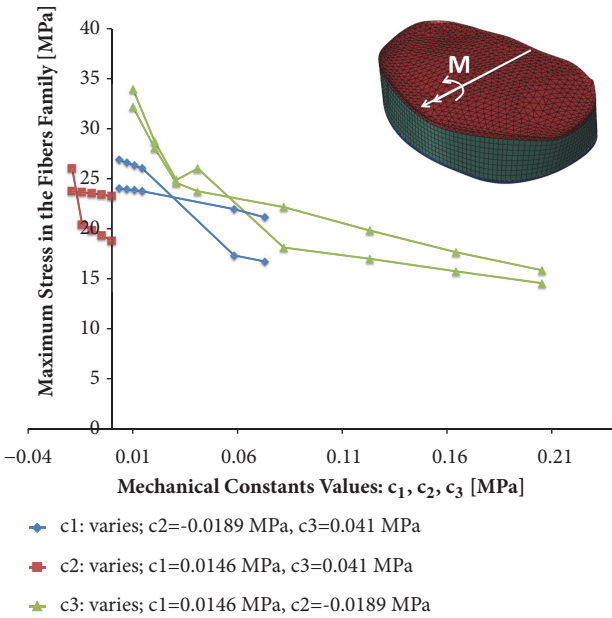


FIGURE 18: Maximum stress in the fibers family of AF versus mechanical constants values for the lateral flexion movement, using Yeoh function.

and 69.9% for axial rotation. In the second case, when  $c_1$  (0.0146 MPa) and  $c_3$  (0.041 MPa) were constant and  $c_2$  was varied, the stress differences between the two fiber families were 2.3% for flexion, 16.4% for extension, 15.1% for lateral flexion, and 68.7% for axial rotation. In the last case, when  $c_1$  (0.0146 MPa) and  $c_2$  (-0.0189 MPa) were constant and  $c_3$  was varied, the stress differences between the two families of fibers were 3.3% for flexion, 26.2% for extension, 8.8% for lateral flexion, and 73.6% for axial rotation. In general, for all values

of  $c_1$ ,  $c_2$ , and  $c_3$ , the stress differences between the two families of fibers were 2.6% for flexion, 32.9% for extension, 12.7% for lateral flexion, and 70.5% for axial rotation.

#### 4. Discussion

In general, increases in the values of the mechanical constants produce an increase in the stiffness of the disc and decreases in the ROM and stress of the fibers. The decrease in stress in the fibers as a result of the increase of the mechanical constants of the ground substance can be explained by the fact that the matrix takes a greater part of the applied moment, decreasing the stress in the fiber.

Using the Mooney-Rivlin function to represent the ground substance, the values of the mechanical constants that obtained the best fit to the experimental data were  $c_{10} = 0$  and  $c_{01} = 0.14$  MPa; here  $c_{01}$  is equal to the value reported by Heuer et al. [43, 47] and Rohlmann et al. [45]. However, these researchers reported values of  $c_{10}$  that differed from zero. On the other hand, the  $c_{01}$  value is very close to that reported ( $c_{01} = 0.25$ ) by Campbell and Petrella [48]. With regard to the stress in the fiber families (flexion: 35.58 and 41.09 MPa; extension: 90.15 and 125.5 MPa; lateral flexion: 16.97 and 16.93 MPa; axial rotation: 11.95 and 82.5 MPa) for previous values of the mechanical constants, the values of the stress were within the range of the experimental ultimate strength reported by Iatridis et al. [49] of  $88 \pm 61$  MPa, but out of the range of the data reported by Fujita et al. [50] ( $0.37 \pm 0.20$  MPa), Skaggs et al. [51] ( $10.3 \pm 8.4$ ), and Green et al. [52] ( $8.6 \pm 4.3$  MPa).

Using the Yeoh function to represent the mechanical behavior of the ground substance produced several set of values of the mechanical constants with a good fit to the experimental data. Calculating the median and standard deviation for the set of values with the best fit to the

experimental ROM in all movements, we obtain  $c_1 = 0.0292 \pm 0.0146$  MPa,  $c_2 = -0.0189 \pm 0$  MPa, and  $c_3 = 0.025625 \pm 0.015375$  MPa. The last values of  $c_1$ ,  $c_2$ , and  $c_3$  are within the experimental range reported by O'Connell et al. [53] but are out of the experimental range reported by Cortes et al. [38]. The differences found may be due to the regional variation of the mechanical properties of the matrix [39] and the significant differences between the values reported in the literature [50–52, 54, 55] for these mechanical properties which are produced by the different protocols used to obtain them. Now, if we wish to obtain a good fit to the experimental ROM and the fiber stress below the ultimate strength, it is necessary to use the obtained values of superior limits of the mechanical constants, so  $c_1 = 0.0438$  MPa,  $c_2 = -0.0189$  MPa, and  $c_3 = 0.041$  MPa. With these constants, the fiber stresses are 47.44 and 48.56 MPa, which are within the experimental range reported by Iatridis et al. [49].

## 5. Conclusion

It is necessary to underline that the Yeoh function produced, as a result, an important set of values that fit the experimental ROM better than the Mooney-Rivlin function. Besides, the Yeoh function has a better fit in the nonlinear region of the experimental ROM than the Mooney-Rivlin function, due to the fact that the Yeoh function has the invariants of second and third grade, whereas the Mooney-Rivlin function has invariants of first grade.

## Data Availability

The data used to support the findings of this study are included within the article.

## Conflicts of Interest

The author declares that there are no conflicts of interest regarding the publication of this paper.

## Acknowledgments

The author appreciates the support of the Universidad Autónoma de Occidente (Cali, Colombia).

## References

- [1] R. N. Natarajan, J. R. Williams, and G. B. J. Andersson, "Recent advances in analytical modeling of lumbar disc degeneration," *The Spine Journal*, vol. 29, no. 23, pp. 2733–2741, 2004.
- [2] J.-L. Wang, M. Parnianpour, A. Shirazi-Adl, and A. E. Engin, "Viscoelastic finite-element analysis of a lumbar motion segment in combined compression and sagittal flexion: Effect of loading rate," *The Spine Journal*, vol. 25, no. 3, pp. 310–318, 2000.
- [3] R. K. Wilcox, T. O. Boerger, D. J. Allen et al., "A dynamic study of thoracolumbar burst fractures," *The Journal of Bone and Joint Surgery—American Volume*, vol. 85, no. 11, pp. 2184–2189, 2003.
- [4] R. K. Wilcox, D. J. Allen, R. M. Hall, D. Limb, D. C. Barton, and R. A. Dickson, "A dynamic investigation of the burst fracture process using a combined experimental and finite element approach," *European Spine Journal*, vol. 13, no. 6, pp. 481–488, 2004.
- [5] P. Tropiano, L. Thollon, P. J. Arnoux et al., "Using a finite element model to evaluate human injuries application to the HUMOS model in whiplash situation," *The Spine Journal*, vol. 29, no. 16, pp. 1709–1716, 2004.
- [6] C. E. Tschirhart, A. Nagpurkar, and C. M. Whyne, "Effects of tumor location, shape and surface serration on burst fracture risk in the metastatic spine," *Journal of Biomechanics*, vol. 37, no. 5, pp. 653–660, 2004.
- [7] T. Belytschko and R. F. Kulak, "A finite-element method for a solid enclosing an inviscid, incompressible fluid," *Journal of Applied Mechanics*, vol. 40, no. 2, pp. 609–610, 1973.
- [8] S. A. Shirazi-Adl, S. C. Shrivastava, and A. M. Ahmed, "Stress analysis of the lumbar disc-body unit in compression. A three-dimensional nonlinear finite element study," *The Spine Journal*, vol. 9, no. 2, pp. 120–134, 1984.
- [9] V. K. Goel, B. T. Monroe, L. G. Gilbertson, and P. Brinckmann, "Interlaminar shear stresses and laminae separation in a disc: Finite element analysis of the l3-l4 motion segment subjected to axial compressive loads," *The Spine Journal*, vol. 20, no. 6, pp. 689–698, 1995.
- [10] H. Schmidt, F. Heuer, U. Simon et al., "Application of a new calibration method for a three-dimensional finite element model of a human lumbar annulus fibrosus," *Clinical Biomechanics*, vol. 21, no. 4, pp. 337–344, 2006.
- [11] F. Ezquerro, F. G. Vacas, S. Postigo, M. Prado, and A. Simón, "Calibration of the finite element model of a lumbar functional spinal unit using an optimization technique based on differential evolution," *Medical Engineering & Physics*, vol. 33, no. 1, pp. 89–95, 2011.
- [12] Y. Guan, N. Yoganandan, J. Zhang et al., "Validation of a clinical finite element model of the human lumbosacral spine," *Medical & Biological Engineering & Computing*, vol. 44, no. 8, pp. 633–641, 2006.
- [13] W. M. Park, K. Kim, and Y. H. Kim, "Effects of degenerated intervertebral discs on intersegmental rotations, intradiscal pressures, and facet joint forces of the whole lumbar spine," *Computers in Biology and Medicine*, vol. 43, no. 9, pp. 1234–1240, 2013.
- [14] A.-P. Zhang, H.-M. Wang, S.-L. Xu, and R.-Q. Chen, "Experimental study on the photoelasticity of lumbosacral joint model and finite element," *Chinese Journal of Clinical Rehabilitation*, vol. 8, no. 29, pp. 6367–6369, 2004.
- [15] H. Schmidt, F. Galbusera, A. Rohlmann, T. Zander, and H.-J. Wilke, "Effect of multilevel lumbar disc arthroplasty on spine kinematics and facet joint loads in flexion and extension: A finite element analysis," *European Spine Journal*, vol. 21, no. 5, pp. S663–S674, 2012.
- [16] H. Schmidt, A. Kettler, F. Heuer, U. Simon, L. Claes, and H.-J. Wilke, "Intradiscal pressure, shear strain, and fiber strain in the intervertebral disc under combined loading," *The Spine Journal*, vol. 32, no. 7, pp. 748–755, 2007.
- [17] T. Liu, K. Khalaf, S. Naserkhaki, and M. El-Rich, "Load-sharing in the lumbosacral spine in neutral standing & flexed postures – A combined finite element and inverse static study," *Journal of Biomechanics*, vol. 70, pp. 43–50, 2018.
- [18] W. Fan and L.-X. Guo, "Finite element investigation of the effect of nucleus removal on vibration characteristics of the lumbar spine under a compressive follower preload," *Journal of the Mechanical Behavior of Biomedical Materials*, vol. 78, pp. 342–351, 2018.

- [19] E. Charriere, F. Sirey, and P. K. Zysset, "A finite element model of the L5-S1 functional spinal unit: Development and comparison with biomechanical tests in vitro," *Computer Methods in Biomechanics and Biomedical Engineering*, vol. 6, no. 4, pp. 249–261, 2003.
- [20] C. M. Puttlitz, V. K. Goel, V. C. Traynelis, and C. R. Clark, "A finite element investigation of upper cervical instrumentation," *The Spine Journal*, vol. 26, no. 22, pp. 2449–2455, 2001.
- [21] U. M. Ayturk, B. Gadowski, D. Schuldt, V. Patel, and C. M. Puttlitz, "Modeling degenerative disk disease in the lumbar spine: A combined experimental, constitutive, and computational approach," *Journal of Biomechanical Engineering*, vol. 134, no. 10, Article ID 101003, 2012.
- [22] U. M. Ayturk and C. M. Puttlitz, "Parametric convergence sensitivity and validation of a finite element model of the human lumbar spine," *Computer Methods in Biomechanics and Biomedical Engineering*, vol. 14, no. 8, pp. 695–705, 2011.
- [23] U. M. Ayturk, J. J. Garcia, and C. M. Puttlitz, "The micromechanical role of the annulus fibrosus components under physiological loading of the lumbar spine," *Journal of Biomechanical Engineering*, vol. 132, no. 6, 2010.
- [24] G. Marini and S. J. Ferguson, "Modelling the influence of heterogeneous annulus material property distribution on intervertebral disk mechanics," *Annals of Biomedical Engineering*, vol. 42, no. 8, pp. 1760–1772, 2014.
- [25] M. Sharabi, K. Wade, and R. Haj-Ali, "Chapter 7 - the mechanical role of collagen fibers in the intervertebral disc," in *Biomechanics of the Spine*, F. Galbusera and H.-J. Wilke, Eds., vol. 7, pp. 105–123, 2018.
- [26] M. Mengoni, K. Vasiljeva, A. C. Jones, S. M. Tarsuslugil, and R. K. Wilcox, "Subject-specific multi-validation of a finite element model of ovine cervical functional spinal units," *Journal of Biomechanics*, vol. 49, no. 2, pp. 259–266, 2016.
- [27] H. E. Jaramillo, L. Gómez, and J. J. García, "A finite element model of the L4-L5-S1 human spine segment including the heterogeneity and anisotropy of the discs," *Acta of Bioengineering and Biomechanics*, vol. 17, no. 2, pp. 15–24, 2015.
- [28] G. J. M. Meijer, J. Homminga, E. E. G. Hekman, A. G. Veldhuizen, and G. J. Verkerke, "The effect of three-dimensional geometrical changes during adolescent growth on the biomechanics of a spinal motion segment," *Journal of Biomechanics*, vol. 43, no. 8, pp. 1590–1597, 2010.
- [29] J. Huyghe, R. Roos, R. Petterson et al., "Characterisation of intervertebral disc tissue and its substitutes," *Journal of Biomechanics*, vol. 39, pp. S27–S28, 2006.
- [30] D. G. T. Strange, S. T. Fisher, P. C. Boughton, T. J. Kishen, and A. D. Diwan, "Restoration of compressive loading properties of lumbar discs with a nucleus implant—a finite element analysis study," *The Spine Journal*, vol. 10, no. 7, pp. 602–609, 2010.
- [31] N. Bogduk, *Clinical Anatomy of the Lumbar Spine & Sacrum*, 1995, <http://www.lavoisier.fr/livre/notice.asp?id=OKKW2RAORR6OWX> [Accessed: 14-Aug-2012].
- [32] S. H. Reynolds, *The Vertebrate Skeleton*, Create Space Independent Publishing Platform, 2013.
- [33] N. Newell, J. P. Little, A. Christou, M. A. Adams, C. J. Adam, and S. D. Masouros, "Biomechanics of the human intervertebral disc: A review of testing techniques and results," *Journal of the Mechanical Behavior of Biomedical Materials*, vol. 69, pp. 420–434, 2017.
- [34] J. J. Cassidy, A. Hiltner, and E. Baer, "Hierarchical structure of the intervertebral disc," *Connective Tissue Research*, vol. 23, no. 1, pp. 75–88, 1989.
- [35] R. Eberlein, G. A. Holzapfel, and C. A. J. Schulze-Bauer, "An anisotropic model for annulus tissue and enhanced finite element analyses of intact lumbar disc bodies," *Computer Methods in Biomechanics and Biomedical Engineering*, vol. 4, no. 3, pp. 209–229, 2001.
- [36] H. E. Jaramillo, C. M. Puttlitz, K. McGilvray, and J. J. García, "Characterization of the L4-L5-S1 motion segment using the stepwise reduction method," *Journal of Biomechanics*, vol. 49, no. 7, pp. 1248–1254, 2016.
- [37] M. Dreischarf, T. Zander, A. Shirazi-Adl et al., "Comparison of eight published static finite element models of the intact lumbar spine: Predictive power of models improves when combined together," *Journal of Biomechanics*, vol. 47, no. 8, pp. 1757–1766, 2014.
- [38] D. H. Cortes and D. M. Elliott, "Extra-fibrillar matrix mechanics of annulus fibrosus in tension and compression," *Biomechanics and Modeling in Mechanobiology*, vol. 11, no. 6, pp. 781–790, 2012.
- [39] D. H. Cortes, W. M. Han, L. J. Smith, and D. M. Elliott, "Mechanical properties of the extra-fibrillar matrix of human annulus fibrosus are location and age dependent," *Journal of Orthopaedic Research*, vol. 31, no. 11, pp. 1725–1732, 2013.
- [40] N. T. Jacobs, D. H. Cortes, J. M. Peloquin, E. J. Vresilovic, and D. M. Elliott, "Validation and application of an intervertebral disc finite element model utilizing independently constructed tissue-level constitutive formulations that are nonlinear, anisotropic, and time-dependent," *Journal of Biomechanics*, vol. 47, no. 11, pp. 2540–2546, 2014.
- [41] N. T. Jacobs, D. H. Cortes, E. J. Vresilovic, and D. M. Elliott, "Biaxial tension of fibrous tissue: using finite element methods to address experimental challenges arising from boundary conditions and anisotropy," *Journal of Biomechanical Engineering*, vol. 135, no. 2, Article ID 021004, 2013.
- [42] F. Heuer, H. Schmidt, and H.-J. Wilke, "Stepwise reduction of functional spinal structures increase disc bulge and surface strains," *Journal of Biomechanics*, vol. 41, no. 9, pp. 1953–1960, 2008.
- [43] F. Heuer, H. Schmidt, L. Claes, and H.-J. Wilke, "Stepwise reduction of functional spinal structures increase vertebral translation and intradiscal pressure," *Journal of Biomechanics*, vol. 40, no. 4, pp. 795–803, 2007.
- [44] F. Heuer, U. Wolfram, H. Schmidt, and H.-J. Wilke, "A method to obtain surface strains of soft tissues using a laser scanning device," *Journal of Biomechanics*, vol. 41, no. 11, pp. 2402–2410, 2008.
- [45] A. Rohlmann, S. Neller, L. Claes, G. Bergmann, and H. J. Wilke, "Influence of a follower load on intradiscal pressure and intersegmental rotation of the lumbar spine," *The Spine Journal*, vol. 26, no. 24, pp. 557–561, 2001.
- [46] "Welcome to Python.org," Python.org, Available: <https://www.python.org/>. [Accessed: 16-Mar-2017].
- [47] F. Heuer, H. Schmidt, Z. Klezl, L. Claes, and H.-J. Wilke, "Stepwise reduction of functional spinal structures increase range of motion and change lordosis angle," *Journal of Biomechanics*, vol. 40, no. 2, pp. 271–280, 2007.
- [48] J. Q. Campbell and A. J. Petrella, "Automated finite element modeling of the lumbar spine: Using a statistical shape model to generate a virtual population of models," *Journal of Biomechanics*, vol. 49, no. 13, pp. 2593–2599, 2016.
- [49] S. Ebara, J. C. Iatridis, L. A. Setton, R. J. Foster, C. Van Mow, and M. Weidenbaum, "Tensile properties of nondegenerate human lumbar annulus fibrosus," *The Spine Journal*, vol. 21, no. 4, pp. 452–461, 1996.

- [50] Y. Fujita, N. A. Duncan, and J. C. Lotz, "Radial tensile properties of the lumbar annulus fibrosus are site and degeneration dependent," *Journal of Orthopaedic Research*, vol. 15, no. 6, pp. 814–819, 1997.
- [51] D. L. Skaggs, M. Weidenbaum, J. C. Latridis, A. Ratcliffe, and V. C. Mow, "Regional variation in tensile properties and biochemical composition of the human lumbar annulus fibrosus," *The Spine Journal*, vol. 19, no. 12, pp. 1310–1319, 1994.
- [52] T. P. Green, M. A. Adams, and P. Dolan, "Tensile properties of the annulus fibrosus," *European Spine Journal*, vol. 2, no. 4, pp. 209–214, 1993.
- [53] G. D. O'Connell, H. L. Guerin, and D. M. Elliott, "Theoretical and uniaxial experimental evaluation of human annulus fibrosus degeneration," *Journal of Biomechanical Engineering*, vol. 131, no. 11, Article ID 111007, 2009.
- [54] J. C. Iatridis, J. P. Laible, and M. H. Krag, "Influence of fixed charge density magnitude and distribution on the intervertebral disc: Applications of a poroelastic and chemical electric (PEACE) model," *Journal of Biomechanical Engineering*, vol. 125, no. 1, pp. 12–24, 2003.
- [55] S. V. Beekmans, K. S. Emanuel, T. H. Smit, and D. Iannuzzi, "Stiffening of the nucleus pulposus upon axial loading of the intervertebral disc: An experimental in situ study," *JOR Spine*, vol. 1, no. 1, p. e1005, 2018.

## Research Article

# A Reliability-Based Consensus Model for Multiattribute Group Decision-Making with Analytically Evidential Reasoning Approach

Yuan-Wei Du <sup>1,2</sup>, Ning Yang,<sup>1</sup> Wen Zhou <sup>1</sup>, and Chang-Xing Li<sup>3</sup>

<sup>1</sup>Management College, Ocean University of China, Qingdao 266100, China

<sup>2</sup>Marine Development Studies Institute of OUC, Key Research Institute of Humanities and Social Sciences at Universities, Ministry of Education, Qingdao 266100, China

<sup>3</sup>School of Economics, Shanghai University of Finance & Economics, Shanghai 200443, China

Correspondence should be addressed to Wen Zhou; [zwzhouwen9572@163.com](mailto:zwzhouwen9572@163.com)

Received 27 July 2018; Accepted 10 September 2018; Published 10 October 2018

Guest Editor: Shouzhen Zeng

Copyright © 2018 Yuan-Wei Du et al. This is an open access article distributed under the Creative Commons Attribution License, which permits unrestricted use, distribution, and reproduction in any medium, provided the original work is properly cited.

Expert reliability is the ability to make unmistakable evaluations on attributes for the performance of an alternative in multiattribute group decision making (MAGDM). It has a significant effect on the group consensus calculation and group decision-making; unfortunately the reliability has not been considered in the consensus-reaching model yet. This study focuses on providing a reliability-based consensus model for MAGDM with analytically evidential reasoning (analytical ER for short) approach. The basic probability assignment (BPA) function which can be discounted by expert reliability is introduced to describe the performance judgments of each expert, by combining which of the group judgments could be determined with analytical ER rule. Then the consensus degrees of three levels (attribute level, alternative level, and expert level) are defined by Jusselme distance to identify the experts who should revise their judgments and point out revised suggestions, based on which a decision-making method within interaction is proposed to determine the effective BPA functions of all experts and make final decision-making. Finally, a numerical case study is carried out to illustrate the effectiveness of the method.

## 1. Introduction

In multiattribute group decision-making (MAGDM), a group of experts make an evaluation on alternatives by several attributes and interact with each other to derive a common solution [1]. However, experts usually have different knowledge and backgrounds on the decision-making problems since they are from diverse professional fields, which may lead to confliction or inconsistency among experts in the group [2]. It is a hot and relevant topic about how to reach a consensus in the decision-making process. The group interaction consensus model (consensus model for short) has been proved to be an effective method to increase consensus, because it supports inconsistent experts, whose inconsistency values are higher than the predefined threshold, with advice on how to modify their evaluation information [2]. In order to assist with group interaction consensus model, three

aspects of researches have been proposed as follows. The first aspect focuses on applying the fuzziness tools to construct consensus models. The fuzziness tools such as fuzzy theory [3–10], hesitant fuzzy set [11–15], and linguistic/preference information [12, 13, 15–22] were introduced into consensus model to extract experts' subjective judgments. The second aspect focuses on constructing the feedback mechanisms. The minimum cost feedback mechanism [19, 23, 24], maximum utility feedback mechanism [25], and cost chance constraint mechanism [26] were proposed to achieve the optimum balance between individual independence and group consensus. The third aspect focuses on extending consensus models to different situations. Dynamic consensus model [27–30], consensus models considering social networks [2, 19, 22], soft consensus model [5], adaptive consensus model [20, 30], and interactive consensus model [2, 31] were proposed to make consensus models play better roles to meet different

requirements and characteristics. It is obvious to find that a few of new ideas for solving the problems have been put forward in consensus models.

Dempster-Shafer theory of evidence (DST) was originally investigated in the 1960's by Dempster, formalized in the 1970's by Shafer, and has been researched ever since widely. The basic probability assignment (BPA) function which is frequently regarded as a piece of evidence is a key concept in the DST, and it can be well combined by the Dempster's rule. The BPA function enables the commitment of belief in a hypothesis that does not necessarily mean that the remaining belief must be assigned to the complement of the hypothesis, but to the whole sample space. The BPA functions and Dempster's rule make the DST able to well handle the uncertainties in decision making [32]. These attractive features have motivated the use of this method in MAGDM problems. For example, Yang introduced the DST into MAGDM and proposed a well-known evidential reasoning (ER) approach [33]. The ER approach is much flexible in dealing with uncertainty in the MAGDM, since it divides the global uncertainty into ignorance and residual support without changing the nature of evidence [32]. Note that the ER approach is a recursive algorithm and it is hard to be modeled and computed sometimes; then the analytical ER methodology is developed [34]. In the framework of ER approach, studying how to reach a consensus and make decision has attracted the attention of scholars. For examples, the consensus framework and consensus model with interval-values for the MAGDM analysis in the ER context have been proposed [35–37]. However, there still exist a lot of problems that need to be solved.

There are two primary methods for reaching consensus, modifying assessments of experts, and adjusting the weights of experts, in both ER framework and other frameworks. The impact of expert reliability on the consensus of MAGDM has not been noticed yet. Reliability is an important concept in various fields [38], such as engineering [39], industry [40], transportation [41], computer networks [42], wireless networks [43], and software [44]. In information fusion field, reliability is defined as an ability of evidence source to provide correct assessment/solution for the given problem, and the reliability of an evidence source should be estimated by statistics or other techniques [45]. In MAGDM, expert reliability can be defined as the ability to make an unmistakable evaluation on the specific attribute for an alternative. Obviously, the higher the reliability of the expert, the more accurate the evaluation information given by the expert. Conversely, the lower the reliability of the expert, the less accurate the evaluation information given by the expert. In the process of calculating the group consensus degree and making group decision-making, if the expert reliability is not considered, or the accuracy of the evaluation information given by the expert is not taken into consideration, it will inevitably lead to the problems such as inaccurate group consensus or poor quality of decision results.

The motivation of this paper is to propose a reliability-based consensus model for MAGDM with analytical ER approach as follows. The ER discounting method is used to reflect the influence of weight and reliability on the expert

evaluation information, based on which the analytically evidential reasoning (analytical ER for short) rule is employed to obtain the group opinion by integrating individual evaluation information on a specific attribute for alternatives. Then the corresponding reliabilities of experts as well as the degrees of nonconsensus of experts are calculated with the help of Jousselme distance. The method of modifying expert's evaluation information and interaction consensus model for MAGDM are proposed finally.

The rest of this study is organized as below. Section 2 briefly reviews the main concepts introduced in the analytical ER approach which is the preliminaries of this paper. In Section 3, a reliability-based consensus model is presented to solve the MAGDM problem with the help of analytical ER approach. In Section 4, we use a numerical case study to illustrate the interaction process of the proposed method. The conclusions are discussed in Section 5.

## 2. Preliminaries

In order to facilitate the later formulation, some basic concepts of the analytical ER approach are given here.

*Definition 1* (see [10, 33, 34, 46]). Let  $H = \{H_1, \dots, H_N\}$  be a set of mutually exclusive and collectively exhaustive propositions, with  $H_i \cap H_j = \emptyset$  for any  $i, j \in \{1, \dots, N\}$  and  $i \neq j$ .  $H$  is then referred to as a frame of discernment. A Basic Probability Assignment (BPA) is a function  $m : 2^H \rightarrow [0, 1]$ , satisfying

$$m(\emptyset) = 0, \sum_{A \subseteq H} m(A) = 1, \quad (1)$$

where  $\emptyset$  is an empty set,  $A$  is any subset of  $H$ , and  $2^H$  is the power set of  $H$ , which consists of all subsets of  $H$ , i.e.,

$$2^H = \{\emptyset, H_1, \dots, H_N, \{H_1, H_2\}, \dots, \{H_1, H_N\}, \dots, \{H_1, \dots, H_{N-1}\}, H\}. \quad (2)$$

The assigned probability  $m(A)$  measures the belief exactly assigned to  $A$  and represents how strongly the evidence supports  $A$ . The sum of all the assigned probabilities is 1 and there is no belief in the empty set  $\emptyset$ . The assigned probability to  $H$ , i.e.,  $m(H)$ , is called the degree of ignorance. For convenience, let  $m(H) = m(N + 1)$ .

*Definition 2* (see [46]). A belief measure, Bel, and a plausibility measure, Pl, are associated with each BPA and they are both functions:  $2^H \rightarrow [0, 1]$ , defined by

$$Bel(A) = \sum_{B \subseteq A} m(B), \quad (3)$$

$$Pl(A) = \sum_{A \cap B \neq \emptyset} m(B), \quad (4)$$

where  $A$  and  $B$  are subsets of  $H$ .  $Bel(A)$  represents the exact support for  $A$ , i.e., the belief of the hypothesis of  $A$  being true;  $Pl(A)$  represents the possible support for  $A$ , i.e., the

total amount of belief that could be potentially placed in  $A$ .  $[Bel(A), Pl(A)]$  constitutes the interval of support to  $A$  and can be seen as the lower and upper bounds of the probability to which  $A$  is supported. The two functions can be connected by

$$Pl(A) = 1 - Bel(\bar{A}). \quad (5)$$

Because the functions  $m$ ,  $Bel$ , and  $Pl$  are one-to-one corresponding, it is equivalent to talk about one of them, or also about the corresponding the evidence.

*Definition 3* (see [10, 33]). Let the grades for assessing alternatives be  $H = \{H_n \mid n = 1, \dots, N\}$  and the belief degree that an alternative is assessed to  $H_n$  be  $\beta_n$  derived from a piece of evidence; then the assessment is profiled by

$$B = \{(H_n, \beta_n), n = 1, \dots, N; (H, \beta_H)\}, \quad (6)$$

where  $\sum_{n=1}^N \beta_n \leq 1$ ,  $\beta_n \geq 0$ , for  $n = 1, \dots, N$ , and  $\beta_H = 1 - \sum_{n=1}^N \beta_n$  represents the degree of global ignorance. If  $\beta_H = 0$ , the assessment is complete; otherwise, it is incomplete. For convenience, let  $(H_{N+1}, \beta_{N+1}) = (H, \beta_H)$  and the assessment as (1) can be denoted as  $B = \{(H_n, \beta_n), n = 1, \dots, N, N + 1\}$ .

*Definition 4* (see [10, 34, 47]). The ER approach first transforms the original belief degrees into BPAs by combining the relative weights and the belief degrees using

$$m = m(H_n) = \begin{cases} \lambda \beta_n, & n = 1, \dots, N, \\ 1 - \lambda \sum_{n=1}^N \beta_n, & n = N + 1. \end{cases} \quad (7)$$

where  $m_H = \bar{m}_H + \tilde{m}_H$ ,  $\bar{m}_H = 1 - \lambda$ ,  $\tilde{m}_H = \lambda(1 - \sum_{n=1}^N \beta_n)$ ,  $\bar{m}_H$  depicts the role extents of the evidence to be combined, and  $\tilde{m}_H$  represents the incompleteness of the assessment.

*Definition 5* (see [10, 33, 47]). There are  $I$  pieces of evidence to be combined, let the BPA function of the  $i^{\text{th}}$  one be  $m_n^i$  generated by (7),  $i = 1, \dots, I$ ,  $n = 1, \dots, N + 1$ , and then the combined belief degree for  $I$  pieces of evidence is calculated by the analytical ER approach as follows:

$$B = B(H_n) = \begin{cases} \frac{m_n}{(1 - \bar{m}_H)}, & n = 1, \dots, N, \\ \frac{\tilde{m}_n}{(1 - \bar{m}_H)}, & n = N + 1. \end{cases} \quad (8a)$$

where

$$m_n = \delta \left[ \prod_{i=1}^I (m_n^i + \bar{m}_H^i + \tilde{m}_H^i) - \prod_{i=1}^I (\bar{m}_H^i + \tilde{m}_H^i) \right], \quad (8b)$$

$$n = 1, \dots, N,$$

$$\bar{m}_H = \delta \left[ \prod_{i=1}^I (\bar{m}_H^i + \tilde{m}_H^i) - \prod_{i=1}^I \bar{m}_H^i \right], \quad (8c)$$

$$\tilde{m}_H = \delta \left[ \prod_{i=1}^I \tilde{m}_H^i \right], \quad (8d)$$

$$\delta = \left[ \sum_{n=1}^N \prod_{i=1}^I (m_n^i + \bar{m}_H^i + \tilde{m}_H^i) - (N - 1) \prod_{i=1}^I (\bar{m}_H^i + \tilde{m}_H^i) \right]^{-1}. \quad (8e)$$

Note that the argument  $\delta$  in (8e) is the reciprocal of the sum of BPA functions assigned to all nonempty sets and is used as a normalization factor.

### 3. The Proposed Method

A reliability-based consensus model to increase the consistency among experts is proposed in analytical ER approach context. In this section, the evidence distance and the expert reliability are firstly introduced based on Jousselme distance. The consensus degrees on three levels are defined, based on which the interaction method for group consensus is presented. Finally the method for information fusion and decision-making is summarized.

*3.1. Evidence Distance and Expert Reliability.* Suppose a set of experts  $E = \{e_i \mid i = 1, \dots, I\}$  is invited to make an evaluation for alternatives  $Y = \{y_k \mid k = 1, \dots, K\}$  on attribute set  $C = \{c_l \mid l = 1, \dots, L\}$ . Experts are invited to evaluate alternatives on each attribute with BPAs. The assessment of alternative  $y_k$  given by expert  $e_i$  with respect to attribute  $c_l$  is expressed as a piece of evidence  $B_{i,l}^k = \{(H_n, \beta_{i,l}^{k,n}) \mid \beta_{i,l}^{k,n} > 0, \sum_{n=1}^{N+1} \beta_{i,l}^{k,n} = 1, n = 1, \dots, N, N + 1\}$ ,  $\forall i, l, k$ .

Distance is a tool that measures the consistency or inconsistency between evidence. There are at least two types of distance measure: one type measures the degree of difference among evidence and the other measures the degree of similarity or compatibility among evidence. The greater the difference among them, the lower the similarity. We should choose a distance measure according to the purpose of the application and the fusion. It is hoped that the opinions of the experts are highly consistent, and we can reasonably assume that the information given by most of experts is reasonable and basically consistent. The high conflict experts who need to be identified are a minority.

In order to depict conflicts or inconsistencies among evidence (expert information), many classical calculation methods, with their own advantages and disadvantages, have

been proposed. For instance, conflict distance  $\sigma$  may reflect the conflicting or inconsistent situation where both  $m_1(A)$  and  $m_2(B)$  are not equal to zero, but the intersection such as  $A \cap B$  is empty. Nevertheless,  $\sigma$  cannot depict the following inconsistency: that is, when  $m_1(A) = 0.9$ ,  $m_2(A) = 0.1$ ,  $m_1$  is more sure whilst  $m_2$  is likely uncommitted about its preference [48]. Pignistic probability distance  $P - dist$  based on the expected utility theory and betting commitments is proposed by Smets [49], which has ability to identify well the inconsistency when  $m_1(A) = 0.9$ ,  $m_2(A) = 0.1$ . Let  $m_1(A) = 0.2$ ,  $m_1(B) = 0.2$ ,  $m_2(A) = 0.2$ ,  $m_2(B) = 0.2$ ; however, the Pignistic probability distance is  $P_{1,2} - dist = \max(|BetP_{m_1}(A) - BetP_{m_2}(A)|) = 0$ , which manifests that there is no difference to  $A$  from the two evidence sources, whilst the  $\sigma$  after combination is still very high. This high conflict or inconsistency cannot come from the difference between betting commitments but from other reasons. Consequently, neither  $\delta$  nor  $P - dist$  could describe a conflict between two BPAs accurately. Fortunately, Jousselme put forward a distance as in Definition 6, which is regarded as a standard metric for two pieces of evidence [50]. Jousselme distance has the ability to measure conflicts or inconsistencies among evidence [51], and it is adopted to measure the opinions' inconsistency between each individual expert and the group of experts.

*Definition 6* (Jousselme distance). Let  $m_i$  and  $m_j$  be two BPAs on the same frame of discernment  $H$ , containing  $N$  mutually exclusive and exhaustive hypotheses. The distance between  $m_i$  and  $m_j$  is

$$J = \sqrt{\frac{1}{2} (\vec{m}_i - \vec{m}_j)^T D (\vec{m}_i - \vec{m}_j)} \quad (9)$$

where  $D$  is a  $(2^H \times 2^H)$ -dimensional matrix whose elements are  $D(A, B) = |A \cap B|/|A \cup B|$  and  $A, B \in 2^H$  defines a metric distance and represents the similarity among the subsets of  $H$ . Given a BPA  $m$  on frame  $H$ ,  $\vec{m}$  is a  $2^H$ -dimensional column vector (can also be called a  $2^H \times 1$  matrix).  $(\vec{m}_i - \vec{m}_j)$  stands for vector subtraction and  $(\vec{m})^T$  is the transpose of vector (or matrix) [50].

In MAGDM problem, experts are not all completely reliable since their knowledge and backgrounds are different. Expert reliability can be defined as the ability to make an unmistakable evaluation on the specific attribute for an alternative in MAGDM. In the process of calculating the group consensus degree and making group decision-making, if the expert reliability is not considered, or the accuracy of the evaluation information given by the expert is not taken into consideration, it will inevitably lead to problems such as inaccurate group consensus or poor quality of decision results. Expert reliability could be estimated by statistics or other techniques.

In our opinion, the expert reliability could be indirectly calculated by Jousselme distance between expert and the group. The reason is that group opinion can be regarded as relatively accurate information. The more consistent of the opinions between the expert and the group (the smaller

the distance of opinions between the expert and the group), the higher the reliability of the expert. Expert reliability is inversely proportional to the distance between expert opinion and group opinion. So we give the following definition.

Setting a threshold, if the Jousselme distance between expert and the group is equal to or less than the threshold, the reliability of the expert is considered to be absolutely reliable, or the degree is 1.

*Definition 7.* Supposing the BPA function given by expert  $e_i$  is  $B_i$  and that of the group of experts is  $B$ , the Jousselme distance between  $B_i$  and  $B$  is  $J_i$ ,  $\varepsilon$  is a threshold to judge whether the distance satisfies the requirement, and then the reliability degree of expert  $e_i$  can be determined as follows:

$$r_i = \begin{cases} 1, & J_i \leq \varepsilon \\ \frac{\varepsilon}{J_i}, & J_i > \varepsilon \end{cases} \quad (10)$$

The expert reliability calculated based on Definition 7 has the following properties: (1) the reliability of the experts with the satisfied distance from group opinion is equal to 1. (2) The smaller the distance between the expert opinion and the group opinion, the more reliable the expert. (3) Expert reliability must be between 0 and 1, that is,  $0 \leq r_i \leq 1$ . It is worth noting that the threshold  $\varepsilon$  is suggested to be equal to the threshold defined in the consensus model in this paper.

*3.2. Consensus Degree on Three Levels.* Following the framework of consensus reaching model defined by [1], the consensus indexes are used to describe the inconsistency or conflict among experts on three hierarchical and progressive consensus levels. They are, respectively, the attribute, the alternative, and the expert levels. The attribute level is the most basic, which could reflect the original conflict among the expert  $e_i$  on a specific attribute  $c_l$  for an alternative  $y_k$ , and experts make amendments to increase their consistency in group also on this level. The alternative level is intermediate, that is, the conflict between experts and the group for the evaluation result on a specific alternative  $y_k$ . The expert level is the highest, that is, the conflict between a specific expert and the group for the evaluation results on all alternatives, which reflects the conflict between the expert and the group as a whole [2].

Note that the dual effects of attribute weight and expert reliability should be taken into account when calculating consensus index, because the weight and the reliability of evidence are two kinds of parameters. The weight is often defined as the attribute weight, and it is relative. The reliability can be defined as the ability to make an unmistakable evaluation on the specific attribute for an alternative, and it's absolute. The reliability of the expert  $e_i$  on each attribute  $c_l$  is different, because each attribute reflects one aspect for a given problem, and the required expert knowledge experience is different. We could combine expert information with the help of analytical ER approach. Based on ER discount, the discounted BPA function of alternative  $y_k$  on attribute  $c_l$  is obtained, which incorporates weight and reliability. Let the weight of attribute  $c_l$  be  $w_l$  and  $w_l \geq 0$ . Note that the sum

of weights  $\sum_{l=1}^L w_l$  is frequently defined to be one, but such a requirement is not necessary. Let the reliability of expert  $e_i$  on attitude  $c_l$  be  $r_i^{k,l}$ ,  $0 \leq r_i^{k,l} \leq 1$ ,  $i = 1, \dots, I$ ,  $k = 1, \dots, K$ ,  $l = 1, \dots, L$ . Obviously,  $r_i^{k,l} = 1$  describes that expert  $e_i$  is most reliable and  $r_i^{k,l} = 0$  describes that he/she is most unreliable. The common discount method is the double discount formula of Definition 4. The discount factor is

$$\lambda_i^{k,l} = \frac{w_l}{1 + w_l - r_i^{k,l}}. \quad (11)$$

Based on the discounted BPA function, the analytical ER approach is used to calculate the group opinion. The analytical ER approach is used to combine the derived BPAs for two times. In order to obtain group evaluation result on an attribute  $c_l$  for an alternative  $y_k$ , we only need combine BPAs for an alternative  $y_k$  on an attribute  $c_l$  with respect to all experts, i.e.,  $m_{l,k} = m_{i,l,k} \oplus \dots \oplus m_{l,k}$ ,  $\forall l, k$ . The symbol  $\oplus$  denotes combine BPAs by using the analytical ER approach,  $m_{l,k} = m_{1,l,k} \oplus \dots \oplus m_{I,l,k}$ ,  $\forall l, k$ . The fusion on the attribute  $c_l$  for the alternative  $y_k$  with respect to all experts is

$$B = B(H_n) = \begin{cases} \frac{m_{l,k}(H_n)}{(1 - \bar{m}_{l,k}(H))}, & n = 1, \dots, N, \\ \frac{\bar{m}_{l,k}(H_n)}{(1 - \bar{m}_{l,k}(H))}, & n = N + 1. \end{cases} \quad (12a)$$

where

$$\begin{aligned} m_{l,k}(H_n) &= \delta_{l,k} \left[ \prod_{i=1}^I (m_{i,l,k}(H_n) + \bar{m}_{i,l,k}(H) + \bar{m}_{1,l,k}(H)) \right. \\ &\quad \left. - \prod_{i=1}^I (\bar{m}_{i,l,k}(H) + \bar{m}_{1,l,k}(H)) \right], \quad n = 1, \dots, N, \end{aligned} \quad (12b)$$

$$\begin{aligned} \bar{m}_{l,k}(H) &= \delta_{l,k} \left[ \prod_{i=1}^I (\bar{m}_{i,l,k}(H) + \bar{m}_{i,l,k}(H)) \right. \\ &\quad \left. - \prod_{i=1}^I \bar{m}_{i,l,k}(H) \right], \end{aligned} \quad (12c)$$

$$\bar{m}_{l,k}(H) = \delta_{l,k} \left[ \prod_{i=1}^I \bar{m}_{i,l,k}(H) \right], \quad (12d)$$

$$\begin{aligned} \delta_{l,k} &= \left[ \sum_{n=1}^N \prod_{i=1}^I (m_{i,l,k}(H_n) + \bar{m}_{i,l,k}(H) + \bar{m}_{i,l,k}(H)) \right. \\ &\quad \left. - (N - 1) \prod_{i=1}^I (\bar{m}_{i,l,k}(H) + \bar{m}_{i,l,k}(H)) \right]^{-1}. \end{aligned} \quad (12e)$$

The Jousselme distance is used to calculate the inconsistency among experts and group as a consensus index. The above three levels of consensus indexes are employed to find

the inconsistent among experts, and the corresponding calculation methods are given by considering the characteristics of the analytical ER approach.

(1) *The Consensus Index on Attribute.* The consensus index on attribute  $c_l$ , denoted  $J_{i,l}^{k,l}$ , is defined to measure the inconsistency or conflict between the expert  $e_i$  and the group for alternative  $y_k$  with respect to the attribute  $c_l$ .

$$J_{i,l}^{k,l} = \sqrt{\frac{1}{2} (\vec{m}_{l,k} - \vec{m}_{i,l,k})^T D (\vec{m}_{l,k} - \vec{m}_{i,l,k})}. \quad (13)$$

$J_{i,l}^{k,l}$  means that the Jousselme distance between the combined BPAs  $m_{l,k}$ ,  $\forall l, k$ , the fusion on all experts for the alternative  $y_k$  with respect to the attribute  $c_l$ , and  $m_{i,l,k}$ ,  $\forall i, l, k$  the expert  $e_i$  makes evaluation on the attribute  $c_l$  for the alternative  $y_k$ .

(2) *The Consensus Index on Alternative.* The consensus degree on alternative  $y_k$ , denoted  $J_{i,I}^k$ , is defined to measure the inconsistency or conflict between the expert  $e_i$  and the group on that alternative. It could be obtained by adding the consensus index values of all attributes on the alternative  $y_k$  for the expert  $e_i$ .

$$J_{i,I}^k = \sum_{l=1}^L J_{i,l}^{k,l} \quad (14)$$

$J_{i,I}^k$  means the distance between the combined BPAs  $m_k$ ,  $\forall k$ , the overall evaluation result for alternative  $y_k$  with respect to all experts, and  $m_{i,k}$ ,  $\forall i, k$  the evaluation result for alternative  $y_k$  with respect the expert  $e_i$ .

(3) *The Consensus Index on Expert.* The consensus degree on expert  $e_i$ , denoted  $J_{i,I}$ , is defined to measure the inconsistency or conflict among expert overall. It could be obtained by adding the consensus index values of all alternatives for expert  $e_i$ .

$$J_{i,I} = \sum_{k=1}^K J_{i,I}^k \quad (15)$$

$J_{i,I}$  means the overall distance between the expert  $e_i$  and the group.

Traditionally, the closer the value  $J$  to 1, the greater the degree of conflict;  $J = 1$  indicates complete conflict; the closer the value to 0, the smaller the conflict;  $J = 0$  means no conflict between them. Algorithm 1 is summarized to compute the distance on three levels.

3.3. *The Interaction Method for Group Consensus.* All experts agree each other unanimously, however, this case is rare in reality and it is not desirable in the decision making process. We should identify the inconsistent information with the values of consensus indexes higher than the threshold in terms of the Jousselme distance. Since the ‘‘absolutely meaningful threshold’’ of conflict tolerance, which has the ability of satisfying all pairs of BPAs, hardly exists, so as to

**Input:** Expert assessments  $B_{i,l}^k = \{(H_n, \beta_{i,l}^{k,n}) \mid \beta_{i,l}^{k,n} > 0, \sum_{n=1}^{N+1} \beta_{i,l}^{k,n} = 1, n = 1, \dots, N, N+1\}$ ,  $i = 1, \dots, I$ ,  $k = 1, \dots, K$ ,  $l = 1, \dots, L$ ; Attribute set  $C = \{c_l \mid l = 1, \dots, L\}$ ; Reliability set of experts on attributes  $r_i^{k,l}, \forall i, k, l$ ; Weight set of attributes  $W = (w_1, \dots, w_L)$ .

**Output:** Distance on the attribute  $J_{i,l}^{k,l}$ ; Distance on the alternative  $J_{i,I}^k$ ; Distance on the expert  $J_{i,I}$ .

**Begin**

  Compute the discounting factor for  $B_{i,l}^k$  by using  $\lambda_i^{k,l} = w_l / (1 + w_l - r_i^{k,l})$ .

  Establish the models as in Eq. (12a), (12b), (12c), (12d), and (12e) and compute  $m_{l,k} = m_{1,l,k} \oplus \dots \oplus m_{I,l,k}$ .

  % Compute the distance between experts and group on three levels

  For  $i=1$  to  $I$

    For  $k=1$  to  $K$

      For  $l=1$  to  $L$

        % Compute the distance between experts and group on attribute

$$J_{i,l}^{k,l} = \sqrt{\frac{1}{2} (\vec{m}_{l,k} - \vec{m}_{i,l,k})^T D (\vec{m}_{l,k} - \vec{m}_{i,l,k})}$$

      EndFor

      % Compute the distance between experts and group on alternative

$$J_{i,I}^k = \sum_{l=1}^L J_{i,l}^{k,l}$$

      EndFor

      % Compute the distance between experts and group on expert

$$J_{i,I} = \sum_{k=1}^K J_{i,I}^k$$

    EndFor

  End

ALGORITHM 1: The algorithm to compute the distances on three levels.

the choice of threshold  $\varepsilon$  is largely subjective and application oriented [52]. Generally, a consensus threshold such as 90%, 80%, and two-thirds is often used as a minimum level that the decision-making required to be achieved [53]. When a consensus level is lower than  $\varepsilon$ , the interaction method for group consensus would be activated to identify inconsistent information and give the recommendation for inconsistent experts to revise her/his assessment. In order to identify the information with high conflicts on three levels, we follow the order of the highest, the intermediate, and the basic level. The order in which the inconsistent information is determined is exactly the opposite of the process of calculating the distance. Assume that the thresholds on the expert level, the alternative level, and the attribute levels are  $\varepsilon_1$ ,  $\varepsilon_2$ , and  $\varepsilon_3$ . The steps of the proposed method can be summarized as follows:

*Step 1.* Experts whose consensus indexes on expert level are higher than the threshold value  $\varepsilon_1$  are identified:

$$e = \{e_i \mid J_{i,I} > \varepsilon_1\} \quad (16)$$

*Step 2.* For the identified experts in Step 1, their alternatives with the values of consensus index higher than the threshold  $\varepsilon_2$  are identified:

$$y = \{y_k \mid J_{i,I}^k > \varepsilon_2\} \quad (17)$$

*Step 3.* Finally, the preference values to be changed are those with the values of consensus index higher than the threshold  $\varepsilon_3$  are identified:

$$c = \{c_l \mid J_{i,l}^{k,l} > \varepsilon_3\} \quad (18)$$

When the expert level's consensus index value  $J_{i,I}$  for  $e_i$  higher than the set thresholds value is identified, the interaction consensus procedure should be carried out to assist the inconsistent experts in modifying their opinion based on the recommendations given to enhance their consensus of the group. Since the attribute level is the most basic, it contains the original information of the expert and the source of the conflict. Therefore, expert  $e_i$  only needs to make corrections at this level. In this process here, only the experts whose consensus index values are higher than the threshold may get revised suggestion. Besides, it does not command those inconsistent experts to accept the revised suggestion regardless of their will; instead, it allows experts to modify the opinions by discounting original opinions and group opinion. The discount factors ( $\gamma \in [0, 1]$ ) are determined by the experts themselves.

“You are suggested to revise your assessment for alternative  $y_k$  on attribute  $c_j$ , to be closer to  $m_{l,k}$ .”

$$\hat{m}_{i,l,k}(H_n) = \begin{cases} (1 - \gamma) m_{i,l,k}(H_n) + \gamma m_{l,k}(H_n), & n = 1, \dots, N \\ 1 - \sum_{n=1}^N (1 - \gamma) m_{i,l,k}(H_n) + \gamma (m_{l,k}(H_n) - 1), & n = N + 1 \end{cases} \quad (19)$$

where  $\gamma \in [0, 1]$  is a parameter to control the degree of advice and  $\bar{m}_{i,l,k}$  is the corrected result.

If the parameter is 0.8, the expert original information is discounted by 0.2 and the group opinion is discounted by 0.8; that is, the expert is more inclined to trust the group opinion. If the parameter is 0.2, the expert original information is discounted by 0.8 and the group opinion is discounted by 0.2; that is, the expert is more inclined to believe her/his original information. If the parameter is 0.5, the expert original information and the group opinion are both discounted by 0.5, that is, the expert remains neutral. When expert determines the parameter to modify her/his opinion, the interaction process is activated. In the process, experts continuously interact with each other and modify the conflict information based on the recommendations given until the consensus level is reached or the maximum time of interaction is achieved. The maximum time of interaction is determined by experts, according to the data and the problem to be solved.

At the beginning, the reliability of the experts could not be determined, so it is a reasonable assumption that all experts are absolutely reliable, that is,  $r_i^{k,l} = 1, \forall i, k, l$ . After the first round of calculation, the actual reliability of the experts can be obtained in light of the Jousselme distance. At this point, the reliability of the identified experts with higher conflict is relatively low. However, in the later interaction, some expert reliability may increase and the Jousselme distance may decrease. This is because the experts get more information and become more reliable, which does not conflict with the objectivity and absoluteness of reliability. Algorithm 2 is summarized to the proposed model.

**3.4. The Method for Information Fusion and Decision Making.** There are two ways to integrate about the analytical ER approach, both of them combine the derived BPAs for two times.

*The First way* is more common: (1) The first time is to fuse BPAs on all attributes for expert  $e_i$ , i.e.,  $m_{i,k} = m_{i,l,k} \oplus \dots \oplus m_{i,L,k}, \forall i, k$ , also called individual information fusion. Obviously,  $m_{i,k}$  is the collected evaluation value given by expert  $e_i$  for alternative  $y_k$ . (2) The second time is to fuse the fused BPAs for all experts for alternative  $y_k$ , i.e.,  $m_k = m_{1,k} \oplus \dots \oplus m_{L,k}, \forall k$ , also called group information fusion,  $m_k$  is the overall evaluation value of alternative  $y_k$  for all experts.

*The Second way* is less common: (1) The first time is to fuse BPAs on all experts for attribute  $c_l$ , i.e.,  $m_{l,k} = m_{1,l,k} \oplus \dots \oplus m_{L,l,k}, \forall l, k$ . Obviously,  $m_{l,k}$  is the collective evaluation value given by all experts for alternative  $y_k$  on attribute  $c_l$  for all experts. (2) The second time is to fuse the fused BPAs for all attributes for alternative  $y_k$ ; i.e.,  $m_k = m_{1,k} \oplus \dots \oplus m_{L,k}, \forall k$ ,  $m_k$  is the collective evaluation value for alternative  $y_k$  on all attributes. Since the analytical ER rule is associative and commutative, the fusion results are the same whether by the first way or the second way.

According to Section 3.3, when the requirements of the consensus model are met, the evaluation information of all experts for the alternative  $y_k$  on the attribute  $c_l$  has been fused, i.e.,  $m_{l,k} = m_{1,l,k} \oplus \dots \oplus m_{L,l,k}, \forall l, k$ . Therefore, the second way

is adopted here for its first time of fusion has been conducted, and only the second time of fusion should be made. In other words, the computational complexity of the decision-making process will be decreased when the second way is adopted.

Combining the evaluation information on all attributes for the alternative  $y_k, m_k = m_{1,k} \oplus \dots \oplus m_{L,k}, \forall k$ , the overall evaluation value for alternative  $y_k$  is

$$B = B(H_n) = \begin{cases} \frac{m_k(H_n)}{(1 - \bar{m}_k(H))}, & n = 1, \dots, N, \\ \frac{\bar{m}_k(H_n)}{(1 - \bar{m}_k(H))}, & n = N + 1. \end{cases} \quad (20a)$$

where

$$m_k(H_n) = \delta_k \left[ \prod_{l=1}^L (m_{l,k}(H_n) + \bar{m}_{l,k}(H) + \tilde{m}_{l,k}(H)) \right. \quad (20b)$$

$$\left. - \prod_{l=1}^L (\bar{m}_{l,k}(H) + \tilde{m}_{l,k}(H)) \right], \quad n = 1, \dots, N,$$

$$\bar{m}_k(H) = \delta_k \left[ \prod_{l=1}^L (\bar{m}_{l,k}(H) + \tilde{m}_{l,k}(H)) \right. \quad (20c)$$

$$\left. - \prod_{l=1}^L \bar{m}_{l,k}(H) \right],$$

$$\bar{m}_k(H) = \delta_k \left[ \prod_{l=1}^L \bar{m}_{l,k}(H) \right], \quad (20d)$$

$$\delta_k = \left[ \sum_{n=1}^N \prod_{l=1}^L (m_{l,k}(H_n) + \bar{m}_{l,k}(H) + \tilde{m}_{l,k}(H)) \right. \quad (20e)$$

$$\left. - (N - 1) \prod_{l=1}^L (\bar{m}_{l,k}(H) + \tilde{m}_{l,k}(H)) \right]^{-1}.$$

The interaction consensus model consists of three stages: (1) consensus degrees on three levels to describe the inconsistency or conflict among experts based on Jousselme distance; (2) the interaction method for group consensus to make experts continuously interact with each other and modify the conflict information based on the recommendations given until the consensus level is reached; (3) the method for information fusion and decision-making in MAGDM. Algorithm 3 is summarized to the proposed model.

## 4. Illustration Example

In this section, A numerical case study is carried out to illustrate the decision making process by the proposed method. Suppose that a MAGDM problem consists of three alternatives  $y_1, y_2, y_3$ , four attributes  $c_1, c_2, c_3, c_4$ , and five experts  $e_1, e_2, e_3, e_4, e_5$ . The frame of discernment is composed of five levels, namely, excellent ( $H_1$ ), good ( $H_2$ ), average ( $H_3$ ), poor ( $H_4$ ), and very poor ( $H_5$ ), i.e.,  $H = \{H_1, \dots, H_5\}$ . Assume

**Input:** Expert assessments  $B_{i,l}^k = \{(H_n, \beta_{i,l}^{k,n}) \mid \beta_{i,l}^{k,n} > 0, \sum_{n=1}^{N+1} \beta_{i,l}^{k,n} = 1, n = 1, \dots, N, N+1\}$ ,  $i = 1, \dots, I$ ,  $k = 1, \dots, K$ ,  $l = 1, \dots, L$ ; Attribute set  $C = \{c_l \mid l = 1, \dots, L\}$ ; Reliability set of experts  $e_i$  on attribute  $c_l$   $r_i^{k,l} = 1, \forall i, k, l$ ; The correction times  $t = 0$ ; The maximum time of interaction  $T$ .

**Output:** Group opinions on attributes that meet the model requirements,  $\widehat{m}_{l,k} = \widehat{m}_{1,l,k} \oplus \dots \oplus \widehat{m}_{I,l,k}$ .

Begin  
 Do:  
 Call Algorithm 1 to compute the distance on three levels.  
 $m_{i,l,k}^t = m_{i,l,k}$   
 $m_{l,k}^t = m_{1,l,k} \oplus \dots \oplus m_{I,l,k}$   
 % Determine the evaluation information that needs to be revised.  
 While  $J_{i,l} > \varepsilon_1$   
   While  $J_{i,l}^k > \varepsilon_2$   
     While  $J_{i,l}^{k,l} > \varepsilon_3$   
       Modify the conflict information as follows  
        $t = t + 1$   
        $m_{i,l,k}(H_n) = (1 - \gamma) m_{i,l,k}^{t-1}(H_n) + \gamma m_{l,k}^{t-1}(H_n)$ ,  $n = 1, \dots, N$   
        $m_{i,l,k}(H_n) = 1 - \sum_{n=1}^N (1 - \gamma) m_{i,l,k}^{t-1}(H_n) + \gamma (m_{l,k}^{t-1}(H_n) - 1)$ ,  $n = N + 1$   
     End  
   End  
 End  
 End  
 End  
 Establish the models as in Eq. (12a), (12b), (12c), (12d), and (12e) and compute  $\widehat{m}_{l,k} = m_{1,l,k} \oplus \dots \oplus m_{I,l,k}$ .  
 Compute the reliability of experts as follows  
 If  $J_{i,l}^{k,l} \leq \varepsilon$ ,  $r_i^{k,l} = 1$   
 else  $r_i^{k,l} = \varepsilon / J_{i,l}^{k,l}$   
 While (The distances between experts and group at expert level is all up to model requirements or  $t \leq T$ )  
 End

ALGORITHM 2: The algorithm to the interaction consensus model for experts.

**Input:** Expert assessments  $B_{i,l}^k = \{(H_n, \beta_{i,l}^{k,n}) \mid \beta_{i,l}^{k,n} > 0, \sum_{n=1}^{N+1} \beta_{i,l}^{k,n} = 1, n = 1, \dots, N, N+1\}$ ,  $i = 1, \dots, I$ ,  $k = 1, \dots, K$ ,  $l = 1, \dots, L$ ; Attribute set  $C = \{c_l \mid l = 1, \dots, L\}$ ; Reliability set of experts  $e_i$  on attribute  $c_l$   $r_i^{k,l} = 1, \forall i, k, l$ ; Weight set of attributes  $W = (w_1, \dots, w_L)$ .

**Output:** Evaluation results for each alternative  $m_k, \forall k$ .

Begin  
 Call Algorithm 1 to compute the distance on three levels.  
 Call Algorithm 2 to compute group opinions on attributes that meet the model requirements,  
 $\widehat{m}_{l,k}, k = 1, \dots, K, l = 1, \dots, L$ .  
 For  $k=1$  to  $K$   
   For  $l=1$  to  $L$   
     Establish the models as in Eq. (20a), (20b), (20c), (20d), and (20e) and compute  $m_k = m_{1,k} \oplus \dots \oplus m_{L,k}$ .  
   EndFor  
 EndFor  
 End

ALGORITHM 3: The algorithm to MAGDM with reliability-based consensus model.

the weights of attributes in the set  $C = \{c_1, \dots, c_4\}$  are  $w_1 = w_2 = 0.2$  and  $w_3 = w_4 = 0.3$ . At the very beginning, the reliabilities of experts on all attributes are assumed as  $r_i^{k,l} = 1, \forall i, k, l$ . Experts are invited to evaluate alternatives on each attribute with BPAs. The assessment of alternative  $y_k$  given by expert  $e_i$  on attribute  $c_l$  is expressed as  $B_{i,l}^k = \{(H_n, \beta_{i,l}^{k,n}) \mid \beta_{i,l}^{k,n} > 0, \sum_{n=1}^{N+1} \beta_{i,l}^{k,n} = 1, n = 1, \dots, 6\}$ ,  $i = 1, \dots, 5, l = 1, \dots, 4, k = 1, \dots, 3$ , can be regarded as a piece of evidence.

For example,  $y_1$  evaluated by expert  $e_1$  with respect to  $c_1$  is  $B_{1,1}^1 = \{H_2 = 0.7, H_2 = 0.15, H = 0.15\}$ . All the assessments for alternatives on are attribute simultaneously listed in Table 1–3.

In the light of the discounting method with both weight and reliability, take the weight  $w_l$  and the reliability  $r_i^{k,l}$  into (11), and we obtain the values of discounting factor. Take  $\lambda_i^{k,l}$  and  $B_{i,l}^k$  into (5), the double discount formula and then the

TABLE 1: Assessments given by experts for alternative  $y_1$ .

Attribute	Expert	$H_1$	$H_2$	$H_3$	$H_4$	$H_5$	$H$
$c_1$	$e_1$	0.0000	0.7000	0.1500	0.0000	0.0000	0.1500
	$e_2$	0.5000	0.2000	0.0000	0.0000	0.0000	0.3000
	$e_3$	0.6000	0.1000	0.0000	0.0000	0.0000	0.3000
	$e_4$	0.5000	0.1500	0.0000	0.0000	0.0000	0.3500
	$e_5$	0.6000	0.3000	0.0000	0.0000	0.0000	0.1000
$c_2$	$e_1$	0.4000	0.4000	0.0000	0.0000	0.0000	0.2000
	$e_2$	0.7500	0.0000	0.0000	0.0000	0.0000	0.2500
	$e_3$	0.0000	0.4000	0.3000	0.0000	0.0000	0.3000
	$e_4$	0.7000	0.2000	0.0000	0.0000	0.0000	0.1000
	$e_5$	0.6000	0.2000	0.0000	0.0000	0.0000	0.2000
$c_3$	$e_1$	0.8500	0.0000	0.0000	0.0000	0.0000	0.1500
	$e_2$	0.7000	0.0000	0.0000	0.0000	0.0000	0.3000
	$e_3$	0.0000	0.2000	0.4000	0.0000	0.0000	0.4000
	$e_4$	0.0000	0.2000	0.4000	0.0000	0.0000	0.4000
	$e_5$	0.600	0.2000	0.0000	0.0000	0.0000	0.2000
$c_4$	$e_1$	0.0000	0.3000	0.0000	0.0000	0.0000	0.2000
	$e_2$	0.9000	0.0000	0.0000	0.0000	0.0000	0.1000
	$e_3$	0.0000	0.0000	0.6000	0.0000	0.0000	0.4000
	$e_4$	0.6000	0.0000	0.0000	0.0000	0.0000	0.4000
	$e_5$	0.0000	0.2000	0.4000	0.0000	0.0000	0.4000

TABLE 2: Assessments given by experts for alternative  $y_2$ .

Attribute	Expert	$H_1$	$H_2$	$H_3$	$H_4$	$H_5$	$H$
$c_1$	$e_1$	0.0000	0.6000	0.1500	0.0000	0.0000	0.2500
	$e_2$	0.2000	0.7000	0.0000	0.0000	0.0000	0.1000
	$e_3$	0.0000	0.6000	0.0000	0.0000	0.0000	0.4000
	$e_4$	0.4000	0.4000	0.0000	0.0000	0.0000	0.2000
	$e_5$	0.0000	0.7000	0.2000	0.0000	0.0000	0.1000
$c_2$	$e_1$	0.7000	0.2000	0.0000	0.0000	0.0000	0.1000
	$e_2$	0.5000	0.4000	0.0000	0.0000	0.0000	0.1000
	$e_3$	0.0000	0.4000	0.3000	0.0000	0.0000	0.3000
	$e_4$	0.3000	0.5000	0.0000	0.0000	0.0000	0.2000
	$e_5$	0.0000	0.6000	0.2000	0.0000	0.0000	0.2000
$c_3$	$e_1$	0.8500	0.0000	0.0000	0.0000	0.0000	0.1500
	$e_2$	0.0000	0.7000	0.0000	0.0000	0.0000	0.3000
	$e_3$	0.0000	0.6000	0.4000	0.0000	0.0000	0.0000
	$e_4$	0.0000	0.5000	0.4000	0.0000	0.0000	0.1000
	$e_5$	0.0000	0.7500	0.0000	0.0000	0.0000	0.2500
$c_4$	$e_1$	0.4000	0.4000	0.0000	0.0000	0.0000	0.2000
	$e_2$	0.9000	0.0000	0.0000	0.0000	0.0000	0.1000
	$e_3$	0.0000	0.0000	0.8000	0.0000	0.0000	0.2000
	$e_4$	0.0000	0.4000	0.0000	0.0000	0.0000	0.6000
	$e_5$	0.4000	0.2000	0.0000	0.0000	0.0000	0.4000

BPA functions  $m_{i,l,k}$  ( $\forall i, j, k$ ) are obtained. Take these BPA functions into the model as (12a), (12b), (12c), (12d), and (12e) to obtain the group evaluation result on an attribute  $c_l$  for an alternative  $y_k$ , i.e.,  $m_{l,k} = m_{i,l,k} \oplus \dots \oplus m_{l,k}$ ,  $\forall l, k$ . All the results on four attributes for three alternatives are derived as shown in Table 4.

Calculate the consensus index values on the attribute level, alternative level, and expert level according to (13)-(15) for expert  $e_i$ . And then the reliability of the expert  $e_i$  on an attribute  $c_l$  for an alternative  $y_k$  is calculated according to Definition 7. For convenience, we present the values of distance and reliability in an array. For example, (0.5403,

TABLE 3: Assessments given by experts for alternative  $y_3$ .

Attribute	Expert	$H_1$	$H_2$	$H_3$	$H_4$	$H_5$	$H$
$c_1$	$e_1$	0.0000	0.4000	0.4000	0.0000	0.0000	0.2000
	$e_2$	0.0000	0.2000	0.7000	0.0000	0.0000	0.1000
	$e_3$	0.0000	0.4000	0.5000	0.0000	0.0000	0.1000
	$e_4$	0.0000	0.0000	0.4000	0.4000	0.0000	0.2000
	$e_5$	0.0000	0.0000	0.6000	0.0000	0.0000	0.4000
$c_2$	$e_1$	0.0000	0.2000	0.5000	0.0000	0.0000	0.3000
	$e_2$	0.0000	0.4000	0.5000	0.0000	0.0000	0.1000
	$e_3$	0.0000	0.4000	0.5000	0.0000	0.0000	0.1000
	$e_4$	0.0000	0.0000	0.8000	0.1000	0.0000	0.1000
	$e_5$	0.0000	0.6000	0.2000	0.0000	0.0000	0.2000
$c_3$	$e_1$	0.0000	0.6000	0.2000	0.0000	0.0000	0.2000
	$e_2$	0.0000	0.0000	0.7000	0.1000	0.0000	0.2000
	$e_3$	0.0000	0.2000	0.6000	0.0000	0.0000	0.2000
	$e_4$	0.0000	0.2000	0.5000	0.0000	0.0000	0.3000
	$e_5$	0.0000	0.0000	0.7500	0.1500	0.0000	0.1000
$c_4$	$e_1$	0.0000	0.4000	0.4000	0.0000	0.0000	0.2000
	$e_2$	0.0000	0.0000	0.7500	0.0000	0.0000	0.2500
	$e_3$	0.0000	0.1000	0.7500	0.0000	0.0000	0.1500
	$e_4$	0.0000	0.2000	0.5000	0.0000	0.0000	0.3000
	$e_5$	0.0000	0.2000	0.6000	0.0000	0.0000	0.2000

TABLE 4: Results of expert fusion for attribute.

Attribute	Expert	$H_1$	$H_2$	$H_3$	$H_4$	$H_5$	$H$
$y_1$	$c_1$	0.6492	0.3412	0.0048	0.0000	0.0000	0.0048
	$c_2$	0.8991	0.0962	0.0023	0.0000	0.0000	0.0023
	$c_3$	0.9214	0.0367	0.0315	0.0000	0.0000	0.0105
	$c_4$	0.7007	0.0803	0.1168	0.0730	0.0000	0.0292
$y_2$	$c_1$	0.0049	0.9922	0.0023	0.0000	0.0000	0.0006
	$c_2$	0.1944	0.7990	0.0049	0.0000	0.0000	0.0016
	$c_3$	0.0000	0.9600	0.0400	0.0000	0.0000	0.0000
	$c_4$	0.8369	0.0922	0.0567	0.0000	0.0000	0.0142
$y_3$	$c_1$	0.0000	0.0391	0.9583	0.0018	0.0000	0.0009
	$c_2$	0.0000	0.0874	0.9115	0.0005	0.0000	0.0005
	$c_3$	0.0000	0.0148	0.9806	0.0033	0.0000	0.0012
	$c_4$	0.0000	0.0200	0.9787	0.0000	0.0000	0.0013

0.7403) means that the distance between expert  $e_1$  and the group on attribute  $c_1$  for alternative  $y_1$  is 0.5575 and the corresponding reliability of expert  $e_1$  0.7175 is shown in the second row and second column of Table 5.

According to the characteristic of the data, we select the thresholds on the expert level, the alternative level, and the attribute level, respectively, that is,  $\varepsilon_1 = 5.5$ ,  $\varepsilon_2 = 2.0$ , and  $\varepsilon_3 = 0.4$ . According to the above, the order of the highest (expert) level, the intermediate (alternative) level, and the most basic (attribute) level are used to determine the experts, alternatives, and attributes that need to be modified. It can be seen from Table 5 that expert  $e_1$  differs greatly from the group opinions on the  $2^{th}, 3^{th}, 4^{th}$  attributes for alternative  $y_2$  and the  $1^{th}, 3^{th}, 4^{th}$  attributes for alternative

$y_3$ . Expert  $e_3$  differs greatly from the group opinions on the  $2^{th}, 3^{th}, 4^{th}$  attributes for alternative  $y_1$ . They both need to modify their opinion based on (19). Suppose that experts  $e_1$  and  $e_3$  simultaneously have adopted the same discount factor values as  $\gamma = [0.0, 0.1, 0.2, 0.3, 0.4, 0.5, 0.6, 0.7, 0.8, 0.9, 1.0]$  to modify their opinions on the corresponding alternatives and attributes. The relationship between the distance and the discount factor after the expert correction is shown in Figure 1.

It can be seen from Figure 1 that when the discount factor takes values as 0, 0.8, 0.9, and 1.0, the experts could reach the consensus level after correction. When the discount factor takes a value in (0.1, 0.7), the requirement of the consensus level is not reached and the experts stop interacting after

TABLE 5: Evidence distance and expert reliability.

	$e_1$	$e_2$	$e_3$	$e_4$	$e_5$
$c_1$	(0.5403, 0.7403)	(0.2174, 1.0000)	(0.2376, 1.0000)	(0.2553, 1.0000)	(0.0692, 1.0000)
$c_2$	(0.4271, 0.9366)	(0.1848, 1.0000)	(0.7219, 0.5541)	(0.1675, 1.0000)	(0.2486, 1.0000)
$c_3$	(0.0977, 1.0000)	(0.2254, 1.0000)	(0.7424, 0.5388)	(0.7424, 0.5388)	(0.2761, 1.0000)
$c_4$	(0.6135, 0.6520)	(0.1846, 1.0000)	(0.6398, 0.6252)	(0.2430, 1.0000)	(0.5803, 0.6894)
$y_1$	(1.6786, -)	(0.8121, -)	(2.3418, -)	(1.4082, -)	(1.1742, -)
$c_1$	(0.3263, 1.0000)	(0.2544, 1.0000)	(0.3532, 1.0000)	(0.5151, 0.7765)	(0.2554, 1.0000)
$c_2$	(0.5569, 0.7183)	(0.3595, 1.0000)	(0.4108, 0.9737)	(0.2492, 1.0000)	(0.2637, 1.0000)
$c_3$	(0.9108, 0.4392)	(0.2482, 1.0000)	(0.3600, 1.0000)	(0.4167, 0.9600)	(0.2040, 1.0000)
$c_4$	(0.3934, 1.0000)	(0.1003, 1.0000)	(0.8006, 0.4996)	(0.7086, 0.5645)	(0.3841, 1.0000)
$y_2$	(2.1874, -)	(0.9623, -)	(1.9247, -)	(1.8896, -)	(1.1071, -)
$c_1$	(0.4826, 0.8509)	(0.2219, 1.0000)	(0.4160, 0.9615)	(0.4978, 0.8035)	(0.3357, 1.0000)
$c_2$	(0.3434, 1.0000)	(0.3694, 1.0000)	(0.3694, 1.0000)	(0.1340, 1.0000)	(0.6296, 0.6353)
$c_3$	(0.6984, 0.5727)	(0.2367, 1.0000)	(0.3185, 1.0000)	(0.3993, 1.0000)	(0.2010, 1.0000)
$c_4$	(0.5015, 0.7976)	(0.2119, 1.0000)	(0.1897, 1.0000)	(0.3969, 1.0000)	(0.3159, 1.0000)
$y_3$	(2.0259, -)	(1.0400, -)	(1.2937, -)	(1.4280, -)	(1.4822, -)
$y_1 + y_2 + y_3$	(5.8919, -)	(2.8144, -)	(5.5602, -)	(4.7258, -)	(3.7635, -)

TABLE 6: Results of modification for inconsistent expert.

Expert	Alternative	Attribute	$H_1$	$H_2$	$H_3$	$H_4$	$H_5$	$H$
$e_1$	$y_2$	$c_2$	0.8592	0.1170	0.0019	0.0000	0.0000	0.0219
		$c_3$	0.1700	0.7680	0.0320	0.0000	0.0000	0.0300
	$y_3$	$c_1$	0.0049	0.9913	0.0029	0.0000	0.0000	0.0009
		$c_3$	0.9199	0.0376	0.0317	0.0000	0.0000	0.0108
$e_3$	$y_1$	$c_4$	0.8355	0.0927	0.0573	0.0000	0.0000	0.0145
		$c_2$	0.6695	0.1538	0.1054	0.0000	0.0000	0.0713
	$y_1$	$c_3$	0.5193	0.3130	0.0838	0.0000	0.0000	0.0838
		$c_4$	0.1556	0.6392	0.1239	0.0000	0.0000	0.0813

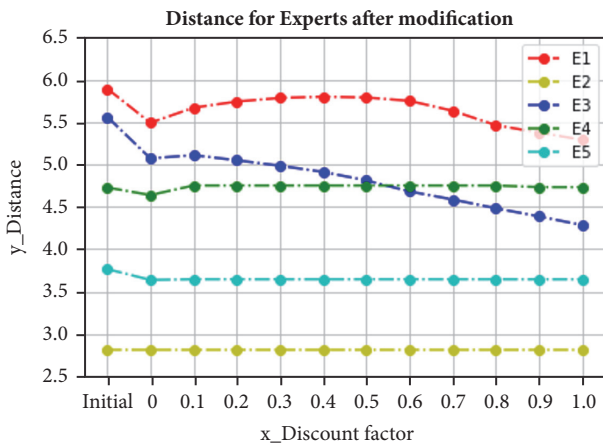


FIGURE 1: Distance for experts after modification.

four times of interaction. Note that the maximum time of interaction is determined by experts. According to the results of many experiments,  $T = 4$  is selected.

Suppose that experts  $e_1$  and  $e_3$  simultaneously have adopted the value of discount factor as  $\gamma = 0.8$  to modify their

opinions on the corresponding alternatives and attributes. The experts interacted four times and reached the required level of consensus. The results for inconsistent expert who have made four times of modification are shown in Table 6.

After the each time of modification, we obtain the new discounting factors by taking the weight  $w_l$  and the new reliability  $r_i^{k,l}$  (as shown in Table 5) into (11). Take  $\lambda_i^{k,l}$  and  $B_{i,l}^k$  into (5), the double discount formula and then the new BPA functions  $\widehat{m}_{i,l,k} (\forall i, j, k)$  are obtained. Take these BPA functions into the model as (12a), (12b), (12c), (12d), and (12e) to obtain the new group evaluation result on an attribute  $c_l$  for an alternative  $y_k$ , i.e.,  $\widehat{m}_{l,k} = \widehat{m}_{i,l,k} \oplus \dots \oplus \widehat{m}_{1,k}, \forall l, k$ . Calculate the new consensus index values on the attribute level, the alternative level, and the expert level according to (13)-(15) for expert  $e_i$ . And then the reliability of the expert  $e_i$  on an attribute  $c_l$  for an alternative  $y_k$  is recalculated according to Definition 7. The results of distance for inconsistent expert who have made four times of modification are shown in Table 7.

From Table 7, we can see that the consensus index values of all experts are less than the threshold of 5.5 at the expert level, reaching the expected level of consensus. It is not difficult to find that there are consensus index values greater

TABLE 7: Evidence distance after modification.

	$e_1$	$e_2$	$e_3$	$e_4$	$e_5$
$c_1$	0.4615	0.2174	0.2376	0.2553	0.0692
$c_2$	0.4471	0.1848	0.1864	0.1675	0.2486
$c_3$	0.0977	0.2254	0.4481	0.6471	0.2761
$c_4$	0.5222	0.1846	0.4856	0.243	0.5026
$y_1$	1.5287	0.8121	1.3577	1.3129	1.0965
$c_1$	0.3263	0.2544	0.3532	0.5974	0.2554
$c_2$	0.5511	0.3595	0.4085	0.2492	0.2637
$c_3$	0.1822	0.2482	0.3600	0.4989	0.2040
$c_4$	0.3934	0.1003	0.6281	0.5923	0.3841
$y_2$	1.4530	0.9623	1.7498	1.9378	1.1071
$c_1$	0.7043	0.2219	0.4957	0.5686	0.3357
$c_2$	0.3434	0.3694	0.3694	0.134	0.5876
$c_3$	0.7156	0.2367	0.3185	0.3993	0.2010
$c_4$	0.7165	0.2119	0.1897	0.3969	0.3159
$y_3$	2.4798	1.0400	1.3733	1.4989	1.4402
$y_1 + y_2 + y_3$	5.4615	2.8144	4.4808	4.7495	3.6439

TABLE 8: Results of attribute fusion for alternative.

Alternative	$H_1$	$H_2$	$H_3$	$H_4$	$H_5$	$H$
$y_1$	1.0000	0.0000	0.0000	0.0000	0.0000	0.0000
$y_2$	0.0000	1.0000	0.0000	0.0000	0.0000	0.0000
$y_3$	0.0000	0.0000	1.0000	0.0000	0.0000	0.0000

than the thresholds on the alternative and the attribute level. This is one of the advantages of our model. If the consensus level on the upper level meets the requirements, the expert does not need to modify the conflict information on the sublevel. In other words, experts do not need to modify all conflict information.

Combine the evaluation information on all attributes for the alternative  $y_k$ ,  $m_k = m_{1,k} \oplus \dots \oplus m_{L,k}$ ,  $\forall k$ , according to (20a), (20b), (20c), (20d), and (20e). All the results are shown in Table 8.

From Table 8, we can see that the evaluation grades of alternatives  $y_1$ ,  $y_2$ , and  $y_3$  are absolutely excellent ( $H_1$ ), good ( $H_2$ ), and average ( $H_4$ ), respectively. The consistency among experts is greatly improved.

## 5. Conclusions

Expert reliability has a significant effect on the group consensus calculation and group decision-making; however it has not been considered in the consensus-reaching model of MAGDM yet. This study aims at providing a reliability-based consensus model for MAGDM with analytically evidential reasoning (ER) approach. A numerical case study is carried out to illustrate the effectiveness of the method. The main contributions of this paper can be summarized as following three aspects.

Firstly, expert reliability is innovatively defined by Joussemle distance of the BPA functions between each expert

and expert group in consensus-reaching model of MAGDM. The individual BPA functions given by each expert are well discounted by both expert reliability and attribute weight, by combining which of the group BPA functions can be determined.

Secondly, the consensus degrees of three levels (attribute level, alternative level, and expert level) are defined by Joussemle distance between individual and group to identify the experts who should revise their judgments and point out revised suggestions.

Thirdly, an analytical ER-based decision-making method within interaction is proposed to determine the effective BPA functions of all experts and make final decision-making.

The established method proposed in this paper is very important for solving MAGDM problems for the following reasons. If the expert reliability is not considered or the accuracy of the evaluation information given by the expert is not taken into consideration, it will inevitably lead to the problems such as inaccurate group consensus degree calculation or poor quality of decision results. For future research, we will investigate how to deal with the more complex issues such that the judgments given by experts are made by fuzzy sets or include local ignorance.

## Data Availability

The data used to support the findings of this study are included within the article.

## Conflicts of Interest

The authors declare that there are no conflicts of interest regarding the publication of this paper.

## Acknowledgments

This research was supported by the National Natural Science Foundation of China (NSFC) under Grant nos. 71874167 and 71462022, the Fundamental Research Funds for the Central Universities under Grant no. 201762026, and the Special Funds of Taishan Scholars Project of Shandong Province under Grant no. tsqn20171205.

## References

- [1] E. Herrera-Viedma, S. Alonso, F. Chiclana, and F. Herrera, "A consensus model for group decision making with incomplete fuzzy preference relations," *IEEE Transactions on Fuzzy Systems*, vol. 15, no. 5, pp. 863–877, 2007.
- [2] J. Wu, F. Chiclana, H. Fujita, and E. Herrera-Viedma, "A visual interaction consensus model for social network group decision making with trust propagation," *Knowledge-Based Systems*, vol. 122, pp. 39–50, 2017.
- [3] J. Chu, X. Liu, Y. Wang, and K.-S. Chin, "A group decision making model considering both the additive consistency and group consensus of intuitionistic fuzzy preference relations," *Computers & Industrial Engineering*, vol. 101, pp. 227–242, 2016.
- [4] H. Liao, Z. Xu, X.-J. Zeng, and D.-L. Xu, "An enhanced consensus reaching process in group decision making with intuitionistic fuzzy preference relations," *Information Sciences*, vol. 329, pp. 274–286, 2016.
- [5] E. Herrera-Viedma, F. J. Cabrerizo, J. Kacprzyk, and W. Pedrycz, "A review of soft consensus models in a fuzzy environment," *Information Fusion*, vol. 17, no. 1, pp. 4–13, 2014.
- [6] S. Zeng, J. Gonzalez, and C. Lobato, "The effect of organizational learning and Web 2.0 on innovation," *Management Decision*, vol. 53, no. 9, pp. 2060–2072, 2015.
- [7] S. Zeng and Y. Xiao, "A method based on topsis and distance measures for hesitant fuzzy multiple attribute decision making," *Technological and Economic Development of Economy*, vol. 24, no. 3, pp. 905–919, 2018.
- [8] S. Zeng, Z. Mu, and T. Bale Entis, "Entis, A novel aggregation method for Pythagorean fuzzy multiple attribute group decision making," *International Journal of Intelligent Systems*, vol. 33, no. 3, pp. 573–585, 2018.
- [9] S. Zeng, N. Wang, C. Zhang, and W. Su, "A Novel Method Based on Induced Aggregation Operator for Classroom Teaching Quality Evaluation with Probabilistic and Pythagorean Fuzzy Information," *EURASIA Journal of Mathematics, Science and Technology Education*, vol. 14, no. 7, pp. 3205–3212, 2018.
- [10] Y. Du, N. Yang, and J. Ning, "IFS/ER-based large-scale multiattribute group decision-making method by considering expert knowledge structure," *Knowledge-Based Systems*, 2018.
- [11] Z. Wu and J. Xu, "A consensus model for large-scale group decision making with hesitant fuzzy information and changeable clusters," *Information Fusion*, vol. 41, pp. 217–231, 2018.
- [12] J. Montserrat-Adell, N. Agell, M. Sánchez, and F. Javier Ruiz, "Consensus, dissension and precision in group decision making by means of an algebraic extension of hesitant fuzzy linguistic term sets," *Information Fusion*, vol. 42, pp. 1–11, 2018.
- [13] B. Zhang, H. Liang, and G. Zhang, "Reaching a consensus with minimum adjustment in MAGDM with hesitant fuzzy linguistic term sets," *Information Fusion*, vol. 42, pp. 12–23, 2018.
- [14] W. Zhou and Z. Xu, "Group consistency and group decision making under uncertain probabilistic hesitant fuzzy preference environment," *Information Sciences*, vol. 414, pp. 276–288, 2017.
- [15] Y. Du, Y. Wang, and M. Qin, "New evidential reasoning rule with both weight and reliability for evidence combination," *Computers & Industrial Engineering*, vol. 124, pp. 493–508, 2018.
- [16] X.-F. Xu, J. Hao, Y.-R. Deng, and Y. Wang, "Design optimization of resource combination for collaborative logistics network under uncertainty," *Applied Soft Computing*, vol. 56, pp. 684–691, 2017.
- [17] X. Xu, W. Zhang, N. Li, and H. Xu, "A bi-level programming model of resource matching for collaborative logistics network in supply uncertainty environment," *Journal of The Franklin Institute*, vol. 352, no. 9, pp. 3873–3884, 2015.
- [18] Z. Wu and J. Xu, "Managing consistency and consensus in group decision making with hesitant fuzzy linguistic preference relations," *OMEGA - The International Journal of Management Science*, vol. 65, pp. 28–40, 2016.
- [19] J. Wu, L. Dai, F. Chiclana, H. Fujita, and E. Herrera-Viedma, "A minimum adjustment cost feedback mechanism based consensus model for group decision making under social network with distributed linguistic trust," *Information Fusion*, vol. 41, pp. 232–242, 2018.
- [20] Y. Zhang, Z. Xu, and H. Liao, "A consensus process for group decision making with probabilistic linguistic preference relations," *Information Sciences*, vol. 414, pp. 260–275, 2017.
- [21] J. Pang, J. Liang, and P. Song, "An adaptive consensus method for multi-attribute group decision making under uncertain linguistic environment," *Applied Soft Computing*, vol. 58, pp. 339–353, 2017.
- [22] J. Wu, F. Chiclana, and E. Herrera-Viedma, "Trust based consensus model for social network in an incomplete linguistic information context," *Applied Soft Computing*, vol. 35, pp. 827–839, 2015.
- [23] Y. Li, H. Zhang, and Y. Dong, "The interactive consensus reaching process with the minimum and uncertain cost in group decision making," *Applied Soft Computing*, vol. 60, pp. 202–212, 2017.
- [24] N. Zhang, Z. Gong, and F. Chiclana, "Minimum cost consensus models based on random opinions," *Expert Systems with Applications*, vol. 89, pp. 149–159, 2017.
- [25] Z. Gong, X. Xu, L. Li, and C. Xu, "Consensus modeling with nonlinear utility and cost constraints: A case study," *Knowledge-Based Systems*, vol. 88, pp. 210–222, 2015.
- [26] X. Tan, Z. Gong, F. Chiclana, and N. Zhang, "Consensus modeling with cost chance constraint under uncertainty opinions," *Applied Soft Computing*, vol. 67, pp. 721–727, 2018.
- [27] I. J. Pérez, F. J. Cabrerizo, S. Alonso, Y. C. Dong, F. Chiclana, and E. Herrera-Viedma, "On dynamic consensus processes in group decision making problems," *Information Sciences*, vol. 459, pp. 20–35, 2018.
- [28] X.-H. Xu, X.-Y. Zhong, X.-H. Chen, and Y.-J. Zhou, "A dynamical consensus method based on exit-delegation mechanism for large group emergency decision making," *Knowledge-Based Systems*, vol. 86, pp. 237–249, 2015.
- [29] Q. Dong and O. Cooper, "A peer-to-peer dynamic adaptive consensus reaching model for the group AHP decision making," *European Journal of Operational Research*, vol. 250, no. 2, pp. 521–530, 2016.

- [30] Z. Shi, X. Wang, I. Palomares, S. Guo, and R. Ding, "A novel consensus model for multi-attribute large-scale group decision making based on comprehensive behavior classification and adaptive weight updating," *Knowledge-Based Systems*, vol. 158, pp. 196–208, 2018.
- [31] M. Zhao, X.-Y. Ma, and D.-W. Wei, "A method considering and adjusting individual consistency and group consensus for group decision making with incomplete linguistic preference relations," *Applied Soft Computing*, vol. 54, pp. 322–346, 2017.
- [32] J.-B. Yang and M. G. Singh, "An Evidential Reasoning Approach for Multiple-Attribute Decision Making with Uncertainty," *IEEE Transactions on Systems, Man, and Cybernetics*, vol. 24, no. 1, pp. 1–18, 1994.
- [33] J.-B. Yang and D.-L. Xu, "Evidential reasoning rule for evidence combination," *Artificial Intelligence*, vol. 205, pp. 1–29, 2013.
- [34] Y.-M. Wang, J.-B. Yang, D.-L. Xu, and K.-S. Chin, "The evidential reasoning approach for multiple attribute decision analysis using interval belief degrees," *European Journal of Operational Research*, vol. 175, no. 1, pp. 35–66, 2006.
- [35] C. Fu, M. Huhns, and S. Yang, "A consensus framework for multiple attribute group decision analysis in an evidential reasoning context," *Information Fusion*, vol. 17, no. 1, pp. 22–35, 2014.
- [36] C. Fu and S. Yang, "An evidential reasoning based consensus model for multiple attribute group decision analysis problems with interval-valued group consensus requirements," *European Journal of Operational Research*, vol. 223, no. 1, pp. 167–176, 2012.
- [37] C. Fu and S.-L. Yang, "The group consensus based evidential reasoning approach for multiple attributive group decision analysis," *European Journal of Operational Research*, vol. 206, no. 3, pp. 601–608, 2010.
- [38] C. Fu, J.-B. Yang, and S.-L. Yang, "A group evidential reasoning approach based on expert reliability," *European Journal of Operational Research*, vol. 246, no. 3, pp. 886–893, 2015.
- [39] V. Sriramdas, S. K. Chaturvedi, and H. Gargama, "Fuzzy arithmetic based reliability allocation approach during early design and development," *Expert Systems with Applications*, vol. 41, no. 7, pp. 3444–3449, 2014.
- [40] D. Gonzalez-Gonzalez, M. Cantu-Sifuentes, R. Praga-Alejo, B. Flores-Hermosillo, and R. Zuñiga-Salazar, "Fuzzy reliability analysis with only censored data," *Engineering Applications of Artificial Intelligence*, vol. 32, pp. 151–159, 2014.
- [41] R. S. Prabhu Gaonkar, M. Xie, and X. Fu, "Reliability estimation of maritime transportation: a study of two fuzzy reliability models," *Ocean Engineering*, vol. 72, pp. 1–10, 2013.
- [42] Y.-K. Lin and L. C.-L. Yeng, "Network reliability based decision of Internet with multiple sources and multiple sinks," *Decision Support Systems*, vol. 54, no. 3, pp. 1477–1487, 2013.
- [43] X. Chen and M. R. Lyu, "Reliability analysis for various communication schemes in wireless CORBA," *IEEE Transactions on Reliability*, vol. 54, no. 2, pp. 232–242, 2005.
- [44] S. Yacoub, B. Cukic, and H. H. Ammar, "A scenario-based reliability analysis approach for component-based software," *IEEE Transactions on Reliability*, vol. 53, no. 4, pp. 465–480, 2004.
- [45] F. Smarandache, J. Dezert, and J. Tacnet, "Fusion of sources of evidence with different importances and reliabilities," *IEEE*, pp. 1–8, 2010.
- [46] A. P. Dempster, "Upper and lower probabilities induced by a multivalued mapping," *Annals of Mathematical Statistics*, vol. 38, pp. 325–339, 1967.
- [47] Y.-W. Du and W.-M. Xu, "Multiattribute group decision making based on interval-valued intuitionistic fuzzy sets and analytically evidential reasoning methodology," *Journal of Intelligent & Fuzzy Systems: Applications in Engineering and Technology*, vol. 33, no. 5, pp. 2953–2960, 2017.
- [48] P. Smets and R. Kennes, "The transferable belief model," *Artificial Intelligence*, vol. 66, no. 2, pp. 191–234, 1994.
- [49] P. Smets, "Decision making in the TBM: the necessity of the pignistic transformation," *International Journal of Approximate Reasoning*, vol. 38, no. 2, pp. 133–147, 2005.
- [50] A. L. Jousselme, D. Grenier, and É. Bossé, "A new distance between two bodies of evidence," *Information Fusion*, vol. 2, no. 2, pp. 91–101, 2001.
- [51] A.-L. Jousselme and P. Maupin, "Distances in evidence theory: comprehensive survey and generalizations," *International Journal of Approximate Reasoning*, vol. 53, no. 2, pp. 118–145, 2012.
- [52] W. Liu, "Analyzing the degree of conflict among belief functions," *Artificial Intelligence*, vol. 170, no. 11, pp. 909–924, 2006.
- [53] P. Pérez-Asurmendi and F. Chiclana, "Linguistic majorities with difference in support," *Applied Soft Computing*, vol. 18, pp. 196–208, 2014.

## Research Article

# An Evacuation Route Model of Crowd Based on Emotion and Geodesic

Bangquan Liu <sup>1,2</sup>, Zhen Liu <sup>2</sup>, Dechao Sun <sup>3</sup>, and Chunyue Bi <sup>3</sup>

<sup>1</sup>College of Information Engineering, Ningbo Dahongying University, Ningbo, China

<sup>2</sup>Faculty of Electrical Engineering and Computer Science, Ningbo University, Ningbo, China

<sup>3</sup>College of Electronics and Computer, Zhejiang Wanli University, Ningbo, China

Correspondence should be addressed to Zhen Liu; [liuzhen@nbu.edu.cn](mailto:liuzhen@nbu.edu.cn) and Dechao Sun; [sundechnao123@163.com](mailto:sundechnao123@163.com)

Received 27 July 2018; Accepted 12 September 2018; Published 1 October 2018

Guest Editor: Carlos Llopis-Albert

Copyright © 2018 Bangquan Liu et al. This is an open access article distributed under the Creative Commons Attribution License, which permits unrestricted use, distribution, and reproduction in any medium, provided the original work is properly cited.

Making unconventional emergent plan for dense crowd is one of the critical issues of evacuation simulations. In order to make the behavior of crowd more believable, we present a real-time evacuation route approach based on emotion and geodesic under the influence of individual emotion and multi-hazard circumstances. The proposed emotion model can reflect the dynamic process of individual in group on three factors: individual emotion, perilous field, and crowd emotion. Specifically, we first convert the evacuation scene to Delaunay triangulation representations. Then, we use the optimization-driven geodesic approach to calculate the best evacuation path with user-specified geometric constraints, such as crowd density, obstacle information, and perilous field. Finally, the Smooth Particle Hydrodynamics method is used for local avoidance of collisions with nearby agents in real-time simulation. Extensive experimental results show that our algorithm is efficient and well suited for real-time simulations of crowd evacuation.

## 1. Introduction

With the rapid development of society, densely populated places are increasing, and the security safety of the crowds is becoming more and more prominent, and the crowd trampling is an extreme event in natural crowd motion. Due to time and space constraints, it is difficult to complete the whole process of experimental exercises in the real life. Evacuation simulation is using computer to establish an effective simulation scene model to help solve the crowd evacuation behaviour in public environment. It is of great significance to prevent and deal with all kinds of major public safety incidents and reduce personal injury and economic loss [1]. In the real world, the emotional state of an individual plays a vital role in his/her decision-making and is easily influenced by others emotions. This process can be called emotional contagion [2]. In a specific group environment, emotional contagion will have an important influence on individual's emotions, behaviours, and decisions [3]. For example, during the emergency evacuation of a fire accident, emotional contagion will exacerbate the panic of the individual and prompt an individual to take immediate evacuation

measures to reduce the time. Traditional multiagent navigation algorithms, like Reciprocal Velocity Obstacles (RVO) [4], have not considered the emotion of individuals. Emotional Reciprocal Velocity Obstacles (ERVO) model [5] improved the RVO with integrating the emotional effect into velocity decision, but it is limited for path planning. Path planning is one of the core technologies of evacuation simulation, which is used to simulate the behaviour of agents in the emergency scene. With the development of crowd simulation technology, although the traditional path planning method has been improved, the real-time path planning in evacuation simulation still faces many challenges.

Inspired by the above challenge, we proposed a novel evacuation simulation approach based on emotion and geodesic. Specifically, we first discussed the construction of individual emotional models in the process of emotional impact, where the individual emotional intensity, emotional infection, and emotional attenuation in evacuation process are described in detail. Based on the emotional impact method, we can add environmental information into a triangular mesh. By using the optimization-driven geodesic approach on triangle meshes, we could realize path planning

in evacuation simulation. The evacuation path can be calculated in real time according to the dynamic state environment information. A complete evacuation simulation system is implemented, and the simulation experiments are carried out for different scenes. The experimental results verify the effective of the proposed model.

## 2. Related Work

In recent years, different types of evacuation simulation models have been proposed to simulate the behavior of evacuation of pedestrians in emergency situations [6–8]. According to the different objects of concern, these models can be divided into macroscopic [9, 10] and microscopic models [11–15]. The former is concerned with evacuating as a whole, assuming that all pedestrians have the same behavior pattern in the evacuation process. The latter is concerned with the simulation of individual behavior of pedestrians, which can generate different individual evacuation details. Compared with the macro model, the micro model can reproduce the influence of individual behavior on the evacuation process and make the simulation results truer. Therefore, the model gradually becomes the mainstream of the current evacuation simulation at home and abroad. This paper is in the micro frame. Under the frame, we focus on the path planning problem in evacuation simulation. Environmental modelling is the preparation of path planning. The evacuation environment is abstracted as a navigation map. The navigation map is usually represented as a graph structure composed of nodes and arcs. Different modelling methods [16, 17] can generate different navigation maps. Path planning means searching a path from the initial node to the target node on the map. In fact, the shortest path planning has become a widely used path planning method. There have been a lot of works on the shortest path planning in the fields of computer and robot. The Floyd algorithm, Dijkstra algorithm, and A\* algorithm and its variant [18] can effectively find a shortest path on the navigation map.

However, when in a dangerous scene, pedestrians cannot find the shortest path under the influence of many factors and choose the safe area to move forward, or even ignore the optimal escape route to follow the flow passively [11]. The shortest path method is no longer applicable. In order to solve this problem, the extra decision module is introduced to evacuation simulation [15, 19, 20]. The decision module confirms the current subgoal according to the current status of the virtual human and then searches for a shortest path to the target. After arriving at the target, the decision module will continue to choose the next target and repeat until it reaches the security exit. This method can produce a good result when the rule is sufficient and reasonable. But the rule set used by the decision must fully reflect the characteristics of the crowd evacuation behavior under different circumstances and avoid the conflict among different rules. In addition, the local path planning among the subtargets is constantly carried out, ignoring the influence of the global environment information on the path selection.

Compared with the explicit formulation of rules set, the path of individual behavior can be naturally planned by

introducing the influence of different factors in the scene directly into the path search process. Toll et al. [21] considered the dynamic population density of various regions in the field environment, and the path of virtual human planning can bypass the crowded area. Jaklin et al. [22] provided a method which can modify the initial path of the plan according to the role identity, and simulate the preference of different individuals to different terrain. The influence of individual emotion on its choice of evacuation path was also reflected in the path planning [23, 24]. The above works considered individual differences in the path planning of pedestrians from different aspects. There is also lack of a path planning method which can take into account the individual psychology, the cognition of the scene, and the ability to act autonomously.

Compared with the real-time path planning method, the optimization method pays attention to the generation of the optimal path in evacuation. This kind of method establishes the optimization function with factors which need to be considered in evacuation and iteratively optimizes it to solve the optimal evacuation route. Usually, the evacuation time is the primary consideration. In recent years, the constraints of the path complexity are also taken into account [1, 25].

The above work can obtain the optimal path to satisfy various constraints; however, the path obtained by the optimization method will be restricted by the constraints considered. Even if sufficient constraints are added, the path generated by this method is too ideal, while the pedestrian in the reality is lacking in the panic and the global environment in the emergency scene. It is difficult to follow such a perfect path, so this kind of method is more suitable for the design of safety route. In addition, the optimization method needs to be solved iteratively. It takes a lot of time to calculate, it is difficult to achieve real time, and it is not suitable for real-time evacuation simulation.

## 3. Materials and Methods

*3.1. Emotional Impact from Hazards and Agents.* During the evacuation process, people often choose to stay away from dangerous sources so as not to cause injury to them. The environmental information of pedestrians will directly affect the planning of evacuation routes. We use triangulated mesh to create environmental information and specify a density function to represent the crowd density and information of hazard which will be updated dynamically during the simulation process. The dangerous value of sources to agents is limited, the closer they are to source, the danger is higher, and, to a certain region, the threat decreases rapidly. Assume that the dangerous area is circular, the Gauss function can be used to calculate the hazard value  $\psi_i$  of  $p_i$ :

$$\psi_i = \frac{1}{\sqrt{2\pi}} \exp^{-(v_i - v_0)^2 / 2} \times \psi_0 \quad (1)$$

where  $v_i$  is the  $i$ -th vertex of the mesh,  $v_0$  is the source vertex of hazards on the mesh, and  $\psi_0$  is the danger value in hazard source  $v_0$ .

In this paper we use triangulation grid to establish navigation grid and record the area  $s$  of each triangle. According to the position of agents, we can compute the number of agent

in each triangle, then the crowd density of triangle can be calculated using the following:

$$\rho = \frac{\sum \pi r_i^2}{s} \quad (2)$$

where  $r_i$  is the radius of agent which is in the crowd.  $s$  is the area of the triangle in which the crowd is located. After computing the density, the crowd density information of surface will be stored in the triangle mesh.

Agents are easily affected by the environment and dangerous information in the process of movement; the closer they are to the hazard, the stronger the agent's willingness to escape the hazard is. At the same time, agents have different reactions to the crowd based on their emotions and environmental factors. In a group environment, the individual is bound to be affected by emotion, but the degree of influence is different. The reason is that the individual has different emotional preferences, the ability to capture emotional clues, and emotional feeling. The group with the same purpose is in the same situation. Although the individual has different degrees of cognition and evaluation to the same stimulus, the emotion of the experience is consistent, only the degree is different. In the calculation of emotional impact, we mainly consider two sources of emotion: special individual emotion and the emotions created by the group. The emotional contagion value  $I_i(t+1)$  of the  $i$ -th agent  $AG_i$  at the time of  $T+1$  is

$$I_i(t+1) = P_i^t \times (\omega \times \psi_d + (1 - \omega) \times GE \times I_i(t)) + I_i(t) \quad (3)$$

where  $I_i(t)$  is the emotional value of the  $AG_i$  at the time of  $T$  and  $\omega$  is an individual's attention to the danger value  $\psi_d$  of hazard source in the current position.  $P_i^t$  is the optimistic mood at the time of  $t$ , expressing the ability of individual emotion to feel positive influence from other groups.  $GE$  is the group emotion, defined as follows:

$$GE = \sum (\beta_i \times \mu_i \times I_i(t)) \quad (4)$$

Although crowd emotion is composed of individual emotions, it is not simply a cumulative accumulation of individual emotions.  $\beta_i$  is the leadership coefficient which indicates the influence of  $AG_i$ 's emotion on group emotion.  $\mu_i$  defines the influence of  $Agent_i$  on group emotion in a group, and the formula is as follows:

$$\mu_i = \frac{P_i^t}{\sum_{i \in G} P_i^t} \quad (5)$$

Personality is the unique mental and psychological characteristics of individuals formed in social activities and is different from other individuals. The possible emotional states of  $AG_i$  include negative emotional state and positive emotional state. Agents who are in positive emotional state are calmer and easier to integrate into groups to reach the destination quickly. The emotion of the agent will be changed with the emotion of the surrounding, in easy step of simulation process, the optimistic emotion  $P_i^t$  of  $AG_i$  also will be updated with a certain randomness, and the formula is as follows:

$$P_i^{t+1} = P_i^t \times (1 + \alpha_p) \quad (6)$$

where  $\alpha_p$  is the change value of indicates optimistic emotion, which can be calculated by the following formula:

$$\alpha_p = \frac{\sum_{i=1}^{N_p} \lambda_p(i)}{N_p} \chi_p \quad (7)$$

where  $N_p$  is the number of agents who could affect the emotion of  $AG_i$ .  $\chi_p$  represents the coefficient factor of an agent's optimism.  $\lambda_p(i)$  indicates the optimistic emotion value from other agents around  $AG_i$ , and it can be calculated by the following formula:

$$\lambda_p(i) = (1 - \eta) \times (1 - \rho) \quad (8)$$

where  $\rho$  is the crowd density of triangle that can be calculated by (2). The weight value  $\psi$  of an agent that has emotions is calculated using the following:

$$\eta = \frac{\alpha}{1 + B e^{b\omega}} \quad (9)$$

$\eta$  takes a value in the range  $[0, 1]$ .  $\omega$  is composed of two emotions. The two emotions, which are orthogonal dimensions of the emotion space and selected from the OCC model [26], are hope and fear. An agent's emotion is a two-dimensional vector, where each dimension is represented by an emotion:

$$\Pi = \langle \psi_H, \psi_F \rangle \quad (10)$$

The variable  $\omega$  of (9) can be calculated by the following:

$$\omega = \psi_H - \psi_F \quad (11)$$

where  $\psi_H + \psi_F = 1$ ,  $\psi_H$  is the hope emotion and  $\psi_F$  is the fear emotion. Generally, agents will choice a suitable way to escape the dangerous area based on their own emotional state and environmental information. There are always two ways: one is to join an appropriate group and follow the leader to evacuate, and the other is to choose the shortest path to move away from the dangerous area and avoid the crowd. When the agent meets a crowd, the value of the agent following the crowd is calculated as follows:

$$T_{flow} = \frac{Q}{\sum_{i=1}^{N_p} I_i(t)} \quad (12)$$

$Q$  is an adjustment coefficient. The way to update the action of an agent can take the following rules: if  $T_{flow} < P^t$ , the agent will keep away from the crowd and take the crowd as an obstacle to recalculate the appropriate path. If  $T_{flow} > P^t$ , the agent will back out the original path planning and join into the crowd and evacuate with others.

**3.2. Geodesic Path with Non-Uniform Density.** Let  $\mathcal{S}$  be a triangulated polyhedral surface in  $\mathcal{R}^3$ , defined by a set of vertices, edges, and faces. Given two points  $s, t \in \mathcal{S}$ , there are infinitely many paths between them. Our task is to calculate the shortest path that passes the obstacles and meet other



**Input:** A triangle Mesh  $\mathcal{S}$ ; two points  $s, t \in \mathcal{S}$  and an initial path between them; A error tolerance  $\epsilon$ .  
**Output:** A geodesic path between  $s$  and  $t$ .  
 Calculate the hazard value  $\psi_i$  of  $p_i$  using equation (1)  
 Calculate crowd density  $\rho$  of triangle  $f_i$  using equation (2)  
 Set density function  $\rho(f_i)$  of  $f_i$  according to  $\psi_i$  and  $\rho$   
 Compute the current length  $L^t$  of initial path  
 Let  $L^{t-1} = 0$   
**while**  $\|L^{t-1} - L^t\| > \epsilon$  **do**  
   Let  $L^{t-1} = L^t$   
   Compute the length of path using equation (13)  
   Compute the gradient of length using equation (14)  
   Get the resulting path;  
   Collect the vertices  $\{v_i\}$  on the path;  
   Traverse and update the face sequence such that each  $v \in \{v_i\}$  is on the other side of the new face sequence.  
   Compute the new length  $L^t$  of path  
**end**

ALGORITHM 1: An optimization based method for computing the shortest path with hazard information.

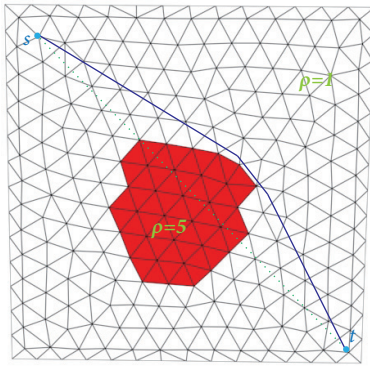


FIGURE 2: The green path is geodesic path assuming the density is uniform on the surface, while the blue path is geodesic path in the density  $\rho = 5$  set on red faces and the other with  $\rho = 1$ .

range. In our experiment of crowd evacuation simulation, taking  $\alpha = 1$ ,  $\beta = 1$ . When using the SPH method to calculate the force, it is important to search other agents in the agent's scope and the time complexity is  $O(n^2)$ , where  $n$  is the number of agents. The computational efficiency decreases slowly with the increasing rate of  $n$ . In order to improve the computational efficiency, we use the Approximate Nearest Neighbor (ANN) method [31] to find the agents in its self-scope.

#### 4. Results and Discussion

We implemented and experimented with our algorithm on a computer with a 64-bit version of Win7 system, a 3.07 GHz Intel(R) Core(TM) i7 CPU, and 6 GB memory. The coding language is C++. We shall use extensive experimental results to exhibit demonstrate the algorithm's efficiency, as well as its insensitiveness to scene resolution, and its robustness to small surface variations and topology. To demonstrate

TABLE 1: Timing statistics (seconds) for geodesic computation on a workstation with a 3.07 GHz CPU and 6GB RAM.

scenario	#Faces	Average time(s)	Max time(s)
scenel(Figure 3)	2,000	0.05	0.08
scenel(Figure 3)	10,196	0.11	0.19
scenel(Figure 3)	51,265	0.34	0.40
scenel(Figure 3)	105,767	0.64	0.41
scene2(Figure 4)	20,852	0.15	0.20
scene3(Figure 5)	12,987	0.11	0.15
scene4(Figure 6)	25,632	0.17	0.19
scene5(Figure 7)	22,572	0.15	0.21

specific features and analyze capability of our method, we carry out the evacuation simulation in different scenarios.

To demonstrate the path planning algorithms efficiency, we developed a program to automatically generate triangulated mesh for scenes and simple interface for users to interactively specify obstacle regions. The radius  $\gamma_i$  of agent is set to 3; other parameters in our system are set experimentally:  $\omega = 0.5$ ,  $\varphi_0 = 20$ ,  $Q = 2$ ,  $B = 1$ ,  $\alpha = 2$ ,  $b = 5$ . To measure the geodesic algorithm performance, we randomly sample 1K pairs of vertices to take down the average computation time and the max computation time. As shown in Table 1, for scene with around 20K faces, our algorithm takes 0.15s averagely to compute a geodesic path and can be used for real-time path planning.

*4.1. Evacuate Simulation under Different Scenarios.* Our method can handle mesh information changes during the simulation. Taking a simple scenario shown in Figure 3 as an example, a group evacuate from sources to targets with the geodesic path which is calculated based on obstacles and hazard information. This scene has  $300 \times 300$  units with 5k triangulated faces and two exports. The group with a leader move from the source position  $s$  to the target position  $t$ , respectively. As shown in Figure 3(a), there are some obstacles

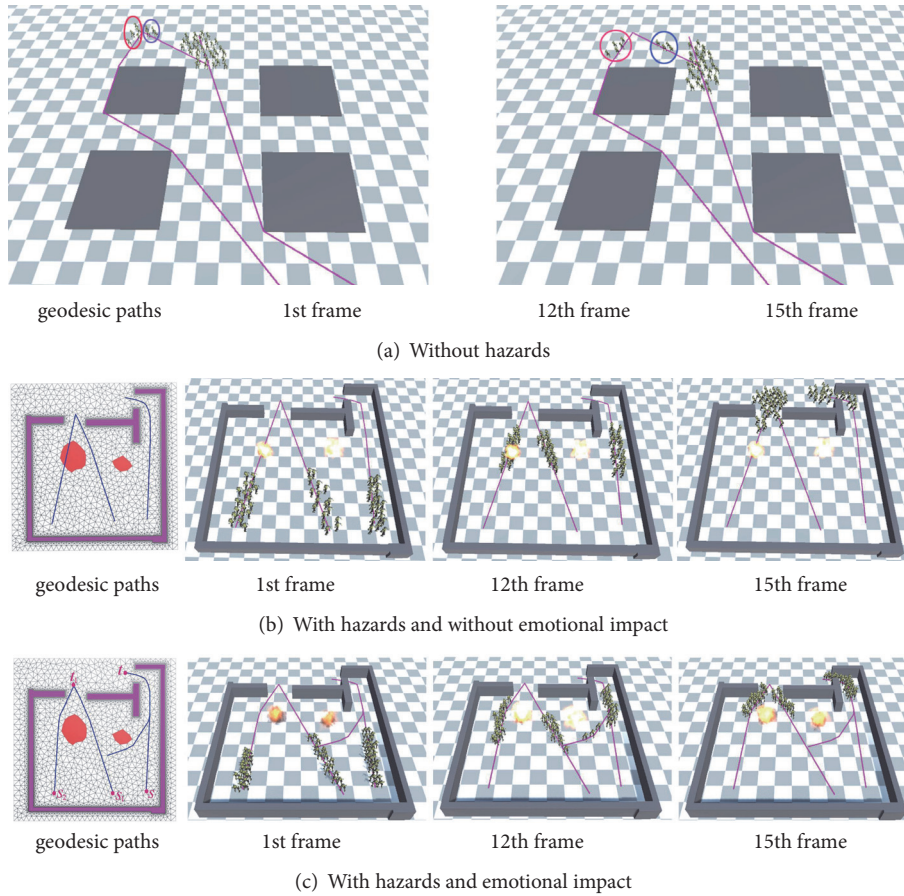


FIGURE 3: Snapshots of crowd simulation in the same scenarios with different hazard and emotional impact. Images in the left line represent the geodesic paths on the triangle mesh. The other three images represent the different snapshots of the simulation process at 1st, 12th, and 15th frame, respectively.

in the scene; we set density  $\rho = 5$  in the region where the obstacles are located and can get the geodesic path in real-time. The geodesic is the shortest path, so the crowd can reach their destination as quickly as possible under their own speed. In Figure 3(b), we add an explosion hazard in the region and agents without emotion will keep moving along the original planned directions. In Figure 3(c), we add the sample hazard into scene and agents with emotion impact, the agents will recalculate their moving path to escape away from the hazard source. We also specify a dangerous factor  $\rho = 10$  to the affected triangulation faces and can get the safety geodesic path less than 0.1 seconds. The simulation results show that the crowd completely avoids the hazards and obstacles.

We also simulate evacuation behaviors in a crowd with the following hazard situations: persistent hazards occur at different moments time. The simulation runs in a simple maze field with two exits. Figure 4 shows some snapshots of crowd movement in this simulation. All the agents move randomly at the beginning of simulation. If a persistent hazard occurs at a specific time as shown in the 10-th frame of Figure 4(a), those agents will keep far away from the hazards continually as long as they evacuated to an exit along the geodesic path. When another persistent hazard occurs at the evacuating exit as shown in the 20-th frame of Figures 4(a) and

4(b), all the agents will escape away from both of the hazards and choose to evacuate from another safe exit.

In order to validate the effectiveness of individual emotions and group information, we run crowd simulations in a scene with a crowd and agents with different emotions. There are four obstacles in the scene and each agent has different emotional values  $\varphi_H$  and  $\varphi_F$ . The agents with  $\varphi_F = 0.6$  and  $\varphi_H = 0.4$  in red circle choose to stay away from the crowd for evacuating. We use (2) to set the crowd density value  $\rho$  in the region where the crowd is located when calculating the geodesic path for those agents. In Figure 5, when the agents in the red circle see a group of crowd in scene, the crowd is seen as an obstacle, and the geodesic path is recalculated for evacuating. On the contrary, the agents with  $\varphi_F = 0.3$  and  $\varphi_H = 0.7$  in the blue circle choose to join the crowd and move forward with the crowd.

**4.2. Analysis of Emotional Impact.** Some simulations of crowd movement with and without emotion model, shown in Figure 6, are used to validate the effectiveness of emotional impact in our method. As shown in Figure 6(a), agents without emotion will keep moving along the geodesic path rendered in red line. In contrast, the agents with emotion will replan the evacuation geodesic path to escape away from the

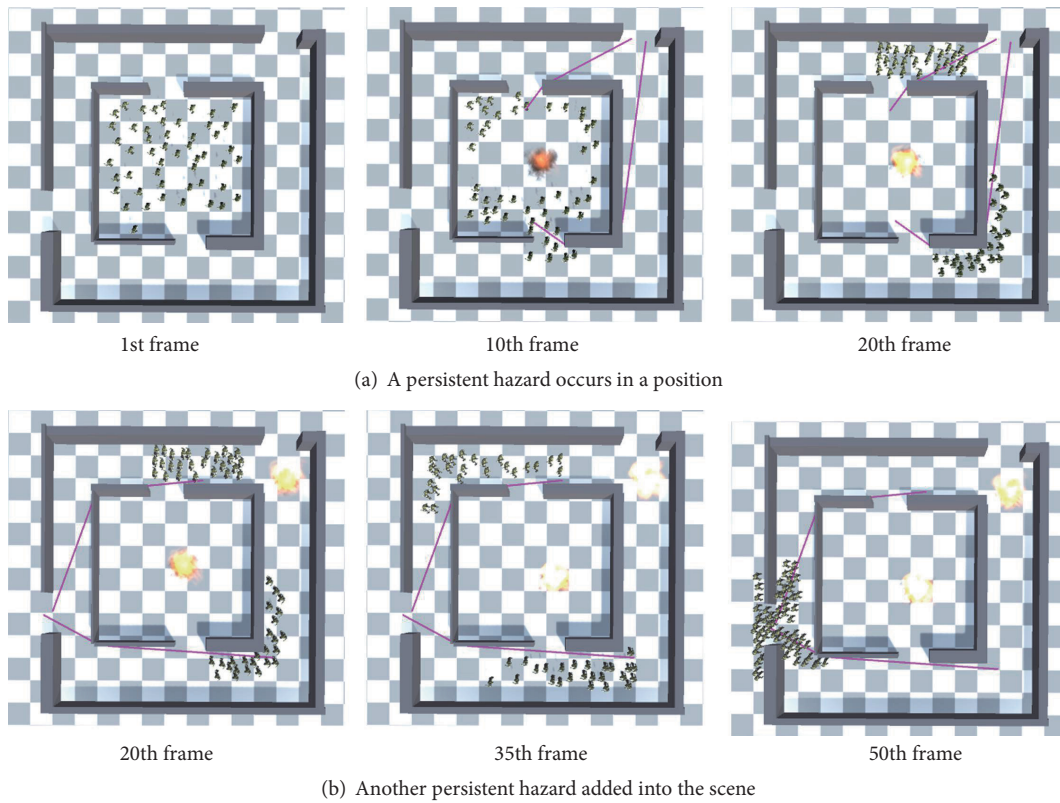


FIGURE 4: Snapshots of crowd simulation in different types of hazard scenarios.

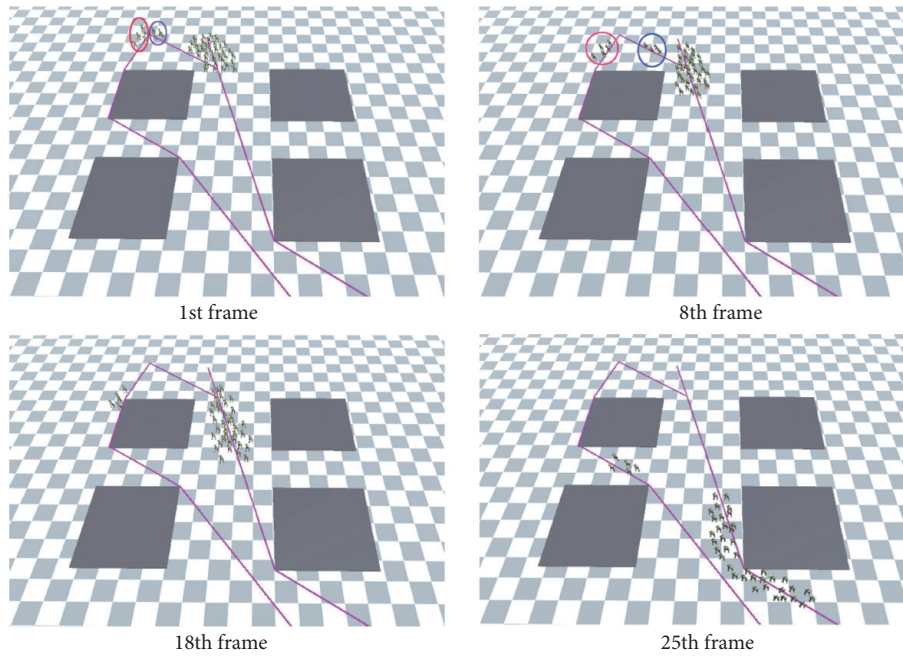


FIGURE 5: Agents with different hope emotion  $\psi_H$  and fear emotion  $\psi_N$  choose different evacuation when they meet another group. Four images represent the different snapshots of the simulation process at different moments.

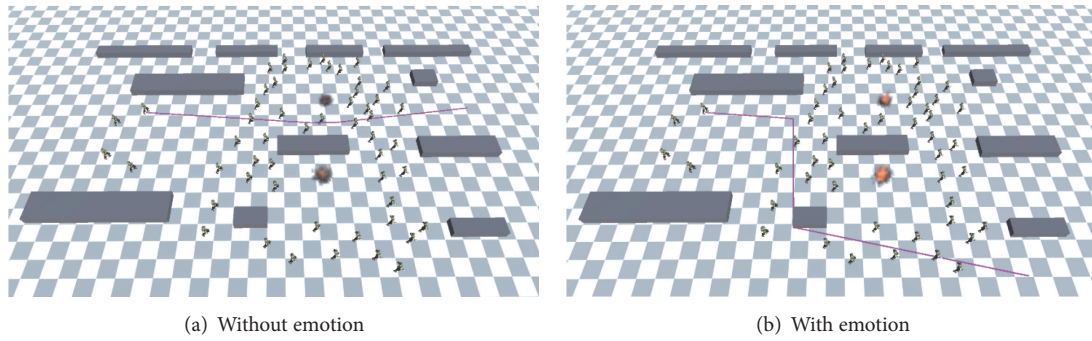


FIGURE 6: The comparison of crowd movements with and without emotion.

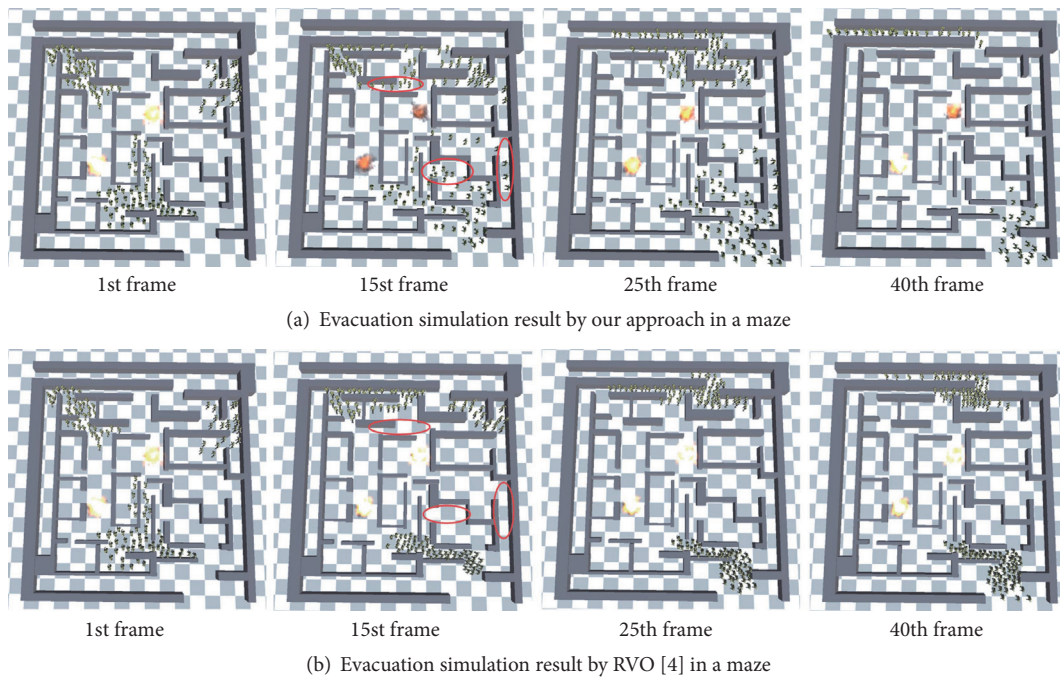


FIGURE 7: Performance comparison. Our algorithm has a performance advantage compared with the existing algorithms.

hazards even when they have not reached the nearby region of the hazard, as shown in Figure 6(b). As we can see from Figure 6, the crowd movement in a hazard environment is affected by the panic emotion significantly.

**4.3. Comparisons with Other Methods.** We compare our algorithm with RVO algorithm in a maze scene with some hazards and multigroups. The effect in Figure 7(b) evacuation result using RVO method, Figure 7(a) is the result of using our algorithm. Figures 7(a) and 7(b) are frames of the same time in the simulation process, they can be observed that if the RVO method is used, agents with similar positions tend to concentrate on the exit and cause blockage. By using our method, we can get all the possible paths in the scene by setting the emotional value of agents. The 40th frame of Figures 7(a) and 7(b) shows that when the evacuation time comes to the end of the simulation, there is still a

local blockage in the simulation results of RVO methods and the simulation with our algorithm is close to the end of evacuation.

We use the same scenario with different numbers of agents from 100 to 2000 to evaluate its performance and compared it with two representative methods: Reciprocal Velocity Obstacles (RVO) algorithm [4] and Emotion Reciprocal Velocity Obstacles (ERVO) algorithm [5]. Figure 8(a) shows the timing statistics and Figure 8(b) shows the Frames Per Second (FPS) statistics, from which we can clearly see a performance advantage compared with the existing algorithms, whether it is simulation time or FPS.

## 5. Conclusions

In this paper, we analyzed the importance of exploring the model of emotional impact and evacuation simulation. In

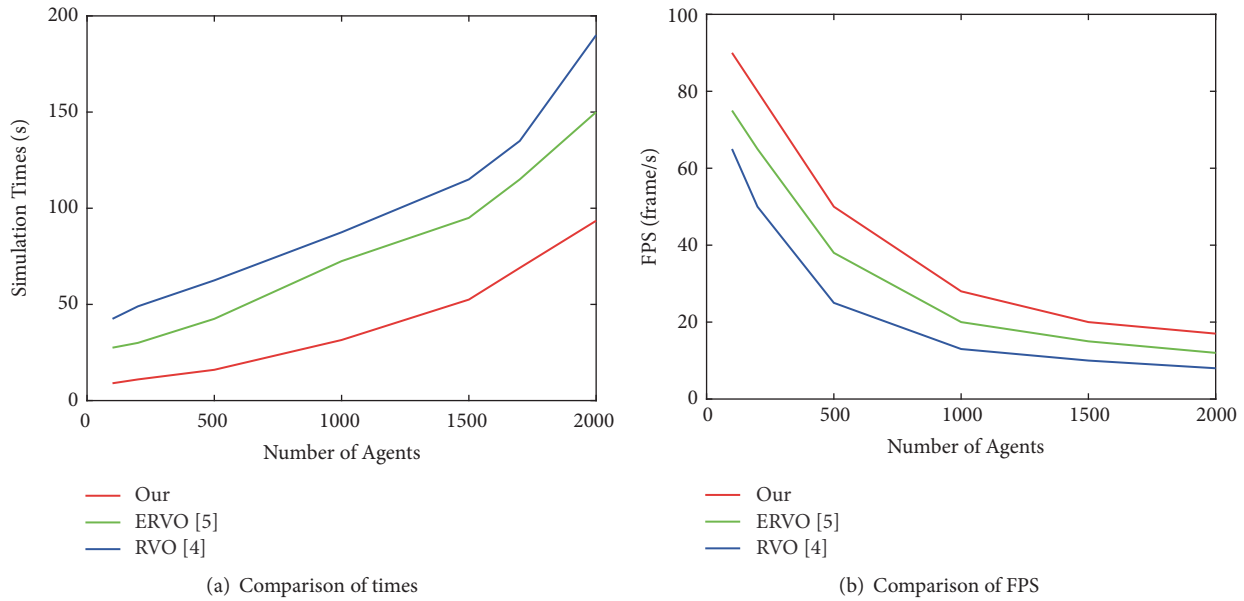


FIGURE 8: Performance comparison.

view of the deficiencies in the emotional simulation of the population, a model of crowd emotional evacuation is proposed from the perspective of social computing, and a real-time path planning method is proposed for the application of evacuation simulation. The results are as follows.

(1) In the process of constructing emotion model, we fully take into account the effect of personality, emotion, and crowd emotion. The influence of group emotion and special individual emotion on the emotional experience of virtual individuals is taken into account in the intensity of emotional infection.

(2) The individual emotion in the crowd is divided into two types of positive and negative emotions. The key to emergency management of the crowd needs to control the infection of negative emotions in the crowd and avoid the crowd in the negative state.

(3) Based on the emotion method, we can add environmental information into a triangular mesh and use the optimization-driven geodesic approach on triangle meshes, we can realize path planning in evacuation simulation.

The evacuation simulation of dense crowd is a challenging research topic, and there are many problems worthy of further study. The work of this paper is still to be further deepened. The next step is to combine computer vision technology to collect crowd motion parameters and supplement the experiment of crowd calculation.

## Data Availability

The simulation data used to support the findings of this study are available from the corresponding author upon request.

## Conflicts of Interest

The authors declare that they have no conflicts of interest.

## Acknowledgments

This work is supported in part by the Science and Technology Plan Project of Zhejiang (LGG18F020001, 2017C33079), NSF of Zhejiang (LY17F020002), Philosophy and Social Sciences Project of Zhejiang (19NDJC0103YB), and NSF of Ningbo (2016A610040, 2016A610042, 2017A610120).

## References

- [1] Z. Ren, W. Gai, and Q. Peng, "Ego-centered path planning in evacuation simulation," *Journal of Computer-Aided Design & Computer Graphics*, 2015.
- [2] E. Hatfield, J. T. Cacioppo, and R. L. Rapson, "Emotional Contagion," *Current Directions in Psychological Science*, vol. 2, no. 3, pp. 96–100, 1993.
- [3] Z. Liu, W. Jin, P. Huang, and Y. Chai, "An emotion contagion simulation model for crowd events," *Computer Research and Development*, vol. 50, no. 12, pp. 2578–2589, 2013.
- [4] J. D. Van Berg, M. Lin, and D. Manocha, "Reciprocal velocity obstacles for real-time multi-agent navigation," in *Proceedings of the 2008 IEEE International Conference on Robotics and Automation, ICRA 2008*, pp. 1928–1935, Pasadena, Calif, USA, May 2008.
- [5] M. Xu, X. Xie, P. Lv et al., "Crowd behavior simulation with emotional contagion in unexpected multi-hazard situations," *Multiagent Systems*, 2018.
- [6] E. Ronchi, P. A. Reneke, and R. D. Peacock, "A conceptual fatigue-motivation model to represent pedestrian movement during stair evacuation," *Applied Mathematical Modelling*, vol. 40, no. 7-8, pp. 4380–4396, 2016.
- [7] X. Zheng, T. Zhong, and M. Liu, "Modeling crowd evacuation of a building based on seven methodological approaches," *Building and Environment*, vol. 44, no. 3, pp. 437–445, 2009.
- [8] Z. Liu and P. Huang, "Study of panic behavior model for crowd on pedestrian bridge in emergent event," *Journal of System Simulation*, vol. 24, no. 9, pp. 1950–1953, 2012.

- [9] R. L. Hughes, "A continuum theory for the flow of pedestrians," *Transportation Research Part B: Methodological*, vol. 36, no. 6, pp. 507–535, 2002.
- [10] R. M. Colombo and M. D. Rosini, "Pedestrian flows and non-classical shocks," *Mathematical Methods in the Applied Sciences*, vol. 28, no. 13, pp. 1553–1567, 2005.
- [11] D. Helbing, I. Farkas, and T. Vicsek, "Simulating dynamical features of escape panic," *Nature*, vol. 407, no. 6803, pp. 487–490, 2000.
- [12] A. Braun, B. E. J. Bodmann, and S. R. Musse, "Simulating virtual crowds in emergency situations," in *Proceedings of the VRST'05 - ACM Symposium on Virtual Reality Software and Technology 2005*, pp. 244–252, Monterey, Calif, USA, November 2005.
- [13] C. Wang and Z. Hangzhou, "Physically based realistic simulation of crowd evacuation during a fire," *Journal of Computer-Aided Design Computer Graphics*, vol. 20, no. 8, pp. 1033–1037, 2008.
- [14] D. Sun, S. Xin, Y. Zhou, S. Chen, R. Wang, and Z. Shu, "Importance driven medial axis," *Journal of Computer-Aided Design & Computer Graphics*, 2016.
- [15] N. Pelechano and N. I. Badler, "Modeling crowd and trained leader behavior during building evacuation," *IEEE Computer Graphics and Applications*, vol. 26, no. 6, pp. 80–86, 2006.
- [16] O. B. Bayazit, J.-M. Lien, and N. M. Amato, "Roadmap-based flocking for complex environments," in *Proceedings of the 10th Pacific Conference on Computer Graphics and Applications, PG 2002*, pp. 104–113, Beijing, China, October 2002.
- [17] W. Van Toll, A. F. Cook, and R. Geraerts, "Navigation meshes for realistic multi-layered environments," in *Proceedings of the 2011 IEEE/RSJ International Conference on Intelligent Robots and Systems: Celebrating 50 Years of Robotics, IROS'11*, pp. 3526–3532, San Francisco, Calif, USA, September 2011.
- [18] T. H. Cormen, C. E. Leiserson, R. Rivest, and C. Stein, "Introduction to algorithms (third edition)," *Computer Education*, vol. 39, no. 4, pp. 643–674, 2013.
- [19] J. Joo, N. Kim, R. A. Wysocki et al., "Agent-based simulation of affordance-based human behaviors in emergency evacuation," *Simulation Modelling Practice and Theory*, vol. 32, no. 2, pp. 99–115, 2013.
- [20] S. Zeng, Z. Mu, and T. Balezentis, "A novel aggregation method for pythagorean fuzzy multiple attribute group decision making," *International Journal of Intelligent Systems*, vol. 33, no. 3, pp. 573–585, 2017.
- [21] W. G. Van Toll, A. F. Cook IV, and R. Geraerts, "Real-time density-based crowd simulation," *Computer Animation and Virtual Worlds*, vol. 23, no. 1, pp. 59–69, 2012.
- [22] N. Jaklin, A. Cook IV, and R. Geraerts, "Real-time path planning in heterogeneous environments," *Computer Animation and Virtual Worlds*, vol. 24, no. 3-4, pp. 285–295, 2013.
- [23] T. Donaldson, A. Park, and I. Lin, "Emotional Pathfinding," in *Advances in Artificial Intelligence*, vol. 3060 of *Lecture Notes in Computer Science*, pp. 31–43, Springer, Berlin, Germany, May 2004.
- [24] A. Johansson and P. Dell'Acqua, "Pathfinding with emotion maps," in *Intelligent Computer Graphics*, vol. 374 of *Studies in Computational Intelligence*, pp. 139–155, Springer, Berlin, Germany, 2012.
- [25] W. Chan and C. Armenakis, "3D building evacuation route modelling and visualization," *International Archives of the Photogrammetry Remote Sensing and Spatial Information*, vol. 2, no. 2, pp. 221–226.
- [26] A. Ortony, G. L. Clore, and A. Collins, "The cognitive structure of emotions," *Contemporary Sociology*, vol. 18, no. 6, pp. 2147–2153, 1988.
- [27] B. Liu, S. Chen, S.-Q. Xin, Y. He, Z. Liu, and J. Zhao, "An optimization-driven approach for computing geodesic paths on triangle meshes," *Computer-Aided Design*, vol. 90, pp. 105–112, 2017.
- [28] A. Gingold R and J. Monaghan J, "Smoothed particle hydrodynamics: theory and application to non-spherical stars," *Monthly Notices of the Royal Astronomical Society*, vol. 181, no. 3, pp. 375–389, 1977.
- [29] L. B. Lucy, "A numerical approach to the testing of the fission hypothesis," *The Astronomical Journal*, vol. 82, pp. 1013–1024, 1977.
- [30] H. D. Young, R. A. Freedman, A. L. Ford, and F. W. Sears, "Sears and zemanskys university physics with modern physics," June 2012.
- [31] D. M. Mount, "ANN: A library for approximate nearest neighbor searching," pp. 783–792, 1998.

## Research Article

# Position Tracking Control of PMSM Based on Fuzzy PID-Variable Structure Adaptive Control

Pei Pei , Zhongcai Pei, Zhiyong Tang , and Han Gu 

*School of Automation Science and Electrical Engineering, Beihang University, Beijing 100191, China*

Correspondence should be addressed to Zhiyong Tang; zyt\_76@buaa.edu.cn

Received 29 May 2018; Revised 14 August 2018; Accepted 7 September 2018; Published 30 September 2018

Guest Editor: Carlos Llopi-Albert

Copyright © 2018 Pei Pei et al. This is an open access article distributed under the Creative Commons Attribution License, which permits unrestricted use, distribution, and reproduction in any medium, provided the original work is properly cited.

A novel Fuzzy PID-Variable Structure Adaptive Control is proposed for position tracking of Permanent Magnet Synchronous Motor which will be used in electric extremity exoskeleton robot. This novel control method introduces sliding mode variable structure control on the basis of traditional PID control. The variable structure term is designed according to the sliding mode surface which is designed by system state equation, so it could compensate for the disturbance and uncertainty. Considering the chattering of sliding mode system, the fuzzy inference method is adopted to adjust the parameters of PID adaptively in real time online, which can attenuate chattering and improve control precision and dynamic performance of system correspondingly. In addition, compared with the traditional sliding mode control, this method takes the fuzzy PID control item to replace the equivalent control item of sliding mode variable structure control, which could avoid the control performance reduction resulted from modeling error and parameter error of system. It is proved that this algorithm can converge to the sliding surface and guarantee the stability of system by Lyapunov function. Simulation results show that Fuzzy PID-Variable Structure Adaptive Control enjoys better control precision and dynamic performance compared with traditional control method, and it improves the robustness of system significantly. Finally, the effectiveness and practicability of the algorithm are verified by the method of Rapid Control Prototyping on the semiphysical simulation test bench.

## 1. Introduction

Lower extremity exoskeleton system is a kind intelligent assist robot, which is wearable, combines the operator with machine, and could be used in medical and military fields wildly [1–3]. Accurate and fast trajectory tracking is one of the core issues of extremity exoskeleton robot [4, 5]. Therefore, the high precision control of the extremity exoskeleton robot driven by Permanent Magnet Synchronous Motor (PMSM) is one of the core problems of robot control. Conventional PID control which has weak robustness is incapable of dealing with nonlinear control, although it has the advantage of simple structure and easy implementation. PMSM is a multivariable and strongly coupled nonlinear system, thus having many factors in its control system, such as current coupling, system saturation, parameter perturbation, and external disturbance, which affect the performance of system directly [6]. Therefore, designing a control method with strong robustness, good dynamic performance, high control

precision, and easy engineering implementation is the focus of research.

Sliding Mode Control (SMC) is widely used as a nonlinear control method currently. By designing the sliding mode surface reasonably, the control performance of system will not be affected by internal parameter perturbation and external disturbance, and the system will have strong robustness and high control precision. However, the equivalent control term of sliding mode control depends on the accuracy of system model and parameters, while in practical application, only an approximate mathematical model of motor can be obtained. And there are still some uncertain factors, such as parameter error and external interference, which will reduce the performance of the sliding mode control and even cause the instability of system [7]. To solve the problem that SMC cannot obtain the accurate model and parameters of system, some intelligent methods are introduced to compensate the equivalent control item. Reference [8] introduced neural network into the variable structure control to compensate

for the lack of accurate system models and parameters and proposed a neural network controller online training method which was applied to the speed loop of electric drive and improved the adaptability and robustness greatly based on variable structure control. An adaptive fuzzy sliding mode control strategy was designed to compensate for the influence of nonlinear, disturbances, and uncertain parameters in asymmetric hydraulic cylinder position servo control system in [9]. In this paper, the uncertain factors of the models and parameters were treated as interference. In [10], by using the linear feedback RBF, the sliding mode controller was compensated, and the control effect was further improved. Reference [11] proposed a method that achieved good results combining fast terminal sliding mode (FTSM) with radial basis function (RBF), which was applied to the vector control of PMSM. The method of combining neural network control and sliding mode variable structure control was proposed in [12, 13] with the main idea of meeting the sliding mode condition by adjusting the gain coefficient of control law online. Simply introducing the intelligent control method will make the controller structure complicated, increase the cost of controlling, and reduce the usability of control system. An ideal controller is designed to strive to reach an optimal tradeoff between performance and complexity.

As is known, PID control is a simple, easy to implement, and widely used control method. In the face of the traditional SMC the accurate models and parameters of system cannot be obtained. It is natural to think of the combination of sliding mode variable structure control and PID control. In the design of sliding surface, the integral term was introduced to form a sliding surface which was similar to PID structure in [14]. Two novel methods, integral approach law and PID-like approach law, were proposed in [15], to control Electro-Hydraulic Actuator (EHA). Among these control methods, PID control was only introduced to design sliding surface; however, the controller also consists of equivalent control item based on mode of system. In [16], PID control and sliding mode variable structure control were combined to be variable structure PID control (VSPID). PID control was introduced to replace the variable structure coefficient in SMC, so that the VSPID became a strict nonlinear controller. However, there was a risk that only nonlinear control cannot guarantee the optimal performance of the system. A similar approach was proposed in [17], and due to the use of PID control instead of the variable structure factor, it is still a switch value control.

Since the variable structure control is introduced in the design of controller in this paper, the chattering caused by variable structure control must be considered. References [18, 19] put forward an adaptive fuzzy sliding mode controller, which realized the self-adaptation of variable structure parameters and attenuated the chattering caused by sliding mode control. Reference [20] proposed a method of fuzzy reaching law for robot control system, which greatly attenuated the chattering of traditional sliding mode system and made the system achieve better control performance. In order to give full play to the performance of the variable structure control item, the fuzzy inference method is introduced to attenuate the chattering of the system by adaptively modifying the

parameters of PID. Since fuzzy PID control is a mature control method applied in engineering, it does not make the control structure too complex.

In this paper, the Fuzzy PID-Variable Structure Adaptive Control, which is mutual compensation of sliding mode variable structure control and fuzzy PID control, is proposed for trajectory tracking of PMSM used in extremity exoskeleton system. Firstly, this algorithm ensures stability of system by PID control instead of equivalent control. Then, a sliding mode surface based on state equation of system is designed for sliding mode variable structure control which compensates for insensitivity of PID control to parameter perturbations and external disturbances. Finally, the fuzzy reasoning method is added to adjust the parameters of PID adaptively online in real time, which improves robustness of system again and attenuates chattering of sliding mode system as well.

## 2. Mathematical Model of PMSM

The mathematical model of PMSM in the rotating shaft ( $d, q$ ) is

$$\begin{aligned} \dot{i}_d &= -\frac{R_s}{L}i_d + p_n\omega i_q + \frac{u_d}{L} \\ \dot{i}_q &= -p_n\omega i_q - \frac{R_s}{L}i_d - \frac{p_n\psi_f}{L}\omega + \frac{u_q}{L} \\ \dot{\omega} &= \frac{p_n\psi_f}{J}i_q - \frac{B}{J}\omega - \frac{T_L}{J} \\ \dot{\theta} &= \omega, \end{aligned} \quad (1)$$

where  $u_d$  and  $u_q$  are voltage component of d axis and q axis of the stator, respectively (V),  $i_d$  and  $i_q$  are current component of d axis and q axis of the stator, respectively (A),  $R_s$  is the resistance of stator winding ( $\Omega$ ),  $\psi_f = \sqrt{3}/2\psi_{fm}$  is electronic flux linkage,  $L = L_d = L_q$  is the inductance of motor,  $B$  is friction coefficient proportional to rotational speed,  $T_L$  is load torque (N.m),  $J$  is moment of inertia ( $kg.m^2$ ),  $\theta = \theta_e/p_n$  is mechanical angle position of motor rotor (rad), and  $\omega = \omega_e/p_n$  is mechanical angle velocity of motor rotor (rad/s).

PMSM servo system is a three-closed-loop control system based on flux orientation, including position control loop, speed control loop, and current control loop. The three-closed-loop control of PMSM is shown in Figure 1 while  $i_d = 0$ . Besides PMSM, the system also includes a SVPWM inverter, a power rectifier, a position sensor, a current controller (ACR), a speed controller (ASR), and a position controller (APR). The position controller (APR) is our focus; meanwhile the speed controller (ASR) and the position controller (APR) are designed based on the traditional PID algorithm.

In order to design the position loop controller conveniently, it is assumed that the speed control loop, the current control loop, and the inverter are ideal. Therefore,

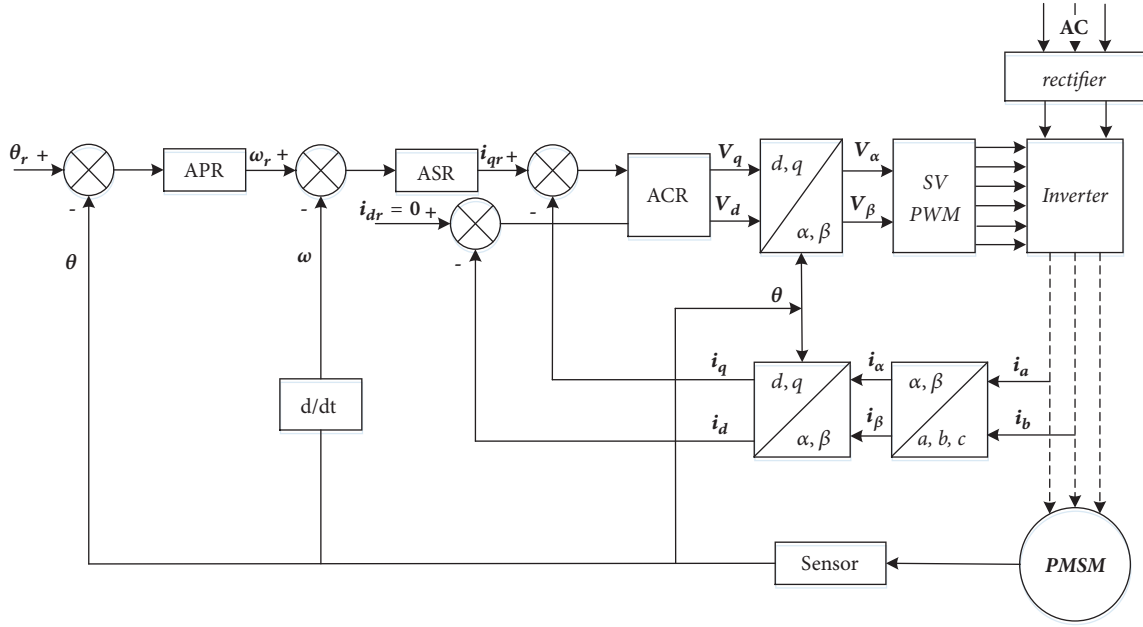


FIGURE 1: Control schematic of PMSM.

the mathematical model of the PMSM can be simplified as a second-order differential link [21] as

$$\begin{aligned} \dot{\theta} &= \omega \\ \dot{\omega} &= \frac{P_n \psi_f}{J} i_q - \frac{B}{J} \omega - \frac{T_L}{J}. \end{aligned} \quad (2)$$

It can be also expressed as

$$\ddot{\theta} = \frac{P_n \psi_f}{J} i_q - \frac{B}{J} \dot{\theta} - \frac{T_L}{J}. \quad (3)$$

Let  $p_n \psi_f / J = f$ ,  $-B/J = g$ ,  $-T_L/J = d$ , and  $i_q = u$ . Then (3) can be simplified as

$$\ddot{\theta} = g\dot{\theta} + fu + d, \quad (4)$$

where  $u$  represents the control input parameter.

The control target of the PMSM position loop is to enable the output to track the reference value quickly and accurately. Let  $e = \theta_r - \theta = e_1$ ,  $\dot{e} = \dot{\theta}_r - \dot{\theta} = e_2$ ; then the state equation of the PMSM can be expressed as

$$\begin{aligned} \dot{e}_1 &= e_2 \\ \dot{e}_2 &= \dot{\theta}_r - \ddot{\theta}. \end{aligned} \quad (5)$$

### 3. Design of Fuzzy PID-Variable Structure Adaptive Controller

**3.1. Design of Fuzzy PID Controller.** The fuzzy PID controller is designed as a system with two-dimensional input and three-dimensional output. The inputs are the error ( $e$ ) and the error change rate ( $e_c$ ) of system. The output ( $\Delta K_p$ ,  $\Delta K_i$ , and

$\Delta K_d$ ) is parameters compensation of PID controller. The PID parameters in practical applications can be expressed as

$$\begin{aligned} K_p &= K_p' + \Delta K_p \\ K_i &= K_i' + \Delta K_i \\ K_d &= K_d' + \Delta K_d, \end{aligned} \quad (6)$$

where  $K_p'$ ,  $K_i'$ , and  $K_d'$  are the preset parameter values of PID controller.

The control principle of fuzzy PID control is shown in Figure 2.

The core of fuzzy PID is the design of fuzzy inference rules. Firstly, fuzzify the input variables  $e$  and  $e_c$  by membership function, and then the inference is carried out according to predefined fuzzy rules. Finally, the barycenter method is used to defuzzify the reasoning results to achieve dynamic real-time update of PID parameters.

The fuzzy subset of two-dimensional input variables and three-dimensional output variables is defined as

$$\{NB, NM, NS, ZO, PS, PM, PB\}. \quad (7)$$

The same membership function is applied to the input variables and the output variables for real-time calculation and online adjustment. The membership functions  $NB$  and  $PB$  adopt Gaussian distribution function, while the rest adopt triangular distribution function [22], as is shown in Figure 3.

The fuzzy rules of  $\Delta K_p$ ,  $\Delta K_i$ , and  $\Delta K_d$  are shown in Table 1, where the first column is the fuzzy rules of  $\Delta K_p$ , the second column is the fuzzy rules of  $\Delta K_i$ , and the third column is the fuzzy rules of  $\Delta K_d$ . 49 fuzzy control rules can be obtained from Table 1, which will be adopted for fuzzy controller designing.

TABLE 1: Fuzzy rules table.

e	ec																				
	NB		NM		NS		ZO		PS		PM		PB								
NB	PS	PM	NB	PS	NB	NB	PB	NB	NB	PM	NB	NM	PM	NB	NS	ZO	NB	ZO	ZO	PM	ZO
NM	PB	PS	NB	PB	NM	NB	PB	NM	NM	PS	NM	NS	PS	NM	NS	ZO	NM	ZO	ZO	PS	ZO
NS	PM	PS	NM	PM	NM	NM	PM	NM	NS	PS	NM	NS	ZO	NM	ZO	NS	NM	PS	NS	PS	PS
ZO	PM	ZO	NM	PM	NS	NS	PS	NS	NS	ZO	NS	ZO	NS	NS	PS	NM	NS	NM	NM	ZO	NM
PS	PS	ZO	NS	PS	ZO	NS	ZO	ZO	ZO	NS	ZO	PS	NS	ZO	PS	NM	ZO	PM	NM	ZO	PM
PM	ZO	PB	ZO	ZO	PS	ZO	NS	PS	PS	NM	PS	PS	NM	PS	PM	NM	PS	PB	NB	PB	PB
PB	ZO	PB	ZO	ZO	PM	ZO	NM	PM	PM	NB	PM	PM	NM	PM	PM	NB	PM	PB	NB	PM	PB

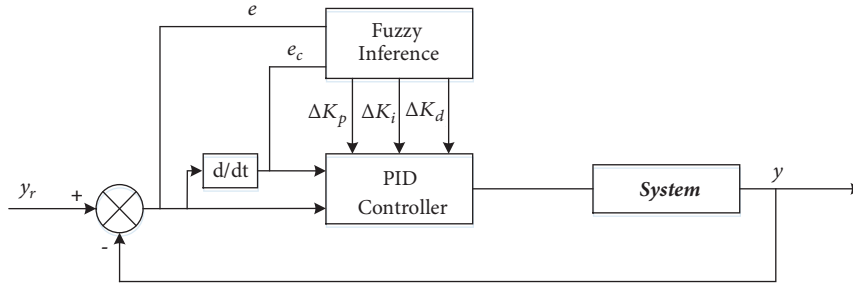


FIGURE 2: Control schematic of Fuzzy PID.

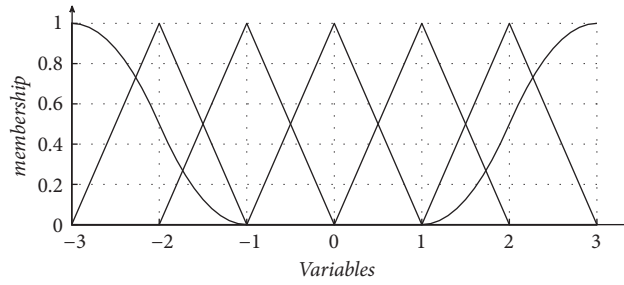


FIGURE 3: Membership function curve.

The process of adaptively adjusting PID parameters should follow the following principles:

- (1)  $K_p$ : When  $e$  is a positive and larger value,  $\Delta K_p$  is positive, that is, to increase  $K_p$ . However, when  $e$  is negative and its absolute value is increasing, the system is in overshoot state, so  $K_p$  should be reduced. When  $e$  is near zero, if  $e_c$  is negative, the system overshoot will become larger and larger, so  $K_p$  should be reduced; if  $e_c$  is positive, in order to reduce the deviation,  $\Delta K_p$  should be positive.
- (2)  $K_i$ : Following the principle of integral separation, its regulation is similar to that of  $K_p$ , but the situation of integral saturation should be prevented, for fear of system overshoot. If  $K_p$  increases,  $K_i$  should be reduced accordingly.
- (3)  $K_d$ : When  $e$  is positive and increasing, increasing  $K_p$  may cause differential spillover. Therefore, if the larger  $K_p$  is taken, the smaller  $K_d$  should be taken.

Finally, the fuzzy quantity of the output variable is defuzzified as the output of the controller by barycenter

method as

$$u(t) = \frac{\sum_{i=1}^n u_i A(u_i)}{\sum_{i=1}^n A(u_i)}, \quad (8)$$

where  $u_i$  is the  $i$ th element of  $u$  and  $A(u_i)$  is the  $u_i$ th membership function of  $A$  on  $u(t)$ .

Then, the output of Fuzzy PID controller can be expressed as

$$u_{PID} = K_p e + K_i \int e + K_d \frac{de}{dt}, \quad (9)$$

where  $K_p = K_p' + \Delta K_p$ ,  $K_i = K_i' + \Delta K_i$ , and  $K_d = K_d' + \Delta K_d$ .

3.2. Design of Sliding Mode Variable Structure Controller. According to state equations (5), the sliding mode surface is defined as

$$s = ce_1 + e_2, \quad (10)$$

where  $c$  is a positive constant.

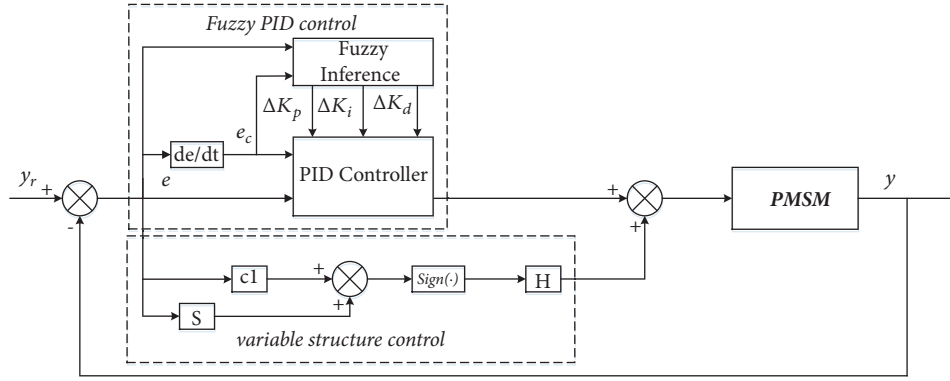


FIGURE 4: Control schematic of Fuzzy PID-Variable Structure Adaptive Control.

$s = \dot{s} = 0$  can be obtained according to the condition that the system maintains the motion on the sliding surface. That is,

$$\dot{s} = c\dot{e} + \ddot{e} = c\dot{e} + (\ddot{\theta}_r - \ddot{\theta}), \quad (11)$$

where  $\theta_r$  is the desired trajectory.

From (4), (10), and (11), we have

$$u^* = \frac{1}{f} (c\dot{e} + \ddot{\theta}_r - g\dot{\theta} - d). \quad (12)$$

From (12), it can be seen that the result of equivalent control quantity  $u^*$  includes  $f$ ,  $g$ , and  $d$ .  $f$  and  $g$  are determined by the system parameters  $B$  and  $J$ .  $d$  is determined by the system parameters  $J$  and  $T_L$ . It can be inferred that the equivalent control amount will be changed with system parameter perturbation and load disturbance, and then the input will make the moving point away from the sliding surface, which will even lead to negative effect on servo system.

The switch item should be designed as

$$u_r = k \text{sign}(s), \quad (13)$$

where  $k > 0$  is the variable structure gain;  $s$  is the sliding mode surface; and  $\text{sign}(\bullet)$  is the sign function.

**3.3. Design of Fuzzy PID-Variable Structure Adaptive Controller.** Considering that the equivalent control item in SMC will affect the servo control performance due to modeling error and inaccurate parameters of system, the effect of the equivalent control item in SMC is compensated by PID control item, and then the effect of the nonlinear is compensated by the variable structure control item. Meanwhile, the fuzzy inference method is used to adjust the parameters of PID in real time online, which can attenuate chattering. The fuzzy PID controller can ensure the stability of system, limit the error to a narrow range, and attenuate the chattering of SMC as well. On the other hand, the variable structure control item is used to compensate the effect of nonlinear, which can suppress the effect of parameter perturbation and load disturbance. The schematic diagram of Fuzzy PID-Variable Structure Adaptive Control is shown in Figure 4.

The output of Fuzzy PID-Variable Structure Adaptive Controller is

$$u = \left[ (K_p' + \Delta K_p) e + (K_i' + \Delta K_i) \int e + (K_d' + \Delta K_d) \frac{de}{dt} \right] + h \text{sign}(s), \quad (14)$$

where  $s$  is the sliding mode surface,  $[(K_p' + \Delta K_p) e + (K_i' + \Delta K_i) \int e + (K_d' + \Delta K_d) (de/dt)]$  is the approximate linear control item, and  $h \text{sign}(s)$  is the nonlinear control item.

#### 4. Proof of Stability

The controller designed by (14) is used to control PMSM position loop described in (4) and (5). If the control parameters are selected according to the constraints of (15), the system state can converge to the sliding surface and ensure global stability of the system.

$$\alpha_3 < g\alpha_2 + fh + \alpha_4 \quad (15)$$

$$f_i k_{di} > c_i + g_i + p_i,$$

where  $\alpha_1$ ,  $\alpha_2$ ,  $\alpha_3$ , and  $\alpha_4$  are the upper bounds of given position target ( $\theta_r$ ), derivative of given position target ( $\dot{\theta}_r$ ), the second derivative of given position target ( $\ddot{\theta}_r$ ), and load disturbance  $d$ , respectively, and  $p$  is the parameter of positive definite matrix defined later. It can be also expressed as

$$\begin{aligned} \|\theta_r\| &\leq \alpha_1 \\ \|\dot{\theta}_r\| &\leq \alpha_2 \\ \|\ddot{\theta}_r\| &\leq \alpha_3 \\ \|d\| &\leq \alpha_4, \end{aligned} \quad (16)$$

where  $\|\bullet\|$  is the Euclidean norm.

In the actual control system, the position target input of the system is bounded, and the perturbation of system parameters and the disturbance of external load will change within a certain range. Thus the assumption in (16) is reasonable in the actual control system.

For  $n$ -dimensional system the sliding surface can be expressed as

$$S = [s_1 \ s_2 \ \dots \ s_n]^T \quad n = 1, 2, \dots, n \quad (17)$$

$$s_i = c_i e_{1i} + e_{2i}. \quad (18)$$

The control item in (13) can be expressed as

$$U = \left( K_P E + K_I \int E + K_D \frac{dE}{dt} \right) + H \text{sign}(S). \quad (19)$$

To construct a control matrix for an  $n$ -dimensional system reasonably, set

$$\begin{aligned} K_P &= \text{diag} \{K_{p1} \ K_{p2} \ \dots \ K_{pn}\} \\ K_I &= \text{diag} \{K_{i1} \ K_{i2} \ \dots \ K_{in}\} \\ K_D &= \text{diag} \{K_{d1} \ K_{d2} \ \dots \ K_{dn}\} \\ E &= [e_1 \ e_2 \ \dots \ e_n]^T \\ H &= \text{diag} \{h_1 \ h_2 \ \dots \ h_n\} \end{aligned} \quad (20)$$

$$\text{sign}(S) = \text{diag} \{\text{sign}(s_1) \ \text{sign}(s_2) \ \dots \ \text{sign}(s_n)\}.$$

Construct a positive definite Lyapunov function as

$$V = \frac{S^T S}{2} + \frac{[E^T \ \dot{E}^T] \begin{bmatrix} Q & P \\ P & G \end{bmatrix} \begin{bmatrix} E \\ \dot{E} \end{bmatrix}}{2}. \quad (21)$$

In order to guarantee the positive definiteness of the Lyapunov function (21), the definition of the symmetry matrix  $\begin{bmatrix} Q & P \\ P & G \end{bmatrix}$  is

$$\begin{aligned} Q &= \text{diag} (q_1 \ q_2 \ \dots \ q_n) \\ P &= \text{diag} (p_1 \ p_2 \ \dots \ p_n) \\ G &= \text{diag} (g_1 \ g_2 \ \dots \ g_n), \end{aligned} \quad (22)$$

where  $q_i$ ,  $p_i$ , and  $g_i$  satisfy the following relationship:

$$c_i^2 - c_i f_i k_{di} + c_i g_i - f_i k_{pi} + q_i = 0. \quad (23)$$

Differentiating  $V$ , we obtain

$$\begin{aligned} \dot{V} &= S^T \dot{S} + [E^T \ \dot{E}^T] \begin{bmatrix} Q & P \\ P & G \end{bmatrix} \begin{bmatrix} \dot{E} \\ \ddot{E} \end{bmatrix} \\ &= \sum_{i=1}^n (s_i \dot{s}_i + q_i e_{1i} e_{2i} + p_i e_{2i}^2). \end{aligned} \quad (24)$$

From (4), (5), (11), and (14), (25) can be obtained:

$$\begin{aligned} \dot{s}_i &= \ddot{\theta}_{ri} - g_i \dot{\theta}_{ri} - f_i k_{pi} e_{1i} + (c_i + g_i - f_i k_{di}) e_{2i} \\ &\quad - f_i k_{ii} \int e_{1i} - f_i h_i \text{sign}(s_i) - d_i. \end{aligned} \quad (25)$$

In the process of stability analysis, as there is no integral term in the design of sliding mode surface, the integral term in fuzzy PID can be ignored. Then (26) can be obtained:

$$\begin{aligned} s_i \dot{s}_i &= (c_i e_{1i} + e_{2i}) [\ddot{\theta}_{ri} - g_i \dot{\theta}_{ri} - f_i h_i \text{sign}(s_i) - d_i] \\ &\quad - c_i f_i k_{pi} e_{1i}^2 \\ &\quad + (c_i^2 + c_i g_i - c_i f_i k_{di} - f_i k_{pi}) e_{1i} e_{2i} \\ &\quad + (c_i + g_i - f_i k_{di}) e_{2i}^2. \end{aligned} \quad (26)$$

Substituting (26) into (24), the following equation can be obtained:

$$\begin{aligned} \dot{V} &= \sum_{i=1}^n \{ (c_i e_{1i} + e_{2i}) [\ddot{\theta}_{ri} - g_i \dot{\theta}_{ri} - f_i h_i \text{sign}(s_i) - d_i] \\ &\quad - c_i f_i k_{pi} e_{1i}^2 + (c_i + g_i - f_i k_{di} + p_i) e_{2i}^2 \\ &\quad + (c_i^2 + c_i g_i - c_i f_i k_{di} - f_i k_{pi} + q_i) e_{1i} e_{2i} \}. \end{aligned} \quad (27)$$

Because of (23), we can obtain

$$\begin{aligned} \dot{V} &= \sum_{i=1}^n \{ s_i [\ddot{\theta}_{ri} - g_i \dot{\theta}_{ri} - f_i h_i \text{sign}(s_i) - d_i] \\ &\quad - c_i f_i k_{pi} e_{1i}^2 + (c_i + g_i - f_i k_{di} + p_i) e_{2i}^2 \}. \end{aligned} \quad (28)$$

Combining (16), then (28) can be expressed as

$$\begin{aligned} \dot{V} &\leq - \sum_{i=1}^n [ \|s_i\| (g_i \alpha_2 + f_i h_i + \alpha_4 - \alpha_3)] \\ &\quad - \sum_{i=1}^n [(c_i f_i k_{pi}) e_{1i}^2] \\ &\quad - \sum_{i=1}^n [(-c_i - g_i + f_i k_{di} - p_i) e_{2i}^2]. \end{aligned} \quad (29)$$

It can be deduced that  $\dot{V}$  is a negative definite matrix when (15) is satisfied. According to Lyapunov's second method, it can be concluded that the system is globally stable based on Fuzzy PID-Variable Structure Adaptive Control.

## 5. Simulation Verification

The model of the position-speed-current three-closed-loop control system for PMSM vector control is built based on Matlab/Simulink. The speed loop and the current loop adopt the conventional PID control while the position loop adopts the Fuzzy PID-Variable Structure Adaptive Control which is introduced in this paper. The simulation model is shown in Figure 5.

The parameters of the simulation model are shown in Table 2.

Figures 6–10 show the step response. The input reference position is a step signal of  $\theta_r = 0.6(\text{rad})$ , and the load disturbance of  $50\text{Nm}$  is added at  $0.75\text{s}$ . The simulation results

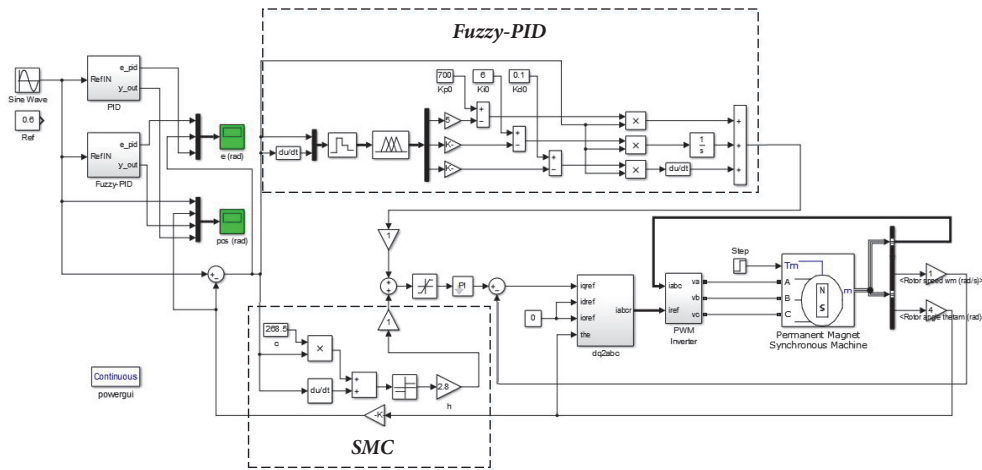


FIGURE 5: Simulink model.

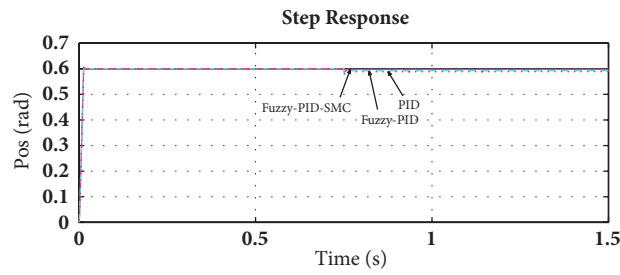


FIGURE 6: Step response (a).

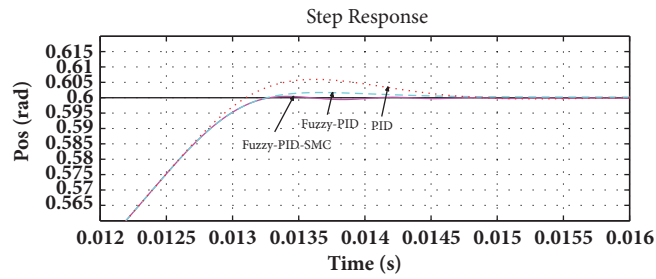


FIGURE 7: Step response (b).

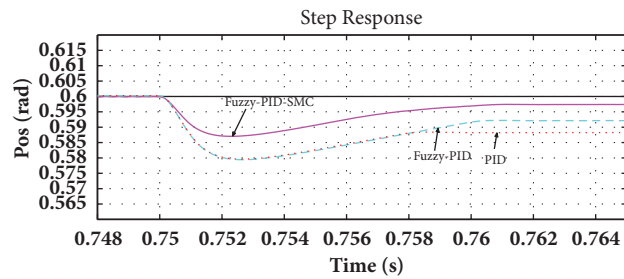


FIGURE 8: Step response (c).

TABLE 2: The parameters of the simulation model.

Parameter	Value	Parameter	Value
$R_s$	2.875Ω	$K_{p0}$	700
$L$	0.00153H	$K_{i0}$	6
$\psi_f$	0.175Wb	$K_{d0}$	0.1
$J$	0.0008Kgm <sup>2</sup>	$c$	268.5
$P_n$	4	$h$	2.8
$K_T$	1.05		

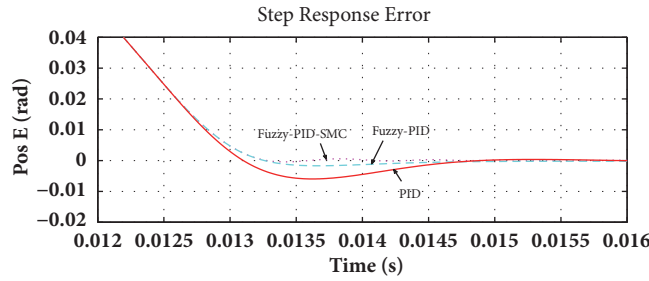


FIGURE 9: Step response error (a).

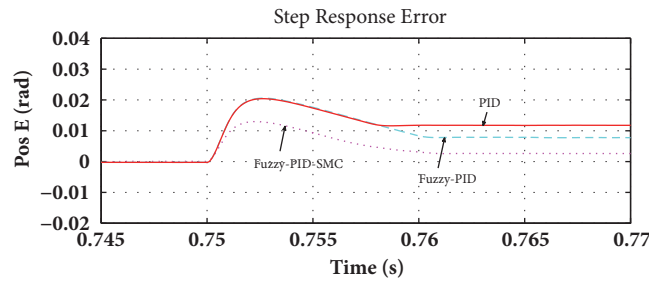


FIGURE 10: Step response error (b).

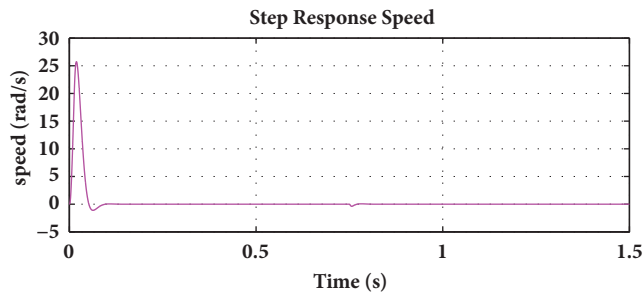


FIGURE 11: Step response speed under Fuzzy PID-Variable Structure Adaptive Control.

are compared with conventional PID control and fuzzy PID control.

From Figure 6, it can be seen that all the three control algorithms can obtain better results based on the condition that the parameters of the control system are appropriate. However, it can be seen from the details that compared with PID control and fuzzy PID control, the Fuzzy PID-Variable Structure Adaptive Control can accelerate system convergence, reduce system response time, and obtain better dynamic performance and robustness. Especially after adding load disturbances, the Fuzzy PID-Variable Structure Adaptive

Control responds fastest and converges to the reference position in the shortest time. In addition, the simulation results show that the chattering of variable structure control is attenuated obviously due to the adaptive adjustment of PID control parameters online. Figure 11 is the speed curve (after a low-pass filter) of PMSM controlled by Fuzzy PID-Variable Structure Adaptive Controller. Figure 12 shows the current curve (after a low-pass filter) of the  $q$  axis (the deceleration ratio of 50 is considered).

Figures 13–15 show the sinusoidal response. The input reference position of system is a sinusoidal signal (amplitude:

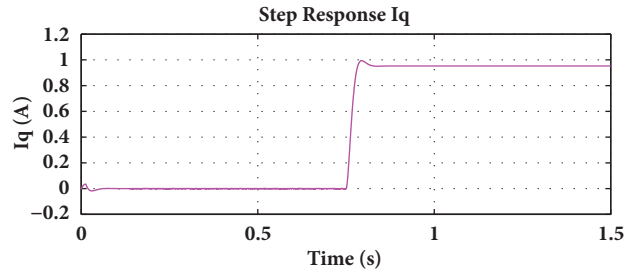


FIGURE 12: Step response  $i_q$  under Fuzzy PID-Variable Structure Adaptive Control.

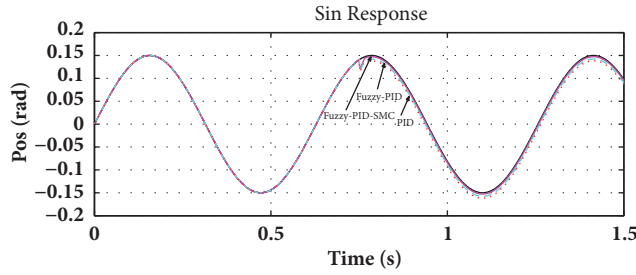


FIGURE 13: Sinusoidal response (a).

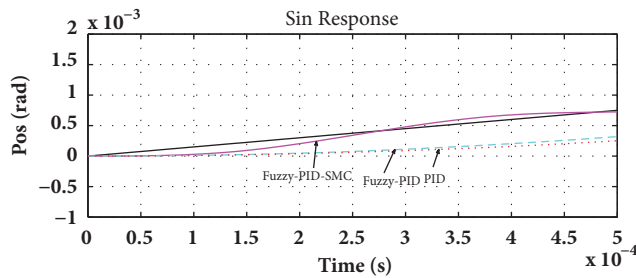


FIGURE 14: Sinusoidal response (b).

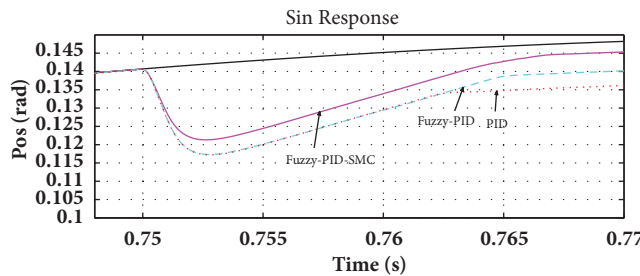


FIGURE 15: Sinusoidal response (c).

0.15rad, frequency: 10Hz), and the load disturbance of 50Nm is added at 0.75s. Compared with Fuzzy PID-Variable Structure Adaptive Control, the other two algorithms exhibit phase lag. Especially after adding load disturbance, PID control and fuzzy PID control exhibit a large static deviation. In addition, the simulation results show that the chattering of variable structure control is attenuated obviously due to the adaptive adjustment of PID control parameters online. Figure 16 is the speed curve (after a low-pass filter) of PMSM controlled by Fuzzy PID-Variable Structure Adaptive

Controller. Figure 17 shows the current curve (after a low-pass filter) of the  $q$  axis (the deceleration ratio of 50 is considered).

By analyzing the step response and sinusoidal response with load disturbance, the Fuzzy PID-Variable Structure Adaptive Control can improve the servo precision, the dynamic performance, and the robustness of system. At the same time, the chattering of variable structure control is also attenuated obviously because the PID parameters can be adjusted online adaptively by fuzzy inference.

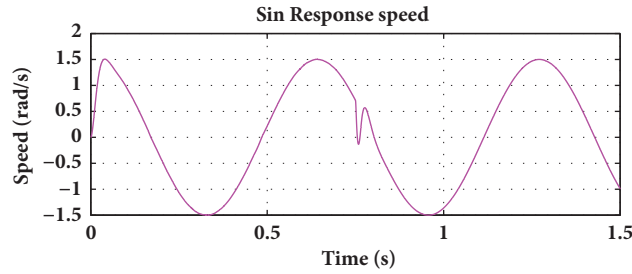


FIGURE 16: Sinusoidal response speed under Fuzzy PID-Variable Structure Adaptive Control.

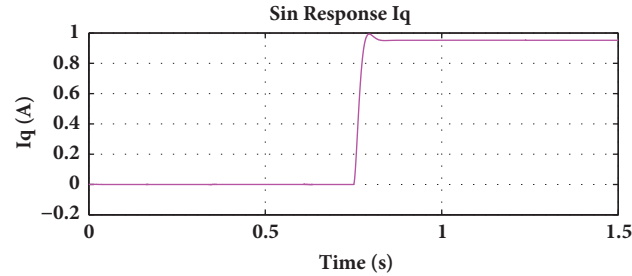


FIGURE 17: Sinusoidal Response  $i_q$  under Fuzzy PID-Variable Structure Adaptive Control.

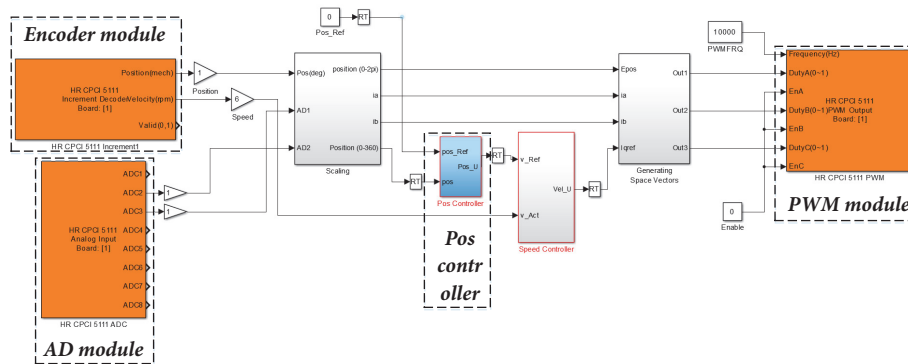


FIGURE 18: RCP model.

### 6. Experiment Verification

The Rapid Control Prototype (RCP) is a kind of semiphysical simulation. After the mathematical simulation of the system control model meets the desired effect, the control algorithm model of the servo system will be extracted individually. Then the Real-Time Driver (RTD) of actual controlled object, feedback original, and drive unit are added to the control algorithm, which will constitute a closed-loop system [23, 24]. Before the structure design and processing completion of extremity exoskeleton, the effectiveness of Fuzzy PID-Variable Structure Adaptive Control is verified on a semi-physical simulation test bench. The RCP model is shown in Figure 18.

The control system test bench is shown in Figure 19.

The control principle of test bench is shown in Figure 20.

6.1. Static Testing. The step response performances of conventional PID control and Fuzzy PID-Variable Structure

Adaptive Control are compared by a step signal. The step response testing is performed with a constant torque of 5Nm, and the step motion mode is a reciprocating motion with the range of  $100^\circ$  to  $200^\circ$ . The experimental results are shown in Figures 21–25; Figure 21 is the position tracking curve, Figure 22 is the position tracking error curve, and Figure 23 is the speed curve. Figure 24 is the original curve of torque sensor under Fuzzy PID-Variable Structure Adaptive Control (it is basically consistent with the curve of torque sensor under PID control), and Figure 25 is the curve of torque sensor after a low-pass filter.

It can be seen from Figures 21 and 22 that the positioning accuracy of conventional PID control and Fuzzy PID-Variable Structure Adaptive Control is almost the same. However, it is evident that the dynamic response of Fuzzy PID-Variable Structure Adaptive Control outperforms that of conventional PID control. Because of the unidirectional constant torque, the forward step response and reverse step response of the same control will be different. Through comparison,

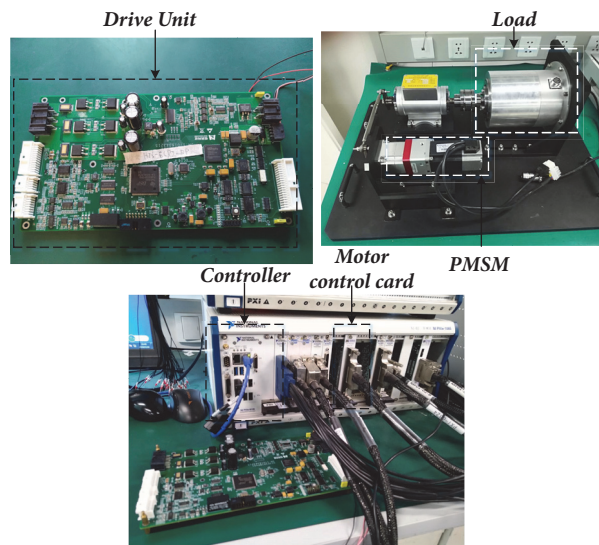


FIGURE 19: The control system test bench.

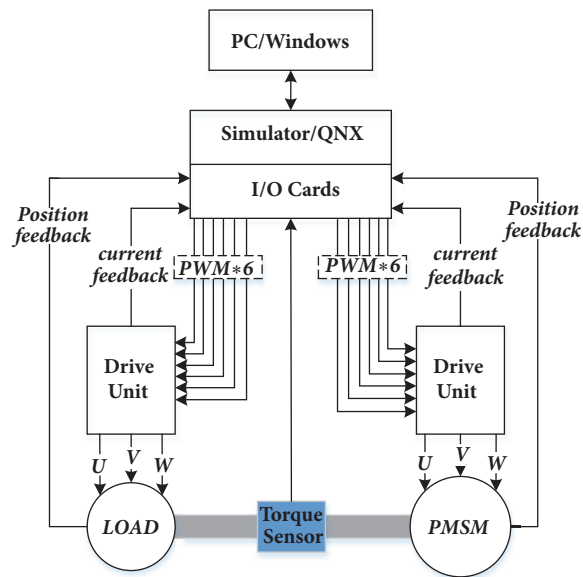


FIGURE 20: The control principle.

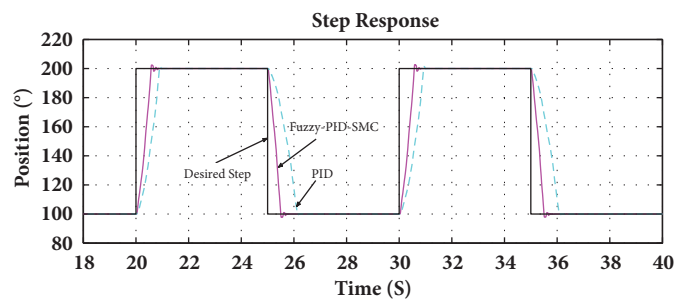


FIGURE 21: Step response position tracking.

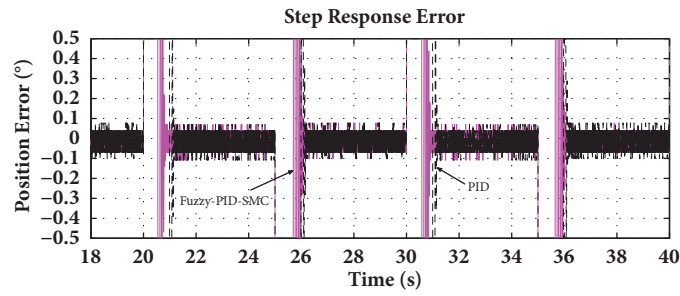


FIGURE 22: Step response position tracking error.

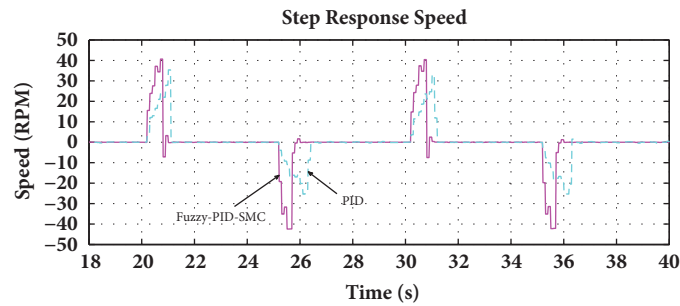


FIGURE 23: Step response speed.

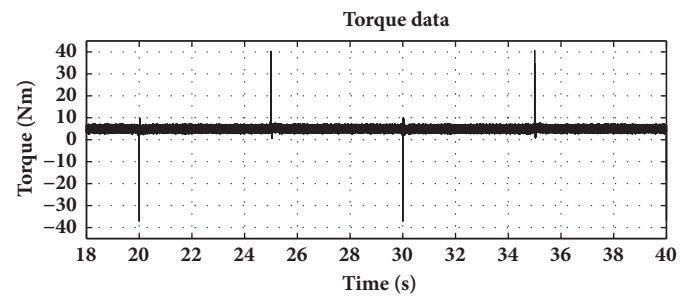


FIGURE 24: Step response original torque data.

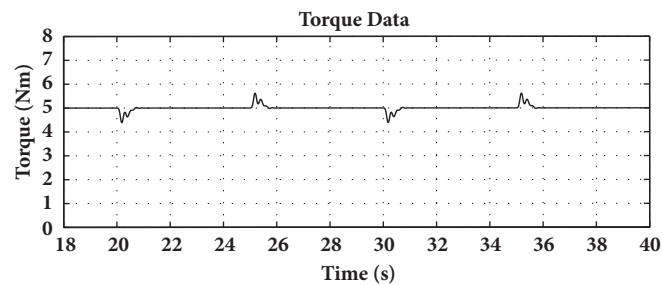


FIGURE 25: Step response torque data after low-pass filter.

it is observed that the forward step response and reverse step response under Fuzzy PID-Variable Structure Adaptive Control are more consistent.

**6.2. Dynamic Testing.** The dynamic response performances of conventional PID control and Fuzzy PID-Variable Structure Adaptive Control are compared by sinusoidal response by a sinusoidal signal (amplitude:  $100^\circ$ , frequency: 2Hz) with

a constant torque of 5Nm. The experimental results are shown in Figures 26–30; Figure 26 is the position tracking curve, Figure 27 is the position tracking error curve, and Figure 28 is the speed curve. Figure 29 is the original curve of torque sensor under Fuzzy PID-Variable Structure Adaptive Control (it is basically consistent with the curve of torque sensor under PID control), and Figure 30 is the curve of torque sensor after a low-pass filter.

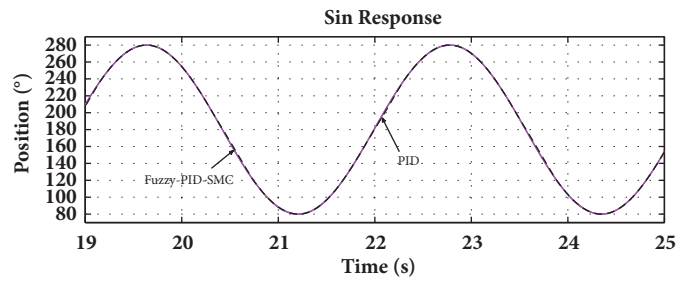


FIGURE 26: Sinusoidal response position tracking.

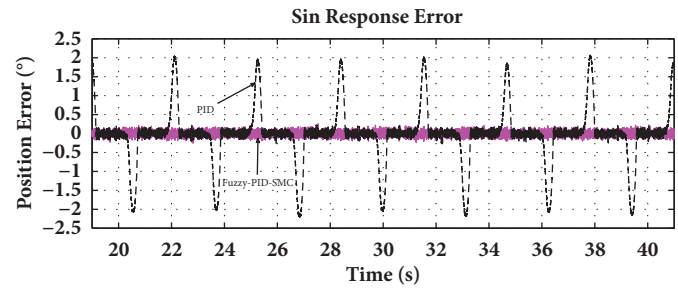


FIGURE 27: Sinusoidal response position tracking error.

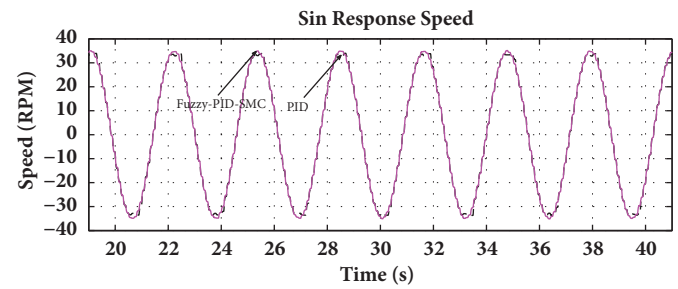


FIGURE 28: Sinusoidal response speed.

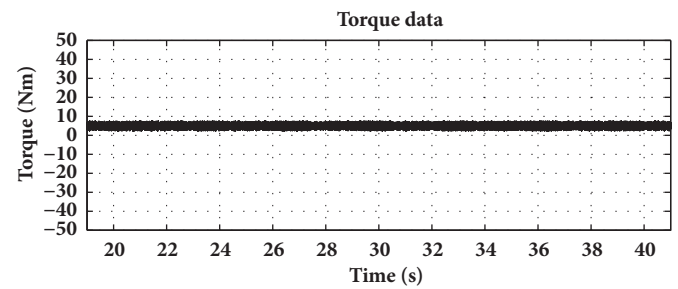


FIGURE 29: Sinusoidal response original torque data.

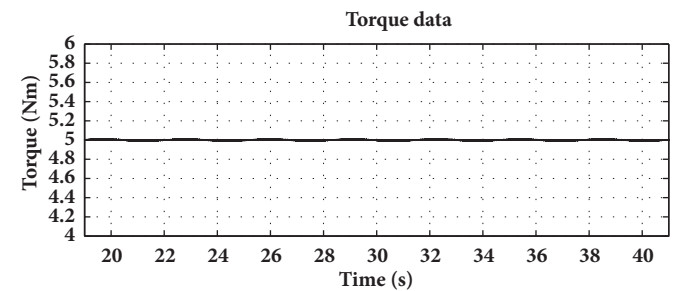


FIGURE 30: Sinusoidal response torque data after low-pass filter.

Both conventional PID control and Fuzzy PID-Variable Structure Adaptive Control achieve good performances under the proper parameter as shown Figure 26. Since the conventional PID control performances are good enough, the advantages of Fuzzy PID-Variable Structure Adaptive Control will be more persuasive when we illustrate the tracking errors in Figure 27. It is observed that the dynamic response of Fuzzy PID-Variable Structure Adaptive Control outperforms that of conventional PID control, especially at the near place of the position curve crossing time axis (at this time, the speed reaches the maximum.).

There is no obvious chattering in the response curve of static testing and dynamic testing under Fuzzy PID-Variable Structure Adaptive Control, which indicates that it is feasible to introduce fuzzy inference into PID control to attenuate chattering. Finally, we conclude the advantages of the proposed Fuzzy PID-Variable Structure Adaptive Control method as high precision, good robustness, and simplicity based on experiments.

## 7. Conclusion

The Fuzzy PID-Variable Structure Adaptive Control algorithm for the position tracking control of PMSM which will be used in electric extremity exoskeleton robot is proposed. The controller consists of two parts which are mutual compensation: one is a nonlinear part (Variable structure control), and the other is an approximate linear part (fuzzy PID control). Variable structure control has high robustness. Fuzzy PID control is used to compensate the equivalent control item in SMC and attenuate chattering. The simulation results show that the algorithm can improve control accuracy, dynamic performance, and robustness. The chattering of sliding mode system is attenuated to some extent. At the same time, the Fuzzy PID-Variable Structure Adaptive Control algorithm has the advantages of simple structure and easy engineering realization as well. Finally, the effectiveness and practicability of the algorithm are verified based on a semiphysical simulation test bench with the method of RCP.

Undoubtedly, the control algorithm proposed in this paper as the lower level control method can be applied in our designed electric exoskeleton successfully. And it is also the foundation and origin of designing the higher level control method in our later works on this electric extremity exoskeleton.

## Data Availability

The simulation and experimental data used to support the findings of this study are available from the corresponding author upon request.

## Conflicts of Interest

The authors declare that there are no conflicts of interest regarding the publication of this paper.

## Acknowledgments

This work was supported by the Chinese National Science Foundation (no. 51075017).

## References

- [1] X. Zhang, Z. Yue, and J. Wang, "Robotics in lower-limb rehabilitation after stroke," *Behavioural Neurology*, vol. 2017, Article ID 3731802, 13 pages, 2017.
- [2] S. Yu, Z. Wang, and K. Zhang, "Sequential time-dependent reliability analysis for the lower extremity exoskeleton under uncertainty," *Reliability Engineering & System Safety*, vol. 170, pp. 45–52, 2018.
- [3] Z. Li, W. Ma, Z. Yin, and H. Guo, "Tracking control of time-varying knee exoskeleton disturbed by interaction torque," *ISA Transactions*, vol. 71, pp. 458–466, 2017.
- [4] B. Brahmi, M. Saad, C. Ochoa Luna, M. H. Rahman, and A. Brahmi, "Adaptive Tracking Control of an Exoskeleton Robot with Uncertain Dynamics Based on Estimated Time Delay Control," *IEEE/ASME Transactions on Mechatronics*, 2018.
- [5] Q. Wu, X. Wang, F. Du, and R. Xi, "Modeling and position control of a therapeutic exoskeleton targeting upper extremity rehabilitation," *Proceedings of the Institution of Mechanical Engineers, Part C: Journal of Mechanical Engineering Science*, vol. 231, no. 23, pp. 4360–4373, 2017.
- [6] J. Qian, A. Xiong, and W. Ma, "Extended state observer-based sliding mode control with new reaching law for pmsm speed control," *Mathematical Problems in Engineering*, vol. 2016, Article ID 6058981, 10 pages, 2016.
- [7] S. Wang, Y. Gao, J. Liu, and L. Wu, "Saturated sliding mode control with limited magnitude and rate," *IET Control Theory & Applications*, vol. 12, no. 8, pp. 1075–1085, 2018.
- [8] A. V. Topalov, G. L. Cascella, V. Giordano, F. Cupertino, and O. Kaynak, "Sliding mode neuro-adaptive control of electric drives," *IEEE Transactions on Industrial Electronics*, vol. 54, no. 1, pp. 671–679, 2007.
- [9] J. F. Wu, J. Z. Wang, and L. P. Wang, "Adaptive fuzzy sliding mode control of asymmetrical hydraulic cylinder based on DSP," *Advanced Materials Research*, vol. 655, pp. 1474–1478, 2013.
- [10] J. C. Zhou, J. P. Tian, and A. H. Tang, "Adaptive Sliding Mode Variable Structure Control for Turn Over Robot Based on RBF Neural Network," *Automation Instrumentation*, pp. 34–36, 2018.
- [11] L. Qi and H. Shi, "Adaptive position tracking control of permanent magnet synchronous motor based on RBF fast terminal sliding mode control," *Neurocomputing*, vol. 115, pp. 23–30, 2013.
- [12] F.-J. Lin and R.-J. Wai, "Sliding-mode-controlled slider-crank mechanism with fuzzy neural network," *IEEE Transactions on Industrial Electronics*, vol. 48, no. 1, pp. 60–70, 2001.
- [13] D. X. Phu, T. D. Huy, V. Mien, and S.-B. Choi, "A new composite adaptive controller featuring the neural network and prescribed sliding surface with application to vibration control," *Mechanical Systems and Signal Processing*, vol. 107, pp. 409–428, 2018.
- [14] T. Su, W. Kuo, V. Giap, H. Q. Vu, and Q. Nguyen, "Active Magnetic Bearing System Using PID-surface Sliding Mode Control," in *Proceedings of the 2016 Third International Conference on Computing Measurement Control and Sensor Network (CMCSN)*, pp. 5–8, Matsue, Japan, May 2016.

- [15] Z. Tang, P. Pei, M. Wen, and Z. Shi, "Two novel reaching laws and their use in sliding mode control of EHA," in *Proceedings of the 2015 IEEE International Conference on Information and Automation, ICIA 2015 - In conjunction with 2015 IEEE International Conference on Automation and Logistics*, pp. 1441–1446, China, August 2015.
- [16] E. M. Jafarov, M. N. A. Parlakçi, and Y. Istefanopulos, "A new variable structure PID-controller design for robot manipulators," *IEEE Transactions on Control Systems Technology*, vol. 13, no. 1, pp. 122–130, 2005.
- [17] W. H. Jiang, Y. C. Fan, Z. Liu, and D. Zeng, "Design of servo positioning system based on PID variable structure," *Applied Mechanics and Materials*, vol. 321–324, pp. 1463–1467, 2013.
- [18] S. Liu and L. Ding, "Application of adaptive fuzzy sliding mode controller in PMSM servo system," in *Proceedings of the 1st International Conference on Computing Control and Industrial Engineering, CCIE 2010*, pp. 95–98, China, June 2010.
- [19] A. Ayadi, M. Smaoui, S. Aloui, S. Hajji, and M. Farza, "Adaptive sliding mode control with moving surface: Experimental validation for electropneumatic system," *Mechanical Systems and Signal Processing*, vol. 109, pp. 27–44, 2018.
- [20] Z. M. Chen, W. J. Meng, and J. G. Wang, "Fuzzy reaching law sliding mode control of robot manipulators," *IEEE Pacific-Asia Workshop on Computational Intelligence and Industrial Application*, vol. 2, pp. 393–397, 2008.
- [21] S. S. Yeoh, T. Yang, L. Tarisciotti, C. I. Hill, S. Bozhko, and P. Zanchetta, "Permanent-Magnet Machine-Based Starter-Generator System With Modulated Model Predictive Control," *IEEE Transactions on Transportation Electrification*, vol. 3, no. 4, pp. 878–890, 2017.
- [22] C.-C. Tsai, F.-C. Tai, Y.-L. Chang, and C.-T. Tsai, "Adaptive predictive PID control using fuzzy wavelet neural networks for nonlinear discrete-time time-delay systems," *International Journal of Fuzzy Systems*, vol. 19, no. 6, pp. 1718–1730, 2017.
- [23] A. Deep, N. K. Pilli, A. K. Chauhan, and S. K. Singh, "Design and development of rapid prototype controlled PMSM drive," in *Proceedings of the 2015 IEEE IAS Joint Industrial and Commercial Power Systems / Petroleum and Chemical Industry Conference, ICPSPIC 2015*, pp. 134–139, India, November 2015.
- [24] W. Zhang, Y. Zhang, R. Wang, and X. Pan, "A model-based DSP control platform for rapid prototype of SVPWM," in *Proceedings of the 2010 IEEE 10th International Conference on Signal Processing, ICSP2010*, pp. 2523–2526, China, October 2010.

## Research Article

# Human-Robot Interaction and Demonstration Learning Mode Based on Electromyogram Signal and Variable Impedance Control

Rui Wu , He Zhang , Tao Peng, Le Fu, and Jie Zhao 

State Key State Key Laboratory of Robotics and System, Harbin Institute of Technology, Harbin, Heilongjiang, China

Correspondence should be addressed to He Zhang; zhanghe0451@hit.edu.cn

Received 2 July 2018; Accepted 9 September 2018; Published 30 September 2018

Guest Editor: Shouzhen Zeng

Copyright © 2018 Rui Wu et al. This is an open access article distributed under the Creative Commons Attribution License, which permits unrestricted use, distribution, and reproduction in any medium, provided the original work is properly cited.

In this research, properties of variable admittance controller and variable impedance controller were simulated by MATLAB firstly, which reflected the good performance of these two controllers under trajectory tracking and physical interaction. Secondly, a new mode of learning from demonstration (LfD) that conforms to human intuitive and has good interaction performances was developed by combining the electromyogram (EMG) signals and variable impedance (admittance) controller in dragging demonstration. In this learning by demonstration mode, demonstrators not only can interact with manipulator intuitively, but also can transmit end-effector trajectories and impedance gain scheduling to the manipulator for learning. A dragging demonstration experiment in 2D space was carried out with such learning mode. Experimental results revealed that the designed human-robot interaction and demonstration mode is conducive to demonstrators to control interaction performance of manipulator directly, which improves accuracy and time efficiency of the demonstration task. Moreover, the trajectory and impedance gain scheduling could be retained for the next learning process in the autonomous compliant operations of manipulator.

## 1. Introduction

With the intensifying aging trend and proposal of new industrial development strategies in recent years, the cooperative robots which have variable impedance compliant operation abilities and can accomplish complicated interaction tasks with human beings are attracting wide attention. Nevertheless, the past robot programming mode and teaching box obviously cannot meet the need of learning and demonstration of diversified human-robot collaboration or interaction tasks. Therefore, it is very necessary to develop new human-robot interaction and task learning mode of robots.

Robot learning and implementation of complicated variable impedance human-robot interaction and cooperation tasks involve following research contents. (1) The variable impedance control algorithm is the basis for compliant operation of robots, which can also be used to improve the intuitiveness of interaction and demonstration process. (2) The new human-robot interaction and demonstration mode can help robot to get more better learning data and reduce workload of demonstrators by using appropriate data

collection (visions and EMG signals as well as encoder and force sensor of the robot [1, 2]) and control methods (variable impedance or admittance control). (3) The collected data are conformed into the commands that robot can understand and implement by the appropriate learning algorithm. In the same time, the robot is empowered with adaptation to task environmental changes.

Generally speaking, variable impedance operation of manipulator can be realized by the variable impedance joints on the structure [3, 4] or the variable impedance algorithm based on rigid or flexible joints [5, 6]. The later one not only avoids the complicated engineering problems in the former one and is conducive to thorough theoretical researches, but also can realize equivalent interaction effect of the former one to a large extent [5, 7]. Of course, variable impedance control algorithm has some problems. For instance, the stability of variable impedance control has attracted extensive attentions of scholars in recent years [8, 9].

How to acquire appropriate impedance gain scheduling is an important problem of the variable impedance control

algorithm. Impedance gain scheduling represents the interaction performance of manipulator to specific interaction tasks. This requires design and study of human-robot interaction and demonstration mode and learning algorithm. Existing studies mainly include the following:

(1) Impedance parameters were adjusted based on intelligence control methods, such as adaptive control, optimal control, fuzzy control, and machine learning [10–12]. For example, Dimeas et al. adjusted the impedance gain scheduling through fuzzy learning and reinforcement learning [11, 13, 14].

(2) Robots learn the complicated operation skills that humans are good at from human demonstrators through learning from demonstration [15–17], such as learning from demonstration based on kinesthetic teaching [15] (Kronander et al.), learning from teleoperation mode based on EMG signals [1, 2] (Yang), and interaction task online learning based on EMG signals [16–18] (Peternel et al.).

Learning from demonstration or developing new controllers by observing and summarizing the laws of human motion [19] are two promising directions to develop the new variable impedance control algorithm and human-robot interaction mode. Firstly, high-quality initial learning data are provided to the robot by human demonstrator's learning and cognition ability of variable impedance operation [20], which can save the learning time and enhance the final learning effect of robot. Secondly, the movement trajectory and impedance parameters of human arms are easy to be acquired by many ways. Trajectory data could be acquired by dragging demonstration [6], vision [21], and teleoperation [18], while impedance parameters can be acquired through EMG signal [21] or kinesthetic teaching [15]. By combining the algorithm of learning from demonstration, demonstrators can make intuitive teaching and simplify the teaching process to the maximum extent. Moreover, robots can learn not only representation (trajectory) of human actions, but also dynamic changes and intentions (impedance parameters of human arms) of human in movement. If robot can extract some skills of human operation, reaction ability and fault tolerance ability of robots in independent execution of tasks might be improved.

This study mainly addressed the problem of how humans transmit the complication operation ability of human arm to manipulator effectively and how robots learn and reproduce operation skills of human. Main research contents included the following. (1) Influences of parameter changes of variable impedance controller and variable admittance controller on trajectory tracking and physical interaction were analyzed through simulations, which can give an intuitive understanding of control method. It also shows the interaction effect of the variable impedance (admittance) controller. (2) Based on new human-robot interaction and demonstration mode by combining variable impedance (admittance) control and EMG signals, more intuitive interaction and demonstration can be achieved; the manipulator end-effector trajectory and demonstrator's arm end-point stiffness are recorded and estimated by demonstrator dragging the manipulator and collecting EMG signals in the same time, which is beneficial to get the robot end-effector desired trajectory and impedance

gain scheduling of one task which is planned by human brain. (3) Existing styles of learning from demonstration were introduced. And the data recorded from variable impedance controller and human-robot interaction mode can be used in a best way to generate command of robot independent operation through searching and discussion the appropriate LfD algorithm; this part of work is laying foundations for future studies. The remainder of this paper is organized as follows. Section 2 introduces the proposed method, including theoretical induction of variable impedance controlling and end-point stiffness estimation of human arm. Section 3 conducts simulation and experiments and generates executable end-effector trajectory and impedance gain scheduling of manipulator. Section 4 shows results of analysis and discussion. Section 5 is the conclusion and introduction of the future work.

## 2. Proposed Approach

*2.1. Impedance and Admittance Control.* Impedance control has two feasible forms, namely, impedance control based on robot position control and impedance control based on joint torque control. Some people divided them into admittance control and impedance control.

*2.1.1. Cartesian Space Admittance Control.* Firstly, the Cartesian space admittance control of the robot was simulated. The trajectory changes were observed according to adjustment of impedance parameters to experience the compliant control effect intuitively, and the result can help us select impedance parameters more conveniently in the future. Since admittance control involves no dynamic control of manipulator, but makes the manipulator flexible by setting position commands on the basis of the admittance control law, so the robotic toolbox of MATLAB is used in this part of work. The 7 degrees of freedom (DOFs) manipulator model of iiwa was constructed for simulation.

Generally, the end-effector expected dynamic equation of the end-effector which is realized by admittance control is

$$F_{ext} = M_d \Delta \ddot{x} + D_d \Delta \dot{x} + K_d \Delta x \quad (1)$$

where  $M_d, D_d, K_d \in \mathbb{R}^{6 \times 6}$  are expected inertia matrix, expected damping matrix, and expected stiffness matrix, respectively. The expected damping matrix and the expected stiffness matrix can vary with tasks.  $\Delta x, \Delta \dot{x}, \Delta \ddot{x}$  are positional deviation, speed deviation, and acceleration deviation at the end-effector of manipulator:

$$\begin{aligned} \Delta x &= x_d - x_r, \\ \Delta \dot{x} &= \dot{x}_d - \dot{x}_r, \\ \Delta \ddot{x} &= \ddot{x}_d - \ddot{x}_r \end{aligned} \quad (2)$$

where  $x_d$  is the expected trajectory, which is the expected point set in the program.  $x_r$  is the reference position which is solved according to the expected dynamic model and it is used as the destination of actual movement of manipulator. In other words, the position controller at the manipulator

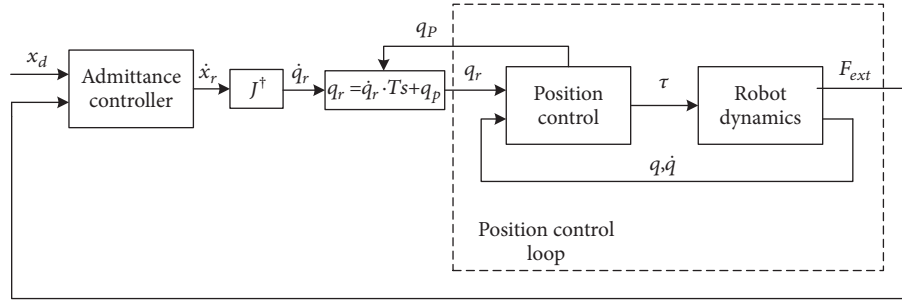


FIGURE 1: Concept of admittance control.

controls different joints to move to this reference position. Therefore, the end-effector of manipulator represents characteristics of the spring-damped second-order system. Figure 1. shows the concept of admittance control.

To simplify the programming and retain the elasticity, the expected dynamic equation of the end-effector was modified as

$$F_{ext} = D_d \Delta \dot{x} + K_d \Delta x \quad (3)$$

For the manipulator, the Jacobian matrix is necessary which can convert the reference position in the Cartesian space into the reference position in the joint space. With respect to the manipulator of 7 DOFs, the pseudoinverse Jacobian matrix  $J^\dagger$  is

$$J^\dagger = J^T \cdot \text{inv}(J \cdot J^T + 0.001 \cdot I) \quad (4)$$

where  $J$  is the Jacobian matrix of manipulator,  $J^T$  is the transpose of Jacobian matrix, and  $I \in \mathbb{R}^{6 \times 6}$  is one unit matrix.

Given the end-effector force  $F_{ext}$ , expected position  $x_d$ , velocity  $\dot{x}_d$ , and the last reference position  $x_{r-p}$  of the manipulator, the reference position  $x_r$  of the manipulator end-effector can be gained by solving (3). Then, the reference speed  $\dot{x}_r$  is feasible to solve the joint velocity by Jacobian pseudoinverse.

$$\dot{q}_r = J^\dagger \dot{x}_r \quad (5)$$

With reference to the previous joint position  $q_p$ , the position command  $q_r$  which is sent to the manipulator at the next moment is

$$q_r = \dot{q}_r \cdot Ts + q_p \quad (6)$$

while another kind of modification in [6] can let the robot easily be dragged by human in free-space cooperation:

$$F_{ext} = M_d \Delta \ddot{x} + D_d \Delta \dot{x} \quad (7)$$

And the reference speed  $\dot{x}_r$  can be calculated by (4) directly. Redoing (5) and (6), the position command  $q_r$  can be got easily.

These two kinds of admittance controller have different function; the first controller can be used to execute some

interaction tasks and make sure the robot will not generate overlarge interaction force, while the second one can be used to accomplish the demonstration teaching, and changing the impedance gain can give the demonstrator different interaction feeling.

**2.1.2. Joint Space Impedance Control.** Later, the impedance control of the manipulator was simulated. Impedance control shall be realized from dynamics of the manipulator. Appropriate feedforward and feedback shall be introduced as dynamics compensation of the manipulator and to generate the dynamic characteristic of impedance. Without consideration to end-effector trajectory, single-joint simulation can approximately represent simulation of the whole manipulator. In this paper, the impedance control law was given from the perspective of 7 DOFs and the single-joint model was constructed by Simulink and an impedance controller was designed to control single-joint of manipulator. The concept of impedance control is shown in Figure 2.

Firstly, it is hypothesized that the rigid body dynamics of single-joint of the manipulator is known accurately:

$$M_r(q) \ddot{q} + C_r(\dot{q}, q) \dot{q} + G(q) = \tau_c + \tau_e \quad (8)$$

where  $q, \dot{q}, \ddot{q} \in \mathbb{R}^N$  are position, speed, and acceleration of each joint of the manipulator.  $M_r(q) \in \mathbb{R}^{N \times N}$  is the inertia positive-definite matrix of the robot joint space.  $C_r(\dot{q}, q) \in \mathbb{R}^{N \times N}$  is the Coriolis force and centrifugal force.  $G(q) \in \mathbb{R}^N$  is the gravity moment on different joints, while  $\tau_c \in \mathbb{R}^N$  and  $\tau_e \in \mathbb{R}^N$  are control moment and the external moment of the robot, respectively.

In the joint space, the expected dynamic relationship of impedance control can be expressed as

$$\tau_e = M_d \Delta \ddot{q} + D_d \Delta \dot{q} + K_d \Delta q \quad (9)$$

where  $M_d, D_d,$  and  $K_d \in \mathbb{R}^{N \times N}$  are expected inertia, expected damping, and expected stiffness, respectively. The expected inertia is a fixed value, but the damping and stiffness matrix is variable.

$$\Delta q = q - q_d \quad (10)$$

where  $q_d$  is the expected joint position.

The inverse dynamic command  $\tau_c$  is set as

$$\tau_c = M_r(q) u + C_r(\dot{q}, q) \dot{q} + G(q) - \tau_e \quad (11)$$

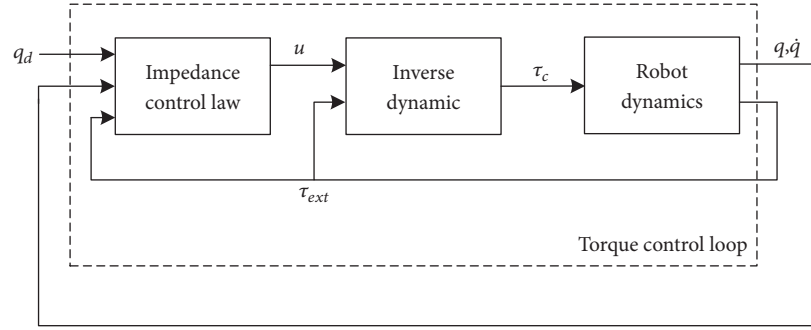


FIGURE 2: Concept of impedance control.

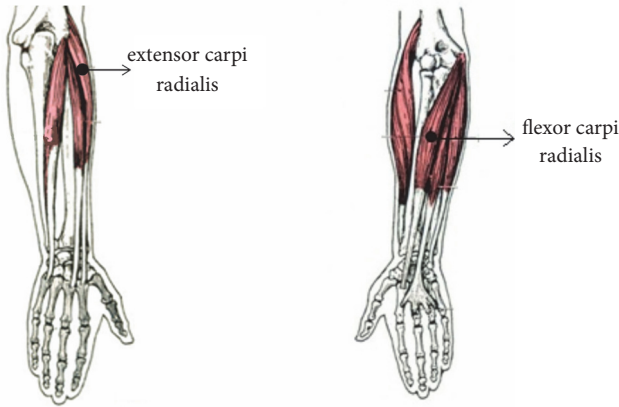


FIGURE 3: Locations of flexor carpi radialis (FCR) and extensor carpi radialis (ECR).

It can be understood as the control feedforward to offset influences of manipulator dynamic characteristics and the external force in control moment. Next, a new control law  $u$  was designed:

$$u = \ddot{q}_d + M_d^{-1} (-D_d \Delta \dot{q} - K_d \Delta q + \tau_c) \quad (12)$$

Obviously, when the expected inertia is equal to the actual inertia of manipulator  $M_d = M_r$ , it is not necessary to measure the external force in this controller. This hypothesis is set true in the single-joint simulation.

Based on the deduced Simulink simulation, the sin signal tracking by single-joint and its interaction with the external force under variable impedance control are tested. Simulation results are introduced in Section 4.

**2.2. Human-Robot Interaction and Demonstration Mode Based on EMG Signals.** In this section, end-point stiffness of human arm was estimated by measuring EMG signals of the antagonistic muscles and then mapped onto controlling parameters of the robot. Flexor carpi radialis (FCR) and extensor carpi radialis (ECR) were chosen as the antagonistic muscles for estimation of end-point impedance parameters of human arms. The locations of these two muscles are shown in Figure 3.

Based on measurement of the EMG signals  $E^i$  of these two muscles and the corresponding maximum voluntary contraction  $E_{MVA}^i$ , the activation percentage  $P^i$  of muscle  $i$  is

$$P^i = \frac{E^i}{E_{MVA}^i} \quad (13)$$

Next, the collaborative contraction degree of muscles  $C_W$  could be calculated and used to estimate the end-effector stiffness  $S$  of the arm.

$$C_W = \min P^{FCR}(t), P^{ECR}(t) \quad (14)$$

$$S = \begin{cases} S^{high} & \text{if } C_W > T \\ S^{low} & \text{if } C_W < T \end{cases} \quad (15)$$

In fact  $C_W$  represents stiffness of wrist joint. Dynamics of the arm were neglected during slow movement and it is viewed simply that  $C_W$  can be used to estimate  $S$ . After  $S$  is gained, two functions could be realized.

(1) The first function is real-time adjustment of interaction performance in interactive teaching through the change of stiffness of human arm. The estimated end-effector stiffness of the arm is used as one reflection of movement intention of the demonstrator. When the end-point stiffness of the demonstrator's arm is high, the demonstrator is attempting to guide the manipulator to make one action that requires accurate position or the act that shall make strong force interaction with the environment, i.e., running through one narrow crack or inserting the hinge pin into the hole. Therefore, the manipulator shall be kept in high damping control status of the impedance controller in order to assure movement accuracy and interaction stability. On the contrary, if the end-point stiffness of demonstrator's arm is low, the demonstrator has no requirements on trajectory accuracy of the manipulator but focuses on flexibility and fast movement of the manipulator. Hence, the manipulator shall be in the low damping state.

(2) Moreover, impedance parameter changes and trajectory of the manipulator in the demonstration process are stored, which can be used in next learning step. And at this process, the human arm stiffness level should be transformed into robot end-effector stiffness and damping, so the robot

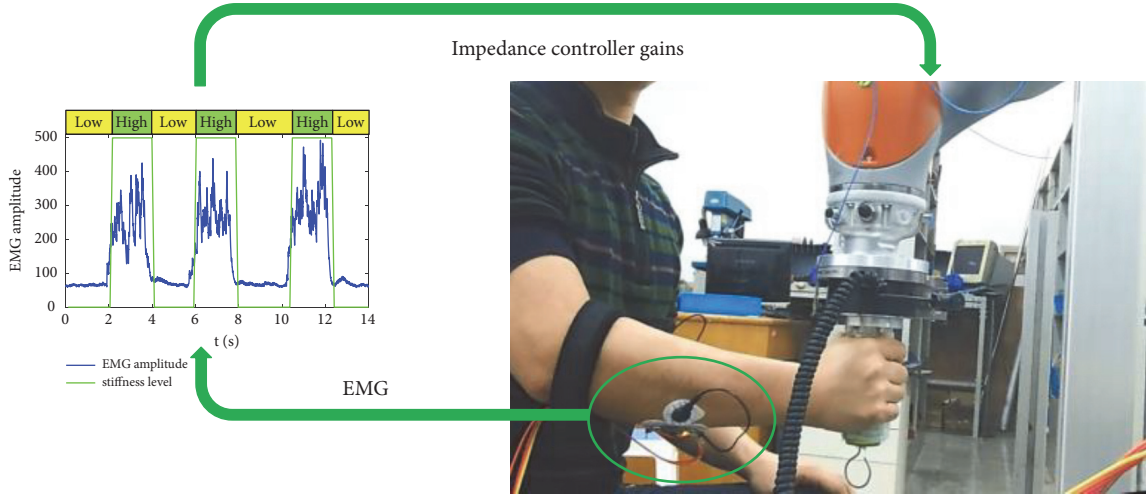


FIGURE 4: Variable impedance interaction and demonstration mode based on human arm end-point stiffness estimation of EMG signals.

can show a good interaction performance in an interaction task by imitating human demonstrator.

In this way, the demonstrator not only can transmit impedance gain scheduling and trajectory easily in the demonstration teaching, but also gains very intuitive and comfortable interaction outcomes. And Figure 4 shows the Basic structure of the variable impedance interaction and demonstration mode based on human arm end-point stiffness estimation of EMG signals.

**2.3. Leaning and Reproduction of Trajectory.** A certain amount of demonstration trajectories could be acquired easily based on the abovementioned design and simulation of the variable impedance controller as well as design and realization of human-robot interaction mode. These trajectories include end-effector trajectory planned by the demonstrator by using the complicated human sensory perceptual system and end-effector stiffness variation sequence of human arms which are generated by the human central nervous system. Therefore, the appropriate end-effector trajectories and impedance variation sequence are collected by the learning from demonstration (LfD) algorithm from the complicated perception ability of human. On the one hand, these data conform to that human habits and robot dynamics are the best and can be used as initial learning data well. On the other hand, kinematics and dynamic characteristics of manipulator are different from those of human. Therefore, self-learning based on characteristics of manipulator is needed in the future, aiming to acquire the moving trajectory of the manipulator and impedance gain scheduling of the controller in accordance with operation characteristics of the manipulator and even adapting to changes of task requirements. Currently, associated popular learning algorithms include GMM-GMR [15] and DMP [2]. After learning based on these algorithms, the manipulator can get the task command suitable for movement of the manipulator through the demonstration trajectory and even

adaptation data of trajectory and impedance scheduling to the changing task requirements.

### 3. Simulation and Experiments

#### 3.1. Simulation

**3.1.1. Admittance Control Simulation.** The admittance control (see (3)) of the manipulator was simulated using MATLAB robotic toolbox according to theoretical deduction in Section 2, and the other admittance controller (see (4)) was used for demonstration, and see part 2.2 of the video in the Supplementary Material for effect of this controller. In the simulation process, when end-effector of the manipulator is below the  $z = 0.2$  plane, the damping matrix and stiffness matrix are

$$\begin{aligned} D_d &= 10 \text{diag}\{I\}, \\ K_d &= 156 \text{diag}\{I\} \end{aligned} \quad (16)$$

where  $I \in \mathbb{R}^{6 \times 6}$  is one unit matrix. On the contrary, when end-effector of the manipulator is above the  $z = 0.2$  plane, the damping matrix and stiffness matrix are

$$\begin{aligned} D_d &= 5 \text{diag}\{I\}, \\ K_d &= 56 \text{diag}\{I\} \end{aligned} \quad (17)$$

In addition, an external force of 5N was applied in these two regions at a certain moment along  $y$  and it was kept for one second to observe phenomenon. The simulation results are shown in Figure 5. See part 1 of the video in the Supplementary Material for details of this simulations.

Changes of joint velocity, constraining force, and Cartesian position of the manipulator are shown in Figure 6.

Hence, influences of damping and stiffness on responses of the manipulator to disturbances can be reflected intuitively. The manipulator makes smaller responses to disturbance

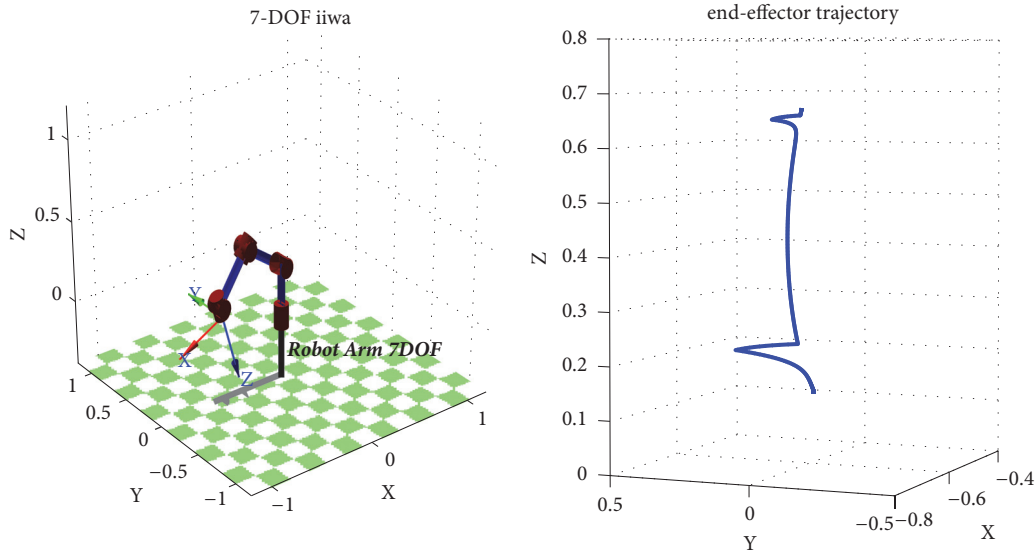


FIGURE 5: MATLAB robotic toolbox simulation.

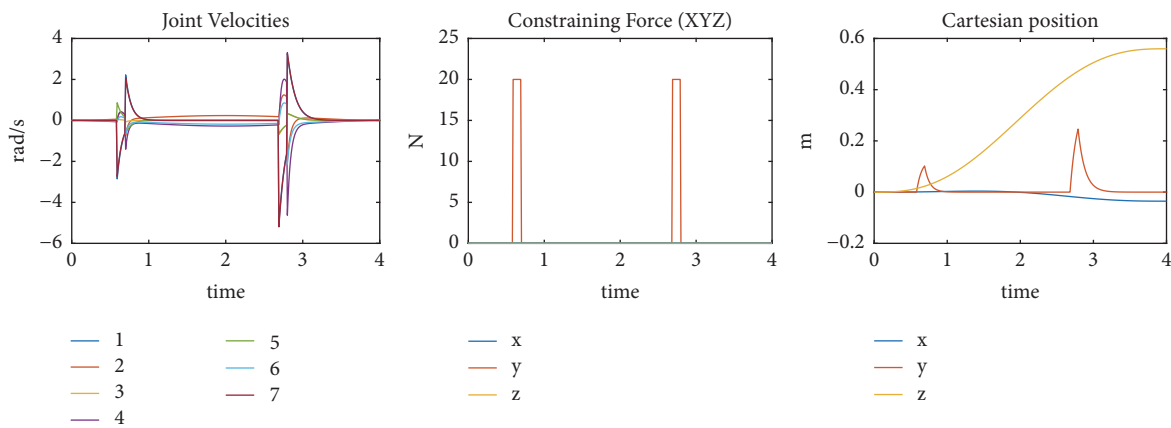


FIGURE 6: Joint velocities, constraining force, and Cartesian position during simulation.

under the larger stiffness and damping. This is similar to the operation mechanism of human arms. Joint stiffness of human arms increases upon contractions of antagonistic muscles, resulting in the increased end-effector stiffness and weakening influences of disturbance on end-point position of human hands. Furthermore, given high end-point stiffness, interaction force in the interaction task can influence end-point trajectory of human hand or hand tool slightly.

**3.1.2. Simulation of Impedance Control.** The single-joint impedance control simulation was carried with Simulink in MATLAB. Since impedance control needs an accurate dynamic model for the purpose of feedforward control, a dynamic model of rigid joint with force sensor was constructed in Simulink.

In this paper, three Simulink simulations were chosen. In the first simulation, single-joint impedance control tracks

the trajectory of sin curve under the changing stiffness. The changing stiffness  $K_d(t)$  is

$$K_d(t) = 18 + 10 \sin(t) \quad (18)$$

Trajectory  $q(t)$  of the sin curve is

$$q(t) = 10 \sin(0.1t) \quad (19)$$

It can be seen from Figure 7 that the variable impedance controller can track the expected trajectory well in the given stiffness range. Although the trajectory error is relatively large in the beginning, it converges gradually as time goes on. This simulation reflects the tracking stability of the variable impedance controller under specific changes of impedance parameters. According to [8], the variable impedance controller has certain stability problems, which, however, were not discussed thoroughly in this paper.

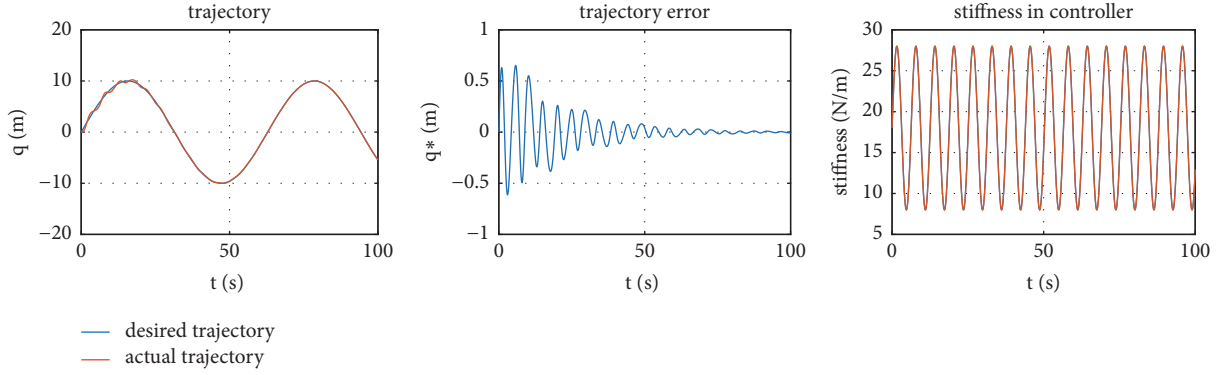


FIGURE 7: Trajectory, trajectory error, and stiffness of controller during first simulation.

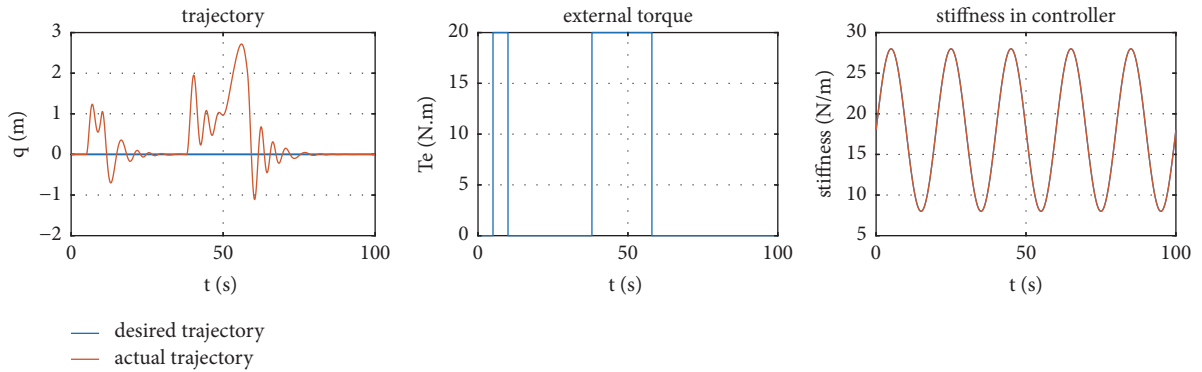


FIGURE 8: Trajectory, external torque, and stiffness of controller during second simulation.

The second simulation focuses on the twice disturbance of the static manipulator by the applied force under changing stiffness  $K_d(t)$ . Under this circumstance,  $K_d(t)$  is

$$K_d(t) = 18 + 10 \sin\left(\frac{\pi}{10}t\right) \quad (20)$$

The external force of 20 N was applied at  $t = 5s$ ,  $t = 38s$  and was kept by 5s and 20s, respectively. It can be seen from Figure 8 that due to changes of the impedance parameter, the external force disturbs the trajectory differently, but the trajectory returns to the stable position after the removal of the external force. This reflects the ability of variable impedance controller to cope with different disturbances of the external force.

The third simulation lets the joint movement track trajectory of sin signal based on the second simulation. Similarly, it can be seen from Figure 9 that the variable impedance controller can interact with external disturbances well. The joint still can maintain stable tracking of the trajectory and cope with external disturbances well when impedance changes.

**3.2. Experiment.** This experiment is to verify whether the operator can increase the dragging damping of manipulator by increasing the arm stiffness under the assistance of the constructed variable impedance human-robot interaction mode. What is more, the experiment also wants to show

the better interaction performance of variable impedance controller during the demonstration teaching than fixed gain impedance controller. As a result, the robot can achieve high trajectory accuracy in copper wire path. On the other hand, decreasing the dragging damping of the manipulator by relieving arm stiffness can help the operator move quickly at less effort. To accomplish this experiment, the dragging handle for demonstration was designed and processed, and an open circular ring was installed at the end of the handle (Figure 10). This open circular ring was used as constraint in the trajectory demonstration and reference trajectory is a piece of copper wire in the shape of Figure 10. KUKA IIWA manipulator is used in this experiment and controlled by ROS system. We can change the impedance gains of the robot by ROS commands.

The collection principle of sEMG signals is shown in Figure 11. Pasting positions of surface electrodes are shown in Figure 12. Skin surface shall be cleaned before the signal acquisition. The EMG signal collection module can rectify and amplify the surface electrode signals and output two signal modes: (1) EMG integrated signals and (2) EMG original signals. Arduino development board converts the analog voltage signals into digital signals by the muscle electric transducer and then transmits data to the computer for later processing.

After getting the EMG signal, we use these two functions of ROS: Publisher and Subscriber, Service, and Client to build

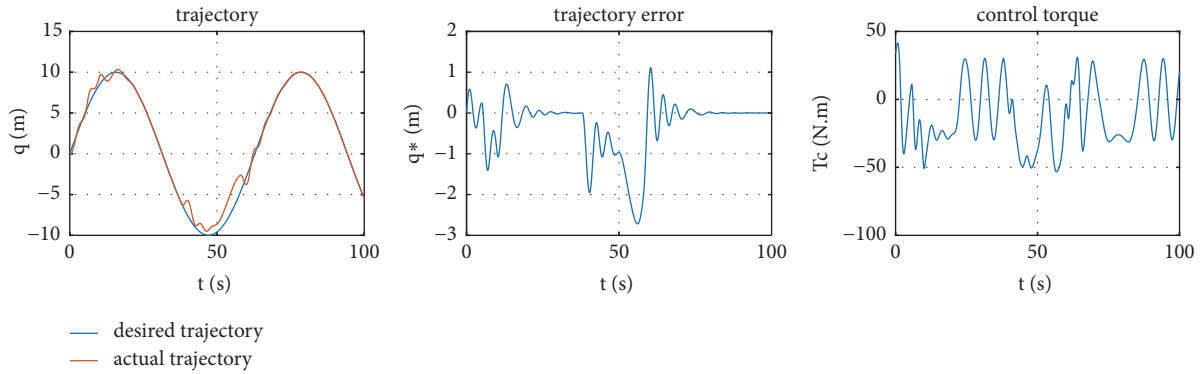


FIGURE 9: Trajectory, trajectory error, and control torque during second simulation.

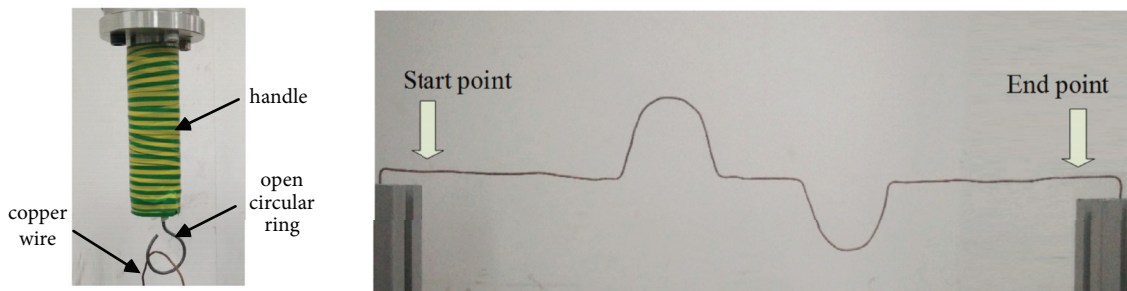


FIGURE 10: Demonstration handle and trajectory of the demonstration copper wire.

the connect between EMG signal and `iiva_stack` software package (which can send commend to KUKA sunrise and get state feedback form it). Then we use a C++ program to complete the calculation of impedance gain on the basis of EMG signal and send the commend to KUKA sunrise controller, so achieving the impedance gain change on the basis of EMG signal.

The interaction and demonstration experiment are shown in Figure 13. See part 3 of video in the Supplementary Material for details of this experiments. The circular ring was covered on the copper wire and the operator dragged the manipulator to move along the trajectory of copper wire as soon as possible. At the same time, the ring centre shall run through the copper wire as much as possible, preventing the ring from the copper wire. According to this experimental rule, the manipulator arrived at the destination and the circular ring was removed from the copper wire. Next, the manipulator returned to the starting point quickly and started to move again. This process was repeated several times. The experiments were mainly divided into two groups: (1) fixed admittance control experiment and (2) variable admittance control experiment.

## 4. Results and Discussion

**4.1. Fixed Admittance Control Experiment.** This experiment is to verify performance of the impedance controllers with low and high damping parameters in the demonstration process.

Two impedance controllers with high and low fixed damping were set for abovementioned trajectory demonstration. At the same time, the demonstration trajectory was recorded. Moreover, 20 trajectory demonstration experiments were carried out to each admittance controller. In each experiment, the mean absolute error between the demonstration trajectory and reference trajectory (trajectory of the copper wire) was calculated and each demonstration time was recorded. The demonstration trajectories of manipulator end-effector of the admittance controllers with low and high damping are shown in Figures 14 and 15, respectively.

After multiple experiments, the mean demonstration experiment time under low damping parameters was 5s and the mean trajectory error was 17 mm. However, the mean demonstration experiment time under high damping parameters was 12s and the mean trajectory error was 8 mm.

**4.2. Experiment of Variable Admittance Control.** This experiment focuses on sEMG measurement and mapping of stiffness changes of human arms, thus enabling realizing online adjustment of impedance controllers with high and low damping parameters. As a result, operators can accomplish the trajectory demonstration task quickly and accurately. The experimental process was consistent with the fixed admittance control experiment. One demonstration trajectory is shown in Figure 16. The mean demonstration time in multiple experiments is 8s and the mean trajectory error is 11 mm.

It can be concluded from experimental data that the admittance controller with low damping parameters has high

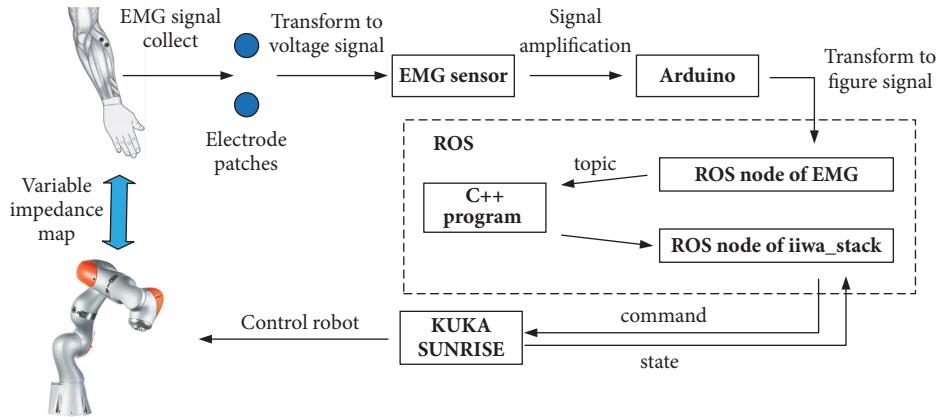


FIGURE 11: Principle of sEMG signal acquisition and conversion.

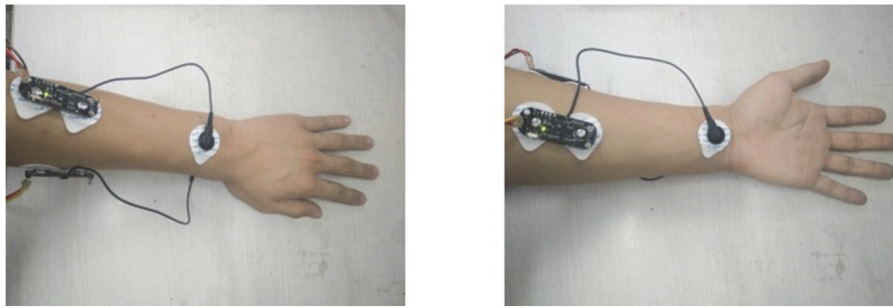


FIGURE 12: EMG sensor locations of FCR and ECR.



FIGURE 13: Variable admittance flexible control experiment based on sEMG.

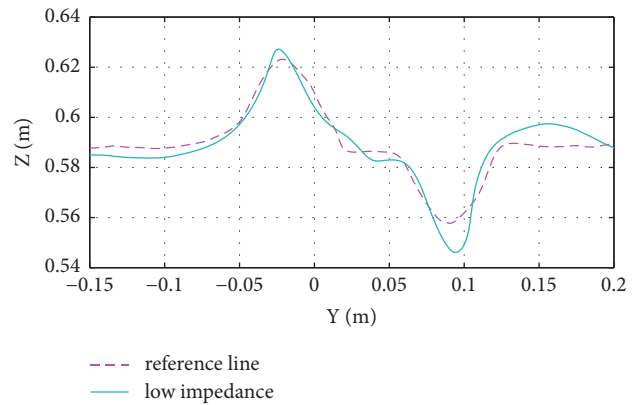


FIGURE 14: Admittance control demonstration trajectory under low damping parameters ( $D_d=10\text{Ns/m}$ ,  $M_d=2\text{kg}$ , and  $K_d=10\text{N/m}$ ).

demonstration speed, but large demonstration trajectory error. On the contrary, the admittance controller with high damping parameters has high demonstration accuracy, but low demonstration speed. The variable impedance controller has advantages of these two controllers. It achieves high demonstration accuracy and high demonstration speed simultaneously.

### 5. Conclusion and Future Work

Some conclusions could be drawn from the above simulations and experiments.

(1) Changing the impedance parameters by variable impedance controller can change responses of the manipulator to external disturbances directly while protecting effects and stability of the flexible interaction, without influencing trajectory tracking significantly. This reflects the fact that variable impedance control can give the manipulator a good interactive control model and flexibility, thus meeting requirements on the complicated operation task. On the one hand, research on human arms proves directly that

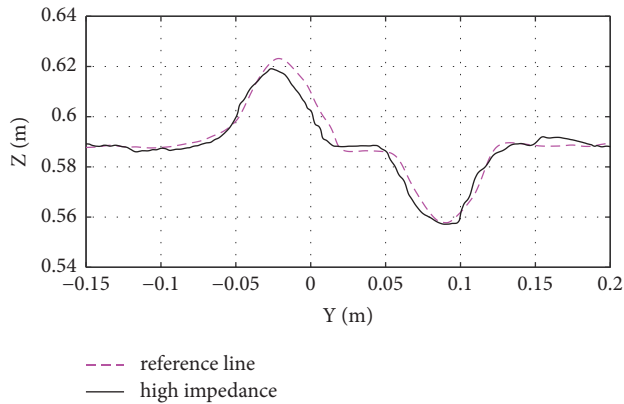


FIGURE 15: Admittance control demonstration trajectory under high damping parameters ( $D_d=100\text{Ns/m}$ ,  $M_d=2\text{kg}$ , and  $K_d=10\text{N/m}$ ).

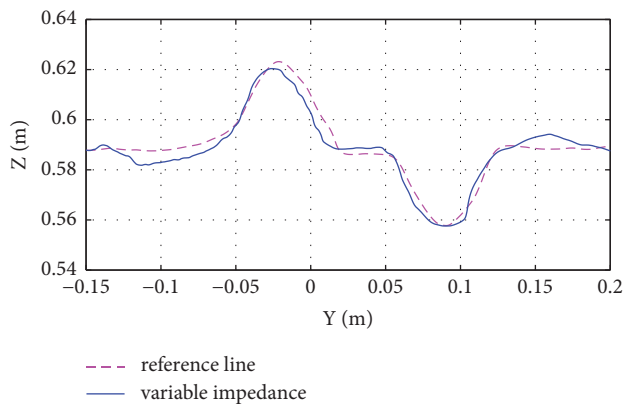


FIGURE 16: Admittance control demonstration trajectory under variable damping parameters ( $D_{\text{Low}}=10\text{Ns/m}$ ,  $D_{\text{High}}=100\text{Ns/m}$ ,  $M_d=2\text{kg}$ , and  $K_d=10\text{N/m}$ ).

impedance control of the manipulator is a bionic control method conforming to the biological organism.

(2) Real-time human arm stiffness estimation and interactive demonstration by combining the variable impedance control and human-robot interaction mode can contribute better interaction and demonstration effects. They can not only increase human-robot interaction efficiency and accuracy and improve interaction intuitive, but also lower requirements on operation experiences of demonstrators as well as energy consumption of demonstrators in the interaction and demonstration process.

(3) Skill features (e.g., planning trajectory and impedance gain scheduling) of human movement can be collected reasonably through demonstration base on the designed human-robot interaction mode, which can be applied onto the manipulator in late processing. Therefore, the control command suitable for operation of manipulator could be gained by late learning optimization of data.

This paper only involves simple end-effector stiffness estimation of human arms and simple production of demonstration trajectory. In future studies, mapping accuracy of

human arm end-effector stiffness shall be increased appropriately to conform better to the principle of imitating human behaviours and learning by demonstration. For example, the EMG signals as well as accurate mapping between human arm postures and end-effector stiffness of human arms are constructed through the recognition method and then used in the interaction mode. As a result, intention of the demonstrator can be reflected more truly and thoroughly. This is beneficial for the manipulator to make more careful imitation. On the other hand, it is necessary to learn the acquired end-effector trajectory and impedance gain scheduling by searching and using some appropriate learning algorithms. Hence, the controller that can execute tasks effectively and even can cope with changes of task conditions as well as disturbances in a certain range is gained. Moreover, future studies shall pay attention to stability of the manipulator throughout the imitation of the human expected variable impedance trajectory. Offline calculation or online adjustment of the executing trajectories and impedances should be studied, aiming to protect stability and safety during execution of tasks by the manipulator itself.

## Data Availability

As the project will not be finished until July 2019 and we have confidentiality agreement with State Key State Key Laboratory of Robotics and System, the data could not be released so far. For any information about the article, please contact us via zhanghe0451@hit.edu.cn.

## Conflicts of Interest

The authors declare that there are no conflicts of interest regarding the publication of this paper.

## Acknowledgments

This work was supported by the National Key R&D Program of China (Grant No. 2017YFB1302701), National Natural Science Foundation of China (Grants Nos. 61503098, and 61473102), Major Research Plan of the National Natural Science Foundation of China (Grant No. 91648201), Natural Science Foundation of Heilongjiang Province (QC2016088), National High Technology Research and Development Program (2015BAF09B02), and Foundation for Innovative Research Groups (Grant No. 51521003) of the National Natural Science Foundation of China.

## Supplementary Materials

Video of simulations and experiments are provided. (*Supplementary Materials*)

## References

- [1] C. Yang, C. Zeng, Y. Cong, N. Wang, and M. Wang, "A Learning Framework of Adaptive Manipulative Skills from Human to Robot," *IEEE Transactions on Industrial Informatics*, pp. 1-1.

- [2] C. Yang, C. Zeng, C. Fang, W. He, and Z. Li, "A DMPs-Based Framework for Robot Learning and Generalization of Human-like Variable Impedance Skills," *IEEE/ASME Transactions on Mechatronics*, vol. 23, no. 3, pp. 1193–1203, 2018.
- [3] S. Wolf and G. Hirzinger, "A new variable stiffness design: Matching requirements of the next robot generation," in *Proceedings of the 2008 IEEE International Conference on Robotics and Automation, ICRA 2008*, pp. 1741–1746, USA, May 2008.
- [4] M. Howard, D. J. Braun, and S. Vijayakumar, "Transferring human impedance behavior to heterogeneous variable impedance actuators," *IEEE Transactions on Robotics*, vol. 29, no. 4, pp. 847–862, 2013.
- [5] F. Ficuciello, L. Villani, and B. Siciliano, "Variable impedance control of redundant manipulators for intuitive human-robot physical interaction," *IEEE Transactions on Robotics*, vol. 31, no. 4, pp. 850–863, 2015.
- [6] S. Grafakos, F. Dimeas, and N. Aspragathos, "Variable admittance control in pHRI using EMG-based arm muscles co-activation," in *Proceedings of the 2016 IEEE International Conference on Systems, Man, and Cybernetics, SMC 2016*, pp. 1900–1905, Hungary, October 2016.
- [7] F. Dimeas, V. C. Moulianitis, C. Papakonstantinou, and N. Aspragathos, "Manipulator performance constraints in Cartesian admittance control for human-robot cooperation," in *Proceedings of the 2016 IEEE International Conference on Robotics and Automation, ICRA 2016*, pp. 3049–3054, Sweden, May 2016.
- [8] K. Kronander and A. Billard, "Stability Considerations for Variable Impedance Control," *IEEE Transactions on Robotics*, vol. 32, no. 5, pp. 1298–1305, 2016.
- [9] F. Ferraguti, C. Secchi, and C. Fantuzzi, "A tank-based approach to impedance control with variable stiffness," in *Proceedings of the 2013 IEEE International Conference on Robotics and Automation, ICRA 2013*, pp. 4948–4953, Germany, May 2013.
- [10] C. Yang, G. Ganesh, S. Haddadin, S. Parusel, A. Albu-Schäffer, and E. Burdet, "Human-like adaptation of force and impedance in stable and unstable interactions," *IEEE Transactions on Robotics*, vol. 27, no. 5, pp. 918–930, 2011.
- [11] F. Dimeas and N. Aspragathos, "Fuzzy learning variable admittance control for human-robot cooperation," in *Proceedings of the 2014 IEEE/RSJ International Conference on Intelligent Robots and Systems, IROS 2014*, pp. 4770–4775, USA, September 2014.
- [12] J. Buchli, F. Stulp, E. Theodorou, and S. Schaal, "Learning variable impedance control," *International Journal of Robotics Research*, vol. 30, no. 7, pp. 820–833, 2011.
- [13] F. Dimeas and N. Aspragathos, "Online Stability in Human-Robot Cooperation with Admittance Control," *IEEE Transactions on Haptics*, vol. 9, no. 2, pp. 267–278, 2016.
- [14] F. Dimeas and N. Aspragathos, "Reinforcement learning of variable admittance control for human-robot co-manipulation," in *Proceedings of the 2015 IEEE/RSJ International Conference on Intelligent Robots and Systems (IROS)*, pp. 1011–1016, Hamburg, Germany, September 2015.
- [15] K. Kronander and A. Billard, "Learning compliant manipulation through kinesthetic and tactile human-robot interaction," *IEEE Transactions on Haptics*, vol. 7, no. 3, pp. 367–380, 2014.
- [16] L. Peternel, T. Petrič, E. Oztop, and J. Babič, "Teaching robots to cooperate with humans in dynamic manipulation tasks based on multi-modal human-in-the-loop approach," *Autonomous Robots*, vol. 36, no. 1-2, pp. 123–136, 2014.
- [17] L. Peternel, N. Tsagarakis, and A. Ajoudani, "A human-robot co-manipulation approach based on human sensorimotor information," *IEEE Transactions on Neural Systems and Rehabilitation Engineering*, vol. 25, no. 7, pp. 811–822, 2017.
- [18] L. Peternel, T. Petric, and J. Babič, "Human-in-the-loop approach for teaching robot assembly tasks using impedance control interface," in *Proceedings of the 2015 IEEE International Conference on Robotics and Automation (ICRA)*, pp. 1497–1502, Seattle, WA, USA, May 2015.
- [19] E. Burdet, G. Ganesh, C. Yang, and A. Albu-Schäffer, "Interaction force, impedance and trajectory adaptation: By humans, for robots," *Springer Tracts in Advanced Robotics*, vol. 79, pp. 331–345, 2014.
- [20] E. Burdet, R. Osu, D. W. Franklin, T. E. Milner, and M. Kawato, "The central nervous system stabilizes unstable dynamics by learning optimal impedance," *Nature*, vol. 414, no. 6862, pp. 446–449, 2001.
- [21] A. Ajoudani, N. Tsagarakis, and A. Bicchi, "Tele-impedance: teleoperation with impedance regulation using a body-machine interface," *International Journal of Robotics Research*, vol. 31, no. 13, pp. 1642–1655, 2012.

## Research Article

# Mass Collaboration-Driven Method for Recommending Product Ideas Based on Dempster-Shafer Theory of Evidence

Yuan-Wei Du <sup>1,2</sup>, Yu-Kun Shan,<sup>1</sup> Chang-Xing Li,<sup>3</sup> and Rui Wang <sup>1</sup>

<sup>1</sup>Management College, Ocean University of China, Qingdao 266100, China

<sup>2</sup>Marine Development Studies Institute of OUC, Key Research Institute of Humanities and Social Sciences at Universities, Ministry of Education, Qingdao 266100, China

<sup>3</sup>School of Economics, Shanghai University of Finance & Economics, Shanghai 200443, China

Correspondence should be addressed to Rui Wang; wangrui@sailunjinyu.com

Received 27 July 2018; Accepted 6 September 2018; Published 27 September 2018

Guest Editor: Shouzhen Zeng

Copyright © 2018 Yuan-Wei Du et al. This is an open access article distributed under the Creative Commons Attribution License, which permits unrestricted use, distribution, and reproduction in any medium, provided the original work is properly cited.

In the mass collaboration mode, there exist a large number of product ideas with low value density and thousands of participants who are differed on their professional backgrounds, knowledge structures, and value orientations. It is impossible for each participant to give a comprehensive evaluation of each idea as that in traditional methods for the reasons as mentioned above. In order to solve this problem, a mass collaboration-driven method for recommending product ideas is proposed based on Dempster-Shafer theory of evidence (DST). Firstly, the method for computing basic probability assignment (BPA) function, which can effectively reflect the facticity of experts' evaluations, is introduced by discounting belief degrees with weights to extract the evaluation information of product ideas. Then, Dempster's combination rule is used to combine the derived BPA functions for two times: the first one is to combine the discounted BPA functions on all criteria with respect to a specified expert and the other is to combine the combined BPA functions for all experts with respect to a specified alternative. Finally, the steps of mass collaboration-driven method for recommending product ideas based on the DST are proposed. An illustrative example is provided to demonstrate the applicability of the proposed method.

## 1. Introduction

Product idea refers to the production of novel and useful idea to complex, novel, and ill-defined problems [1–3]. Successful innovation requires high-quality ideas and how to effectively generate novel and useful product ideas continues to be a critical issue for both design scholars and practitioners.

At present, research on product ideas is mainly divided into two processes: one is idea generation, whereby ideas emerge in an associative manner, and the other is idea evaluation, whereby generated ideas are evaluated and screened. From the perspective of idea generation, Chou presented an ideation method for generating new product ideas [4]; Kazmi and Kytola attempted to explore assessment of a company's new product ideas generation potential linked to their industrial teams' diversified capabilities as well as their work potential [5]; Banović et al. used projective and creative research techniques to involve consumers in the

process of modification and generation of new product ideas [6]; Shroyer et al. presented a qualitative case study of a professional design team's use of ideas generation with analyses at five emergent timescales [7]; Giller et al. suggested that either unbounded or prohibitive task instructions should be used when crowdsourcing innovative ideas [8]; Kwon et al. proposed a methodology to be served as an essential supporting tool for generating creative ideas that could spark innovation [9]; Mirtalaie et al. presented a systemic framework for product designers in the ideation phase of new product development. From the perspective of product ideas evaluation, Steele et al. developed a measure of ideas evaluation self-efficacy [10, 11]; Özaygen and Balagué proposed a methodology to reduce crowd innovation voting bias and to help managers to better select the ideas [12]; Hao et al. explored the neural correlates underlying the effects of ideas evaluation on idea generation in creative thinking [13]; Mayselless et al. proposed an explanatory model of

ideas centered upon the key role of the left temporoparietal regions in evaluating and inhibiting ideas [14]; Hoornaert et al. established a new model that can improve the reliability of ideas ranking by means of automated information retrieval methods, linear methods, and nonlinear machine-learning algorithms [15].

With the development of information technology, more and more subjects can participate in the innovation [16], and many enterprises have carried out product innovation in mass collaboration mode and achieved initial results [17, 18], as mass collaboration mode has reduced BMW's R & D cycle from 2 years to half a year and made Linux Kernel's software system update continuously in weeks; HUAWEI focuses on "user perception" and has established a close cooperative relationship with more than 30 telecom operators, industry alliances and institutions, vertical industry leaders, and so on and has released a new generation of Easy Macro solutions and a new generation of 3D MIMO solutions. Although the mass collaboration mode has helped many enterprises achieve some results, product innovation based on this mode is still an important issue facing the enterprise at present stage. On the one hand, there are a lot of ideas in the generation stage. Thousands of participants can publish their opinions on product innovation with various Internet platforms, thus generating a large number of ideas with low value density. On the other hand, there are many participants in the idea evaluation stage. The participants not only include the internal members of the enterprises but also include the vast number of current and potential users.

Some scholars have done some researches on idea generation and idea evaluation in product innovation, which are of great significance to enrich the research achievements in this field. However, the large number of ideas and participates in the mass collaboration mode leads to the existing achievements which are not suitable for solving the problem of product idea evaluation. The reason is that the participants may come from the relevant subjects such as the internal members and social public, and the knowledge, preference and ability of each participant may be different from each other. It is impossible for each participant to give a comprehensive evaluation of each idea as that in the traditional methods.

In order to solve the above problems, this paper puts forward a mass collaboration-driven method for recommending product ideas based on Dempster-Shafer theory of evidence (DST), on the basis of taking full consideration of the characteristics of the large number of ideas and the large number of participants. Existing methods in this field require all experts to give complete evaluation information on all criteria for each idea, but this is difficult to achieve in the mass collaboration mode. In contrast, considering the incompleteness of expert knowledge, the proposed method allows each expert to evaluate only one or more criteria for an idea in his/her field of expertise. Moreover, it allows each expert to be assigned different weights in each criterion, so as to obtain more reasonable and effective evaluation information. However, the proposed method can only sort the ideas from a static point of view and cannot achieve real-time sorting for the added ideas and evaluation information.

The rest of this paper is organized as follows. In Section 2, we introduce the framework of evaluating product ideas. In Section 3, we propose the method for recommending product ideas based on the DST and analyze the specific steps of the proposed method. In Section 4, we use an example to illustrate the combination process of the proposed method. Section 5 concludes the paper.

## 2. Framework of Evaluating Product Ideas

*2.1. Generation of Ideas.* Ever since the publication of Osborn's (1953) influential book *Applied Imagination*, many organizations consider group brainstorming as a particularly effective technique for generating large numbers of creative ideas [19]. To stimulate creativity, a group idea-generation technique was developed and popularized under the name of brainstorming [20]. This technique has been extended to electronic brainstorming, in which group members simultaneously produce as many ideas as possible on computers in a short period of time [21]. In view of the advantages of electronic brainstorming that electronic brainstorming groups perform better than face-to-face groups, in both the number of high-quality ideas and the average originality of ideas, we decide to use this method to generate the needed ideas.

In order to get effective product ideas, enterprises should publish innovative requirements on the Internet platform. For example, on the premise of guaranteeing the quality of the product, compared with the extravagant outer packaging, the enterprise can require a simple and clear design in the appearance and packaging of the product. It cannot only reduce the cost of packaging but also attract consumers' attentions. In other words, the enterprise can require new product ideas to be differentiated in terms of product functionality, durability, style design, delivery, installation, customer training, and consulting services, so that new products are distinguished from the same products on the market.

After the enterprise announces the innovation request, the public can be the participants in the mass collaboration mode and all of them can express their opinions and discuss freely on the various interactive platforms. In order to get as much product ideas as possible, enterprises adopt electronic brainstorming method and make full use of all kinds of online platforms to encourage participants to participate in the process of product ideas generation around innovative requirements. The goal of electronic brainstorming is to generate a list of ideas, applying four rules: (a) focus on quantity, (b) withhold criticism, (c) welcome unusual ideas, and (d) combine and improve one's own ideas. Thus, a large number of product ideas have been generated.

*2.2. Classification of Participants.* Nowadays, many companies rely on online innovation communities to collaborate together with users and integrate external user knowledge within firm boundaries for new product development purposes [22]. All people except internal members of the enterprise can be regarded as users, who either have bought a product (current users) or are likely to buy a product

(potential users). Numerous studies have shown that positive interaction between users and enterprises is conducive to the transformation of new technologies and the development of new products. In addition, employees, as insiders, have a deeper understanding of the real situation of the enterprise and the goal of product innovation and can participate in the whole process of product innovation. To sum up, according to the differences in value orientation and knowledge structure, this paper divides the participants in the mass collaborative mode into three categories: internal members of the enterprise, current users, and potential users.

(1) Internal members of the enterprise: As the originator and manager of the product ideas, internal members of the enterprise participate in the formation of the ideas in the whole process, which can be divided into managers, technical developers, production managers, and marketers. Managers mainly evaluate an idea from the perspective of economic benefits; technical developers mainly evaluate an idea from the perspective of enterprises' ability to transform existing technologies into product characteristics; production managers mainly evaluate an idea from the perspective of the production parameters (such as environment, medium temperature, pressure, etc.) and the technological design method; marketers mainly evaluate an idea from the perspective of marketing requirements.

(2) Current users: The current users refer to the users of a technology, product, or service, who have used one product. They are the actual experiencers of the product, have a more comprehensive understanding of the advantages and disadvantages of the product, can provide the corresponding information for the problems existing in the product, and can also evaluate the existing ideas.

(3) Potential users: The potential users are those users who have not been used but have the desire to buy some kind of product or service, have the ability to buy, have the right to make a decision, and have a demand for the function provided by the product. They can evaluate an idea from the perspective of whether the product can satisfy their needs.

**2.3. Evaluation Criteria for Product Ideas.** Early research on idea used the number of creative ideas as the only criterion to measure the quality of idea. With the deepening of idea evaluation, the quantitative evaluation method in the past is no longer applicable. At present, the general view of the research on product idea evaluation criteria is multicriteria comprehensive decision-making. This view holds that idea evaluation depends on multiple criteria and comprehensive decision-making [23].

Plucker et al. proposed the idea that the evaluation of product idea should include two dimensions: novelty and practicality [24]. Chan et al. suggested that the customer lifetime value (CLV) calculated can be regarded as the final evaluation criterion used to support idea screening decisions [25]. Rietzschel et al. proposed that a good idea should be new and practical and put forward two criteria: novelty and feasibility [26]. Diedrich et al. believed that the primary criterion for judging an idea is novelty, followed by usefulness [27]. Schwarz and Bodendorf suggested that

a good idea should be feasible, novel, profitable, useful, and highly mature [28]. Hart et al. pointed out that technical feasibility is the most commonly used evaluation criterion in idea evaluation [29]. MacCrimmon and Wagner believed that the criteria of idea decision-making need to take into account five aspects: novelty, nonobvious, relevance, practicality, and thoroughness [30]. Carbonell-Foulquié et al. believed that strategic conformity, technical feasibility, customer acceptability, economic performance, and marketing opportunity are 5 major criteria for evaluating an idea [31]. Dean et al. pointed out that the essence of an idea is novelty, based on which four first level criteria of evaluation, novelty, feasibility, relevance and particularity, are established, and two level criteria are established under each criterion [32].

The above evaluation criteria are based on many angles and discussed the idea itself, but this is not to be ignored that the fundamental purpose of ideas research and development is to better maintain the enterprise's own development. Therefore, the economic and technological benefits of ideas should also be emphasized. Hietikko proposed a model with two 2-dimensional tables, one for customer and the other for producer [33]. The value for customer is divided into two factors: usefulness and economic efficiency, and the table of producer is divided into marketability and productivity. Eling et al. put forward that when evaluating an idea, we should consider the speed of evaluation and whether it can bring benefits to enterprises [34]. Lauto and Valentin proposed that the decision time and the technological achievements contained in the idea must be taken into consideration [35]. Ferioli et al. further refined the practicability of the idea evaluation criteria into two aspects: technology executable and economic benefits [36]. Gutierrez put forward six principles of idea evaluation, which are core competitiveness, market position, module economic value, R & D capital, risk awareness, and organizational goal contribution [37].

On the basis of referring to the relevant literature, we select 4 criteria as the evaluation criteria of product ideas, as shown in Table 1.

**2.4. Framework of Idea Evaluation.** Each product idea can be regarded as an alternative. Suppose that a set of alternative ideas is expressed as  $A = \{a_k \mid k = 1, \dots, K\}$ , a set of three types of experts is expressed as  $E = \{E_i \mid i = 1, 2, 3\}$ , and a set of criteria is expressed as  $C = \{c_j \mid j = 1, \dots, 4\}$ . Suppose the number of individuals in the experts  $E_i$  is  $I_i$  and  $e_s^i$  is the  $s^{th}$  individual in  $E_i$ , then the set of individuals in  $E_i$  can be expressed as  $E_i = \{e_s^i \mid s = 1, \dots, I_i\}$ ,  $i = 1, 2, 3$ . According to the above,  $E_1 = \text{Internal members of the enterprise}$ ,  $E_2 = \text{Current users}$ ,  $E_3 = \text{Potential users}$ ,  $c_1 = \text{Novelty}$ ,  $c_2 = \text{Acceptability}$ ,  $c_3 = \text{Usefulness}$ , and  $c_4 = \text{Feasibility}$ . After the generation of the ideas, for each idea, every expert can give an evaluation information on the performance of a certain criterion according to his own knowledge and experience. For examples, internal members of enterprise can evaluate the above 4 criteria according to the principle of whether an idea can bring benefits to enterprises. Current users and potential users can evaluate the above 4 criteria according to the principle of whether an idea meets their needs. Suppose

TABLE 1: Evaluation criteria of ideas.

Evaluation criteria	Meaning of the criteria
Novelty( $c_1$ )	Degree to which an idea is not only rare, but is also ingenious, imaginative, or surprising.
Acceptability( $c_2$ )	Acceptability of the market or user, or the popularity of new products in the market.
Usefulness( $c_3$ )	Value of an idea that can be brought to users and enterprises after implementation.
Feasibility( $c_4$ )	Possibility of product development, the feasibility of existing technology, and the possibility of mass production.

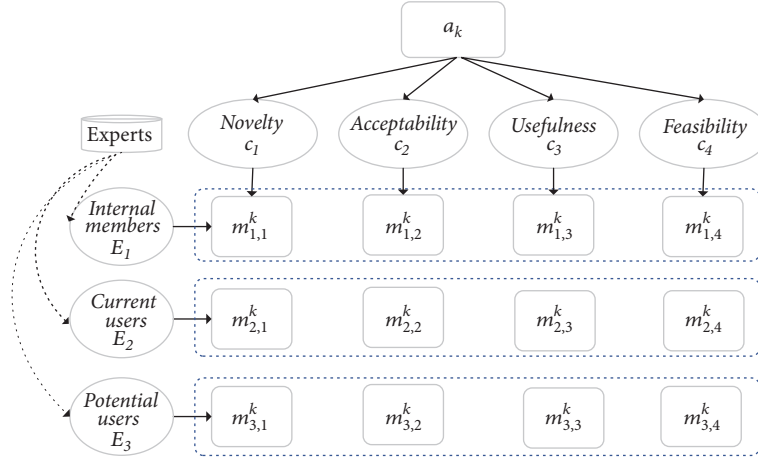


FIGURE 1: Framework of idea evaluation.

that the evaluation information of alternative  $a_k$  evaluated by experts  $E_i$  with respect to criterion  $c_j$  is expressed as  $m_{i,j}^k$ . Thus, the framework of idea evaluation can be shown in Figure 1.

### 3. The Proposed Method

In this paper, based on the comprehensive consideration of weight, the DST and the Pignistic probability are used for ideas selection and ranking. The DST is an extension of classical probability theory by generalization of the Bayesian theory of subjective probability. Being a mathematical framework for representation of uncertainty, the DST combines the degrees of belief derived from independent items of evidences. It mainly deals with four concepts: frame of discernment, basic probability assignment (BPA), the belief or mass function, and the plausibility [38]. Its advantages are mainly manifested in the following three aspects: first, it can handle more uncertainty in real world; second, no prior distribution is needed before the combination of evidence from individual information sources; third, it allows one to specify a degree of ignorance in some situations instead of being forced to be assigned for probabilities [39]. The relevant definitions are shown as follows [40–43].

**3.1. Information Extraction Method.** In the mass collaboration mode, considering the differences in knowledge structure, cognitive ability, and value orientation, every expert can only evaluate one or several criteria of an idea, which determines that there may be uncertain information about

“incomplete known” or “completely unknown” in the evaluation information. Compared with the fact that each expert can evaluate all the criteria in traditional methods, the BPA function, as an expression of uncertain information, allows each expert to evaluate the criteria that he has the ability to evaluate, thereby maximally ensuring the authenticity of the evaluation information [44–46]. In view of this, we use the BPA function to extract the evaluation information.

**Definition 1.** Suppose the grade of an idea is expressed as  $\theta_n$  ( $n = 1, \dots, N$ ), each grade is exclusive, and the finite set of mutually exclusive and exhaustive propositions  $\Theta = \{\theta_1, \theta_2, \dots, \theta_n\}$  is the frame of discernment.

**Definition 2.** Supposing that the set of every subset of  $\Theta$  is  $2^\Theta$ ,  $\theta$  is any subsets of  $\Theta$ , and  $m(\theta)$  represents the degree of belief, if the mapping function  $m : 2^\Theta \rightarrow [0, 1]$  could fulfill

$$m(\emptyset) = 0, \quad \sum_{\theta \in \Theta} m(\theta) = 1 \quad (1)$$

then  $m(\theta)$  is called the BPA function of  $\Theta$ . If  $m(\theta) > 0$ ,  $\theta$  is called a focal element.

In this paper, let the frame of discernment is  $\Theta = \{\theta_1, \theta_2\}$ ,  $\theta_1 = \text{Excellent}$ , and  $\theta_2 = \text{Non-excellent}$ , which represents the answer of “Is the alternative  $a_k$  excellent or not on criterion  $c_j$  for experts  $E_i$ ?”. In order to obtain the evaluation information of three types of experts within the same framework of discernment  $\Theta$ , we assume that the choice of  $e_s^i$  with respect to criterion  $c_j$  on alternative  $a_k$  is  $\theta_{s \rightarrow n}^i$ . For example, if  $e_s^i$  thinks

that the alternative  $a_k$  is excellent on criterion  $c_j$ , then  $\theta_{s \rightarrow n}^i = \theta_1$ ; if  $e_s^i$  could not give any evaluation information on the performance of  $a_k$  on criterion  $c_j$ , then  $\theta_{s \rightarrow n}^i = \Theta = \{\theta_1, \theta_2\}$ .

Suppose  $\bar{\theta}_{s \rightarrow n}^i$  is the complementary set of  $\theta_{s \rightarrow n}^i$ , and we use  $\theta_{s \rightarrow n}^i$  and  $\bar{\theta}_{s \rightarrow n}^i$  to define the discriminant function  $f_{s \rightarrow n}^i$  of the performance of  $a_k$  on criterion  $c_j$ , so we can obtain the degree of belief of alternative  $a_k$  evaluated by experts  $E_i$  with respect to criterion  $c_j$ , expressed as  $m_{i,j}^k$ . The calculation methods of  $f_{s \rightarrow n}^i$  and  $m_{i,j}^k$  are shown as

$$m_{i,j}^{k,n}(\theta) = \sum_{s=1}^{I_i} \frac{f_{s \rightarrow n}^i(\theta)}{I_i}, \quad (2)$$

where  $f_{s \rightarrow n}^i(\theta) = \{1, \theta = \theta_{s \rightarrow n}^i; 0, \theta = \bar{\theta}_{s \rightarrow n}^i\}$ ,  $\theta \subseteq \Theta$ , and  $m_{i,j}^{k,\theta_1} + m_{i,j}^{k,\theta_2} + m_{i,j}^{k,\Theta} = 1$ .

When  $\theta \subset \Theta$  and  $\theta \neq \forall \theta_n$ ,  $m_{i,j}^{k,\theta}$  reflects the degree of local ignorance; when  $\theta = \Theta$ ,  $m_{i,j}^{k,\Theta}$  reflects the degree of global ignorance. In particular, when  $m_{i,j}^{k,\Theta} = 1$ ,  $m_{i,j}^{k,\theta_1} = m_{i,j}^{k,\theta_2} = 0$ , which means that the experts  $E_i$  do not give any evaluation information on the performance of  $a_k$  on criterion  $c_j$ .

**3.2. Weight Determination Method for Three Types of Experts.** Because of the differences in knowledge structure and value orientation, the weights of the three types of experts on a criterion are different [47]. Weight is the subjectively relative importance degree of an expert to another with respect to a criterion and usually can be determined by some computing methods such as Analytic Hierarchy Process (AHP) and Analytic Network Process (ANP). In this paper, we suggest using AHP method to determine the weights of three experts on a criterion. Three types of experts are compared two by two, thus the judgment matrix is constructed [48]. The relative importance of each expert is obtained through normalization and a series of calculation steps. The weight of experts  $E_i$  on criterion  $c_j$  can be expressed as  $w_{ij}$ ,  $w_{ij} \geq 0$ ,  $\sum_{i=1}^3 w_{ij} = 1$ ,  $\forall j$ .

In addition, in order to ensure that the evaluation information is more scientific and reasonable, the weight of each criterion should also be considered. We also suggest using AHP method to determine the weights of each criterion, which can be expressed as  $w_j$ ,  $w_j \geq 0$ ,  $\sum_{j=1}^4 w_j = 1$ .

**3.3. Information Combination Method.** In this paper, Dempster's combination rule is used to combine the derived BPA functions for two times. The first time is to combine BPA functions on all criteria with respect to the specified experts  $E_i$ , so we can obtain the overall evaluation value for alternative  $a_k$  on all criteria given by experts  $E_i$  (called individual combination). The second time is to combine the combined BPAs for all experts with respect to a specified alternative  $a_k$ , so we can obtain the overall evaluation value for alternative  $a_k$  for all experts (called group combination).

Due to the weight of each criterion and the weight of various experts on each criterion being different, in order

to ensure the authenticity of evidence sources, we adopt the Shafer's discounting method to discount the obtained BPA function  $m_{i,j}^k$ , and the discounting method is shown in

$$m_{i,j}^{k,w} = \begin{cases} 0 & \theta = \emptyset \\ w_j w_{ij} m_{i,j}^{k,\theta} & \theta \subset \Theta \\ w_j w_{ij} m(\theta) + 1 - w_j w_{ij} & \theta = \Theta \end{cases} \quad (3)$$

After making the Shafer's discounting,  $m_{i,j}^{k,w}$  is integrated with the weight of each criterion and the weight of each type of expert, and then Dempster's combination rule can be used to make companion. Dempster's combination rule can be expressed as

$$\begin{aligned} m(\theta) &= [m_1(\theta_A) \oplus m_2(\theta_B)] \\ &= \frac{1}{1-K} \sum_{\theta_A \cap \theta_B = \theta} m_1(\theta_A) m_2(\theta_B) \end{aligned} \quad (4)$$

with  $K = \sum_{\theta_A \cap \theta_B = \emptyset} m_1(\theta_A) m_2(\theta_B)$ , where  $\theta$ ,  $\theta_A$ , and  $\theta_B$  are subsets of  $\Theta$ ,  $\oplus$  is the orthogonal sum operator, and  $K$  is a normalization constant, called the conflict coefficient of two BPAs

Through the first combination, we can get the comprehensive evaluation value of experts  $E_i$  on all criteria of alternative  $a_k$ , that is,  $m_i^k$ . Then Dempster's combination rule is used again to combine the combined BPA functions  $m_i^k$ . Obviously, the combination process can be represented as  $m_1^k \oplus m_2^k \oplus m_3^k = m_k$ , so we can obtain the overall evaluation value for alternative  $a_k$  for all experts, expressed as  $m_k$ .

**3.4. Method Steps.** The steps of mass collaboration-driven method for recommending product ideas based on the DST are as follows.

*Step 1.* Identify alternative ideas. In the mass collaboration mode, the product ideas are identified by various participants based on product innovation requirements. A set of ideas can be expressed as  $A = \{a_k \mid k = 1, \dots, K\}$ , and the main purpose of this paper is to rank them.

*Step 2.* Set decision parameters. Suppose a set of criteria is expressed as  $C = \{c_j \mid j = 1, \dots, 4\}$ , a set of three types of experts is expressed as  $E = \{E_i \mid i = 1, 2, 3\}$ , a set of grades is expressed as  $\Theta = \{\theta_1, \theta_2\}$ , a set of utilities for grades is expressed as  $U = \{0 \leq u_1 \leq u_2 \leq 1\}$ , a set of weights of experts' type is expressed as  $W_{ij} = \{w_{ij} \mid w_{ij} \geq 0; \sum_{i=1}^3 w_{ij} = 1, \forall j\}$ , and a set of weights of criteria is expressed as  $W_j = \{w_j \mid w_j \geq 0; \sum_{j=1}^4 w_j = 1\}$ .

*Step 3.* Select the first idea. Let  $k=1$  and take  $a_1$  as the initial evaluation idea to be evaluated.

*Step 4.* Expert evaluation. In the mass collaboration mode, three kinds of experts, internal members of the enterprises,

current users, and potential users, can evaluate the various attributes of existing ideas. The evaluation value of alternative  $a_k$  evaluated by experts  $E_i$  with respect to criterion  $c_j$  can be expressed as  $m_{i,j}^k = \{(\theta, m_{i,j}^{k,\theta}) \mid \theta \in \Theta, \sum_{\theta \in \Theta} m_{i,j}^{k,\theta} = 1\}$ ,  $\forall i, j, k$ .

*Step 5.* Make individual combination. Taking the specific experts  $E_i$  as the combination target, based on  $w_{ij}$  and  $w_j$ , Shafer's discounting is used to discount  $m_{i,j}^k$  and get the discounted BPA functions  $m_{i,j}^{k,w}$ . Then Dempster's combination rule is used to combine  $m_{i,j}^{k,w}$  and we get the comprehensive evaluation value of experts  $E_i$  on all criteria of alternative  $a_k$ , expressed as  $m_i^k$ .

*Step 6.* Make group combination. Taking all experts as the combination target, Dempster's combination rule is used to combine  $m_i^k$ , and we get the overall evaluation value for alternative  $a_k$  for all experts, expressed as  $m_k$ .

*Step 7.* Determine probability distribution. The BPA functions  $m_k$  obtained by Step 6 are converted to the form of probability distribution by the Pignistic probability. So we can obtain

$$p_n^k = Bel_k(\theta_n) + \varepsilon_k \cdot Pl_k(\theta_n), \quad n = 1, 2, \quad (5)$$

where  $Bel_k(\theta_n) = \sum_{X \subseteq \theta_n} m_k(X)$  is the concept of belief,  $Pl_k(\theta_n) = \sum_{\theta_n \cap X \neq \emptyset} m_k(X)$  is the concept of plausibility, and  $\varepsilon_k = [1 - \sum_{\theta_n \in \Theta} Bel_n(\theta_n)] / \sum_{\theta_n \in \Theta} Pl_k(\theta_n)$ .

*Step 8.* Change the alternative idea. Let  $k=k+1$ ; if  $k \leq K$ , it means taking  $a_k$  as the current evaluation idea, and going back to Step 4; if  $k > K$ , it indicates that the combination of all the ideas has been completed and going to Step 9.

*Step 9.* Rank alternatives. By combining grade with probability, we can get the probability distribution of the overall value of  $a_k$ , which can be expressed as  $P_k = \{(\theta_n, p_n^k) \mid n = 1, 2\}$ ,  $k = 1, \dots, K$ . According to the rank utility and the expected utility theory, the total utility of  $a_k$  is calculated as

$$U_k = \sum_n u_n p_n^k, \quad k = 1, \dots, K \quad (6)$$

The greater the total utility  $U_k$  is, the better  $a_k$  is. Then we can get the rank of all the ideas.

#### 4. Illustrative Example

HUAWEI Technologies is a private high-tech firm based in Shenzhen, China, focusing on the provision of next generation telecommunications networks. Huawei is committed to providing Internet-protocol (IP)-based fixed & mobile communication (FMC) solutions to ensure that end users are able to experience consistent communication services at anytime, anywhere. HUAWEI's vision is "to enrich life through communication," and its mission is to "to focus on

our customers' market challenges and needs by providing excellent communications network solutions and services in order to consistently create maximum value for customers." HUAWEI focuses on "user perception" and has established a close cooperative relationship with more than 30 telecom operators, industry alliances and institutions, vertical industry leaders, and so on. In order to give full play to the wisdom of group users, HUAWEI set up HUAWEI interactive community on the official website to encourage the majority of participants to participate in the platform exchange. It aims at providing a platform for direct communication with users, collecting users' opinions and needs, allowing users to define the next product of HUAWEI, discussing and communicating in circles in the form of a community, providing a rich data document, and allowing users to release their opinions on the platform. As a result, HUAWEI can receive a lot of product ideas, but how to select effective product ideas among a large number of product ideas with low value density is an urgent problem to be solved. This paper takes HUAWEI innovation as the background, and assumes that there are several product ideas, which can be evaluated by three types of experts: internal members of enterprise, current users, and potential users, so as to illustrate the decision making process of the proposed method.

In August, 2018, HUAWEI interactive community Managers released a post entitled "What new APP features do you want? Say it, and win M3 panel computer!". All participants can respond to this post, either by presenting new ideas, or by evaluating existing ones. This post is valid for one month. In the meantime, the enterprise received 45 ideas and needed to rank these ideas for easy selection. In this paper, we take 3 ideas as the representative to introduce the ranking process of ideas. So, the set of ideas can be expressed as  $A = \{a_k \mid k = 1, 2, 3\}$ ,  $a_1$ = Change the theme color of APP according to the color of cell phone shell,  $a_2$ = Home service center makes a manageable-sorted look, and  $a_3$ = Add automatic save draft function.

This paper proposes the following assumptions: (a) there are 300, 500 and 200 individuals in three types of experts, namely,  $E_1$ = *Internal members of the enterprise*,  $E_2$ =*Current users*,  $E_3$ = *Potential users*; (b) there are four criteria  $c_1$ = *Novelty*,  $c_2$ = *Acceptability*, and  $c_3$ = *Usefulness*,  $c_4$ = *Feasibility*; (c) the weights of the four criteria are assumed to be 0.17, 0.28, 0.26, 0.29; (d) on criterion  $c_1$ , the weights of three types of experts are assumed to be 0.2, 0.4, and 0.4; on criterion  $c_2$ , the weights of three types of experts are assumed to be 0.3, 0.4, and 0.3; On criterion  $c_3$ , the weights of three types of experts are assumed to be 0.2, 0.5, and 0.3; On criterion  $c_4$ , the weights of three types of experts are 0.4, 0.3, and 0.3; (e) the evaluation set of grades can be expressed as  $\Theta = \{\theta_1, \theta_2\}$ ,  $\theta_1$ =*Excellent*, and  $\theta_2$ =*Non-excellent*, which represents that each expert is asked by the question "Is the alternative  $a_k$  excellent or not on criterion  $c_j$ ?", and the utility of each grade is set as  $u_1 = 1$ ,  $u_2 = 0$ . In this paper, the evaluation information of the 1000 experts on alternative  $a_k$  is obtained through simulation, as shown in Table 2.

The numbers in Table 2 indicate the number of individuals in  $E_i$  who think alternative  $a_k$  is excellent, nonexcellent, or

TABLE 2: Evaluation information of all experts.

		Criterion $c_1$			Criterion $c_2$			Criterion $c_3$			Criterion $c_4$		
		$\theta_1$	$\theta_2$	$\Theta$									
$E_1$	$a_1$	90	210	0	180	90	30	60	240	0	90	120	90
	$a_2$	120	120	60	210	60	30	150	90	60	60	210	30
	$a_3$	90	180	30	150	90	60	210	60	30	150	60	90
$E_2$	$a_1$	200	250	50	150	350	0	250	50	200	350	50	100
	$a_2$	450	50	0	150	250	100	350	50	100	250	100	150
	$a_3$	150	350	0	150	300	50	350	100	50	250	150	100
$E_3$	$a_1$	180	0	20	100	100	0	140	40	20	80	60	60
	$a_2$	60	80	60	100	60	40	80	120	0	40	140	20
	$a_3$	100	80	20	120	60	20	140	40	20	80	120	0

TABLE 3: BPA functions for all experts.

		Criterion $c_1$			Criterion $c_2$			Criterion $c_3$			Criterion $c_4$		
		$\theta_1$	$\theta_2$	$\Theta$									
$E_1$	$a_1$	0.3000	0.7000	0.0000	0.6000	0.3000	0.1000	0.2000	0.8000	0.0000	0.3000	0.4000	0.3000
	$a_2$	0.4000	0.4000	0.2000	0.7000	0.2000	0.1000	0.5000	0.3000	0.2000	0.2000	0.7000	0.1000
	$a_3$	0.3000	0.6000	0.1000	0.5000	0.3000	0.2000	0.7000	0.2000	0.1000	0.5000	0.2000	0.3000
$E_2$	$a_1$	0.4000	0.5000	0.1000	0.3000	0.7000	0.0000	0.5000	0.1000	0.4000	0.7000	0.1000	0.2000
	$a_2$	0.9000	0.1000	0.0000	0.3000	0.5000	0.2000	0.7000	0.1000	0.2000	0.5000	0.2000	0.3000
	$a_3$	0.3000	0.7000	0.0000	0.3000	0.6000	0.1000	0.7000	0.2000	0.1000	0.5000	0.3000	0.2000
$E_3$	$a_1$	0.9000	0.0000	0.1000	0.5000	0.5000	0.0000	0.7000	0.2000	0.1000	0.4000	0.3000	0.3000
	$a_2$	0.3000	0.4000	0.3000	0.5000	0.3000	0.2000	0.4000	0.6000	0.0000	0.2000	0.7000	0.1000
	$a_3$	0.5000	0.4000	0.1000	0.6000	0.3000	0.1000	0.7000	0.2000	0.1000	0.4000	0.6000	0.0000

TABLE 4: Discounted BPA functions.

		Criterion $c_1$			Criterion $c_2$			Criterion $c_3$			Criterion $c_4$		
		$\theta_1$	$\theta_2$	$\Theta$									
$E_1$	$a_1$	0.0102	0.0238	0.9660	0.0504	0.0252	0.9244	0.0104	0.0416	0.9480	0.0348	0.0464	0.9188
	$a_2$	0.0136	0.0136	0.9728	0.0588	0.0168	0.9244	0.0260	0.0156	0.9584	0.0232	0.0812	0.8956
	$a_3$	0.0102	0.0204	0.9694	0.0420	0.0252	0.9328	0.0364	0.0104	0.9532	0.0580	0.0232	0.9188
$E_2$	$a_1$	0.0272	0.0340	0.9388	0.0336	0.0784	0.8880	0.0650	0.0130	0.9220	0.0609	0.0087	0.9304
	$a_2$	0.0612	0.0068	0.9320	0.0336	0.0560	0.9104	0.0910	0.0130	0.8960	0.0435	0.0174	0.9391
	$a_3$	0.0204	0.0476	0.9320	0.0336	0.0672	0.8992	0.0910	0.0260	0.8830	0.0435	0.0261	0.9304
$E_3$	$a_1$	0.0612	0.0000	0.9388	0.0420	0.0420	0.9160	0.0546	0.0156	0.9298	0.0348	0.0261	0.9391
	$a_2$	0.0204	0.0272	0.9524	0.0420	0.0252	0.9328	0.0312	0.0468	0.9220	0.0174	0.0609	0.9217
	$a_3$	0.0340	0.0272	0.9388	0.0504	0.0252	0.9244	0.0546	0.0156	0.9298	0.0348	0.0522	0.9130

uncertain on criterion  $c_j$ . Combined with Table 2, the evaluation information can be transformed into BPA functions  $m_{i,j}^k$  by (2), which are shown in Table 3.

The evaluation value of alternative  $a_k$  evaluated by experts  $E_i$  with respect to criterion  $c_j$  is shown in Table 3, expressed as  $m_{i,j}^k$ . The weights of each criterion and the weights of experts on each criterion are substituted into (3), and the Shafer's discounting is used to discount  $m_{i,j}^k$ , so the BPA functions  $m_{i,j}^{k,w}$  discounted by weight can be obtained. The discounted BPA functions are shown in Table 4.

According to Dempster's combination rule, we use (4) to combine the discounted BPA functions  $m_{i,j}^{k,w}$ . For the

first time of combination, we can get the comprehensive evaluation value of experts  $E_i$  on all criteria of alternative  $a_k$ , expressed as  $m_i^k$ . Then, using Dempster's combination rule to combine  $m_i^k$  again, we can get the overall evaluation value for alternative  $a_k$  for all experts, expressed as  $m_k$ . By substituting  $m_k$  in (5), we can get the probability distribution of comprehensive performance at all grades of alternative  $a_k$  (see the 2-3 columns of Table 5). By substituting grade utility  $u_1 = 1, u_2 = 0$  and probability distribution into (6), we can calculate the total utility  $U_k$  of alternative  $a_k$  (see the 4<sup>th</sup> column of Table 5). According to the total utility  $U_k$ , we can know that the ranking is  $a_3 > a_1 > a_2$ .

TABLE 5: Probability distribution and utility.

Alternative ideas	Grades		Utility
	$\theta_1$	$\theta_2$	
$a_1$	0.5490	0.4510	0.5490
$a_2$	0.5310	0.4690	0.5310
$a_3$	0.5540	0.4460	0.5540

## 5. Conclusions

In the mass collaboration mode, the large number of ideas and participates leads to the existing methods which are not suitable for solving the problem of product idea evaluation. In this paper, we propose a mass collaboration-driven method for recommending product ideas based on DST. Firstly, the BPA function computing method is introduced by discounting belief degrees with weights to extract the evaluation information of product ideas, which can effectively reflect the facticity of experts' evaluation. Secondly, Dempster's combination rule is used to combine the derived BPA functions for two times: the first one is to combine the discounted BPA functions on all criteria with respect to a specified expert and the other is to combine the combined BPA functions for all experts with respect to a specified alternative. Finally, the steps of mass collaboration-driven method for recommending product ideas based on the DST are proposed. An example is proposed to illustrate the recommendation mechanism by the proposed method. The main contribution of this paper is that the DST is innovatively introduced to solve the problem of recommending product ideas in the mass collaboration mode, in which each participant can expediently give real assessments with his/her experiences and their assessments can be reasonably combined with Dempster's rule. It is worth noting that this paper only proposes the mass collaboration-driven method for recommending product ideas from the static combination perspective but does not consider the dynamic interaction. As a result, studying the dynamic interaction recommendation problem for the product ideas in the mass collaboration mode will be the next research direction.

## Data Availability

The data used to support the findings of this study are available from the corresponding author upon request.

## Conflicts of Interest

The authors declare that there are no conflicts of interest regarding the publication of this paper.

## Acknowledgments

This research was supported by the National Natural Science Foundation of China (NSFC) under Grant Nos. 71874167 and 71462022, the Fundamental Research Funds for the Central Universities under Grant No. 201762026, and the Special

Funds of Taishan Scholars Project of Shandong Province under Grant No. tsqn20171205.

## References

- [1] T. M. Amabile, "The social psychology of creativity: A componential conceptualization," *Journal of Personality and Social Psychology*, vol. 45, no. 2, pp. 357–376, 1983.
- [2] M. D. Mumford and S. B. Gustafson, "Creativity Syndrome: Integration, Application, and Innovation," *Psychological Bulletin*, vol. 103, no. 1, pp. 27–43, 1988.
- [3] M. A. Runco and G. J. Jaeger, "The Standard Definition of Creativity," *Creativity Research Journal*, vol. 24, no. 1, pp. 92–96, 2012.
- [4] J.-R. Chou, "An ideation method for generating new product ideas using TRIZ, concept mapping, and fuzzy linguistic evaluation techniques," *Advanced Engineering Informatics*, vol. 28, no. 4, pp. 441–454, 2014.
- [5] S. A. Kazmi, M. Naarananoja, and J. K. Wartsila, "Identifying Dissimilarities among Global Teams while Pursuing New Product Idea Generation Practices," *Procedia - Social and Behavioral Sciences*, vol. 229, pp. 376–386, 2016.
- [6] M. Banović, A. Krystallis, L. Guerrero, and M. J. Reinders, "Consumers as co-creators of new product ideas: An application of projective and creative research techniques," *Food Research International*, vol. 87, pp. 211–223, 2016.
- [7] K. Shroyer, T. Lovins, J. Turns, M. E. Cardella, and C. J. Atman, "Timescales and ideaspaces: An examination of idea generation in design practice," *Design Studies*, vol. 57, pp. 9–36, 2018.
- [8] T. Gillier, C. Chaffois, M. Belkhouja, Y. Roth, and B. L. Bayus, "The effects of task instructions in crowdsourcing innovative ideas," *Technological Forecasting & Social Change*, vol. 134, pp. 35–44, 2018.
- [9] H. Kwon, Y. Park, and Y. Geum, "Toward data-driven idea generation: Application of Wikipedia to morphological analysis," *Technological Forecasting & Social Change*, vol. 132, pp. 56–80, 2018.
- [10] M. A. Mirtalaie, O. K. Hussain, E. Chang, and F. K. Hussain, "A decision support framework for identifying novel ideas in new product development from cross-domain analysis," *Information Systems*, vol. 69, pp. 59–80, 2017.
- [11] L. M. Steele, G. Johnson, and K. E. Medeiros, "Looking beyond the generation of creative ideas: Confidence in evaluating ideas predicts creative outcomes," *Personality and Individual Differences*, vol. 125, pp. 21–29, 2018.
- [12] A. Özyaygen and C. Balagué, "Idea evaluation in innovation contest platforms: A network perspective," *Decision Support Systems*, vol. 112, pp. 15–22, 2018.
- [13] N. Hao, Y. Ku, M. Liu et al., "Reflection enhances creativity: Beneficial effects of idea evaluation on idea generation," *Brain and Cognition*, vol. 103, pp. 30–37, 2016.

- [14] N. Maysseles, J. Aharon-Peretz, and S. Shamay-Tsoory, "Unleashing creativity: The role of left temporoparietal regions in evaluating and inhibiting the generation of creative ideas," *Neuropsychologia*, vol. 64, pp. 157–168, 2014.
- [15] S. Hoornaert, M. Ballings, E. C. Malthouse, and D. Van den Poel, "Identifying New Product Ideas: Waiting for the Wisdom of the Crowd or Screening Ideas in Real Time," *Journal of Product Innovation Management*, vol. 34, no. 5, pp. 580–597, 2017.
- [16] S. Zeng, J. Gonzalez, and C. Lobato, "The effect of organizational learning and Web 2.0 on innovation," *Management Decision*, vol. 53, no. 9, pp. 2060–2072, 2015.
- [17] X.-F. Xu, J. Hao, Y.-R. Deng, and Y. Wang, "Design optimization of resource combination for collaborative logistics network under uncertainty," *Applied Soft Computing*, vol. 56, pp. 684–691, 2017.
- [18] X. Xu, W. Zhang, N. Li, and H. Xu, "A bi-level programming model of resource matching for collaborative logistics network in supply uncertainty environment," *Journal of The Franklin Institute*, vol. 352, no. 9, pp. 3873–3884, 2015.
- [19] E. F. Rietzschel, B. A. Nijstad, and W. Stroebe, "Productivity is not enough: A comparison of interactive and nominal brainstorming groups on idea generation and selection," *Journal of Experimental Social Psychology*, vol. 42, no. 2, pp. 244–251, 2006.
- [20] N. Michinov, E. Jamet, N. Métyayer, and B. Le Hénaff, "The eyes of creativity: Impact of social comparison and individual creativity on performance and attention to others' ideas during electronic brainstorming," *Computers in Human Behavior*, vol. 42, pp. 57–67, 2015.
- [21] D. M. DeRosa, C. L. Smith, and D. A. Hantula, "The medium matters: Mining the long-promised merit of group interaction in creative idea generation tasks in a meta-analysis of the electronic group brainstorming literature," *Computers in Human Behavior*, vol. 23, no. 3, pp. 1549–1581, 2007.
- [22] J. Füller, G. Jaweck, and H. Mühlbacher, "Innovation creation by online basketball communities," *Journal of Business Research*, vol. 60, no. 1, pp. 60–71, 2006.
- [23] P.-A. Verhaegen, D. Vandevenne, J. Peeters, and J. R. Duflou, "Refinements to the variety metric for idea evaluation," *Design Studies*, vol. 34, no. 2, pp. 243–263, 2013.
- [24] J. A. Plucker, R. A. Beghetto, and G. T. Dow, "Why Isn't Creativity More Important to Educational Psychologists Potentials, Pitfalls, and Future Directions in Creativity Research," *Journal of Educational Psychology*, vol. 39, no. 2, pp. 83–96, 2004.
- [25] S. L. Chan, W. H. Ip, and C. K. Kwong, "Closing the loop between design and market for new product idea screening decisions," *Expert Systems with Applications*, vol. 38, no. 6, pp. 7729–7737, 2011.
- [26] E. F. Rietzschel, B. A. Nijstad, and W. Stroebe, "The selection of creative ideas after individual idea generation: Choosing between creativity and impact," *British Journal of Psychology*, vol. 101, no. 1, pp. 47–68, 2010.
- [27] J. Diedrich, M. Benedek, E. Jauk, and A. C. Neubauer, "Are creative ideas novel and useful?" *Psychology of Aesthetics, Creativity, and the Arts*, vol. 9, no. 1, pp. 35–40, 2015.
- [28] S. Schwarz and F. Bodendorf, "Attributive Idea Evaluation," *International Journal of Knowledge-Based Organizations*, vol. 2, no. 1, pp. 77–91, 2012.
- [29] S. Hart, E. J. Hultink, N. Tzokas, and H. R. Commandeur, "Industrial companies' evaluation criteria in new product development gates," *Journal of Product Innovation Management*, vol. 20, no. 1, pp. 22–36, 2003.
- [30] K. R. MacCrimmon and C. Wagner, "Stimulating ideas through creativity software," *Management Science*, vol. 40, no. 11, pp. 1514–1532, 1994.
- [31] P. Carbonell-Foulquié, J. L. Munuera-Alemán, and A. I. Rddríguez-Escudero, "Criteria employed for go/no-go decisions when developing successful highly innovative products," *Industrial Marketing Management*, vol. 33, no. 4, pp. 307–316, 2004.
- [32] D. Dean, J. Hender, T. Rodgers, and E. Santanen, "Identifying Quality, Novel, and Creative Ideas: Constructs and Scales for Idea Evaluation," *Journal of the Association for Information Systems*, vol. 7, no. 10, pp. 646–699, 2006.
- [33] E. Hietikko, "A Two Dimensional Matrix Presentation for Idea Evaluation," *International Journal of Engineering Research and Applications*, vol. 3, pp. 1673–1676, 2013.
- [34] K. Eling, F. Langerak, and A. Griffin, "The Performance Effects of Combining Rationality and Intuition in Making Early New Product Idea Evaluation Decisions," *Creativity and Innovation Management*, vol. 24, no. 3, pp. 464–477, 2015.
- [35] G. Lauto and F. Valentin, "How preference markets assist new product idea screening," *Industrial Management & Data Systems*, vol. 116, no. 3, pp. 603–619, 2016.
- [36] M. Ferioli, E. Dekoninck, S. Culley, B. Roussel, and J. Renaud, "Understanding the rapid evaluation of innovative ideas in the early stages of design," *International Journal of Product Development*, vol. 12, no. 1, pp. 67–83, 2010.
- [37] E. Gutierrez, I. Kihlander, and J. Eriksson, "What's a good idea? Understanding evaluation and selection of new product ideas," in *Proceedings of the International Conference on Engineering Design Stanford*, pp. 121–132, USA, 2009.
- [38] G. S. Mitra Thakur, R. Bhattacharyya, and S. Sarkar Mondal, "Stock portfolio selection using Dempster-Shafer evidence theory," *Journal of King Saud University - Computer and Information Sciences*, vol. 30, no. 2, pp. 223–235, 2018.
- [39] C. Zhang, Y. Hu, F. T. Chan, R. Sadiq, and Y. Deng, "A new method to determine basic probability assignment using core samples," *Knowledge-Based Systems*, vol. 69, pp. 140–149, 2014.
- [40] S. Zeng and Y. Xiao, "A method based on topsis and distance measures for hesitant fuzzy multiple attribute decision making," *Technological and Economic Development of Economy*, vol. 24, no. 3, pp. 969–983, 2018.
- [41] S. Zeng, Z. Mu, and T. Baležentis, "A novel aggregation method for Pythagorean fuzzy multiple attribute group decision making," *International Journal of Intelligent Systems*, vol. 33, no. 3, pp. 573–585, 2018.
- [42] S. Zeng, "Pythagorean fuzzy multiattribute group decision making with probabilistic information and OWA approach," *International Journal of Intelligent Systems*, vol. 32, no. 11, pp. 1136–1150, 2017.
- [43] Y. Du, Y. Wang, and M. Qin, "New evidential reasoning rule with both weight and reliability for evidence combination," *Computers & Industrial Engineering*, vol. 124, pp. 493–508, 2018.
- [44] X. Deng, Q. Liu, Y. Deng, and S. Mahadevan, "An improved method to construct basic probability assignment based on the confusion matrix for classification problem," *Information Sciences*, vol. 340–341, pp. 250–261, 2016.
- [45] Y.-W. Du and W.-M. Xu, "Multiattribute group decision making based on interval-valued intuitionistic fuzzy sets and analytically evidential reasoning methodology," *Journal of Intelligent & Fuzzy Systems: Applications in Engineering and Technology*, vol. 33, no. 5, pp. 2953–2960, 2017.

- [46] Y.-W. Du and Y.-M. Wang, "Evidence combination rule with contrary support in the evidential reasoning approach," *Expert Systems with Applications*, vol. 88, pp. 193–204, 2017.
- [47] Y. Du, N. Yang, and J. Ning, "IFS/ER-based large-scale multiattribute group decision-making method by considering expert knowledge structure," *Knowledge-Based Systems*, 2018.
- [48] A. Gnanavelbabu and P. Arunagiri, "Ranking of MUDA using AHP and Fuzzy AHP algorithm," *Materials Today: Proceedings*, vol. 5, no. 5, pp. 13406–13412, 2018.

## Research Article

# Decision-Maker's Risk Preference Based Intuitionistic Fuzzy Multiattribute Decision-Making and Its Application in Robot Enterprises Investment

Liandong Zhou  and Qifeng Wang 

*Logistics and E-Commerce College, Zhejiang Wanli University, Ningbo 315100, China*

Correspondence should be addressed to Qifeng Wang; [lhywqf@163.com](mailto:lhywqf@163.com)

Received 29 June 2018; Accepted 4 September 2018; Published 24 September 2018

Guest Editor: Carlos Llopis-Albert

Copyright © 2018 Liandong Zhou and Qifeng Wang. This is an open access article distributed under the Creative Commons Attribution License, which permits unrestricted use, distribution, and reproduction in any medium, provided the original work is properly cited.

At present, the utilization of hesitation information of intuitionistic fuzzy numbers is insufficient in many methods which were proposed to solve the intuitionistic fuzzy multiple attribute decision-making problems. And also there exist some flaws in the intuitionistic fuzzy weight vector constructions in many research papers. In order to solve these insufficiencies, this paper defined three construction equations of weight vectors based on the risk preferences of decision-makers. Then we developed an intuitionistic fuzzy dependent hybrid weighted operator (IFDHW) and proposed an intuitionistic fuzzy multiattribute decision-making method. Finally, the effectiveness of this method is verified by a robot manufacturing investment example.

## 1. Introduction

In 1986, the fuzzy theory of Zadeh [1] was extended to the intuitionistic fuzzy theory by Atanassov [2]. Intuitionistic fuzzy sets contain three parts: membership, nonmembership, and hesitation. With these three parts, intuitionistic fuzzy sets (IFSs) can describe the fuzzy nature world better than the traditional fuzzy sets.

Researchers have made great achievements in the study of intuitionistic fuzzy information aggregation. By using the IFS which are characterized by a membership function and nonmembership functions, Xu [3, 4] developed intuitionistic fuzzy weighted averaging (IFWA) operator, intuitionistic fuzzy ordered weighted averaging (IFOWA) operator, and intuitionistic fuzzy hybrid aggregation (IFHA) operator. S Zeng [5] considered the probabilities and the OWA in the same formulation and proposed the Pythagorean fuzzy probabilistic ordered weighted averaging (PFPOWA) operator. Over the past decades, researchers have developed many operators to solve the multiple attribute group decision-making (MAGDM) problems. Wei [6] proposed induced intuitionistic fuzzy ordered weighted geometric (I-IFOWG) operator and induced interval-valued intuitionistic

fuzzy ordered weighted geometric (I-IIFOWG) to solve the MAGDM problems. Su et al. [7] extended the induced generalized ordered weighted averaging (IGOWA) operator and developed induced generalized intuitionistic fuzzy ordered weighted averaging (IG-IFOWA) operator. Zeng et al. [8] considered both ordered weighted average operator and induced ordered weighted average and proposed pythagorean fuzzy induced ordered weighted averaging weighted average (PFIOAWA) operator for MAGDM. Combining intuitionistic fuzzy operators and TOPSIS method together, many multiattribute decision-making (MADM) methods have been developed [9–11]. Based on the TOPSIS method, intuitionistic fuzzy VIKOR methods were introduced [12, 13] and the problem of choosing the best alternative due to the incommensurability between attributes had been well solved. Chatterjee et al. [14] integrated the Analytic Hierarchy Process and the VIKOR compromise-ranking method together and constructed a flexible multicriteria decision-making (MCDM) framework. Huang et al. [15] extend the VIKOR method to MAGDM with interval neutrosophic numbers (INNs). Meng et al. [16] introduced the prospect theory into MADM with interval-valued intuitionistic fuzzy information. Qin et al. [17] proposed a decision-making

model by integrating VIKOR method and prospect theory. Xie et al. [18] applied prospect theory and grey relational analysis to stochastic decision-making. Li et al. [19] aggregated the decision-making information in different natural states by using the prospect theory.

Although there are many research achievements on intuitionistic fuzzy information aggregation and methods for solving MADM and MAGDM problems, there are still some drawbacks and research gaps for further research:

(1) Intuitionistic fuzzy numbers (IFNs) contain three parts: membership, nonmembership, and hesitation. Therefore, when using the aggregation operator to rank IFNs, these three aspects should be taken into account simultaneously. But most of the existing aggregation operators are only concerned about two parts: membership and nonmembership. The uncertainty (hesitation degree) of IFNs is often ignored.

(2) In the process of MADM, common aggregation operators often assume that attributes are independent from each other. Xu [20] proposed a weighting method based on normal distribution. The characteristic of this method is giving a smaller weight to the data that is too high or too low; therefore the effect of larger deviations on integration results can be eliminated as much as possible. However, there is a flaw in this method, the weight is independent of the data which to be integrated and cannot reflect the relationship between data. If the interaction factors of attributes are taken into account in the aggregation operators, decision-makers will be assisted to obtain more accurate decision results.

(3) The existing weight determination methods are mostly focused on subjective weighting [21]. Some objective weight determination methods need to solve the linear or non-linear programming model [22, 23]. And computation of these methods is relatively cumbersome and is not suitable for decision-making problems with lots of alternatives and attributes.

(4) Recently, researchers made some progresses in decision-making with risk preferences. Adding risk preferences can affect the decision-maker's psychological factors into the decision-making process. That can reduce the error of decision results and improve the quality of the decision-making. Liu, J. et al. [24] proposed a new model involved risk preferences of decision-makers based on the prospect theory and criteria reduction. Wan et al. [25] developed a new method with interval-valued intuitionistic fuzzy preference relations for solving group decision-making problems. Y. Lin et al. [26] developed a method to determine relative weights of decision-makers depending on preference information. However, the most existing research on risk preferences focuses on priority weights and less researches from the perspective of decision-maker's attitude.

(5) Recently, IFS has been applied to many decision-making fields, such as supplier selection [10, 27, 28] and pattern recognition [29–31]. But there is no application in robot enterprises investment field.

Considering all the problems listed above, this paper focused on the study of intuitionistic fuzzy multiattribute decision-making with decision-makers' different attitudes. And in order to give decision-makers most desirable results, we combined intuitionistic fuzzy theory and risk preference

partition theory which is from expected utility theory. In risk preference partition theory, the risk preference attitude of decision-makers can be divided into three categories: risk proneness, risk aversion, and risk neutralness. Then we defined the weight vectors equations according to the attitudes of decision-makers based on the three parts of IFNs. They're objective weights and easy to be calculated. By taking interaction factors of attributes into account, we defined the intuitionistic fuzzy dependent hybrid weighted operator and proposed a decision-making method. The effectiveness of this method is verified by a robot enterprises investment example.

## 2. Preliminaries

Atanassov [1] introduced nonmembership to the Zadeh fuzzy sets (FS)[2] and defined IFS, shown as follows.

*Definition 1.*  $X = \{x_1, x_2, \dots, x_n\}$  is an universe of discourse; then

$$A = \{\langle x, \mu_A(x), \nu_A(x) \rangle \mid x \in X\} \quad (1)$$

is an IFS, where for each element  $x \in X$ ,  $\mu_A(x) : X \rightarrow [0, 1]$  represents the membership, and  $\nu_A(x) : X \rightarrow [0, 1]$  represents the nonmembership, with the condition satisfying  $0 \leq \mu_A(x) + \nu_A(x) \leq 1, \forall x \in X$ . And  $\pi_A(x) = 1 - \mu_A(x) - \nu_A(x)$  is a degree that characterizes the uncertainty or hesitancy of each element  $x \in X$  in IFS set  $A$ . In particular, if  $\pi_A(x) = 0, \forall x \in X$ , then set  $A$  degenerate into Zadeh fuzzy sets. The membership degree, nonmembership degree, and hesitation degree of the IFS effectively extend the representation ability of classical fuzzy sets. For convenience, we can define  $\alpha = (\mu_\alpha, \nu_\alpha)$  as an IFN, where  $\mu_\alpha \in [0, 1], \nu_\alpha \in [0, 1]$ , and  $\mu_\alpha + \nu_\alpha \leq 1$ . Xu [4] introduced the IFNs operational laws, shown as follows.

*Definition 2.*  $\alpha = (\mu_\alpha, \nu_\alpha)$  and  $\beta = (\mu_\beta, \nu_\beta)$  are two IFNs; then five operational laws are as follows:

$$\bar{\alpha} = (\nu_\alpha, \mu_\alpha), \quad (2)$$

$$\alpha \oplus \beta = (\mu_\alpha + \mu_\beta - \mu_\alpha \mu_\beta, \nu_\alpha \nu_\beta), \quad (3)$$

$$\alpha \otimes \beta = (\mu_\alpha \mu_\beta, \nu_\alpha + \nu_\beta - \nu_\alpha \nu_\beta), \quad (4)$$

$$\lambda \alpha = (1 - (1 - \mu_\alpha)^\lambda, \nu_\alpha^\lambda), \quad \lambda > 0, \quad (5)$$

$$\alpha^\lambda = (\mu_\alpha^\lambda, 1 - (1 - \nu_\alpha)^\lambda), \quad \lambda > 0. \quad (6)$$

Based on operational laws of IFNs above, a weighted averaging operator of IFNs is given by Xu [4].

*Definition 3.*  $\alpha_i = (\mu_i, \nu_i)(i = 1, 2, \dots, n)$  is a set of IFNs, and letting  $\Theta$  be the set of intuitionistic fuzzy numbers, then  $IFWA : \Theta^n \rightarrow \Theta$  is defined as follows:

$$IFWA_\omega(\alpha_1, \alpha_2, \dots, \alpha_n) = \sum_{i=1}^n \omega_i \alpha_i \tag{7}$$

$$= \left( 1 - \prod_{i=1}^n (1 - \mu_i)^{\omega_i}, \prod_{i=1}^n \nu_i^{\omega_i} \right);$$

then  $IFWA$  is called intuitionistic fuzzy weighted averaging operator, where  $\omega = (\omega_1, \omega_2, \dots, \omega_n)^T$  is the weight vector of  $\alpha_i(i = 1, 2, \dots, n)$  with the condition satisfying  $\omega_i \in [0, 1](i = 1, 2, \dots, n), \sum_{i=1}^n \omega_i = 1$ . Obviously, by using the  $IFWA$  operator to aggregate IFNs, the aggregated value is also an IFN. Thus the loss of information is avoided.

### 3. Intuitionistic Fuzzy Dependent Hybrid Weighted Operator

The  $IFWA$  operator only considers the importance of IFNs by using the weight vector, but the risk attitude information inside the IFNs is also very important. In order to exploit the risk attitude information inside the IFNs, we need to introduce similarity degree defined by Xu [32].

*Definition 4.*  $\alpha_1 = (\mu_{\alpha_1}, \nu_{\alpha_1})$  and  $\alpha_2 = (\mu_{\alpha_2}, \nu_{\alpha_2})$  are any two IFNs;  $\bar{\alpha}_2 = (\nu_{\alpha_2}, \mu_{\alpha_2})$  is the complement of  $\alpha_2$ ; then

$$S(\alpha_1, \alpha_2) = \begin{cases} 0.5, & \alpha_1 = \alpha_2 = \bar{\alpha}_2 \\ \frac{d(\alpha_1, \bar{\alpha}_2)}{d(\alpha_1, \bar{\alpha}_2) + d(\alpha_1, \alpha_2)}, & \text{others} \end{cases} \tag{8}$$

is the similarity degree between  $\alpha_1$  and  $\alpha_2$ , where

$$d(\alpha_1, \alpha_2) = \frac{1}{2} (|\mu_{\alpha_1} - \mu_{\alpha_2}| + |\nu_{\alpha_1} - \nu_{\alpha_2}| + |\pi_{\alpha_1} - \pi_{\alpha_2}|) \tag{9}$$

is the standard Hamming distance between  $\alpha_1$  and  $\alpha_2$ .

*Definition 5.*  $\alpha_i = (\mu_i, \nu_i)(i = 1, 2, \dots, n)$  is a set of IFNs; then the average of the IFNs is defined as

$$\alpha = \frac{1}{n} (\alpha_1 \oplus \alpha_2 \oplus \dots \oplus \alpha_n) \tag{10}$$

$$= \left( 1 - \prod_{i=1}^n (1 - \mu_i)^{1/n}, \prod_{i=1}^n \nu_i^{1/n} \right)$$

In order to reflect the preferences of decision-makers, we divide the risk attitude information into three kinds: risk proneness, risk aversion, and risk neutrality. Then we redefine the weight equations to extract risk attitude information that inside the IFNs.

*Definition 6.*  $\alpha_i = (\mu_i, \nu_i)(i = 1, 2, \dots, n)$  is a set of IFNs; then three kinds of risk attitudes are introduced by using different weight equations.

(i) Risk proneness weight equation for  $\alpha_i$  is defined as

$$\omega_i = \frac{\pi_i}{\sum_{i=1}^n \pi_i} \tag{11}$$

with the condition satisfying  $\sum_{i=1}^n \omega_i = 1 (i = 1, 2, \dots, n), \omega_i \in [0, 1]$ . The degree of hesitancy is  $\pi_i = 1 - \mu_i - \nu_i$ . Obviously, the greater the degree of hesitancy, the greater the corresponding weight. Risk proneness decision-makers consider hesitancy as advantage.

(ii) Risk aversion weight equation for  $\alpha_i$  is defined as

$$\omega_i = \frac{1 - \pi_i}{\sum_{i=1}^n (1 - \pi_i)} \tag{12}$$

with the condition satisfying  $\sum_{i=1}^n \omega_i = 1 (i = 1, 2, \dots, n), \omega_i \in [0, 1]$ . Because of  $1 - \pi_i = \mu_i + \nu_i$ , the greater the degree of hesitancy, the smaller the corresponding weight. Risk aversion decision-makers consider hesitancy as disadvantage.

(iii) Risk neutrality weight equation for  $\alpha_i$  is based on similarity degree and average of IFNs, defined as follows:

$$\omega_i = \frac{S(\alpha_{\sigma(i)}, \alpha)}{\sum_{i=1}^n S(\alpha_{\sigma(i)}, \alpha)}, \quad i = 1, 2, \dots, n \tag{13}$$

with the condition satisfying  $\sum_{i=1}^n \omega_i = 1(i = 1, 2, \dots, n), \omega_i \in [0, 1]$ , where  $S(\alpha_{\sigma(i)}, \alpha)$  is the similarity degree between  $\alpha_{\sigma(i)}$  and  $\alpha$  is calculated by (8).  $\alpha$  is the average value of  $\alpha_i$  which is calculated by (10). And  $\alpha_{\sigma(i)}$  is  $i$ th largest of  $\alpha_i$  and with the condition satisfying  $\alpha_{\sigma(i-1)} \geq \alpha_{\sigma(i)}, (i = 1, 2, \dots, n)$ . The weight calculations depend on the membership, nonmembership, and hesitation of IFNs. If the intuitionistic fuzzy value is closer to the average value, the weight value will be greater. If the intuitionistic fuzzy value is far away from the average value, the weight value will be smaller. It can represent the risk neutrality decision-makers' attitude.

In order to aggregate risk attitude information, both the importance of IFNs and the risk factors brought by the hesitation of IFNs should be taken into consideration. We proposed an intuitionistic fuzzy dependent hybrid weighted operator ( $IFDHW$ ), defined as follows.

*Definition 7.*  $\alpha_i = (\mu_i, \nu_i)(i = 1, 2, \dots, n)$  is a set of IFNs, and letting  $\Theta$  be the set of intuitionistic fuzzy numbers, then  $IFDHW : \Theta^n \rightarrow \Theta$  is defined as follows:

$$IFDHW_\omega(\alpha_1, \alpha_2, \dots, \alpha_n) = \sum_{i=1}^n \omega_i \dot{\alpha}_{\sigma(i)} \tag{14}$$

$$= \left( 1 - \prod_{i=1}^n (1 - \mu_i)^{\omega_i}, \prod_{i=1}^n \nu_i^{\omega_i} \right);$$

then  $IFDHW$  is an intuitionistic fuzzy dependent hybrid weighted operator, where  $\dot{\alpha}_i = n\omega_i \alpha_i, \dot{\alpha}_{\sigma(i-1)} \geq \dot{\alpha}_{\sigma(i)}$  for all  $i$  and  $W = (w_1, w_2, \dots, w_n)^T$  is the weight vector of  $\alpha_i$  with the condition  $\sum_{i=1}^n w_i = 1 (i = 1, 2, \dots, n), w_i \in [0, 1]$ .  $n$  is called the balancing coefficient.  $\omega_i$  is decided by decision-makers' three kinds of attitude: risk proneness, risk aversion, and risk neutrality.  $\omega_i$  can be calculated by using (11)-(13).

#### 4. Intuitionistic Fuzzy Multiple Attribute Decision-Making Method Based on Decision-Maker's Risk Attitude

For solving a MADM problem with intuitionistic fuzzy information, let us suppose that  $A = \{A_1, A_2, \dots, A_n\}$  ( $i = 1, 2, \dots, n$ ) is a set of  $n$  alternatives to be selected;  $G = \{G_1, G_2, \dots, G_m\}$  ( $j = 1, 2, \dots, m$ ) is a set of  $m$  attributes and whose weight vector is  $W = (w_1, w_2, \dots, w_m)^T$ , where  $w_j$  is the weight for attribute  $G_j$  with the condition  $\sum_{i=1}^n w_i = 1$  ( $i = 1, 2, \dots, n$ ),  $w_i \in [0, 1]$ .  $D = (\alpha_{ij})_{m \times n} = ((\mu_{ij}, \nu_{ij}))_{m \times n}$  is the decision matrix, where  $\alpha_{ij}$  is provided by decision-maker for alternative  $A_i$  with respect to attribute  $G_j$ .

In the following three steps, we will use the IFDHW operator to solve MADM problems by developing a method based on decision-maker's risk attitude.

*Step 1.* The decision-maker gives the decision matrix  $D = (\alpha_{ij})_{m \times n}$  according to the actual situation with weight vector  $W = (w_1, w_2, \dots, w_m)^T$ . Meanwhile, decision-maker chooses the appropriate risk weight equation to calculate  $w_i$  according to the decision-maker's risk preference.

*Step 2.* Utilize the IFDHW operator and calculate overall values  $r_{A_i}$  for all the alternatives  $A_i$  ( $i = 1, 2, \dots, n$ ) by using (14).

*Step 3.* Based on aggregated value  $r_{A_i}$  for all  $A_i$  ( $i = 1, 2, \dots, n$ ), the score values  $S(\alpha_i)$  are calculated and ranked. The best one(s) of all the alternatives  $A_i$  would be selected.

#### 5. Illustrated Example

There is an investment company who want to invest in one of the robot manufacturing enterprises  $A_i$  ( $i = 1, 2, 3, 4$ ). The investment company has determined five attributes  $G_j$  ( $j = 1, 2, 3, 4, 5$ ) to evaluate the robot manufacturing enterprises: production capacity; technological innovation ability; marketing ability; management ability; risk aversion ability.  $w = (0.25, 0.2, 0.2, 0.1, 0.25)^T$  is the weight vector of these attributes. The intuitionistic fuzzy decision matrix is provided by the company which is listed in Table 1. The investment decision-making steps are shown as follows.

*Step 1.* Using weight equation to calculate alternatives' risk weight vector, we take the one kind of decision-maker's attitude for an example. Using risk proneness weight equation  $w_i = (1 - \mu_i - \nu_i) / \sum_{i=1}^n (1 - \mu_i - \nu_i)$  to calculate four robots manufacturing enterprises' risk weight vector

$$\begin{aligned} \omega_1 &= (0.1667, 0.3333, 0.1667, 0.1667, 0.1667)^T, \\ \omega_2 &= (0.1250, 0.1250, 0.1250, 0.3750, 0.2500)^T, \\ \omega_3 &= (0.1000, 0.3000, 0.2000, 0.3000, 0.1000)^T, \\ \omega_4 &= (0.1667, 0.1667, 0.000, 0.1667, 0.5000)^T. \end{aligned} \quad (15)$$

*Step 2.* Use the IFDHW operator. First, calculate  $\hat{\alpha}_i = nw_i \alpha_i$ , taking alternative  $A_1$  for example.  $\hat{\alpha}_1 = (0.4054, 0.503)$   $\hat{\alpha}_2 = (0.7000, 0.1000)$ ,  $\hat{\alpha}_3 = (0.7000, 0.2000)$ ,  $\hat{\alpha}_4 = (0.3183, 0.5946)$ , and  $\hat{\alpha}_5 = (0.6464, 0.2530)$ . Then calculate overall values  $r_{A_i}$  for every  $A_i$  ( $i = 1, 2, \dots, n$ ) by using (14):

$$\begin{aligned} r_{A_1} &= (0.6038, 0.2308), \\ r_{A_2} &= (0.5356, 0.2753), \\ r_{A_3} &= (0.5146, 0.2321), \\ r_{A_4} &= (0.5033, 0.2669). \end{aligned} \quad (16)$$

*Step 3.* Sort the alternatives by calculating the score functions  $S(r_{A_i})$ , ( $i = 1, 2, 3, 4$ ) for every alternatives based on overall values  $r_{A_1}, r_{A_2}, r_{A_3}$ , and  $r_{A_4}$ . If two or more score values are equal, then we can use accuracy function  $H(r_{A_i})$  to get the ranking results.

$$\begin{aligned} S(r_{A_1}) &= 0.3729, \\ S(r_{A_2}) &= 0.2603, \\ S(r_{A_3}) &= 0.2825, \\ S(r_{A_4}) &= 0.2364. \end{aligned} \quad (17)$$

According to the results of  $S(r_{A_i})$ , ( $i = 1, 2, 3, 4$ ), and thus  $A_1 > A_3 > A_2 > A_4$ , where " $>$ " denotes "be superior to," therefore, for a decision-maker in the risk proneness attitude,  $A_1$  is the best investment company. Using the same steps, the ranking results in other two cases are shown in Table 2.

Table 2 shows that rest on different risk attitudes the best alternatives can be different. For risk proneness attitude that the best investment company is  $A_1$ , for risk aversion attitude it is  $A_2$  and for risk neutralness attitude it is  $A_3$ . This ranking method can reflect the impact of risk factors on the ranking results and can also choose the best alternative according to different risk attitudes of decision-makers.

#### 6. Conclusions

In this paper, we want to solve the MADM problems when decision-makers take different risk attitude. The innovations of this paper are listed as follows:

(1) We introduced three risk preference attitudes of decision-makers to MADM field. Three risk preference attitudes are from risk preference partition theory which is contained in expected utility theory.

(2) Considering the hesitation information of IFNs, we defined three equations for constructing weight vectors according to different decision-makers' attitudes. The weight vectors are subjective and easy to calculate for solving the MADM problems with lots of alternatives and attributes.

(3) This decision-making method can provide decision-making basis for many different fields when decision-makers want to check if there are any differences while they are

TABLE 1: Intuitionistic fuzzy decision matrix for investment.

	$G_1$	$G_2$	$G_3$	$G_4$	$G_5$
$A_1$	(0.5,0.4)	(0.7,0.1)	(0.7,0.2)	(0.4,0.5)	(0.5,0.4)
$A_2$	(0.6,0.3)	(0.5,0.4)	(0.7,0.2)	(0.3,0.4)	(0.6,0.2)
$A_3$	(0.7,0.2)	(0.6,0.1)	(0.5,0.3)	(0.4,0.3)	(0.5,0.4)
$A_4$	(0.5,0.4)	(0.5,0.4)	(0.6,0.4)	(0.6,0.3)	(0.4,0.3)

TABLE 2: Ranking results of different risk attitudes.

Risk attitudes	Ranking results
Risk proneness	$A_1 > A_3 > A_2 > A_4$
Risk aversion	$A_2 > A_3 > A_1 > A_4$
Risk neutralness	$A_3 > A_2 > A_1 > A_4$

in different attitudes. Then they can get the most desirable alternative(s).

In the future, we should study the accuracy of this proposed method. Meanwhile, we can also extend the proposed method to solve the MAGDM problems.

### Data Availability

The intuitionistic fuzzy data used to support the findings of this study are included within the article.

### Conflicts of Interest

The authors declare that there are no conflicts of interest regarding the publication of this paper.

### Acknowledgments

This paper is supported by the Key Research Institute of Philosophy and Social Science of Zhejiang Province (Modern Port Service Industry and Creative Culture Research Center) (nos. 16JDGH067, 15JDLG01YB), Research Project of Philosophy and Social Science of Zhejiang Province (no. 18NDJC283YB), and Soft Science Project of Ningbo (nos. 2017A10085, 2017A10068)

### References

- [1] L. A. Zadeh, "Fuzzy sets," *Information and Control*, vol. 8, pp. 338–353, 1965.
- [2] K. T. Atanassov, "Intuitionistic fuzzy sets," *Fuzzy Sets and Systems*, vol. 20, no. 1, pp. 87–96, 1986.
- [3] Z. S. Xu and R. R. Yager, "Some geometric aggregation operators based on intuitionistic fuzzy sets," *International Journal of General Systems*, vol. 35, no. 4, pp. 417–433, 2006.
- [4] Z. Xu, "Intuitionistic fuzzy aggregation operators," *IEEE Transactions on Fuzzy Systems*, vol. 15, no. 6, pp. 1179–1187, 2007.
- [5] S. Zeng, "Pythagorean fuzzy multiattribute group decision making with probabilistic information and OWA approach," *International Journal of Intelligent Systems*, vol. 32, no. 11, pp. 1136–1150, 2017.
- [6] G. Wei, "Some induced geometric aggregation operators with intuitionistic fuzzy information and their application to group decision making," *Applied Soft Computing*, vol. 10, no. 2, pp. 423–431, 2010.
- [7] Z. Su, G. Xia, M. Chen, and L. Wang, "Induced generalized intuitionistic fuzzy OWA operator for multi-attribute group decision making," *Expert Systems with Applications*, vol. 39, no. 2, pp. 1902–1910, 2012.
- [8] S. Zeng, Z. Mu, and T. Baležentis, "A novel aggregation method for Pythagorean fuzzy multiple attribute group decision making," *International Journal of Intelligent Systems*, vol. 33, no. 3, pp. 573–585, 2018.
- [9] C. Q. Tan, "A multi-criteria interval-valued intuitionistic fuzzy group decision making with Choquet integral-based TOPSIS," *Expert Systems with Applications*, vol. 38, no. 4, pp. 3023–3033, 2011.
- [10] F. E. Boran, S. Genç, M. Kurt, and D. Akay, "A multi-criteria intuitionistic fuzzy group decision making for supplier selection with TOPSIS method," *Expert Systems with Applications*, vol. 36, no. 8, pp. 11363–11368, 2009.
- [11] S. Zeng and Y. Xiao, "A method based on topsis and distance measures for hesitant fuzzy multiple attribute decision making," *Technological and Economic Development of Economy*, vol. 24, no. 3, pp. 969–983, 2018.
- [12] K. Chatterjee, M. B. Kar, and S. Kar, "Strategic Decisions Using Intuitionistic Fuzzy Vikor Method for Information System (IS) Outsourcing," in *Proceedings of the International Symposium on Computational and Business Intelligence IEEE Computer Society*, pp. 123–126, 2013.
- [13] H. Liao and Z. Xu, "A VIKOR-based method for hesitant fuzzy multi-criteria decision making," *Fuzzy Optimization and Decision Making*, vol. 12, no. 4, pp. 373–392, 2013.
- [14] K. Chatterjee and S. Kar, "Unified Granular-number-based AHP-VIKOR multi-criteria decision framework," *Granular Computing*, vol. 2, no. 3, pp. 199–221, 2017.
- [15] Y. Huang, G. Wei, and C. Wei, "VIKOR Method for Interval Neutrosophic Multiple Attribute Group Decision-Making," *Information*, vol. 8, no. 4, p. 144, 2017.
- [16] F. Meng, C. Tan, and X. Chen, "An approach to Atanassov's interval-valued intuitionistic fuzzy multi-attribute decision making based on prospect theory," *International Journal of Computational Intelligence Systems*, vol. 8, no. 3, pp. 591–605, 2015.
- [17] J. D. Qin, X. W. Liu, and W. Pedrycz, "An extended VIKOR method based on prospect theory for multiple attribute decision making under interval type-2 fuzzy environment," *Knowledge-Based Systems*, vol. 86, pp. 116–130, 2015.
- [18] N. Xie, Z. Li, and G. Zhang, "An intuitionistic fuzzy soft set method for stochastic decision-making applying prospect theory and grey relational analysis," *Journal of Intelligent & Fuzzy Systems: Applications in Engineering and Technology*, vol. 33, no. 1, pp. 15–25, 2017.

- [19] Peng Li, Yingjie Yang, and Cuiping Wei, "An Intuitionistic Fuzzy Stochastic Decision-Making Method Based on Case-Based Reasoning and Prospect Theory," *Mathematical Problems in Engineering*, vol. 2017, Article ID 2874954, 13 pages, 2017.
- [20] Z. S. Xu, "An overview of methods for determining OWA weights," *International Journal of Intelligent Systems*, vol. 20, no. 8, pp. 843–865, 2005.
- [21] X. Guo, Z. Yuan, and B. Tian, "Supplier selection based on hierarchical potential support vector machine," *Expert Systems with Applications*, vol. 36, no. 3, pp. 6978–6985, 2009.
- [22] A. Zouggari and L. Benyoucef, "Simulation based fuzzy TOPSIS approach for group multi-criteria supplier selection problem," *Engineering Applications of Artificial Intelligence*, vol. 25, no. 3, pp. 507–519, 2012.
- [23] G. Wang, S. H. Huang, and J. P. Dismukes, "Product-driven supply chain selection using integrated multi-criteria decision-making methodology," *International Journal of Production Economics*, vol. 91, no. 1, pp. 1–15, 2004.
- [24] J. Liu, S.-F. Liu, P. Liu, X.-Z. Zhou, and B. Zhao, "A new decision support model in multi-criteria decision making with intuitionistic fuzzy sets based on risk preferences and criteria reduction," *Journal of the Operational Research Society*, vol. 64, no. 8, pp. 1205–1220, 2013.
- [25] S. Wan, F. Wang, and J. Dong, "A Three-Phase Method for Group Decision Making with Interval-Valued Intuitionistic Fuzzy Preference Relations," *IEEE Transactions on Fuzzy Systems*, vol. 26, no. 2, pp. 998–1010, 2018.
- [26] Y. Lin and Y. Wang, "Group decision making with consistency of intuitionistic fuzzy preference relations under uncertainty," *IEEE/CAA Journal of Automatica Sinica*, vol. 5, no. 3, pp. 741–748, 2018.
- [27] R. Roostaei, M. Izadikhah, F. H. Lotfi, and M. Rostamy-Malkhalifeh, "A multi-criteria intuitionistic fuzzy group decision making method for supplier selection with vikor method," *International Journal of Fuzzy System Applications*, vol. 2, no. 1, pp. 1–17, 2012.
- [28] G. Büyükoçkan and F. Göçer, "Application of a new combined intuitionistic fuzzy MCDM approach based on axiomatic design methodology for the supplier selection problem," *Applied Soft Computing*, vol. 52, pp. 1222–1238, 2017.
- [29] W. L. Hung and M. S. Yang, "On the J -divergence of intuitionistic fuzzy sets with its application to pattern recognition," *Information Sciences*, vol. 178, no. 6, pp. 1641–1650, 2008.
- [30] S.-H. Cheng, S.-M. Chen, and T.-C. Lan, "A New Similarity Measure between Intuitionistic Fuzzy Sets for Pattern Recognition Based on the Centroid Points of Transformed Fuzzy Numbers," in *Proceedings of the IEEE International Conference on Systems, Man, and Cybernetics IEEE*, pp. 1125–1129, 2015.
- [31] H. Nguyen, "A novel similarity/dissimilarity measure for intuitionistic fuzzy sets and its application in pattern recognition," *Expert Systems with Applications*, vol. 45, pp. 97–107, 2016.
- [32] Z. S. Xu and R. R. Yager, "Intuitionistic and interval-valued intuitionistic fuzzy preference relations and their measures of similarity for the evaluation of agreement within a group," *Fuzzy Optimization and Decision Making*, vol. 8, no. 2, pp. 123–139, 2009.

## Research Article

# Extension Dependent Degree Method with Mapping Transformation for Three-Parameter Interval Number Decision Making

Li-Bo Xu <sup>1</sup>, Xing-Sen Li,<sup>2</sup> Jun-kai Shao,<sup>1</sup> and Kai-jie Wang<sup>1</sup>

<sup>1</sup>Zhejiang University Ningbo Institute of Technology, Ningbo, Zhejiang 315000, China

<sup>2</sup>Guangdong University of Technology, Guangzhou, Guangdong 510006, China

Correspondence should be addressed to Li-Bo Xu; [xu\\_libo@163.com](mailto:xu_libo@163.com)

Received 22 July 2018; Accepted 28 August 2018; Published 12 September 2018

Academic Editor: Carlos Llopis-Albert

Copyright © 2018 Li-Bo Xu et al. This is an open access article distributed under the Creative Commons Attribution License, which permits unrestricted use, distribution, and reproduction in any medium, provided the original work is properly cited.

In view of the multiattribute decision making problem that the attribute values and weights are both three-parameter interval numbers, a new decision making approach and framework based on extension simple dependent degree are proposed. According to traditional extension simple dependent function, the new approach proposes a new extension dependent function for three-parameter interval number. Then through an interval mapping transformation method, the process for obtaining dependent degree for the interval with its optimal value not being the endpoint is transformed to the monotonous process for the interval with its optimal value being the endpoint. The method can not only perform uncertain analysis of decision results by different settings of attitude coefficients, but also take dynamic analysis and rule finding by some extension transformation. At last, an example is presented to examine the effectiveness and stability of our method.

## 1. Introduction

In multiattribute decision making (MADM), attributes information often shows some ambiguity and uncertainty due to the complexity from objective things and the finiteness from decision makers, so it is difficult to describe by some accurate numerical values. Therefore, several methods that can describe this uncertainty information, such as interval number [1], fuzzy number [2], gray number [3], and connection number [4, 5], have been widely studied and applied. Among them, interval number theory, as one of the most possible solutions, has produced many valuable research results. However, the traditional interval number is too rough to describe the uncertain information. It only focuses on the upper and lower bounds of the interval and possibly ignores its intrinsic preference information from users, which greatly limits its practicability in many actual application scenarios. In comparison, the three-parameter interval number [6] not only retains the upper and lower bounds of the interval, but also emphasizes the gravity value which has the maximum hit possibility in all values. Therefore, it is superior to the

traditional interval number method in describing the uncertainty information. In recent years, the three-parameter interval number theory has become the research focus in uncertainty decision making domain. Literature [7–9] establishes the concept of three-parameter interval gray number, correlation degree, and closeness calculation method according to the gray system theory. In literature [10], the ratio of the sums of three parameters is directly used as the interval comparison results, and then the pairwise comparison matrix is built to sort the scheme. In literature [11], the traditional interval likelihood ranking method is extended to the three-parameter interval ranking, and the TOPSIS model is established for three-parameter interval number. Literature [12] also adopts TOPSIS method to sort three-parameter interval numbers by redefining an Euclidean distance. In literature [13], combining the center value, the gravity value, and the interval's length of the three-parameter interval gray number, an exact score function is defined as the basis for comparison. Literature [14] proposes to convert the three-parameter interval into traditional two-parameter interval, so that the likelihood sorting method for the traditional

interval can be used directly. In some earlier literature [15, 16], some triangle fuzzy numbers are used to describe the three-parameter interval, and the scheme order was determined based on the fuzzy number operation process and the distance measure of ideal point. Literature [17] defines the concept of three-parameter interval fuzzy set, its operation rules, and distance measure formula. Literature [18] proposes a three-parameter interval gray linguistic variable decision making method based on projection model and prospect theory.

In general, although the existing research has made some great progress, there are still some things to be improved. First, most of the research is based on the fuzzy number correlation theory including score function, fuzzy distance, fuzzy similarity, and likelihood method. These fuzzy number concepts and measures are only extended to the three-parameter interval number field, so there is no new method and framework. Second, many decision making models are too deterministic and lose their uncertainty in the process. Hence, it is difficult to carry out stability checking and uncertainty analysis for the decision results in the later stage. In this regard, the set pair analysis method is proposed [19], which converts the three-parameter interval number into the connection number expression and maintains the uncertainty of the result and the calculation simplicity. Therefore, it is another idea worthy of further study. Third, the existing decision making model is basically static. Researches on dynamic decision judgment and rule discovery are very inadequate.

In order to solve the above problems, the paper attempts to propose a new multiattribute decision making method and framework based on extension dependent degree. This thinking and method are rarely seen in the existing research literature. In this method, firstly, according to the extension simple dependent degree calculation method and its mapping transformation rule, the dependent degree calculation expression for the three-parameter interval and its interval map transformation method are given. This will transform the process of calculating dependent degree of the interval with its optimal value not being the endpoint to the monotonous process of the interval with its optimal value being the endpoint. It not only makes the calculation process simple and unified, but also expresses a new three-parameter interval sorting method. Secondly, six typical coefficient setting schemes are given for the attitude coefficient in the dependent degree calculation expression, which can reflect the different preference attitudes from the decision makers for the upper, lower, and average evaluation scores. It can make the model perform some uncertainty analysis for the decision results. After that, the comparison between our method and the existing other research results is shown by numerical examples, which illustrates the effectiveness and stability of the proposed method and its ability to perform uncertainty analysis. Finally, based on the extension dependent degree calculation, the dynamic analysis and rule discovery of the decision process through extension transformation are proposed, which shows the dynamic applicability of our method.

## 2. Extension Simple Dependent Degree for Three-Parameter Interval

### 2.1. Three-Parameter Interval Number

*Definition 1.* Let  $R$  be the real number set, and for any  $a, b \in R, a \leq b, X = [a, b]$  is noted as interval number. Here  $a$  is the lower bound of the interval, and  $b$  is the upper bound. When  $a = b, X$  degenerates into a real number.

*Definition 2* (see [10–12]). Let  $R$  be a real number set, and for any  $a, b, m \in R, a \leq m \leq b, \bar{X} = [a, m, b]$  is noted as a three-parameter interval number. Here  $a$  and  $b$ , respectively, represent the lower and upper bound of the interval number.  $m$  represents a special point with some statistical meaning in this interval such as mean value or maximum possibility value, which is called gravity value or ideal value.

In fact, the three-parameter interval number is the expansion of the traditional interval number but may describe uncertainty and fuzzy numbers more abundantly and accurately. For example, there is an evaluation score for the performance of a product noted as a three-parameter interval number [4, 6, 8]. The number may mean that the lower and upper bounds from user group evaluations are 4 and 8, respectively. It can also mean that the score from one user covers between 4 and 8, and 6 is the most preferred score. It can also indicate that the lowest score and highest score for single attribute are 4 and 8, and the average score is 6. By some means, the three-parameter interval number is similar to the triangular fuzzy number [20, 21] expression. Both of them consider that the left and right interval endpoints are the critical points, and the middle points are the most representative ones. However, the triangular fuzzy number focuses more on the degree of the elements belonging to some fuzzy set. The three-parameter interval number pays more attention to the probability or the statistical meaning for the interval, and so its meaning is more universal and rich. It is worthy of further research and application.

*2.2. Extension Simple Dependent Degree and Mapping Transformation.* In extenics [22], extension simple dependent function describes the relationship between a point  $x$  and interval covering  $X$ . Its calculation is based on the given range of values and does not need to rely on subjective judgment or empirical value from decision makers, so it is convenient to quantitatively describe the nature of things. It has been used in some evaluation and forecasting applications [23, 24].

*Definition 3* (see [22]). Suppose a finite interval  $X = [a, b]$ , and its optimal value is  $m \in X$ ; then

$$k(x, X) = \begin{cases} \frac{x-a}{m-a}, & x \leq m \\ \frac{b-x}{b-m}, & x \geq m. \end{cases} \quad (1)$$

Here  $k(x, X)$  is called extension simple dependent degree of the point  $x$  and interval  $X$ , as shown in Figure 1, and it satisfies the following properties:

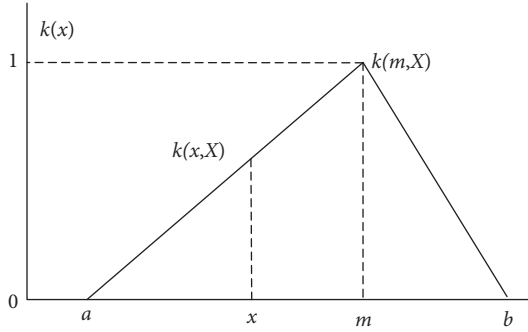


FIGURE 1: The extension simple dependent degree.

- (1) When  $x=m$ ,  $k(x, X)$  reaches the maximum value and  $k(x, X)=k(m, X)=1$ .
- (2) When  $x \in X$  and  $x \neq a, b$ , then  $k(x, X) > 0$ .
- (3) When  $x \notin X$  and  $x \neq a, b$ , then  $k(x, X) < 0$ .
- (4) When  $x=a$  or  $x=b$ , then  $k(x, X) = 0$ .

A special case is when  $m=a$  or  $b$ , and  $x \in X$ ; then

$$k(x, X) = \begin{cases} \frac{b-x}{b-a}, & (m = a) \\ \frac{x-a}{b-a}, & (m = b). \end{cases} \quad (2)$$

Obviously, as shown in formula (2), when the optimal point  $m$  is just at the endpoint of the interval, extension simple dependent degree formula becomes a monotonic increasing or monotonic decreasing function, and its calculation process is very concise and intuitive. However, as shown in formula (1), when the optimal point  $m$  is not at the endpoint, the dependent degree formula must be changed according to the location of  $m$ , which will bring some complexity and inconveniences. Therefore, here we propose a mapping transformation method which will transform the dependent degree calculation with the optimal point not being the endpoint into the calculation with the optimal point being the endpoint, so as to keep the monotonicity and simplicity of the process.

**Definition 4.** Suppose a finite interval  $X=[a, b]$  and its optimal value is  $m \in X, m \neq a, b$ . For  $\forall x \in X$ , there is a transformation  $\theta(x) = x'$  that can make  $x' \in [a, m)$  and  $k(x', X) = k(x, X)$  hold. Then,  $x'$  is called the dependent degree mapping point of  $x$ , and  $\theta$  is called the dependent degree mapping transformation.

**Theorem 5.** Suppose a finite interval  $X = [a, b]$  and its optimal value is  $m \in X, m \neq a, b$ . For  $\forall x \in X$ , if  $x'$  is the dependent degree mapping point of  $x$ , then  $x' \in [a, m)$ , and

$$\begin{aligned} x' &= \theta(x) \\ &= \begin{cases} k(x, X)(m-a) + a = \frac{b-x}{b-m}(m-a) + a & x \in (m, b) \\ x & x \in [a, m]. \end{cases} \quad (3) \end{aligned}$$

*Proof.* From Definition 3, when  $x \in (m, b)$ ,  $k(x, X) \in [0, 1)$ , then  $a \leq x' = k(x, X)(m-a) + a < m$ ; i.e.,  $x' \in [a, m)$ . By Definition 3,  $k(x', X) = (x' - a)/(m - a) = (k(x, X)(m - a) + a - a)/(m - a) = k(x, X)$ .  $\square$

Obviously, for a finite interval  $X = [a, b]$  with its optimal value  $m \in X, m \neq a, b$ , through the above mapping transformation, any point in the interval  $X$  and its dependent degree calculation are mapped to the left half of  $X$ , that is, the monotonic increasing interval  $[a, m)$ . Here, this leads to Theorem 6.

**Theorem 6.** Suppose a finite interval  $X = [a, b]$  with its optimal value  $m \in X, m \neq a, b, \forall x_0 \in X$ , taking a mapping transformation  $\theta(x_0) = x'_0$ , and transforming interval  $X$  as its left half interval  $X' = [a, m]$ . Then  $k(x'_0, X') = k(x_0, X)$  holds.

The proof is very easy according to Theorem 5, so it is omitted. As we seen, this theorem successfully transforms the dependent degree calculation with the optimal point not at the endpoint of the interval to the calculation with the optimal point at the right endpoint. That makes dependent degree calculation process very simple and unified.

According to the above content, we will deduce extension dependent degree for three-parameter interval and its mapping transformation method.

### 2.3. Three-Parameter Interval Extension Dependent Degree and Mapping Transformation

**Definition 7.** Suppose a finite interval  $X = [a, b]$  with its optimal value  $m \in X$ ; there is a subinterval  $X_0=[a_0, b_0]$  and  $X_0 \subseteq X$ ; then

$$k(X_0, X) = \alpha k(a_0, X) + (1 - \alpha) k(b_0, X), \quad (4)$$

$\alpha \in [0, 1]$ .

$k(X_0, X)$  is called the interval extension dependent degree of the subinterval  $X_0$  and the interval  $X$ , and it satisfies the following properties,

- (1) When  $a_0 = b_0, k(X_0, X)$  degenerates into the extension simple dependent degree in Definition 3.
- (2) When  $a_0 = b_0 = m, k(X_0, X)$  reaches the maximum value and  $k(X_0, X) = k(m, X) = 1$ .
- (3) When  $a_0 = a, b_0 = b, k(X_0, X)$  reaches the minimum value and  $k(X_0, X) = 0$ .
- (4) When  $X_0 \subset X, 0 < k(X_0, X) < 1$ .

Obviously, when  $m=a$  or  $b$ , according formula (2) and (4), the interval dependent degree function is simplified to a monotonic increasing or monotonic decreasing function.

**Definition 8.** Suppose a finite interval  $X = [a, b]$  with its optimal value  $m \in X$ ; there is a three-parameter subinterval  $\overline{X}_0 = [a_0, m_0, b_0]$  and  $\overline{X}_0 \subseteq X$ ; then,

$$\begin{aligned} k(\overline{X}_0, X) &= \alpha k(a_0, X) + (1 - \alpha - \beta) k(m_0, X) \\ &\quad + \beta k(b_0, X), \quad (5) \\ &\quad (\alpha, \beta \in [0, 1], \alpha + \beta \leq 1) \end{aligned}$$

$k(\overline{X_0}, X)$  is called the three-parameter interval extension dependent degree of the subinterval  $\overline{X_0}$  and the interval  $X$ , and it satisfies the following properties:

(1) When  $a_0 = b_0 = m_0$ ,  $k(\overline{X_0}, X)$  degenerates into the extension simple dependent degree.

(2) When  $a_0 = b_0 = m_0 = m$ ,  $k(\overline{X_0}, X)$  reaches the maximum value and  $k(\overline{X_0}, X) = k(m_0, X) = k(m, X) = 1$ .

(3) When  $a_0 = a$ ,  $b_0 = b$ ,  $k(\overline{X_0}, X) = (1 - \alpha - \beta)k(m_0, X)$ . In particular, when  $m_0 = a_0$  or  $m_0 = b_0$ ,  $k(\overline{X_0}, X)$  reaches the minimum value and  $k(\overline{X_0}, X) = 0$ .

(4) When  $\overline{X_0} \subset X$ ,  $0 < k(\overline{X_0}, X) < 1$ .

Obviously, when  $m=a$  or  $b$ , the three-parameter interval extension dependent degree function is simplified to a monotonic increasing or monotonic decreasing function. The three-parameter interval extension dependent degree shows the relationship between the three-parameter subinterval  $\overline{X_0}$  and the interval  $X$ . In it,  $\alpha$  and  $\beta$  represent the preference attitude coefficient of the decision makers, which will reflect the degree of tendency from the decision makers to the upper bound, the lower bound, and the gravity value of the interval  $\overline{X_0}$ . That means that for an attribute, the decision makers either pay more attention to the high evaluation or pay more attention to the low evaluation or the overall statistical value of the evaluation.

As above, when  $m=a$  or  $b$ , the three-parameter interval extension dependent degree calculation is simple and intuitive. However, when  $m \neq a, b$ , the calculation and comparison of the three-parameter interval dependent degree become complicated. The calculation formula of the dependent degree will be complicatedly changed due to the difference relative position of the upper bound, the lower bound, and the optimal point  $m$ . The attitude coefficients also cannot directly correspond to the dependent degree of the upper and lower bounds of the interval. This paper proposes a method of interval mapping transformation. It will transform the interval dependent degree calculation with the optimal point not at the endpoint to the calculation with the optimal point at the endpoint. That keeps monotonicity and simplicity of the interval dependent degree calculation process.

*Definition 9.* Suppose a finite interval  $X = [a, b]$  with its optimal value  $m \in X$ ,  $m \neq a, b$ . For the three-parameter subinterval  $\overline{X_0} = [a_0, m_0, b_0]$  and  $\overline{X_0} \subseteq X$ , there is a mapping transformation  $\theta(\overline{X_0}) = \overline{X_0}'$  which makes  $\overline{X_0}' \subseteq [a, m]$  and  $k(\overline{X_0}', X) = k(\overline{X_0}, X)$  hold. Then  $\overline{X_0}'$  is called the dependent degree mapping interval of  $\overline{X_0}$ .

**Theorem 10.** Suppose a finite interval  $X = [a, b]$  and its optimal value  $m \in X$ ,  $m \neq a, b$ . For the three-parameter subinterval  $\overline{X_0} = [a_0, m_0, b_0]$  and  $\overline{X_0} \subseteq X$ , if  $\overline{X_0}'$  is the dependent degree mapping interval of  $\overline{X_0}$ , then,

$$\overline{X_0}' = \theta(\overline{X_0})$$

$$= \begin{cases} [a_0, m_0, b_0] = \overline{X_0} & (a_0, m_0, b_0 \in [a, m]) \\ [a_0, m_0, b_0'] = \left[ a_0, m_0, \frac{b-b_0}{b-m}(m-a) + a \right] & (a_0, m_0 \in [a, m], b_0 \in (m, b]) \\ \text{or } [b_0', m_0, a_0] = \left[ \frac{b-b_0}{b-m}(m-a) + a, m_0, a_0 \right] & \\ [a_0, m_0', b_0'] = \left[ a_0, \frac{b-m_0}{b-m}(m-a) + a, \frac{b-b_0}{b-m}(m-a) + a \right] & (a_0 \in [a, m], m_0, b_0 \in (m, b]) \\ \text{or } [b_0', m_0', a_0] = \left[ \frac{b-b_0}{b-m}(m-a) + a, \frac{b-m_0}{b-m}(m-a) + a, a_0 \right] & \\ [b_0', m_0', a_0'] = \left[ \frac{b-b_0}{b-m}(m-a) + a, \frac{b-m_0}{b-m}(m-a) + a, \frac{b-a_0}{b-m}(m-a) + a \right] & (a_0, m_0, b_0 \in (m, b]). \end{cases} \quad (6)$$

*Proof.* Without loss of generality, suppose  $\alpha$  is the preference coefficient of low dependent degree,  $\beta$  is the preference coefficient of high dependent degree, and  $1 - \alpha - \beta$  is the preference coefficient of the dependent degree of gravity value. Here, we proved the second case. When  $a_0, m_0 \in [a, m]$ ,  $b_0 \in (m, b]$ , there are two cases:

(1) When  $k(a_0, X) > k(b_0, X)$ , as shown in Figure 2(a). Since  $b_0 \in (m, b]$ , according to Theorem 5, it takes a mapping transformation  $\theta(b_0) = b_0' = k(b_0, X)(m-a) + a$  which makes  $k(b_0', X) = k(b_0, X)$  and  $b_0' \in [a, m]$  hold. Then, since the dependent degree increases monotonically in the interval

$[a, m]$ , and  $k(b_0', X) < k(a_0, X)$ , there is  $b_0' < a_0$ . Thus,  $\overline{X_0}' = [b_0', m_0, a_0]$ ; then,

$$\begin{aligned} k(\overline{X_0}', X) &= \alpha k(b_0', X) + (1 - \alpha - \beta) k(m_0, X) \\ &\quad + \beta k(a_0, X) \\ &= \alpha k\left(\frac{b-b_0}{b-m}(m-a) + a, X\right) \\ &\quad + (1 - \alpha - \beta) k(m_0, X) + \beta k(a_0, X) \end{aligned}$$

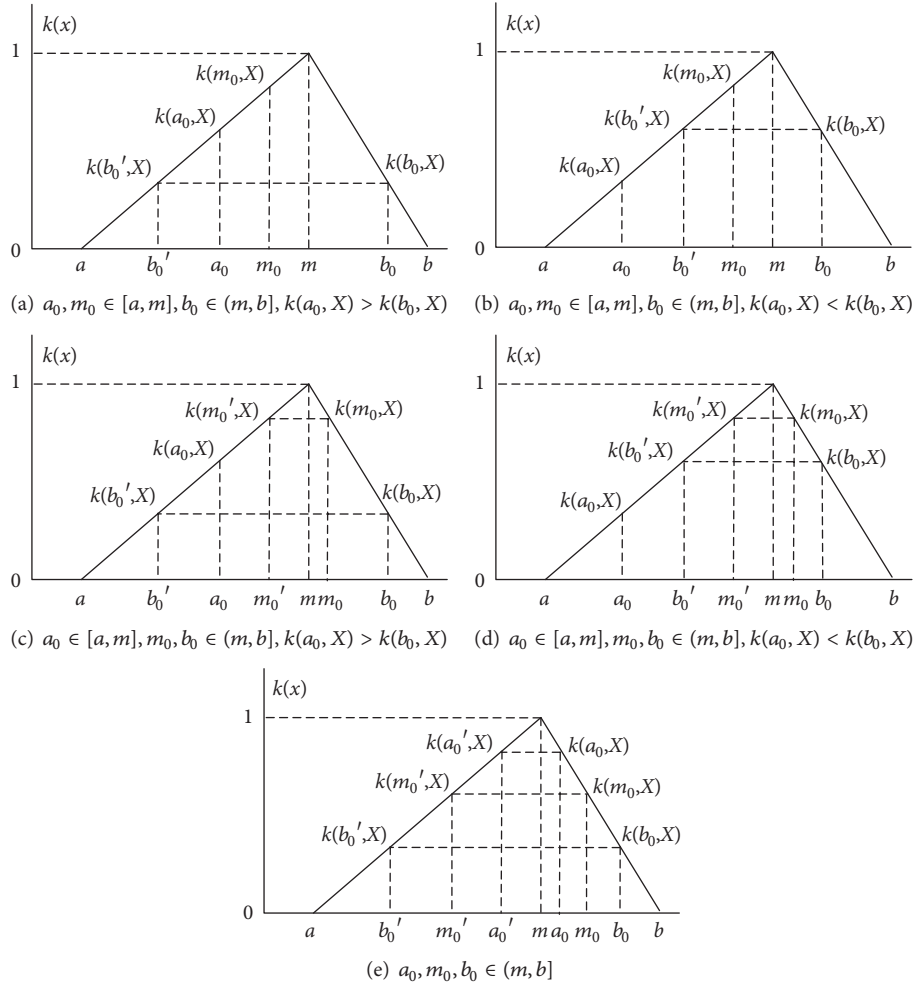


FIGURE 2: The interval dependent degree mapping transformation.

$$\begin{aligned}
 &= \alpha k(k(b_0, X)(m-a) + a, X) \\
 &\quad + (1 - \alpha - \beta) k(m_0, X) + \beta k(a_0, X) \\
 &= \alpha \left( \frac{k(b_0, X)(m-a) + a}{m-a} \right) \\
 &\quad + (1 - \alpha - \beta) k(m_0, X) + \beta k(a_0, X) \\
 &= \alpha k(b_0, X) + (1 - \alpha - \beta) k(m_0, X) \\
 &\quad + \beta k(a_0, X) = k(\overline{X_0}, X).
 \end{aligned}
 \tag{7}$$

(2) When  $k(a_0, X) < k(b_0, X)$ , as shown in Figure 2(b). Similarly, it is easy to get  $\theta(b_0) = b'_0 = k(b_0)(m-a) + a, b'_0 \in [a, m]$  and  $b'_0 > a_0$ . Therefore,  $\overline{X'_0} = [a_0, m_0, b'_0]$ ; then,

$$\begin{aligned}
 k(\overline{X'_0}, X) &= \alpha k(a_0, X) + (1 - \alpha - \beta) k(m_0, X) \\
 &\quad + \beta k(b'_0, X) \\
 &= \alpha k(a_0, X) + (1 - \alpha - \beta) k(m_0, X)
 \end{aligned}$$

$$\begin{aligned}
 &\quad + \beta k\left(\frac{b-b_0}{b-m}(m-a) + a, X\right) \\
 &= \alpha k(a_0, X) + (1 - \alpha - \beta) k(m_0, X) \\
 &\quad + \beta k(k(b_0, X)(m-a) + a, X) \\
 &= \alpha k(a_0, X) + (1 - \alpha - \beta) k(m_0, X) \\
 &\quad + \beta \left( \frac{k(b_0, X)(m-a) + a - a}{m-a} \right) \\
 &= \alpha k(a_0, X) + (1 - \alpha - \beta) k(m_0, X) \\
 &\quad + \beta k(b_0, X) = k(\overline{X_0}, X).
 \end{aligned}$$

(8)  $\square$

Therefore, when  $k(a_0, X) > k(b_0, X)$ , there is  $\overline{X'_0} = [b'_0, m_0, a_0]$ . When  $k(a_0, X) < k(b_0, X)$ , there is  $\overline{X_0} = [a_0, m_0, b'_0]$ . The other cases are shown in Figures 2(c)-2(e) and may be proved at the same way. Here we will no longer repeat them.

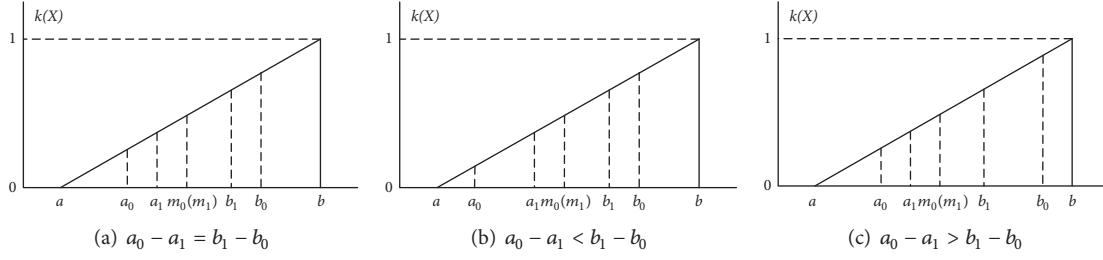


FIGURE 3: The interval dependent degree of benefit attribute interval.

Obviously, for a finite interval  $X = [a, b]$  and its optimal value  $m \in X$ ,  $m \neq a, b$ , by performing the interval mapping transformation defined above, all of the subintervals and their dependent degree calculations are mapped to the left half of the  $X$ , i.e.,  $[a, m]$ . It leads to Theorem 11.

**Theorem 11.** Suppose a finite interval  $X = [a, b]$  with its optimal value  $m \in X$ ,  $m \neq a, b$ . For the three-parameter subinterval  $\overline{X}_0 = [a_0, m_0, b_0]$  and  $\overline{X}_0 \subseteq X$ , by taking interval mapping transformation  $\theta(\overline{X}_0) = \overline{X}'_0$  for  $X_0$ , and transforming interval  $X$  to its left half interval  $X' = [a, m]$ , then  $k(\overline{X}'_0, X') = k(\overline{X}_0, X)$  holds.

The proof is very easy according to Theorem 10, so it is omitted.

As we see, this theorem successfully transforms the three-parameter interval extension dependent degree calculation with the optimal point not at the endpoint to the calculation with the optimal point at the endpoint. That makes the three-parameter interval dependent degree calculation process very simple and uniform.

Different from the traditional interval theories such as gray correlation analysis, interval closeness, and the other measurement methods, the three-parameter interval extension dependent degree not only measures the relationship between two intervals, but also measures the relationship between the gravity points of them. Therefore, the measure is more comprehensive and reasonable. Compared to some existing methods in recent years such as three-parameter interval gray correlation degree, three-parameter interval closeness, three-parameter set pair connection number, and three-parameter interval projection sorting [25], the extension dependent degree method is not only simpler in calculation process but also capable of performing dynamic and uncertainty analysis.

#### 2.4. Dependent Degree Sorting Methods for Different Attribute Types

**Theorem 12.** Suppose a benefit attribute interval  $X = [a, b]$ ; there are three-parameter subintervals  $\overline{X}_0 = [a_0, m_0, b_0]$  and  $\overline{X}_1 = [a_1, m_1, b_1]$ ,  $\overline{X}_0, \overline{X}_1 \subseteq X$ . Then,

(1) when  $\alpha a_0 + (1 - \alpha - \beta)m_0 + \beta b_0 = \alpha a_1 + (1 - \alpha - \beta)m_1 + \beta b_1$ , there is  $k(\overline{X}_0, X) = k(\overline{X}_1, X)$ ;

(2) when  $\alpha a_0 + (1 - \alpha - \beta)m_0 + \beta b_0 < \alpha a_1 + (1 - \alpha - \beta)m_1 + \beta b_1$ , there is  $k(\overline{X}_0, X) < k(\overline{X}_1, X)$ ;

(3) when  $\alpha a_0 + (1 - \alpha - \beta)m_0 + \beta b_0 > \alpha a_1 + (1 - \alpha - \beta)m_1 + \beta b_1$ , there is  $k(\overline{X}_0, X) > k(\overline{X}_1, X)$ .

*Proof.* Since  $X = [a, b]$  is the benefit attribute interval,  $b$  is the optimal value. Then,

$$\begin{aligned}
 & k(\overline{X}_0, X) - k(\overline{X}_1, X) \\
 &= \alpha k(a_0, X) + (1 - \alpha - \beta)k(m_0, X) + \beta k(b_0, X) \\
 &\quad - (\alpha k(a_1, X) + (1 - \alpha - \beta)k(m_1, X) + \beta k(b_1, X)) \\
 &= \alpha \left( \frac{a_0 - a}{b - a} \right) + (1 - \alpha - \beta) \left( \frac{m_0 - a}{b - a} \right) + \beta \left( \frac{b_0 - a}{b - a} \right) \\
 &\quad - \left( \alpha \left( \frac{a_1 - a}{b - a} \right) + (1 - \alpha - \beta) \left( \frac{m_1 - a}{b - a} \right) + \beta \left( \frac{b_1 - a}{b - a} \right) \right) \\
 &= \frac{\alpha a_0 + (1 - \alpha - \beta)m_0 + \beta b_0 - (\alpha a_1 + (1 - \alpha - \beta)m_1 + \beta b_1)}{b - a}.
 \end{aligned} \tag{9}$$

□

**Corollary 13.** Suppose a benefit attribute interval  $X = [a, b]$ ; there are three-parameter subintervals  $\overline{X}_0 = [a_0, m_0, b_0]$  and  $\overline{X}_1 = [a_1, m_1, b_1]$ ,  $\overline{X}_0, \overline{X}_1 \subseteq X$ . When  $m_0 = m_1$ , then,

(1) when  $\alpha a_0 + \beta b_0 = \alpha a_1 + \beta b_1$ , there is  $k(\overline{X}_0, X) = k(\overline{X}_1, X)$ ;

(2) when  $\alpha a_0 + \beta b_0 < \alpha a_1 + \beta b_1$ , there is  $k(\overline{X}_0, X) < k(\overline{X}_1, X)$ ;

(3) when  $\alpha a_0 + \beta b_0 > \alpha a_1 + \beta b_1$ , there is  $k(\overline{X}_0, X) > k(\overline{X}_1, X)$ .

The following part analyzes the practical significance of Corollary 13 in the decision making for benefit attributes. For no loss of generality and more intuitive process, it is assumed that  $\alpha = \beta$ . At this point,  $a_0 + b_0$  and  $a_1 + b_1$  determine the values of the dependent degree, respectively.

As shown in Figure 3(a), for a benefit attribute interval  $X = [a, b]$ , there are two evaluation intervals  $\overline{X}_0 = [a_0, m_0, b_0]$  and  $\overline{X}_1 = [a_1, m_1, b_1]$  with the same gravity value  $m_0 (m_1)$ , which indicates that their overall evaluation is consistent. Although  $\overline{X}_0$  has a higher upper bound and a lower bound, it expands out to the same extent on the upper and lower bounds for  $\overline{X}_1$ ; i.e.,  $a_0 - a_1 = b_1 - b_0$ . This only illustrates that the evaluation of  $\overline{X}_0$  is more relatively controversial but cannot distinguish which is better. Therefore,  $k(\overline{X}_0, X) = k(\overline{X}_1, X)$ , which is in line with people's habit of making decision. As shown in Figure 3(b), the overall evaluation of  $\overline{X}_0$  and  $\overline{X}_1$  is consistent, but relative to  $\overline{X}_1$ , the expanding segment of the lower bound of  $\overline{X}_0$  is larger than that of the upper bound; i.e.,  $a_0 - a_1 < b_1 - b_0$ . This indicates that  $\overline{X}_0$

TABLE 1: An example of the interval dependent degree calculation for benefit attribute interval.

$\alpha = \beta = 1/3$	$\overline{X}_1 = [2, 4, 8]$	$\overline{X}_0 = [3, 4, 7]$	$\overline{X}_0 = [1, 4, 7]$	$\overline{X}_0 = [2, 4, 9]$
$X = [0, 10]$	$k(\overline{X}_1, X) = 0.467$	$k(\overline{X}_0, X) = 0.467$	$k(\overline{X}_0, X) = 0.4$	$k(\overline{X}_0, X) = 0.5$
Sorting result		$k(\overline{X}_0, X) = k(\overline{X}_1, X)$	$k(\overline{X}_0, X) < k(\overline{X}_1, X)$	$k(\overline{X}_0, X) > k(\overline{X}_1, X)$

TABLE 2: An example of the interval dependent degree calculation for fixed attribute interval.

$\alpha = \beta = 1/3$	$\overline{X}_1 = [2, 4, 8]$	$\overline{X}_0 = [3, 4, 7]$	$\overline{X}_0 = [1, 4, 7]$	$\overline{X}_0 = [2, 4, 9]$
$X = [0, 10], m = 4$	$\theta(\overline{X}_1) = \overline{X}'_1 = [4/3, 4, 2]$	$\theta(\overline{X}_0) = \overline{X}'_0 = [2, 4, 3]$	$\theta(\overline{X}_0) = \overline{X}'_0 = [1, 4, 2]$	$\theta(\overline{X}_0) = \overline{X}'_0 = [2/3, 4, 2]$
$X' = [0, 4]$	$k(\overline{X}_1, X) = k(\overline{X}'_1, X') = 0.611$	$k(\overline{X}_0, X) = k(\overline{X}'_0, X') = 0.75$	$k(\overline{X}_0, X) = k(\overline{X}'_0, X') = 0.583$	$k(\overline{X}_0, X) = k(\overline{X}'_0, X') = 0.556$
Sorting result		$k(\overline{X}_0, X) > k(\overline{X}_1, X)$	$k(\overline{X}_0, X) < k(\overline{X}_1, X)$	$k(\overline{X}_0, X) < k(\overline{X}_1, X)$

contains a lower evaluation value, so the overall evaluation of  $\overline{X}_0$  should be slightly lower than  $\overline{X}_1$ ; i.e.,  $k(\overline{X}_0, X) < k(\overline{X}_1, X)$ . This is also in line with people's thinking habits of making decision. On the contrary, as shown in Figure 3(c), when  $a_0 - a_1 > b_1 - b_0$ , the expanding segment of the upper bound of  $\overline{X}_0$  is larger than that of the lower bound, which means  $\overline{X}_0$  contains a higher evaluation value. Therefore, the overall evaluation of  $\overline{X}_0$  should be slightly higher than  $\overline{X}_1$ . Table 1 shows a simple example of the above content.

**Corollary 14.** Suppose a benefit attribute interval  $X = [a, b]$ ; there are three-parameter subintervals  $\overline{X}_0 = [a_0, m_0, b_0]$  and  $\overline{X}_1 = [a_1, m_1, b_1]$ ,  $\overline{X}_0, \overline{X}_1 \subseteq X$ . When  $a_0 = a_1, b_0 = b_1$ , then,

- (1) when  $m_0 = m_1$ , there is  $k(\overline{X}_0, X) = k(\overline{X}_1, X)$ ;
- (2) when  $m_0 < m_1$ , there is  $k(\overline{X}_0, X) < k(\overline{X}_1, X)$ ;
- (3) when  $m_0 > m_1$ , there is  $k(\overline{X}_0, X) > k(\overline{X}_1, X)$ .

The practical significance of Corollary 14 is that when the upper and lower bounds of two evaluation intervals both are the same, the one with the larger gravity value is better.

**Theorem 15.** Suppose a cost attribute interval  $X = [a, b]$ ; there are three-parameter subintervals  $\overline{X}_0 = [a_0, m_0, b_0]$  and  $\overline{X}_1 = [a_1, m_1, b_1]$ ,  $\overline{X}_0, \overline{X}_1 \subseteq X$ . Then,

- (1) when  $\alpha a_0 + (1 - \alpha - \beta)m_0 + \beta b_0 = \alpha a_1 + (1 - \alpha - \beta)m_1 + \beta b_1$ , there is  $k(\overline{X}_0, X) = k(\overline{X}_1, X)$ ;
- (2) when  $\alpha a_0 + (1 - \alpha - \beta)m_0 + \beta b_0 > \alpha a_1 + (1 - \alpha - \beta)m_1 + \beta b_1$ , there is  $k(\overline{X}_0, X) < k(\overline{X}_1, X)$ ;
- (3) when  $\alpha a_0 + (1 - \alpha - \beta)m_0 + \beta b_0 < \alpha a_1 + (1 - \alpha - \beta)m_1 + \beta b_1$ , there is  $k(\overline{X}_0, X) > k(\overline{X}_1, X)$ .

The proof is the same as that of Theorem 12.

**Corollary 16.** Suppose a cost attribute interval  $X = [a, b]$ ; there are three-parameter subintervals  $\overline{X}_0 = [a_0, m_0, b_0]$  and  $\overline{X}_1 = [a_1, m_1, b_1]$ ,  $\overline{X}_0, \overline{X}_1 \subseteq X$ . When  $m_0 = m_1$ , then,

- (1) when  $\alpha a_0 + \beta b_0 = \alpha a_1 + \beta b_1$ , there is  $k(\overline{X}_0, X) = k(\overline{X}_1, X)$ ;
- (2) when  $\alpha a_0 + \beta b_0 > \alpha a_1 + \beta b_1$ , there is  $k(\overline{X}_0, X) < k(\overline{X}_1, X)$ ;
- (3) when  $\alpha a_0 + \beta b_0 < \alpha a_1 + \beta b_1$ , there is  $k(\overline{X}_0, X) > k(\overline{X}_1, X)$ .

The practical significance of Corollary 16 is the same as that of Corollary 13.

**Corollary 17.** Suppose a cost attribute interval  $X = [a, b]$ ; there are three-parameter subintervals  $\overline{X}_0 = [a_0, m_0, b_0]$  and  $\overline{X}_1 = [a_1, m_1, b_1]$ ,  $\overline{X}_0, \overline{X}_1 \subseteq X$ . When  $a_0 = a_1, b_0 = b_1$ , then,

- (1) when  $m_0 = m_1$ , there is  $k(\overline{X}_0, X) = k(\overline{X}_1, X)$ ;
- (2) when  $m_0 < m_1$ , there is  $k(\overline{X}_0, X) > k(\overline{X}_1, X)$ ;
- (3) when  $m_0 > m_1$ , there is  $k(\overline{X}_0, X) < k(\overline{X}_1, X)$ .

The practical significance of Corollary 17 is that when the upper and lower bounds of two evaluation intervals both are the same, the one with the smaller gravity value is better.

**Theorem 18.** Suppose a fixed attribute interval  $X = [a, b]$  with its optimal value  $m \in X, m \neq a, b$ . For the three-parameter subintervals  $\overline{X}_0 = [a_0, m_0, b_0]$  and  $\overline{X}_1 = [a_1, m_1, b_1]$ ,  $X_0, X_1 \subseteq X$ , by taking the interval mapping transformation  $\theta(\overline{X}_0) = \overline{X}'_0$  and  $\theta(\overline{X}_1) = \overline{X}'_1$  and transforming interval  $X$  to the benefit interval  $X' = [a, m]$ , then,  $k(\overline{X}'_0, X') = k(\overline{X}_0, X)$ ,  $k(\overline{X}'_1, X') = k(\overline{X}_1, X)$  hold.

The proof is easy by Definition 9 and Theorem 11, so it is omitted.

Theorem 18 successfully transforms the three-parameter interval dependent degree calculation for the fixed attribute interval into the calculation for the benefit attribute interval with monotonic increasing feature. It not only makes the calculation process in multiattribute decision making application more simple and uniform, but also facilitates performing uncertainty and dynamic analysis. Table 2 shows an example of the interval dependent degree calculation for fixed attribute interval.

**2.5. Preference Attitude Coefficient.** In the three-parameter interval extension dependent degree formula of Definition 8,  $\alpha$  and  $\beta$  represent the preference attitude coefficient of the decision maker. Different coefficients reflect the tendency extent from decision makers to the dependent degree of the upper bound, the lower bounds, and gravity value. Table 3 shows various typical coefficient settings.

Among them, type I represents decision makers having no preference. Type II represents that decision makers focusing more on the dependent degree of gravity values. Type III represents that decision makers preferring the dependent degree of the upper and the lower bounds. Type IV represents that decision makers preferring the dependent degree of gravity values and considering the evaluation values within

TABLE 3: Setting of preference attitude coefficient.

	I	II	III	IV	V	VI
$\alpha$	0.333	0.25	0.4	0.1065	0.222	0.444
$\beta$	0.333	0.25	0.4	0.1065	0.444	0.222
$1 - \alpha - \beta$	0.333	0.5	0.2	0.787	0.333	0.333

the interval presenting a standard normal distribution. Type V and IV, respectively, represent decision makers tending to the dependent degree of the upper bound and the lower bound.

In type IV, assuming the evaluation value  $x$  obeying the standard normal distribution with  $\mu = 0, \sigma = 1$ , the probability density function is  $\varphi(x) = (1/\sqrt{2\pi})e^{-x^2/2}$ . According to the  $2\sigma$  principle, the probability of gravity value is  $\varphi(\mu) = 0.399$ , the probabilities of the upper and lower bounds are  $\varphi(\mu + 2\sigma) = \varphi(\mu - 2\sigma) = 0.054$ . Then, the preference attitude coefficient of gravity value is  $(1 - \alpha - \beta) = 0.399/(0.399 + 2 \times 0.054) = 0.787$ , and the coefficients of the dependent degree of the upper and lower bounds are  $\alpha = \beta = 0.1065$ .

### 3. The Process of Decision Making

Suppose, for multiattribute decision making, there are solution set  $S = \{s_1, s_2, \dots, s_m\}$  and attribute set  $U = \{u_1, u_2, \dots, u_n\}$ . The evaluation value of attribute  $u_j$  of solution  $s_i$  is the three-parameter interval number  $\overline{X}_{ij} = [a_{ij}, m_{ij}, b_{ij}]$ . Then, the evaluation value matrix is  $(\overline{X}_{ij})_{m \times n}$  ( $i = 1, 2, \dots, m; j = 1, 2, \dots, n$ ).

*Step 1.* According to Theorems 10 and 11, make interval mapping transformation towards the evaluation matrix  $(\overline{X}_{ij})_{m \times n}$  and transform the fixed attribute intervals and their three-parameter interval evaluations value into the appropriate benefit attribute intervals and the appropriate evaluations value. A new evaluation matrix  $(\overline{X}'_{ij})_{m \times n}$  is obtained.

*Step 2.* Determine the coefficient setting of  $\alpha$  and  $\beta$  in Table 3 as needed.

*Step 3.* Get the value range of each attribute  $u_j$ . If the value range of the attribute is determined in advance, this range is taken as the value interval of the attribute. If not, take  $X'_j = [\min(\overline{X}'_{ij}), \max(\overline{X}'_{ij})]$  ( $i = 1, 2, \dots, m$ ) as the value interval of the attribute according to the max-min principle. Then calculate the three-parameter interval dependent degree of each evaluation value  $k(\overline{X}'_{ij}, X'_j)$  according to Definition 8.

*Step 4.* If the attribute weight set has been given  $W = \{w_1, w_2, \dots, w_n\}$ , then get the comprehensive three-parameter interval dependent degree towards each solution  $s_i$ , which is described as  $K(s_i) = \sum_{j=1}^n w_j k(\overline{X}'_{ij}, X'_j)$  and sorted. Turn to Step 6.

*Step 5.* If the attribute weights have been given in the form of three-parameter interval number set  $W = \{\overline{W}_1, \overline{W}_2, \dots, \overline{W}_n\}$

and each weight value is  $\overline{W}_j = [w_j^a, w_j^m, w_j^b]$  ( $j = 1, 2, \dots, n$ ),  $w_j^a \leq w_j^b$ , then calculate the comprehensive interval dependent degree under three weights of each solution  $s_i$ , which are described as  $K(s_i)^a = \sum_{j=1}^n w_j^a k(\overline{X}'_{ij}, X'_j)$ ,  $K(s_i)^m = \sum_{j=1}^n w_j^m k(\overline{X}'_{ij}, X'_j)$ , and  $K(s_i)^b = \sum_{j=1}^n w_j^b k(\overline{X}'_{ij}, X'_j)$ . Then, perform the stability test and comprehensive sorting according to the three dependent degrees. Turn to Step 6.

*Step 6.* Perform uncertainty analysis for decision result through different settings of  $\alpha$  and  $\beta$ .

*Step 7.* Perform dynamics analysis and rule discovery on decision result through the interval extension transformation.

### 4. Example Analysis

*4.1. Multiattribute Decision Making Process and Its Uncertainty Analysis.* For convenience of comparison and illustration, the example uses the data from [15, 26]. One organization decides to give an annual evaluation for 5 candidates ( $s_1, s_2, s_3, s_4, s_5$ ) according to 6 evaluation attributes ( $u_1, u_2, u_3, u_4, u_5, u_6$ ) which include moral quality, working attitude, working style, educational level, leadership, and development ability. Each attribute of each candidate was scored, respectively, from the group decisions and then the evaluation of each attribute of each one is obtained by some basic statistical processing. The score range was determined in advance. Obviously, the evaluation for the same candidate varies from person to person; as a result, the attribute value is given in the form of three-parameter interval number. The first five are benefit attributes which are the bigger the better, ranging from 0.80 to 1.00. The last one is a fixed attribute, ranging from 0.80 to 1.20. For the fixed attribute, 1.00 is the optimal score, and the score beyond it means too radical and vice versa (too conservative). The attribute values are shown in Table 4. Here, the optimal candidate is determined according to the above information.

(1) The evaluation matrix is obtained according to Table 4.

(2) According to Step 1, do the interval mapping transformation for the evaluation matrix. The evaluation values in the benefit attribute intervals keep unchanged, and those belonging to the fixed attribute intervals are transformed to those in the benefit attribute, as shown in Table 5.

(3) Determine the setting scheme of coefficient  $\alpha$  and  $\beta$  according to Step 2. For comparing consistency, the setting of type I in Table 3 is used ( $\alpha = \beta = 1/3$ ).

(4) Determine the value range of each attribute according to Step 3. In this example, the first five have the same

TABLE 4: Evaluation value table.

candidate	$u_1$	$u_2$	$u_3$	$u_4$	$u_5$	$u_6$
$s_1$	[0.80 0.85 0.90]	[0.90 0.92 0.95]	[0.91 0.94 0.95]	[0.93 0.96 0.99]	[0.90 0.91 0.92]	[0.95 0.97 1.01]
$s_2$	[0.90 0.95 1.00]	[0.89 0.90 0.93]	[0.90 0.92 0.95]	[0.90 0.92 0.95]	[0.94 0.97 0.98]	[0.90 0.93 1.05]
$s_3$	[0.88 0.91 0.95]	[0.84 0.86 0.90]	[0.91 0.94 0.97]	[0.91 0.94 0.96]	[0.86 0.89 0.92]	[1.06 1.08 1.09]
$s_4$	[0.85 0.87 0.90]	[0.91 0.93 0.95]	[0.85 0.88 0.90]	[0.86 0.89 0.93]	[0.87 0.90 0.94]	[1.04 1.07 1.08]
$s_5$	[0.86 0.89 0.95]	[0.90 0.92 0.95]	[0.90 0.95 0.97]	[0.91 0.93 0.95]	[0.90 0.92 0.96]	[1.10 1.13 1.15]

TABLE 5: The evaluation table after the interval mapping transformation.

candidate	$u_1$	$u_2$	$u_3$	$u_4$	$u_5$	$u_6$
$s_1$	[0.80 0.85 0.90]	[0.90 0.92 0.95]	[0.91 0.94 0.95]	[0.93 0.96 0.99]	[0.90 0.91 0.92]	[0.95 0.97 0.99]
$s_2$	[0.90 0.95 1.00]	[0.89 0.90 0.93]	[0.90 0.92 0.95]	[0.90 0.92 0.95]	[0.94 0.97 0.98]	[0.90 0.93 0.95]
$s_3$	[0.88 0.91 0.95]	[0.84 0.86 0.90]	[0.91 0.94 0.97]	[0.91 0.94 0.96]	[0.86 0.89 0.92]	[0.91 0.92 0.94]
$s_4$	[0.85 0.87 0.90]	[0.91 0.93 0.95]	[0.85 0.88 0.90]	[0.86 0.89 0.93]	[0.87 0.90 0.94]	[0.92 0.93 0.96]
$s_5$	[0.86 0.89 0.95]	[0.90 0.92 0.95]	[0.90 0.95 0.97]	[0.91 0.93 0.95]	[0.90 0.92 0.96]	[0.85 0.87 0.90]

TABLE 6: Dependent degree of the three-parameter interval attribute values.

	$u_1$	$u_2$	$u_3$	$u_4$	$u_5$	$u_6$
$k_{1j}$	0.2500	0.6167	0.6667	0.8000	0.5500	0.8500
$k_{2j}$	0.7500	0.5333	0.6167	0.6167	0.8167	0.6333
$k_{3j}$	0.5667	0.3333	0.7000	0.6833	0.4500	0.6167
$k_{4j}$	0.3667	0.6500	0.3833	0.4667	0.5167	0.6833
$k_{5j}$	0.5000	0.6167	0.7000	0.6500	0.6333	0.3667

TABLE 7: The three-parameter interval weight values.

$w_j$	$u_1$	$u_2$	$u_3$	$u_4$	$u_5$	$u_6$
$[w_j^a, w_j^m, w_j^b]$	[0.10, 0.15, 0.20]	[0.05, 0.10, 0.15]	[0.20, 0.25, 0.30]	[0.05, 0.10, 0.15]	[0.15, 0.20, 0.25]	[0.10, 0.15, 0.20]

TABLE 8: Dependent degree of the three-parameter interval weight values.

$K(s_i)$	$s_1$	$s_2$	$s_3$	$s_4$	$s_5$
$[K(s_i)^a, K(s_i)^m, K(s_i)^b]$	[0.397, 0.583, 0.770]	[0.442, 0.640, 0.838]	[0.377, 0.544, 0.712]	[0.315, 0.468, 0.622]	[0.385, 0.558, 0.732]

TABLE 9: The scheme sorting results and their stability test.

	$s_1$	$s_2$	$s_3$	$s_4$	$s_5$	sorting result
$K(s_i)^a$	0.3967	0.4417	0.3767	0.3150	0.3850	$s_2 > s_1 > s_5 > s_3 > s_4$
$K(s_i)^m$	0.5833	0.6400	0.5442	0.4683	0.5583	$s_2 > s_1 > s_5 > s_3 > s_4$
$K(s_i)^b$	0.7700	0.8383	0.7117	0.6217	0.7317	$s_2 > s_1 > s_5 > s_3 > s_4$

determined range [0.80, 1.00]. The range of the last one is also changed to [0.80, 1.00] after the interval mapping transformation. Then, the three-parameter interval dependent degree of each attribute evaluation value is calculated, as shown in Table 6.

(5) In order to maintain comparison consistency and validity, the weights of the attributes are set the same as those in [15, 26], as shown in the form of three-parameter interval number in Table 7. According to Step 5, the comprehensive dependent degree of each scheme under three weight parameters is calculated, respectively, as shown in Table 8. Then, the scheme sorting results and their stability test are shown in Table 9. By sorting under the upper bound, lower bound,

and the gravity value of weight parameter, respectively, the sorting results are all the same, which means higher stability of the sorting results. The results are also the same as those in [26].

(6) According to the different settings of  $\alpha$  and  $\beta$  in Table 3, the uncertainty analysis is performed.  $\alpha$  and  $\beta$  show the different tendency from decision makers for the dependent degree of the upper bound, the lower bound, and the gravity value. Table 10 shows the sorting results under six different settings of  $\alpha$  and  $\beta$ . The results illustrate that the sorting results are still the same under different attitude coefficient settings, which means the current sorting result has lower level of uncertainty and it does not change when

TABLE 10: the sorting results under different attitude coefficient settings.

coefficient settings	$s_1$	$s_2$	$s_3$	$s_4$	$s_5$	sorting result
I	0.5833	0.6400	0.5442	0.4683	0.5583	$s_2 > s_1 > s_5 > s_3 > s_4$
II	0.5850	0.6400	0.5425	0.4662	0.5569	$s_2 > s_1 > s_5 > s_3 > s_4$
III	0.5820	0.6400	0.5455	0.4700	0.5595	$s_2 > s_1 > s_5 > s_3 > s_4$
IV	0.5879	0.6400	0.5396	0.4627	0.5544	$s_2 > s_1 > s_5 > s_3 > s_4$
V	0.5578	0.6111	0.5147	0.4400	0.5253	$s_2 > s_1 > s_5 > s_3 > s_4$
VI	0.6089	0.6689	0.5736	0.4966	0.5913	$s_2 > s_1 > s_5 > s_3 > s_4$

TABLE 11: Sorting reversion caused by the move transformation of evaluation of attribute  $s_1$ .

move transformation $T(\overline{X}_{1j})$	$K(s_1)$	$K(s_2)$	sorting reversion
$\overline{X}_{11}[0.80, 0.85, 0.90] \rightarrow [0.88, 0.93, 0.98]$	0.6433	0.6400	$s_1 > s_2 > s_5 > s_3 > s_4$
$\overline{X}_{13}[0.91, 0.94, 0.95] \rightarrow [0.96, 0.99, 1.00]$	0.6458	0.6400	$s_1 > s_2 > s_5 > s_3 > s_4$
$\overline{X}_{15}[0.90, 0.91, 0.92] \rightarrow [0.96, 0.97, 0.98]$	0.6433	0.6400	$s_1 > s_2 > s_5 > s_3 > s_4$

the preference tendency from decision makers for the upper or lower bound of attribute evaluations changes.

**4.2. Extension Transformation Analysis.** At above, the sorting method and uncertainty analysis of multiattribute decision making under static environment have been described precisely though building extension interval dependent degree function. In addition, according to Step 7, the dependent degree will change by performing extension transformation of the dependent degree formula, which can precisely describe the changes and rule discoveries of decision results under dynamic environment. In this case, a most common extension transformation is element transformation. For example, the evaluation value of attribute  $u_1$  of candidate  $s_1$  changes from [0.80 0.85 0.90] to [0.85 0.90 0.95] after element transformation. Will it influence the decision results? Or what the extent of the influence that it makes? Literature [22] puts forward five basic interval extension transformations such as movement, expansion and contraction, replacement, addition and deletion, and decomposition. Here, movement transformation, which is the most common one, is used to analyze decision results under some dynamic environment.

**Definition 19.** Suppose a three-parameter interval  $\overline{X} = [a, m, b]$  and a constant  $l$ . There is transformation  $T$  towards them, and it makes  $T(\overline{X}) = [a+l, m+l, b+l]$  hold. Then,  $T$  is called the move transformation of  $\overline{X}$ . While  $l \geq 0$ ,  $T$  is called positive direction move transformation.

**Theorem 20.** Suppose a benefit attribute interval  $X = [a, b]$  and a three-parameter subinterval  $\overline{X}_0 = [a_0, m_0, b_0]$ ,  $\overline{X}_0 \subseteq X$ . If a move transformation  $T(\overline{X}_0) = [a_0+l, m_0+l, b_0+l]$  ( $0 \leq l \leq b-b_0$ ) exists, then  $k(T(\overline{X}_0), X) - k(\overline{X}_0, X) = l/(b-a)$  holds.

*Proof.* Since  $X = [a, b]$  is a benefit attribute interval,  $b$  is the optimal value, so

$$k(T(\overline{X}_0), X) - k(\overline{X}_0, X) = \alpha k(a_0 + l) + (1 - \alpha - \beta) k(m_0 + l) + \beta k(b_0 + l) - (\alpha k(a_0) + (1 - \alpha - \beta) k(m_0) + \beta k(b_0)) = \alpha \left( \frac{a_0 + l - a}{b - a} \right) + (1 - \alpha - \beta) \left( \frac{m_0 + l - a}{b - a} \right) + \beta \left( \frac{b_0 + l - a}{b - a} \right) - \left( \alpha \left( \frac{a_0 - a}{b - a} \right) + (1 - \alpha - \beta) \left( \frac{m_0 - a}{b - a} \right) + \beta \left( \frac{b_0 - a}{b - a} \right) \right) = \frac{\alpha l + (1 - \alpha - \beta) l + \beta l}{b - a} = \frac{l}{b - a}.$$

(10)  
□

For multiattribute decision making, each evaluation value may be performed by the movement transformation. As a result, the combination result of all movement transformations tends to be quite complex. Here, we only discuss the impact from movement transformation of one attribute. For example, for a positive direction move transformation of one attribute of candidate  $s_1$ , the transformation is established as

$$T(\overline{X}_{1j}) = [a_{1j} + l_j, m_{1j} + l_j, b_{1j} + l_j] \quad (j = 1, 2, \dots, n, 0 \leq l_j \leq 1 - m_{1j}). \quad (11)$$

According to Theorem 20, by iteration calculation with step size of 0.01, the transformation rule and the threshold value that is able to bring some sorting reversion are obtained, as shown in Table 11. It illustrates that, if the evaluation of scheme  $s_1$  wants to overtake that of  $s_2$ , the evaluation of any of the attributes  $u_1, u_3, u_5$  should be chosen to be promoted. Among them, attribute  $u_3$  needs a minimum level of promotion. However, except for  $u_1, u_3, u_5$ , promoting the evaluation of any of the other attributes will not change the results.

Here is another example, by taking positive direction move transformation of one attribute of candidate  $s_3$ , transformation analysis will be performed. By iteration calculation with step size of 0.01, the transformation rule and the threshold value that is able to bring some sorting reversion

TABLE 12: Sorting reversion caused by the move transformation of evaluation of attribute  $s_3$ .

move transformation $T(\overline{X}_{3j})$	$K(s_3)$	$K(s_5)$	sorting reversion
$\overline{X}_{31}[0.88, 0.91, 0.95] \rightarrow [0.90, 0.93, 0.97]$	0.5592	0.5583	$s_2 \succ s_1 \succ s_3 \succ s_5 \succ s_4$
$\overline{X}_{32}[0.84, 0.86, 0.90] \rightarrow [0.87, 0.89, 0.93]$	0.5592	0.5583	$s_2 \succ s_1 \succ s_3 \succ s_5 \succ s_4$
$\overline{X}_{33}[0.91, 0.94, 0.97] \rightarrow [0.93, 0.96, 0.99]$	0.5692	0.5583	$s_2 \succ s_1 \succ s_3 \succ s_5 \succ s_4$
$\overline{X}_{34}[0.91, 0.94, 0.96] \rightarrow [0.94, 0.97, 0.99]$	0.5592	0.5583	$s_2 \succ s_1 \succ s_3 \succ s_5 \succ s_4$
$\overline{X}_{35}[0.86, 0.89, 0.92] \rightarrow [0.88, 0.91, 0.94]$	0.5642	0.5583	$s_2 \succ s_1 \succ s_3 \succ s_5 \succ s_4$
$\overline{X}_{36}[0.91, 0.92, 0.94] \rightarrow [0.93, 0.94, 0.96]$ $\Rightarrow \overline{X}_{36} \Rightarrow [1.06, 1.08, 1.09] \rightarrow [1.04, 1.06, 1.07]$	0.5592	0.5583	$s_2 \succ s_1 \succ s_3 \succ s_5 \succ s_4$

are obtained, as shown in Table 12. It illustrates that, if the evaluation of  $s_3$  is going to overtake that of  $s_5$ , the evaluation of any of the attributes can be chosen to be promoted. Among them, attributes  $u_1, u_3, u_5, u_6$  need relatively low levels of promotion. It must be noted that the interval of  $u_6$  has been processed by mapping transformation and, as a result, and needs to map back after movement transformation.

**5. Conclusion**

By adopting the extension dependent degree function, the paper researches the multiattribute decision making with attribute information being three-parameter interval number. It is a new thinking in the related research field. The main contributions are listed as follows: (1) Based on extension dependent function, a new decision making method and framework towards the multiattribute decision with attribute information being three-parameter interval number are put forward. (2) A formula of extension three-parameter interval dependent degree function is given, which reflects the different tendency from decision makers towards the lower bound, the upper bound, and the gravity point of the attribute evaluation by setting preference attitude coefficients. (3) Through defining the interval dependent degree mapping method, the calculation of the interval dependent degree with the optimal point not at the endpoint is transformed to the calculation with the optimal point at the endpoint, which has monotonic and simple process. (4) Six typical settings of attitude coefficients are given and the uncertainty analysis of decision results is made accordingly. (5) Based on the framework of the extension dependent degree calculation, dynamic analysis and rule discovery on decision results are performed through some extension element transformation.

The research work is quite abundant in the future. As a new thinking and framework, the decision method based on extension dependent function still needs further development and promotion. Next, the model will consider the combination of psychological behavior from decision makers such as prospect theory or regret theory, which can better reflect decision makers' risk preferences. By improving the extension dependent function, the model can describe some more complex decision processes. The model may be revised to adapt to some more complex extension transformations. Furthermore, the model can also need to be expanded to many other decision environments including mixed type data, incomplete information, and fuzzy hesitant set.

**Data Availability**

The data used to support the findings of this study are included within the article.

**Conflicts of Interest**

The authors declare that there are no conflicts of interest regarding the publication of this paper.

**Acknowledgments**

This research was supported by Zhejiang Science Foundation Project of China (No. Y16G010010, LY18F020001) and Ningbo Innovative Team: the intelligent big data engineering application for life and health (Grant No. 2016C11024).

**References**

- [1] Q.-W. Cao and J. Wu, "The extended COWG operators and their application to multiple attributive group decision making problems with interval numbers," *Applied Mathematical Modelling*, vol. 35, no. 5, pp. 2075–2086, 2011.
- [2] Z. Xu and H. Liao, "A survey of approaches to decision making with intuitionistic fuzzy preference relations," *Knowledge-Based Systems*, vol. 80, pp. 131–142, 2015.
- [3] P. Wang, P. Meng, J.-Y. Zhai, and Z.-Q. Zhu, "A hybrid method using experiment design and grey relational analysis for multiple criteria decision making problems," *Knowledge-Based Systems*, vol. 53, no. 11, pp. 100–107, 2013.
- [4] J. Ma and C. Ji, "Generalized grey target decision method for mixed attributes based on connection number," *Journal of Applied Mathematics*, vol. 2014, 2014.
- [5] K. Kumar and H. Garg, "Connection number of set pair analysis based TOPSIS method on intuitionistic fuzzy sets and their application to decision making," *Applied Intelligence*, vol. 48, no. 8, pp. 2112–2119, 2018.
- [6] G. Z. Pu and Y. W. Zhang, "Grey Fuzzy Comprehensive Evaluation Method Based on Interval Numbers of Three Parameters," *Systems Engineering and Electronic*, vol. 23, no. 9, pp. 43–45, 2001.
- [7] D. Luo and X. Wang, "The multi-attribute grey target decision method for attribute value within three-parameter interval grey number," *Applied Mathematical Modelling*, vol. 36, no. 5, pp. 1957–1963, 2012.
- [8] D. Luo, "Decision-making methods with three-parameter interval grey number," *Systems Engineering - Theory & Practice*, vol. 29, no. 1, pp. 124–130, 2009.

- [9] D. Luo, X. Wang, and B. Song, "Multi-attribute decision-making methods with three-parameter interval grey number," *Grey Systems: Theory and Application*, vol. 3, no. 3, pp. 305–315, 2013.
- [10] Q. Z. Hu, W. H. Zhang, and L. Yu, "The Research and Application of Interval Numbers of Three Parameters," *Engineering Science*, vol. 9, pp. 47–51, 2007.
- [11] S. L. Yan, S. F. Liu, J. J. Zhu et al., "TOPSIS Decision-Making Method with Three-Parameter Interval Number Based on Entropy Measure," *Chinese Journal of Management Science*, vol. 21, no. 6, pp. 145–151, 2013.
- [12] Y. Rong and Y. Liu, "TOPSIS multiple attribute decision making method based on three parameters interval number," in *Proceedings of the 4th IEEE International Conference on Progress in Informatics and Computing, PIC 2016*, pp. 123–127, China, December 2016.
- [13] C.-B. Li, K. Zhao, and Z.-Q. Qi, "A risky multi-criteria decision-making method with three-parameter interval grey number," *Zidonghua Xuebao/Acta Automatica Sinica*, vol. 41, no. 7, pp. 1306–1314, 2015.
- [14] ZW. Chen, XF. Wang, YJ. Shao, and i. e, "Regret theory approach to multiple attribute decision making with three-parameter interval number," *Control Theory & Applications*, vol. 33, no. 9, pp. 1214–1224, 2016.
- [15] Y.-J. Xu and Q.-L. Da, "Method for triangular fuzzy number multiple attribute decision making based on ideal solution," *Xi Tong Gong Cheng Yu Dian Zi Ji Shu*, vol. 29, no. 9, pp. 1469–1471, 2007.
- [16] X.-H. Chen and X. Yang, "Multiple attributive group decision making method based on triangular fuzzy numbers," *Xi Tong Gong Cheng Yu Dian Zi Ji Shu*, vol. 30, no. 2, pp. 278–282, 2008.
- [17] J. L. LanR Fan, "TOPSIS decision-making method on three parameters interval-valued fuzzy sets," *Engineering Theory & Practice*, vol. 29, no. 5, pp. 129–136, 2009.
- [18] C. Li and J. Yuan, "A new multi-attribute decision-making method with three-parameter interval grey linguistic variable," *International Journal of Fuzzy Systems*, vol. 19, no. 2, pp. 292–300, 2017.
- [19] W. X. Jin, X. M. Liu, and K. Q. Zhao, "Multiple Attribute Decision-making with the Interval Number and with the Hybrid Qualitative and Quantitative Based on the Connection Number," *Mathematics in Practice and Theory*, vol. 44, pp. 166–173, 2014.
- [20] F. Molinari, "A new criterion of choice between generalized triangular fuzzy numbers," *Fuzzy Sets and Systems*, vol. 296, pp. 51–69, 2016.
- [21] S. Zeng, J. Chen, and X. Li, "A hybrid method for pythagorean fuzzy multiple-criteria decision making," *International Journal of Information Technology & Decision Making*, vol. 15, no. 2, pp. 403–422, 2016.
- [22] C. Y. Yang and W. Cai, *Extenics: Theory, Method and Application*, SciencePress, Columbus, The Educational Publisher, Beijing, China, 2013.
- [23] M. Wang, X. Xu, J. Li, J. Jin, and F. Shen, "A novel model of set pair analysis coupled with extenics for evaluation of surrounding rock stability," *Mathematical Problems in Engineering*, vol. 2015, Article ID 892549, 9 pages, 2015.
- [24] X. Li, Y. Tian, F. Smarandache, and R. Alex, "An extension collaborative innovation model in the context of big data," *International Journal of Information Technology & Decision Making*, vol. 14, no. 1, pp. 69–91, 2015.
- [25] Q. Z. Hu, L. Yu, and A. P. Zhang, "Research about Multi-objective Decision Making Method Based on Interval Numbers of Three Elements," *Journal of Systems & Management*, vol. 19, no. 1, pp. 25–30, 2010.
- [26] X. M. Liu and K. Q. Zhao, "Multiple attribute decision making of interval numbers based on analysis of the uncertainty of connection numbers," *Fuzzy Systems and Mathematics*, vol. 24, no. 5, pp. 141–148, 2010.

## Research Article

# Bifurcation Analysis of Stick-Slip Motion of the Vibration-Driven System with Dry Friction

Peng Li  and Ziwang Jiang

*School of Aerospace Engineering and Applied Mechanics, Tongji University, Shanghai 200092, China*

Correspondence should be addressed to Peng Li; [1310548@tongji.edu.cn](mailto:1310548@tongji.edu.cn)

Received 9 March 2018; Revised 26 June 2018; Accepted 12 August 2018; Published 27 August 2018

Academic Editor: Carlos Llopis-Albert

Copyright © 2018 Peng Li and Ziwang Jiang. This is an open access article distributed under the Creative Commons Attribution License, which permits unrestricted use, distribution, and reproduction in any medium, provided the original work is properly cited.

This paper is concerned with the vibration-driven system which can move due to the periodic motion of the internal mass and the dry friction; the system can be modeled as Filippov system and has the property of stick-slip motion. Different periodic solutions of stick-slip motion can be analyzed through sliding bifurcation, two-parameter numerical continuation for sliding bifurcation is carried out to get the different bifurcation curves, and the bifurcation curves divide the parameters plane into different regions which stand for different stick-slip motion of the periodic solution. Furthermore, continuations with additional condition  $v = 0$  are carried out for the directional control of the vibration-driven system in one period; the curves divide the parameter plane into different progressions.

## 1. Introduction

Recently, mobile mechanisms that can move due to the vibration of the internal mass have been widely researched, and these mechanisms have many advantages over conventional mobile systems (driven by legs, wheels, wings, etc.), for example, easy fabrication, hermetic structure, and locomotion in the narrow environment. Thus they have extensive application in pipeline inspection, life detection in disaster, and medical endoscopy.

Chernousko [1] first proposed the horizontal motion of the system driven by the movable internal mass; the friction which acted on the body is anisotropic, which means the coefficient of friction in forward and backward direction is different. The two periodic control modes, velocity-controlled mode and acceleration-controlled mode, are constructed for the relative motion of the internal mass, and optimal parameters of periodic control were decided to realize the maximum mean velocity of the body. Fang et al. [2] used the method of averaging to obtain an approximate expression of the average steady-state velocity when the stick-slip phenomenon was not considered, optimal parameters of the internal controlled mass were determined to maximize the average velocity, and some control strategies were given

to control the motion of system under the stick-slip effect. Liu et al. [3] studied the vibroimpact capsule system which has a main body interacting with an internal harmonically driven mass, when the internal mass contact with the plate impact occurs, and the parameters for the maximum mean velocity can be determined through nonlinear dynamics analysis, the energy consumption was also considered, and the parameters for the maximum mean velocity and the minimum energy consumption were not the same. Fang et al. [4, 5] and Zimmermann et al. [6–8] studied the two and more modules vibration-driven systems; the approximate expression of steady-state motion was obtained when the friction is small and the optimal parameters were got to achieve the maximum mean velocity. Bolotnik et al. [9] modeled the system driven by the movable internal mass which can move in the horizontal direction and the vertical direction (change the normal force for anisotropic friction in the different direction). Then the approximate expression of average steady-state velocity was obtained through the method of averaging; optimal parameters (the amplitude and the phase shift of the horizontal and vertical vibration excitation forces) were determined to realize the maximum average velocity and to control the direction of motion. In the paper, we study the model.

The dry friction plays an important role in vibration-driven system motion. The systems with dry friction belong to Filippov piecewise-smooth dynamical systems [10, 11]. The Filippov systems may exhibit different types of limit cycles caused by the interaction of a trajectory with the boundary of the sliding regions; the features of Filippov system are called the sliding bifurcation. Kowalczyk et al. [12] investigated a dry friction oscillator through numerical continuation of sliding bifurcation and revealed the codimension two sliding bifurcation points. Marcel Guardia et al. [13] analytically considered sliding bifurcations of periodic orbits in the dry friction oscillator, and the results agreed with the numerical calculation [12]. Fang et al. [14] studied the vibration-driven system through sliding bifurcation, and a two-parameter bifurcation problem was theoretically analyzed. For the numerical continuation of piecewise-smooth system, the software SlideCont [15] and TC-HAT [16] based on ATUO have been developed. Joseph Páez Chávez used the software TC-HAT to study the bifurcation of some mechanical models, the nonsmooth Jeffcott rotor [17], the impact oscillator [18], the piecewise-linear capsule system [19], etc. The continuation toolbox COCO was developed for continuation and bifurcation analysis of smooth and nonsmooth dynamical systems [20, 21]; the soft impact oscillator [22] and the impulsively coupled oscillators [23] were analyzed through the COCO. In this paper, the COCO will be employed to numerically study the sliding bifurcation of vibration-driven system; the sliding bifurcation will help us to understand the stick-slip property of periodic solution and give some instructive ideas to design and control the system.

The paper is organized as follows. In Section 2, the model of the vibration-driven system is described. The mathematical model of vibration-driven system is studied in detail in order to perform the numerical analysis by the mean of COCO in Section 3. Two-parameter sliding bifurcations are analyzed and the directional control of the vibration-driven system is tackled by the numerical continuation in Section 4, and some conclusions are given in Section 5.

## 2. Modeling of Vibration-Driven System

The vibration-driven system is considered as depicted in Figure 1. The vibration-driven system is composed of a rigid body and an internal mass; the rigid body realizes the translational motion along a straight line in the resistive environment. The internal mass can move relative to the rigid body in horizontal and vertical direction. The internal mass is considered a point mass. Dry friction acts between the rigid body and the ground.

Two Cartesian reference frames are introduced: the inertial reference frame  $Oxy$  and the coordinate system  $O'\xi\eta$  attached to the rigid body. The  $x$ - and  $\xi$ -axes are horizontal; the  $y$ - and  $\eta$ -axes are vertical. We denote  $x$  as the coordinate of the point  $O'$  in the inertial reference frame  $Oxy$ ,  $x$  denotes the displacement of the rigid body,  $\xi$  and  $\eta$  denote the coordinates of the internal body in the reference frame  $O'\xi\eta$ ,  $m$  and  $m_1$  are the masses of the rigid body and the internal body, respectively, and  $g$  is the gravitational acceleration.

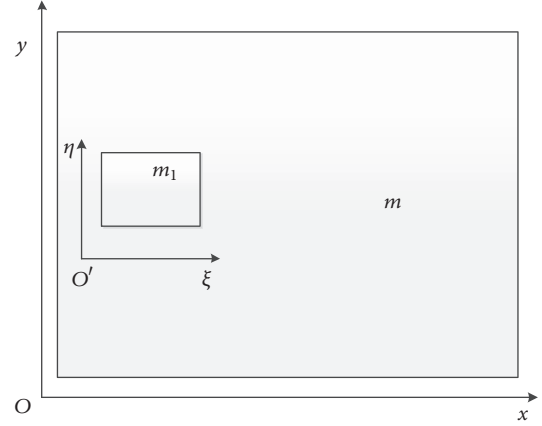


FIGURE 1: Vibration-driven system.

The dynamics equation of the system along  $x$ -axis can be governed by Newton's second laws as follows:

$$(m + m_1) \ddot{x} + m_1 \ddot{\xi} = F_f, \quad (1)$$

where  $F_f$  is the frictional force. The force  $F_f$  is described by Coulomb law:

$$F_f = \begin{cases} -\mu F_N \operatorname{sgn} \dot{x}, & \text{if } \dot{x} \neq 0, \\ -F_0, & \text{if } \dot{x} = 0 \& |F_0| \leq \mu F_N, \\ -\mu F_N \operatorname{sgn} F_0, & \text{if } \dot{x} = 0 \& |F_0| > \mu F_N, \end{cases} \quad (2)$$

where  $F_0$  is the resultant force on the body except for the dry friction in the horizontal direction,  $F_N$  is the normal force exerted on the system by the ground, and  $\mu$  is the coefficient of dry friction. The asymmetrical friction in forward and backward motions arises from the time-varying normal force  $F_N$ . The force  $F_0$  and force  $F_N$  can be expressed:

$$F_0 = -m_1 \ddot{\xi}, \quad (3)$$

$$F_N = (m + m_1) g + m_1 \ddot{\eta}. \quad (4)$$

The rigid body keeps the contact with the ground; therefore, the force  $F_N$  must be satisfied the inequality  $F_N \geq 0$ . So we have

$$(m + m_1) g + m_1 \ddot{\eta} \geq 0. \quad (5)$$

Next, we assume the control acceleration is harmonic function with the same frequency but shifted in the phase; particularly,

$$\begin{aligned} \ddot{\xi} &= -A \sin \omega t, \\ \ddot{\eta} &= B \sin(\omega t + \phi). \end{aligned} \quad (6)$$

Here  $A$  and  $B$  are the driving-amplitudes, respectively,  $\omega$  is the driving-frequency, and  $\phi$  is the phase difference between the forces.

Substituting (6) into (1)-(5),

$$M\dot{x} = F_x \sin \omega t + F_f, \quad (7)$$

$$F_f = \begin{cases} -\mu F_N \operatorname{sgn} \dot{x}, & \text{if } \dot{x} \neq 0, \\ -F_x \sin \omega t, & \text{if } \dot{x} = 0 \& |F_x \sin \omega t| \leq \mu F_N, \\ -\mu F_N \operatorname{sgn} \sin \omega t, & \text{if } \dot{x} = 0 \& |F_x \sin \omega t| > \mu F_N, \end{cases} \quad (8)$$

$$F_N = Mg + F_y \sin(\omega t + \phi), \quad F_N \geq 0, \quad (9)$$

where  $M = m + m_1$ ,  $F_x = m_1 A$ , and  $F_y = m_1 B$ .

To reduce the number of parameters of the system, the nondimensional variables  $x^*$  and  $t^*$  and the parameters  $\varepsilon$  and  $\alpha$  are introduced:

$$\begin{aligned} x^* &= \frac{M\omega^2}{F_x} x, \\ t^* &= \omega t, \\ \varepsilon &= \mu \frac{Mg}{F_x}, \\ \alpha &= \frac{F_y}{Mg} \end{aligned} \quad (10)$$

Substituting these variables above into (7)-(9) (omit the asterisks),

$$\ddot{x} = \sin t + f_c, \quad (11)$$

$$f_c = \begin{cases} -\varepsilon f_n \operatorname{sgn} \dot{x}, & \text{if } \dot{x} \neq 0, \\ -\sin t, & \text{if } \dot{x} = 0 \& |\sin t| \leq \varepsilon f_n, \\ -\varepsilon f_n \operatorname{sgn} \sin t, & \text{if } \dot{x} = 0 \& |\sin t| > \varepsilon f_n, \end{cases} \quad (12)$$

$$f_n = 1 + \alpha \sin(t + \phi), \quad \alpha \leq 1. \quad (13)$$

The expressions  $f_c$  and  $f_n$  stand for the normalized dry friction and the normal force, respectively. The parameter  $\varepsilon$  represents the ratio of the possible maximum value of the dry friction force to the amplitude  $F_x$ . We assume the value of the parameter  $\varepsilon$  is in the interval  $(0, 1)$ . Due to periodicity, the phase difference  $\phi$  ranges from 0 to  $2\pi$ .

### 3. Modeling of the Vibration-Driven System as Filippov System

The mathematical model of vibration-driven system can be defined as a piecewise-smooth system of the Filippov type. We can transform (11) into vector fields, event functions, and reset functions through the approach of multisegment periodic orbits. Let  $\mathbf{y} = (y_1, y_2)^T = (\dot{x}, t)^T$  and  $\mathbf{p} = (\varepsilon, \alpha, \phi)^T$  represent the state variables of the system and the parameters, respectively.

The multisegment periodic orbits of the vibration-driven system consist of two or more segments, which can be modeled as follows.

**Stick:** This segment occurs when  $\sin y_2 < |\varepsilon f_n|$ ; the motion during this segment is governed by the equation

$$\dot{\mathbf{y}} = f_s = \begin{pmatrix} 0 \\ 1 \end{pmatrix}. \quad (14)$$

This segment terminates when the resultant force on the body except for the dry friction equals the threshold of the dry friction force. The event functions are detected as follows:

$$h_f(\mathbf{y}) = \sin y_2 - \varepsilon(1 + \alpha \sin(y_2 + \phi)) = 0 \quad (\text{transition to forward slip})$$

$$h_b(\mathbf{y}) = \sin y_2 + \varepsilon(1 + \alpha \sin(y_2 + \phi)) = 0 \quad (\text{transition to backward slip})$$

The next segment initial point is defined by the reset function  $g_{id}(\mathbf{y}) = \mathbf{y}$ .

**Forward slip:** this segment occurs when the force is larger than the maximum value of the dry friction; that is,  $\sin y_2 > \varepsilon(1 + \alpha \sin(y_2 + \phi))$ ; the motion during this segment is governed by the equation

$$\dot{\mathbf{y}} = f_f = \begin{pmatrix} \sin y_2 - \varepsilon(1 + \alpha \sin(y_2 + \phi)) \\ 1 \end{pmatrix}. \quad (15)$$

This segment ends when the velocity becomes zero; that is,  $h(\mathbf{y}) = y_1 = 0$ . The next segment is connected by the reset function  $g_{id}(\mathbf{y}) = \mathbf{y}$ .

**Backward slip:** this segment occurs when  $\sin y_2 < -\varepsilon(1 + \alpha \sin(y_2 + \phi))$ ; the motion of the system during this segments is described by the equation

$$\dot{\mathbf{y}} = f_b = \begin{pmatrix} \sin y_2 + \varepsilon(1 + \alpha \sin(y_2 + \phi)) \\ 1 \end{pmatrix}. \quad (16)$$

This segment ends when the velocity becomes zero; the event function is defined:  $h(\mathbf{y}) = y_1 = 0$ . The next segment is connected by the reset function  $g_{id}(\mathbf{y}) = \mathbf{y}$ .

**Stick  $2\pi$ :** this segment is introduced to keep the variable  $y_2$  within the interval  $[0, 2\pi)$ , when  $\sin y_2 < |\varepsilon f_n|$ , the motion of the system is governed by (14), the segment ends when  $h_{2\pi}(\mathbf{y}) = 2\pi - y_2 = 0$ , and the reset function is

$$g_{2\pi}(\mathbf{y}) = \begin{pmatrix} y_1 \\ y_2 - 2\pi \end{pmatrix}. \quad (17)$$

**Forward slip  $2\pi$ :** this segment is introduced to keep the variable  $y_2$  within the interval  $[0, 2\pi)$ , when  $\sin y_2 > \varepsilon(1 + \alpha \sin(y_2 + \phi))$ , the motion of the system is governed by (15), the segment ends when  $h_{2\pi}(\mathbf{y}) = 2\pi - y_2 = 0$ , and the reset function is  $g_{2\pi}(\mathbf{y})$ .

**Backward slip  $2\pi$ :** this segment is introduced to keep the variable  $y_2$  within the interval  $[0, 2\pi)$ , when  $\sin y_2 < -\varepsilon(1 + \alpha \sin(y_2 + \phi))$ , the motion of the system is governed by (16), the segment ends when  $h_{2\pi}(\mathbf{y}) = 2\pi - y_2 = 0$ , and the reset function is  $g_{2\pi}(\mathbf{y})$ .

A periodic solution of Filippov system can be described as a sequence of triplet  $I_i = (f_i, h_i, g_i)$ ; the segment of system is governed by the vector field  $f_i$ , terminates at the

event function  $h_i$ , and connects the next segment by the reset function  $g_i$ . Any periodic trajectory of the system is described by solution signature  $\{I_i\}_{i=1}^M$ ;  $M$  is the length of signature. Therefore the periodic solution of the vibration-driven can be described by combinations of the seven triplets corresponding to above statement:

$$\begin{aligned}
 I_1 &= (f_s, h_f, g_{id}), \\
 I_2 &= (f_s, h_b, g_{id}), \\
 I_3 &= (f_f, h, g_{id}), \\
 I_4 &= (f_b, h, g_{id}), \\
 I_5 &= (f_s, h_{2\pi}, g_{2\pi}), \\
 I_6 &= (f_f, h_{2\pi}, g_{2\pi}), \\
 I_7 &= (f_b, h_{2\pi}, g_{2\pi}).
 \end{aligned} \tag{18}$$

In the Filippov system, there are four possible sliding bifurcations in the limit cycle because of the interaction of a trajectory with the boundary of a sliding region, including crossing-sliding bifurcation, gazing-sliding bifurcation, switching-sliding bifurcation, and adding-sliding bifurcation. Nondegeneracy conditions for the four sliding bifurcation are given [10, 11]. The sliding bifurcation does not change the number and stability of the system's solutions, but it will induce the different interaction between the limit cycle and the sliding regions.

#### 4. Numerical Bifurcation Analysis

In this section, we will perform the sliding bifurcation and directional control to analyze the dynamics response of the vibration-driven system.

**4.1. Sliding Bifurcation Analysis.** When  $\varepsilon = 0.6, \alpha = 0.456, \phi = 2\pi/3$ , the periodic trajectory of the motion is shown by Figure 2. The cycle signature is  $\{I_1, I_3, I_4, I_5\}$ . We start the numerical continuation of the periodic solution by the method of path-following using the parameter value as an initial value. The additional boundary  $h_b(\mathbf{y}) = \sin y_2 + \varepsilon(1 + \alpha \sin(y_2 + \phi)) = 0$  may be applied to the start point of the third segment for the crossing-sliding bifurcation continuation. We will use the COCO to carry out the numerical continuation concerning parameters  $\phi$  and  $\varepsilon$ ; the curve  $cs_1$  which is the result of this numerical continuation is shown in Figure 3.

Similarly, the numerical continuation is performed in parameter space  $\phi \times \varepsilon$  with different cycle signatures and different additional boundary condition for different segment boundary point and the results are depicted in Figure 3. The signature of cycle trajectory in  $E_1$  is  $\{I_1, I_3, I_5\}$ , when the additional conditions  $h_b(\mathbf{y}) = \sin y_2 + \varepsilon(1 + \alpha \sin(y_2 + \phi)) = 0$  and  $\cos y_2 + \varepsilon \alpha \cos(y_2 + \phi) = 0$  are applied to the point of the segment  $I_5$  according to nondegeneracy conditions of adding-sliding bifurcation; hence we can get the adding-sliding bifurcation curve  $ad_1$ . The adding-sliding bifurcation

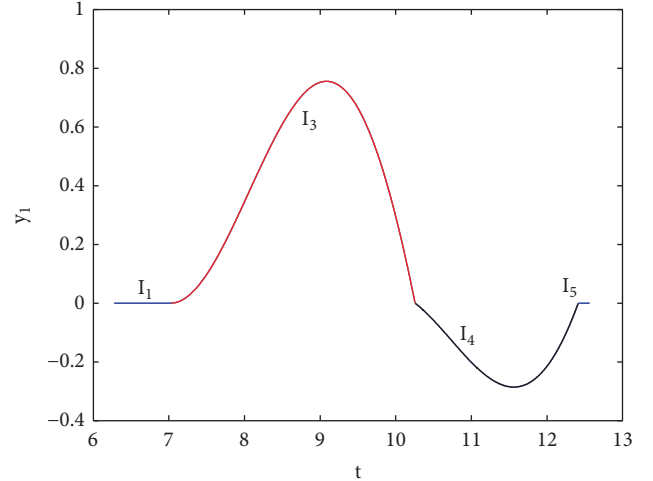


FIGURE 2: Periodic solution of vibration-driven system (11) computed for the parameter values  $\varepsilon = 0.6, \alpha = 0.456, \phi = 2\pi/3$ . The trajectory consists of the segments  $I_1, I_3, I_4, I_5$ .

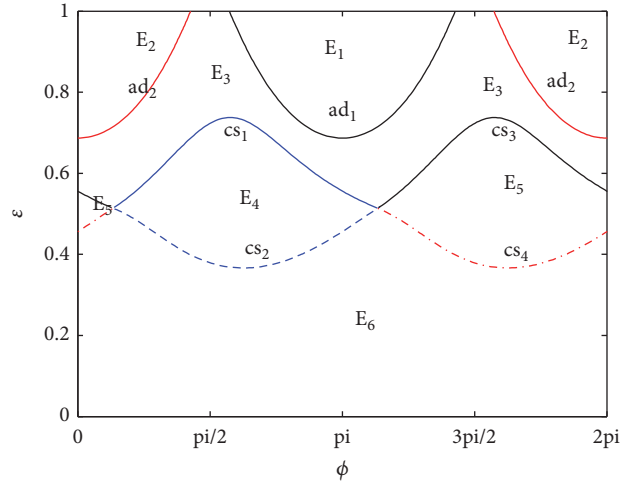


FIGURE 3: Two-parameter continuation of sliding bifurcation with respect to  $\phi$  and  $\varepsilon$  for  $\alpha = 0.456$ .  $ad_i$  represent adding-sliding bifurcations,  $cs_i$  represent crossing-sliding bifurcations, and the regions  $E_i$  denote the different stick-slip motions of the periodic solutions.

branch  $ad_2$  is got similarly. The curves  $cs_1, cs_2, cs_3$ , and  $cs_4$  represent crossing-sliding bifurcation branches. The sliding bifurcation curves divide the two parameters plane into eight regions and there are six different stick-slip periodic solutions in the parameter plane. The periodic solution of system in  $E_1$  with signature  $\{I_1, I_3, I_5\}$  is depicted in Figure 4(a), which means the velocity of the system is always greater than or equal to 0. The signature of the periodic trajectory in  $E_2$  is  $\{I_4, I_2, I_7\}$  as depicted in Figure 4(b), which means the velocity of the system is always lower than or equal to 0. The velocity in the two regions does not change its sign; it is important for the practical application to do some work, such as medical robot for intestinal therapy. Furthermore, when the velocity of system changes its sign, the efficiency will decrease because

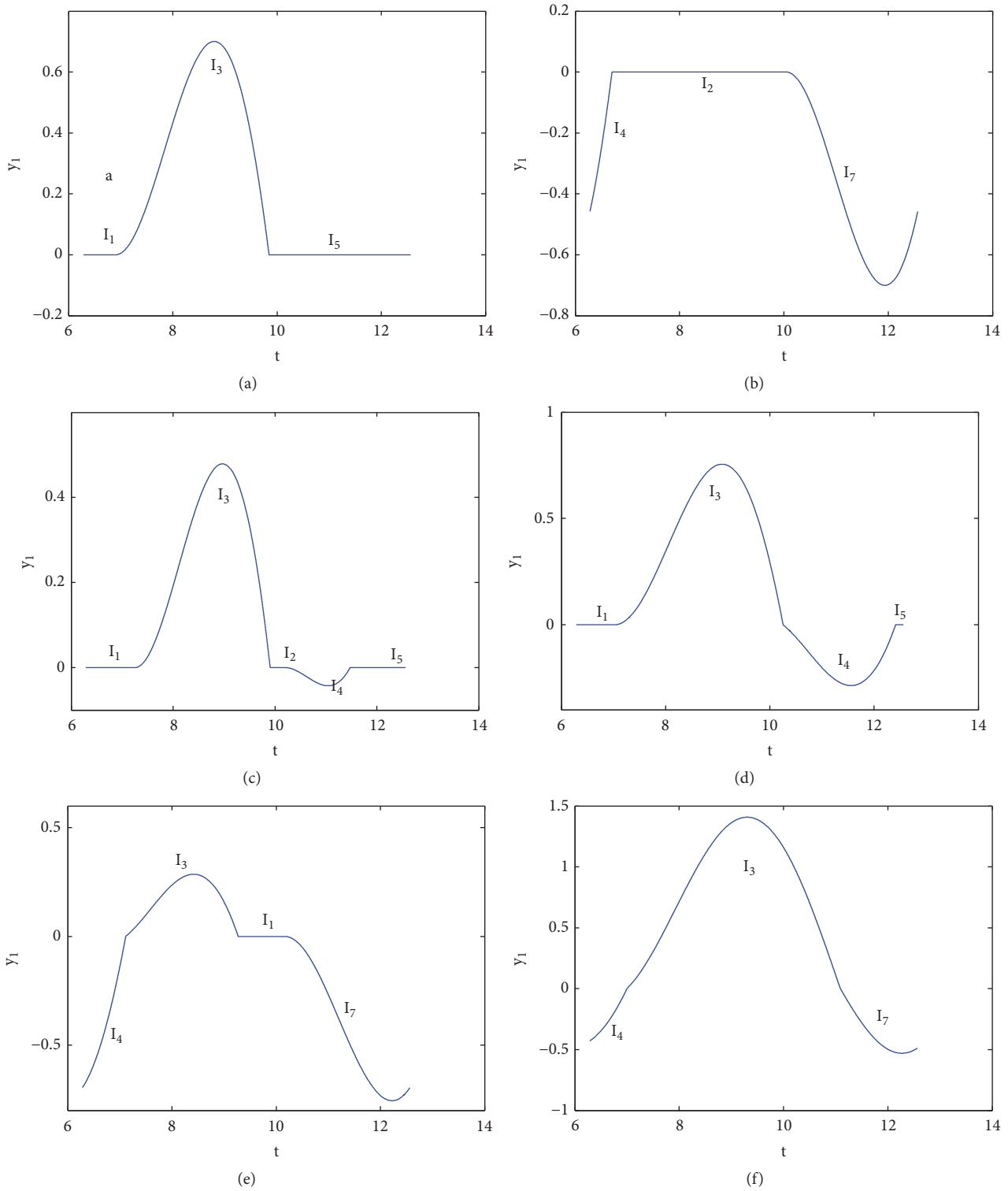


FIGURE 4: The velocity of the vibration-driven system for  $\alpha = 0.456$ , (a)  $\epsilon = 0.8, \phi = \pi$  in  $E_1$ . (b)  $\epsilon = 0.8, \phi = 0$  in  $E_2$ . (c)  $\epsilon = 0.8, \phi = 2\pi/3$  in  $E_3$ . (d)  $\epsilon = 0.6, \phi = 2\pi/3$  in  $E_4$ . (e)  $\epsilon = 0.6, \phi = 5\pi/3$  in  $E_5$ . (f)  $\epsilon = 0.2, \phi = 2\pi/3$  in  $E_6$ .

of more energy dissipated by opposite slip. The limit cycle of system in  $E_3$  can be described by the signature  $\{I_1, I_3, I_2, I_4, I_5\}$  depicted in Figure 4(c). The signature of periodic solution in  $E_4$  is  $\{I_1, I_3, I_4, I_5\}$  showed in Figure 4(d); the signature of the

periodic solution in  $E_5$  is  $\{I_4, I_3, I_1, I_7\}$  depicted in Figure 4(e). The cyclic signature in Figure 4(f) is  $\{I_4, I_3, I_7\}$ .

The result of two-parameter continuation for the sliding bifurcation with respect to the parameters  $\phi$  and  $\epsilon$  by fixing

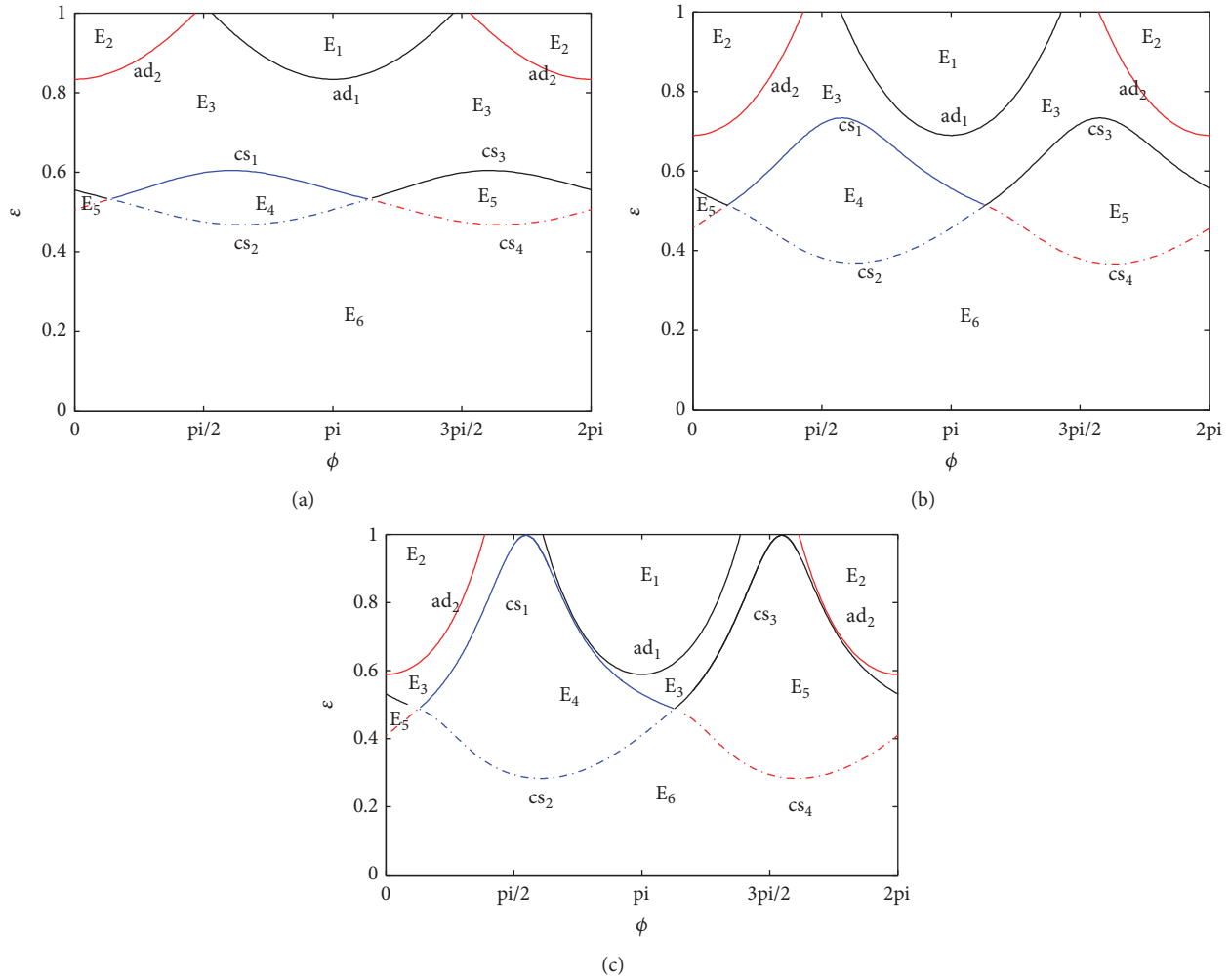


FIGURE 5: Two-parameter continuations of sliding bifurcation with respect to  $\phi$  and  $\varepsilon$  for different parameter  $\alpha$ : (a)  $\alpha = 0.2$ ; (b)  $\alpha = 0.45$ ; (c)  $\alpha = 0.7$ ;  $ad_i$  represent adding-sliding bifurcations,  $cs_i$  represent crossing-sliding bifurcations, and the regions  $E_i$  denote the different stick-slip motions of the periodic solutions.

different value  $\alpha$  ((a)  $\alpha = 0.2$ ; (b)  $\alpha = 0.45$ ; (c)  $\alpha = 0.7$ ) is shown in Figure 5. The regions  $E_3$  and  $E_6$  are shrinking and the regions  $E_1$ ,  $E_2$ ,  $E_4$ , and  $E_5$  are expanding as the  $\alpha$  increases. Therefore it is easy to realize directional motion in  $E_1$  or  $E_2$  through changing the parameters when the parameter  $\alpha$  increases.

We carry out the numerical continuation with respect to the parameters  $\varepsilon, \alpha$  in  $[0, 1] \times [0, 1]$  for the different  $\phi$  and the results are depicted in Figure 6 ((a)  $\phi = \pi/3$ ; (b)  $\phi = 2\pi/3$ ; (c)  $\phi = 4\pi/3$ ). The periodic solutions in region  $E_i$  in Figures 3 and 6 have the same stick-slip motion; the curve  $ss_1$  represents the switching-sliding bifurcation branch. As shown from Figure 6, there are different regions of stick-slip motion of system in the parameter plane when  $\phi$  is different; the motion in  $E_2$  which is always equal to or lower than 0 can be realized by changing the parameter  $\varepsilon$  and  $\alpha$  when  $\phi = \pi/3$ , but the motion in  $E_1$  could not happen no matter the value of  $\varepsilon$  and  $\alpha$ . The velocity of system which is always equal to or larger than zero can be controlled through changing the

parameter when  $\phi$  is  $2\pi/3$  or  $4\pi/3$ . Therefore the value of  $\phi$  is important for realizing directional motion.

The numerical continuation for the parameters  $\phi, \alpha$  in the  $[0, 2\pi] \times [0, 1]$  by fixing the value of the parameter  $\varepsilon$  is carried out and the results are depicted in Figure 7. From Figure 7, there are no regions  $E_1$  and  $E_2$  in the parameter plane when  $\varepsilon = 0.4$ , but the regions  $E_1$  and  $E_2$  appear in the parameter plane as  $\varepsilon$  increases to 0.6; the regions  $E_1$  and  $E_2$  expand when  $\varepsilon = 0.8$ .

**4.2. Directional Control.** Based on the above analysis, we can see that the direction of the system progression in one period can be forward (the region  $E_1$  in Figure 3) or backward (the region  $E_2$  in Figure 3) owing to different parameters.

The average velocity of the system in one period is

$$v = \frac{1}{T} \int_0^T y_1(t) dt. \quad (19)$$

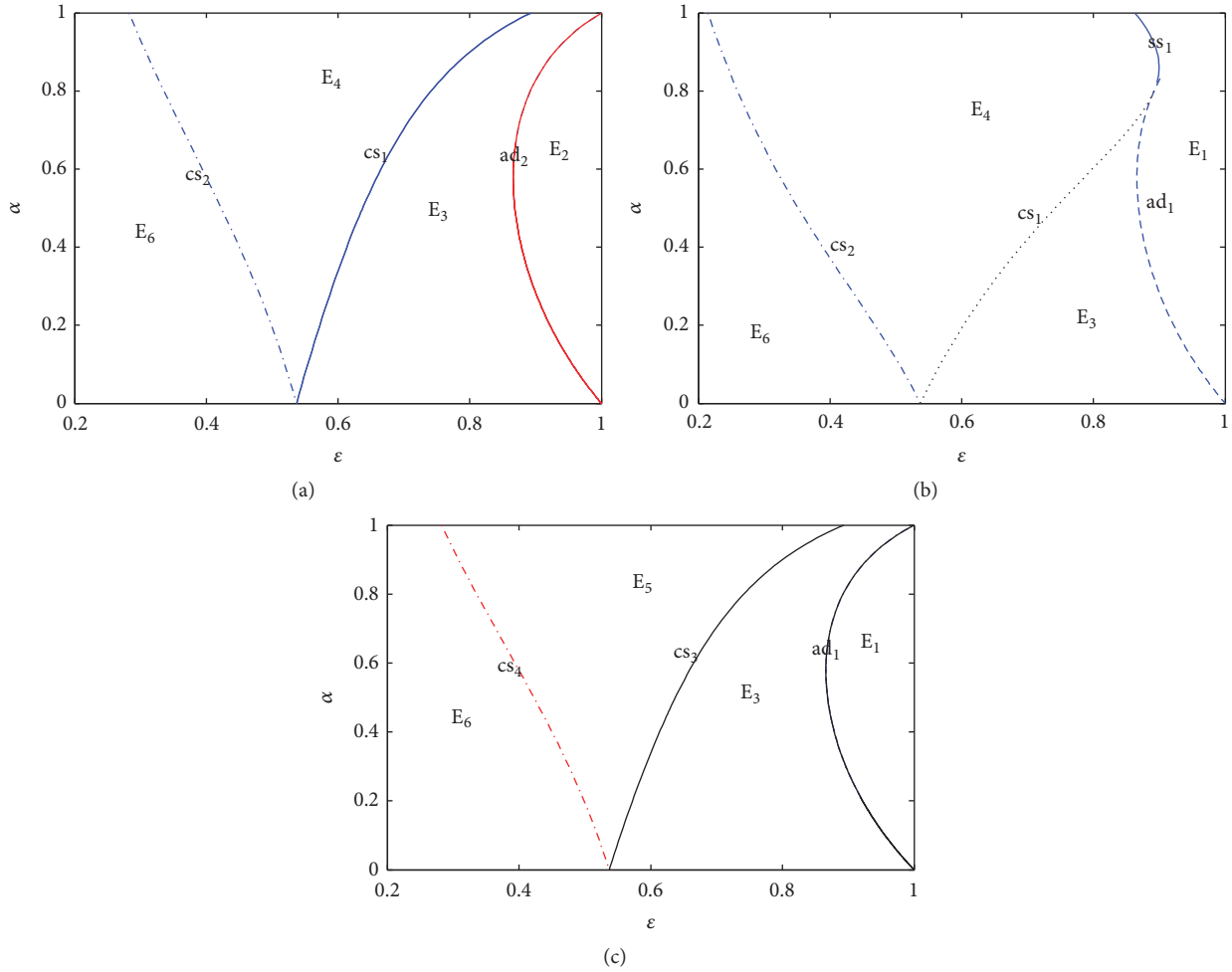


FIGURE 6: Two-parameter continuation of sliding bifurcation with respect to  $\epsilon$  and  $\alpha$  for different  $\phi$ : (a)  $\phi = \pi/3$ ; (b)  $\phi = 2\pi/3$ ; (c)  $\phi = 4\pi/3$ ;  $ad_i$  represent adding-sliding bifurcations,  $cs_i$  represent crossing-sliding bifurcations,  $ss_i$  represent switching-sliding bifurcations, and the regions  $E_i$  denote the different stick-slip motions of the periodic solutions.

The regions of different directional progression in one period can be determined by implementing the parameters continuation of the periodic solution with additional condition  $v = 0$ .

When  $\alpha = 0.456$ , there are six different stick-slip period solutions in the parameter plane in Figure 3; two parameters  $\phi, \epsilon$  can be continued numerically based on different period solutions with the additional condition  $v = 0$ . The result is presented in Figure 8. The curves divide the parameters into three regions: forward drift ( $v > 0$ ), backward drift ( $v < 0$ ), and zero drift ( $v = 0$ , on the curves). They are shown in Figures 9(a), 9(b), and 9(c), respectively. According to Figure 8, it can be seen that, for any value of the parameter  $\epsilon$ , the direction of system progression can be controlled by changing the phase  $\phi$ , the direction of progression is forward when  $\phi$  is in  $(\pi/2, \pi)$ , and the direction of progression is backward when  $\phi$  is in  $(3\pi/2, 2\pi)$ . When  $0.7239 < \epsilon < 1$ , the direction of progression is forward when  $\phi$  is in  $(\pi/2, 3\pi/2)$ ; and the direction of progression is backward when  $\phi$  is in  $(0, \pi/2)$  and  $(3\pi/2, 2\pi)$ .

When  $\phi = 2\pi/3$ , there is no solution with additional condition  $v = 0$  in the parameter  $\epsilon - \alpha$  plane, which indicates

that the direction of the progression does not change. The direction of the progression is forward because the average velocity is larger than zero in the region  $E_1$  seen from Figure 6(b).

When  $\epsilon = 0.6$ , the parameter  $\phi - \alpha$  plane for directional continuation is presented in Figure 10, some conclusions are drawn from Figure 10 similarly: for any parameter  $\alpha$ , the direction of system progression can be controlled by changing the phase  $\phi$ ; the direction of progression is forward when  $\phi$  is in  $(\pi/2, 4.4211)$ ; and the direction of progression is backward when  $\phi$  is in  $(3\pi/2, 2\pi)$  and  $(0, 1.2795)$ . When  $0 < \alpha < 0.2278$ , the direction of progression is forward when  $\phi$  is in  $(\pi/2, 3\pi/2)$ ; and the direction of progression is backward when  $\phi$  is in  $(0, \pi/2)$  and  $(3\pi/2, 2\pi)$ .

## 5. Conclusions

This paper studies the dynamical response of the vibration-driven system which is composed of a body with movable internal mass. The asymmetry of friction in forward and backward direction is essential to the motion of system,

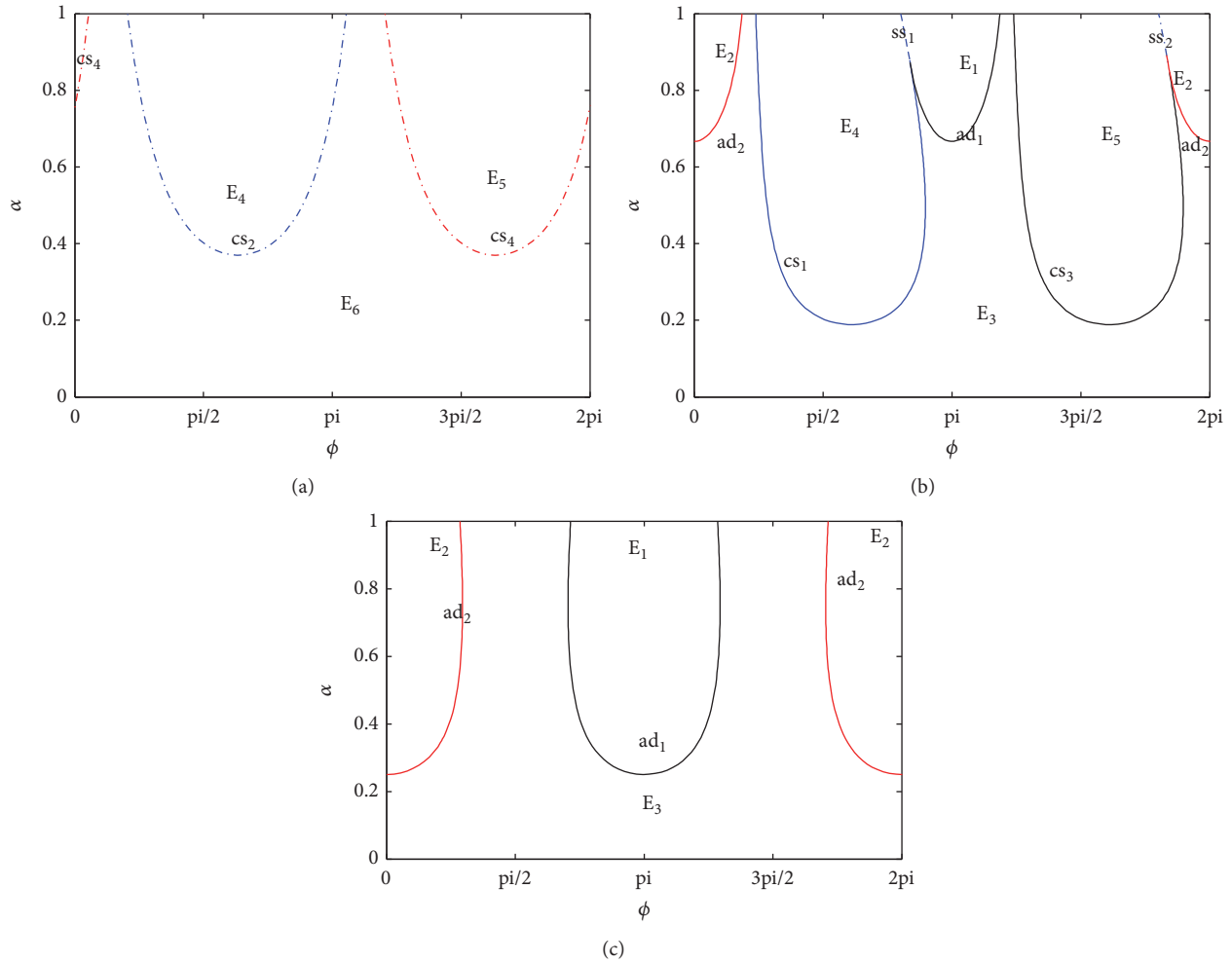


FIGURE 7: Two-parameter continuation of sliding bifurcation with respect to  $\phi$  and  $\alpha$  for different  $\varepsilon$ : (a)  $\varepsilon = 0.4$ ; (b)  $\varepsilon = 0.6$ ; (c)  $\varepsilon = 0.8$ ;  $ad_i$  represent adding-sliding bifurcations,  $cs_i$  represent crossing-sliding bifurcations,  $ss_i$  represent switching-sliding bifurcations, and the regions  $E_i$  denote the different stick-slip motions of the periodic solutions.

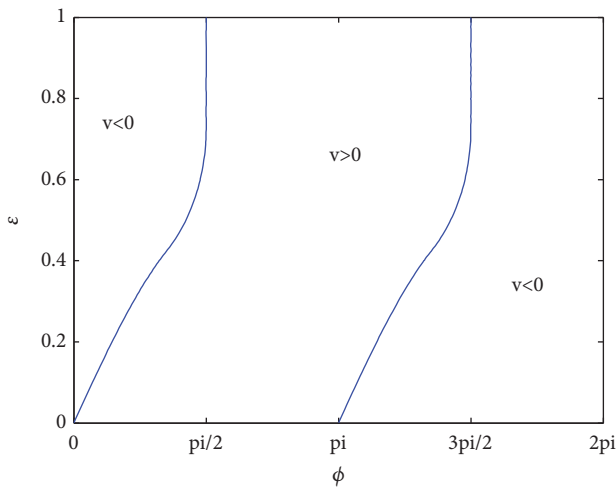


FIGURE 8: Two-parameter continuations of the periodic orbits for the parameter  $\alpha = 0.456$ . The average velocity is zero along the curves in the plane.

which arises from the normal force change due to the vertical motion of the internal mass. The vibration-driven system involving dry friction belongs to the Filippov system, the cycle trajectory of the system can be divided into smooth segments, the event functions defined the terminal point of the segments, and the reset functions connected the segments. We take advantage of the software COCO to carry out the bifurcation analysis.

Two-parameter sliding bifurcations are carried out by performing the numerical continuation. Different period solutions of stick-slip motion are obtained through the sliding bifurcation curves. For directional control of the vibration-driven system, the drift of the vibration-driven system in one period may change sign, the continuation with additional condition  $v = 0$  is carried out in the parameters plane, and the curves are obtained. The curves divide the parameters plane into three modes of drift (backward, forward, and zero). So the direction of the vibration-driven system progression can be controlled by changing the parameters.

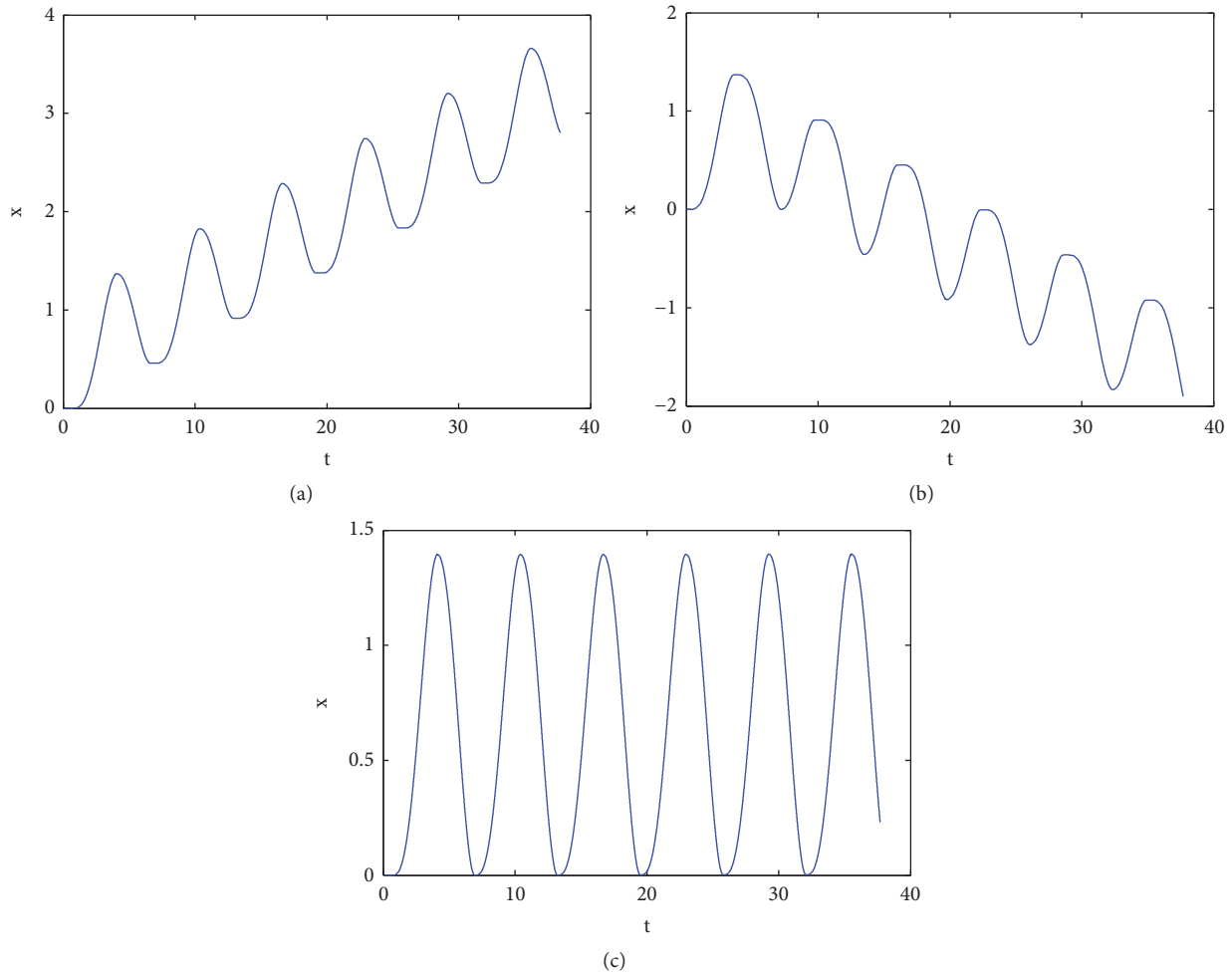


FIGURE 9: The progression of the vibration-driven system for (a)  $\varepsilon = 0.5$ ,  $\alpha = 0.456$ ,  $\phi = \pi/2$ ; (b)  $\varepsilon = 0.5$ ,  $\alpha = 0.456$ ,  $\phi = 3\pi/2$ ; (c)  $\varepsilon = 0.4271$ ,  $\alpha = 0.456$ ,  $\phi = 1.1121$ .

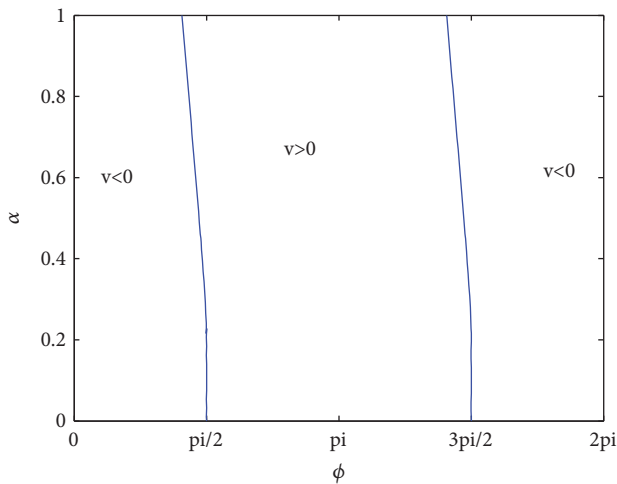


FIGURE 10: Two-parameter continuation of the periodic orbits for the parameter  $\varepsilon = 0.6$ . The average velocity is zero along the curves in the plane.

The particular contribution of this research is the numerical continuation of the parameters for the vibration-driven system and detailed classifications of parameter space where different system dynamic behaviors can be obtained. The bifurcation analysis improves our understanding of the dynamical behaviors of the vibration-driven system and is of benefit to devise control strategies for the vibration-driven system.

**Data Availability**

No data were used to support this study.

**Disclosure**

The research did not receive specific funding.

**Conflicts of Interest**

The authors declare that they have no conflicts of interest.

## References

- [1] F. L. Chernous'ko, "Analysis and optimization of the motion of a body controlled by means of a movable internal mass," *Journal of Applied Mathematics and Mechanics*, vol. 70, no. 6, pp. 819–842, 2006.
- [2] H.-B. Fang and J. Xu, "Dynamics of a mobile system with an internal acceleration-controlled mass in a resistive medium," *Journal of Sound and Vibration*, vol. 330, no. 16, pp. 4002–4018, 2011.
- [3] Y. Liu, M. Wiercigroch, E. Pavlovskaia, and H. Yu, "Modelling of a vibro-impact capsule system," *International Journal of Mechanical Sciences*, vol. 66, pp. 2–11, 2013.
- [4] H.-B. Fang and J. Xu, "Controlled motion of a two-module vibration-driven system induced by internal acceleration-controlled masses," *Archive of Applied Mechanics*, vol. 82, no. 4, pp. 461–477, 2012.
- [5] H.-b. Fang and J. Xu, "Dynamics of a three-module vibration-driven system with non-symmetric Coulomb's dry friction," *Multibody System Dynamics*, vol. 27, no. 4, pp. 455–485, 2012.
- [6] K. Zimmermann, I. Zeidis, and C. Behn, *Mechanics of Terrestrial Locomotion: With a Focus on Non-pedal Motion Systems*, Springer, Heidelberg, Germany, 2009.
- [7] K. Zimmermann, I. Zeidis, N. Bolotnik, and M. Pivovarov, "Dynamics of a two-module vibration-driven system moving along a rough horizontal plane," *Multibody System Dynamics*, vol. 22, no. 2, pp. 199–219, 2009.
- [8] K. Zimmermann, I. Zeidis, M. Pivovarov, and C. Behn, "Motion of two interconnected mass points under action of non-symmetric viscous friction," *Archive of Applied Mechanics*, vol. 80, no. 11, pp. 1317–1328, 2010.
- [9] N. N. Bolotnik, I. M. Zeidis, K. Zimmermann, and S. F. Yatsun, "Dynamics of controlled motion of vibration-driven systems," *Journal of Computer and Systems Sciences International*, vol. 45, no. 5, pp. 831–840, 2006.
- [10] Y. A. Kuznetsov, S. Rinaldi, and A. Gagnani, "One-parameter bifurcations in planar Filippov systems," *International Journal of Bifurcation and Chaos*, vol. 13, no. 8, pp. 2157–2188, 2003.
- [11] M. Bernardo, C. Budd, A. R. Champneys, and P. Kowalczyk, *Piecewise-Smooth Dynamical Systems: Theory And Applications*, Springer, Berlin, Germany, 2008.
- [12] P. Kowalczyk and P. T. Piironen, "Two-parameter sliding bifurcations of periodic solutions in a dry-friction oscillator," *Physica D: Nonlinear Phenomena*, vol. 237, no. 8, pp. 1053–1073, 2008.
- [13] M. Guardia, S. J. Hogan, and T. M. Seara, "An analytical approach to codimension-2 sliding bifurcations in the dry-friction oscillator," *SIAM Journal on Applied Dynamical Systems*, vol. 9, no. 3, pp. 769–798, 2010.
- [14] H. Fang and J. Xu, "Stick-Slip Effect in a Vibration-Driven System With Dry Friction: Sliding Bifurcations and Optimization," *Journal of Applied Mechanics*, vol. 81, no. 5, p. 051001, 2013.
- [15] F. Dercole and Y. A. Kuznetsov, "SlideCont: an Auto97 driver for bifurcation analysis of Filippov systems," *ACM Transactions on Mathematical Software*, vol. 31, no. 1, pp. 95–119, 2005.
- [16] P. Thota and H. Dankowicz, "TC-HAT: A Novel Toolbox for the Continuation of Periodic Trajectories in Hybrid Dynamical Systems," *SIAM Journal on Applied Dynamical Systems*, vol. 7, no. 4, pp. 1283–1322, 2008.
- [17] J. Páez Chávez and M. Wiercigroch, "Bifurcation analysis of periodic orbits of a non-smooth Jeffcott rotor model," *Communications in Nonlinear Science and Numerical Simulation*, vol. 18, no. 9, pp. 2571–2580, 2013.
- [18] J. Páez Chávez, E. Pavlovskaia, and M. Wiercigroch, "Bifurcation analysis of a piecewise-linear impact oscillator with drift," *Nonlinear Dynamics*, vol. 77, no. 1-2, pp. 213–227, 2014.
- [19] J. Páez Chávez, Y. Liu, E. Pavlovskaia, and M. Wiercigroch, "Path-following analysis of the dynamical response of a piecewise-linear capsule system," *Communications in Nonlinear Science and Numerical Simulation*, vol. 37, pp. 102–114, 2016.
- [20] H. Dankowicz and F. Schilder, "An Extended Continuation Problem for Bifurcation Analysis in the Presence of Constraints," *Journal of Computational and Nonlinear Dynamics*, vol. 6, no. 3, 2011.
- [21] H. Dankowicz and F. Schilder, *Recipes for continuation*, Society for Industrial and Applied Mathematics, Philadelphia, Pennsylvania, 2013.
- [22] H. Jiang and M. Wiercigroch, "Geometrical insight into non-smooth bifurcations of a soft impact oscillator," *IMA Journal of Applied Mathematics*, vol. 81, no. 4, pp. 662–678, 2016.
- [23] H. Jiang, Y. Liu, L. Zhang, and J. Yu, "Anti-phase synchronization and symmetry-breaking bifurcation of impulsively coupled oscillators," *Communications in Nonlinear Science and Numerical Simulation*, vol. 39, pp. 199–208, 2016.

## Research Article

# Nonlinear Vibration of an Elastic Soft String: Large Amplitude and Large Curvature

De-Min Zhao, Shan-Peng Li, Yun Zhang, and Jian-Lin Liu 

*Department of Engineering Mechanics, College of Pipeline and Civil Engineering, China University of Petroleum (East China), Qingdao 266580, China*

Correspondence should be addressed to Jian-Lin Liu; [liujianlin@upc.edu.cn](mailto:liujianlin@upc.edu.cn)

Received 12 April 2018; Accepted 7 June 2018; Published 22 July 2018

Academic Editor: Carlos Llopis-Albert

Copyright © 2018 De-Min Zhao et al. This is an open access article distributed under the Creative Commons Attribution License, which permits unrestricted use, distribution, and reproduction in any medium, provided the original work is properly cited.

Mechanical nonlinear vibration of slender structures, such as beams, strings, rods, plates, and even shells occurs extensively in a variety of areas, spanning from aerospace, automobile, cranes, ships, offshore platforms, and bridges to MEMS/NEMS. In the present study, the nonlinear vibration of an elastic string with large amplitude and large curvature has been systematically investigated. Firstly, the mechanics model of the string undergoing strong geometric deformation is built based on the Hamilton principle. The nonlinear mode shape function was used to discretize the partial differential equation into ordinary differential equation. The modified complex normal form method (CNFM) and the finite difference scheme are used to calculate the critical parameters of the string vibration, including the time history diagram, configuration, total length, and fundamental frequency. It is shown that the calculation results from these two methods are close, which are different with those from the linear equation model. The numerical results are also validated by our experiment, and they take excellent agreement. These analyses may be helpful to engineer some soft materials and can also provide insight into the design of elementary structures in sensors, actuators and resonators, etc.

## 1. Introduction

Mechanical vibration of slender structures, such as beams, strings, rods, plates, and even shells, occurs widely in a variety of areas, spanning from aerospace, automobile, cranes, ships, offshore platforms, and bridges to MEMS/NEMS (micro/nanoelectromechanical system) [1–5]. On one hand, the huge vibration amplitude can shorten the lifetime of the whole structures, with the accumulation of damage or fatigue of materials [6]. On the other hand, the advantage of mechanical vibration can be successfully utilized in a lot of spectrums. For instance, at the nanoscale, Wang et al. used a situ transmission electron microscopy (TEM) to measure the dynamic deflection of a cantilever made of multiwalled carbon nanotube, which was excited to resonance in TEM [7, 8]. Besides this, Zheng and Jiang proposed the concept of creation of nanomechanical systems of operating frequency up to several gigahertz, based on the oscillation of a core in a multiwall carbon nanotube [9].

The most intriguing issue on vibration is its nonlinear effect, as the strong nonlinearity can lead to many special phenomena. Up to now, the nonlinear vibration of structures has aroused extensive attention in the past decades. A central task of the nonlinear vibration of beams is to seek their nonlinear frequencies, and much effort has been devoted to this problem. For example, Hemmatnezhad and Ansari [10] studied the frequency of a functionally graded beam by means of a finite element formulation. In their model, the von Karman type nonlinear strain–displacement relationship is employed, and the effects of transverse shear deformation are included based upon the Timoshenko beam theory. Similarly, to further seek the nonlinear frequencies, Gunda and Gupta [11] investigated the vibration of a composite beam, Nikkar and Bagheri [12] explored the cantilever beam with an intermediate lumped mass, and Yu and Wu et al. [13] studied the beam with immovable spring-hinged ends. More related works include that Raju and Rao [14] formulated the nonlinear vibration of the beam using multiterm admissible

functions for the first mode. Then He [15] used the variational approach to investigate the vibration frequency of a uniform cantilever beam carrying an intermediate lumped mass. Hoseini and Pirbodaghi et al. [16] presented the homotopy analysis method to study the accurate analytical solution for the nonlinear fundamental natural frequency of a tapered beam with large amplitude vibration.

At the micro/nanoscale, Gheshlaghi [17] developed the Euler-Bernoulli beam model and calculated the nonlinear natural frequencies of the first two modes of a nanowire. In succession, the harmonic balance method and the asymptotic numerical method were combined to solve the equations of a comprehensive multiphysics model of cantilever made of carbon nanotube [18]. Moreover, using the different model, i.e., the Eringen's nonlocal elasticity theory, Simsek [19] calculated the nonlinear vibration frequency of a nanobeam with axially immovable ends. Similarly, Nazemnezhad et al. [20] got the exact solution for the nonlinear vibration of a nanobeam, in use of the nonlocal Euler-Bernoulli theory. For the applications of devices, Feng et al. [1] studied the nonlinear vibration of a dielectric elastomer-based microbeam resonator, where the gas damping and excitation are considered. Han and Zhang [2] designed a doubly clamped microresonator based on the large amplitude vibration model. Furthermore, in the experiments, several measurement methods for the nonlinear vibration of slender beams were proposed [21, 22].

Although much work has been done on the nonlinear vibration of beams and in most of references this behavior was termed as "large amplitude," however, it should be stressed that only the normal strain with von Karman type was considered in most of works. In practice, when a beam vibrates with large displacement, its amplitude can even amount to the value on the same order as its length. That is to say, the large amplitude vibration of the string should be associated with large displacement, large rotation, and large curvature, which should be taken into consideration [23]. Pai and Nayfeh [24] studied the large deformation body especially considering the large deformation and rotation, which is a bit complex. Babilioa and Lenci [25, 26] gave definitions on mechanical and geometric curvatures and, similarly, Kopmaz and Gündođdu [27] presented different concepts on mathematical and physical curvatures. With the same idea, Semler et al. [28] developed a beam equation on the nonlinear vibration of a pipe conveying fluid. Zhao et al. [29] used the similar model to investigate the nonlinear vibration of a nanobeam with surface effects. In addition, Vljajic and Fitzgerald et al. [30] studied the prestressed beam with large variable curvature, and they provided the analytical formulation for static configurations, natural frequencies, and mode shapes, which were validated by the experiment and finite element method. It is clearly seen that the above-mentioned bibliography mostly focuses on beams, and little literature on string vibration has been mentioned. Although Nayfeh and Mook [31] analyzed the nonlinear (free and forced) vibrations of strings and Benedetti and Rega [32] studied the forced vibration of a suspended cable associated with quadratic and cubic nonlinearities, only small amplitude of the string is considered. The vibration characteristics of a light axially moving band were investigated by Koivurova in

use of the Fourier–Galerkin–Newton method [33], where the von Karman strain was taken into account.

In the present study, we do not concentrate on the vibration of beams or plates but mainly on an elastic string or rod made of soft materials such as rubber materials, where large deformation and curvature can often happen when it vibrates. In this situation, the string will experience a very large displacement and especially a large curvature. This issue is not trivial, as the equation is associated with very strong nonlinearity. Although the complex normal form method (CNFM) developed by Nayfeh [34] was adopted to analyze the nonlinear vibration [29] it works very well in weak nonlinear vibration system. Then Leung et al. and Zhang et al. [35, 36] modified the traditional CNFM to predict the natural frequency in the strong nonlinear dynamics. For the CNFM introduced by Nayfeh [34], the fundamental frequency is independent of parameters of the nonlinear terms of the equation, which equals to the natural frequency of the derived linear system. However, for the modified CNFM [35, 36], the fundamental frequency is unknown and needs to be determined by the parameters of the nonlinear terms of the equation.

The outline of the paper is organized as follows. In Section 2, the dynamics equation of an elastic string with large amplitude and large mechanical curvature is derived based on the Hamilton principle. Next, in Section 3, the Galerkin method using the nonlinear mode shape function is used to discretize the partial differential equation to ordinary differential equation. Then, the modified complex normal CNFM is adopted to get the semianalytical solution of the strong nonlinear vibration of the string in Section 4. In Section 5, the semianalytical results including the time history diagram, string configuration, total string length, and fundamental frequency are calculated, which are compared with those from the numerical computation and our self-designed experiment. Finally, the conclusion is given in Section 6. Although the analysis is aiming to investigate the string vibration, the route of line can be extended to explore the vibration of some other elastic structures, such as rods, beams, plates, and shells.

## 2. Model Formulation

We consider an elastic string, with an initial configuration of Line  $OB$ , as shown in Figure 1. Refer to the Cartesian coordinate system  $O-\bar{x}\bar{y}$ , where the origin is located at point  $O$ . The original length of the string is  $L$ , and its cross-section area is  $A$ . Young's modulus and mass density of the string are  $E$  and  $\rho$ , respectively, and point  $D_0$  is the midpoint of the string. When the string starts to vibrate in the  $(\bar{x}, \bar{y})$  plane, its axis is elongated and the morphology is curvilinear, which is schematized in Figure 1. We examine two arbitrary adjacent material points  $C_0(\bar{x}, 0)$  and  $C'_0(\bar{x} + d\bar{x}, 0)$ , both in  $\bar{x}$ -axis with infinitesimal distance  $d\bar{x}$  in the original configuration; then they transfer to the positions  $C_1(\bar{x}_1, \bar{y}_1)$  and  $C'_1(\bar{x}_2, \bar{y}_2)$  after deformation. Considering the large deformation of the string, the curvilinear coordinate is introduced, where the arc length  $\bar{s}$  is measured from the origin point  $O$  along the axis of the string.

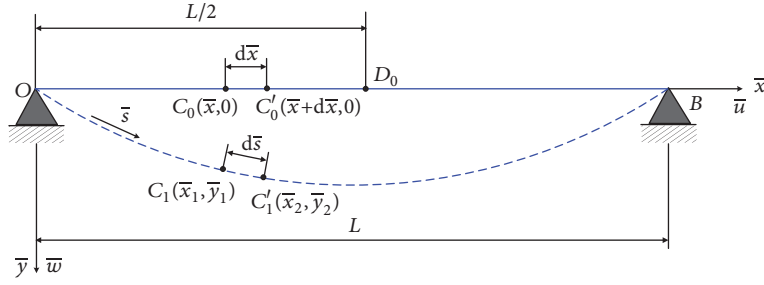


FIGURE 1: Schematic of the vibrational configuration of an elastic string with large deformation.

According to Figure 1, the geometric relations of the string are given as [28, 29, 31]

$$\begin{aligned} \bar{x}_1 - \bar{x} &= \bar{u} \\ \bar{y}_1 &= \bar{w} \\ \bar{x}_2 - (\bar{x} + d\bar{x}) &= \bar{u} + d\bar{u} \\ \bar{y}_2 &= \bar{w} + d\bar{w}, \end{aligned} \quad (1)$$

where  $\bar{u}$  and  $\bar{w}$  are the displacements of point  $C_0$  along  $\bar{x}$  and  $\bar{y}$  directions, respectively. It can be seen that, before deformation, the microelement between  $C_0$  and  $C'_0$  has the length  $d\bar{x}$  and it becomes  $d\bar{s}$  after deformation. As a result, the expression of  $d\bar{s}$  is derived as

$$d\bar{s} = \sqrt{(\bar{x}_2 - \bar{x}_1)^2 + (\bar{y}_2 - \bar{y}_1)^2} = \sqrt{(1 - \bar{u}'^2)^2 + \bar{w}'^2}, \quad (2)$$

where  $\bar{u}' = d\bar{u}/d\bar{x}$  and  $\bar{w}' = d\bar{w}/d\bar{x}$ . Due to the fact that the value of  $\bar{u}$  is much smaller than that of  $\bar{w}$ , the contribution of  $\bar{u}'$  can be negligible in the vibration process. Therefore, the strain of an arbitrary point in the string is given by

$$\varepsilon = \frac{d\bar{s} - d\bar{x}}{d\bar{x}} = \sqrt{1 + \bar{w}'^2} - 1. \quad (3)$$

In order to obtain the governing equation of the string, we deal with this problem by way of energy principle. Firstly, the kinetic energy of the string can be written as

$$T = \int_0^L \rho A \dot{\bar{w}}^2 d\bar{x}, \quad (4)$$

where  $\dot{\bar{w}} = d\bar{w}/dt$  and  $t$  is the time variable.

The elastic strain energy is decomposed into two portions; i.e., the first contribution originates from the pretension force of the string  $N_0$  and the second one comes from the elongation in the vibration process. Consequently, in a period from  $t_1$  to  $t_2$ , the strain energy can be expressed as

$$U = \frac{EA}{2} \int_{t_1}^{t_2} \int_0^L \left( \frac{N_0}{EA} + \varepsilon \right)^2 d\bar{x} dt. \quad (5)$$

Considering there is no work from the nonconservative forces, the application of Hamilton principle yields

$$\delta \int_{t_1}^{t_2} (T - U) dt = 0. \quad (6)$$

Because we study the soft slender string, the mechanical curvature is sufficiently accurate and used more conveniently for the integration [25, 26]. Therefore, in use of the principle of variation, the governing equation of the string in vibration with large amplitude and large mechanical curvature can be deduced as

$$\begin{aligned} \rho A \ddot{\bar{w}} - (N_0 - EA) \left( \frac{\bar{w}''}{\sqrt{1 + \bar{w}'^2}} - \frac{\bar{w}'^2 \bar{w}''}{(1 + \bar{w}'^2)^{3/2}} \right) \\ - EA \bar{w}'' = 0. \end{aligned} \quad (7)$$

The boundary conditions at two ends are

$$\begin{aligned} \bar{w}(0, t) &= 0, \\ \bar{w}(L, t) &= 0, \end{aligned} \quad (8)$$

where  $\ddot{\bar{w}} = d^2\bar{w}/dt^2$  and  $\bar{w}'' = d^2\bar{w}/d\bar{x}^2$ .

It can be seen that when the amplitude of the string is big enough, the term  $\bar{w}'^2$  cannot be ignored in (7), and thus the governing equation is more complicated, as it has a very great mechanical curvature. As is well known, the value of  $\bar{w}'$  is close to zero when the vibration amplitude is small. If this term is omitted, (7) can degenerate to the classical string vibration equation, whose amplitude and curvature are both small and the equation is linear:

$$\ddot{\bar{w}} = \frac{N_0}{\rho A} \bar{w}'' . \quad (9)$$

For convenience, the following nondimensional quantities are defined as

$$\begin{aligned} w &= \frac{\bar{w}}{L}, \\ x &= \frac{\bar{x}}{L}, \\ r &= \frac{1}{L} \sqrt{\frac{N_0}{\rho A}}, \\ \omega &= \pi r, \\ \tau &= \omega t, \end{aligned}$$

$$\begin{aligned}\beta_1 &= \frac{(1 - EA/N_0)}{\pi^2}, \\ \beta_2 &= \frac{EA}{N_0\pi^2}.\end{aligned}\quad (10)$$

Accordingly, (7) can be recast as

$$\ddot{w} = \frac{\beta_1 w''}{(1 + w'^2)^{1/2}} - \frac{\beta_1 w'^2 w''}{(1 + w'^2)^{3/2}} + \beta_2 w'', \quad (11)$$

and this equation is termed as the dimensionless large amplitude vibration (LAV) equation throughout this study.

Then the boundary conditions and initial conditions are rewritten as

$$\begin{aligned}w(0, \tau) &= 0, \\ w(1, \tau) &= 0, \\ w(x, 0) &= a \sin(\pi x), \\ \dot{w}(x, 0) &= 0.\end{aligned}\quad (12)$$

At the same time, the linear equation is nondimensionalized as

$$\ddot{w} = \frac{1}{\pi^2} w''. \quad (13)$$

In the above equations, the related expressions are  $\ddot{w} = d^2w/d\tau^2$ ,  $w' = dw/dx$ , and  $w'' = d^2w/dx^2$ , and  $a$  is the amplitude of the middle point in the string, i.e., point  $D_0$ .

### 3. Mode Discretization with Exact Mode Shape

The following task is to solve (11), which is an intractable problem. Clearly, it seems impossible to directly get the analytical solution of this highly nonlinear equation. Therefore, in use of the Taylor series, (11) can be expanded into the following polynomial expansion until 5th-order terms, where the terms of higher order are ignored:

$$\ddot{w} = \frac{w''}{\pi^2} + \beta_1 \left( -\frac{3w'^2}{2} + \frac{15w'^4}{8} \right) w''. \quad (14)$$

It is clear that (14) is still a high order and nonlinear partial differential equation (PDE), and seeking the closed form solution is not at hand. Herein, the Galerkin discretization method is utilized to transform the PDE into the ordinary differential equation (ODE). The previous result [18] tells us that the first-mode analysis of vibration is sufficient to capture the main nonlinear characteristics and can get the fundamental frequency accurately enough. Hence, we take the trial to only consider the first mode of the vibration, aiming to get an approximate solution for the first step. Moreover, the mode shape is a critical factor to affect the vibration of the continuously beam, rod, and string. For the small amplitude vibration of string with simply supported condition, the first-mode shape function is often assumed by linear mode shape

function [31] described by  $\sin(\pi x)$ . However, for the large curvature vibration, especially the amplitude of the middle point nearly 0.4-0.5 times of span of simply supported string, the mode shape function,  $\sin(\pi x)$ , based on the linear the mode shape, fails. The exact mode shape function should be selected considering the physical experiments given in Section 5.3. Assume that the displacement  $w(x, \tau)$  can be described as

$$w(x, \tau) = q(\tau) W(x) \quad (15)$$

and

$$W(x) = \sin(\pi x) \sqrt{1 + \cos^2(\pi x)}. \quad (16)$$

Substituting (15) and (16) into (14), multiplying both sides of the equation by  $W(x)$  and then integrating both sides from 0 to 1 yields the following ODE equation with strong nonlinearities:

$$\ddot{q} + \omega_0^2 q + k_1 q^3 + k_2 q^5 = 0, \quad (17)$$

where  $\omega_0^2 = 1.0745$ ,  $k_1 = -8.1836\beta_1$ , and  $k_2 = -53.5149\beta_1$ .

In order to compare the large curvature vibration with the small amplitude vibration, for the linear equation in (13), the classic mode shape function  $\sin(\pi x)$  is adopted; thus the classic the dimensionless ODE can degenerate to  $\ddot{q} + q = 0$ . Then one can obtain the theoretical solution easily, which is named as theoretical solution of the linear equation throughout the paper.

### 4. Semianalytical Solution Using CNFM Method

Equation (17) is strong nonlinear system due to the nonlinear terms  $q^3$  and  $q^5$  which are far more large than the linear term  $q$ . Although He's variational method [6, 12, 15, 19], harmonic balance method [18], and Homotopy analysis method [16] are used widely in the strong nonlinear system, the modified CNFM method [29, 34-36] gives more accurate results based on the experience of the authors. Next, we use the modified CNFM approach to solve (17). We assume that the solution of (17) can be formulated as

$$\begin{aligned}q &= \xi + \bar{\xi}, \\ \dot{q} &= i\omega_1 (\xi - \bar{\xi}),\end{aligned}\quad (18)$$

where  $\bar{\xi}$  is the complex conjugate of  $\xi$  and  $\omega_1$  is the unknown fundamental natural frequency to be determined. Introduce a nonlinear transformation from  $\xi$  to  $\eta$  in the form of

$$\xi = \eta + h(\eta, \bar{\eta}), \quad (19)$$

where  $\eta$  and  $\bar{\eta}$  are complex conjugates and they are both complex functions.

The near identity transformation function  $h$  including the variables  $\eta$  and  $\bar{\eta}$  is expressed as

$$\begin{aligned}h(\eta, \bar{\eta}) &= \Delta_1 \eta + \Delta_2 \bar{\eta} + \Delta_3 \eta^3 + \Delta_4 \eta^2 \bar{\eta} + \Delta_5 \eta \bar{\eta}^2 \\ &\quad + \Delta_6 \bar{\eta}^3 + \Delta_7 \eta^5 + \Delta_8 \eta^4 \bar{\eta} + \Delta_9 \eta^3 \bar{\eta}^2 \\ &\quad + \Delta_{10} \eta^2 \bar{\eta}^3 + \Delta_{11} \eta \bar{\eta}^4 + \Delta_{12} \bar{\eta}^5\end{aligned}\quad (20)$$

where  $\Delta_i$  ( $i=1..12$ ) are real numbers.

Substituting (18)–(20) into (17), one can get

$$\begin{aligned} \dot{\eta} = & i\omega_1\eta + i\omega_1\bar{h} - \frac{\partial h}{\partial \eta}\dot{\eta} - \frac{\partial h}{\partial \bar{\eta}}\dot{\bar{\eta}} + \frac{i\omega_1}{2} \left( \frac{\omega_0^2}{\omega_1^2} - 1 \right) \\ & \cdot (\eta + \bar{\eta} + h + \bar{h}) \\ & + \frac{i}{2\omega_1} \left[ k_1 (\eta + \bar{\eta} + h + \bar{h})^3 + k_2 (\eta + \bar{\eta} + h + \bar{h})^5 \right], \end{aligned} \quad (21)$$

where  $h$  and  $\bar{h}$  are complex conjugates. Substituting (19) and (20) into (18) leads to

$$\begin{aligned} q = & \eta + \bar{\eta} + (\Delta_1 + \Delta_2)(\eta + \bar{\eta}) + (\Delta_3 + \Delta_6)(\eta^3 + \bar{\eta}^3) \\ & + (\Delta_4 + \Delta_5)(\eta^2\bar{\eta} + \eta\bar{\eta}^2) + (\Delta_7 + \Delta_{12})(\eta^5 + \bar{\eta}^5) \\ & + (\Delta_8 + \Delta_{11})(\eta^4\bar{\eta} + \eta\bar{\eta}^4) \\ & + (\Delta_9 + \Delta_{10})(\eta^3\bar{\eta}^2 + \eta^2\bar{\eta}^3). \end{aligned} \quad (22)$$

To eliminate the secular terms  $\eta$ ,  $\eta^2\bar{\eta}$ , and  $\eta^3\bar{\eta}^2$  in (22), the following conditions should be met:

$$\Delta_1 + \Delta_2 = 0; \quad (23)$$

$$\Delta_4 + \Delta_5 = 0 \quad (24)$$

$$\Delta_9 + \Delta_{10} = 0. \quad (25)$$

Moreover, let the coefficients of terms  $\bar{\eta}$ ,  $\eta^3$ ,  $\eta\bar{\eta}^2$ ,  $\bar{\eta}^3$ ,  $\eta^5$ ,  $\eta^4\bar{\eta}$ ,  $\eta^2\bar{\eta}^3$ ,  $\eta\bar{\eta}^4$ , and  $\bar{\eta}^5$  in the right side of (22) vanish, as they are the nonresonant terms, which are much smaller than term  $\eta$ . Thus twelve equations are obtained in Appendix. Solving (23)–(25) and the related equations in Appendix, we can acquire the parameters  $\Delta_i$  ( $i=1, \dots, 12$ ), which are given in Appendix.

After these operations, the resonant terms  $\eta$ ,  $\eta^2\bar{\eta}$ , and  $\eta^3\bar{\eta}^2$  will remain in (21), and the equation is simplified to

$$\begin{aligned} \dot{\eta} = & i \frac{1 + \omega_1^2}{2\omega_1} \eta + i \frac{3k_1}{2\omega_1} \eta^2\bar{\eta} \\ & + i \frac{1}{2\omega_1} (10k_2 - 3k_1\Delta_6) \eta^3\bar{\eta}^2, \end{aligned} \quad (26)$$

where the real parameters  $\Delta_6$  is given in Appendix.

Assume

$$\eta = \frac{1}{2} a e^{i\omega_1 t}, \quad (27)$$

where  $a$  is the dimensionless vibration amplitude and  $\omega_1$  is the fundamental frequency which is to be determined. Substituting (27) into (26) leads to

$$\begin{aligned} \dot{a} = & 0 \\ \omega_1 = & \frac{\omega_0^2 + \omega_1^2}{2\omega_1} + \frac{3k_1}{8\omega_1} a^2 + \frac{10k_2 - 3k_1\Delta_6}{32\omega_1} a^4. \end{aligned} \quad (28)$$

The first equation in (28) indicates that the amplitude  $a$  is a constant determined by the initial condition, and the second equation determines the fundamental frequency  $\omega_1$ . Substituting  $\Delta_i$  ( $i=1, \dots, 12$ ),  $a$  and  $\omega_1$  into (22), one can get the final solution of (17) as

$$\begin{aligned} q = & a \cos(\omega_1 t) \\ & + \left[ \frac{1}{4} (\Delta_3 + \Delta_6) a^3 + \frac{1}{16} (\Delta_8 + \Delta_{11}) a^5 \right] \\ & \cdot \cos(3\omega_1 t) + \frac{1}{16} (\Delta_7 + \Delta_{12}) a^5 \cos(5\omega_1 t). \end{aligned} \quad (29)$$

## 5. Results and Discussion

**5.1. Numerical Scheme.** To get a more accurate solution, the finite difference method (FDM) is used to directly calculate the PDE, which manifests a robust method. The central difference is adopted, i.e.,  $w' = (w_{j+1}^n - w_{j-1}^n)/2(\Delta x)$ ,  $w'' = (w_{j+1}^n - 2w_j^n + w_{j-1}^n)/(\Delta x)^2$ , and  $\ddot{w} = (w_j^{n+1} - 2w_j^n + w_j^{n-1})/(\Delta \tau)^2$ , where  $j$  and  $n$  are both integers and  $\Delta x$  and  $\Delta \tau$  are the space and time steps, respectively. In the simulation process, the string is made of soft material such as rubber. The physical parameters of the string are measured as follows: mass density  $\rho=798 \text{ kg/m}^3$ , length  $L=68.77 \text{ mm}$ , cross-section area  $A=2.282 \text{ mm}^2$ , pretension force along the axial direction  $N_0=0.68 \text{ N}$ , and Young's modulus  $E=0.85 \text{ MPa}$ . The computational program is written in MATLAB 12, where the time step  $\Delta \tau$  is set as 0.001 and the space step  $\Delta x$  is set as 0.01. In the FDM discretization, when  $\tau = 0$  and  $\tau = \Delta \tau$ , the displacement  $w_j^i = a \sin[\pi(\Delta x)(j-1)]$ , ( $i=1, 2$ ), and  $j$  takes the value from 1 to 101.

**5.2. Time History Diagram of the Midpoint.** Evidently, the midpoint  $D_0$  is a critical point which should be carefully examined, as it may be associated with the largest amplitude of the string. When the initial amplitude of  $D_0$  is bigger, such as  $a=0.4$  and  $0.45$ , the related curves in the time history diagram are displayed in Figure 2. It can be seen that, with the evolution of time, the difference between the LAV model and the linear equation becomes more obvious; and the result from the semianalytical solution is in agreement with the numerical result, although there is slight difference as shown in Figure 2. As displayed in Figure 2(a), in the time interval from 0 to 20, there are nearly 4 periods in the LAV model and only 3 periods in the linear equation model. It can also be observed when  $\tau = 15.7$  that the motion of the point predicted by the LAV equation is nearly one-half period faster than that by the linear equation. This indicates that the whole motion of the string predicted by the LAV equation is quicker than that predicted by the linear equation.

**5.3. Vibrational Configurations.** In what follows, we compute the configurations of the string with large amplitude  $a=0.4$  in one period, which are shown in Figures 3(a)–3(h). Firstly, it is noted that there is great difference between the results from the LAV model and the linear equation model as shown in Figure 3. This again stresses that the linear equation is

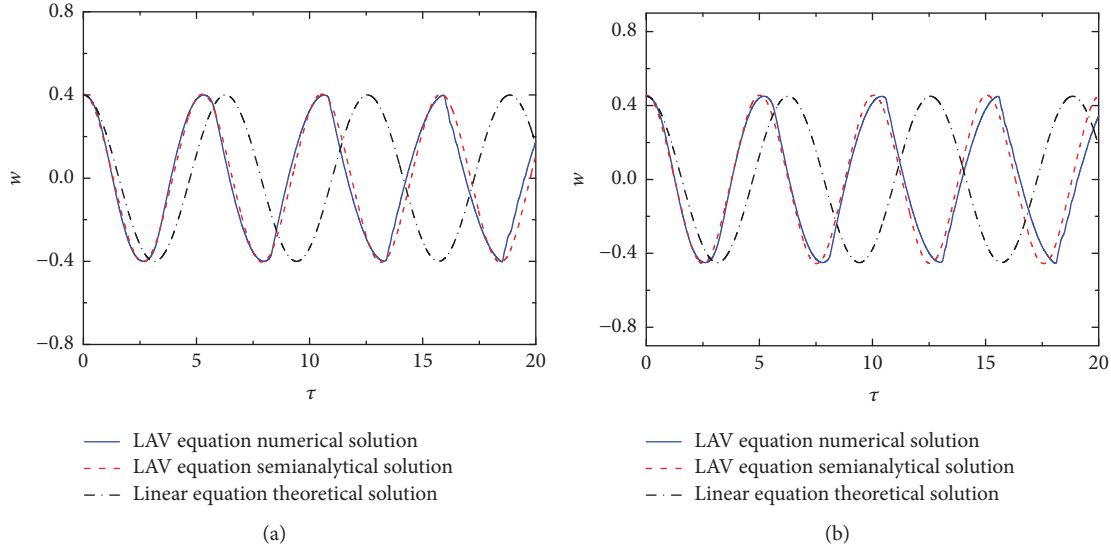


FIGURE 2: Time history diagram of point  $D_0$ , with the initial amplitudes (a)  $a = 0.4$  and (b)  $a = 0.45$ .

insufficient to depict the vibration with large amplitude and large curvature. However, in the whole period, although there is difference between the results from the semianalytical method and numerical simulation, the configurations predicted by the two methods are close. Therefore, it should be mentioned that the calculated string morphologies by the semianalytical are more similar to those from the numerical results than those from the linear equation model.

The next phenomenon is that the numerical morphologies of the string are very complicated in the vibration process. For instance, when  $\tau=5.3, 6.0, 8.0,$  and  $10.5$  in Figures 3(a), 3(b), 3(d), and 3(h), there are some nearly horizontal segments appearing in the curves. This strange behavior may be attributed to the complex nonlinear dynamics response, where the clamped ends exert strong constraints on the string and vice versa; near the middle part of the string, the constraint is much weaker. Another possible reason is that the first-mode analysis of the string may be an oversimplified model and the higher-mode behaviors must be further considered to illustrate this phenomenon. Furthermore our semianalytical solution can also have the similar shapes in this figures, especially near the middle part of the string.

To verify this numerical result, we perform an experiment as a comparison, where the string configurations in the vibration are shown in Figures 4(a)–4(h). A rubber string with  $1.408 \times 1.630 \text{ mm}^2$  cross-section is fixed horizontally on a desktop at room temperature, whose original length  $L$  is 50.85 mm. To add the pretension force on the string, the deformed length of the string is elongated to  $l=68.77$  mm and origin area of the cross-section is  $2.282 \text{ mm}^2$ . Thus the prestrain can be given as  $\varepsilon=(l-L)/L=0.3524$ , and using the measured value of Young's modulus  $E=0.85 \text{ MPa}$ , the pretension force is  $N_0=0.68 \text{ N}$ . At first, in the vertical plane the midpoint of the string is excited by an original amplitude, which is 0.4 times of the string length  $L$ . Next, the string is released, and

then its vibration sequences are recorded by the high speed camera (Phantom v2512 with 10000 frames per second). As shown in Figures 4(a), 4(b), 4(c), and 4(d), we find that there are really platform segments appearing in the string and the total configurations in these situations are close to the shape of trapezoid. Meanwhile, the string is no longer a straight line when it approaches the equilibrium position as shown in Figures 4(e) and 4(f), implying that the length of the string is bigger than its original length. These behaviors are beyond our imagination, as they demonstrate the complexity of the nonlinear dynamics.

**5.4. Total String Length.** It can be seen that in both the LAV equation and the linear equation, the extensibility of the string is considered; thus its length can be calculated and the two curves are compared in Figure 5. The nondimensional length of the string after deformation is expressed as  $l/L = \int_0^L \sqrt{1 + \bar{w}^2} d\bar{x}/L$ . For the linear equation model, this nondimensional length is a periodic function with respect to the time  $\tau$ , i.e.,  $l/L(\tau + T/2) = l/L(\tau)$ . This means that the maximum and minimum values of the string length do not alter in the vibration process. Especially, when the string approaches the  $x$ -axis, it is really a straight line, and thus the value of  $l/L$  is of the smallest value, i.e., one. This feature reemphasizes that the small amplitude vibration has linear properties. On the contrary, the oscillation behavior of the string length is more complex in the LAV model, where its minimum value increases with the elapsing time. In this situation, the dimensionless string length is always bigger than one, indicating that the string is always in the elongation state, even when it approaches the  $x$ -axis. In the experiment, such as in Figures 4(e), 4(f), 3(e), and 3(f), the shapes of the string are not merely straight lines and its length at this critical time must be larger than one. Evidently, this consistence on the experimental phenomenon can validate the efficiency of our numerical method.

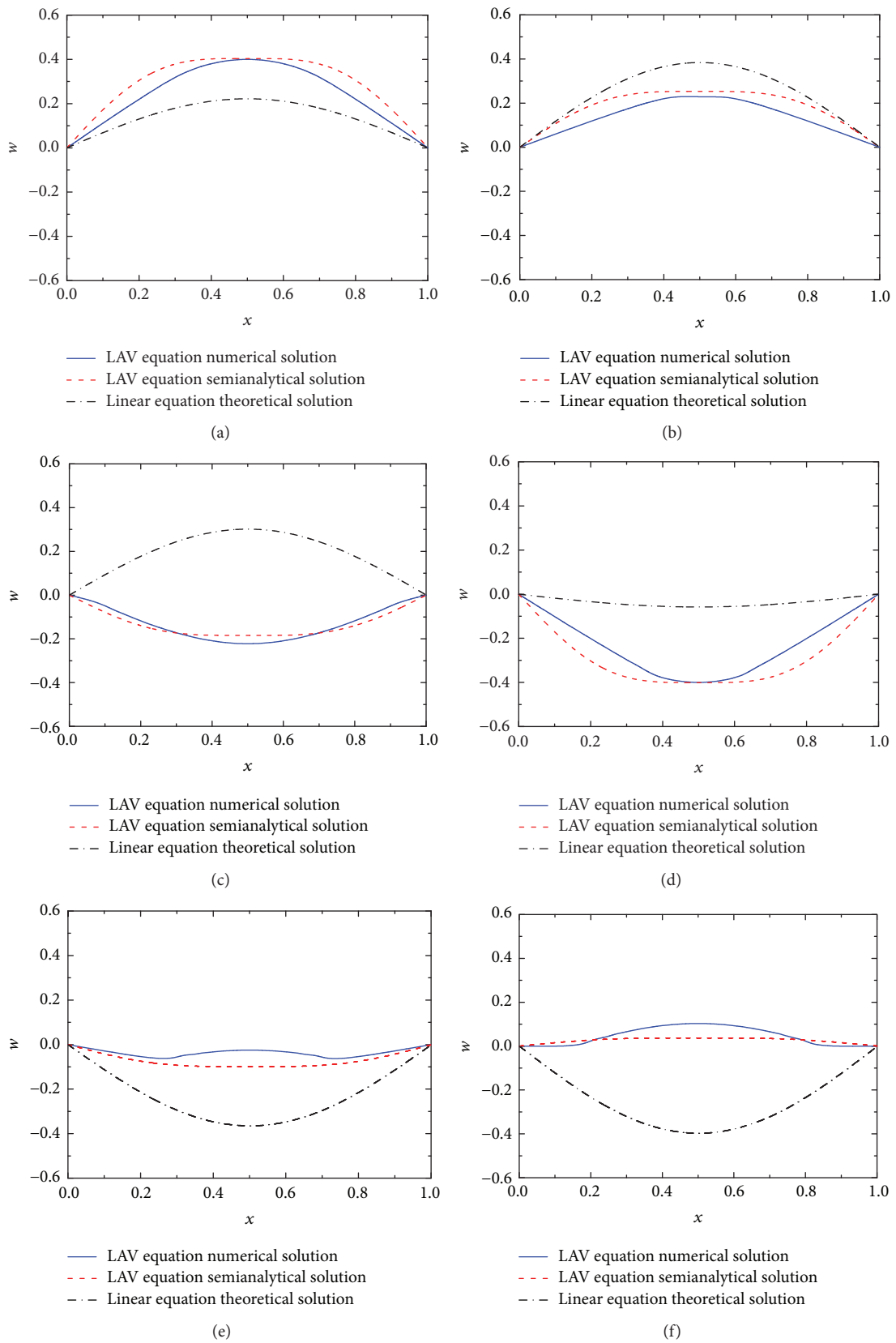


FIGURE 3: Continued.

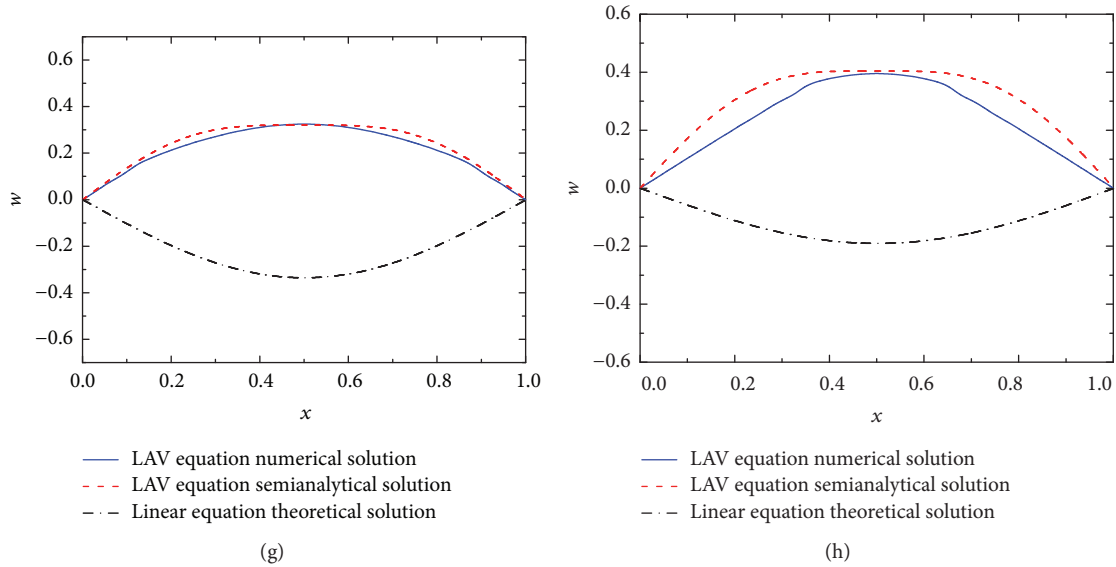


FIGURE 3: Vibrational configurations of an elastic string, when (a)  $\tau=5.3$ ; (b)  $\tau = 6.0$ ; (c)  $\tau = 7.0$ ; (d)  $\tau = 8.0$ ; (e)  $\tau = 9.0$ ; (f)  $\tau = 9.3$ ; (g)  $\tau = 10$ ; (h)  $\tau = 10.5$ .

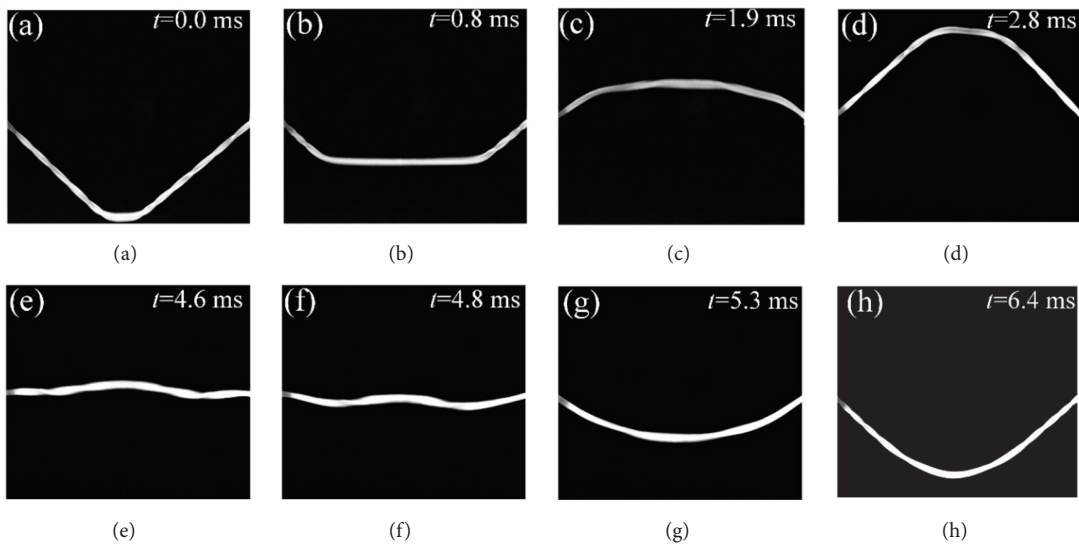


FIGURE 4: Vibrational configurations of the string in the experiment.

5.5. *Fundamental Frequency.* Another vibration characteristic parameter about vibration is the frequency, and in the current study, the value of the fundamental frequency is obtained by the solution of (28), and it is also tested by the experimental measurement. When the vibration has a small amplitude, vibration of the string, its dynamic behavior can be formulated by the linear equation  $\ddot{q} + q = 0$ , with the natural frequency always being  $\omega_1 = 1$ , which is irrelative to the initial amplitude. We observed in Figure 6 the difference between the semianalytical method and experiment method is great. The main reason is that, for the small amplitude, the mode shape function should be  $\sin(\pi x)$  rather than  $\sin(\pi x)\sqrt{1 + \cos^2(\pi x)}$ . The frequency exhibited in Figure 6 demonstrates that our mode shape function should not be

used for the small amplitude vibration. However, for the large amplitude vibration, the fundamental frequency is not a constant and its value is greatly affected by the initial amplitude. As shown in Figure 6, with the increase of the amplitude, the fundamental frequency also increases, which is verified by the experimental results. Although there exists value difference between the semianalytical solution and the experimental data, their tendencies are the same and both of the two results are bigger than one with the increase of initial amplitude  $a$ . This behavior again demonstrates the complicated response of the nonlinear dynamics, which is very sensitive to the initial value. It should be clarified that our mode shape function only for the large amplitude vibration with the ratio (amplitude of the middle part of the string

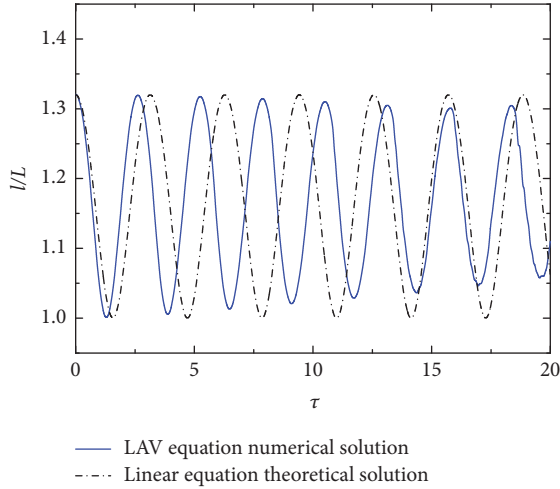


FIGURE 5: Total length of the string based on the LAV equation and linear equation.

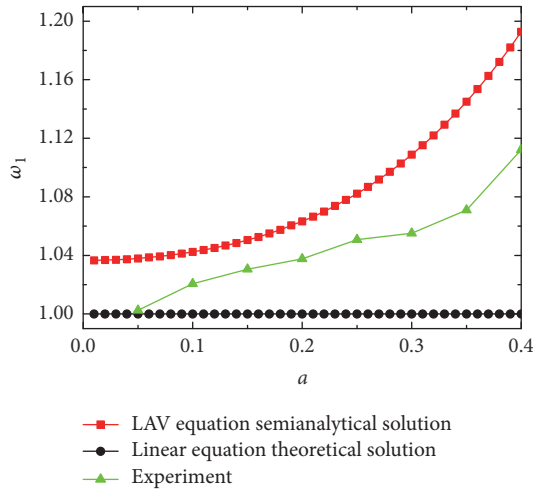


FIGURE 6: Relation between the fundamental  $\omega_1$  and the initial amplitude  $a$ .

to the whole span) is nearly 0.2-0.5. If the ratio is greater, different mode shape functions should be selected and the similar analysis process can be carried out.

## 6. Conclusion

In conclusion, the nonlinear vibration of a soft elastic string with large amplitude and large curvature has been systematically investigated in this study. The mathematical model in the absence of damping is developed based on the Hamilton principle. The exact mode shape function different from the counterpart derived from the linear equation was selected based on the experiment. For the large amplitude vibration, the time history diagram from the semianalytical is very close to that from the numerical result and these two results are very different from that of the linear model. The vibration configurations of the elastic string have the similar laws as those of the time history diagrams based on

the comparison of the three models. We find that, in the numerical calculations, there are platform segments with the shape of trapezoid appearing in the configuration curves, and this phenomenon has been verified by our semianalytical solution and the experiment. The total length of the string in the large deformation shows that it is not a periodic function with respect to the time, which is distinct with the result of the linear model. We also point out that the fundamental frequency of the string with large amplitude vibration is greatly affected by the initial amplitude, which has the same tendency as our experiment result.

It should be mentioned that this study is only the first trial on the nonlinear vibration of elastic structures with large amplitude and large curvatures. The following work is expected, which will be extended to some other engineering structures, such as beams, rods, plates, and shells. These analyses may be beneficial to engineer some soft materials and can also shed light on the design of elementary structures in sensors, actuators and resonators, etc.

## Appendix

### A. Equations to Determine Coefficients of Nonresonant Terms

Besides (23)-(25), the other equations to determine the value of  $\Delta_i$  ( $i=1, \dots, 12$ ) are

$$2i\omega_1\Delta_2 + \frac{i(\omega_0^2 - \omega_1^2)}{2\omega_1} = 0;$$

$$2i\omega_1\Delta_3 - \frac{i(\omega_0^2 - \omega_1^2)}{2\omega_1}(\Delta_3 + \Delta_6) - \frac{ik_1}{2\omega_1} = 0;$$

$$2i\omega_1\Delta_5 + \frac{3ik_1}{2\omega_1} = 0;$$

$$4i\omega_1\Delta_6 + \frac{i(\omega_0^2 - \omega_1^2)}{2\omega_1}(\Delta_3 + \Delta_6) + \frac{ik_1}{2\omega_1} = 0;$$

$$4i\omega_1\Delta_7 - \frac{i(\omega_0^2 - \omega_1^2)}{2\omega_1}(\Delta_7 + \Delta_{12}) - \frac{3ik_1}{2\omega_1}(\Delta_3 + \Delta_6) - \frac{ik_2}{2\omega_1} = 0;$$

$$2i\omega_1\Delta_8 - \frac{i(\omega_0^2 - \omega_1^2)}{2\omega_1}(\Delta_8 + \Delta_{11}) - \frac{6ik_1}{2\omega_1}(\Delta_3 + \Delta_6) - \frac{5ik_2}{2\omega_1} = 0;$$

$$2i\omega_1\Delta_{10} + \frac{3ik_1}{2\omega_1}(\Delta_3 + \Delta_6) + \frac{10ik_2}{2\omega_1} = 0;$$

$$4i\omega_1\Delta_{11} + \frac{i(\omega_0^2 - \omega_1^2)}{2\omega_1}(\Delta_8 + \Delta_{11})$$

$$+ \frac{6ik_1}{2\omega_1}(\Delta_3 + \Delta_6) + \frac{5ik_2}{2\omega_1} = 0;$$

$$\begin{aligned}
& 6i\omega_1\Delta_{12} + \frac{i(\omega_0^2 - \omega_1^2)}{2\omega_1} (\Delta_7 + \Delta_{12}) \\
& + \frac{3ik_1}{2\omega_1} (\Delta_3 + \Delta_6) + \frac{ik_2}{2\omega_1} = 0.
\end{aligned}
\tag{A.1}$$

## B. Formulas of Parameters $\Delta_i$

The parameters  $\Delta_i$  ( $i=1, \dots, 12$ ) are

$$\begin{aligned}
\Delta_1 &= -\Delta_2, \\
\Delta_2 &= \frac{\omega_1^2 - \omega_0^2}{4\omega_1^2}, \\
\Delta_3 &= -2\Delta_6, \\
\Delta_6 &= \frac{k_1}{\omega_0^2 - 9\omega_1^2}, \\
\Delta_4 &= -\Delta_5, \\
\Delta_5 &= -\frac{3k_1}{4\omega_1^2}, \\
\Delta_7 &= -\frac{3}{2}\Delta_{12}, \\
\Delta_{12} &= \frac{6k_1\Delta_6 - 2k_2}{25\omega_1^2 - \omega_0^2}, \\
\Delta_8 &= -2\Delta_{11}, \\
\Delta_{11} &= \frac{6k_1\Delta_6 - 5k_2}{9\omega_1^2 - \omega_0^2}, \\
\Delta_9 &= -\Delta_{10}, \\
\Delta_{10} &= \frac{3k_1\Delta_6 - 10k_2}{4\omega_1^2}.
\end{aligned}
\tag{B.1}$$

## Data Availability

No data were used to support this study.

## Ethical Approval

Ethical approval was obtained for this study.

## Conflicts of Interest

The authors declare that they have no conflicts of interest.

## Acknowledgments

This study was supported by the National Natural Science Foundation of China (nos. 11672334, 11672335 and 11611530541) and the Endeavour Australia Cheung Kong Research Fellowship Scholarship from the Australian government.

## References

- [1] C. Feng, L. Yu, and W. Zhang, "Dynamic analysis of a dielectric elastomer-based microbeam resonator with large vibration amplitude," *International Journal of Non-Linear Mechanics*, vol. 65, pp. 63–68, 2014.
- [2] J. Han, Q. Zhang, and W. Wang, "Design considerations on large amplitude vibration of a doubly clamped microresonator with two symmetrically located electrodes," *Communications in Nonlinear Science and Numerical Simulation*, vol. 22, no. 1–3, pp. 492–510, 2015.
- [3] T. Beléndez, C. Neipp, and A. Beléndez, "Large and small deflections of a cantilever beam," *European Journal of Physics*, vol. 23, no. 3, pp. 371–379, 2002.
- [4] L. Wang and Y. Zhao, "Large amplitude motion mechanism and non-planar vibration character of stay cables subject to the support motions," *Journal of Sound and Vibration*, vol. 327, no. 1–2, pp. 121–133, 2009.
- [5] M. Spagnuolo and U. Andreaus, "A targeted review on large deformations of planar elastic beams: extensibility, distributed loads, buckling and post-buckling," *Mathematics and Mechanics of Solids*, pp. 1–23, 2018.
- [6] M. P. Omran, A. Amani, and H. G. Lemu, "Analytical approximation of nonlinear vibration of string with large amplitudes," *Journal of Mechanical Science and Technology*, vol. 27, no. 4, pp. 981–986, 2013.
- [7] Z. L. Wang, P. Poncharal, and W. A. De Heer, "Measuring physical and mechanical properties of individual carbon nanotubes by in situ TEM," *Journal of Physics and Chemistry of Solids*, vol. 61, no. 7, pp. 1025–1030, 2000.
- [8] Z. L. Wang, R. P. Gao, P. Poncharal, W. A. De Heer, Z. R. Dai, and Z. W. Pan, "Mechanical and electrostatic properties of carbon nanotubes and nanowires," *Materials Science and Engineering C: Materials for Biological Applications*, vol. 16, no. 1–2, pp. 3–10, 2001.
- [9] Q. Zheng and Q. Jiang, "Multiwalled Carbon Nanotubes as Gigahertz Oscillators," *Physical Review Letters*, vol. 88, no. 4, 2002.
- [10] M. Hemmatnezhad, R. Ansari, and G. H. Rahimi, "Large-amplitude free vibrations of functionally graded beams by means of a finite element formulation," *Applied Mathematical Modelling: Simulation and Computation for Engineering and Environmental Systems*, vol. 37, no. 18–19, pp. 8495–8504, 2013.
- [11] J. B. Gunda, R. K. Gupta, G. Ranga Janardhan, and G. Venkateswara Rao, "Large amplitude vibration analysis of composite beams: Simple closed-form solutions," *Composite Structures*, vol. 93, no. 2, pp. 870–879, 2011.
- [12] A. Nikkar, S. Bagheri, and M. Saravi, "Dynamic model of large amplitude vibration of a uniform cantilever beam carrying an intermediate lumped mass and rotary inertia," *Latin American Journal of Solids and Structures*, vol. 11, no. 2, pp. 320–329, 2014.
- [13] Y. P. Yu, B. S. Wu, Y. H. Sun, and L. Zang, "Analytical approximate solutions to large amplitude vibration of a spring-hinged beam," *Meccanica*, vol. 48, no. 10, pp. 2569–2575, 2013.
- [14] K. K. Raju and G. V. Rao, "Towards improved evaluation of large amplitude free-vibration behaviour of uniform beams using multi-term admissible functions," *Journal of Sound and Vibration*, vol. 282, no. 3–5, pp. 1238–1246, 2005.
- [15] J.-H. He, "Variational approach for nonlinear oscillators," *Chaos, Solitons and Fractals*, vol. 34, no. 5, pp. 1430–1439, 2007.
- [16] S. H. Hoseini, T. Pirbodaghi, M. T. Ahmadian, and G. H. Farrahi, "On the large amplitude free vibrations of tapered beams:

- an analytical approach," *Mechanics Research Communications*, vol. 36, no. 8, pp. 892–897, 2009.
- [17] B. Gheshlaghi, "Large-amplitude vibrations of nanowires with dissipative surface stress effects," *Acta Mechanica*, vol. 224, no. 7, pp. 1329–1334, 2013.
- [18] S. Souayeh and N. Kacem, "Computational models for large amplitude nonlinear vibrations of electrostatically actuated carbon nanotube-based mass sensors," *Sensors and Actuators A: Physical*, vol. 208, pp. 10–20, 2014.
- [19] M. Şimşek, "Large amplitude free vibration of nanobeams with various boundary conditions based on the nonlocal elasticity theory," *Composites Part B: Engineering*, vol. 56, pp. 621–628, 2014.
- [20] R. Nazemnezhad and S. Hosseini-Hashemi, "Exact solution for large amplitude flexural vibration of nanobeams using non-local Euler-Bernoulli theory," *Journal of Theoretical and Applied Mechanics (Poland)*, vol. 55, no. 2, pp. 649–658, 2017.
- [21] K. Nakamura, K. Kakihara, M. Kawakami, and S. Ueha, "Measuring vibration characteristics at large amplitude region of materials for high power ultrasonic vibration system," *Ultrasonics*, vol. 38, no. 1, pp. 122–126, 2000.
- [22] A. Mozuras and E. Podzharov, "Measurement of large harmonic vibration amplitudes," *Journal of Sound and Vibration*, vol. 271, no. 3-5, pp. 985–998, 2004.
- [23] J. C. Simo, "A finite strain beam formulation. The three-dimensional dynamic problem. Part I," *Computer Methods Applied Mechanics and Engineering*, vol. 49, no. 1, pp. 55–70, 1985.
- [24] P.-F. Pai and A.-H. Nayfeh, "A new method for the modeling of geometric nonlinearities in structures," *Computers & Structures*, vol. 53, no. 4, pp. 877–895, 1994.
- [25] E. Babilio and S. Lenci, "On the notion of curvature and its mechanical meaning in a geometrically exact plane beam theory," *International Journal of Mechanical Sciences*, vol. 128-129, pp. 277–293, 2017.
- [26] S. Lenci, F. Clementi, and G. Rega, "Comparing Nonlinear Free Vibrations of Timoshenko Beams with Mechanical or Geometric Curvature Definition," *Procedia IUTAM*, vol. 20, pp. 34–41, 2017.
- [27] O. Kopmaz and Ö. Gündoğdu, "On the curvature of an Euler-Bernoulli beam," *International Journal of Mechanical Engineering Education*, vol. 31, no. 2, pp. 132–142, 2003.
- [28] C. Semler, G. X. Li, and M. P. Paidoussis, "The non-linear equations of motion of pipes conveying fluid," *Journal of Sound and Vibration*, vol. 169, no. 5, pp. 577–599, 1994.
- [29] D. Zhao, J. Liu, and L. Wang, "Nonlinear free vibration of a cantilever nanobeam with surface effects: Semi-analytical solutions," *International Journal of Mechanical Sciences*, vol. 113, pp. 184–195, 2016.
- [30] N. Vljajic, T. Fitzgerald, V. Nguyen, and B. Balachandran, "Geometrically exact planar beams with initial pre-stress and large curvature: Static configurations, natural frequencies, and mode shapes," *International Journal of Solids and Structures*, vol. 51, no. 19-20, pp. 3361–3371, 2014.
- [31] A. H. Nayfeh and D. T. Mook, *Nonlinear Oscillations*, John Wiley & Sons, New York, NY, USA, 1979.
- [32] F. Benedettini and G. Rega, "Non-linear dynamics of an elastic cable under planar excitation," *International Journal of Non-Linear Mechanics*, vol. 22, no. 6, pp. 497–509, 1987.
- [33] H. Koivurova, "The numerical study of the nonlinear dynamics of a light, axially moving string," *Journal of Sound and Vibration*, vol. 320, no. 1-2, pp. 373–385, 2009.
- [34] A. H. Nayfeh, *The Method of Normal Forms*, Wiley-VCH, Weinheim, Germany, 2nd edition, 2011.
- [35] A. Y. Leung and Q. C. Zhang, "Complex normal form for strongly non-linear vibration systems exemplified by Duffing-van der Pol equation," *Journal of Sound and Vibration*, vol. 213, no. 5, pp. 907–914, 1998.
- [36] W. Wang, Q. C. Zhang, and X. J. Wang, "Application of the undetermined fundamental frequency method for analyzing the critical value of chaos," *Acta Physica Sinica*, vol. 58, no. 8, pp. 5162–5168, 2009.

## Research Article

# A Study on the Application of Coordinated TOPSIS in Evaluation of Robotics Academic Journals

Liping Yu,<sup>1</sup> Wenhua Yang,<sup>2</sup> Yunlong Duan ,<sup>2</sup> and Xinwen Long<sup>3</sup>

<sup>1</sup>School of Management and E-Business, Zhejiang Gongshang University, Hangzhou 310018, China

<sup>2</sup>International Business School, Yunnan University of Finance and Economics, Kunming 650221, China

<sup>3</sup>Library, Southeast University, Nanjing 211189, China

Correspondence should be addressed to Yunlong Duan; [duanyl1977@126.com](mailto:duanyl1977@126.com)

Received 26 April 2018; Accepted 28 June 2018; Published 11 July 2018

Academic Editor: Carlos Llopis-Albert

Copyright © 2018 Liping Yu et al. This is an open access article distributed under the Creative Commons Attribution License, which permits unrestricted use, distribution, and reproduction in any medium, provided the original work is properly cited.

While TOPSIS is a widely used evaluation method, it lacks evaluation from the perspective of indicator coordination. Based on the analysis of TOPSIS evaluation methods, this paper proposes a new assessment method, coordinated TOPSIS, which takes into account the advantages of TOPSIS evaluation methods and the coordination level of evaluation indicators. Taking the robotics academic journals as an example, the TOPSIS evaluation and the coordinated TOPSIS evaluation results are compared. The research shows that the weights of the coordinated TOPSIS method can be manually adjusted according to the purpose of evaluation and have a good flexibility; the TOPSIS evaluation results and coordinated TOPSIS evaluation results have a high degree of correlation, but the difference from the perspective of the ranking is big; the coordinated TOPSIS is very suitable for evaluation field that needs to consider the coordinated development, and it can be replicated.

## 1. Introduction

It is of great significance to evaluate academic journals of robotics. With the rapid development of artificial intelligence, the development of robotics disciplines is very fast. In recent years, robotic academic journals have become increasingly influential, and their influence factors are getting higher and higher, which makes it very important to promote the development of robotics disciplines. The evaluation of robotic academic journals not only helps the competition between different journals and improves the academic quality, but also facilitates the selection of appropriate journals by the author when posting. It provides great value to journals and scholars and they can jointly support the development of robotics disciplines.

TOPSIS is a widely used evaluation method. Since Huang proposed the TOPSIS evaluation method [1], it has been widely applied in an extensive range of fields such as economy, society, and natural sciences. It evaluates the relative distance between the evaluation object and the ideal solution and negative ideal solution. On March 17, 2018, based on Scopus database, a total of 5,630 papers were searched

by title, abstract and keyword “TOPSIS”. Based on the Ei/Compendex database, a total of 4,144 papers were retrieved when “TOPSIS” was searched in “all fields”. Based on the Web of Science database, a total of 2823 papers were found using the search topic “TOPSIS”.

In the evaluation of science and technology, TOPSIS has also been widely used. Xu et al. use the TOPSIS method to evaluate the output of scientific research institutions [2]. Yu et al. use TOPSIS to evaluate academic journals based on panel data [3]. Li et al. adopt fuzzy TOPSIS in multicriteria group decision-making in the study of research institutions output [4]. Yu and Pan study the characteristics and differentiation of TOPSIS under high power and applied it to academic journal evaluation [5].

Just as any evaluation method has its own advantages and disadvantages; TOPSIS also has some room for optimization. Jahanshahloo et al. study the distance calculation formula of the TOPSIS method when the attribute data is a fuzzy number [6] and proposed an improved method. Yu, Pan, et al. put forward a modified TOPSIS method based on the reverse order problem as the points of evaluation value on the vertical line of the line segment between ideal solution

and negative ideal solutions move [7]. Li and Zhang's study suggests that when the TOPSIS evaluation is conducted [8], if the negative ideal solution of the newly added evaluation object is lower, the problem of disordered sorting will occur, and they recommend some ideas for improvement. Lu and Tang believe that the TOPSIS method has problems in the determination of positive and negative ideal points [9], the determination of weights, and the calculation of closeness, which all lead to disordered sorting. It is proposed to use absolute positive and negative ideal points, and use projection methods to improve the closeness formula. Li, Zhang et al. employ gray correlation closeness to evaluate instead of TOPSIS positive and negative ideal solution distance [10].

Sun et al. evaluate the impact of green technology innovation on ecological-economic efficiency of strategic emerging industries with the entropy weighted TOPSIS method [11]. Based on the proposed distance measure, Shen and Ma et al. developed an extended intuitionistic fuzzy TOPSIS approach to handle multicriteria decision-making problems [12]. Chen et al. adopt the improved TOPSIS method and sequence weighting to evaluate the level of transformation and upgrading of six resource-based cities in Shanxi province from 2001 to 2015 [13]. Mishra et al. propose a new integrated approach using analytical hierarchy process (AHP) and technique for order of preference by similarity to ideal solution (TOPSIS) methods for evaluation and prioritization of appropriate manufacturing flexibility type required in the context of multiple environmental uncertainties [14]. Existing research advances the optimization of TOPSIS evaluation method. The improvement of the TOPSIS evaluation method needs to be comprehensively analyzed. Some of them are indeed problems with the TOPSIS evaluation method itself, which of course needs to be enhanced. Others do not belong to the TOPSIS method itself, for example, increasing the evaluation objects. If the evaluation object contains a negative ideal solution, it will disarrange the entire order. This is very normal. Some scholars have proposed to optimize the setting of TOPSIS weights, but the weighting problem is the basic issue of multiattribute evaluation method and is not specific to the TOPSIS evaluation method. In general, TOPSIS is an excellent evaluation method, but it is meaningful to improve TOPSIS from the perspective of the evaluation index coordination. Currently, there are few related studies in this field, and it is necessary to take a deep dive into it.

First, evaluation of academic journals can be done from a variety of perspectives, including academic quality, journal influence, timeliness, and editorial quality. An excellent journal should strive to achieve comprehensive and coordinated development. Each evaluation index should not be lacking. However, for the current TOPSIS evaluation method, when certain indicators are low, they can be complemented when the other indicators are high.

Second, the coordinated development of academic journals is also in line with the laws of journal development. For example, the timely delivery of the robot journals is efficient, which is a manifestation of their academic quality. Editing and publishing excellence is also an integral part of journal quality. Journals with better academic quality are bound to have higher influence.

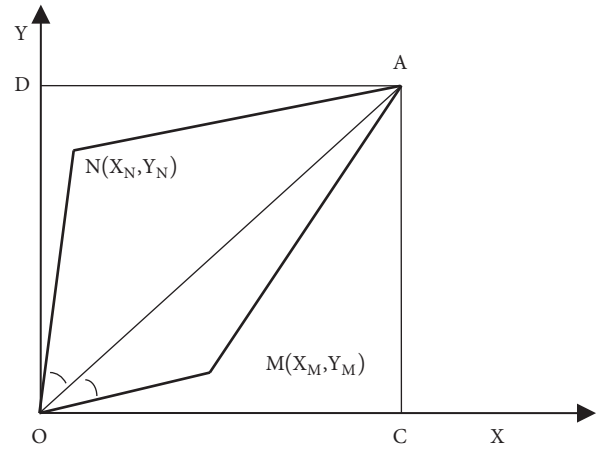


FIGURE 1: Coordination issues for evaluation.

Third, there are not many multiattribute methods which evaluate from the perspective of coordination. There are dozens of multiattribute evaluation methods. TOPSIS is only one of the evaluation methods. When TOPSIS is designed initially, the coordination of evaluation indicators is not considered. If improved, it can not only optimize the TOPSIS evaluation method and enrich the basic theory of evaluation but also have important practical significance for the evaluation of academic journals. It can also promote the all-round and balanced development of academic journals.

Based on the analysis of TOPSIS method principle, this paper proposes a coordinated TOPSIS evaluation method. Taking the JCR2016 Robotics Journal as an example, this paper studies the differences between the evaluation method and the original TOPSIS evaluation method and then summarizes the results.

## 2. The Principles of Coordinated TOPSIS Evaluation Method

2.1. *Introduction to TOPSIS Evaluation Method.* The traditional TOPSIS calculation formula is

$$C_i = \frac{\sqrt{\sum_{j=1}^n \omega_j (x_{ij} - x_j^-)^2}}{\sqrt{\sum_{j=1}^n \omega_j (x_{ij} - x_j^+)^2} + \sqrt{\sum_{j=1}^n \omega_j (x_{ij} - x_j^-)^2}} \quad (1)$$

In formula (1),  $x_{ij}$  represents the standardized evaluation index,  $x_j^+$  is the positive ideal solution, its value is  $\max(x_j)$ ;  $x_j^-$  is the negative ideal solution, its value is  $\min(x_j)$ , and  $n$  is the number of evaluation indicators.  $C_i$  indicates the evaluation result of TOPSIS, and its value is between 0 and 1, the larger the evaluation result, the better the evaluation object.

Figure 1 can further illustrate the TOPSIS evaluation principle. Assume that there are only two evaluation indicators X, Y, and A is normalized ideal solution with coordinates (1, 1). OA is 45° straight line, also called the coordinated straight line. All points on OA line have the same value of the two evaluation indexes. The position of the negative ideal

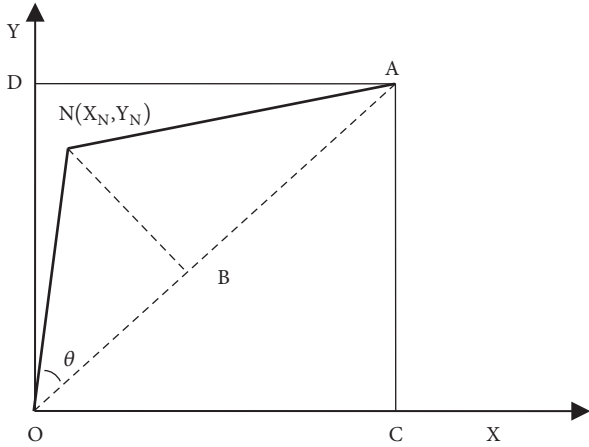


FIGURE 2: Calculation of coordination degree.

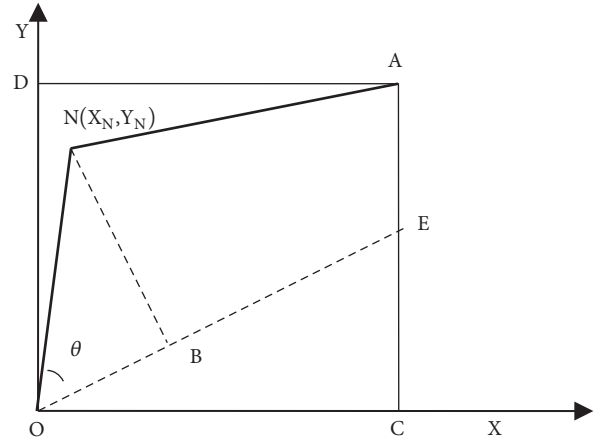


FIGURE 3: Weighted TOPSIS reference.

solution is uncertain. For simplicity, assume that the negative ideal solution is the origin and the coordinates are (0, 0). M is any point that needs to be evaluated and its coordinate value is  $(X_M, Y_M)$ . The distance from M to the ideal solution is MA, and the distance to the negative ideal solution is OM. At this time, the TOPSIS evaluation value is

$$C_M = \frac{OM}{OM + MA} \quad (2)$$

**2.2. Reflecting the Coordinated Development of Indicators.** As shown in Figure 1, it is assumed that there are two evaluation objects M  $(X_M, Y_M)$  and N  $(X_N, Y_N)$ , and for point M,  $X_M > Y_M$ ; for point N,  $X_N < Y_N$ . However, from the deviation degree of X, Y evaluation index at points M and N, N point deviates further from the OA line. This is because the abscissa  $X_N$  of point N is much smaller than its ordinate  $Y_N$ , showing  $\angle NOA > \angle AOM$ . In other words, if the two indicators X, Y are more coordinated, the gap between the values of the two should be smaller. In the case of limit,  $X = Y$ , that is located on the coordination line OA. The size of the coordination level can be represented by the angle of the line from the origin to the point and line OA. For point M, the angle is  $\angle AOM$ . For point N, the angle is  $\angle NOA$ . The smaller the angle is, the more coordinated it is.

**2.3. The Degree of Coordination.** As shown in Figure 2, in order to reflect the coordinated development of indicators in TOPSIS evaluation, which means the horizontal coordinate value should be close to its vertical coordinate value for any indicator, it is necessary to calculate the degree of coordination. The size of  $\angle NOA$  indicates the level of coordination. The larger the angle is, the less coordinated it is. In other words, the bigger the indicator is, the less coordinated it is, just use  $45^\circ - \angle NOA$ .

In order to find out the size of  $\angle NOA$ , you need to calculate the cosine of the angle first and then convert it by the inverse cosine function. Yu and Zhang proved that the length of OB is  $(X_N + Y_N)/2$ , and the length of ON is the Euclidean distance from the point N to the origin, so that the cosine of the  $\angle NOA$  is solved [15].

It can be utilized across the board. Assuming in general  $\angle NOA = \theta$ , its cosine is

$$\cos(\theta_i) = \frac{\sum_{j=1}^n x_{ij}}{n \sqrt{\sum_{j=1}^n x_{ij}^2}} \quad (3)$$

The value of  $\theta$  can be calculated using the inverse cosine function. The larger  $\theta$  is, the more uncoordinated it is. The value of  $\theta$  is  $0^\circ - 45^\circ$ , if 45 is subtracted from  $\theta$  and then divided by 45, the degree of coordination can be obtained with a slight conversion. The maximum value is 1 and a minimum value is 0:

$$p_i = \frac{45 - \theta_i}{45} \quad (4)$$

This method can also be applied to weighted TOPSIS. There is no concept of weighting when the TOPSIS method was developed. Scholars such as Shyr, Deng et al., Yue and Zeng, and Xiao (2018) introduced weights to TOPSIS. The indicator coordination line of the weighted TOPSIS is not  $45^\circ$  straight line [16–19]. As shown in OE in Figure 3, because the weight of X is greater than that of Y, resulting in the coordination reference line becoming OE, closer to the X-axis, the angle  $\theta$  further increases and N is even more inconsistent. Angle  $\theta$  may be greater than  $45^\circ$ . It may be less than  $45^\circ$ . However, it will certainly be less than  $90^\circ$ . Therefore, it is more reasonable to consider the use of  $90$  minus  $\theta$  for the calculation of the degree of coordination after weighting.

In the weighted TOPSIS evaluation, the  $\theta$  cosine size is

$$\cos(\theta_i) = \frac{\sum_{j=1}^n \omega_j x_{ij}}{n \sqrt{\sum_{j=1}^n \omega_j x_{ij}^2}} \quad (5)$$

Due to the weighted TOPSIS, the reference baseline is not  $45^\circ$ . Therefore, when calculating the degree of coordination, it is better to convert using 90, that is,

$$p_i = \frac{90 - \theta_i}{90} \quad (6)$$

**2.4. Coordinated TOPSIS Method.** To revise TOPSIS from the point of view of coordinated development, two issues must be considered. First, the TOPSIS evaluation results must be considered to reflect the superiority and characteristics of TOPSIS, and the second is coordination. As for the synthesis of the two, there are two ideas, one is to take additive synthesis, and the other is multiplication synthesis. For the multiplication synthesis, for points on X-axis or Y-axis, which are completely uncoordinated, the coordination degree is 0, so the overall evaluation value is 0, which is not in line with the usual; therefore additive synthesis is adopted. The weight of the coordination degree can also be set according to the purpose of the evaluation. For this purpose, the coordination weight  $v$  is introduced,  $0 < v < 1$ . If the assessment is to encourage the coordinated development of the evaluation indicators,  $v$  must be greater than or equal to 0.5.

In addition, we must pay attention to the dimensional issue of the TOPSIS evaluation value and coordination degree. In TOPSIS evaluation, since the positive and negative ideal solutions are often not in the same evaluation object, the theoretical maximum value is 1 and the minimum value is 0. However, this situation often does not exist in actual evaluation. In order to combine TOPSIS evaluation values and coordination degree, the TOPSIS evaluation results must be standardized. In the same way, the degree of coordination also needs to be standardized. This coordination formula is

$$T_i = (1 - v) \frac{C_i}{\max(C_i)} + v \frac{P_i}{\max(P_i)} \quad (7)$$

In this equation,  $C_i$  is the evaluation results;  $P_i$  is coordination degree;  $v$  is the weight of adjustment. The coordination degree is an important adjustment indicator in that coordinated development of various types of indicators needs to be encouraged. The differences between these indicators should not be too big.

**2.5. Explanation of Coordinated TOPSIS Evaluation Using Absolute Negative Ideal Solution.** In TOPSIS evaluation, if a negative ideal solution is used, the line between negative ideal solution to the ideal solution will not normally be  $45^\circ$ . It is not meaningful to use the non- $45^\circ$  line as a criterion to judge whether or not the evaluation indicators are coordinated. This is because the coordination reference standard is not unique. In this circumstance, a more scientific approach is to adopt an absolute negative ideal solution, that is, to use the origin as a negative ideal solution. In addition, the use of an absolute negative ideal solution can also fundamentally eliminate disorder problem in TOPSIS. The sequences of all evaluation results will be changed if the negative ideal solution changes.

It should be noted that, in the following empirical research, in order to conduct a comparative analysis of TOPSIS and coordinated TOPSIS, absolute negative ideal solutions are used in TOPSIS evaluation, and the value at the origin of the coordinate axis is the worst value.

### 3. Sources of Data

This article takes the JCR2016 Robotics Journal as an example to compare and analyze TOPSIS and coordinated TOPSIS evaluation results. The robotics discipline is one of the few disciplines in JCR 2016, with a total of 26. Since the four journals "IEEE Transactions on Cognitive and Developmental Systems," "Intelligent Service Robotics," "IEEE Transactions on Autonomous Mental Development," and "Frontiers in Neurorobotics" have missing data, they are not considered, so there are actually only 22 journals.

JCR2016 published a total of 11 indicators, namely, Total Cites, Journal Impact Factor, Impact Factor without Journal Self Cites, 5-Year Impact Factor, Immediacy Index, Cited Half-Life, Citing Half-life, Eigenfactor Score, and Article Influence Score. Average Journal Impact Factor Percentile, Normalized Eigenfactor, and Since Normalized Eigenfactor is derived linearly from characteristic factors, it is removed to avoid data duplication, Average Journal Impact Factor Percentile is calculated based on the impact factor, and it belongs to the ranking index, which is discontinuous numerical index. Therefore, it is also deleted. Nine indicators are used for evaluation, and the statistics of the data are shown in Table 1.

All indicators must be standardized during the evaluation. The normalization method of the forward indicator is to divide the original indicator value by its maximum value. The cited half-life and the citing half-life are two reverse indexes that need to be processed in a forward direction. The standardized formula is as follows:

$$x_{ij} = \frac{x'_{ij} - \max(x'_j)}{\max(x'_j) - \min(x'_j)} \quad (8)$$

In formula (8),  $x_i$  is the standardized evaluation index,  $x'_{ij}$  is the original index data,  $\max()$  is the maximum value, and  $\min()$  is the minimum value.

### 4. Evaluation Results Comparison

First of all, the TOPSIS method is used for evaluation. For the sake of simplicity, the weights of the nine evaluation indexes are set equal to 0.111. Next, the coordinated TOPSIS is used to evaluate. The weight of the coordination degree is set to 0.5, and the weight of the TOPSIS evaluation is also 0.5. The evaluation results are shown in Table 2.

From the average of all the journals, the overall  $\theta$  is high, the average tilt is  $73.529$  degree, and the gap between the journals is not large, indicating that the coordination of the journal is not good. The root cause is the large data distribution of bibliometric indicators in academic journals. Seglen finds that the citation data exhibited a typical skewed distribution. Outliers caused large variations in the statistical mean [20]. Vinkler also finds the right bias of the citation distribution [21].

From the ranking of evaluation results, after considering the coordination degree, the ranking of the evaluation results of the coordinated TOPSIS differs greatly from that of the TOPSIS. There are only four types of journals that are

TABLE 1: Index description statistics.

Evaluation index	Mean	Median	Maximum	Minimum	Std. Dev.
Total Cites	2301.000	1501.000	12478.000	144.000	2920.082
Journal Impact Factor	2.540	2.380	8.649	0.500	1.915
Impact Factor without Journal Self Cites	2.249	1.902	7.108	0.390	1.703
5-Year Impact Factor	2.950	2.440	9.243	0.406	2.236
Immediacy Index	0.430	0.426	1.390	0.053	0.336
Cited Half-Life	6.241	6.550	10.000	2.300	1.867
Citing Half-life	7.991	8.000	10.000	4.900	1.041
Eigenfactor Score	0.003	0.002	0.013	0.000	0.003
Article Influence Score	0.752	0.481	2.792	0.091	0.682

TABLE 2: Comparison of TOPSIS and coordinated TOPSIS evaluation.

JCR Abbreviated Title	Angle $\Theta$	Coordination Degree $P_i$	TOPSIS Value $C_i$	TOPSIS Ranking	Coordinated TOPSIS Value $T_i$	Ranking
INT J ROBOT RES	71.479	0.206	0.610	2	0.967	1
SOFT ROBOT	72.970	0.189	0.633	1	0.947	2
IEEE ROBOT AUTOM MAG	72.314	0.197	0.507	4	0.864	3
IEEE T ROBOT	73.132	0.187	0.515	3	0.849	4
J FIELD ROBOT	71.539	0.205	0.426	5	0.821	5
BIOINSPIR BIOMIM	71.751	0.203	0.415	6	0.806	6
ROBOT CIM-INT MANUF	72.060	0.199	0.401	7	0.787	7
AUTON ROBOT	70.934	0.212	0.346	8	0.773	8
ROBOT AUTON SYST	71.140	0.210	0.302	13	0.733	9
SWARM INTELL-US	72.320	0.196	0.322	12	0.718	10
J BIONIC ENG	73.465	0.184	0.333	9	0.696	11
J MECH ROBOT	73.416	0.184	0.328	11	0.694	12
INT J SOC ROBOT	73.853	0.179	0.329	10	0.683	13
J INTELL ROBOT SYST	73.478	0.184	0.278	15	0.652	14
ROBOTICA	72.311	0.197	0.167	20	0.596	15
INT J ADV ROBOT SYST	76.305	0.152	0.296	14	0.593	16
ADV ROBOTICS	73.395	0.185	0.193	18	0.588	17
INT J HUM ROBOT	73.707	0.181	0.162	21	0.555	18
IND ROBOT	74.480	0.172	0.171	19	0.542	19
APPL BIONICS BIOMECH	75.557	0.160	0.159	22	0.504	20
INT J ROBOT AUTOM	77.649	0.137	0.203	16	0.484	21
REV IBEROAM AUTOM IN	80.377	0.107	0.195	17	0.407	22
Average	73.529	0.183	0.331	--	0.694	--

completely consistent in the ranking of the two evaluation methods, accounting for 18.18% of all journals. Because the overall number of robotics journals is small, this situation will be more serious for other disciplines that have more journals.

The degree of correlation between TOPSIS and coordinated TOPSIS evaluation results is relatively high. The correlation coefficient is 0.939, indicating a high degree of consistency between the two. From the scatter plot of the evaluation results (Figure 4), when the score is higher, the two have more similar results, and vice versa.

## 5. Conclusions and Discussion

Coordinated TOPSIS is an evaluation method that takes into account the coordination of evaluation indicators and the advantages of TOPSIS evaluation. In accordance with TOPSIS evaluation, this paper proposes a method to determine the degree of coordination. The principle is to measure the angle between the line from the evaluation object to the origin and the ideal solution to the origin. The smaller the angle is, the better the coordination of the indicators is. Based on this result, a new evaluation method, coordinated TOPSIS,

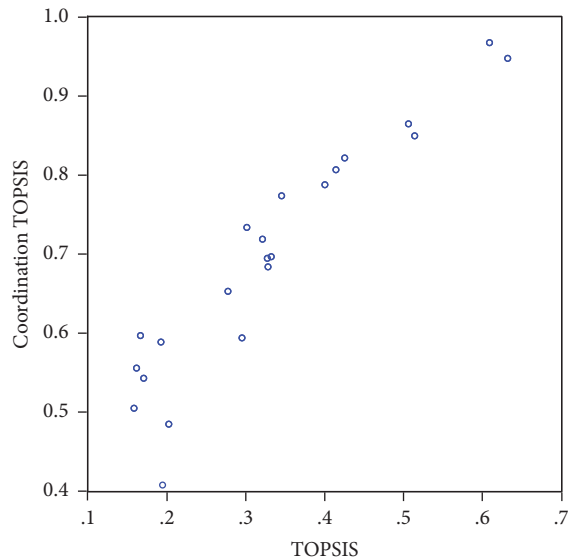


FIGURE 4: Comparison of scatter plots of evaluation results.

is proposed, combining TOPSIS and coordination level. The weight of the coordination degree can be manually adjusted according to the purpose of evaluation, and it can be widely applied when the coordination level of indicators need to be taken into account

The empirical research shows that the TOPSIS evaluation results have a high correlation with the coordinated TOPSIS evaluation results, but they differ significantly from the ranking perspective. Because there are few robot academic journals in this study, this sort of difference has been shown. The ranking difference will be even greater for subjects with more academic journals. The evaluation method cannot be simply chosen for a higher correlation coefficient. It should be based on the purpose of the evaluation and the principle of the evaluation method. After all, the choice of evaluation methods will have a significant impact on the results.

Coordinated TOPSIS is very suitable for evaluation field that needs to consider the coordinated development, and it can be replicated. In the evaluation of science and technology, the balanced development of evaluation indicators has become more and more important, such as academic quality and influence, technology and economy, scientific R&D, and transformation of achievements, etc. As far as the field of economic and social development is concerned, more areas need to consider coordinated development. Therefore, coordinated TOPSIS has a wide range of applications, which can be selected according to the purpose of evaluation and extended to some extent.

## Data Availability

The data used to support the findings of this study are included within the article.

## Conflicts of Interest

The authors declare that they have no conflicts of interest.

## Acknowledgments

This paper is supported by the Major Project of National Social Science Fund of China (No. 16ZDA053), Humanities and Social Sciences Projects of the Ministry of Education (17YJA630125), Philosophy and Social Science Foundation of Zhejiang Province (17NDJC107YB), and China's National Natural Science Foundation Project (71663058). The authors thank them heartedly for supporting the paper funds.

## References

- [1] C. L. Hwang and K. Yoon, "Methods for multiple attribute decision making," in *Multiple Attribute Decision Making*, vol. 186 of *Lecture Notes in Economics and Mathematical Systems*, pp. 58–191, Springer, Heidelberg, Germany, 1981.
- [2] J. Xu, Z. Li, W. Shen, and B. Lev, "Multi-attribute comprehensive evaluation of individual research output based on published research papers," *Knowledge-Based Systems*, vol. 43, pp. 135–142, 2013.
- [3] L. Yu, X. Shen, Y. Pan, and Y. Wu, "Scholarly journal evaluation based on panel data analysis," *Journal of Informetrics*, vol. 3, no. 4, pp. 312–320, 2009.
- [4] Z. Li, M. Liechty, J. Xu, and B. Lev, "A fuzzy multi-criteria group decision making method for individual research output evaluation with maximum consensus," *Knowledge-Based Systems*, vol. 56, pp. 253–263, 2014.
- [5] L. P. Yu, Y. T. Pan, and Y. S. Wu, "Application of TOPSIS in journal evaluation and its promotion under high power," *Journal of Statistical Research*, vol. 29, no. 12, pp. 96–101, 2012.
- [6] G. R. Jahanshahloo, F. H. Lotfi, and M. Izadikhah, "Extension of the TOPSIS method for decision-making problems with fuzzy data," *Applied Mathematics and Computation*, vol. 181, no. 2, pp. 1544–1551, 2006.
- [7] L. P. Yu, Y. T. Pan, and Y. S. Wu, "Revised TOPSIS and its application research in science and technology evaluation," *Intelligence Magazine*, vol. 31, no. 6, pp. 103–107, 2012.
- [8] Y. K. Li and J. R. Zhang, "The reverse order problem," *Science and Technology Journal*, vol. 26, no. 7, pp. 47–50, 2008.
- [9] W. F. Lu and H. X. Tang, "A comprehensive improvement of TOPSIS method for multi-attribute decision making," *Statistics and Decision*, no. 19, pp. 38–40, 2012.
- [10] C. B. Li, J. Y. Zhang, Y. D. Gu, and Z. Q. Qi, "A fuzzy stochastic multi-criteria decision making method and application based on prospect theory and improved TOPSIS," *Operations Research and Management*, vol. 24, no. 2, pp. 92–100, 2015.
- [11] L.-Y. Sun, C.-L. Miao, and L. Yang, "Ecological-economic efficiency evaluation of green technology innovation in strategic emerging industries based on entropy weighted TOPSIS method," *Ecological Indicators*, vol. 73, pp. 554–558, 2017.
- [12] F. Shen, X. Ma, Z. Li, Z. Xu, and D. Cai, "An extended intuitionistic fuzzy TOPSIS method based on a new distance measure with an application to credit risk evaluation," *Information Sciences*, vol. 428, pp. 105–119, 2018.
- [13] W. Chen, Y. Shen, and Y. Wang, "Evaluation of economic transformation and upgrading of resource-based cities in Shaanxi

- province based on an improved TOPSIS method,” *Sustainable Cities and Society*, vol. 37, pp. 232–240, 2018.
- [14] R. Mishra, A. K. Pundir, and L. Ganapathy, “Evaluation and prioritisation of manufacturing flexibility alternatives using integrated AHP and TOPSIS method: Evidence from a fashion apparel firm,” *Benchmarking*, vol. 24, no. 5, pp. 1437–1465, 2017.
- [15] L. P. Yu and Q. Zhang, “A study of the nature of two types of utility function evaluation methods in journal evaluation,” *Journal of Intelligence*, no. 10, pp. 1077–1082, 2014.
- [16] H. J. Shyur, “COTS evaluation using modified TOPSIS and ANP,” *Applied Mathematics and Computation*, vol. 177, no. 1, pp. 251–259, 2006.
- [17] H. Deng, C.-H. Yeh, and R. J. Willis, “Inter-company comparison using modified TOPSIS with objective weights,” *Computers & Operations Research*, vol. 27, no. 10, pp. 963–973, 2000.
- [18] Z. Yue, “An extended TOPSIS for determining weights of decision makers with interval numbers,” *Knowledge-Based Systems*, vol. 24, no. 1, pp. 146–153, 2011.
- [19] S. Zeng and Y. Xiao, “A method based on topsis and distance measures for hesitant fuzzy multiple attribute decision making,” *Technological and Economic Development of Economy*, vol. 24, no. 3, pp. 969–983, 2018.
- [20] P. O. Seglen, “The skewness of science,” *Journal of the Association for Information Science and Technology*, vol. 43, no. 9, pp. 628–638, 1992.
- [21] P. Vinkler, “Introducing the Current Contribution Index for characterizing the recent, relevant impact of journals,” *Scientometrics*, vol. 79, no. 2, pp. 409–420, 2009.

## Research Article

# Workspace Analysis of a Hybrid Kinematic Machine Tool with High Rotational Applications

Haiqiang Zhang,<sup>1</sup> Hairong Fang ,<sup>1,2</sup> Yuefa Fang,<sup>1,2</sup> and Bingshan Jiang<sup>1</sup>

<sup>1</sup>Robotics Research Center, School of Mechanical, Electronic and Control Engineering, Beijing Jiaotong University, Beijing, China

<sup>2</sup>Key Laboratory of Vehicle Advanced Manufacturing, Measuring and Control Technology, Ministry of Education, Beijing, China

Correspondence should be addressed to Hairong Fang; [hrfang@bjtu.edu.cn](mailto:hrfang@bjtu.edu.cn)

Received 14 April 2018; Accepted 22 May 2018; Published 26 June 2018

Academic Editor: Carlos Llopis-Albert

Copyright © 2018 Haiqiang Zhang et al. This is an open access article distributed under the Creative Commons Attribution License, which permits unrestricted use, distribution, and reproduction in any medium, provided the original work is properly cited.

This paper presents a novel parallel manipulator with one translational and two rotational (1T2R) degrees of freedom that can be employed to form a five-degree-of-freedom hybrid kinematic machine tool for large heterogeneous complex structural component machining in aerospace field. Compared with serial or parallel machine, hybrid machine has the merits of high stiffness, high speed, large workspace, and complicated surface processing ability. To increase stiffness, three-degree-of-freedom redundantly actuated and overconstrained 2PRU-PRPS parallel manipulator (P denotes the active prismatic joint) is proposed, which is utilized as the main body of hybrid machine. By resorting to the screw theory, the degree of freedom of the proposed mechanism is briefly addressed including the initial configuration and general configuration and validated by Grübler-Kutzbach (G-K) equation. Next, kinematic inverse solution and parasitic motion of the parallel manipulator are deduced and the transformational relations between the Euler angle and Tilt-Torsion (T-T) angle are identified. Thirdly, the performance evaluation index of orientation workspace is introduced, and the reachable workspace and joint workspace are formulated. Through specific examples, the reachable workspace, task workspace, and joint workspace of the redundant actuation parallel manipulator are depicted. Compared with overstrained 2PRU-PRS parallel manipulator, corresponding analyses illustrate that the proposed parallel manipulator owns much better orientation capability and is very meaningful to the development of the five-axis hybrid machine tool.

## 1. Introduction

Parallel kinematic manipulator tools were claimed to possess the inherent advantages such as high stiffness, high loading capability, high precision, low error accumulation, quick response speed, and high orientation capability. However, parallel manipulators suffer inherently from the unfavorable workspace. Therefore, it is of crucial significance to have a larger workspace so as to satisfy the working capability [1, 2]. While the three-axis NC machine has more advantages in large workspace and good dexterity, however, it is only suitable for simple surface or small parts processing [3, 4]. The five-axis series CNC machine, adding two-degree-of-freedom rotating head attached to its mobile platform or two-degree-of-freedom rotary tables on the three-axis machine, can maintain the favourable orientation, but often sacrificed certain workspace, and may cause poor precision and stiffness by increasing the length of the actuator to

enlarge the workspace [5, 6]. So there is a contradiction between workspace and precision and stiffness for free surface machining by using the traditional series or parallel machine tool, and they cannot be able to satisfy requirements of the high speed milling for large heterogeneous complex surface in aerospace. At present, many complicated freedom surfaces are still milling manually, which inevitably has high cost, low efficiency, and long cycle, and the process not only depends heavily on the expertise and experience of the operators, but also requires much attention be given to processing; what is more, it is difficult to obtain high quality machining surface [7]. So it is of importance to explore a design approach for solving the required reachable workspace to envelope the task workspace, which will offer an ideal solution for machining [8].

Hybrid kinematic machine is expected to integrate the respective merits of pure serial and parallel machine, which has bigger workspace and better dynamic performance,

higher precision and higher rigidity, more complicated surface processing ability, and more flexible orientation capability and has been successfully employed as machine tools and robots for high speed milling, drilling, and welding in aerospace and automotive industry for free surface processing, as well as assembly operations of aluminum structural parts [9]. It has been demonstrated practically by very successful applications such as a typical Sprint Z3 mechanism [10], Tricept hybrid machine tool [11], and Exechon hybrid machine tool [12]. In many practical applications, to increase the workspace of the three-degree-of-freedom parallel manipulator, we can add one or two long tracks. Simultaneously, to improve the orientation adjusting ability of the end effector, one can attach two- or three-degree-of-freedom rotating head and then form a multi-degree-of-freedom hybrid machine tool with large workspace and high stiffness, as well as high orientation capability [13, 14].

Hybrid machine tool underwent fast improvements and drew particular interests for numerous researchers, since they satisfy the increasing demanding task requirements of many various applications such as in machine tools, assembly lines, and high speed machining used in automotive, railway, and construction industries. For instance, the German DS Technologie launched five-axis machining center Ecospeed spindle for aircraft structure components with complex geometries, and the spindle head was mounted on the end effector of parallel manipulator, which can realize rotation about the x- and y-axis and translation along z-axis, and translation in X and Y direction can be realized by two very long tracks [15]. Wang et al. [16] have proposed a 3-SPR parallel mechanism which forms the main body of a 5-DOF hybrid manipulator especially designed for high speed machining in the aircraft industry. A five-axis hybrid machine has been developed to realize lapping and milling for large complex structure component surface, and it is generated by serially adding a 2-DOF A/C-axis head to the coupling three-degree-of-freedom 3RPS parallel manipulator in terms of two rotations and one translation [17, 18]. Hao et al. [19] came up with a novel two-degree-of-freedom parallel manipulator, incorporated a two-degree-of-freedom rotating head with A and C axis arrangement, and supplemented a mobile platform, which can form a gantry type five-axis hybrid machine tool to provide five-DOF movement capabilities. Huang et al. [20] put forward a practical 5-DOF hybrid reconfigurable manipulator module called Trivariant and built a variety of equipment to complete high speed milling for large aluminum structural components and complex molds. Wu et al. [21] have studied the three-degree-of-freedom redundant actuation parallel manipulator, increased the freedom of movement and rotation in the worktable, and applied it to the five-degree-of-freedom hybrid machine tool to perform machining.

The remainder of the paper is organized as follows. The research background of hybrid parallel machine tools and traditional serial-parallel machines is presented firstly. In the subsequent section, the required degree of freedom for high speed milling machining of large heterogeneous complex freedom surface is briefly addressed, and a redundantly actuated and overconstrained 2PRU-PRPS parallel manipulator

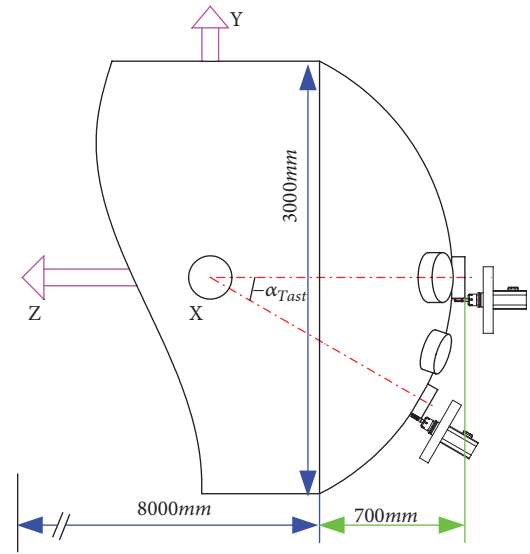


FIGURE 1: Limit rotational angle about x-axis.

configuration is presented and selected as the main body of the hybrid machine tool. Afterward, the degree of freedom of the proposed parallel manipulator was analyzed including initial configuration and general configuration based on the screw theory, and the modified Grübler-Kutzbach (G-K) equation was utilized to verify the correctness for the degree of freedom. Then, the kinematic inverse position and transformational relation between Z-Y-X Euler angle and Tilt-Torsion (T-T) angle are performed. Next, based on the inverse position analysis and constraint conditions, the limit boundary searching algorithms and flowchart are introduced in detail. In the subsequent section, the parasitic motion of the parallel manipulator was carried out by numerical examples; simultaneously, the orientation workspace analysis of the parallel manipulator is performed and the reachable workspace, the task workspace, and the joint workspace of the parallel manipulator are intuitively depicted by using computer code programming. Finally, this article is concluded in "Conclusions" section.

## 2. Design Requirements and Configuration of Hybrid Machine

**2.1. Function Requirement Analysis.** The purpose of this paper is to design a hybrid machine tool used in the aerospace field for a large heterogeneous free surface high speed milling; the workpiece magnitude is shown in Figures 1 and 2, whose span in x-axis is 3000mm and in y-axis is 3600mm, the total length of z-axis is 9400mm, and the feed stroke of the end face in Z direction is 700mm, because the workpiece can only be placed flat and cannot be stood; therefore, the first condition of the overall layout selection of horizontal hybrid machine tool should be considered. In order to achieve the desired machining effects, the machine tool and surface normal are kept reasonable in the process of surface milling, so the machine tool should have at least five degrees of freedom, including three translational degrees and two

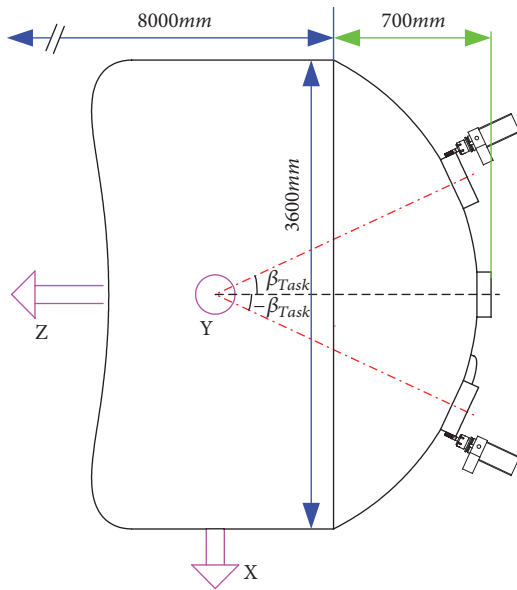


FIGURE 2: Limit rotational angle about y-axis.

rotational degrees. The latter is much more important than the former when it comes to perform three-dimensional milling [22]. Limit rotation angles (i.e.,  $\alpha_{Task}$ ,  $\beta_{Task}$ ) between the tool and the surface during the curved surface machining are shown in Figures 1 and 2.

According to the characteristics of the curve surface, five relative motion between the surface and the cutter are processed, the x- and y-axis motion are configured by the ball screw motion unit in series to satisfy the requirements of large workspace, and translation along z-axis and two rotations that are perpendicular to the z-axis are completed by parallel manipulator to meet the stiffness and orientation requirement of the tool. If the movements are achieved via traditional feed unit and orientation rotating head, then it cannot guarantee stiffness and accuracy of the machine owing to its cantilever. The specific design requirements are as follows:

- Absolute position accuracy: parallel manipulator configuration instead of traditional series configuration can reduce error accumulation.
- Normal precision: the parallel manipulator has good orientation capability to ensure the normal contact between the normal of free surface and machine tool point, so as to keep its normal position precision.
- Workspace: workspace is generated by adopting compound spherical joint to increase orientation workspace and serial X-Y long tracks to expand the position workspace of the hybrid machine tool.
- High stiffness: hybrid machine tool will produce heavy cutting force in the high speed machining process, so as to maintain higher machining accuracy, and the machine tool should be able to bear the heavy force and resist the external force deformation. Thus, the parallel manipulator should have higher stiffness characteristics.
- High quality: the high orientation capability of parallel manipulator is employed instead of manual milling, which is beneficial to ensure the machining quality.

According to the above processing requirements, the parallel manipulator tool requires high stiffness and good orientation capability for the high speed machining of the free surface. Considering development trend of the hybrid machine tool, a five-axis hybrid machine tool can be constructed by adopting 1T2R three-degree-of-freedom parallel manipulator with two long X-Y tracks, which is the best choice to realize the machining task requirements.

**2.2. Configuration Design of the 1T2R Mechanism.** It is configuration innovation of the 1T2R three degrees of freedom that is the kernel of the hybrid machine tool. In order to complete the surface process with high efficiency and high precision, it is of crucial importance and significance for novel 1T2R lower-degree of freedom parallel manipulator with high stiffness, large workspace, and high orientation capability. There is an abundance of research on 1T2R mechanism. Kong and Li [23, 24] divided the 1T2R parallel manipulator into three categories, one of which is PU configuration parallel manipulator, second kind of which is UP configuration parallel manipulator with coupling between rotation and movement, and the third is RPR configuration parallel manipulator, which can eliminate the coupling of rotation and movement and have certain space axis. Li et al. [25] pointed out that a class of one translation and two rotation DOFs parallel manipulator called [PP]S configuration mainly include 3-PRS, 3-RPS, 3-RRS, and 3-PPS. Wang et al. [26] presented the 3-PUU parallel manipulator with rotational and translational coupling degrees of freedom; the difference between proposed mechanism and the 3PRS parallel manipulator is that the former did not have the spherical joint, but yet possesses much larger rotation angle and higher precision. Cui et al. [27] designed a 3RPS parallel manipulator with compound spherical joint that can increase the rotation angle. Li et al. [28] proposed a novel overconstrained parallel manipulator 2RPU&SPR, the degree of freedom was analyzed based on the screw theory, and kinematic inverse position and Jacobian matrix were derived. Yan et al. [29] introduced a comparison study of the kinematics characteristics of two overconstrained 2-RPU&SPR parallel manipulators. Xie et al. [30] conducted performance comparison analysis including motion force transmission performance, parasitic motion, and orientation capability of two overconstrained 2PRU-PRS and 2PRU-UPR parallel manipulator. Pashkevich [31] demonstrated that the overconstrained parallel manipulator can effectively improve the stiffness characteristic of the mechanism.

To increase the workspace of the parallel manipulator, enhance the kinematics performance of the machine tool, and improve the stiffness characteristic and dynamic characteristic, this paper adopts the redundantly actuated and overconstrained 2PRU-PRPS parallel manipulator with compound spherical joint as the main body of the hybrid machine tool. Simultaneously, to obtain a high rotation angle, using single limb double redundantly actuated technology,

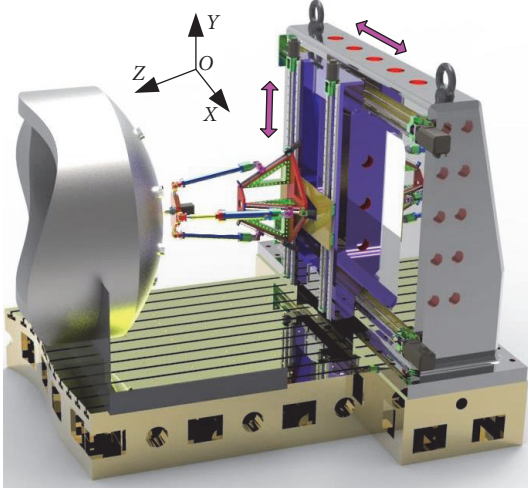


FIGURE 3: A hybrid kinematic machine with five DOFs.

with two long X-Y tracks to form a 5-axis hybrid machine tool, it can be applied to machining for a large complex heterogeneous surface, and the overall structural concept is shown in Figure 3.

### 3. Mobility Analysis of the 2PRU-PRPS Parallel Manipulator

**3.1. Architecture Description of the 2PRU-PRPS Parallel Manipulator.** A novel redundantly actuated and overconstrained 2-PRU-PRPS parallel manipulator with compound spherical joint has been proposed in this paper, as shown in Figure 4, which is composed of a moving platform, a fixed base, and two identical constrained PRU chains and one double actuated PRPS chain together connecting the moving and fixed base. And two of PRU chains are symmetrically arranged and are located in a plane; furthermore two revolute axes are parallel with each other, and the second revolute axes of two Hooke joints are coincident and perpendicular to the third revolute axis of spherical joint. The parasitic motion appears only in an axial direction. The parallel manipulator is actuated by four active prismatic joints, and three actuators are fixed at the base, which reduces the inertia of the parallel manipulator tool. The spindle head is mounted at the end of the moving platform to complete the high speed milling.

To facilitate analysis, a fixed coordinate system  $B-xyz$  is located at the center of the fixed base, and a moving coordinate system  $A-uvw$  is attached at the center of the moving platform, respectively. Let the middle point of hypotenuse  $B_1B_2$  be  $B$ ,  $x$ -axis is perpendicular to  $B_1B_2$ ,  $y$ -axis coincides with  $B_1B_2$ , and  $z$ -axis is perpendicular to the fixed base upward. Similarly, let the middle point of hypotenuse  $A_1A_2$  be  $A$ ,  $u$ -axis is perpendicular to  $A_1A_2$ ,  $v$ -axis coincides with  $A_1A_2$ , and  $w$ -axis is perpendicular to the moving platform upward. Without loss of generality,  $\Delta B_1B_2B_3$  and  $\Delta A_1A_2A_3$  are both isosceles right triangle,  $\angle B_1B_3B_2 = \angle A_1A_3A_2 = 90^\circ$ , and their circumradii are nominated as  $a$  and  $b$ , respectively.  $BB_1=BB_2=BB_3=b$ , and  $AA_1=AA_2=AA_3=a$ . With respect to  $B-xyz$ , the position vectors of points  $B_i$  and  $A_i$  ( $i=1,2,3$ ) are as

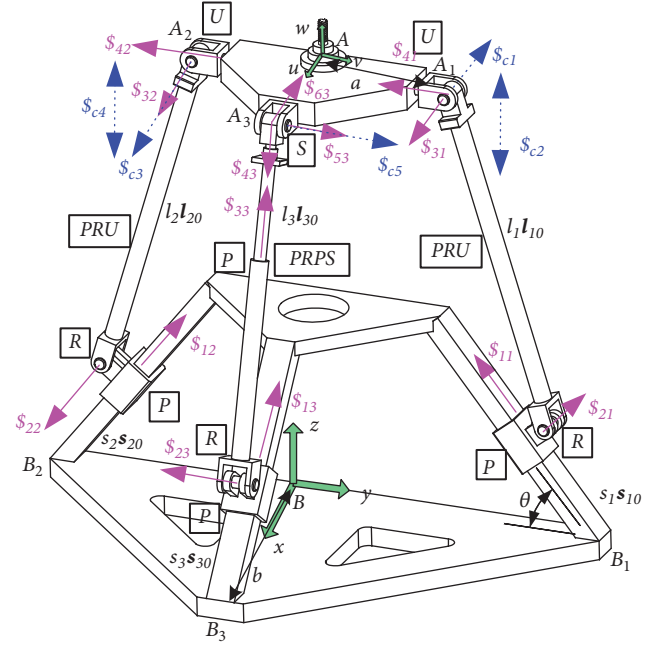


FIGURE 4: The schematic diagram of the 2-PRU-PRPS parallel manipulator.

follows. The coordinates of  $B_1$ ,  $B_2$ , and  $B_3$  are  $(0 \ b \ 0)$ ,  $(0 \ -b \ 0)$ , and  $(b \ 0 \ 0)$ , respectively. The coordinates of  $A_1$ ,  $A_2$ , and  $A_3$  are  $(x_1 \ y_1 \ z_1)$ ,  $(x_2 \ y_2 \ z_2)$ , and  $(x_3 \ y_3 \ z_3)$ , respectively. The layout angle of the fixed actuators is defined as  $\theta$ , and the angle between  $B_i$  joint and  $x$ -axis of the coordinate system  $B-xyz$  is  $\theta_i$ .

**3.2. Mobility Analysis of Initial Configuration.** Lower-mobility parallel manipulators whose independent degrees of freedom of the end effector are usually less than six can be implemented in many applications. In order to determine the motion pattern of the redundantly actuated and overconstrained 2PRU-PRPS parallel manipulator, mobility analysis is indispensable, whereas it is necessary to analyze the constraint screw provided by each chain to the moving platform and comprehensively analyze the constraint type of the moving platform.

It is assumed that the axes of the fixed coordinate system and the moving coordinate system are parallel to each other in the initial pose. Firstly, the first PRU limb is analyzed in the fixed coordinate system, and the twist screw of the chain can be expressed as

$$\begin{aligned} \$_{11} &= (0 \ 0 \ 0; 0 \ -c\theta \ s\theta) \\ \$_{21} &= (1 \ 0 \ 0; 0 \ 0 \ -b) \\ \$_{31} &= (1 \ 0 \ 0; 0 \ z_1 \ -y_1) \\ \$_{41} &= (0 \ -1 \ 0; z_1 \ 0 \ -x_1) \end{aligned} \quad (1)$$

where  $s$  and  $c$  are the abbreviation of *sine* and *cosine*, respectively. Employing reciprocal screw theory, the wrench system of (1) is obtained as

$$\begin{aligned} \$_{c1} &= (1 \ 0 \ 0; 0 \ z_1 \ 0) \\ \$_{c2} &= (0 \ 0 \ 0; 0 \ 0 \ 1) \end{aligned} \quad (2)$$

where  $\$_{c1}$  represents a constraint force passing  $A_1$  point and parallel to  $x$ -axis and  $\$_{c2}$  represents a constraint couple perpendicular to the fixed base.

Similarly, the twist screw of the second PRU limb is given by

$$\begin{aligned} \$_{12} &= (0 \ 0 \ 0; 0 \ c\theta \ s\theta) \\ \$_{22} &= (1 \ 0 \ 0; 0 \ 0 \ b) \\ \$_{32} &= (1 \ 0 \ 0; 0 \ z_2 \ -y_2) \\ \$_{24} &= (0 \ 1 \ 0; -z_2 \ 0 \ x_2) \end{aligned} \quad (3)$$

The wrench screw of (3) is obtained as

$$\begin{aligned} \$_{c3} &= (1 \ 0 \ 0; 0 \ z_2 \ 0) \\ \$_{c4} &= (0 \ 0 \ 0; 0 \ 0 \ 1) \end{aligned} \quad (4)$$

where  $\$_{c3}$  represents a constraint force passing point  $A_2$  and parallel to the  $x$ -axis of the fixed coordinate system and  $\$_{c4}$  represents a constraint couple perpendicular to the fixed base.

The twist screw of the third PRPS limb is given by

$$\begin{aligned} \$_{13} &= (0 \ 0 \ 0; -c\theta \ 0 \ s\theta) \\ \$_{23} &= (0 \ 1 \ 0; 0 \ 0 \ b) \\ \$_{33} &= (0 \ 0 \ 0; l_3 \ 0 \ n_3) \\ \$_{43} &= (-l_3 \ 0 \ -n_3; -n_3y_3 \ n_3x_3 - l_3z_3 \ l_3y_3) \\ \$_{53} &= (0 \ 1 \ 0; -z_3 \ 0 \ x_3) \\ \$_{63} &= (1 \ 0 \ 0; 0 \ z_3 \ -y_3) \end{aligned} \quad (5)$$

where  $l_3$  and  $n_3$  are direction cosines of the three prismatic joints in limb 3.

The wrench screw of (5) is obtained as

$$\$_{c5} = (0 \ 1 \ 0; -z_3 \ 0 \ x_3) \quad (6)$$

where  $\$_{c5}$  represents a constraint force passing point  $A_3$  and parallel to  $y$ -axis of the fixed coordinate system.

The constraint screw of all the limbs acting on the moving platform can be obtained as

$$\begin{aligned} \$_{c1} &= (1 \ 0 \ 0; 0 \ z_1 \ 0) \\ \$_{c2} &= (0 \ 0 \ 0; 0 \ 0 \ 1) \\ \$_{c3} &= (1 \ 0 \ 0; 0 \ z_2 \ 0) \\ \$_{c4} &= (0 \ 0 \ 0; 0 \ 0 \ 1) \\ \$_{c5} &= (0 \ 1 \ 0; -z_3 \ 0 \ x_3) \end{aligned} \quad (7)$$

It is worth noting that  $z_1=z_2=z_3=z$ , and when the mechanism is initial configuration, the twist screw of the moving platform can be obtained by adapting the reciprocity of (7).

$$\begin{aligned} \$_1^m &= (0 \ 1 \ 0; -z \ 0 \ 0) \\ \$_2^m &= (1 \ 0 \ 0; 0 \ z \ 0) \\ \$_3^m &= (0 \ 0 \ 0; 0 \ 0 \ 1) \end{aligned} \quad (8)$$

where (8) represents the moving platform that is capable of rotation about  $x$ - and  $y$ -axes and translation along the  $z$ -axis.

**3.3. Mobility Analysis of General Configuration.** Similarly, the twist screw of the first PRU limb is given in the fixed coordinate system by

$$\begin{aligned} \$_{11} &= (0 \ 0 \ 0; 0 \ -c\theta \ s\theta) \\ \$_{21} &= (1 \ 0 \ 0; 0 \ s_1s\theta \ s_1c\theta - b) \\ \$_{31} &= (1 \ 0 \ 0; 0 \ z_1 \ -y_1) \\ \$_{41} &= (0 \ e_1 \ f_1; f_1y_1 - e_1z_1 \ -f_1x_1 \ e_1x_1) \end{aligned} \quad (9)$$

where  $s_i$  denotes the twist of the P joint and  $e_i$  and  $f_i$  represent the direction cosine of the second revolute axis of the Hooke joint of  $i$  limb.

Then, the wrench screw of limb 1 is easily obtained as

$$\begin{aligned} \$_{c1} &= (e_1 \ 0 \ 0; 0 \ e_1z_1 - f_1y_1 \ 0) \\ \$_{c2} &= (0 \ 0 \ 0; 0 \ -f_1 \ e_1) \end{aligned} \quad (10)$$

where  $\$_{c1}$  represents a constraint force passing point  $A_1$  and parallel to  $\$_{21}$ ;  $\$_{c2}$  represents a constraint couple perpendicular to  $v$  and  $\$_{31}$ .

As previously mentioned, the twist screw of the second PRU limb can be expressed as

$$\begin{aligned} \$_{12} &= (0 \ 0 \ 0; 0 \ c\theta \ s\theta) \\ \$_{22} &= (1 \ 0 \ 0; s_2s\theta \ 0 \ b - s_2c\theta) \\ \$_{32} &= (1 \ 0 \ 0; 0 \ z_2 \ -y_2) \\ \$_{24} &= (0 \ -e_1 \ -f_1; e_1z_2 - f_1y_2 \ f_1x_2 \ -e_1x_2) \end{aligned} \quad (11)$$

The wrench screw of (11) is obtained as

$$\begin{aligned} \$_{c3} &= (e_1 \ 0 \ 0; 0 \ e_1z_2 - f_1y_2 \ 0) \\ \$_{c4} &= (0 \ 0 \ 0; 0 \ -f_1 \ e_1) \end{aligned} \quad (12)$$

where  $\$_{c3}$  represents a constraint force passing point  $A_2$  and parallel to  $\$_{22}$ ;  $\$_{c4}$  represents a constraint couple perpendicular to  $v$  and  $\$_{32}$ .

The twist screw of the third PRPS limb can be expressed as

$$\begin{aligned}
\$_{13} &= (0 \ 0 \ 0; -c\theta \ 0 \ s\theta) \\
\$_{23} &= (0 \ 1 \ 0; -s_3s\theta \ 0 \ b - s_3c\theta) \\
\$_{33} &= (0 \ 0 \ 0; l_3 \ 0 \ n_3) \\
\$_{43} &= (-l_3 \ 0 \ -n_3; -n_3y_3 \ n_3x_3 - l_3z_3 \ l_3y_3) \\
\$_{53} & \\
&= (-n_1 \ e_3 \ l_1; l_1y_3 - e_3z_3 \ -l_1x_3 - n_1z_3 \ e_3x_3 + n_1y_3) \\
\$_{63} & \\
&= (g_1 \ -f_1 \ e_1; e_1y_3 + f_1z_3 \ g_1z_3 - e_1x_3 \ -f_1x_3 - g_1y_3)
\end{aligned} \tag{13}$$

where  $g_1 = (e_1l_1 - f_1e_3)/n_1$ ,  $e_3$  is a constant, and  $l_3$  and  $n_3$  represent the direction cosine of the third joint axis.

Subsequently, the wrench screw of (13) can be expressed as

$$\$_{c5} = (0 \ 1 \ 0; -z_3 \ 0 \ x_3) \tag{14}$$

where  $\$_{c5}$  represents a constraint force passing point  $A_3$  and parallel to  $\$_{23}$ .

So far the constraint screw of the parallel manipulator can be expressed as

$$\begin{aligned}
\$_{c1} &= (e_1 \ 0 \ 0; 0 \ e_1z_1 - f_1y_1 \ 0) \\
\$_{c2} &= (0 \ 0 \ 0; 0 \ -f_1 \ e_1) \\
\$_{c3} &= (e_1 \ 0 \ 0; 0 \ e_1z_2 - f_1y_2 \ 0) \\
\$_{c4} &= (0 \ 0 \ 0; 0 \ -f_1 \ e_1) \\
\$_{c5} &= (0 \ 1 \ 0; -z_3 \ 0 \ x_3)
\end{aligned} \tag{15}$$

It is noteworthy that the direction vector  $A_1A_2$  coincides with the axes of the second joint axis of the Hooke joint in the two PRU limbs, so the relation can be obtained as

$$\frac{z_2 - z_1}{y_2 - y_1} = \frac{f_1}{e_1} \tag{16}$$

By combining (16) and rearranging (15), the twist screw of the moving platform yields the following:

$$\begin{aligned}
\$_1^m &= (1 \ 0 \ 0; 0 \ z_3 \ 0) \\
\$_2^m &= (0 \ e_1 \ f_1; f_1y_2 - e_1z_2 \ 0 \ 0) \\
\$_3^m &= (0 \ 0 \ 0; 0 \ 0 \ 1)
\end{aligned} \tag{17}$$

In (17),  $\$_1^m$  represents one rotational degree of freedom passing point  $A_3$  and parallel to  $x$ -axis,  $\$_2^m$  represents one rotational degree of freedom of the moving platform passing point  $A_2$  and parallel to the  $v$ -axis, and  $\$_3^m$  represents a translational degree of freedom that is perpendicular to the fixed base. There are two instantaneous rotation axes, one of which is a straight line passing point  $A_3$  and parallel to the

$x$ -axis and another is  $v$ -axis, located in the moving platform, and they change with the motion of the moving platform. It is worth noting that the mechanism has the same constraint screw and the degree of freedom with the 2PRU-PRS parallel manipulator.

Generally, the degree of freedom of parallel manipulator can be calculated by the modified *Grübler-Kutzbach* (*G-K*) equations; that is,

$$F = d(n - g - 1) + \sum_{i=1}^g f_i + v - \zeta \tag{18}$$

where  $F$  represents the degree of freedom of the mechanism,  $n$  represents the number of the components,  $g$  represents the number of the kinematic joints,  $d = 6 - \lambda$  represents the order of the mechanism,  $f_i$  represents the degree of freedom of the  $i$ th kinematic joint,  $v$  represents the redundant constraints of the mechanism, and  $\zeta$  represents the local degree of freedom.

There was neither constraint couple in the same direction nor constraint force in collinearity among the constraint screw in the parallel manipulator; therefore, there is no common constraint, that is,  $\lambda = 0$ . Because there are only three linearly independent variables in the five-constraint screw of the parallel manipulator, therefore, the parallel manipulator has two redundant constraints, that is,  $v = 2$ . Because the parallel manipulator has no local degree of freedom, so  $\zeta = 0$ . We can see from the schematic of the mechanism that the number of the components is 6, the number of the kinematic joints is 10, and the relative freedom of all the kinematic joints in the mechanism is 14. Due to the introduction of redundant actuation, there are five linear correlations between the six-twist screw, so there is a local degree of freedom, that is,  $\zeta = 1$  [32, 33].

Thus, based on the revised *Grübler-Kutzbach* (*G-K*) equations, the degree of freedom of the 2PRU-PRPS parallel manipulator can be recalculated as follows:

$$\begin{aligned}
F &= d(n - g - 1) + \sum_{i=1}^g f_i + v - \zeta \\
&= 6 \times (9 - 10 - 1) + 14 + 2 - 1 = 3
\end{aligned} \tag{19}$$

In summary, the redundantly actuated and overconstrained 2PRU-PRPS parallel manipulator has three degrees of freedom, i.e., two rotational degrees of freedom about  $x$ -axis and  $v$ -axis and one translational degree of freedom along  $z$ -axis.

## 4. Inverse Kinematics of the Parallel Manipulator

**4.1. Position Inverse Analysis.** The inverse kinematics solution is based on the determination of the structural parameters of the parallel manipulator, when the position and orientation of the moving platform are given, so as to solve the input displacement of the prismatic joints.

Z-Y-X Euler angles are adopted to describe orientation matrix of the moving coordinate system with respect to the fixed coordinate system, first rotating the moving coordinate

about  $z$ -axis by angle  $\gamma$ , then about  $y$ -axis of the new coordinate system by angle  $\beta$ , and finally about  $x$ -axis of the new coordinate system by angle  $\alpha$ . Thus, the orientation matrix  $\mathbf{R}$  can be expressed as

$$\begin{aligned} \mathbf{R} &= \mathbf{R}(\gamma, z) \mathbf{R}(\beta, y) \mathbf{R}(\alpha, x) \\ &= \begin{bmatrix} c\beta c\gamma & sas\beta c\gamma - cas\gamma & cas\beta c\gamma + sas\gamma \\ c\beta s\gamma & sas\beta s\gamma + cac\gamma & cas\beta s\gamma - sac\gamma \\ -s\beta & sac\beta & cac\beta \end{bmatrix} \end{aligned} \quad (20)$$

$\mathbf{p} = [x \ y \ z]^T$  represents the position vector of the original point  $A$  in the fixed coordinate system  $B - xyz$ .  $\mathbf{a}_i$  and  $\mathbf{b}_i$  represent the position vector in the fixed coordinate of joints  $A_i$  and  $B_i$ , and the coordinate of each joint in the fixed coordinate system can be, respectively, expressed in matrix form as

$$\begin{aligned} \mathbf{a}_1 &= R(0 \ a \ 0)^T \\ \mathbf{a}_2 &= R(0 \ -a \ 0)^T \\ \mathbf{a}_3 &= R(a \ 0 \ 0)^T, \\ \mathbf{b}_1 &= (0 \ b \ 0)^T \\ \mathbf{b}_2 &= (0 \ -b \ 0)^T \\ \mathbf{b}_3 &= (b \ 0 \ 0)^T \end{aligned} \quad (21)$$

Because of the arrangement of revolute joint in  $\underline{PRU}$  and  $\underline{PRPS}$  limbs, the center of Hooke joints and spherical joint cannot move along the axis of the revolute joint, so the following constraint conditions can be structured as

$$\begin{aligned} (\mathbf{p} + \mathbf{a}_1)^T \cdot (1 \ 0 \ 0) &= 0 \\ (\mathbf{p} + \mathbf{a}_2)^T \cdot (1 \ 0 \ 0) &= 0 \\ (\mathbf{p} + \mathbf{a}_3)^T \cdot (0 \ 1 \ 0) &= 0 \end{aligned} \quad (22)$$

Selecting parameters  $\alpha, \beta, z$  as three independent parameters, parasitic motion can be arranged as

$$\begin{aligned} x &= 0 \\ y &= -ac\beta s\gamma \\ \gamma &= \arctan\left(\frac{sas\beta}{ca}\right) \end{aligned} \quad (23)$$

The close-loop vector method is used to establish the equation of vector  $A_i B_i$  in the fixed coordinate system  $B - xyz$

$$\mathbf{L}_i = \mathbf{a}_i + \mathbf{p} - \mathbf{b}_i = l_i \mathbf{l}_{i0} + s_i \mathbf{s}_{i1} \quad (24)$$

Equation (24) squares on both sides; we arrange and obtain

$$s_i^2 - 2\mathbf{L}_i^T \mathbf{s}_{i1} s_i + \mathbf{L}_i^T \mathbf{L}_i - l_i^2 = 0 \quad (25)$$

Position inverse solution of the  $2\underline{PRU}$ - $\underline{PRPS}$  parallel manipulator about  $s_i$  in (25) can be expressed as follows [34].

$$s_i = \mathbf{L}_i^T \mathbf{s}_{i1} \pm \sqrt{(\mathbf{L}_i^T \mathbf{s}_{i1})^2 - \mathbf{L}_i^T \cdot \mathbf{L}_i + l_i^2} \quad (26)$$

where  $\mathbf{s}_{i1} = [-c\theta_i c\theta \ -s\theta_i c\theta \ s\theta]^T$ ,  $l_1=l_2=l$ , and  $l_3$  is an extensible and compressible link.

**4.2. Orientation Description of T-T Angle.** To better describe the orientation capability of the parallel manipulator, Liu and Bonev [35] pointed out that the [PP]S mechanism is three degrees of freedom with zero-torsion angle and systemically studied the relationships between different Euler angles and Tilt-Torsion (T-T) angle; that is, the orientation of the moving platform can be easily described as two variables: the azimuth angle and tilt angle. Therefore, T-T angle is a new orientation description method, which is usually more concise and more efficient to reflect the orientation capability of a class of 3-[PP]S mechanism compared with the description of Euler angles method. When the torsion angle is zero, the orientation matrix of T-T angle can be expressed as

$$\begin{aligned} {}^{T-T} \mathbf{R}(\varphi, \phi, 0) &= \mathbf{R}_z(\varphi) \mathbf{R}_y(\phi) \mathbf{R}_z(-\varphi) \mathbf{R}_z(0) \\ &= \begin{bmatrix} s^2\varphi + c^2\varphi c\phi & s\varphi c\phi(c\phi - 1) & c\varphi s\phi \\ s\varphi c\phi(c\phi - 1) & c^2\varphi + s^2\varphi c\phi & s\varphi s\phi \\ -c\varphi s\phi & -s\varphi c\phi & c\phi \end{bmatrix} \end{aligned} \quad (27)$$

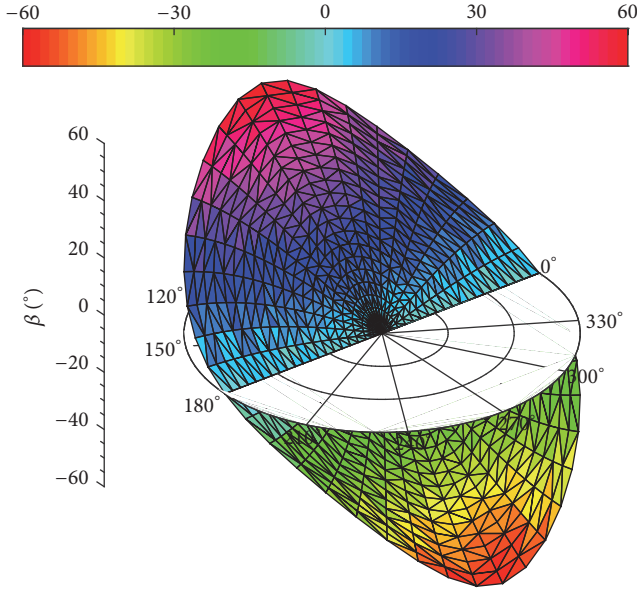
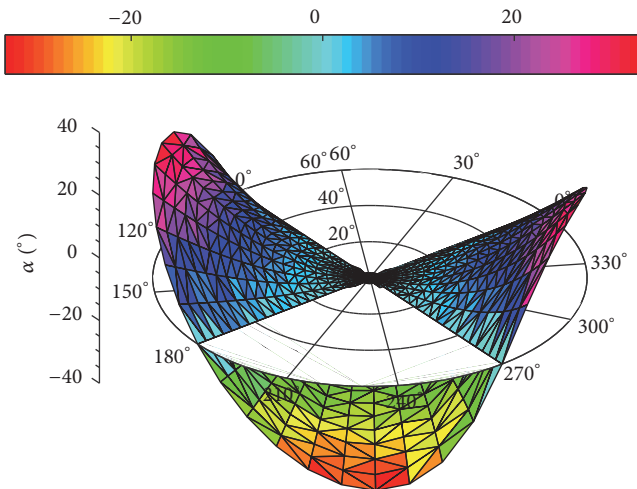
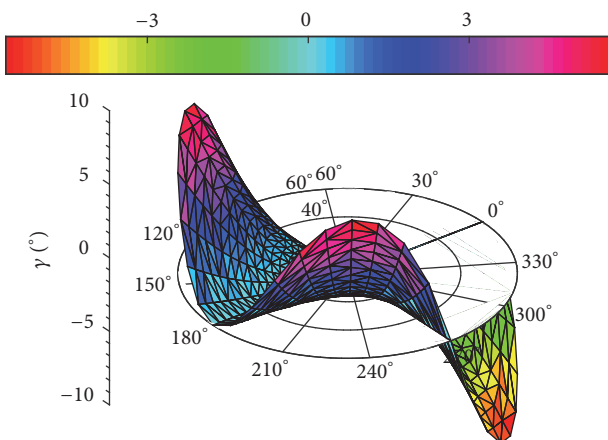
Combining (20) and (27), the T-T angles with zero-torsion can be converted to the Z-Y-X Euler angles via the following equation:

$$\begin{aligned} \beta &= a \sin(c\varphi s\phi) \\ \alpha &= a \sin\left(\frac{-s\varphi s\phi}{c\beta}\right) \\ \gamma &= a \sin\left(\frac{s\varphi c\phi(c\phi - 1)}{c\beta}\right) \end{aligned} \quad (28)$$

Figures 5, 6, and 7 show the relations between  $(\alpha, \beta, \gamma)$  and  $(\varphi, \phi)$ , separately. The circle coordinate denotes azimuth  $\varphi$ , and radial coordinate denotes the tilt angle  $\phi$ .

## 5. Orientation Workspace Analysis

The orientation workspace of parallel manipulator tool is an important performance index, which is the set of all practically feasible orientation of the moving platform. By analyzing the workspace, we can deduce the problem whether the expected machining range can be realized. The main analysis methods contain analytical method and numerical method; in this paper, the limit boundary searching method of reachable workspace was adopted, and the mechanism is divided into several single limbs, and the boundary of single limb space is obtained by using the surface enveloping theory; finally, the whole workspace of the mechanism is obtained by using the surface intersection technique. The difficulty of the

FIGURE 5: The relation of  $\beta$  referring to  $(\varphi, \phi)$ .FIGURE 6: The relation of  $\alpha$  referring to  $(\varphi, \phi)$ .FIGURE 7: The relation of  $\gamma$  referring to  $(\varphi, \phi)$ .

hybrid machine tool workspace is to solve the workspace of parallel manipulator, while the workspace analysis of parallel manipulator is mainly to investigate the reachable workspace of the end effector. For 1T2R parallel manipulator, the workspace of the manipulator mainly considers the rotational capability about the  $x$ -axis and the  $v$ -axis and the translational capability along  $z$ -axis. Over the past decade, workspace was investigated by many scholars with different methods and algorithms. Referring to [36], a discrete boundary searching method was implemented to calculate the workspace of parallel manipulator considering the driving constraint and joints constraint in the polar coordinate system. Pond [37] investigated reachable workspace and dexterous workspace of three parallel manipulators (including 3-PRS, 3-RPS, and Tricept) based on homogeneous Jacobian matrix condition number and conducted quantitative analysis on the workspace. Herero et al. [38] solve the workspace of 2PRU-1PRS parallel manipulator based on the calculation of inverse kinematics and geometrical constraint and singularity constraint; what is more, they pointed out that maximum inscribed ball can be utilized to measure the workspace. Fu and Gao et al. [39] obtained the position workspace and orientation workspace of the parallel manipulator with decoupling three branches of six degrees of freedom by using a numerical searching method and chose the maximum inscribed cylinder and sphere envelope as the specified shade in the workspace.

**5.1. Parameters Constraint Condition.** In the actual machining process of parallel manipulator tool, the following limitations should be considered.

(1) *Limitations of the Actuated Joints  $s_i$*

$$s_{\min} \leq s_i \leq s_{\max} \quad (29)$$

where  $s_{\min}$  and  $s_{\max}$  represent the minimum and maximum stroke of active joint, respectively. Here,  $s_{\min} = 0$  and  $s_{\max} = 650\text{mm}$ .

(2) *Limitation of Redundantly Actuated Joint  $q_4$*

$$q_{\min} \leq q_4 \leq q_{\max} \quad (30)$$

where  $q_{\min}$  and  $q_{\max}$  represent the minimum and maximum displacement of the second-stage active joint of the third limb, respectively. Here  $q_{\min} = 900\text{mm}$  and  $q_{\max} = 1200\text{mm}$ .

(3) *Joint Angle Constraints*

(a) *The Rotation Angle  $R_{2i}$  of the Rotation Joint R Should Be Satisfied*

$$R_{2\min} \leq R_{2i} = a \cos \left( \frac{s_{1i} \cdot l_{i0}}{|s_{1i}| |l_{i0}|} \right) \leq R_{2\max} \quad (31)$$



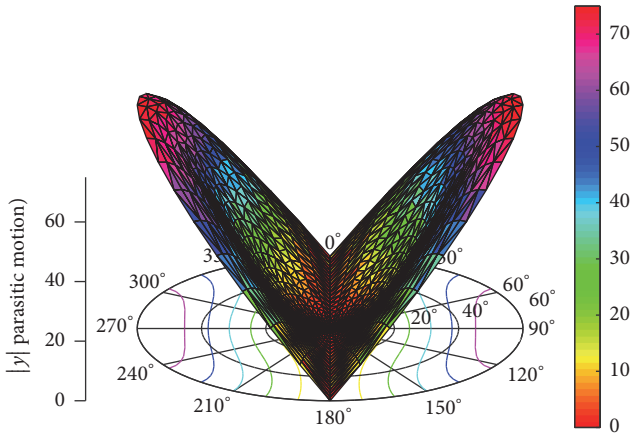


FIGURE 9: Parasitic motion relation between  $|y|$  and  $(\varphi, \phi)$  with  $z=1300$ .

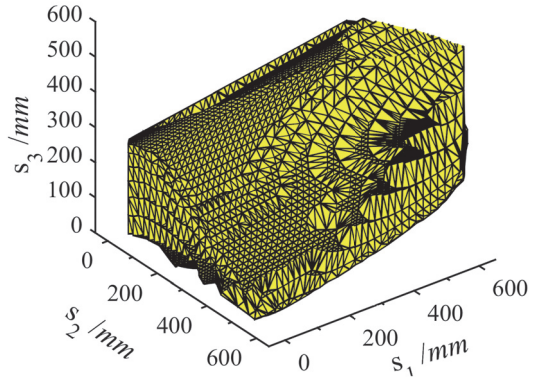


FIGURE 11: Joint workspace of the parallel manipulator.

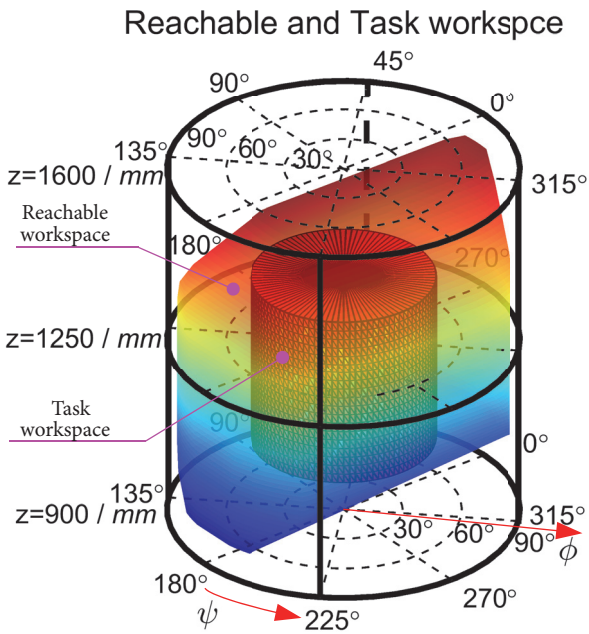


FIGURE 10: Singularity-free reachable and task workspace.

By specifying the value of the  $q_4$  (that is link length of  $l_3$ ), we can get a surface in three-dimensional joint workspace  $(s_1, s_2, s_3)$  formed by the three prismatic joints. And the surface contains all the possible actuated parameters which affect the motion of the moving platform. Figure 11 shows the joint workspace when  $q_4=1150mm$ , which gives us information that various constraints can result in a set of unreachable points and implies that the capability of motions can be efficiently utilized.

The reachable workspace of the proposed parallel manipulator and the overconstrained 2PRU-PRS parallel manipulator, with the same degree of freedom, is illustrated in Figure 12. To facilitate analysis, the same search space is used for comparison of the overconstrained 2PRU-PRS parallel manipulator and the proposed parallel manipulator. The

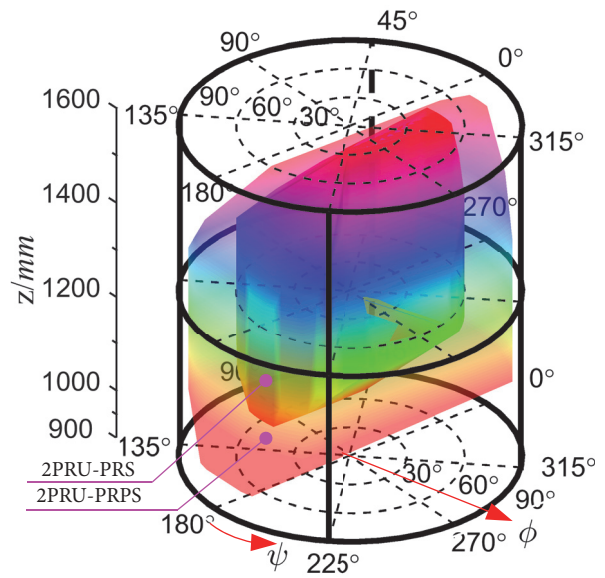


FIGURE 12: Singularity-free workspace comparison of two parallel manipulators.

result shows that the redundant actuation parallel manipulator has a larger workspace and much higher orientation rotation capability than the 2PRU-PRS parallel manipulator. Therefore, it is feasible to select the redundantly actuated and overconstrained 2PRU-PRPS parallel manipulator as the main body of the hybrid machine tool and is very meaningful to the development of the five-axis hybrid machine tool.

### 7. Conclusions

In this paper, a novel serial-parallel hybrid kinematic machine tool with high stiffness, high orientation capability, and large workspace has been presented, which is a combination of 1T2R parallel manipulator and two long X-Y tracks and can be applied to high speed machining of a large heterogeneous complex freedom surface in the aerospace field.

The mobility of proposed redundantly actuated and overconstrained 2PRU-PRPS parallel manipulator has been

detailed and analyzed based on the screw theory and Grübler-Kutzbach (G-K) equations, and the correctness of analysis method is verified. The inverse kinematic position and parasitic motion of the derived parallel manipulator have been sequentially analyzed, and the relationship between Z-Y-X Euler angle and Tilt-Torsion (T-T) angle is briefly expressed.

The orientation workspace, the performance evaluation index, can serve as an alternative for the description of the orientation capability. Compared with overstrained 2PRU-PRS parallel manipulator, the corresponding results illustrate that the redundant actuation parallel manipulator can effectively increase the workspace and potentially improve its orientation capability, which lays a theoretical foundation for the stiffness analysis and optimal design of the parallel manipulator in the future work.

### Data Availability

The data used to support the findings of this study are available from the corresponding author upon request.

### Conflicts of Interest

The authors declared no potential conflicts of interest with respect to the research, authorship, and/or publication of this article.

### Acknowledgments

The authors would like to acknowledge the financial support of the Fundamental Research Funds for the Central Universities under Grant no. 2018JBZ007, no. 2018YJS136, and no. 2017YJS158 and the National Natural Science Foundation of China (NSFC) under Grants 51675037 and 51505023.

### References

- [1] M. Terrier, A. Dugas, and J.-Y. Hascoët, "Qualification of parallel kinematics machines in high-speed milling on free form surfaces," *The International Journal of Machine Tools and Manufacture*, vol. 44, no. 7-8, pp. 865-877, 2004.
- [2] Y. Lu and J. Xu, "Computer simulation machining a 3D free surface by using a 3-RPRU parallel machine tool," *The International Journal of Advanced Manufacturing Technology*, vol. 33, no. 7-8, pp. 782-792, 2007.
- [3] Y. D. Chen, J. Ni, and S. M. Wu, "Real-time CNC tool path generation for machining IGES surfaces," *Journal of Engineering for Industry*, vol. 115, no. 4, pp. 480-486, 1993.
- [4] D. C. H. Yang and Z. Han, "Interference detection and optimal tool selection in 3-axis NC machining of free-form surfaces," *Computer-Aided Design*, vol. 31, no. 5, pp. 303-315, 1999.
- [5] C.-C. Lo, "Real-time generation and control of cutter path for 5-axis CNC machining," *The International Journal of Machine Tools and Manufacture*, vol. 39, no. 3, pp. 471-488, 1999.
- [6] Y. H. Jung, D. W. Lee, J. S. Kim, and H. S. Mok, "NC post-processor for 5-axis milling machine of table-rotating/tilting type," *Journal of Materials Processing Technology*, vol. 130-131, pp. 641-646, 2002.
- [7] P. Xu, C.-F. Cheung, B. Li, L.-T. Ho, and J.-F. Zhang, "Kinematics analysis of a hybrid manipulator for computer controlled ultra-precision freeform polishing," *Robotics and Computer-Integrated Manufacturing*, vol. 44, pp. 44-56, 2017.
- [8] Y. Lu, Y. Shi, and B. Hu, "Solving reachable workspace of some parallel manipulators by computer-aided design variation geometry," *Proceedings of the Institution of Mechanical Engineers, Part C: Journal of Mechanical Engineering Science*, vol. 222, no. 9, pp. 1773-1781, 2008.
- [9] J. Tlustý, J. Ziegert, and S. Ridgeway, "Fundamental comparison of the use of serial and parallel kinematics for machines tools," *CIRP Annals - Manufacturing Technology*, vol. 48, no. 1, pp. 351-356, 1999.
- [10] N. Hennes and D. Staimer, "Application of PKM in aerospace manufacturing-high performance machining centers ECOSPEED, ECOSPEED-F and ECOLINER," in *Proceedings of the 4th Chemnitz Parallel Kinematics Seminar*, pp. 557-577, Zwickau, Verlag Wissenschaftliche Scripten, Chemnitz, Germany, 2004.
- [11] Y. Wang, H. Liu, T. Huang, and D. G. Chetwynd, "Stiffness modeling of the tricept robot using the overall jacobian matrix," *Journal of Mechanisms and Robotics*, vol. 1, no. 2, pp. 1-8, 2009.
- [12] J. Zhang, Y. Q. Zhao, and Y. Jin, "Elastodynamic Modeling and Analysis for an Exechon Parallel Kinematic Machine," *Journal of Manufacturing Science and Engineering*, vol. 138, no. 3, 2016.
- [13] B. Gherman, D. Pisla, C. Vaida, and N. Plitea, "Development of inverse dynamic model for a surgical hybrid parallel robot with equivalent lumped masses," *Robotics and Computer-Integrated Manufacturing*, vol. 28, no. 3, pp. 402-415, 2012.
- [14] M. Weck and D. Staimer, "Parallel kinematic machine tools - Current state and future potentials," *CIRP Annals - Manufacturing Technology*, vol. 51, no. 2, pp. 671-683, 2002.
- [15] N. Hennes, "Ecospeed:an innovative machinery concept for high-performance 5-axis machining of large structural components in aircraft engineering," in *Proceedings of the 3rd Chemnitz Parallel Kinematics Seminar*, pp. 763-774, Zwickau, Germany, 2002.
- [16] M. Wang, H. Liu, T. Huang, and D. G. Chetwynd, "Compliance analysis of a 3-SPR parallel mechanism with consideration of gravity," *Mechanism and Machine Theory*, vol. 84, pp. 99-112, 2015.
- [17] X. Yang, J. Zhao, L. Zhang, D. Li, and R. Li, "A novel surface self-adapting parallel machine tool for blade machining," in *Proceedings of the 2009 IEEE International Conference on Mechatronics and Automation, ICMA 2009*, pp. 3921-3926, August 2009.
- [18] Y. G. Li, H. T. Liu, X. M. Zhao, T. Huang, and D. G. Chetwynd, "Design of a 3-DOF PKM module for large structural component machining," *Mechanism and Machine Theory*, vol. 45, no. 6, pp. 941-954, 2010.
- [19] Q. Hao, L. Guan, and L. Wang, "Intelligent acceleration/deceleration control algorithm for drive force for a heavy duty hybrid machine tool," *Qinghua Daxue Xuebao/Journal of Tsinghua University*, vol. 49, no. 11, pp. 1770-1778, 2009.
- [20] T. Huang, M. Li, X. M. Zhao, J. P. Mei, D. G. Chetwynd, and S. J. Hu, "Conceptual design and dimensional synthesis for a 3-DOF module of the TriVariant - A novel 5-DOF reconfigurable hybrid robot," *IEEE Transactions on Robotics*, vol. 21, no. 3, pp. 449-456, 2005.
- [21] J. Wu, J. Wang, L. Wang, T. Li, and Z. You, "Study on the stiffness of a 5-DOF hybrid machine tool with actuation redundancy," *Mechanism and Machine Theory*, vol. 44, no. 2, pp. 289-305, 2009.
- [22] J. Fan and A. Ball, "Quadric method for cutter orientation in five-axis sculptured surface machining," *The International*

- Journal of Machine Tools and Manufacture*, vol. 48, no. 7-8, pp. 788–801, 2008.
- [23] X. Kong and M. Gosselin C, “Type synthesis of three-DOF up-equivalent parallel manipulators using a virtual-chain approach,” *Advances in Robot Kinematics*, pp. 123–132, 2006.
- [24] Q. Li and J. M. Hervé, “Type synthesis of 3-DOF RPR-equivalent parallel mechanisms,” *IEEE Transactions on Robotics*, vol. 30, no. 6, pp. 1333–1343, 2017.
- [25] Q. Li, Z. Chen, Q. Chen, C. Wu, and Z. Huang, “Structural condition for [PP]S parallel mechanism without parasitic motion,” *Journal of Mechanical Engineering*, vol. 46, no. 15, pp. 31–35, 2010.
- [26] L. Wang, H. Xu, and L. Guan, “Optimal design of a 3-PUU parallel mechanism with 2RIT DOFs,” *Mechanism and Machine Theory*, vol. 114, pp. 190–203, 2017.
- [27] X. Cui, X. Han, and W. Chen, “Continuous stiffness modeling of 3-RPS parallel kinematic machine with special composite spherical joints,” *Beijing Hangkong Hangtian Daxue Xuebao/Journal of Beijing University of Aeronautics and Astronautics*, vol. 36, no. 11, pp. 1275–1280, 2010.
- [28] B. Li, Y. Li, and X. Zhao, “Kinematics analysis of a novel overconstrained three degree-of-freedom spatial parallel manipulator,” *Mechanism and Machine Theory*, vol. 104, pp. 222–233, 2016.
- [29] F. Xie, X. Liu, and T. Li, “A Comparison Study on the Orientation Capability and Parasitic Motions of Two Novel Articulated Tool Heads with Parallel Kinematics,” *Advances in Mechanical Engineering*, vol. 4, pp. 249103–249103, 2015.
- [30] Q. Yan, B. Li, Y. Li, and X. Zhao, “Kinematics comparative study of two overconstrained parallel manipulators,” *Mathematical Problems in Engineering*, vol. 2016, Article ID 5091405, 12 pages, 2016.
- [31] A. Pashkevich, D. Chablat, and P. Wenger, “Stiffness analysis of overconstrained parallel manipulators,” *Mechanism and Machine Theory*, vol. 44, no. 5, pp. 966–982, 2009.
- [32] H. Qu, S. Guo, and Y. Zhang, “A novel relative degree-of-freedom criterion for a class of parallel manipulators with kinematic redundancy and its applications,” *Proceedings of the Institution of Mechanical Engineers, Part C: Journal of Mechanical Engineering Science*, vol. 231, no. 22, pp. 4227–4240, 2017.
- [33] Z. Huang, J. Liu, and Y. Li, *On mobility of mechanisms*, Science Press, Beijing, China, 2011.
- [34] G. Cui, H. Zhang, D. Zhang, and F. Xu, “Analysis of the kinematic accuracy reliability of a 3-DOF parallel robot manipulator,” *International Journal of Advanced Robotic Systems*, vol. 12, pp. 1–11, 2015.
- [35] X. LIU, “Attitude Description Method of [PP]S Type Parallel Robotic Mechanisms,” *Chinese Journal of Mechanical Engineering*, vol. 44, no. 10, p. 19, 2008.
- [36] Z. Z. Chi, D. Zhang, L. Xia, and Z. Gao, “Multi-objective optimization of stiffness and workspace for a parallel kinematic machine,” *International Journal of Mechanics and Materials in Design*, vol. 9, no. 3, pp. 281–293, 2013.
- [37] G. Pong and J. A. Carretero, “Quantitative dexterous workspace comparison of parallel manipulators,” *Mechanism and Machine Theory*, vol. 42, no. 10, pp. 1388–1400, 2007.
- [38] S. Herrero, C. Pinto, O. Altuzarra, and M. Diez, “Workspace study of the 2PRU-1PRS parallel manipulator,” in *Proceedings of the 14th International Federation for the Promotion of Mechanism and Machine Science World Congress, IFToMM 2015*, October 2015.
- [39] J. Fu and F. Gao, “Optimal design of a 3-leg 6-DOF parallel manipulator for a specific workspace,” *Chinese Journal of Mechanical Engineering*, vol. 29, no. 4, pp. 659–668, 2016.